THE

TELSTAR

EXPERIMENT

PART 2

THE BELL SYSTEM

TECHNICAL JOURNAL

Contents, Part 2

The Mechanical Design of the Horn-Reflector Antenna and Radome

By J. C. DOLLING, R. W. BLACKMORE, W. J. KINDERMANN
and K. B. WOODARD

This paper describes the mechanical design of the horn-reflector antenna and the associated radome. The mechanical considerations dictating the final configuration of the antenna structure are discussed, along with the engineering aspects of the design, fabrication, and erection of the structure. The mechanical features of the data take-off and antenna drive systems are given in detail. The final section presents an account of the requirements, manufacture, and installation of the radome and its accessory equipment.

I. INTRODUCTION

The ground-based communication antenna of the Telstar project must figuratively project a needle of energy toward a 3-foot satellite at a distance of several thousand miles and listen for a whisper in return. It must perform in this fashion while moving about both azimuth and elevation axes. Furthermore, it must provide service in all weather conditions.

Many weeks of study preceded the determination of a general configuration for the structure, its support, and the method of control. The mechanical problems involved in achieving the required antenna performance are discussed in this article.*

The first part (Section II) describes the system requirements and the early design concepts. It also outlines the major factors governing the over-all design and points out the necessary compromises. The next part (Section III) describes the mechanical structure which evolved as the final design and tells of a number of the problems encountered during manufacture and erection.

---

* The information on concept consideration was provided by Mr. Dolling; that on the mechanical structure by Mr. Blackmore. Mr. Kindermann was concerned with the position data devices and the power drives, and Mr. Woodard with the radome.

The angles which define the pointing of the antenna must be accurately known at all times. The position data devices are among the most precise components in the entire Telstar system. The accuracy requirements for the data take-offs and their mechanical construction are given in Section IV, which also explains the means for driving the antenna about the two axes of motion.

An air-supported construction shelter provided a controlled environment during erection and alignment of the antenna. Later this was replaced by an air-supported radome which assures all-weather operation of the completed antenna. Section V presents a detailed account of the requirements, manufacture, and installation of the radome and its accessory equipment.

II. CONCEPT CONSIDERATION

2.1 *System Requirements*

The horn-reflector type of antenna was selected for the Telstar project because of its broadband and low-noise properties. It provides an offset feed arrangement with very good shielding between focus and reflector. This configuration also permits placement of the receiver at the focal point, thus minimizing line loss.

The velocities and accelerations necessary for tracking the Telstar satellite imposed the need for azimuth and elevation drives capable of operating over a very wide range of velocities, starting from zero. Fig. 1 shows the azimuth velocity requirements for two angles of peak elevation, φ. Accuracy, rigidity and mass inertia are the three basic parameters which determine the quality of the antenna:

2.1.1. A high order of accuracy is called for in the manufacture of all reflecting, rolling, or sliding surfaces. Accuracy of the reflecting surfaces determines the electrical efficiency of the antenna. Furthermore, provision must be made to let fixed and moving parts of the antenna rotate against one another about perpendicular axes and at very accurately controlled tracking speeds.

2.1.2. The antenna structure must present considerable rigidity against both external and internal forces. It is necessary to maintain true focal point-reflector orientation for all elevation and azimuth angles under the influences of gravity, driving acceleration, and thermal expansion forces. The structure also must exhibit high-frequency response to servo control.

2.1.3. The problem of mass inertia about the rotational axes not only calls for a compact design of short over-all dimensions and small radii
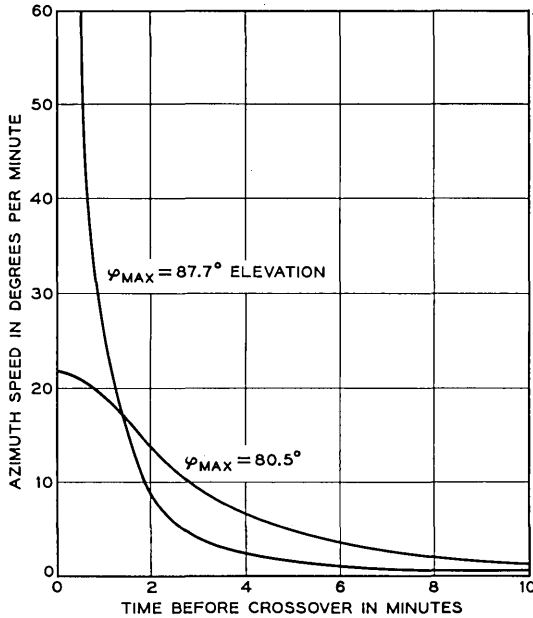
Fig. 1 — Antenna rotational speed for 2200-mile-high satellite in circular orbit.

about the axes but also imposes a very stringent requirement of light weight for every piece that moves with respect to the ground.

Finally, a reliable communication system requires that the antenna be operable under all weather conditions, and that provisions be made for survival in the event of loss of the radome.

2.2 Investigation of Concepts

Several antenna design concepts were investigated to find the one design that would best meet the stated requirements. Although the investigation narrowed down to studies of horn-reflector type antennas, early studies included paraboloidal and hemispherical dishes, and sectional sphere-type antennas. Consideration was given to the designs of the hemispherical dish and sectional sphere-type antennas because of the small mass inertia of those parts which require the most precise positioning, the high structural rigidity and compact design. Some of the major reasons for rejecting these types were feed shadow and long transmission lines, each of which contribute excessive noise.

Of the many horn-reflector antenna concepts investigated, the six
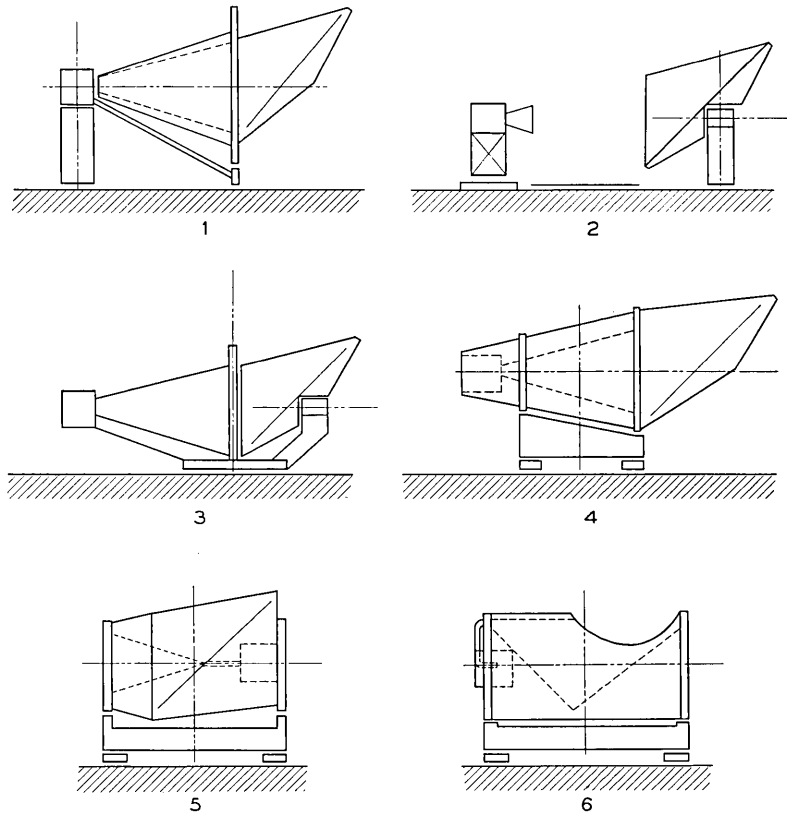
Fig. 2 — Horn-reflector antenna concepts.

that exhibited characteristics falling within system requirements are shown in Fig. 2. The main features of these concepts, the motives that warranted their consideration, and the major reasons for eliminating five of them, are discussed briefly in the following paragraphs.

Concept 1 is a four-sided pyramidal horn-reflector antenna with the horn's symmetry line horizontal and coinciding with the elevation axis. Rotation in azimuth takes place about the horn apex, which is identical with the paraboloid's focal point, so as to avoid translational motions of the equipment room. After study, this concept was abandoned, mainly because of the large turning circles in azimuth and elevation which would result in excessive wind torques and preclude the possibility of a radome because of the very large size.

Concept 2 does away with most of the horn while maintaining the geometry of the paraboloid. A metallic ground plane substitutes in part

for the shielding effect of the horn. The axis of azimuth rotation is co-incident with the reflector center. Both measures aim at minimizing wind and mass inertia torques. Uncertainties about effective noise temperature and synchronization of azimuth motions of reflector and feed excluded this scheme from further consideration.

Concept 3 is an attempt to reduce turning circles by using a conical horn and placing the azimuth axis at the largest diameter of the cone. Only the reflector rotates in elevation, but the entire antenna turns in azimuth on a small-diameter platform. Reasons for not following this layout were the excessive weight of the shell structure, lack of rigidity in the reflector structure, and restriction in the elevation motion.

Concept 4 maintains the advantages of a conical horn and a mid-way location of the azimuth axis but adds full elevating rotation, highest stiffness by one-piece design of the horn and reflector plus equipment room, optimum support against gravitational deflection by a cradle-like azimuth carriage, and lightweight space frame design. This concept incorporated most of the desired features.

Concept 5 essentially takes the elements of No. 4, introduces a plane mirror perpendicular to the horn axis and places equipment room and cradle under the reflector, thereby reducing the antenna's length by 40 per cent and improving the contour stability of the sectional paraboloid reflector. Unknowns about the noise temperature of this shortened horn arrangement precluded its adoption.

Concept 6, for the sake of minimum size and ultimate rigidness. opens the flare angle of the conical horn and tilts its symmetry axis, enclosing the horn-reflector antenna in an elevating structure of cylindrical outer shape. The length reduces by about 30 per cent, height by 35 per cent, compared with the antenna actually built. The necessity of a transmission line between horn apex and equipment room was the reason for rejection of this concept.

In the selection of the final antenna concept, an evaluation was made of each on the basis of its ability to meet system and design requirements. Table I illustrates the method employed of comparing and determining the compatibility of the above antenna concepts with the requirements. The concept numbers correspond to those described above, above, and the check marks indicate where the stated requirement is fully met.

It can be seen by examining the columns of Table I that only concept 4 appears to meet all of the basic requirements. Thus concept 4 was selected as the most suitable design for present use in the Telstar program.

TABLE I—EVALUATION OF ANTENNA CONCEPTS

Basic Requirements	Concept					
	1	2	3	4	5	6
System:						
Rotating equipment rooms	√	√	√	√	√	√
Minimum of 180° elevation coverage	√	√	—	√	√	√
Tracking velocity and acceleration	—	√	√	√	√	√
Pointing accuracy	—	—	—	√	√	√
Beam spread stability	—	—	√	√	√	√
Electrical shielding	√	—	√	√	—	√
Minimum wind torques	—	√	√	√	√	√
Thermal differential expansion:						
Ambient temperature	—	√	√	√	√	√
Radiation heat	—	√	—	√	√	√
Operation in extreme precipitation	√	√	√	√	√	√
Survival (hurricane winds & ice)	√	√	√	√	√	√
Life expectancy	√	√	√	√	√	√
Design:						
No feed shadow	√	√	√	√	√	√
Horizontal RF feed	√	√	√	√	√	√
Short, straight transmission line	√	√	√	√	√	—
Minimum mass inertia about azimuth axis	—	√	√	√	√	√
Torsional and mounting rigidity of drive	√	—	—	√	√	√
Rigid structure	—	—	—	√	√	√
Thermal expansion restraint	—	√	√	√	√	√
Minimum deflection suspension	√	√	—	√	√	√
Stable foundation	√	√	—	√	√	√
Stow position	√	—	—	√	√	√
Accessibility of equipment room	√	√	√	√	√	√
Protective radome adaptability	—	—	√	√	√	√

2.3 *Basic Design Considerations*

With the selection of concept 4 as the most desirable antenna, several fundamental questions had to be answered before detailed design could start. They are discussed in the following paragraphs.

2.3.1. What is the best length-to-height ratio of the entire antenna structure? It had been decided that the effective aperture area for the radio beam should be 3600 square feet,[1,2] that the reflector should be a section of a paraboloid, and that the cone axis should coincide with the horizontal elevation axis. Consideration of the location of the center of gravity, the azimuth turning diameter, and the preferred flare angle influenced the choice of the length-to-diameter ratio.

2.3.2. What kind of structural pattern should be chosen for the skeleton of the horn enclosure? A polygonal pyramid of approximately round cross section requires an elevation turning circle 30 per cent smaller than the elevation circle of a horn with a square cross section. Furthermore, it

can be made much more rigid against bending, shear, torsion, differential thermal expansion, and cross-sectional deformation. Also, deflection of the polygonal structure in the vertical plane remains constant with all elevation angles, and finally a round horn is more suitable electrically. The spiral pattern of the structural members has no parts that are idle at any time and thereby provides the most efficient configuration for a high rigidity-to-weight ratio. The lengths of the members were chosen in accordance with resonance and buckling requirements. A shell design would necessarily become prohibitively heavy to prevent skin buckling.

2.3.3. What is the most suitable type of configuration for the cradle structure? To achieve the highest rigidity-to-weight ratio of the entire structure, lattice-box girders are used for the cradle. The structure has the shortest and most direct load-carrying connections between the elevation assembly and the foundation. Minimum deflection support is provided for the elevation structure in two planes. Stability against overturning moments is achieved by use of a sufficiently large base frame. The least amount of material is required and a high natural frequency of structural members is obtained.

2.3.4. Which structural shapes should be used for building the horn enclosure? Structural tubes are three times lighter than any other structural shape for the same static deflection, and their resonant frequency between joints is about 70 per cent higher than that of other shapes of the same weight.

2.3.5. What material is appropriate as structural building material? Light weight and high rigidity are desirable in view of deflections due to gravity and high-frequency response to servo forces in the structure. Steel was selected because of its high modulus of elasticity. The rigidity of an aluminum structure of the same volume would be intolerably low when attached dead loads are considered, even though the resonant frequencies of the load-bearing skeletons may be equal. Increasing the volume of aluminum for stiffening would cancel the effects of savings in weight and mass inertia. Under a radome, an aluminum horn enclosure could at best save 20 per cent by weight of the present antenna and increase the natural frequency by about 10 per cent. Differential thermal expansions, due to sunlight in the open or because of air stratification in a radome, would double with aluminum. An all-aluminum structure of equal static and dynamic but worse thermal properties would cost about 10 per cent more than a steel structure.

2.3.6. Is damping feasible and needed to limit the amplitude of vibrations? Since the structure is designed to have no play in any of the joints, damping can be expected only from the material. This damping decre-

ment is known to be no more than 0.05. With servo impulses applied directly, the structure may resonate, causing erroneous reactions of the servo. Many of the devices investigated for increasing internal damping proved to be either excessively heavy or ineffective because the permissible vibrational amplitudes were too small. External damping devices were also considered but were found to add drag to the rotational torques, thereby increasing the pointing error. Due to the autotrack's minimizing effect on directional corrections, and due to the need for converting digital information into analog, the torque changes originated at the drives are small. These changes are smoothed by gear and wheel friction so that little of this energy is converted to structural vibration. With the antenna in a radome enclosure, no wind forces are present to excite structural resonance. The relatively high natural frequency of the antenna, 2.2 cps, and the coupling of several antenna components with different higher frequencies, eliminate oscillations at resonance.

2.3.7. How should manufacturing and deflection tolerances be distributed among the structural components and foundation? Tolerance accumulation in an antenna system starts deep in the ground and is traced all the way up through the foundation, rails, trucks, azimuth carriage, elevation structure, and reflector suspension to the last panel surface. The distribution of the total allowable antenna pointing error for each part of the mechanical system has to be accomplished in accordance with the limitations of structural geometry, physical properties of materials, resonant frequency requirements, and currently available manufacturing techniques. Consideration also must be given to directions of errors and the probability of their occurrence.

Equations (1) and (2) below represent the total pointing errors about azimuth and elevation axes. Angular errors about the third axis, perpendicular to both azimuth and elevation axes, can be expressed in azimuth measure. Rotations about the nominal pointing vector result in equivalent elevation errors.

$$
\begin{aligned}
A = 2 &\left\{ \left[\beta_{GE} + \beta_{TE} - \left(\frac{c}{l} \right)_{GE} + \left(\frac{c}{l} \right)_{TE} \right] \tan \varphi \pm \beta_{ME}/\cos \varphi \right\} \\
&+ (\delta_{GA} - \delta_{TE}) \sin \varphi + (\epsilon_{GA} + \epsilon_{TE}) \cos \varphi \pm \delta_{MA} \tan \varphi \\
&+ \delta_{GE} \sin 2\varphi \tan \varphi + \epsilon_{GE} (1 - \cos 2\varphi) \\
&\pm \left\{ \epsilon_{MF}{}^2 + \epsilon_{MA}{}^2 + \epsilon_{ME}{}^2 + \epsilon_{GF}{}^2 + \epsilon_{TF}{}^2 + \epsilon_{TA}{}^2 \right. \\
&+ (\delta_{MF}{}^2 + \delta_{ME}{}^2 + \delta_{GF}{}^2 + \delta_{TA}{}^2 + \delta_{TF}{}^2) \tan^2 \varphi \\
&+ \left. 4 \left(\beta_{MEr}{}^2 + \left(\frac{c}{l} \right)_{ME}^2 \middle/ \cos^2 \varphi \right) \right\}^{1/2}
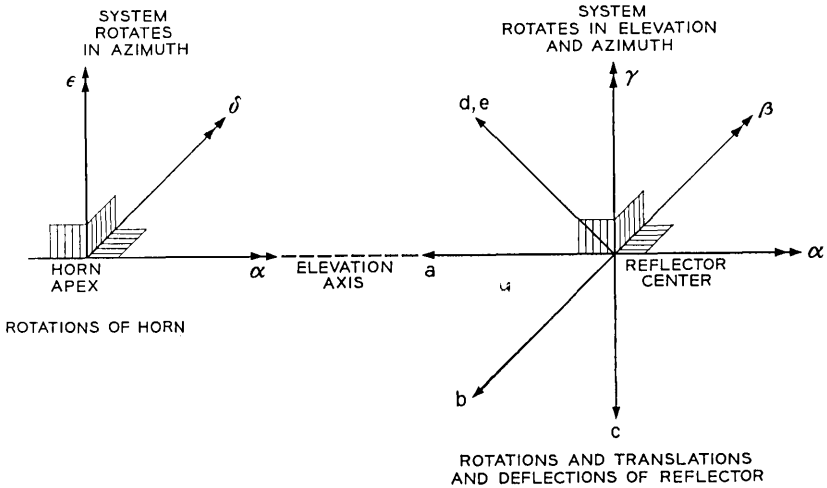\end{aligned}
\tag{1}
$$

$$E = \left[\alpha_{GA} + \alpha_{GE} + \alpha_{TE} - \gamma_{GE} - \gamma_{TE} + \left(\frac{b}{l} \right)_{GE} \right] \cos \varphi$$

$$\pm \left[\alpha_{MF}^2 + \alpha_{MA}^2 + \alpha_{ME}^2 + \alpha_{GF}^2 + \alpha_{TF}^2 + \alpha_{TA}^2 \right. \tag{2}$$

$$\left. + \gamma_{ME}^2 + \left(\frac{b}{l} \right)_{ME}^2 + \left(\frac{b}{l} \right)_{TE}^2 \cos^2 \varphi \right]^{1/2}.$$

In these expressions, note that (*i*) the equations describe electrical pointing deviations with respect to ground due to structural imperfections and varying deformations; (*ii*) β_{ME} is usually chosen negative to compensate for β_{GE} at the zenith position, which is readily measurable at the time of alignment; (*iii*) δ_{MA}, even though preferably a residual value (*r*) after adjustment, has a permanent great influence so that its direction must be known for $+$ or $-$; (*iv*) the equations contain signs for 0 to 90° elevation φ only; and (*v*) the temperature is assumed stratified in the radome for the elevation structure, random for the remaining structure. It is also assumed that there are no wind forces and that operational forces are negligible.

Fig. 3 shows the coordinate systems on which the above equations are based. With the help of this theory, it became possible to generate a tolerance budget for designers, manufacturers and erectors, as presented in Table II. Data for deflections due to servo or wind forces were left out as being negligibly small and zero, respectively. After the antenna design had been completed, the expected total pointing errors were calculated, in part compensated for by mechanical bias against gravitational deflection, and later compared with measurements from radio star tracking, Fig. 4. Agreement between calculations and measurements of variable errors was found to be excellent. The shaded areas in Fig. 4 indicate data scatter, due essentially to the influence of the rolling surfaces. The variable errors then were counteracted by data corrections as functions of elevation angle, so that predictable errors are entirely eliminated. Reflector panels were to be manufactured to within 0.03 inch in contour, and total accumulated deviation from the desired paraboloid was to be kept under $\pm\frac{1}{8}$ inch, so as to insure the least distortion to the beam.

2.4 *Additions to Basic Concept*

After the basic design concept had been selected, some features were added to the antenna to increase its performance and reliability. A radome excludes all influences by the elements such as wind, ice, snow and rain. To obtain the smallest possible azimuth turning clearance, the azimuth axis was shifted closer to the reflector. The four cradle sup-

α = ROTATION ABOUT ELEVATION AXIS
β = ROTATION IN PLANE OF ELEVATION AXIS
    AND POINTING VECTOR
γ = ROTATION ABOUT POINTING VECTOR
δ = ROTATION IN PLANE OF ELEVATION AXIS
    AND AZIMUTH AXIS
ε = ROTATION ABOUT AZIMUTH AXIS
a = DISPLACEMENT ALONG ELEVATION AXIS
b = DISPLACEMENT PERPENDICULAR TO PLANE
    OF ELEVATION AXIS AND POINTING VECTOR
c = DISPLACEMENT ALONG POINTING VECTOR
d = CORRUGATION HEIGHT OF REFLECTOR SURFACE
e = MEMBRANE DISPLACEMENT OF REFLECTOR

POINTING ERRORS:
    A = AZIMUTH
    E = ELEVATION
    P = PITCH

DIRECTIONS:
    +E = DOWN
    +A = COUNTERCLOCKWISE

POINTING ANGLES:
    φ = ELEVATION ABOVE HORIZON
    ψ = AZIMUTH ROTATION

SUBLETTERS:
    A = AZIMUTH STRUCTURE
    E = ELEVATION STRUCTURE
    F = FOUNDATION AND TRACK
    G = GRAVITY
    M = MANUFACTURING
    T = TEMPERATURE

Fig. 3 — Tolerance coordinate systems.

port trucks no longer ride on one common double track but on two individual rails, each mounted on one of two concentric ring foundations. The trucks became two-wheeled and non-self-aligning. Therefore, both a pintle bearing on a central foundation and an extra structure inside the four structural planes of the azimuth carriage had to be added to keep the trucks on the rails against considerable friction forces. More struc-

TABLE II—STRUCTURAL TOLERANCES FOR POINTING ACCURACY

Symbol of Rotation	Tolerances[a] for			Influences[b] on pointing					
	Mfg. (M)	Grav. (G)	Temp. (T)	Azimuth			Elevation		
				A_M	A_G	A_T	E_M	E_G	E_T
Foundation and track (F)									
α	0.10	0.05	0	0	0	0	± 1[c]	± 1	± 1
δ	0.10	0.05	0	$\pm 1u$[d]	$\pm 1u$	$\pm 1u$	0	0	0
ϵ	0.10	0.05	0	± 1	± 1	± 1	0	0	0
Azimuth structure (A)									
α	0	0.05	0.05	0	0	0	± 1	$\pm 1w$	± 1
δ	0.05	0.10	0.05	$\pm 1u$	$+1v$[e]	$\pm 1u$	0	0	0
ϵ	0	0.10	0	± 1	$+1w$[f]	± 1	0	0	0
Elevation structure (E)									
α	0	0.15	0	0	0	0	± 1	$+1w$	$+1w$
β	0.05	0.30	0.15	$-2x$[g]	$+2y$[h]	$+2y$	0	0	0
γ	0.15	0.50	0.15	0	0	0	± 1	$-1w$	$-1w$
δ	0.15	0.05	0.05	$\pm 1u$	$\pm 1u$	$-1w$	0	0	0
ϵ	0.10	0.05	0	± 1	± 1	$+1w$	0	0	0
b/l[i]	0.15	0.30	0	0	0	0	± 1	$+1w$	$\pm 1w$
c/l	0.05	0.10	0	$\pm 2x$	$-2y$	$+2y$	0	0	0

(a) Angular deviations in milliradians; (b) factors of magnification; (c) $+A$ counterclockwise, $+E$ down; (d) $u = \tan \varphi$; (e) $v = \sin \varphi$; (f) $w = \cos \varphi$; (g) $x = 1/\cos \varphi$; (h) $y = (1 - \sin \varphi)/\cos \varphi$; (i) l = horizontal distance between focus and reflector.

ture was added for the transmission of horizontal forces from the rear elevation bearing to the pintle bearing, because the elevation bearing was fixed axially. To allow for expansion at a later date, the equipment room at the apex of the horn was not enclosed within the elevation structure but was placed directly on the azimuth cradle. A lower equipment room located on the azimuth cradle had not been anticipated in the original design but was found to be a necessary addition. Both equipment rooms represent dead loads and therefore impose considerable penalties to the antenna in terms of weight and inertia. Structure-mounted positive drives were employed instead of truck-mounted friction drives to insure slip-free operation under all conceivable conditions, thus imposing high accuracy requirements on the location of the center of azimuth rotation. A view of the antenna model, showing most of the above features, is seen as Fig. 5.
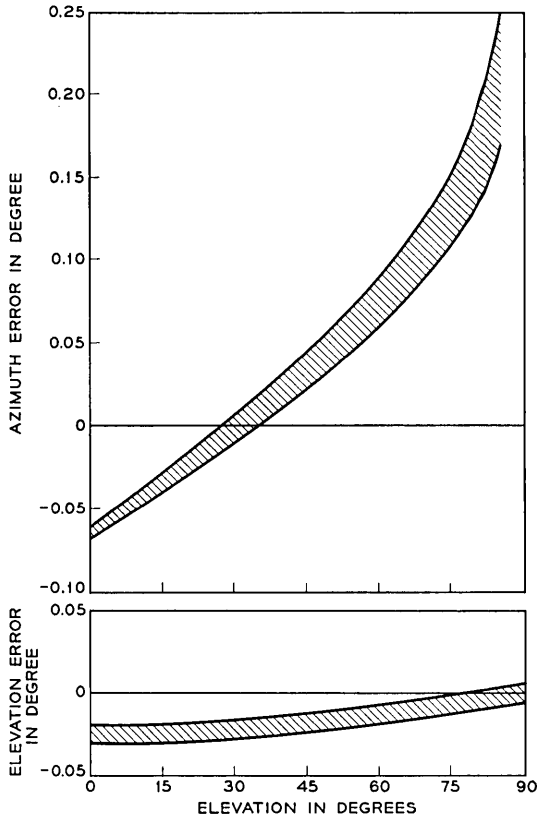
Fig. 4 — Calculated structural variable pointing errors.

III. MECHANICAL STRUCTURE

3.1 General Configuration

Fig. 6 is an outline drawing of the horn-reflector antenna. This antenna, which is a greatly enlarged version of the horn-reflector antennas employed in the Bell System's transcontinental microwave relay network, can best be visualized as two separate structures — an elevation structure rotating about a horizontal axis and an azimuth structure rotating about a vertical axis. The elevation structure is an extremely rigid framework which houses a conical horn some 90 feet long and supports a reflecting surface measuring approximately 100 by 70 feet. The horn terminates at its apex in an enclosed room housing the transmitting
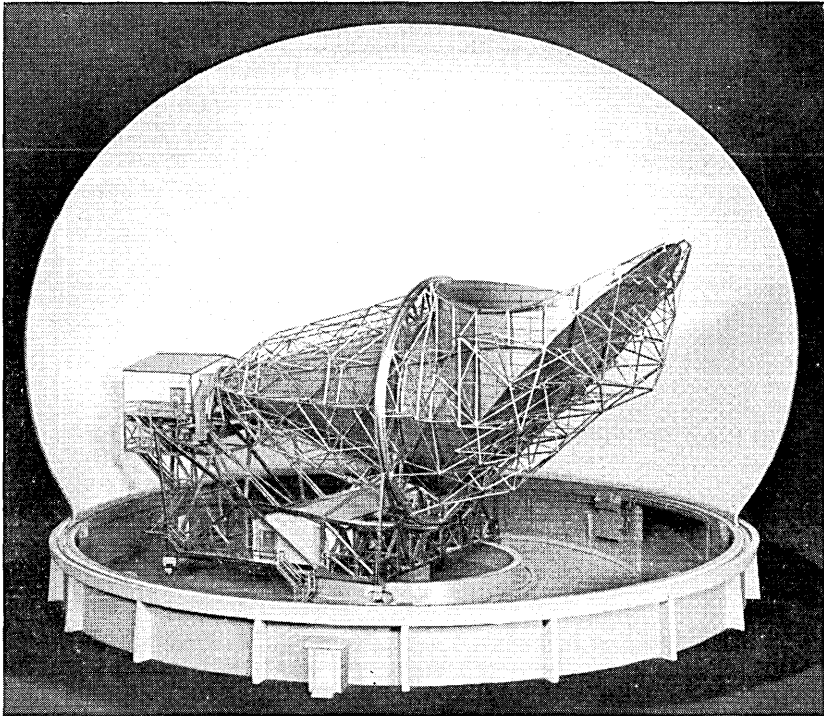
Fig. 5 — Model of Telstar horn-reflector antenna.

and low-noise receiving equipment. At its large end the horn terminates in the reflector, which is a sector of a paraboloid of revolution set at an angle of 45 degrees with the cone axis. The space between horn and reflector is occupied by a cylindrical structure which serves as a shield for the 67.7-foot diameter aperture of the antenna. Fig. 7 illustrates the relation between the conical, cylindrical, and paraboloidal surfaces comprising the horn, shield, and reflector.

The entire antenna structure is 177 feet long, stands some 95 feet above the azimuth rails at maximum elevation angle, and weighs about 380 tons with all equipment installed. The McKiernan-Terry Corporation of Dover and Harrison, New Jersey, were the prime contractors responsible for the detailed design, fabrication, and erection of the structure, guided by the basic design developed by Bell Laboratories. Subcontractors responsible to McKiernan-Terry, and working in close cooperation with Bell Laboratories engineers, included Burns & Roe, Inc., of New York City, responsible for the antenna and radome founda-
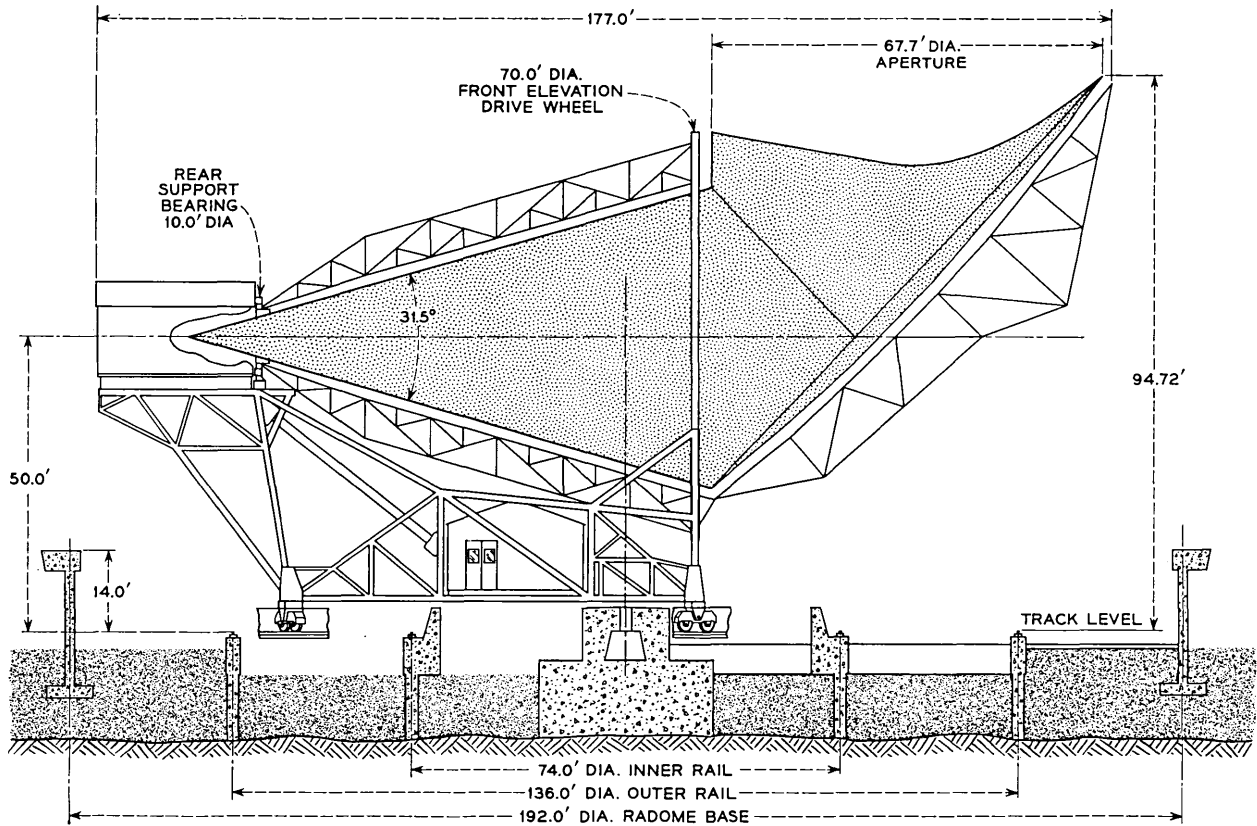
Fig. 6 — Outline drawing of horn-reflector antenna.
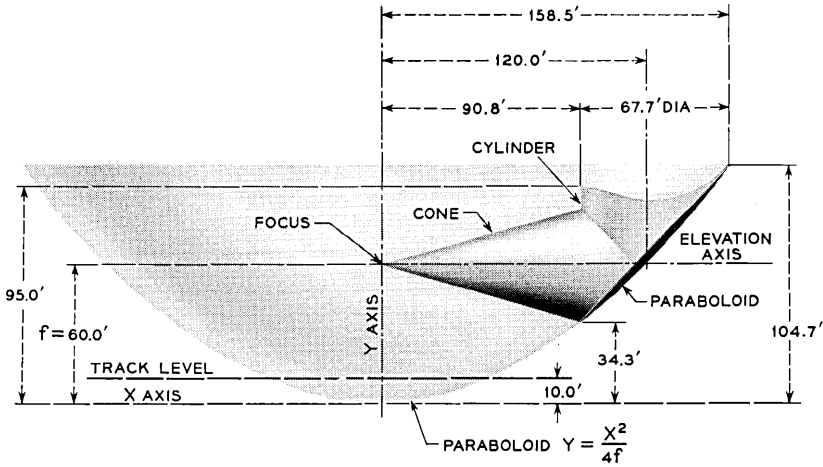
Fig. 7 — Relationship between horn, shield, and reflector surfaces.

tions; Radio Construction Corporation of Pittsburgh, Pennsylvania, erectors of the structure; and Advanced Structures of La Mesa, California, who fabricated and aligned the cone, shield, and reflector surfaces of the elevation structure.

3.1.1 Elevation Structure

The elevation structure is supported at two diameters and is provided with a choke joint near the cone apex to permit continuous rotation about the horizontal axis of the conical horn. At the large end of the cone, this support is provided by a circular track ring, integral with the structure. Near the apex, the support, as well as the axial restraint, is provided by a self-aligning ball bearing 10 feet in diameter. The wheels of the two trucks supporting the 70-foot diameter elevation track ring are provided with ball splines to accommodate any breathing of the elevation structure brought about by temperature differences between it and the supporting structure.

3.1.2 Azimuth Structure

The azimuth structure serves as the cradle to support the elevation structure. Rotation about a vertical axis is provided for by four trucks supporting the entire weight of both structures and running on two circular and concentric tracks. All horizontal reactions associated with azimuth rotation are assumed by a self-aligning roller bearing three feet

in diameter and located at the center of the concentric tracks. This pintle bearing is isolated from vertical reactions by means of a flexible diaphragm that forms the connection between the outer race of the bearing and the rotating structure. Continuous azimuth rotation is afforded by a slip ring assembly for electrical power and signal circuits, and by a rotary joint for the chilled water required for cooling equipment on the structure. The slip ring assembly, which is an adaptation of a previous design, accommodates 295 electrical circuits: 28 for heavy power, 21 for signal circuits and 246 for general purpose.

3.1.3 Equipment Rooms

Two equipment rooms are mounted on the azimuth structure. One, commonly called the upper room, is at the cone apex. Its floor area is 900 square feet, and it houses the Telstar communication transmitters and receivers as well as associated electronic gear and the elevation angle indicating devices. The other room, commonly called the lower room, is located beneath the horn section of the antenna and just to the rear of the pintle bearing. Its floor area is 1600 square feet, and it houses the alarm and signaling equipment, the antenna digital control system, the antenna servo system, the station monitor system, the autotrack system, a transmitter for use in the NASA project Relay experiment, and various items of auxiliary equipment.

3.1.4 Antenna Foundation

The antenna foundation consists of three main elements. At the center of azimuth rotation is the massive reinforced concrete pintle block keyed into granite bedrock some 15 feet below grade to enable it to withstand a horizontal reaction of 300,000 pounds which could develop if, in the event of a hurricane, the protective radome were lost and the structure were subjected directly to the full force of a 100-mph wind. The two concentric reinforced concrete rings for the azimuth tracks are also supported directly on bedrock to minimize localized vertical deflections that would result in antenna pointing errors. These foundations are designed so as to contribute no more than 0.005-inch differential vertical deflection between any two azimuth trucks as the 380-ton antenna rotates in azimuth. The two track rings are tied to each other and to the pintle block by eight radial concrete beams to further increase the stability of the entire foundation. The inner ring has associated with it a wall supporting the azimuth bull gear. Fig. 8 shows the completed antenna

foundation. The outer wall, which the photograph shows still under construction, is the foundation to which the radome was attached.

3.1.5 *Azimuth Rail System*

The outer azimuth track, 136 feet in diameter, is made up of 24 segments of heavy-duty crane rail weighing 171 pounds per yard, and the 74-foot diameter inner track contains twelve segments of the same weight rail. These segments were rolled to the proper curvature by the fabricator, Bethlehem Steel, ground to produce a flat and horizontal upper surface in another shop, and then butt-welded to produce a continuous ring after installation at the site. Jacks were interposed between the rails and the foundation sole plates to permit leveling of the entire track system to within $\frac{1}{32}$ inch. The excess weld material at the butt joints was faired into the adjacent ground surface of the rail head with a rail grinder developed specifically for this task. After this operation, each rail weld was checked for proper hardness with a portable hardness tester, and was subjected to a dye penetrant test to disclose cracks and porosity.

Fig. 8 — Completed antenna foundation and partially constructed foundation for attachment of radome.

The inner rail is the most heavily loaded and deflects approximately 0.018 inch between jacks when subjected to the wheel load. However, because of the relative spacing between wheels and jacks and the equalizing action of the truck, a total vertical movement of only half this amount is realized by the corner of the cradle structure.

3.2 *Azimuth Structure Considerations*

3.2.1 *Structural Details*

The principal members comprising the azimuth structure are steel box girders having a cross section one foot square. These girders were fabricated of four common angle sections laced together by welding smaller angle sections between them in a diagonal pattern. The girders were shop-assembled, where practicable, into subassemblies, but these shop subassemblies had to be limited in size so they could be transported by truck. On-site assembly of these members, as well as those of the elevation structure, was accomplished by bolted connections. High tensile strength bolts, which develop highly efficient and rigid joints by virtue of the clamping action on the bolted members, were used for all critical connections. Every high tensile strength bolt was hand-torqued to a predetermined value to insure that the required clamping forces were developed.

3.2.2 *Truck Alignment*

The design and alignment of the azimuth trucks and wheels were engineered to provide, as nearly as possible, pure rolling contact between wheel and rail. Because the only geometric shape capable of providing pure rolling contact along a circular path on a flat surface is a cone, the azimuth wheels were designed as frustrums of cones, and each wheel was aligned at assembly so that the projected cone apex coincided with the point of intersection of the azimuth axis and the plane formed by the top of the azimuth rails. To accomplish this alignment, a mirror mounted on the inboard end of the wheel axle was used to collimate a transit located at the center of azimuth rotation and at the level of the rail heads. The wheel being adjusted was raised off the track by a few thousands of an inch so that it could be rotated during the alignment procedure to verify orthogonality of the mirror and the wheel axis.

3.3 Elevation Structure Considerations

3.3.1 Elevation Wheel Fabrication

With the installation of the large elevation bearing assembly at the rear and the elevation trucks at the front, the azimuth structure was essentially complete and ready to receive the elevation structure. The first member of the elevation structure to be erected was the 70-foot diameter elevation wheel. This wheel had been fabricated in six separate segments to facilitate truck shipment to the site. Upon arrival at the site, the segments were placed on wooden cribbing some ten feet above the radome arena floor and assembled to form a complete wheel, the plane of which was horizontal. The elevation track, consisting of twelve sections of 104-pound crane rail previously rolled to the proper curvature, was next installed and the twelve rail joints butt-welded to form a continuous track ring. The entire 220-foot circumference of this ring was then ground to produce a smooth and concentric supporting track for the elevation structure. For this operation a grinding rig was devised, consisting of a precision grinding head mounted on a radius arm pivoted about the wheel center from a pintle anchored to the floor. The radius arm was supported near the wheel circumference by a track provided on the upper face of the wheel. The arm was motor-driven to make one circuit of the wheel in about four minutes, and carried a platform at the outer end to accommodate the operator. After some 136 hours of grinding, a continuous track having the required surface finish and width was attained. With the installation of the elevation bull gear segments and a "strongback" to reinforce the wheel during the lifting operation, the complete assembly, weighing close to 50 tons, was then ready for erection.

3.3.2 Elevation Wheel Erection

The lifting of this huge assembly, first to a vertical attitude and then up onto the elevation trucks, was the most spectacular and critical phase of the antenna erection sequence. Because of space limitations imposed by the presence of the radome wall and a temporary construction shelter (see below), the cranes involved in this lift could not be deployed to their best advantage and, consequently, the combined lifting capacity of three large cranes, one 90 ton and two 60 ton, had to be employed. Extreme caution was necessary throughout the entire 8 hours required for the two operations to insure that the lifting efforts of the three cranes were carefully synchronized. Any tendency for one of the cranes
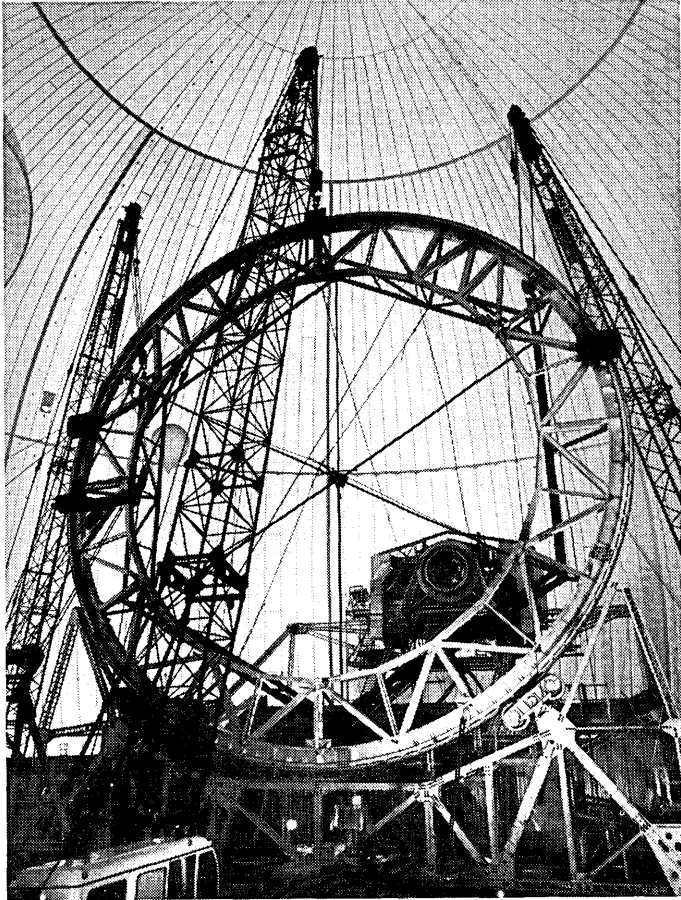
Fig. 9 — Final phase of installation of elevation wheel.

to assume more or less of its proper share of the total load could cause an imbalance, which would have resulted in an overloaded crane and would have led to disaster. Fig. 9 shows the final phase of the operation. The rear elevation bearing can be seen in the background.

3.3.3 *Cone Structure*

The next operation was the installation of the twelve cone rafters connecting the rotating race of the elevation bearing with the elevation wheel and forming the primary support structure for the cone as well as the

means for keeping the wheel erect. These rafters, some 75 feet long by 8 feet deep, had been fabricated as weldments of steel tubing and had been jig-assembled at the shop to insure uniformity of all critical dimensions. Each rafter was made in two sections with a field-bolted joint between the two units to facilitate shipment by truck and passage through the vehicular air lock of the radome.

3.3.4 *Cone Structure Alignment and Panel Installation*

When the cone structure was complete, but before the panels comprising the cone surface could be installed, it was necessary to rotate the cone structure about the elevation axis to establish the center of rotation of the elevation wheel. Because of size and weight considerations it was not feasible to design this wheel to have negligible deflections. Furthermore, the cross section of the wheel had to vary from sector to sector to accommodate the nonsymmetrical loading the reflector structure would impose on it. Consequently, it was necessary to find the actual center of the wheel as it rotated in order to establish the nominal axis for the cone surface. To accomplish this, a theodolite mounted at the theoretical location of the cone apex was used to observe a target suspended in the plane of the wheel. The position of the target was then adjusted to produce a minimum orbit as the wheel rotated. The centroid of this irregular orbit was the desired center of rotation, and the required cone surface was centered about a line connecting this point and the cone apex. For adjusting the cone panels to conform to the desired surface, an optical instrument located at the cone apex and aligned to this centerline was provided with an angle attachment enabling it to sweep the required cone angle. The tolerance on the cone surface is $\pm\frac{1}{32}$ inch at the rear panels and increases linearly to ± 1 inch at the large end of the horn.

3.3.5 *RF Surface Considerations*

The panels comprising the cone, shield, and reflector surfaces were fabricated of aluminum honeycomb. Averaging 3 by 12 feet in area and weighing about 1 pound per square foot, these panels could be readily handled by two men but were strong enough to support safely the weight of the workmen during the installation procedure. To make these panels, two 0.020-inch sheets of aluminum separated by a 1- to $1\frac{1}{2}$-inch thick lightweight aluminum honeycomb core were form molded to conform to the desired curvature to within 0.030 inch. With the curing of the adhesive used to bond the three elements together, this curvature was

"locked in," producing a panel having the required curvature plus an excellent compromise between weight and rigidity.

3.3.6 Reflector Back-Up Structure

Erection of the reflector back-up structure was performed with the structure oriented in elevation to point upward toward the zenith because, for this attitude, the nominal 45-degree angle between the reflector plane and elevation axis could be readily monitored by vertical measurements to a horizontal reference plane. Since this structure rotates about the elevation axis, and consequently with respect to the gravitational vector, its asymmetry results in a departure from the normal 45-degree relationship. This departure had been calculated and found to be within allowable limits. Pointing errors resulting from it could be compensated for by azimuth and elevation motions for any pointing angle except the zenith, where no amount of azimuth or elevation correction could overcome an outward or inward sag of the reflector surface. Hence, the zenith orientation was the most critical (as well as the most convenient) for monitoring the erection of this structure.

3.3.7 Reflector Panel Installation and Alignment

Upon completion of the reflector back-up structure, the entire elevation assembly was again rotated about the elevation axis, this time to determine the average center of rotation of the back-up structure. The centroid of the minimum orbit thus determined would become the starting point for the paneling of the reflector surface.

These panels, like the cone and shield panels, were provided with six threaded studs for attachment to the secondary support structure. The mounting nuts were appropriately positioned on these studs, and slotted clearance holes were used in the supporting members so that adjustment of the panel in three coordinates was possible. The panels, already curved in two directions by the fabrication process, were positioned to conform to the theoretical paraboloid of revolution to within 0.060 inch on a one-sigma basis by an alignment method developed jointly by Advanced Structures and Bell Telephone Laboratories. Paper targets, cemented to the front surface of each panel in locations corresponding to the support points, were observed from two theodolites located on a predetermined base line established on the radome floor. For this procedure the elevation structure had been rotated to the nadir position and the entire reflector was therefore readily observable from the floor-mounted instruments. The angles observed from the two theodolite positions were fed to

a computer located within the construction shelter and programmed to produce numerical values indicating the departure, in a direction normal to the surface, of each observed target from the theoretical paraboloidal surface. These values could be used directly to move the target points of the panels in or out until they coincided with the desired reflector surface. Corrections for gravitationally induced deflections of the back-up structure and for dimensional changes due to temperature variations were incorporated in the computer program. Fig. 10 is a contour plot of the
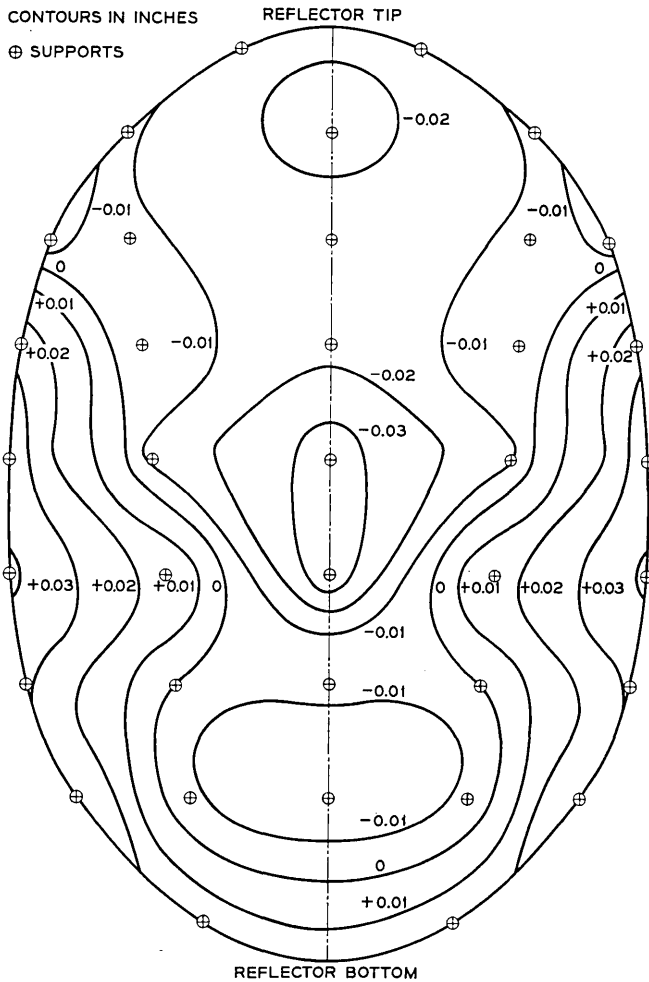

Fig. 10 — Elastic reflector contours.

local deflections compensated in this manner. The downward sag of the plane of the entire reflector frame from the nominal 45° angle also had to be included in the correction, since the effect of the gravitational vector was reversed as the structure was rotated from the zenith position in which it had been aligned to the nadir position employed for panel alignment. Actually, only three-fourths of the full correction was applied. This resulted in a nominally correct reflector surface at 30° elevation angle instead of at 90°. This represented a departure from the original intention to produce an optimum reflector surface at the zenith pointing angle. The compromise was dictated by the consideration that the antenna would never be required to track through the zenith and would spend comparatively little time tracking at the higher elevation angles. Only every other panel was observed, computed, and adjusted. The intervening panels were then faired to the adjusted panels. Shield panel adjustment was a much more simple procedure, the only requirement being that the cylindrical shield not encroach on the radiating aperture of the reflector surface.

With the adjustment of the shield panels and the taping of the joints between horn, shield, and reflector panels with aluminum-faced tape, the antenna structure was essentially complete.

IV. POSITION DATA DEVICES AND ANTENNA DRIVES

Important contributors to the successful performance of the horn-reflector antenna are the precise data take-off devices and the highly responsive hydraulic transmissions with associated low-compliance gearing in the servo drives. This equipment, operating under control of the antenna pointing system, must meet the antenna beam pointing tolerance of ±0.019 degree under satellite tracking conditions.

4.1 Data Take-Off Devices

The narrow beamwidth and stringent pointing error requirements for the antenna dictated the use of extremely accurate data take-off devices on both axes of rotation.

The large primary reference data gears were produced by the Westinghouse Corporation, Lester, Pennsylvania. Type 410 stainless steel $\frac{3}{4}$-inch thick plate stock was used for the gear blanks, and the standard $14\frac{1}{2}$-degree pressure angle, full depth involute tooth forms were produced by hobbing. Table III lists pertinent data applicable to these gears as mounted on the hobbing machine after the final finishing cuts were made.

In addition, very precise reference diameters were machined on the gears just below the root diameter of the teeth. The reference diameters

TABLE III — GEAR DATA

	Azimuth	Elevation
Pitch diameter	40 inches	132 inches
Diametral pitch	32	16
Number of teeth	1280	2112
Tolerance, tooth to any other tooth	10 seconds	12 seconds
Tolerance, tooth-to-tooth	4 seconds	$1\frac{1}{2}$ seconds

were later used to accurately center the gears on the antenna axes for final installation.

The final inspection of the gears was conducted by Bell Telephone Laboratories personnel at the manufacturing plant with the aid of rather specialized instrumentation. Precise measurement of angles subtended by groups of teeth were made by means of autocollimation techniques used in conjunction with an optical polygon mounted on the hobber table axis. At each test position, a mechanical probe engaged a gear tooth at the pitch line. Errors in tooth flank angular position as evidenced by probe displacement were detected by an electronic indicator mounted on the probe support.

Gear tooth-to-tooth error and pitch circle eccentricity checks were made with a certified master gear mounted on a precision slide and rolling in engagement with the gear under test. An electronic indicator sensed radial movement of the master gear slide resulting from variations in pitch circle or tooth contours, and the indicator output was connected to a rectilinear recorder to produce a permanent chart record of the test. In correlation with this test, electronic indicator checks were made on the datum circle runout. Figs. 11 and 12 are photographs of the setups for these tests.

On the horn-reflector antenna, the azimuth data gear is mounted and centered on the stationary pintle post, and the data take-off devices are located on the adjacent rotating structure. The elevation data gear is secured to the rotating inner race of the ten-foot elevation bearing, and the data units are mounted on the face of the large pillow block weldment that secures the bearing to the azimuth structure. Thus the synchros and resolvers, comprising the data take-off units, are part of and revolve with the azimuth cradle of the horn. The associated signal leads can therefore run directly to terminal bays in the lower equipment room without passing through slip rings.

The elevation data take-off devices, driven by the rotating gear through anti-backlash pinions, are as follows:

(a) *Precision resolvers* at 1:1 and 64:1 antenna speed. These outputs
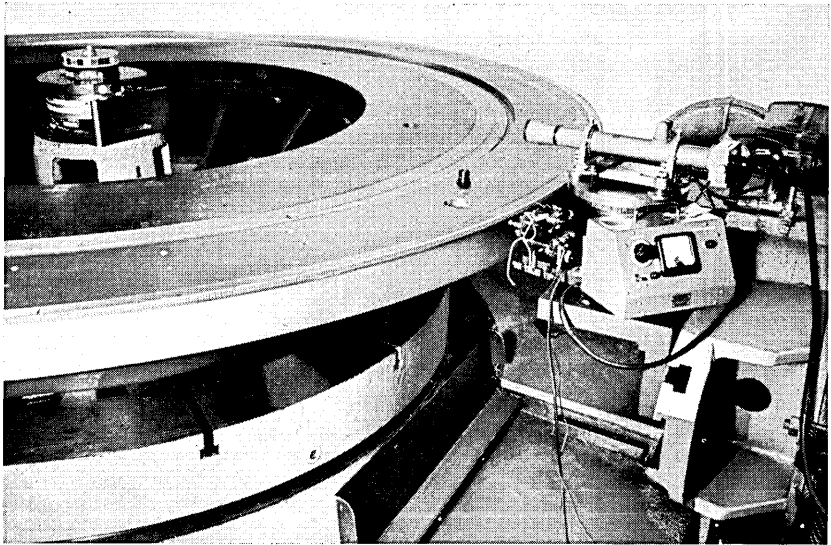
Fig. 11 — Test equipment for checking errors in gear tooth flank angular position.

are time-sequence sampled and translated to digital form for antenna position data input to the antenna pointing system.[3,4]

(b) *Synchros*: torque transmitters at 1:1 and 36:1 speeds are used for remote operation of slaved antenna position dials; control transformers at 1:1 and 64:1 speeds are used for manual servo loop control in position or velocity modes. These are used for off-line operation of the antenna.[5]

(c) *Boresight synchro* at 360:1 for initial boresighting and antenna pattern measurements.[2]

(d) *Autotrack coordinate converter*. This is a 1:1 speed synchro and potentiometer assembly used in conjunction with the autotrack system.[6]

Except for the omission of item (d), a similar arrangement is used for the azimuth data devices.

Fig. 13 is a photograph of the horn apex showing four data units clustered around one side of the 132-inch data gear. Fig. 14 shows two typical data units.

4.2 *Antenna Gear Drives and Hydraulic Transmission Systems*

The antenna utilizes hydraulic servo transmissions made by Vickers, Incorporated, and intermediate speed gear boxes made by the Western Gear Co. Two 25-horsepower and two 10-horsepower hydraulic trans-
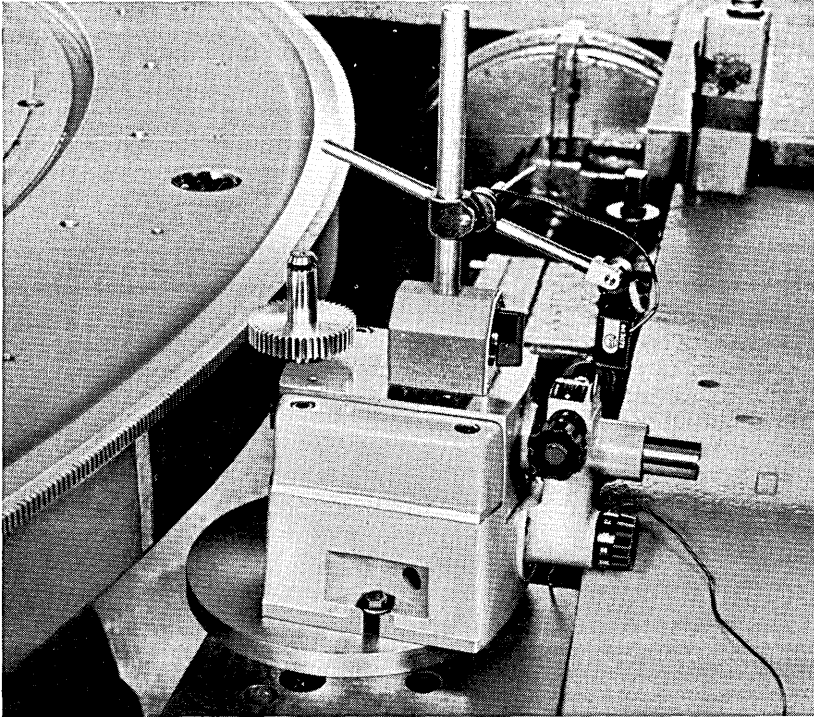
Fig. 12 — Test equipment for checking gear tooth-to-tooth error and pitch circle runout.

missions are used for driving, respectively, in azimuth and in elevation. Each transmission has two motor output shafts — one to drive and the other to provide a reverse torque for anti-backlash purposes as described below. Consequently, four complete gear trains are required for the drives on each axis.

4.2.1 Drive Gearing

The two azimuth drives are mounted at diametrically opposite locations on the horizontal framework of the azimuth structure. Fig. 15 depicts the arrangement of one azimuth drive. Fig. 16 shows the schematic of the gear trains.

It is noted that each transmission output shaft drives into the 11.32:1 input gear box which, in turn, drives the 22.59:1 output gear box. The 13-inch pitch diameter pinions engage the 64-foot pitch diameter bull
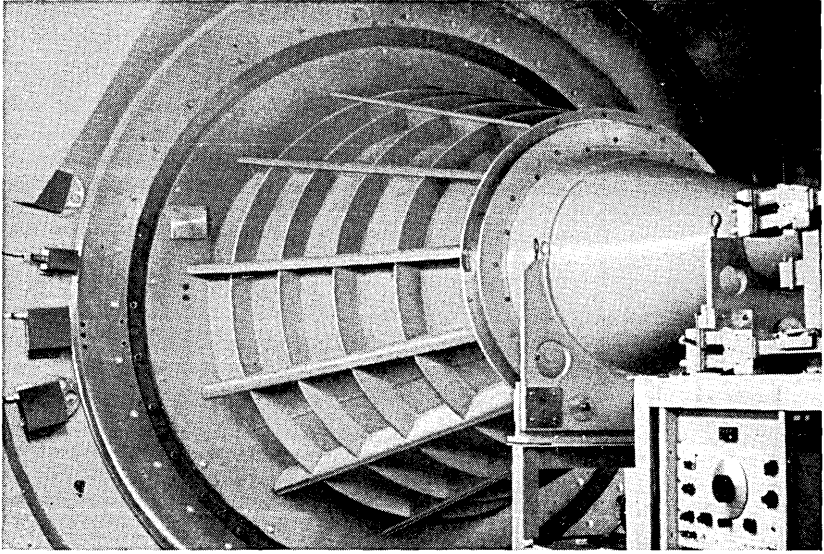
Fig. 13 — Horn apex showing four data units clustered on periphery of 132-inch data gear.

Fig. 14 — Two typical data units.

OVER-ALL RATIO
DRIVE-TO-ANTENNA AXIS
15,107 : 1

EXTERNAL
HYDRAULIC
CIRCUIT

INPUT GEAR BOX
11.32 : 1

25-HP
HYDRAULIC
DRIVE

OUTPUT GEAR BOX
22.59 : 1

GEAR CASE

BULL GEAR

INNER RAIL
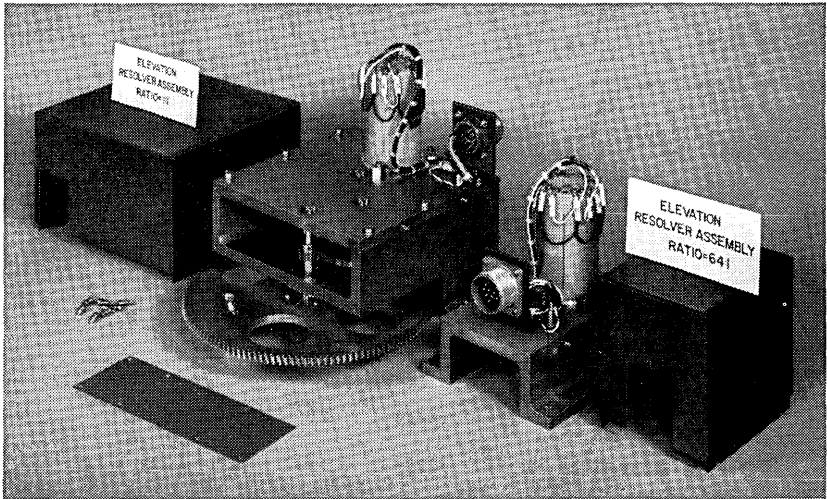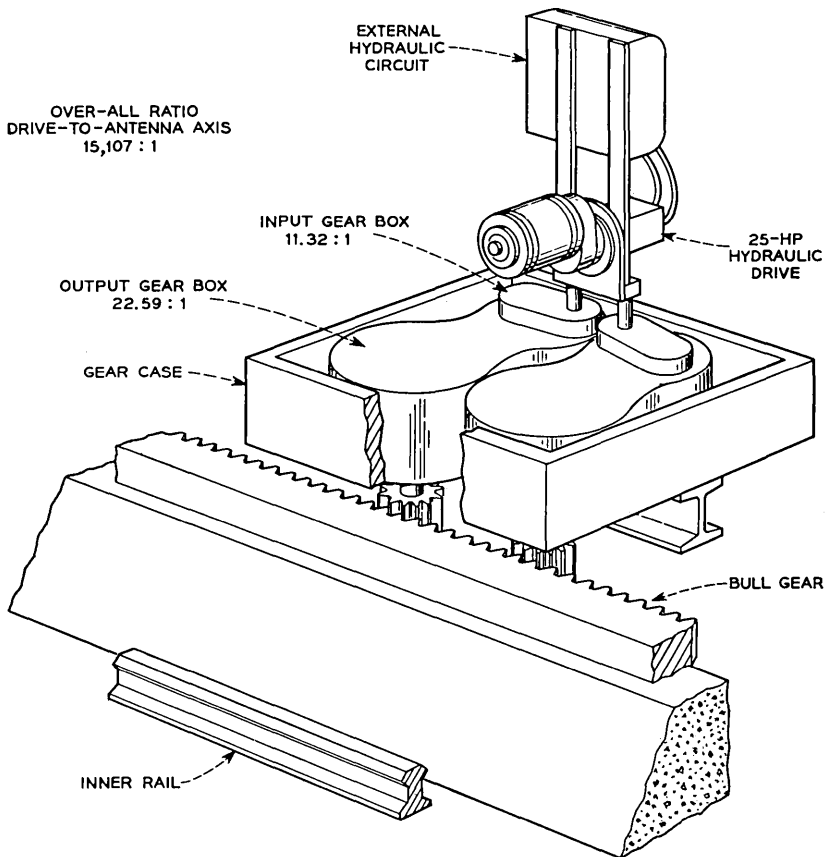
Fig. 15 — Schematic showing arrangement of one azimuth drive.

gear for an over-all drive ratio of 15,107:1; the 13-tooth pinions literally "walk" around the 768-tooth bull gear in rotating the structure.

The azimuth gearing is rather large. The output gear box is 54 inches long, 35 inches wide, and 22 inches high. A pair of boxes mount in a gear case that is 70 by 80 by 28 inches. A complete drive assembly, including the gear boxes and hydraulic unit, weighs $5\frac{1}{2}$ tons. Figs. 17 and 18 are photographs of an azimuth drive mounted on the antenna structure.

The azimuth bull gear is an internal gear of 64-foot pitch diameter and 6-inch face width, and is composed of 32 equal segments. To bring the gear as close as possible to the underside of the horn azimuth framework, the segments are bolted to the top of a five-foot high parapet that is part
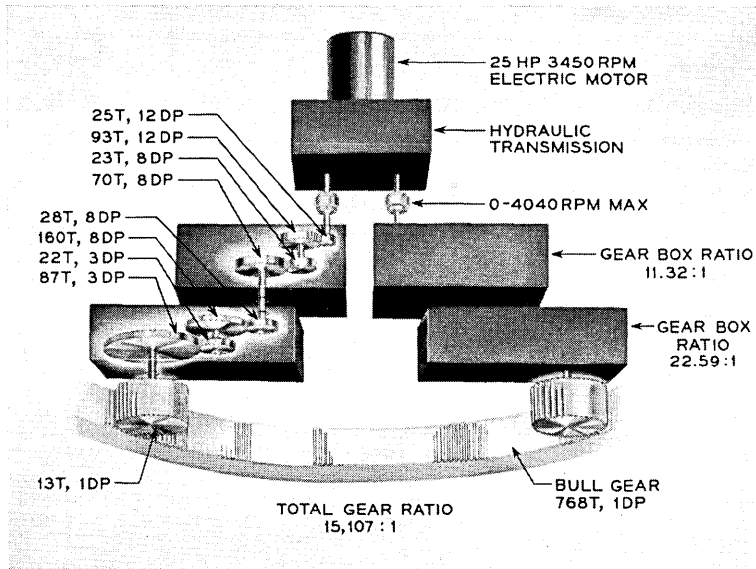
Fig. 16 — Schematic of azimuth gear train.
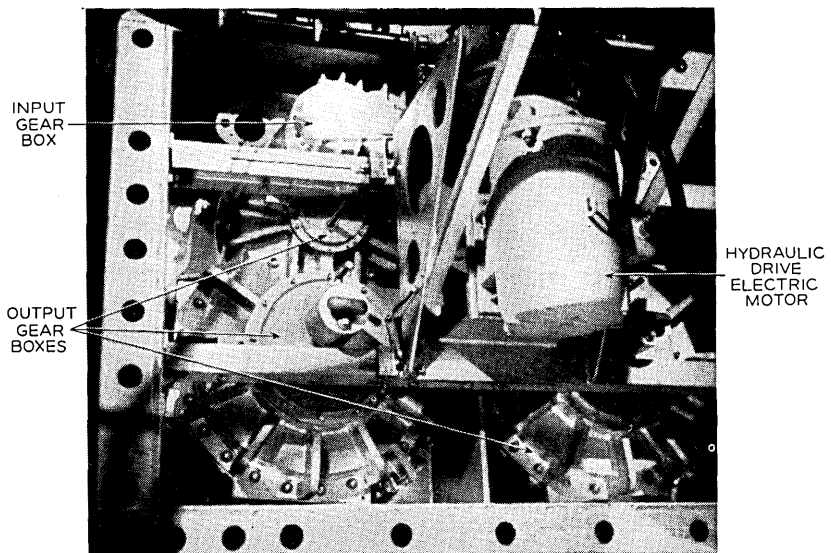
Fig. 17 — Azimuth drive mounted on antenna structure (top view).
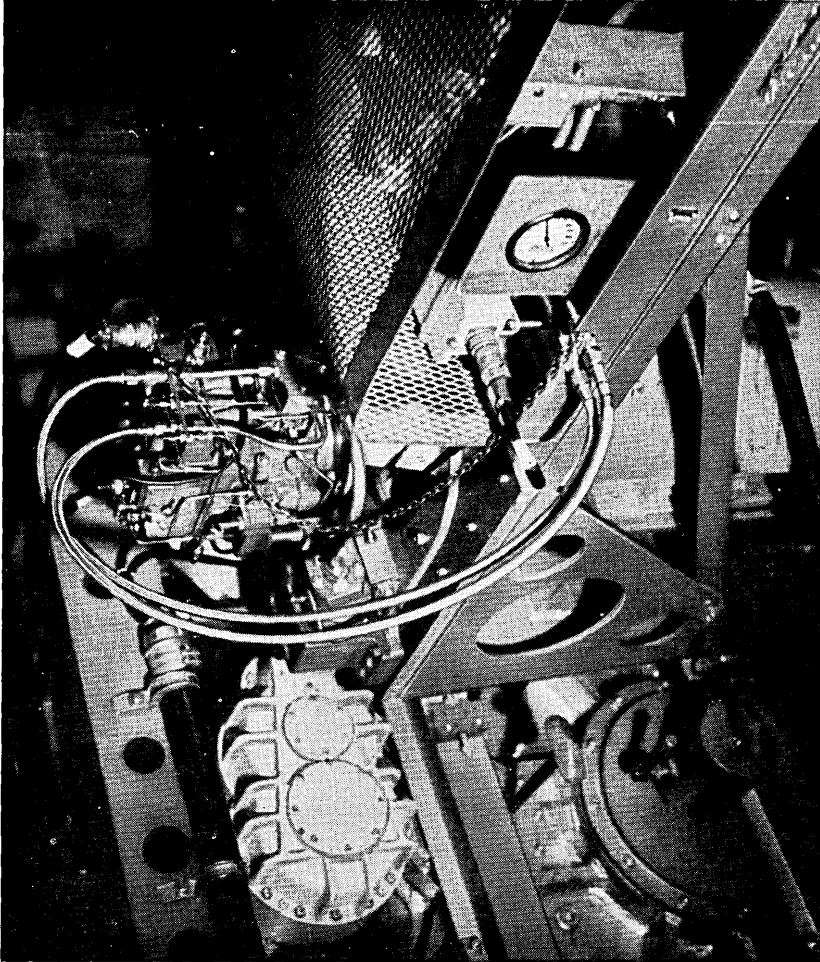
Fig. 18 — Azimuth drive mounted on antenna structure (side view).

of the foundation structure. By this means, the cantilever moment of the gear box and pinion and the resulting azimuth structure compliance are minimized.

Fig. 19 is a photograph of the azimuth drive pinions and a section of the bull gear.

The two elevation drives are mounted on the forward truss of the azimuth structure adjacent to the trucks that support the elevation wheel. Each assembly of the pair consists of the 10-horsepower hydraulic
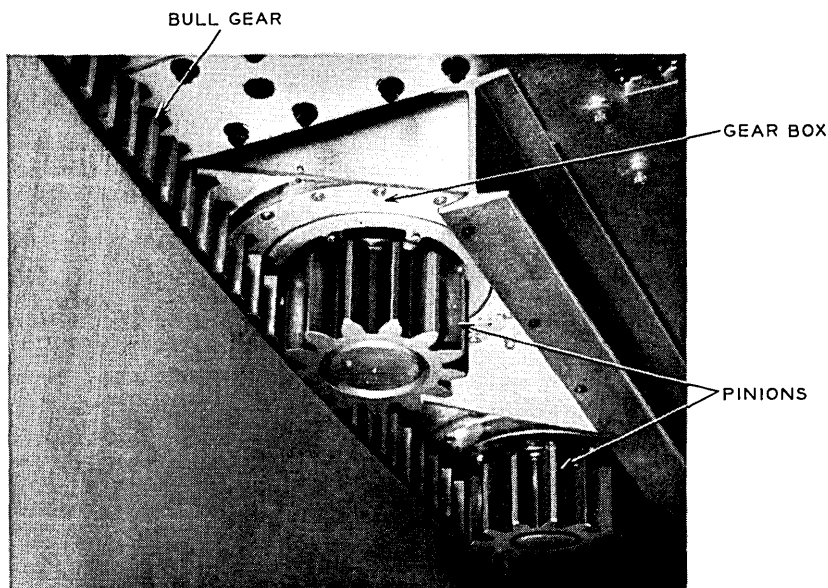
Fig. 19 — Azimuth drive pinions and section of bull gear.

unit which drives the 9.28:1 input gear box. This is the input to the final gear drive box of 23.52:1 ratio. The fifteen-tooth, 10-inch pitch diameter output pinions engage the $1\frac{1}{2}$ diametral pitch, 70-foot pitch diameter bull gear to yield an over-all elevation drive ratio of 18,334:1. The bull gear consists of 36 segments bolted and doweled to the periphery of the elevation wheel. The elevation drive gear schematic is shown in Fig. 20.

Fig. 21 is a photograph of the left-hand elevation drive mounted on the structure. Each gear box measures 48 by 38 by 18 inches, and the pair of boxes are mounted in the gear case of 88 by 90 inches. One complete drive assembly, including the hydraulic package, weighs approximately 3 tons.

4.2.2 *Hydraulic Drives*

The hydraulic drives are the prime movers for the antenna.

The 25-horsepower azimuth drive unit is shown in Fig. 22. The 10-horsepower elevation unit is quite similar in appearance and functioning but is slightly smaller.

The basic hydraulic circuit in somewhat simplified form is shown in Fig. 23. The power input to the system is a three-phase induction motor

RATIO
9.28 : 1

RATIO
23.52 : 1

10 HP ELECTRIC
MOTOR 3450 RPM

HYDRAULIC
TRANS-
0-3930 RPM   MISSION

24T, 16 DP
68T, 16 DP
24T, 12 DP
69T, 12 DP
27T, 10 DP
78T, 10 DP
25T, 8 DP
232T, 8 DP
15T, 1½ DP
BULL GEAR, 1260T, 1½ DP

TOTAL GEAR RATIO
18,334 : 1
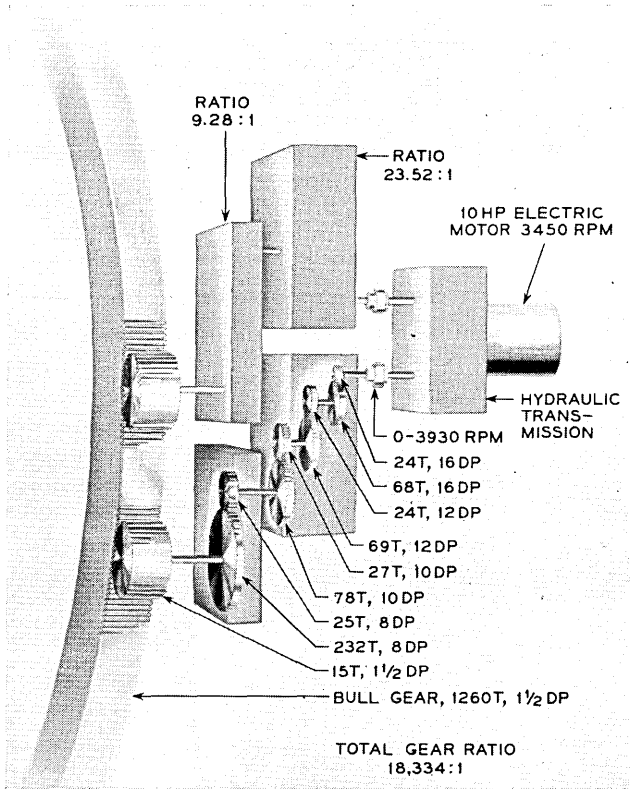
Fig. 20 — Elevation drive gear schematic.

that drives the servo-controlled main pump and two gear-type pumps for control and replenishing fluid pressure. The main pump is a nine-cylinder, variable flow, positive displacement type. As shown in Fig. 24, fluid is displaced when the shaft drives the pistons and cylinder barrel contained within the yoke housing. The yoke is mounted to swing 30 degrees either side of center about a pintle bearing, under control of the stroking cylinder. The flow is directed through ports in the stationary valve plate, and thence through passages in the yoke to the hollow pintle, where connections are made to the hydraulic motor circuit (see Fig. 23). The yoke angular position determines the displacement of the pistons and the direction of output flow.

    The pump is connected in a series circuit with the two nine-cylinder hydraulic motors with intermediate connections through relief or di-
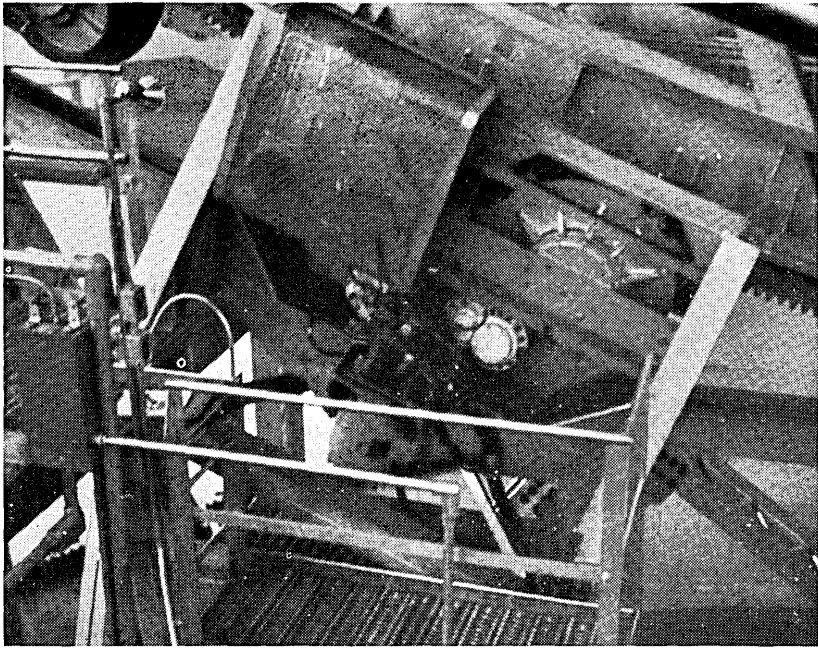
Fig. 21 — Left-hand elevation drive mounted on antenna structure.

rectional valves to the replenishing pump and sump. The hydraulic motors are similar in construction to the pump except that the stroke angle is fixed at 25 degrees. Fluid under pressure acting upon the pistons causes the cylinder barrel assembly to revolve and drive the output shaft. With the fixed angle between the cylinder barrel and shaft, the displacement per stroke is constant. Hence, motor speed is related to fluid flow rate.

For zero input signal, the servo valve, stroking cylinder, and main-pump yoke self adjust to the null or neutral position, and no flow occurs. However, the replenishing pump produces a differential pressure of approximately 60 psi across the two motors, tending to drive them in opposite directions with equal torque. The effect is that clearances in the gear trains are taken up in the direction that the motors normally drive. Because the pressure acting on both motors is equal, net driving torque applied to the bull gear is zero. This arrangement of the replenishing pump in the circuit effectively eliminates backlash in the gearing.

When an input signal actuates the torque motor, the directly coupled servo valve meters fluid at control-pump pressure to the stroking cylinder, causing it to move in magnitude proportional to the signal ampli-
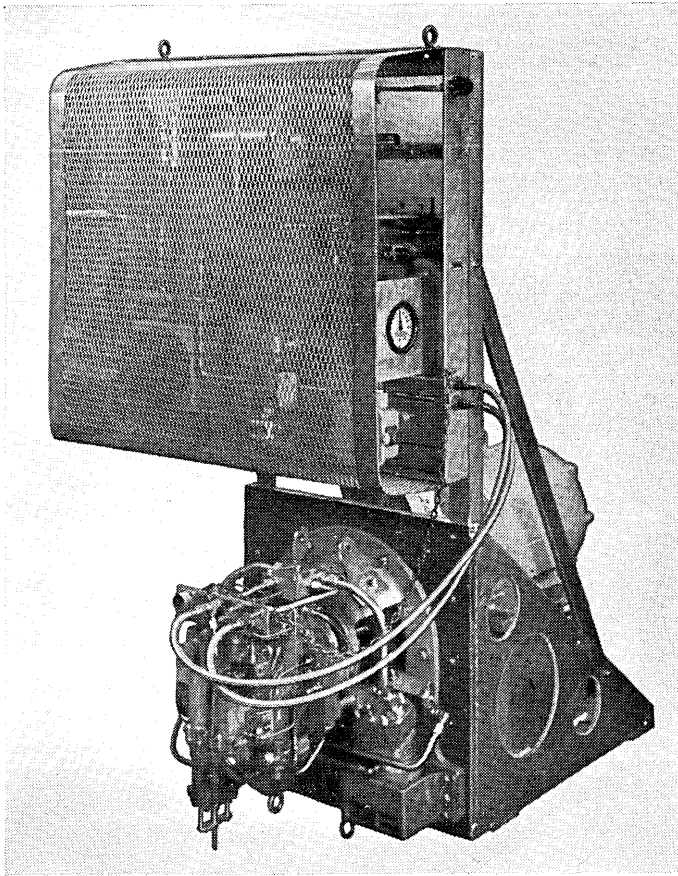
Fig. 22 — Vickers 25-horsepower azimuth drive unit.

tude and in direction in accord with signal polarity. By mechanical connection, the stroking-cylinder piston rod adjusts the position of the main-pump yoke to control a proportional pump output rate in the desired direction of flow.

If it is assumed that the flow is directed to motor 1, the increased pressure closes the directional check valve on the upper side of the re-plenishing pump connection and acts in the motor to produce driving torque. As antenna rotation occurs, the spent fluid passes to motor 2, which is driven by its gear train as a pump discharging fluid against the 60-psi replenishing pump pressure differential. The resulting light load on the gear train eliminates backlash.

When the input signal amplitude is increased, the pump yoke angle
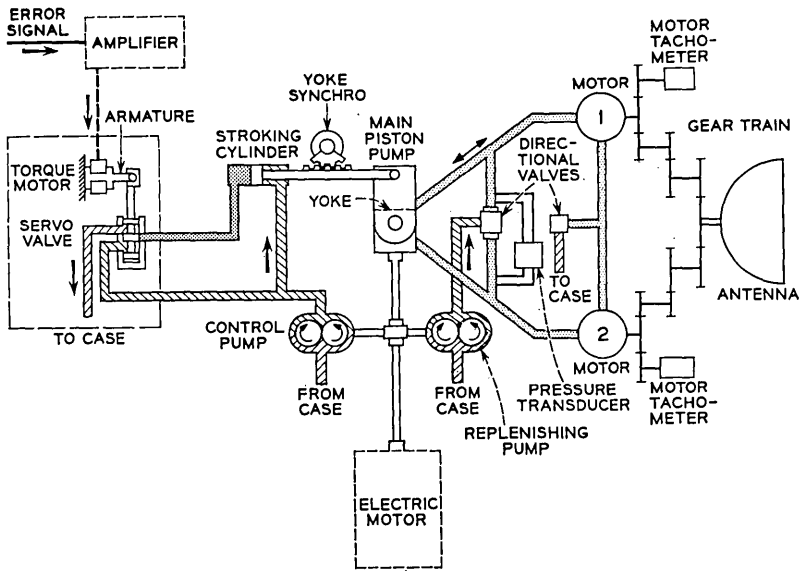
Fig. 23 — Simplified schematic of basic hydraulic drive circuit.
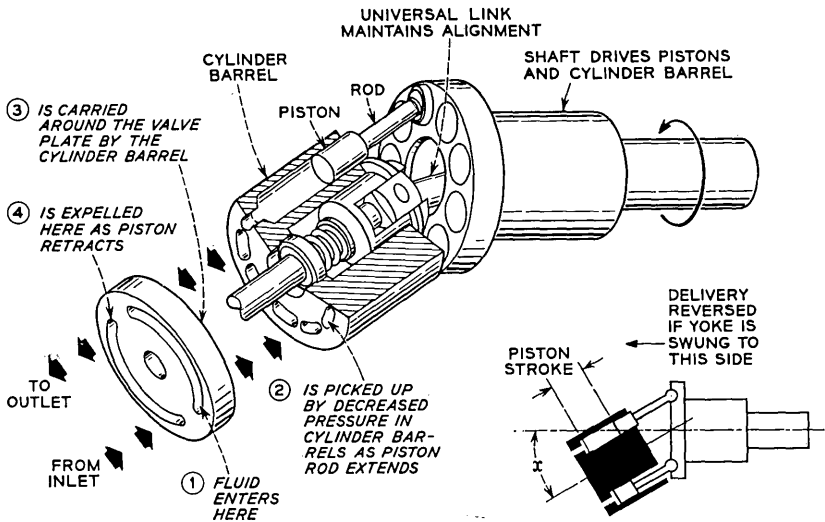
Fig. 24 — Mechanical schematic of piston pump.

increases correspondingly. Motor 1 operates at a higher output, but the retarding torque of motor 2 remains constant.

If a signal of opposite polarity is applied to the torque motor, the same sequence of operations drives the pump yoke to a position on the opposite side of center, direction of flow is reversed, and the two motors interchange their roles, reversing antenna rotation. Because the retarding torque is maintained at all times, reversal is smooth.

The pressure transducer (see Fig. 23) provides an electrical signal proportional to the pressure drop across the main pump, which is proportional to the work load on the hydraulic motor. This signal, as an input to the servo system, is used to equalize the output of the two hydraulic transmissions and to provide system damping. The yoke synchro and motor tachometers are also feedback inputs to the servo system for operational control.

The combination of the Vickers transmission and drive gearing provides remarkable responsiveness and antenna tracking capability. Speeds may vary from zero to maximum antenna slew rates of 1.5 degrees per second in azimuth and 1.4 degrees per second in elevation. As an indication of the acceleration capabilities, it should be noted that at slew speed the drives complete a full reverse command in an interval of less than three teeth on the bull gear. At the other extreme, as in tracking radio stars or under certain conditions during satellite tracking, rotation of one axis may be imperceptible. Particularly impressive is the response to sinusoidal servo input signals as high as 2 cps in frequency.

V. RADOME

5.1 *Need for Radome Coverage*

Early studies at Bell Laboratories and past experience based on tests of military antenna systems have proven that, despite the added system noise, a radome is essential to protect the horn-reflector antenna from the effects of enviornmental conditions. Some of the considerations and the advantages afforded by radome protection are discussed herein.

Without radome coverage, the antenna would be subject to the effects of the common elemental conditions of the area, such as solar heat, wind, snow, ice, rain, and dust. These conditions can seriously affect antenna performance.

(a) Direct solar heat, for example, can disturb the antenna reflecting surface contour accuracy so that the required patterns and gain are not achieved. Furthermore, differential solar thermal distortion can adversely affect beam pointing accuracy.

(b) The influences of wind on an exposed antenna are even more pronounced than those of solar heat. An antenna structure and high-gain antenna servo drive system can become unstable under buffeting winds as low as 30 miles per hour. Excitation or distortion under high wind loading also can jeopardize its tracking performance.

(c) Accumulations of ice, snow, and possibly rain, if suitable drainage is not provided, can substantially interfere with antenna performance. Such accumulations sometimes necessitate limiting the range of antenna motion about its axis; otherwise, there is the risk of introducing too great a turning moment for the servo drives to counteract. This hazard makes disposal of the accumulation difficult, as indicated by a recent experience at a large installation in New England. An attempt to dump a heavy snowfall by tilting the dish caused an excessive moment, resulting in complete lack of control of the moved axis. The snow had to be removed by hand-shoveling and sweeping—a hazardous and time-consuming task that encroached on vital test time.

Under radome protection, however, the antenna is nearly independent of ambient weather conditions and can be scheduled on an optimum basis. Not only does this protection avert the direct adverse effects of the elements on antenna performance, but it also retards physical deterioration. Maintenance requirements are drastically reduced when an antenna is housed in a radome. Moreover, within a radome, antenna maintenance can be conducted with a higher degree of confidence and reliability.

Other less obvious advantages are also derived. If the antenna is to be radome-housed, its structure and servo systems can be built for lighter duty than if it is to be exposed. When no direct provisions are needed to counter the effects of exposure, a greater latitude in design approach is permissible.

5.2 Selection of Structure

When the need for a radome was established, it became necessary to choose the type of protective structure that would meet all requirements. Rigid-foam, space-frame, and air-supported structures were considered on the basis of: (a) state of the art, (b) electrical performance, (c) cost, and (d) effect on the schedule. The air-supported structure won by a sizable margin on all counts.

At that time, the largest radome built, either rigid or air-supported, was 150 feet in diameter. The diameter of the protective radome structure for the horn-reflector antenna is 210 feet, which obviously called

TABLE IV — PERTINENT LOAD FIGURES FOR 210-FT DIAMETER
TRUNCATED SPHERE

Inflation lift at 0.175 lb/in²	=	730,000 lbs
Aerodynamic lift in a 100-mph wind	=	844,000 lbs
Total lift	=	1,574,000 lbs
Aerodynamic drag	=	221,000 lbs
Aerodynamic moment	=	8,700,000 lb-ft
Fabric tension due to above loads	=	463 lbs/linear in

for a major step beyond the state of the art at that time for any kind of radome structure.

5.3 *Radome Design*

The principal loads imposed on the radome fabric under the most severe weather conditions are due to the internal pressure of the supporting air and the effects of the wind. These loads in a 100-mph wind, which requires an internal pressure of 0.175 lb/in², are listed in Table IV.

Fig. 25 is a good illustration of the aerodynamic load factors encountered on a truncated sphere supported on a base and placed in a free wind stream. The contour lines are on the surface of the sphere and
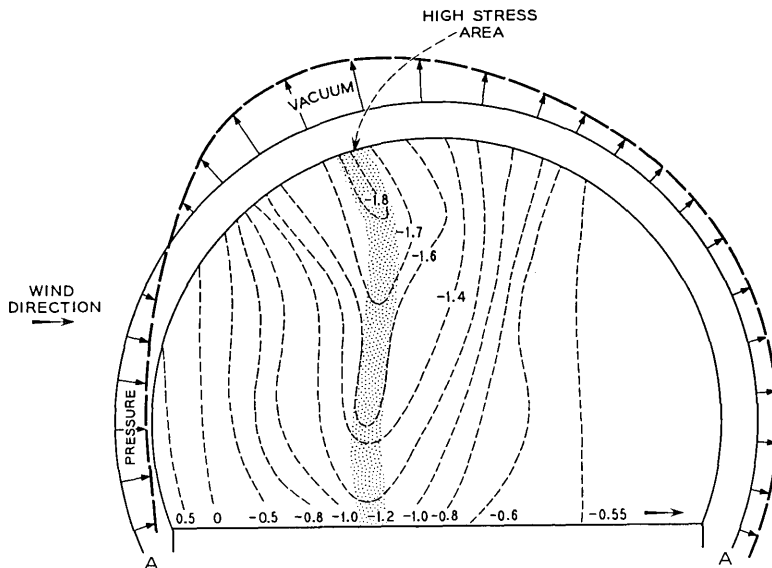

Fig. 25 — Aerodynamic loads on a truncated sphere in a free wind stream.

represent equal aerodynamic pressure of the values shown in the area contoured. A value of 1.0 is equal to the dynamic pressure of the wind for a given air velocity. Plus figures represent inward forces or pressure; minus values stand for outward forces or vacuum.

Fig. 25 reveals that, for a moderately high wind velocity, the aerodynamic suction forces about the sphere add to the internal pressure loading, becoming highest in a circumferential band perpendicular to the wind direction, as shown by the shaded area of high stress. The contour numbers in the figure also reveal that the particular area of highest stress is near the pole or crown. For the sake of clarity, the pressure values in a plane through the center of the radome and parallel to the wind have been plotted from an arc of a circle (A-A) used as a baseline (see Fig. 25). The directions of the arrows from the baseline indicate the direction of the reaction, depending on whether it is pressure or vacuum. The figure also pictorially shows that the aerodynamic drag force and moment about the base are high because of the additive impact pressure on the windward side and the vacuum on the leeward side.

The computations of aerodynamic and inflation pressure loads are straightforward and are all contained in a report by Cornell Aeronautical Laboratory.[7] Therefore, they are not repeated in this paper.

5.4 *Material Development*

The common pneumatic automobile tire could be considered a very distant relative of a large inflatable radome. Since it is a pressure-rigidized structure, it can serve to illustrate just one of the many difficulties in the design of a 210-foot diameter air-supported structure.

At an inflation of 28 pounds per square inch, a passenger automobile tire must withstand a tensile loading of approximately 100 pounds per inch. The tire carcass, of course, is designed to withstand puncturing bruises and road shock; therefore, it is made with a large safety margin of thickness above that required for the tensile load.

Unlike the tire, however, the radome must pass RF energy with minimum loss and pattern distortion. In this case, an undue safety margin of thickness would cause serious degradation of electrical performance. For a given pressure, as the diameter of a spherical pressure vessel increases, the tensile loading per inch of skin increases in direct proportion to the diameter. In the case of the radome, its required inflation pressure is a function of its wind environment. For the Telstar radome, the maximum wind environment capability is 100 miles per hour, and the corresponding inflation pressure is 0.175 pound per square inch (roughly $\frac{1}{100}$ of the tire pressure).

This low pressure might appear to be an insignificant problem in comparison to the 28 pounds per square inch required for the automobile tire. However, with very little calculation it can be shown that, when the 210-foot diameter radome is inflated, its skin is under a tensile loading of 150 pounds per inch, which is 50 per cent higher than the tensile load on the tire. To this load must be added the aerodynamic force of 300 pounds per inch, bringing the total radome skin tension to 450 pounds per inch (based on a 100-mph wind), or about $4\frac{1}{2}$ times the tensile load on the tire.

This load in itself does not appear to be a formidable problem; however, it becomes more drastic in view of the other requirements that are placed on the material. Besides sustaining the tension load, the material must also have the following characteristics:

(a) The base fabric must be stable, little affected by constant exposure to solar ultraviolet radiation, and must be highly rip resistant, with a sufficient margin of safety to allow for factory handling, erection, and anticipated life expectancy under load.

(b) Any protective coating for the base material must be tough, durable, and resistant to both abrasion and erosion from weathering. It must have good adherence to the base material and be capable of being bonded or cemented into joints that will exhibit characteristics equal to or better than the base material. For RF transmission, its moisture absorption must be low.

(c) For electrical reasons, the finished material must have a dielectric constant as low as possible (3.0 in the case of the Telstar system) and a thickness of no more than 0.071 inch, and must be held to an over-all thickness tolerance of ±0.002 inch. The material must be light in weight to permit transportation and erection with a minimum of difficulty. To equalize stress and to preserve the aerodynamic shape, strength and stretch properties of the material in the warp and fill directions must be as close to equal as possible.

With these specifications to be met, the selection and development of the material obviously was a formidable problem. Because no off-the-shelf commercial material was available, the problem was solved by producing a special radome skin from the best raw materials obtainable. The base yarn, selected for high strength and ultraviolet resistance, was Dacron polyester fiber, hot-stretched and heat-stabilized. Investigation of loom capacity revealed that, to meet strength, rip resistance, and elongation requirements, the radome fabric had to be specially woven to the heaviest gauge within loom capacity. After coating, two such fabric layers were laminated. To distribute loads equally, the two
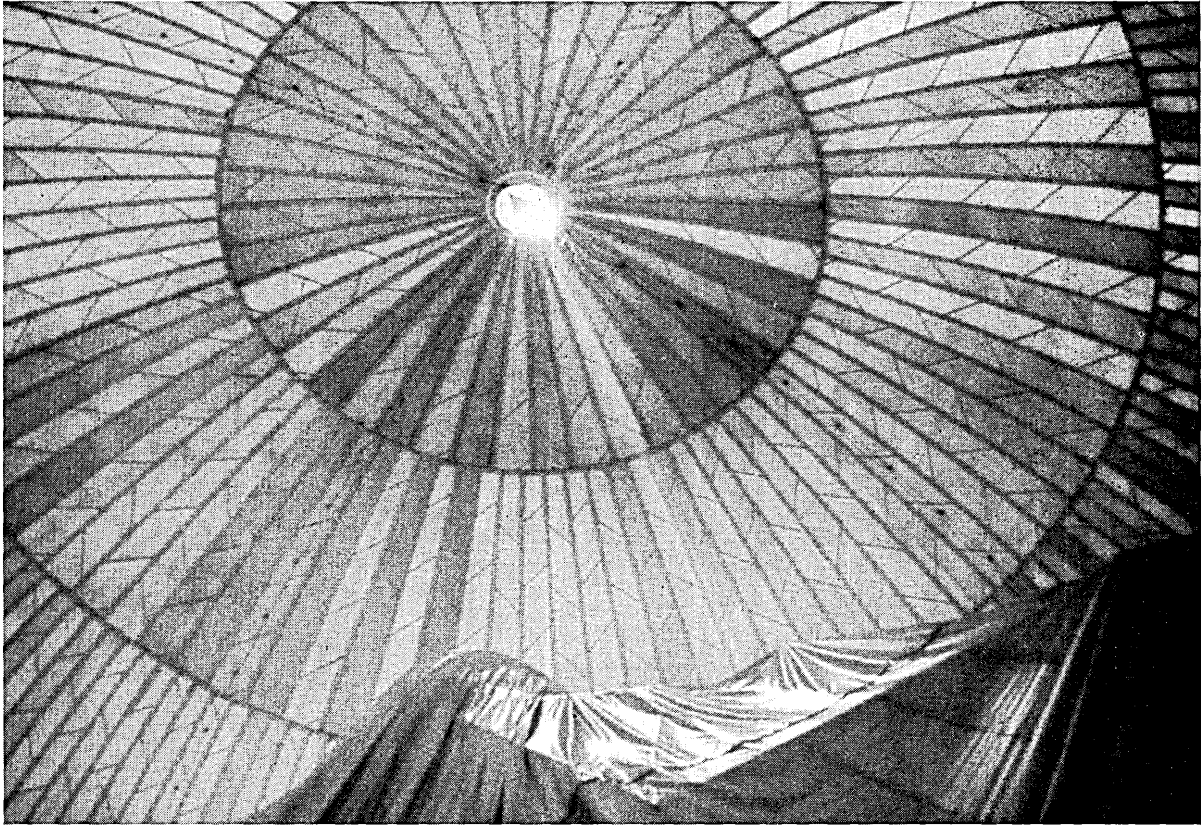
Fig. 26 — Upward view showing herringbone pattern inside Andover radome.

plies were bias-laminated to form a herringbone pattern (see Fig. 26). This laminate was then bonded, piece by piece, to make the full shaped radome shell.

The coating material selected was a synthetic rubber (based on Hypalon, a DuPont proprietary material) specially formulated to minimize RF loss and moisture permeability. This coating, together with commercially available Hypalon air-curing cements, was capable of developing the necessary inter-laminar and joint-bonded strengths, in addition to meeting all the requirements stated above.

To assure quality and uniformity in the finished product, checking was required throughout the entire process — i.e., checks of the yarn, the woven material, the coating material, the coating process, the thickness and quality control of the coated material, the ply laminating process, and the joints. All had to be continuously checked and double checked.

Quality control was a major undertaking because the inflated structure is composed of 6 acres of single-ply material laminated to make 3 acres of 2-ply patterned panels and contains 31,600 feet of hand-cemented joints which bond the patterned panels one to another to produce the final single-piece radome.

5.5 Radome Fabrication

The double-ply material, coated and laminated in the materials processing plant in Beacon, New York, was shipped to the radome fabricating plant of Birdair Structures, Inc., Buffalo, New York. The coated fabric was processed so that a single batch operation produced a continuous roll of a length in excess of that required to fabricate two of the 168 major gores, each 154 feet long. The length which was selected permitted sampling of material for quality-control purposes from each end and the middle of the roll. The samples thus represented the full range of curing-heat history. Quality control included warp-and-fill strength tests, coating-adhesion tests, and tests for elongation under load.

When the material was received at the radome fabricating plant, test samples were cut from the prescribed locations on the roll and forwarded to the receiving inspection laboratory for testing to confirm the prior tests and to check the weight, gauge, tear resistance, ply adhesion, and water permeability. Lap-joint specimens were also made and subjected to dead loads at 160 degrees Fahrenheit to determine the hot-ply adhesion and cementability of the coatings.

Material passing all tests, including 100 per cent visual inspection, was then ready for the next step, the cutting of gores according to templates. Patterning the gores took place on a flat table. The templates, therefore, included compensation factors to adjust the shape of the gore for transition from a plane surface to a spherical sector. Other factors took into account the differential elongation between the straight and alternating bias plies and that between the warp and fill of each ply under load. All of these compensations were made to insure the sphericity, under the required inflation pressure, which must be attained in the radome to realize adequate stress distribution and utilization of fabric strength.

The gore edges were next processed for stress relief at lap-joint terminations by subjecting them to a proprietary slitting process.

A sufficient number of gores was produced to cover the entire range of gauge and weight within the tolerance specified. To maintain uniformity of electrical characteristics, each gore produced was selectively assigned to various sections of the radome.

Bonding of gores commenced when an optimum number of gores was available for suitable dispersal in the radome and for consecutive cementing of adjacent panels sequenced in accordance with the folding scheme, which anticipated the eventual unfolding and deployment of the radome about the foundation at the erection site.

The edges to be bonded were buffed with a power buffer to expose a virgin surface of the Hypalon coating for manual application of two separate precoats of Hypalon cement. Mating edges of the precoated gores were then laid up on a form especially designed for holding and aligning the adjacent panel edges for application of bonding cement and curing in the desired panel-to-panel relationship to produce sphericity in the finished radome under inflation pressure.

The bonding cement was applied manually and the joints were rolled with a power-roller, the weight and speed of which were designed specifically for the Telstar radome. Joints remained in tension on the form for 3 to 4 hours for final room-temperature cure. Each long meridianal joint required 3 moves or positions on the form to complete bonding of the entire length.

Each move on and off the form had to be made without jeopardizing the anticipated sequence of folding the finished radome for placement in the 8 × 10 × 40-foot crate for delivery. This latter point was important since the complete radome weighs 60,000 pounds and is difficult to move when bonded into one piece. The upper edge of the main panels

was bonded to the crown, the lower edge to the roped clamping bead. The crown, like the main gores, was made up of numerous bonded pieces.

Sample joints were made daily with each batch of cement, using production materials, and processed by production cleaning and curing methods. Samples were identified with each joint made and with each day's production. After cure, the samples were subjected to strength and peel tests for assurance that no unknown factors had inadvertently affected the uniformly high quality of the unit. To meet acceptance requirements, the strength of the joint had to exceed that of the material.

After final cure of each cemented joint, every inch of each side was visually inspected and "prodded" with a peel tester to ascertain that it was properly and securely bonded. The minutest area exhibiting the slightest indication of being questionable for any reason whatsoever was immediately reprocessed.

A precoated tape was cemented over the outer seam of each finished lap joint. The tape adds nothing to the joint strength, but it protects the exposed edge from invasion of the elements and improves the appearance.

A final inspection of all seams was made again while the radome was being folded into the shipping crate.

5.6 Erection

Program schedules did not allow sufficient time for the material development and manufacture of the radome prior to assembly of the antenna structure. To provide environmental protection during the antenna construction period and while development and manufacture of the radome material proceeded, a temporary air-supported structure (construction shelter), also 210 feet in diameter, was designed and fabricated. This structure could be provided relatively quickly and inexpensively because the wind requirements were lower than for the radome, and electrical specifications and long life span were not required. This intermediate structure provided protection for antenna construction and also was used in erecting the final radome.

Use of the construction shelter as an erection aid necessitated the addition of a bulge or blister to the fabric envelope, as seen in Fig. 27. This blister provided clearance for the upper equipment room when the construction shelter was lowered to the position required for radome installation, shown in Fig. 28. Erection of the one-piece, 60,000-pound inflatable radome over the pre-erected 95-foot high antenna and con-
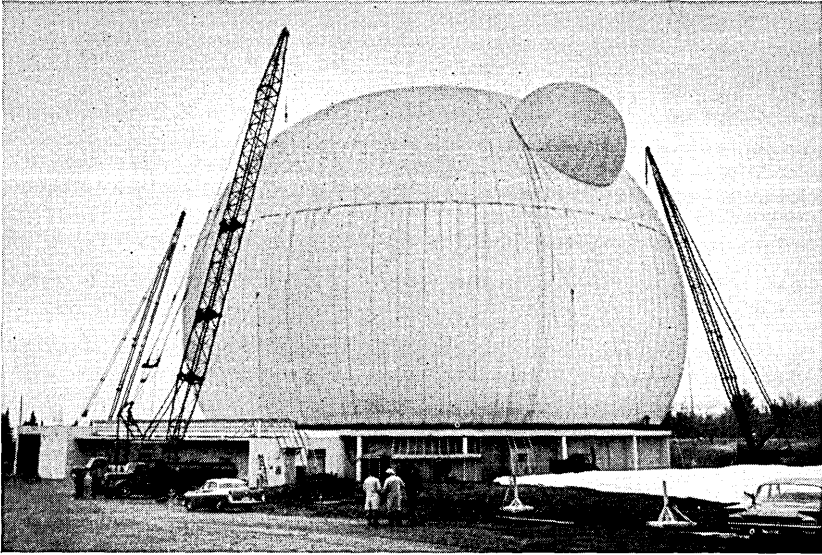
Fig. 27 — Preparing the construction shelter for deflation; permanent radome being unfolded at lower right.
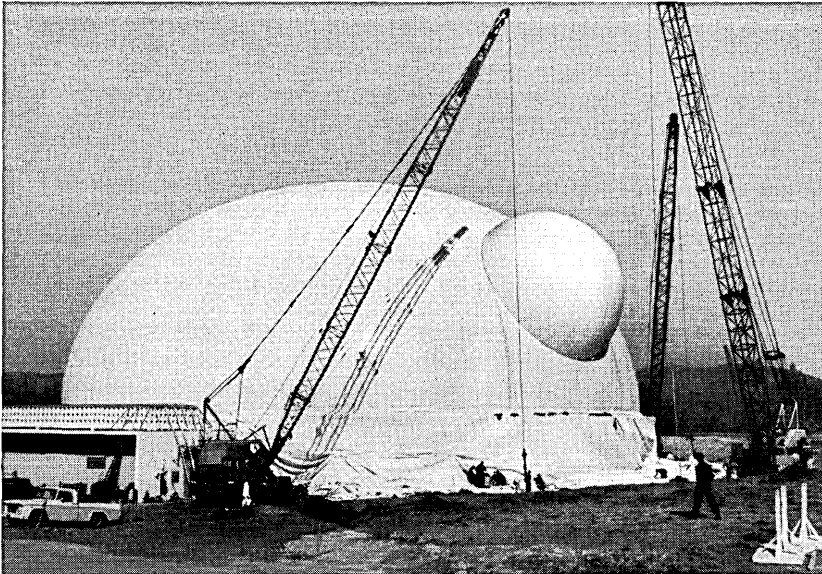
Fig. 28 — Construction shelter lowered and reattached to foundation ring; 160° of the radome is attached to the clamping ring.

struction shelter was a herculean task. Many schemes were considered; some of them included the use of towers, or helicopters or helium bags. Each method considered appeared to be hazardous and expensive or, in many cases, impractical. Strangely enough, the final method utilized air pressure as the main motive force to place the radome over the antenna and construction shelter. The method used is shown in Figs. 27 through 30.

Fig. 27 shows the air-supported construction shelter. The completed antenna has been placed in the stow position inside the construction shelter. In Fig. 28 the temporary construction shelter has been lowered, reattached to its foundation, and reinflated. The radome has been attached to the foundation around 160 degrees of its periphery and has been folded in preparation for lifting the leading edge. In Fig. 29 the leading edge has been lifted over the "blister," and tension is exerted on the leading edge bead by winches at the foundation. Fig. 30 shows

Fig. 29 — Initial raising of the radome over the blister of the construction shelter.
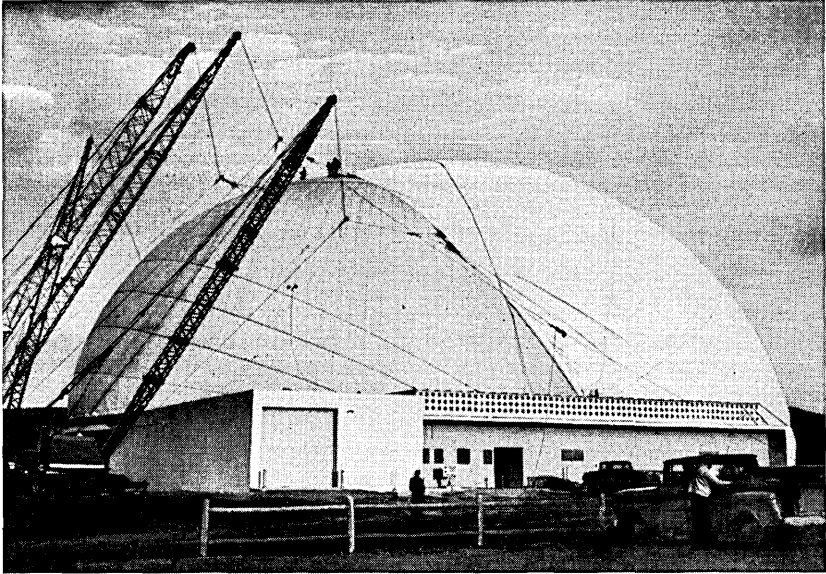
Fig. 30 — Radome being pressurized to allow sliding it over the construction shelter.

crane lines attached to the leading edge of the radome and the radome being pressurized. The pressure reaction on the upper free portion of the radome delivers a net force to the radome toward the cranes and slides the leading edge up and over the inflated construction shelter to engulf it. The radome bead is attached completely and the radome is inflated; the shelter is then removed from within. Fig. 31 shows the final installation with the radome fully inflated.

5.7 Pressurization System

The pressurization system is completely automatic and functions always to keep the radome internally pressurized to a level in excess of the dynamic pressure of the wind.

The system is designed to maintain any one of three pressure levels: $1\frac{1}{2}$ inches of water (0.054 psi) by use of two low-pressure blowers for winds from 0 to 45 miles per hour, 3 inches of water (0.108 psi) by use of one intermediate-pressure blower for winds from 45 to 70 miles per hour, and $5\frac{1}{2}$ inches of water (0.20 psi) by use of two high-pressure blowers for winds from 70 to 100 miles per hour. All blowers operate as
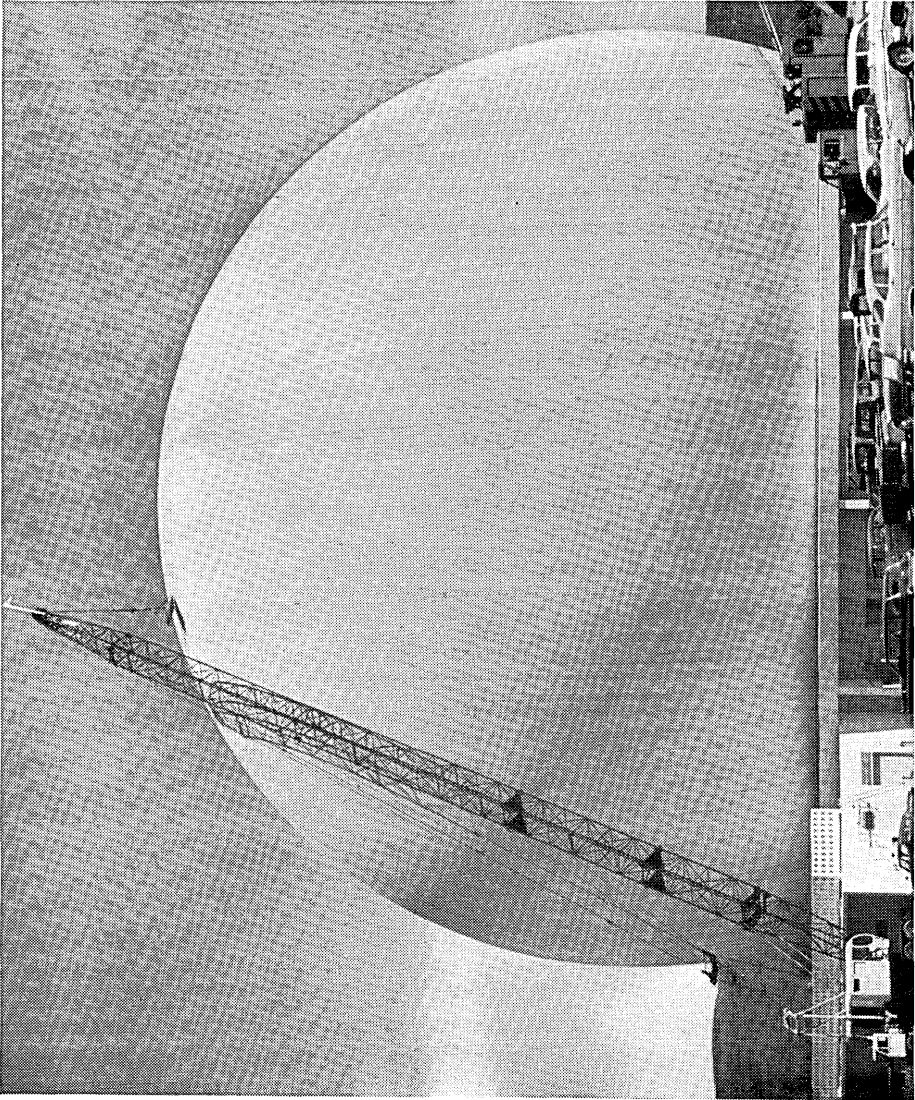
Fig. 31 — Radome installation complete and fully inflated.

a function of the output of an external anemometer and the internal radome pressure. Should a blower fail for any reason, the system is designed so that the next pressure-stage blowers will automatically come on to maintain pressure. For emergency situations, manual remotely controlled vents are provided. Also, high-pressure valves are installed, which will prevent the pressure from ever exceeding the maximum design pressure. All blowers, with the exception of the low-pressure blower, will function automatically from an emergency generator provided at the site.

REFERENCES

1. Hoth, D. F., O'Neill, E. F., and Welber, I., The *Telstar* Satellite System, B.S.T.J., this issue, p. 765.
2. Hines, J. N., Li, Tingye, and Turrin, R. H., The Electrical Characteristics of the Conical Horn-Reflector Antenna, B.S.T.J., this issue, p. 1187.
3. Githens, J. A., Kelly, H. P., Lozier, J. C., and Lundstrom, A. A., Antenna Pointing System: Organization and Performance, B.S.T.J., this issue, p. 1213.
4. Githens, J. A., and Peters, T. R., Digital Equipment for the Antenna Pointing System, B.S.T.J., this issue, p. 1223.
5. Lozier, J. C., Norton, J. A., and Iwama, M., The Servo System for Antenna Positioning, B.S.T.J., this issue, p. 1253.
6. Cook, J. S., and Lowell, R., The Autotrack System, B.S.T.J., this issue, p. 1283.
7. Cornell Aeronautical Laboratory Report, number UB-909-D-2, issued by Rome Air Development Center, March, 1956.

The Electrical Characteristics of the
Conical Horn-Reflector Antenna

By J. N. HINES, TINGYE LI and R. H. TURRIN

(Manuscript received February 11, 1963)

The conical horn-reflector antenna was selected for the satellite communication ground station because of its broadband and low-noise properties. Prior to the construction of the full-size antenna, theoretical and model studies of its electrical characteristics were undertaken. These studies consisted of computing gain and radiation patterns for two modes of excitation, constructing of model antennas and measuring them. Results of these studies are presented in this paper together with results of the measurements of the full size antenna at Andover, Maine.

I. INTRODUCTION

The horn-reflector antenna was selected for the satellite communication ground station because of its broadband and low-noise properties along with certain operational advantages. Two forms of the horn-reflector antenna exist, the pyramidal and the conical. The *pyramidal* horn-reflector antenna has been widely used in the Bell System's microwave radio relay network since its inception at Bell Telephone Laboratories, Holmdel, New Jersey, over 20 years ago.[1] Recently, a large steerable version of this antenna with a 20 × 20-foot aperture[2] was built at Holmdel, New Jersey, and employed in both the Echo and Telstar communications satellite projects. More recently, a very large *conical* horn-reflector antenna was constructed at Andover, Maine, and an identical one at Pleumeur-Bodou, France, for the Telstar communications satellite project. Electrically, the two types of the horn-reflector antenna are very similar, but the conical form possesses certain structural advantages. The suitability and the performance of these antennas are amply reflected in the success of these projects.

Prior to construction of the full-size conical horn-reflector antenna, theoretical and model studies of the electrical characteristics of the antenna were undertaken. These studies consisted of computing gain

and radiation patterns for two modes of excitation, constructing model antennas and measuring them. We present in this paper results of these studies together with results of the measurements of the full-size antenna at Andover, Maine.

II. DESCRIPTION OF ANTENNAS

2.1 General

The geometry of the horn reflector is shown in Fig. 1. The antenna consists of a paraboloidal reflecting section illuminated by a conical horn. The apex of the horn coincides with the focus of the paraboloid,
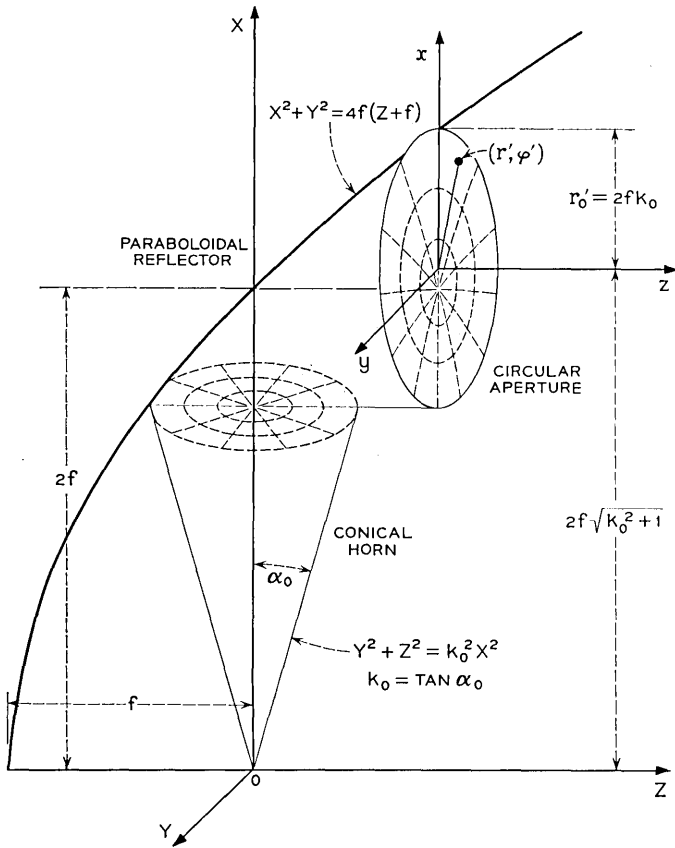

Fig. 1 — Geometry of the conical horn-reflector antenna.

and the axis of the horn is perpendicular to the axis of the paraboloid. The paraboloidal section acts as a combined right-angle reflector and phase corrector for the diverging spherical wave from the conical horn, so that the wave appearing at the circular aperture has a plane wavefront. A cylindrical section encircles the aperture and is attached to both the conical horn and the paraboloidal reflector. This cylindrical aperture shield contributes to the low-noise characteristic of this type of antenna.

The antenna can be excited in as many ways as there are modes in the conical horn.[3,4] For small flare angles the field configurations over the spherical equiphase surfaces are essentially the same as those of a circular waveguide. It is certainly true in this case, where the total flare angle is 31.5 degrees. Therefore, we refer to the dominant wave in the horn as the TE_{11} wave and the second propagating wave as the TM_{01} wave. The former is used for communication and the two are used together for automatic tracking.

2.2 Model Antennas

Two models of the conical horn-reflector antenna were constructed at the Holmdel and at the Whippany, N. J., Bell Laboratories. These are referred to as models one and two, respectively. Photographs of these model antennas are shown in Fig. 2. Model one was employed for extensive TE_{11} mode pattern measurements, while model two was employed primarily to investigate the TM_{01} mode radiation patterns. Neither model was measured to exact scale of the large antenna (in terms of wavelength). Pertinent dimensions and information about the models are given in Table I.

The reflector surface of model one was constructed of $\frac{1}{16}$-inch brass strips which form sectors of the paraboloid. The strips, approximately two inches wide, were bonded to a rigid ribbed frame with a resin cement. The surface accuracy was obtained with the aid of precision templates; the surface was then hand honed. The reflector surface of model two was constructed with the aid of a paraboloidal deep dish which was used as a mold. The dish surface tolerance, therefore, determined the tolerance of the reflector of the model antenna. Both models had aperture shields which were cut in a plane tangent to the cone surface.

2.3 Full Size Antenna

A sketch of the full-size antenna constructed at Andover, Maine, is shown in Fig. 3. The mechanical design of the antenna is reported else-
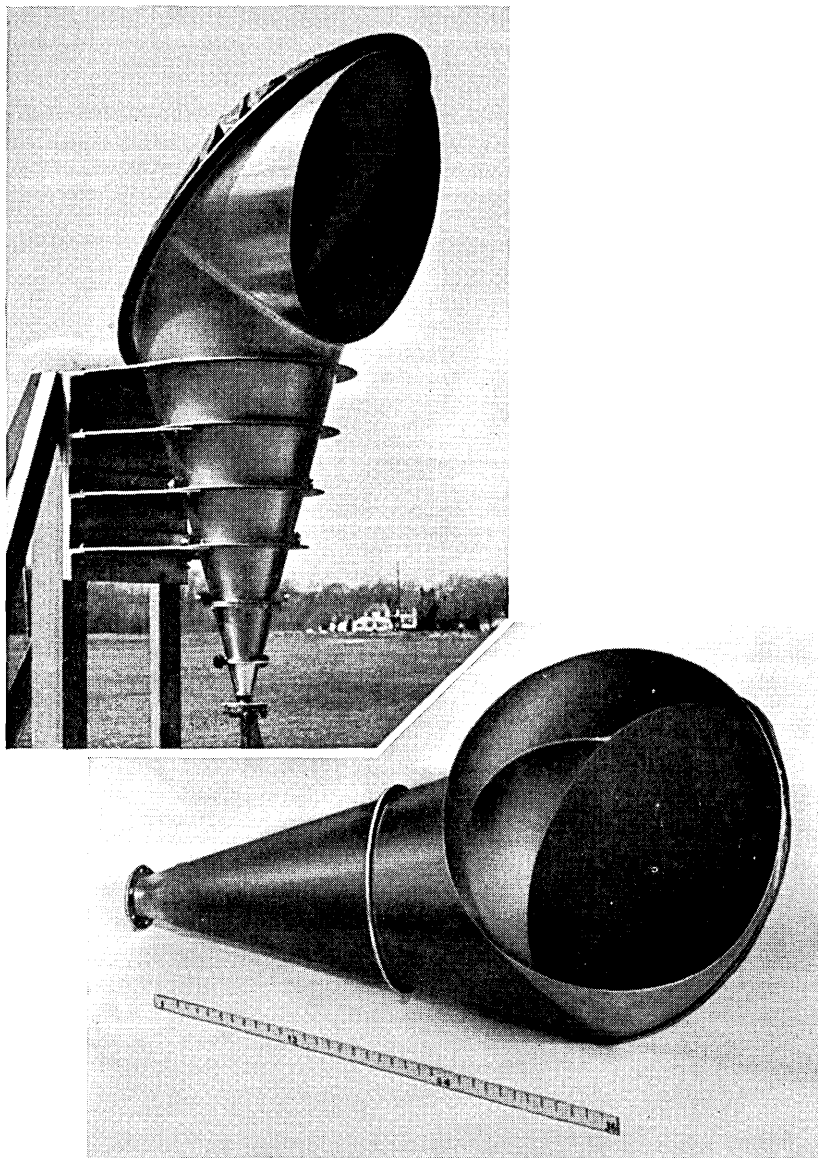
Fig. 2 — Photographs of the model antennas: upper, model one; lower, model two.

TABLE I

	Model One	Model Two
Aperture diameter	27 inches	23 inches
Flare angle	31.5 degrees	27 degrees
Measuring frequency	11.2 kmc	10.0 kmc
Construction material	Brass sheet	Resin-impregnated Fiberglas coated with silver paint
Reflector surface tolerance	±0.010 inch	±0.060 inch

where.[5] Some of the important features of the antenna are given in Table II.

The antenna and support structure rotate about a central pintle bearing on two sets of tracks for azimuth motion. Elevation motion is accomplished by rotating the antenna about its cone axis. A rotary joint is located in the cone section approximately 6 feet from the apex. The entire antenna structure is enclosed in a 210-foot diameter radome.

III. THEORETICAL PATTERN COMPUTATION

The paraboloidal section of the antenna transforms the spherical wave in the conical horn into a plane wave. However, due to the curvature of the reflector and the differences of path length involved, the aperture field configuration is not the same as that in the horn but is somewhat distorted; the field lines tend to crowd toward that edge of the aperture closest to the apex of the horn. The amount of distortion depends upon the flare angle of the horn and becomes more pronounced as the angle increases.

Equations relating coordinates in the cone with coordinates in the aperture plane are derived in Appendix A. In essence, polar coordinates in the cone are transformed into bipolar coordinates in the aperture plane (see Fig. 1). The transformation is therefore conformal.

Once the equations of transformation are known, the linear (x and y) components of the aperture fields for the TE_{11} wave and the TM_{01} wave can be written; these are given in Appendix B. Since the principal electric vector of the TE_{11} wave can be arbitrarily oriented in the aperture plane, we have chosen two principal directions of polarization for our computation. One of these is designated longitudinal polarization, where the principal electric vector in the aperture plane is parallel to the axis of the cone; the other is designated transverse polarization, where the principal electric vector in the aperture plane is orthogonal to the axis

Fig. 3 — Sketch of the full-size conical horn-reflector antenna at Andover, Maine.

TABLE II

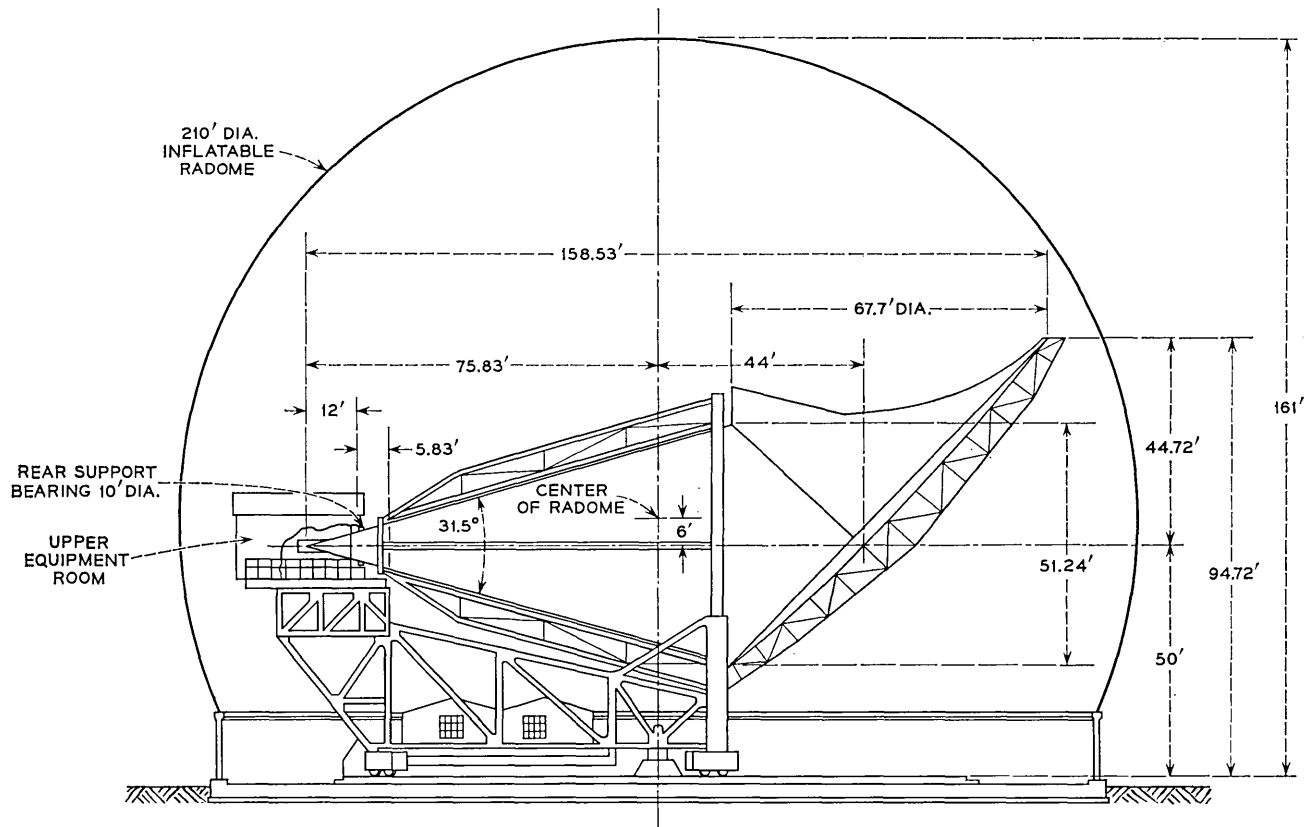| Total flare angle of conical horn	31.5 degrees
Focal length of paraboloid	60 feet
Diameter of aperture	67.7 feet = 280 wavelengths at the receiving frequency of 4079.73 mc and 440 wavelengths at the transmitting frequency of 6389.58 mc.
Aperture area	3600 square feet

of the cone. The TM_{01} wave, however, is axially symmetric in the conical horn and therefore has no principal direction of polarization.

The aperture fields being known, one can calculate the far-field patterns of the antenna near the axis of the beam to good approximation by using the integral[6]

$$g(\theta,\varphi) = \frac{1}{4f^2} \int_0^{2\pi} \int_0^{r_0'} E(r',\varphi') \exp\left[j\beta r' \sin\theta \cos(\varphi - \varphi')\right] r' \, dr' \, d\varphi'$$

$$= \int_0^{2\pi} \int_0^{k_0} E(s,\varphi') \exp\left[jus \cos(\varphi - \varphi')\right] s \, ds \, d\varphi' \tag{1}$$

where $E(r',\varphi')$ represents the components of the aperture field under consideration, $\beta = 2\pi/\lambda$ is the propagation constant of free space, f is the focal length of the paraboloid, $k_0 = \tan \alpha_0 = \tan (\frac{1}{2}$ flare angle of the cone), $r_0' = 2f \, k_0$ is the radius of the aperture, and $u = 2\beta f \sin \theta$. As illustrated in Fig. 1, the polar coordinates $r'(s = r'/2f)$ and φ' are in the aperture plane, and the angles θ and φ refer to the polar (z) axis through the center of the aperture plane.

We have computed the radiation patterns in two principal (longitudinal and transverse) planes and in a 45-degree plane. The longitudinal plane contains the beam and the horn axes; the transverse plane contains the beam axis but is normal to the horn axis (see Fig. 4). Since the aperture fields are symmetric about the longitudinal plane, the integral given by (1) can be reduced further. The reduced integrals for the various cases are listed in Appendix C. These integrals were programmed for numerical integration on an IBM 704 computer.

The computed patterns of the antenna excited by a TE_{11} wave are given in Figs. 5, 6 and 7, which show (as dashed curves) the principal and the cross-polarized patterns for longitudinal and transverse polarizations and in the two principal planes. Because the cross-polarized components of the aperture fields are antisymmetric about the longitudinal plane, the cross-polarized patterns for both polarizations are zero for all angles in that plane and therefore are not shown. Fig. 8 gives the
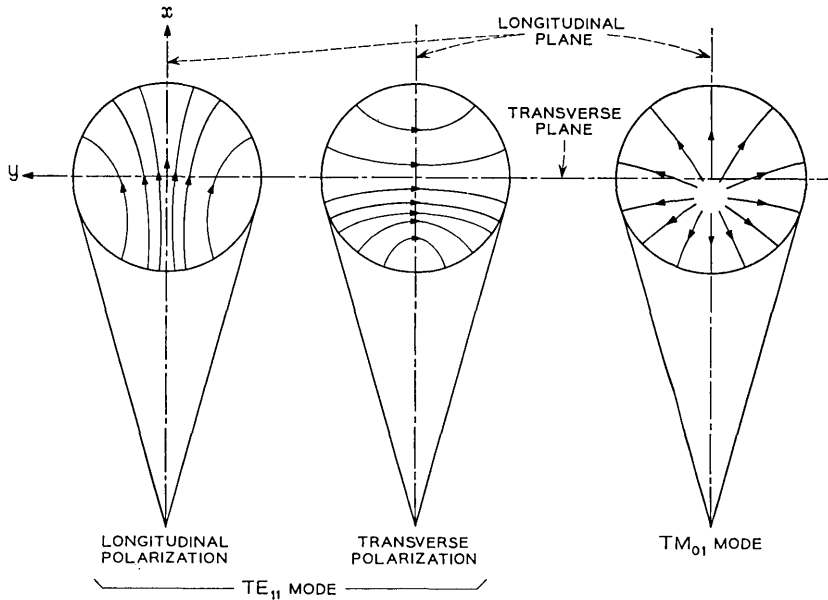
Fig. 4 — Sketch showing the electric field lines in the aperture plane of the antenna for the two modes of excitation. The principal planes in which radiation patterns are calculated and measured are also indicated.

computed radiation patterns of the antenna excited by a TM_{01} wave. Fig. 8(a) shows the pattern in the longitudinal plane for the longitudinal component of the field, and Fig. 8(b) shows the pattern in the transverse plane for the transverse component of the field. The pattern for the transverse component is zero for all angles in the longitudinal plane, and all the lobes of the pattern for the longitudinal component are more than 50 db down in the transverse plane; these patterns therefore are not shown.

The aperture efficiencies of the antenna excited by a TE_{11} wave are calculated to be 0.806 for the longitudinal polarization and 0.807 for the transverse polarization.

The radiation patterns for circular polarization may be calculated by combining the appropriate principal and cross-polarized components of the far field.[2] The computed patterns in the longitudinal and in the transverse planes are shown in Figs. 9 and 10. Due to the presence of the cross-polarized components of the far field in the transverse plane, the circularly polarized radiation patterns in the transverse plane are unsymmetrical; the maximum of the main beam is shifted by 0.97 u off the $u = 0$ axis, which is about one-thirteenth of the 3-db beamwidth. The

direction of this shift is dependent upon the sense of the polarization, the shift being $+0.97\ u$ for one sense and $-0.97\ u$ for the other.

Certain salient features of the antenna are summarized in Table III for linear polarization and in Table IV for circular polarization. For example, at the receiver frequency of 4170 mc the power gain and the half-power beamwidth for circular polarization are 58.17 db and 0.228°, respectively, and at the transmitter frequency of 6390 mc they are 61.86 db and 0.149°, respectively.
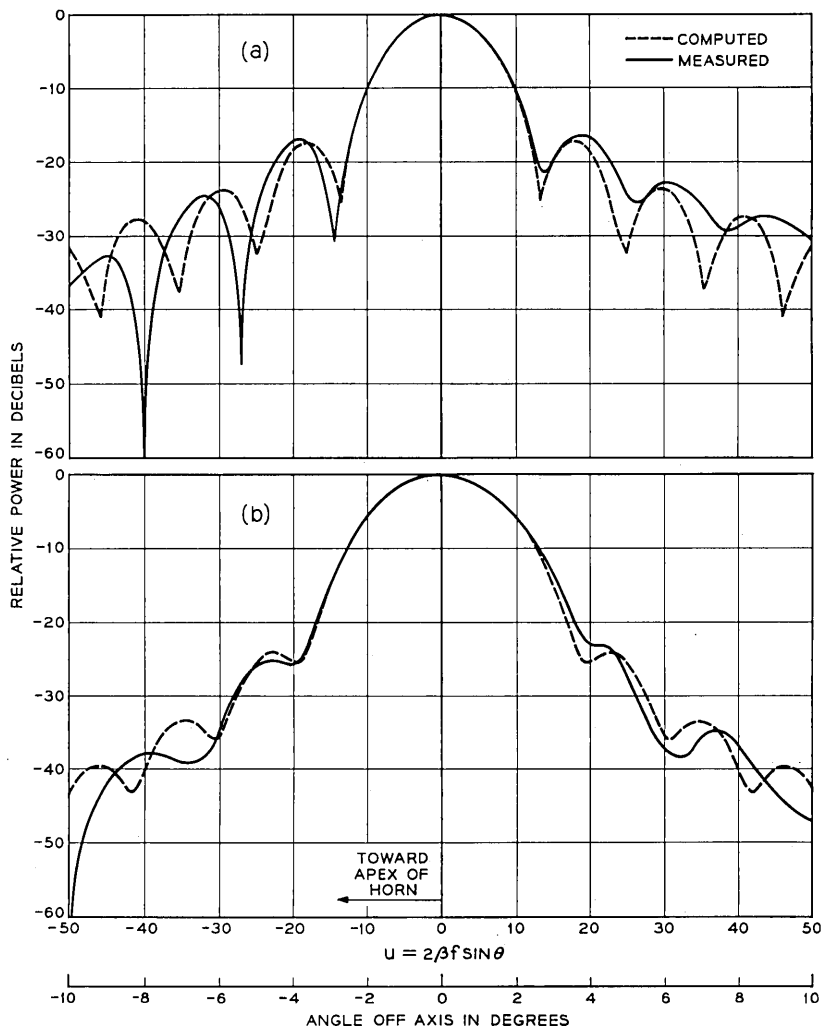
Fig. 5 — Radiation patterns for TE_{11} mode in the longitudinal plane (model one): (a) longitudinal polarization; (b) transverse polarization.
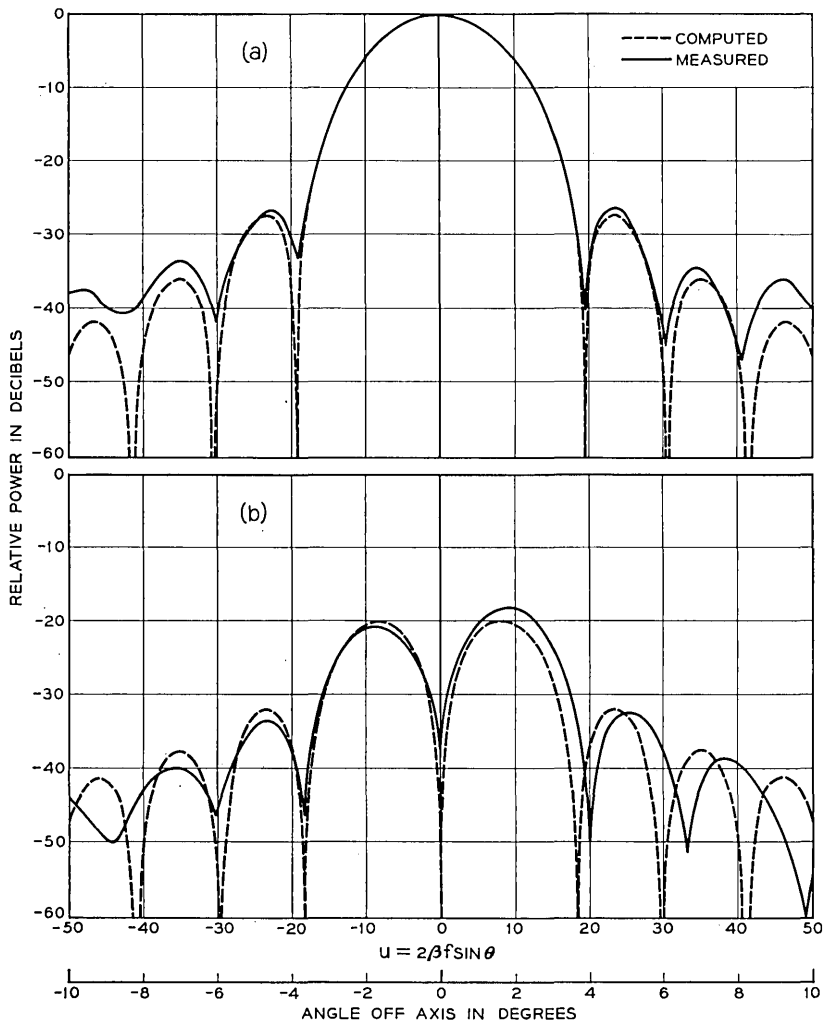
Fig. 6 — Radiation patterns for TE$_{11}$ mode in the transverse plane (model one): (a) principal patterns for longitudinal polarization; (b) cross-polarized patterns for longitudinal polarization.

IV. MEASURED RESULTS

4.1 *Model Antennas*

Far-field radiation pattern measurements for linear polarization were made on both model antennas and showed good agreement with theoretically computed patterns. Both antennas were measured on outdoor

ranges where standard antenna measuring procedure was employed. In particular, TE_{11} mode patterns for both longitudinal and transverse polarizations were measured on model one at 11.2 kmc. The measured patterns in longitudinal and transverse planes are shown as solid curves along with the computed patterns in Figs. 5 through 7. The TM_{01} mode patterns which were important to automatic tracking were measured
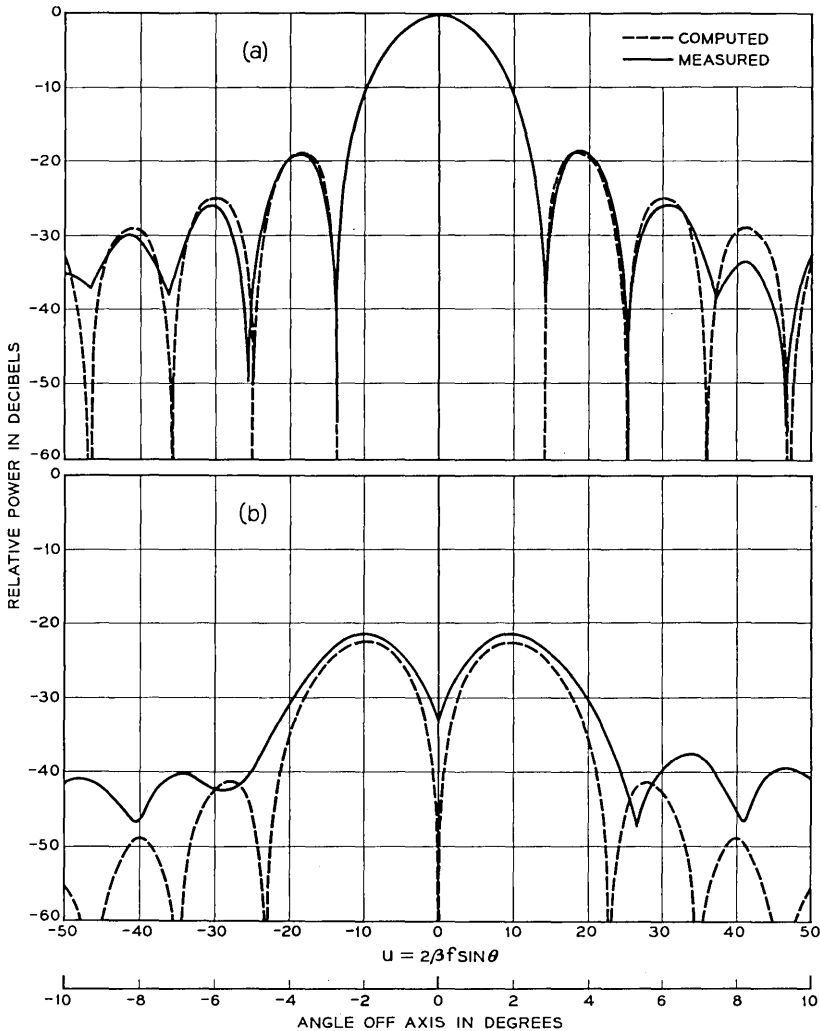
Fig. 7 — Radiation patterns for TE_{11} mode in the transverse plane (model one): (a) principal patterns for transverse polarization; (b) cross-polarized patterns for transverse polarization.
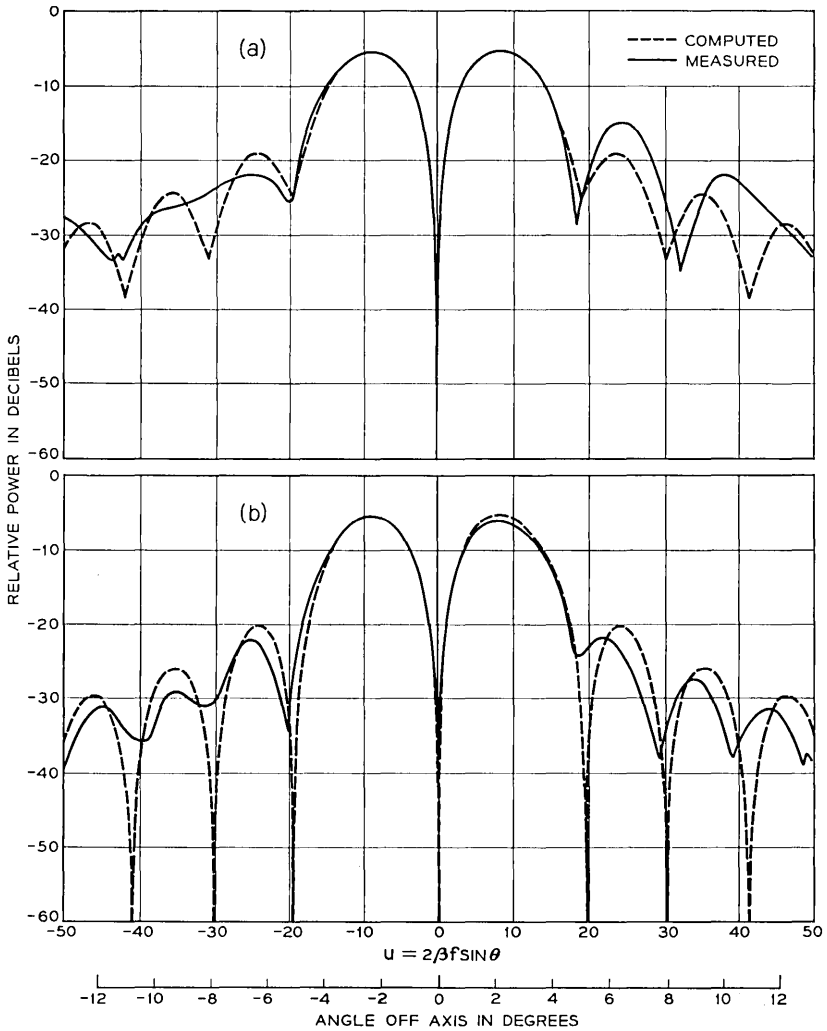
Fig. 8 — Radiation patterns for TM_{01} mode (model two): (a) in the longitudinal plane for the longitudinal component of the aperture field; (b) in the transverse plane for the transverse component of the aperture field.

on model two; these patterns are characterized by nulls in the direction of the TE_{11} beam maxima. The measured and computed patterns for the longitudinal component in the longitudinal plane and for the transverse component in the transverse plane are shown in Fig. 8, where the relative power scales are normalized to the TE_{11} mode beam maxima.

In general, the agreement between measured and computed patterns is good, especially in the region of the main beam and first side lobes. The agreement becomes poor for levels near and below the isotropic level. The discrepancies are probably due to a variety of factors which include higher-order modes, depolarization due to ground roughness, mechanical inaccuracies, and approximations involved in the theoretical analysis.
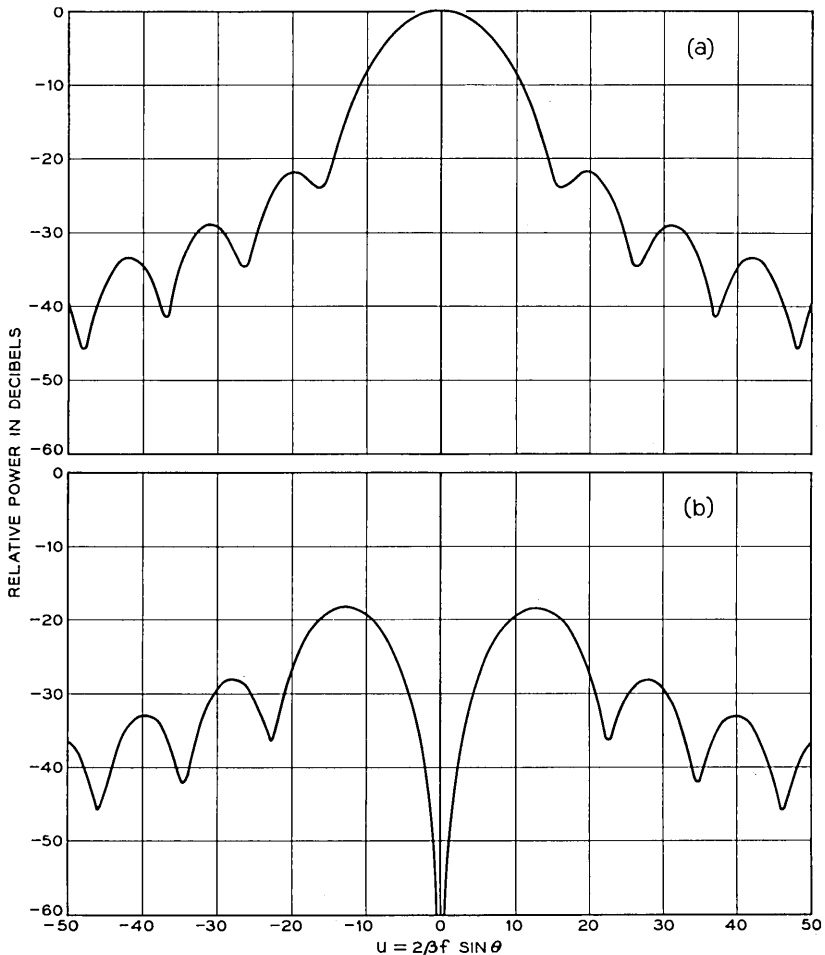
Fig. 9 — Computed circularly polarized radiation patterns for TE_{11} mode in the longitudinal plane: (a) desired sense; (b) undesired sense.
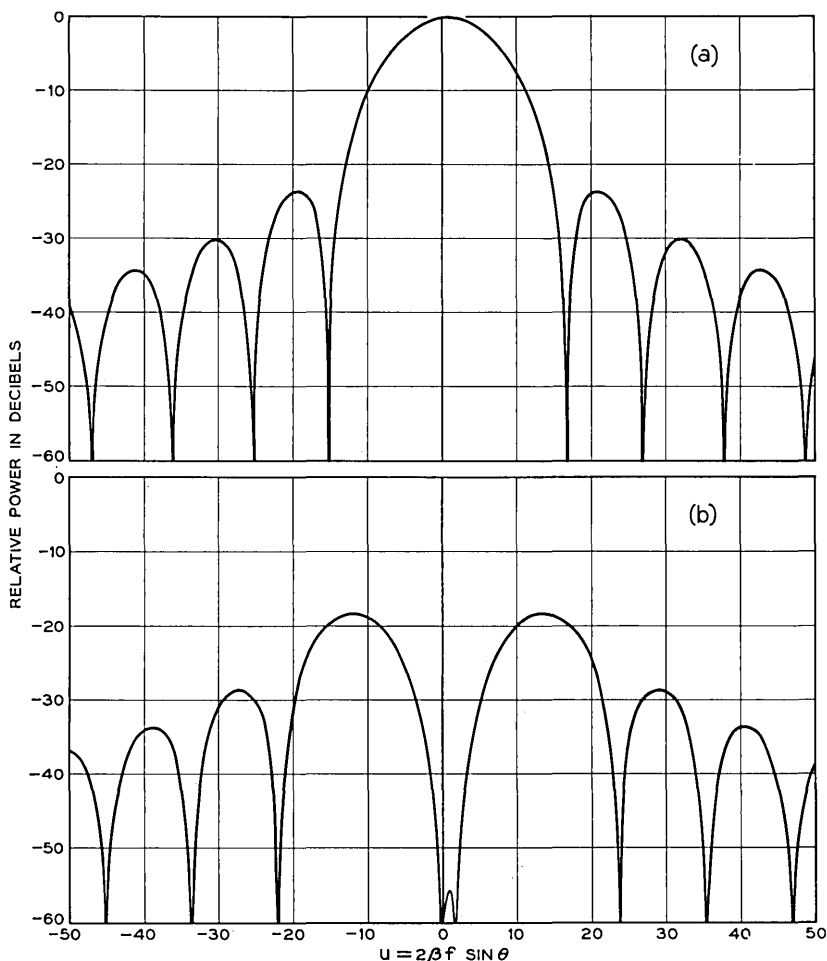
Fig. 10 — Computed circularly polarized radiation patterns for TE$_{11}$ mode in the transverse plane: (a) desired sense; (b) undesired sense.

Gain measurements for both longitudinal and transverse polarization were made on model one, and the difference in gain between the two polarizations was less than the measurement error. The average of the measured gain corresponded to an effective area 1.3 ± 0.2 db less than the actual area. Theoretically the effective area should be 0.94 db less than the actual area.

A characteristic of the horn-reflector antenna is the spillover lobe in

TABLE III — COMPUTED RADIATION CHARACTERISTICS OF THE CONICAL
HORN-REFLECTOR ANTENNA FOR LINEAR POLARIZATION
(FLARE ANGLE = 31.5°)

TE$_{11}$ Mode	Longitudinal Polarization			Transverse Polarization		
	Long. Plane	Trans. Plane	45° Plane	Long. Plane	Trans. Plane	45° Plane
3-db beamwidth ($u = 2\beta f \sin \theta$)	11.2	14.6	12.7	14.0	11.7	12.7
Null beamwidth ($u = 2\beta f \sin \theta$)	27.2	38.4	32.6	39.0	27.4	32.6
Maximum cross-polarization (db)	$-\infty$	-20.0	-17.7	$-\infty$	-22.3	-17.5
First side-lobe level (db)	-17.2	-27.0	-22.1	-24.1	-18.2	-23.1
2nd side-lobe level (db)	-23.5	-35.8	-29.6	-33.4	-24.5	-29.6
3rd side-lobe level (db)	-27.5	-41.8	-34.1	-39.4	-28.5	-33.6

TM$_{01}$ Mode	Longitudinal Component			Transverse Component		
	Long. Plane	Trans. Plane	45° Plane	Long. Plane	Trans. Plane	45° Plane
Principal-lobe level* (db)	-5.5	-52.7	-8.5	$-\infty$	-5.7	-8.7
Null level* (db)	-52.7		-52.7		$-\infty$	$-\infty$
Width between principal lobes ($u = 2\beta f \sin \theta$)	17.0		17.0		17.0	17.0
Null width at 20 db below peak of principal lobe ($u = 2\beta f \sin \theta$)	1.1		1.1		1.1	1.1
First side-lobe level* (db)	-19.0		-22.6		-20.5	-22.9

* Relative to major-lobe level of TE$_{11}$ mode.

the longitudinal plane with longitudinal polarization caused by diffraction over the edge of the reflector.[2] This spillover lobe in the radiation pattern was measured on model one and found to be at +68° with a level of −35 db from the main beam. The spillover does not occur for transverse polarization because of the taper in the aperture field.

TABLE IV — COMPUTED RADIATION CHARACTERISTICS OF THE CONICAL
HORN-REFLECTOR ANTENNA FOR CIRCULAR POLARIZATION
(FLARE ANGLE = 31.5°)

TE$_{11}$ Mode	Longitudinal Plane	Transverse Plane
3-db beamwidth ($u = 2\beta f \sin \theta$)	12.7	12.8
Null beamwidth ($u = 2\beta f \sin \theta$)	33.6	32.4
Beam shift ($u = 2\beta f \sin \theta$)	0	0.97
Maximum level of undesired sense of polarization (db)	-18.3	-18.2
First side-lobe level (db)	-21.7	-23.6
2nd side-lobe level (db)	-28.9	-30.1
3rd side-lobe level (db)	-33.3	-34.3

4.2 *Full-Size Antenna*

4.2.1 *General*

A series of measurements and tests were conducted during February, March, and April, 1962, on the antenna at Andover, Maine. These consisted of boresight, gain, polarization and pattern measurements.

The boresight antenna,* located atop a 250-foot tower on Black Mountain 4.6 miles away, was used to illuminate the horn reflector during these measurements. The beamwidth of the boresight antenna and its height above ground were selected so that the maximum level of the ground reflected signal received by the horn reflector would be 45 db or more below the maximum direct signal when the horn reflector is on boresight. Actual measurements indicated that the reflected signal was more than 50 db below the direct signal. Evidence that the incident field was quite uniform in the azimuth plane was obtained when a comparison was made between patterns measured in the normal and plunged positions (i.e., both azimuth and elevation reversed from normal position). The comparison revealed that the two sets are nearly identical; that is, the patterns "turned over" with the antenna.

4.2.2 *Boresighting*

The electrical boresight axis is defined as the direction of the null in the center of the TM_{01} pattern used in the autotrack system. As the initial step in the calibration of antenna pointing, this axis was located and the angle data readouts were set to the boresight antenna coordinates.

The distance to the boresight antenna is approximately 24,000 feet, which is about 37 per cent shorter than that required for the conventional phase deviation of $\pi/8$ radian across the aperture. The effect of boresighting at a reduced range was investigated theoretically.[7] It was found that at this range the null in the TM_{01} pattern shifts in azimuth 0.007 degree away from the aperture normal toward the apex of the horn feed section.

By using a technique of plunging the antenna first in azimuth and then in elevation so as to again point at the boresight antenna, it is possible to determine the precise electrical pointing direction of the antenna with respect to the rotational axes. This was done, and the results of the tests

---

* The boresight antenna is a two-foot diameter paraboloidal reflector illuminated by a circularly polarized feed. It has a power gain of 25 db and an axial ratio of less than 2 db at 4080 mc.

can be summarized as follows. The magnitude of the parallax with respect to the azimuth axis obtained from the geometry of the ground station is 0.106 degree (the aperture is offset from the axis of azimuthal rotation). Boresighting at the reduced range decreases this angle by 0.007 degree so that the magnitude of the electric azimuth parallax should be 0.099 degree. However, the average measured electrical parallax was 0.123 ± 0.005 degree. This indicates that there is a slight outward pitch of the reflector surface which is equal to one-half this amount, or 0.012 degree, when the antenna is pointing at the boresight tower. The surveyed elevation angle to the boresight tower is 3.960 degrees and the average electrical elevation angle measured by plunging was 3.990 ± 0.005 degrees. The difference indicated an 0.030 ± 0.005 degree droop of the reflector at low elevation. These, along with more recent star-tracking measurements, generally corroborate the sag predicted by structural analysis.

4.2.3 Gain Measurements

Because time was at a premium, the usual technique of measuring the vertical distribution of the incident field with the standard gain horn to determine its average value was not employed in measuring the power gain of the horn-reflector antenna. Instead the standard horn was placed at a convenient point at the edge of the roof of the upper equipment room (see Fig. 3). The measured value of power gain was 57.8 ± 0.3 db. To lend support to this measurement, the directivity of the horn reflector was determined by integrating its measured radiation patterns. The value so obtained is 57.6 ± 0.2 db. These results are to be compared with the theoretical value of 57.97 db. The measurements were made at a frequency of 4080 mc.

4.2.4 Radiation Pattern Measurements

Radiation pattern measurements were made for the TE_{11} mode and the TM_{01} mode at 4080 mc with the antenna in the position in which it is normally operated. The horizontal and vertical components of the circularly polarized TE_{11} field excited in the circular feed section at the apex of the conical horn were measured. The patterns are called the $(TE_{11})_x$ and $(TE_{11})_r$ patterns respectively, because they are measured at the horn apex, which does not rotate in elevation with the rest of the antenna. For small changes in elevation about this position, however, $(TE_{11})_x$ essentially corresponds to longitudinal polarization, and $(TE_{11})_r$ to transverse polarization (see Fig. 4). The TM_{01} patterns were measured

in the same manner. All of these measurements were repeated with the antenna in the plunged position. The normal position patterns are shown and compared with the computed patterns in Figs. 11 to 13. The dashed curves in the figures represent computed patterns of the far field for linear polarization with the exception of the one in Fig. 13(a), which represents the computed pattern in the longitudinal plane at the reduced range.[7]

Agreement between measured and predicted patterns over the sector of the major lobes is excellent and is fairly good in the side-lobe regions. Some discrepancy is to be expected in the side-lobe regions, however, since the measured patterns include the effect of the cross-polarized response of the antenna (the incident field was circularly polarized) while the computed points include only the linearly polarized response of the antenna. In addition, the patterns were measured at a reduced range.
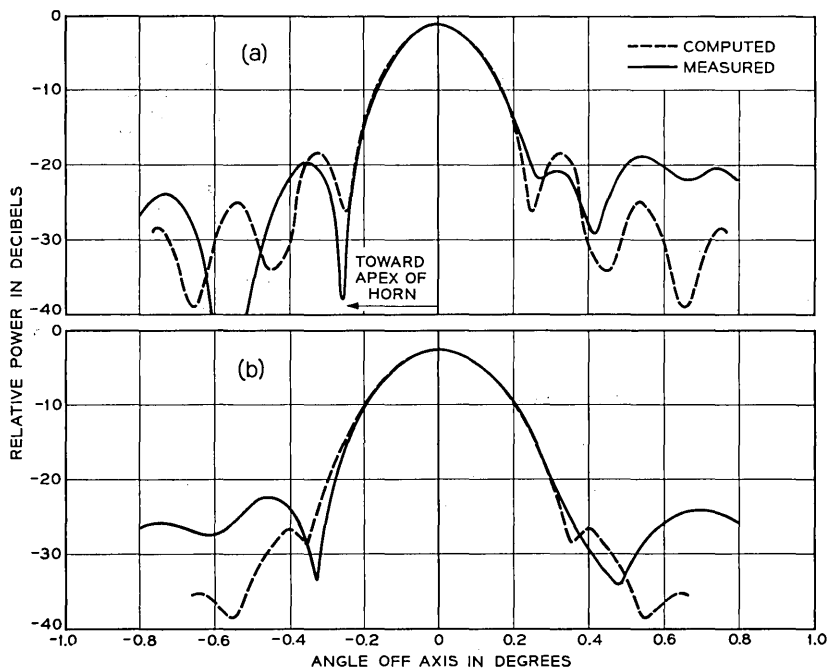
Fig. 11 — Principal radiation patterns of the full size antenna for TE_{11} mode in the longitudinal plane: (a) longitudinal polarization $(TE_{11})_X$; (b) transverse polarization $(TE_{11})_Y$. (The dashed curves are computed far-field patterns.)
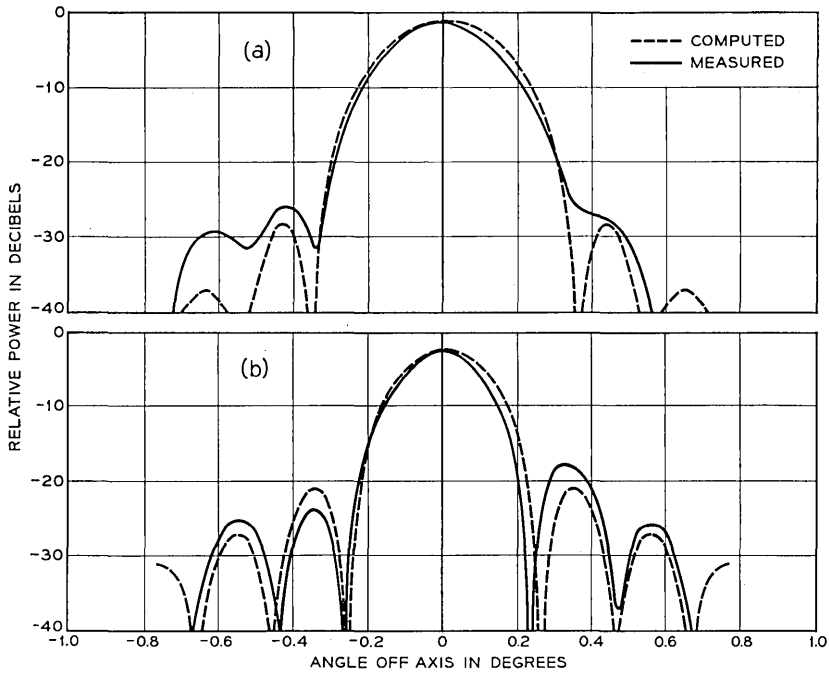
Fig. 12 — Principal radiation patterns of the full size antenna for TE_{11} mode in the transverse plane: (a) longitudinal polarization $(TE_{11})_X$; (b) transverse polarization $(TE_{11})_Y$. (The dashed curves are computed far-field patterns.)

The patterns described above were measured through a construction shelter before the permanent radome was installed. A comparison with those measured later through the permanent radome disclosed no measurable change in the patterns.

V. ACKNOWLEDGMENTS

It is a pleasure to acknowledge the efforts of R. R. Redington for assistance in the construction and adjustment of the boresight antenna and in the measurements on the full-size horn-reflector antenna. E. M. Elam, J. H. Hammond and E. C. Snyder also assisted in the various measurements. Mrs. C. L. Beattie programmed the computer for the pattern and gain computations. The aid and encouragement of A. B. Crawford, J. S. Cook and R. Lowell in these efforts are also acknowledged. In addition, the patience of the people in the servo-control group
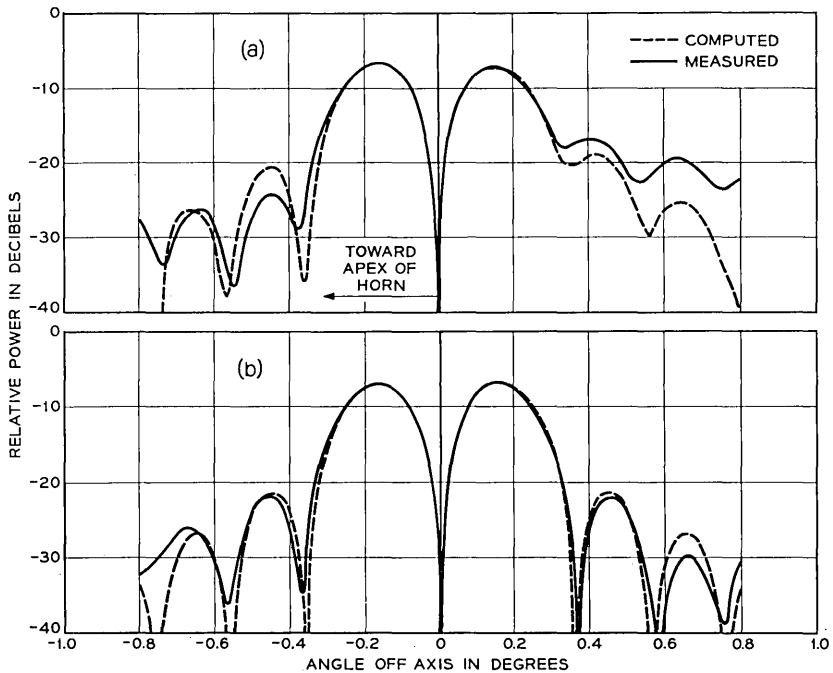
Fig. 13 — Radiation patterns of the full size antenna for TM_{01} mode: (a) in the longitudinal plane for the longitudinal component of the aperture field (the dashed curve is computed for the reduced range); (b) in the transverse plane for the transverse component of the aperture field (the dashed curve is the computed far-field pattern).

and their care exercised in moving the antenna during measurements are greatly appreciated.

APPENDIX A

The Geometry of the Antenna

The geometry of the conical horn-reflector antenna is given in Fig. 1. The apex of the conical section, which is also the focus of the paraboloidal section, is taken to be the origin of the coordinate system (X, Y, Z), and the axis of the cone is taken to be coincident with the X axis.

The equation of a cone coaxial with the conical horn is

$$Y^2 + Z^2 = k^2 X^2, \tag{2}$$

where $k = \tan \alpha$ and $2\alpha = $ flare angle of the cone. The equation of the paraboloid is

$$X^2 + Y^2 = 4f(Z + f), \tag{3}$$

where f is the focal length. Eliminating Z between (2) and (3) gives the equation for the projection of intersection of cone and paraboloid in the X-Y plane. This equation is

$$(X - 2f\sqrt{k^2 + 1})^2 + Y^2 = 4f^2k^2, \tag{4}$$

which is a circle with center at $(2f\sqrt{k^2 + 1}, 0)$ and radius equal to $2fk$. Since (2) also represents circles in the Y-Z plane, we see that the paraboloidal reflector transforms a family of concentric circles in the Y-Z plane into a family of nonconcentric circles in the X-Y plane. Similarly, we can show that a family of radial lines in the Y-Z plane, after reflection from the paraboloid, transforms into a family of circles in the X-Y plane which are described by

$$X^2 + (Y - 2f \cot \eta)^2 = 4f^2 \operatorname{cosec}^2 \eta, \tag{5}$$

where $\eta = \arctan (Y/Z) = $ constant defines the family of radial lines in the Y-Z plane. Equations (4) and (5) describe a set of orthogonal coordinate systems in the X-Y plane. This is the familiar bipolar coordinate system.[8] Therefore, the transformation from the set of polar coordinates in the Y-Z plane into the set of bipolar coordinates in the X-Y plane is a conformal transformation.

APPENDIX B

The Aperture Field

The radial and the circular components of the field in the conical horn are given by

$$E_\rho = \frac{1}{\kappa\rho} J_1(\kappa\rho) \cos \eta \tag{6}$$

$$E_\eta = -\tfrac{1}{2}[J_0(\kappa\rho) - J_2(\kappa\rho)] \sin \eta \tag{7}$$

for TE_{11} mode, longitudinal polarization,

$$E_\rho = \frac{1}{\kappa\rho} J_1(\kappa\rho) \sin \eta \tag{8}$$

$$E_\eta = \tfrac{1}{2}[J_0(\kappa\rho) - J_2(\kappa\rho)] \cos \eta \tag{9}$$

for TE$_{11}$ mode, transverse polarization, and

$$E_\rho = J_1 (\gamma\rho) \tag{10}$$

$$E_\eta = 0 \tag{11}$$

for TM$_{01}$ mode. In the above equations $\rho^2 = X^2 + Z^2$, $\tan \eta = Y/Z$ and J_n is a Bessel function of the first kind and nth order. The arguments of the Bessel function $\kappa\rho$ and $\gamma\rho$ are equal to 1.841184 (k/k_0) and 2.404826 (k/k_0), respectively, where $k_0 = \tan \alpha_0$ and $2\alpha_0$ is the total flare angle of the horn.

After reflection from the paraboloidal section, these polar components of the field transform conformally into the corresponding bipolar components in the aperture plane. E_η will lie along the family of circles given by (4) and E_ρ will lie along the orthogonal family of circles given by (5). Since the bipolar coordinate system is a curvilinear system, it is necessary to obtain the linear components of the field before radiation patterns can be computed.

For the purpose of computing radiation patterns, it is convenient to take the center of the aperture as the origin of the coordinate system. Now, the periphery of the aperture is a circle given by (4) with k replaced by k_0. Letting the center of the circular aperture be the origin of a new coordinate system in which

$$x = X - 2f\sqrt{k_0^2 + 1} \quad \text{and} \quad y = Y,$$

equation (4) becomes

$$(x + 2f\sqrt{k_0^2 + 1} - 2f\sqrt{k^2 + 1})^2 + y^2 = 4f^2k^2. \tag{12}$$

This equation gives the direction of E_η in the aperture plane. The angle, ψ_η, which E_η makes with the x axis is given by

$$\tan \psi_\eta = \frac{dy}{dx} = -(x + 2f\sqrt{k_0^2 + 1} - 2f\sqrt{k^2 + 1})/y. \tag{13}$$

Since E_ρ is perpendicular to E_η, the angle ψ_ρ between E_ρ and the x axis is given by

$$\tan \psi_\rho = -\left(\frac{dy}{dx}\right)^{-1} = -\cot \psi_\eta. \tag{14}$$

Knowing the angles ψ_η and ψ_ρ, we can now write expressions for the linear components of the aperture field; they are:

$$E_x = \frac{2f}{d} [E_\rho \cos \psi_\rho + E_\eta \cos \psi_\eta] \tag{15}$$

and

$$E_y = \frac{2f}{d} [E_\rho \sin \psi_\rho + E_\eta \sin \psi_\eta].$$ (16)

where $d = f + (X^2 + Y^2)/4f$ is the distance from the apex of the horn to the reflector. The factor $2f/d$, therefore, takes into account the attenuation due to path-length difference for the spherical wave in the conical section of the antenna.

APPENDIX C

List of Integrals Used in Pattern Computation

C.1 TE_{11} *Mode*

(*i*) Longitudinal plane ($\varphi = 0°$ and $180°$)
  (a) Principal patterns

$$\begin{matrix} g_L(u) \\ \\ g_T(u) \end{matrix} = \int_0^\pi \int_0^{k_0} \begin{matrix} {}_L E_x(s,\varphi') \\ \\ {}_T E_y(s,\varphi') \end{matrix} \exp (jus \cos \varphi')s \, ds \, d\varphi'$$

  (b) Cross-polarized patterns

$$\begin{matrix} g_L(u) \\ = 0 \\ g_T(u) \end{matrix}$$

(*ii*) Transverse plane ($\varphi = 90°$ and $270°$)
  (a) Principal patterns

$$\begin{matrix} g_L(u) \\ \\ g_T(u) \end{matrix} = \int_0^\pi \int_0^{k_0} \begin{matrix} {}_L E_x(s,\varphi') \\ \\ {}_T E_y(s,\varphi') \end{matrix} \cos (us \sin \varphi')s \, ds \, d\varphi'$$

  (b) Cross-polarized patterns

$$\begin{matrix} g_L(u) \\ \\ g_T(u) \end{matrix} = \int_0^\pi \int_0^{k_0} \begin{matrix} {}_L E_y(s,\varphi') \\ \\ {}_T E_x(s,\varphi') \end{matrix} \sin (us \sin \varphi')s \, ds \, d\varphi'$$

(*iii*) 45° plane ($\varphi = 45°$ and 225°)

   (a) Principal patterns

$$
\begin{aligned}
g_L(u) & \\
& = \int_0^\pi \int_0^{k_0} \frac{{}_L E_x(s,\varphi')}{} \cos\left(\frac{us}{\sqrt{2}} \sin \varphi'\right) \exp\left(j \frac{us}{\sqrt{2}} \cos \varphi'\right) s \, ds \, d\varphi' \\
g_T(u) & \qquad\qquad\qquad {}_T E_y(s,\varphi')
\end{aligned}
$$

   (b) Cross-polarized patterns

$$
\begin{aligned}
g_L(u) & \\
& = \int_0^\pi \int_0^{k_0} \frac{{}_L E_y(s,\varphi')}{} \sin\left(\frac{us}{\sqrt{2}} \sin \varphi'\right) \exp\left(j \frac{us}{\sqrt{2}} \cos \varphi'\right) s \, ds \, d\varphi' \\
g_T(u) & \qquad\qquad\qquad {}_T E_x(s,\varphi')
\end{aligned}
$$

In the above equations the subscripts L and T denote longitudinal and transverse polarizations, respectively.

C.2 TM_{01} Mode

  (*i*) Longitudinal plane ($\varphi = 0°$ and 180°)

   (a) Longitudinal component pattern

$$
g_{\mathrm{TM}}(u) = \int_0^\pi \int_0^{k_0} E_x(s,\varphi') \exp\left(jus \cos \varphi'\right) s \, ds \, d\varphi'
$$

   (b) Transverse component pattern

$$
g_{\mathrm{TM}}(u) = 0
$$

  (*ii*) Transverse plane ($\varphi = 90°$ and 270°)

   (a) Longitudinal component pattern

$$
g_{\mathrm{TM}}(u) = \int_0^\pi \int_0^{k_0} E_x(s,\varphi') \cos\left(us \sin \varphi'\right) s \, ds \, d\varphi'
$$

   (b) Transverse component pattern

$$
g_{\mathrm{TM}}(u) = \int_0^\pi \int_0^{k_0} E_y(s,\varphi') \sin\left(us \sin \varphi'\right) s \, ds \, d\varphi'
$$

  (*iii*) 45° plane ($\varphi = 45°$ and 225°)

   (a) Longitudinal component pattern

$$
g_{\mathrm{TM}}(u) = \int_0^\pi \int_0^{k_0} E_x(s,\varphi') \cos\left(\frac{us}{\sqrt{2}} \sin \varphi'\right) \exp\left(j \frac{us}{\sqrt{2}} \cos \varphi'\right) s \, ds \, d\varphi'.
$$

(b) Transverse component pattern

$$g_{\text{TM}}(u) = \int_0^\pi \int_0^{k_0} E_y(s,\varphi') \sin\left(\frac{us}{\sqrt{2}}\sin\varphi'\right) \exp\left(j\frac{us}{\sqrt{2}}\cos\varphi'\right) s\,ds\,d\varphi'.$$

REFERENCES

1. Friis, H. T., and Beck, A. C., U. S. Patent 2,236,393, filed March 1, 1939, issued March 25, 1941.
2. Crawford, A. B., Hogg, D. C., and Hunt, L. E., A Horn-Reflector Antenna for Space Communication, B.S.T.J., **40**, July, 1961, pp. 1095–1116.
3. Buchholz, H., The Propagation of Electromagnetic Waves in a Conical Horn, Ann. d. Physik, **37**, February, 1940, pp. 173–225.
4. Schorr, M. G. and Beck, F. J., Jr., Electromagnetic Field of the Conical Horn, J. Appl. Phys., **21**, August, 1950, pp. 795–801.
5. Dolling, J. C., Blackmore, R. W., Kindermann, W. J., and Woodard, K. B., The Mechanical Design of the Conical Horn-Reflector Antenna and Radome, B.S.T.J., this issue, p. 1137.
6. Silver, S., *Microwave Antenna Theory and Design*, McGraw-Hill, New York, 1949, p. 192.
7. Lange, J., unpublished work.
8. Stratton, J. A., *Electromagnetic Theory*, McGraw-Hill, New York, 1941, p. 55.

Antenna Pointing System: Organization and Performance

By J. A. GITHENS, H. P. KELLY, J. C. LOZIER
and A. A. LUNDSTROM

This paper is a description of the antenna pointing system used in the satellite ground station at Andover, Maine. It is an introduction to the following five papers in this issue, which describe and discuss in some detail the various major parts and features of the antenna pointing system. In order that the antenna have sufficient gain for the Telstar experiment, it was necessary that it have a "pencil" beam of about $\frac{1}{5}$ degree in diameter. This requires an antenna pointing system of high accuracy. The equipment and methods required to achieve this accuracy are outlined.

I. OBJECTIVES

At the Andover, Maine, satellite ground station the 3600-square-foot aperture horn-reflector antenna[1,2] concentrates the microwave energy in a very narrow beam. This is needed to achieve adequate signal-to-noise ratio in the broadband communications channel provided by the system. Accordingly, it is necessary to provide means for pointing the antenna at the Telstar satellite. The guiding objectives used in engineering and constructing the antenna pointing system are briefly described here.

A demonstration of reliable satellite communications was a primary goal. This required acquisition and tracking of the satellite to an accuracy which would hold the resulting maximum loss in antenna gain to values acceptable to the communication link. It required a system with versatility sufficient to cope with a combination of unfavorable conditions such as deviations of the satellite from the expected orbit, variations in refraction effects, antenna misalignments, and equipment malfunction.

A basic objective of a communications satellite system is reliability. In the current state of the art (weight limitations, etc.) this can be best

realized by designing the satellite so that it will be as rugged as possible and therefore relatively simple. The ground station, on the other hand, may have considerable complexity since it can be maintained and improved.

It was decided that the system must have sufficient flexibility for experiments to evaluate different methods of acquiring and tracking satellites. This required facilities for the recording, reduction, and evaluation of large amounts of pointing data.

1.1 *System Description*

The Telstar antenna pointing system performs two primary functions: (*i*) it establishes the communication connection by causing the horn-reflector communication antenna to acquire and continuously track the satellite throughout a communications pass, and (*ii*) it provides means for determining the satellite orbit so that pointing instructions may be generated for future passes to help meet the requirements of the first function. The most difficult problem encountered in providing these functions is one of accuracy due to the needle-like antenna patterns of the 3600-square-foot aperture of the communications antenna. The beam is nearly circular, with an angular diameter of 0.165° at the transmitting frequency of 6390 mc and 0.225° at the receiving frequency of 4170 mc when measured 3 db down from the beam pattern maximum. Furthermore, the requirement placed on the antenna pointing system is that mispointing of the antenna should contribute no more than 1 db of loss in carrier-to-noise ratio in the communications path. A 1-db decrease in carrier-to-noise ratio would be produced by pointing errors which produce approximately 1-db decrease in the 4170-mc down path transmission. A 1-db contour on the antenna pattern at 4170 mc would approximate a circle of 0.06° radius. Therefore, the maximum tolerable pointing error in antenna azimuth or elevation angle is ±0.06°. To meet this requirement, one must first know where the satellite is with commensurate accuracy and be able to calibrate and control the horn antenna precisely.

A block diagram of the antenna pointing system is shown in Fig. 1. Before a discussion of the operation of this system is undertaken, consider the characteristics of each block. All of the frequencies shown are approximate.

Satellite:[3] The satellite is not part of the pointing system, but it plays an important role in antenna pointing by radiating two CW beacons for tracking purposes, one at 136 mc and the other at 4080 mc. The 136-mc beacon is radiated continuously, but the 4080-mc beacon is
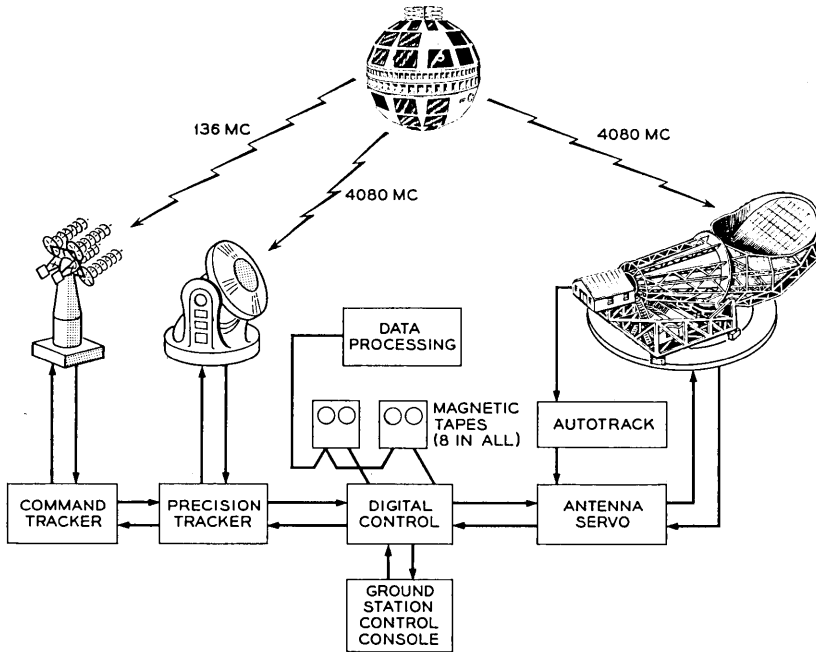
Fig. 1 — Block diagram of pointing system.

transmitted only when the traveling-wave tube amplifier in the satellite is turned on. In addition to its function in the antenna pointing system, the 136-mc beacon also permits the satellite to be tracked by the world-wide NASA Minitrack network. The 4080-mc microwave beacon provides a means of tracking using frequencies in the common-carrier band.

Command Tracker:[4] Tracking of the 136-mc beacon in the satellite is accomplished by the command tracker, a quad-helix antenna having autotrack capabilities. It has a 20° beam diameter and is capable of tracking with an accuracy of about ±1°. In addition to its tracking role, the command tracker also receives telemetry information, which appears as modulation on the 136-mc signal, and transmits commands to the satellite at 120 mc.

Precision Tracker:[5] The 4080-mc beacon is tracked by the precision tracker, a tracking system using an 8-foot Cassegrain dish antenna with a 2° beam. This antenna is capable of autotracking the microwave beacon with an accuracy of about 0.01°. The precision tracker provides the basic data from which the orbital position of the satellite is calculated.

Either of the two trackers, precision or command, can be slaved to the other. This feature is important during initial acquisition, when the position of the satellite is not well known, and will be discussed in more detail later.

Autotrack: The horn-reflector antenna is also capable of tracking the 4080-mc beacon in the satellite by means of its autotrack system.[6] Operating on the nature of the propagation of the received 4080-mc beacon signal in the horn and using a principle similar to the monopulse radar technique, this system produces error signals which indicate the satellite's position relative to the center of the antenna beam. This error signal is used to correct the position of the antenna automatically.

Antenna Servo: The antenna servo[7] controls the hydraulic drive system of the horn antenna. It does this on the basis of commands received from the digital control and/or the error signals received from the autotrack. The servo feedback loop may be closed in the digital control section, where a digital comparison is made between the commanded position and the actual position. An alternative mode of operation is available whereby the servo loop is closed through the autotrack system. This is an autotracking mode and digital control is not involved. These two modes can also be combined so that the autotrack serves to correct any errors in the commanded position.

Data Processing: The data-processing portion of the system consists of two general purpose computers.[8] These facilities perform two primary functions in the antenna pointing system: (*i*) they enable the system to keep track of the satellite by periodically up-dating the basic orbital parameters on the basis of track information derived from the precision tracker and the horn; and (*ii*) they predict future positions of the satellite and generate pointing instructions for both the precision tracker and the horn for future passes. The facilities are also used to record and process data for performance analysis.

Digital Control: The digital control[9] interconnects the various elements of the system and provides a variety of functions. It takes the pointing instructions, which were stored on magnetic tape by the data-processing section, and develops the "program commands" which point the horn-reflector antenna. Similarly, it generates position commands which provide the precision tracker with an acquisition track about which it can search for the satellite. Since, in both instances, these commands must be given at a much higher rate than the rate at which they are recorded on tape, the digital control incorporates interpolation circuits which yield commands at a 128-per-second rate. A second important function is the recording of track information for subsequent use by the

data-processing section in up-dating the orbital elements. The digital control encodes the precision tracker and horn positions and records them on magnetic tape along with the time of each sample. Because of the accuracy requirements in positioning the horn antenna, the digital control also performs the major servo summing operation digitally. That is, the commanded position is compared with the encoded horn position digitally, and only after the error signals are thus derived, and the need for accuracy reduced, is this signal decoded to an analog quantity and used as an input to the antenna servo. The digital control contains the basic time reference in the system and synchronizes the whole operation with real time. Finally, this portion of the system incorporates a number of functions to permit manual supervision and control of the operation and to provide means for establishing the various operational modes and system configurations.

Magnetic Tape Units:[8] The magnetic tape units appear as a separate item on the block diagram because they are shared between the data-processing and digital control sections. These tape units contain a switching feature that permits connection to either the data processing units or the digital control. Thus, tapes which have been connected to digital control and on which track information is recorded during a pass may be switched following the pass to the computers for processing. Similarly, tapes containing pointing instructions prepared by the computers in the data-processing section can be switched onto the digital control to control the antennas during a pass.

Ground Station Control Console:[10] The ground station control console provides facilities for centralized monitoring and control of all antenna pointing operations. The positions of the antennas are displayed, along with the signals necessary to allow the ground station controller to make an instantaneous and continuous appraisal of the tracking performance. Means are provided for remote control of the antenna positions and operating modes, as well as for commanding the satellite itself. The provision of these facilities at a central position permits the operations performed in establishing the communications connection to be closely coordinated.

II. OPERATION

Now that the functions of the components have been briefly described, consider the operation of the system. In preparation for an upcoming communications pass, the data-processing section, using its latest orbital elements, generates the pointing instructions and stores them on mag-

netic tape. The pointing instructions consist of time information, azimuth and elevation position, velocity and acceleration information, and range information. In addition, compensation factors, derived from the horn-reflector antenna calibration curves, are included to correct beam deflections caused by structural deformations which are functions of horn position. Such a set of information is called a data point, and data points are recorded for each four seconds of the pass. For error-correcting purposes, the data points are recorded in triplicate.

In preparation for the upcoming pass, this tape containing pointing instructions is switched to the digital control. Connections within the digital control are made so that these pointing instructions command both the horn antenna and the precision tracker. In addition, the command tracker is slaved to the precision tracker through a synchro connection. Thus, the tape pointing instructions bring all three antennas to the satellite rise point on the horizon. At the predicted rise time, the pointing instructions cause the three antennas to commence moving at the predicted rate along the satellite track.

At this point the satellite is radiating the 136-mc beacon only. In a typical pass, the command tracker acquires and tracks the satellite's 136-mc beacon and then transmits the command at 120 mc to turn on the telemetry and energize the radiation experiment circuits. The received telemetry is examined to determine the "health" of the satellite. The command tracker then transmits a sequence of commands that apply voltage to the traveling-wave tube (TWT) filament, turns on the TWT helix and collector voltages, and energizes the transistor circuits, and, finally, applies voltage to the TWT anode. This enables the 4080-mc beacon, and the precision tracker and autotrack system can then acquire and track its signal. At this point any one of the following modes of operation may be put into effect: (*i*) normal, (*ii*) autotrack, (*iii*) programmed command, (*iv*) precision tracker command, (*v*) initial, or (*vi*) search.

2.1 *Normal Mode*

As soon as autotrack acquires, the communications antenna is locked on the satellite and the communications connection is established. In this mode of operation the function of the pointing instructions (program command) is to place the horn antenna beam on the satellite to within the $\pm 0.15°$ acquisition range of the autotrack. The autotrack system will then center the beam on the satellite. This is considered the normal mode of operation and in the antenna servo, the program command loop has about twice the gain of the autotrack loop.

2.2 *Autotrack Mode*

Other modes are possible and have been used. A full autotrack operation is possible in which, after acquisition, the program command is removed and the autotrack loop has complete control. In this autotrack mode, the autotrack loop can and does have a higher gain than it does in the combined mode. The tracking, therefore, is accurate as long as the velocities required to track are within the maximum system capability of 1.5° per second. As an alternative to using programmed command for acquisition, the antenna may be positioned manually and acquisition effected as the satellite passes through the beam.

2.3 *Programmed Command Mode*

Similarly, a full programmed command can be obtained by removing the autotrack error signals. In this mode the tracking performance is entirely dependent on accurate orbit prediction and on a precise knowledge of antenna calibration. Experience indicates that the accuracy of prediction is sufficient to make this mode feasible. This mode has proven most useful in tracking radio stars or in deliberately offsetting the antenna for experimental purposes, as in measuring antenna patterns using the satellite. It is also useful as a back-up method in the event of an autotrack failure. In this case the full command mode can be supplemented by manual offsets to improve tracking.

2.4 *Precision Tracker Command Mode*

In the normal and autotrack modes described above, it was assumed that the orbit prediction was accurate enough to allow the horn antenna to acquire the satellite with the autotrack, from the pointing instructions, without assistance from the precision tracker or command tracker. That is, it was assumed that the pointing instructions were sufficiently accurate to place the beam center within an angular circle of 0.15° radius of satellite position. In general this is true. However, in unusual cases, as on the first few passes after launch, the orbit may not be accurately known, and the antenna pointing system incorporates a number of features to permit acquisition under these conditions. The command tracker gives a "broad brush" acquisition means with its 20° beam. The slave connection described above can be reversed so that the precision tracker is slaved to the command tracker. Then, the 1° tracking accuracy of the command tracker is sufficient to allow acquisition by the precision tracker with its 2° beam. The horn antenna may be slaved to the precision tracker by use of what is called the "precision tracker com-

mand" mode. In this mode the encoded precision tracker positions are transmitted directly to the antenna servo by the digital control, and these positions are used as the command input to the antenna servo. Thus, the 0.01° tracking accuracy of the precision tracker is more than adequate to enable acquisition by the autotrack. This mode of acquisition was used on the early passes of the Telstar satellite.

2.5 Initial Mode

A second form of slave-type operation is possible with this system in what is known as the "initial mode" type of operation. In this mode, the computer is put on line. The precision tracker positions are read directly into the computer, which smooths the positions and does a short-term prediction to produce pointing instructions with which it commands the antenna servo directly. This mode is designed to yield smoother operation than the precision tracker command mode, since the precision tracker jitter is averaged out and the antenna servo is supplied with rate information as well as the positional information.

2.6 Search Modes

In addition, to aid in acquisition, the precision tracker has a search mode in which it can search about the acquisition track provided by the digital control. Similarly, the horn antenna servo has a spiral scan capability which causes it to spiral scan about the programmed track. Actuation of a spiral scan causes the horn-reflector antenna to perform a ten-turn spiral out to about 2.5° from the programmed track. Two spiraling rates are available.

In the operational experience to date it has not been necessary to use either the spiral scan or the initial mode operation, and they have been used for experimental purposes only.

At the conclusion of the pass, the command tracker transmits a sequence of commands to turn off the transmission channel. Throughout the pass, the precision tracker and horn positions are measured at twice and once per second, respectively, and recorded on magnetic tape. At the conclusion of the pass these tape units are switched from the digital control to the data-processing section so that the information may be used to up-date the orbital elements. Note that the function of the data-processing section is an off-line operation and that the computers are not directly involved in pointing the antennas.

For calibrating the horn antenna, radiometry equipment and the communication maser are used to track the known positions of radio

stars. In addition, a boresight tower on nearby Black Mountain provides a microwave beacon and satellite electronics for routine calibration of pointing and for autotrack adjustments.

III. CONCLUSIONS

The program objectives were met and successful communication performance achieved, beginning with the first visible pass on July 10, 1962. In no case did antenna pointing performance detectably degrade the communication demonstrations and tests. For the first four months after launch, satisfactory acquisition and tracking were accomplished for all scheduled passes.

All of the modes of operation described were successfully tried. They made possible the high level of system reliability achieved.

Full horn autotrack with predicted pointing information for acquisition was found to be the most accurate mode of operation. It is the most economical and holds promise for application in operational systems. The full tape command system has proven useful for making radio star calibrations of the horn-reflector antenna.

Accurate tracking at azimuth velocities of 1.5°/sec has been achieved. This will permit tracking within a degree or two of the zenith for satellites with 5,000-mile circular orbits.

REFERENCES

1. Dolling, J. C., Blackmore, R. W., Kindermann, W. J., and Woodard, K. B., The Mechanical Design of the Horn-Reflector Antenna and Radome, B.S.T.J., this issue, p. 1137.
2. Hines, J. N., Li, Tingye, and Turrin, R. H., The Electrical Characteristics of the Conical Horn-Reflector Antenna, B.S.T.J., this issue, p. 1187.
3. Shennum, R. H., and Haury, P. T., A General Description of the *Telstar* Spacecraft, B.S.T.J., this issue, p. 801.
4. Chapman, R. C., Jr., Critchlow, G. F., and Mann, H., Command and Telemetry Systems, B.S.T.J., this issue, p. 1027.
5. Anders, J. V., Higgins, E. F., Murray, J. L., and Schaefer, F. J., The Precision Tracker, B.S.T.J., this issue, p. 1309.
6. Cook, J. S., and Lowell, R., The Autotrack System, B.S.T.J., this issue, p. 1283.
7. Lozier, J. C., Norton, J. A., and Iwama, M., The Servo System for Antenna Positioning, B.S.T.J., this issue, p. 1253.
8. Claus, A. J., Blackman, R. B., Halline, E. G., and Ridgway, W. C., Orbit Determination and Prediction, and Computer Programs, B.S.T.J., this issue, p. 1357.
9. Githens, J. A., and Peters, T. R., Digital Equipment for the Antenna Pointing System, B.S.T.J., this issue, p. 1223.
10. Smith, D. H., Carlson, C. P., McCune, R. J., Elicker, R. E., and Sageman, R. E., Planning, Operation and External Communications of the Andover Earth Station, B.S.T.J., this issue, p. 1383.

Digital Equipment for the Antenna Pointing System

By J. A. GITHENS and T. R. PETERS

This paper describes the digital control and data processing portions of the antenna pointing system used to track the Telstar satellite. The description is functional in nature, giving the form of the inputs, the functions performed, and the outputs produced. A general description of the digital equipment is followed by a discussion of the functions performed by the subsystems, the operational modes provided, the equipment features, and the operating experience.

I. INTRODUCTION

The primary function of the digital equipment in the Telstar antenna pointing system[1] is to generate pointing information for the horn-reflector antenna. The performance of this function requires the prediction of the ephemeris from previously acquired information on the satellite orbit. Together with the precision tracker[2] and the horn antenna,[3] the digital equipment provides means for the acquisition, recording, and storage of the track information in each pass. These data are used to periodically up-date the parameters which describe the satellite's orbit. These updated parameters are the basis for the generation of the pointing instructions which are stored and used to control the horn antenna and precision tracker during future passes. During a pass the pointing instructions are synchronized with real time, interpolated to provide a smooth flow of data and then compared with the actual antenna postion. To insure accuracy in the conversion of the digital pointing instructions to the analog inputs required by the antenna servo,[4] the input comparison is performed digitally. The conversion to analog voltages is performed on the difference, or error, signals for which the accuracy requirements are not extreme. In addition, the digital equipment performs a variety of other functions which will be described in this paper.

In Section II a general description of the seven functional units mak-

ing up the digital equipment will be given. Sections III through X contain detailed descriptions of the operations performed by these functional units. The paper then discusses the configurations of these functional units as they are used to provide the various operational modes of the system (Section XI). The implementation of these functions and the equipment features are described (Section XII) and, in conclusion, operational experience is discussed in Section XIII.

II. GENERAL DESCRIPTION

The digital equipment is made up of seven functional units, or subsystems, as shown in the block diagram of Fig. 1.

2.1 Data Processors

The data processors are two general-purpose digital computer systems capable of performing the complex programs[5] necessary to define the satellite orbit from track information, predict future passes, and generate the ephemeris for each pass of interest. Normally, the data processors, having completed their function prior to a pass, take no active part in the pointing during a pass.
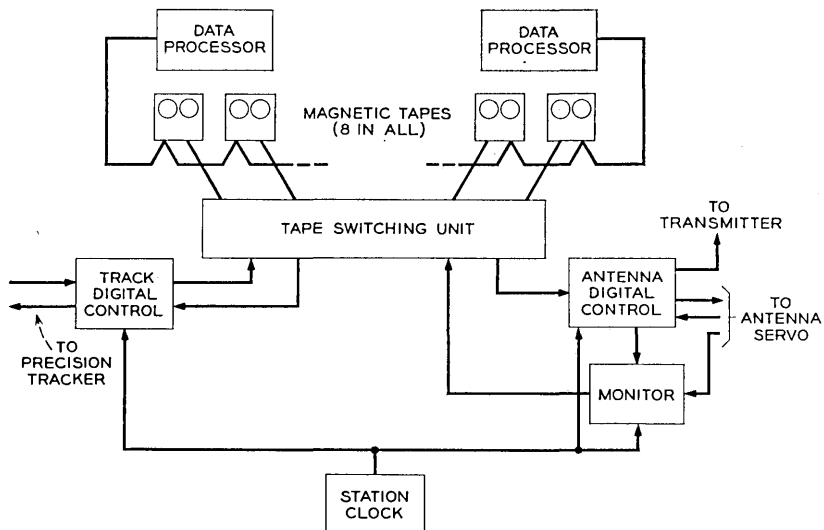

Fig. 1 — Digital equipment block diagram.

2.2 *Magnetic Tape Units*

The magnetic tape units together with the tape switching unit provide for storage and transfer of tracking data and ephemerides within the digital control and data processing system.

2.3 *Antenna Digital Control*

The antenna digital control (ADC) is closely integrated with the antenna servo, which is the actuator of the horn-reflector communications antenna. The ADC, reading pointing instructions from a magnetic tape, synchronizes the pointing operation with time, interprets the pointing instructions in the form and at the rate required by the antenna servo, and closes the servo position loop digitally so that the pointing is achieved with adequate accuracy. In reading the pointing instructions, it performs a variety of tests to check the validity of the data. Careful checking is necessary, because the information is transmitted 1600 feet from the control building and through a slip-ring assembly to the ADC equipment on the antenna structure. Pointing instructions are recorded on tape for each four seconds of the pass, and the ADC provides an interpolator which, using this information, produces position commands at the 128 per second rate required by the antenna servo. Experience has shown that the predominant orbit prediction error is usually in time, and the ADC incorporates means for manually offsetting the predicted pointing instructions in time. This allows the operator to reduce these prediction errors. The ADC also includes features which allow the antenna to be manually offset in position from the predicted track. To meet the system accuracy requirements, the ADC performs the servo position summing operation by comparing the commanded position, as determined from the pointing instructions and the offsets, with the actual antenna position. The actual antenna position is determined from data pick-off units in both axes whose outputs are digitally encoded by the ADC with a precision of 0.003. Only after the position differences, or errors, have thereby been determined, and the need for extreme accuracy reduced, are the ADC outputs converted to analog voltages as inputs to the antenna servo. The output of the ADC may be used in three ways by the antenna pointing system: (a) as the sole source of pointing information; (b) with the autotrack[6] system to provide a combined source of control, in which the autotrack tends to correct for errors in the pointing instructions from the magnetic tapes; and (c) as a means for acquisition of the satellite beacon by the autotrack system, after which autotrack has complete control and the ADC outputs are used only as back-up.

2.4 *Monitor*

The monitor records on tape all the pertinent information on tracking performance from the antenna digital control and the antenna servo. The data processors use the monitor tapes as one source of track data and as a means of performance analysis.

2.5 *Track Digital Control*

The track digital control (TDC) records on tape the precision tracker positions during the pass and provides the data processors another source of track information. These positions are also available in real time as a source of pointing instructions for the horn antenna. This provides a means of slaving the horn antenna to the precision tracker. The TDC also performs a pointing function for the precision tracker similar to that which the antenna digital control performs for the antenna servo and the horn antenna. It provides means for controlling the precision tracker from pointing information stored on magnetic tape. Though the command tracker[7] is not controlled directly by the TDC, it can be slaved to the precision tracker and thereby pointed indirectly by the TDC for acquisition purposes.

2.6 *Tape Switching Unit*

The tape switching unit provides facilities for connecting any of the eight tape units to the antenna digital control, monitor, or track digital control.

2.7 *Clock*

The station clock provides the basic time reference for the system, so that operation may be accurately synchronized with Universal Time.

2.8 *Acquisition Aids*

The digital equipment provides several features to aid in acquisition when the orbit is not precisely known. Since the precision tracker has a relatively broad beam (2°) compared to the beam of the horn-reflector antenna, (0.2°), it can be used as an acquisition aid. This is accomplished by slaving the horn antenna to the precision tracker and performing the initial acquisition of the satellite beacon with the precision tracker. This is called the "PT command" mode. The encoded precision tracker positions produced in the track digital control are used as the command input

in the antenna digital control. The accuracy of the tracker is such that this places the horn antenna well within the acquisition range of the horn autotrack system. A second form of slave operation, initial mode, is possible, in which the data processors are used in real time. In this mode, position information from the track digital control is read directly into the data processors. They smooth the data, perform a short-term prediction and drive the antenna digital control directly with pointing information. This mode yields smoother operation than the PT command mode, since the precision tracker tracking jitter is removed and rate information is supplied.

To aid in acquisition, the antenna servo includes facilities for generating a spiral scan pattern for the horn antenna. The outputs of the spiral scan generator are spiral velocities which are integrated in the antenna digital control and used to offset the programmed position.

In the sections which follow, the functions performed by the seven digital subsystems are described.

III. DATA PROCESSORS

The data processing portion of the antenna pointing system consists of two IBM 1620 Computer systems. Each computer system consists of an IBM 1620 central processing unit, an IBM 1623 core storage unit, an IBM 1622 card reader-punch, and an IBM 1921 tape adapter unit. The 1620 is a desk-sized, solid-state, decimal machine with 20,000 characters of internal magnetic core storage. These units have been equipped with the floating point and automatic divide options. The 1623 core storage unit adds 40,000 characters of core storage, giving each computer a storage capacity of 60,000 characters. The 1921 unit adapts each system for magnetic tape operation and is capable of handling six tape units. The 1622 units provide the systems with card input and output capabilities. The computing systems are pictured in Fig. 2.

The on-site facilities include an IBM 407 printer and an IBM 026 punch. In addition, IBM 7701 magnetic tape transmission terminals working into DATA-PHONE links to the Whippany and Murray Hill Laboratories permit the IBM 7090 computing facilities at these locations to be used as back-up for the on-site facilities.

The primary function of the data processors is to keep an accurate, up-to-date record of the satellite's orbit from which it can predict future passes and generate precise pointing instructions for the site antennas. The orbit is described by a set of basic orbital elements. These elements, or orbit parameters, are periodically refined and updated by the data

Fig. 2 — Two computing systems with four tape units each; three cabinets between tape units contain tape switching equipment.

processors using track information recorded during previous passes by the track digital control and the monitor. The updated orbital elements then are used to predict the upcoming pass and to prepare the mission tape, which contains the pointing instructions. In addition to these functions, the data processors are used for data reduction and performance analysis.

IV. MAGNETIC TAPE UNITS

The Andover installation uses eight IBM 729-II magnetic tape units, shown in Fig. 2. These units are equipped with a switching option which permits each unit to be connected to either the data processors or the digital control. Four units are assigned to each of the data processors. When connected to the digital control, any one of the eight units may be connected by the tape switching unit to the antenna digital control, monitor, or the track digital control input or output. When so connected the tape units operate under the control of these units; the antenna digital control and track digital control input can read tapes and the monitor and track digital control output can write tapes. The low-density mode is always used on these tape units, so that the tape information rate is 15,000 characters per second.

V. MISSION TAPES

The end product of the data processors' efforts is the mission tape for each communications pass. The mission tape, with its pointing instruc-

tions, is the primary input to the antenna digital control and the track digital control. The mission tape consists of data points containing time, pointing angle, and rate information. Normally, a data point is recorded for each four seconds during a pass. To provide for error correction, the information in each data point is recorded redundantly as three separate tape records called blocks. Thus, each data point consists of three redundant blocks of information.

The time information in each block specifies, with a precision of 1/256 second, the time at which the pointing information in that block is to be used. The time information is called tape time. The pointing information consists of azimuth and elevation position, velocity, and acceleration commands. Range information also is given in each block. In addition, compensation factors, somewhat inappropriately called predistortion information, are included in each block. These are correction factors to be added to the pointing information to compensate for mechanical distortions in the horn antenna that cause the electrical axis to differ from the mechanical axis. The use of these factors is discussed further in a later section.

In addition to the time and pointing information, each data block includes a number of unique tape characters called tags. One of these tags identifies the block as the first, second, or third block of a data point. Another tag indicates the checking mode to be used. There are a number of other tags which identify the different types of information and are used to control the disposition of the information by the input circuits.

VI. ANTENNA DIGITAL CONTROL

The antenna digital control equipment is shown in Fig. 3 and is represented by the simplified block diagram of Fig. 4. In this diagram, the antenna digital control (ADC) is shown as three blocks: the input circuits, the ephemeris interpolator, and the output circuits. When a mission tape is connected to the ADC by the tape switching unit, the magnetic tape unit operates under the control of the ADC input circuits. As data blocks are read, the input circuits perform the following functions.

6.1 Data Checking

Before a data block is accepted, it is carefully inspected to determine its validity. The following checks are performed.
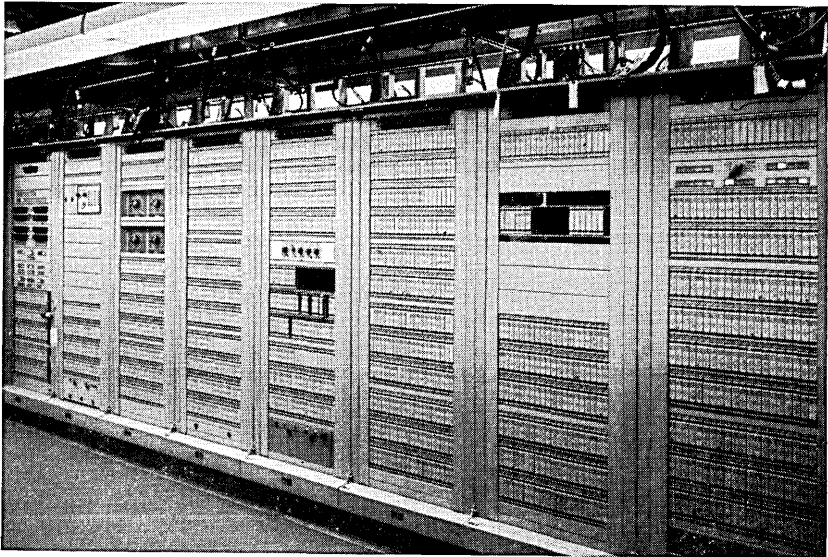
Fig. 3 — Antenna digital control equipment: seven racks at left house ADC equipment; right-hand rack houses monitor equipment.
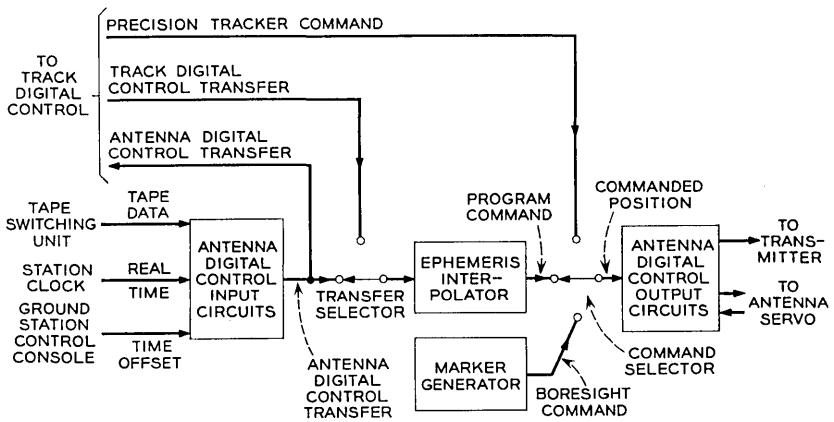
Fig. 4 — Antenna digital control block diagram.

6.1.1 Parity Checks

Since the tapes being read in this operation have been written on IBM equipment, the IBM parity checking conventions are used. Each data block is recorded with two forms of parity check bits, the "vertical" check bits and the "longitudinal" check bits. In the vertical parity check

each tape character is recorded with a parity bit which makes the number of ones in that character even. In the longitudinal parity check, an additional tape character is recorded at the end of each tape record (each data point block in this case). A tape record consists of a sequence of seven-bit tape characters recorded on tape in seven channels. Each bit in the longitudinal check character is chosen to make the number of ones in each channel of the record even. The longitudinal check character thus serves as a check on the block as a whole.

In the reading operation, each character and each channel are inspected to determine that the number of ones is indeed even. As a block is read it is written into buffer storage. As the block is read from the buffer memory, the parity of each character is again inspected to check on the storage operation.

6.1.2 *Time Checks*

As data are read in, the time information in each data block (tape time) is checked against Universal Time. Two checks are performed. In the unconditional time check, the tape time is examined to see that it is later than Universal Time. If tape time were earlier than Universal Time it would represent an impossible situation, since time always advances, and data blocks containing such information are rejected. The second check is called the conditional time check, in which the tape time is inspected to see that it is not later than Universal Time by more than 20 seconds.

6.1.3 *Reasonableness Check*

To check the validity of the commanded data in each data block, the change in position commanded is compared with the previously ordered velocity. This check is performed by subtracting the new position command from the previously accepted position command and comparing this difference with the previously accepted velocity command. If the difference exceeds the maximum acceleration to be expected with the orbits under consideration, the data block is rejected as unreasonable.

6.1.4 *Checking Modes*

Each data block contains a tag character specifying the checking mode to be used by the ADC in checking the data. Two checking modes are used: in the first mode all of the above checks are performed, and in the second the results of the reasonableness and conditional time checks are ignored. The second checking mode is used for data points immedi-

ately following track discontinuities, such as are encountered in shifting between stars in star-tracking routines, where the discontinuities would cause good data points to be rejected due to the reasonableness criterion. This checking mode also can be used for data points following initial pointing commands by which the antenna is brought to the initial pointing angles more than 20 seconds before the start of a pass. This makes it unnecessary to program data points for every four seconds to command the same position until the start of the pass. This second checking mode also makes possible the use of lower data rates.

Data blocks are always rejected if there are parity errors or unconditional time errors. When operating in the first checking mode, rejection of two successive data points (six blocks) causes cancellation of the reasonableness and conditional time checks until a data block is accepted. In other words, after rejection of two successive data points, the checking operation reverts automatically to the second checking mode until a data block is accepted.

6.2 *Compensation Factors*

The most critical surface on the horn-reflector communications antenna is the reflector surface. During construction, the panels making up this surface were very carefully aligned to about 0.06 inch. Yet this is a very large surface, about 70 feet by 100 feet, and as the antenna is rotated in elevation the force of gravity acts on the structure at different angles, causing minute distortions in the surface. These distortions cause the electrical axis of the antenna beam to differ from the mechanical axis, and it was necessary to calibrate the antenna so that these deflections could be compensated for in pointing the antenna. The calibration was measured by tracking radio stars of known positions using radiometry techniques.[8] The calibration thus determined is stored in the data processors as an empirical function of antenna elevation angle. As data points are recorded on the mission tape, the data processors add this calibration information. With only a single communications antenna, as in the present installation, these factors could be added directly to the pointing commands. However, when more than one antenna is in operation at a site, the data processors in preparing the mission tapes have no way of knowing which antenna will be used. Anticipating this requirement, the data point format provides for the transmission of the calibration factors as separate items tagged for each antenna. As the data are read by the ADC input circuits, the calibration factors for the particular antenna controlled by that ADC are selected and added to the

pointing commands. Since these factors can be significantly large at high elevations, velocity and acceleration factors, as well as position factors, are necessary if a smooth track is to be obtained.

6.3 Time Offsets

The ADC input circuits provide the facility for offsetting Universal Time received from the station clock a total of plus or minus 1 minute, 59 seconds in one-second steps. This facility is provided because experience indicates that the predominant orbit prediction error is usually in time. The time offset is under the control of the ground station control console.

6.4 Time Synchronization

The ADC input circuits perform the important function of synchronizing the operation with time. As a good data block is read by the ADC input circuits, it is stored in memory and the tape time is examined 256 times per second and compared with the offset Universal Time. When an exact comparison is obtained, the command data are transferred to the ephemeris interpolator.

6.5 Ephemeris Interpolator

While data points are received generally once every four seconds, the antenna servo requires information at a rate of 128 per second. The function of interpolating the command data between data points is performed by the ephemeris interpolator. The ephemeris interpolator performs a quadratic interpolation, using incremental or digital differential analyzer techniques, and produces azimuth and elevation position and velocity commands 128 times per second. The interpolation is performed with a precision of 0.003° in position as long as the velocity does not exceed 0.49°/sec. For higher velocities, the interpolation is performed with 4 times the granularity, or with a precision of about 0.01°. The use of a quadratic interpolation permits several consecutive data points to be rejected without affecting system accuracy.

As shown in the block diagram of Fig. 4, the input to the ephemeris interpolator can come from one of two sources, depending on the position of the transfer selector. With the selector in the position shown, the interpolator receives command data from the ADC input circuits. In the other position the command data are received from the track digital control input circuits. Similarly, command data are transmitted to a transfer

selector in the track digital control. The use of these selectors will be discussed further in the section on operating modes.

The output of the ephemeris interpolator is called the program command. It is one input to the command selector.

6.6 *Manual Position Offsets*

The command selector provides the command input to the ADC output circuits (Fig. 4). One of three inputs can be selected. The switch position shown is considered the normal position with the ephemeris interpolator providing the program command as input. With the selector in the PT command position, precision tracker encoded positions from the track digital control provide the commands. In the boresight command position, the selector provides position commands from memory which serve to bring the horn antenna to the boresight tower coordinates for testing and calibration routines.

The input provided by the command selector is called the "commanded position." The ADC output circuits provide a means for manually offsetting this commanded position in either axis. Two offsets are provided. One offset can be controlled from the ground station control console and either offset may be operated from the antenna control test position. The offsets can be inserted at two fixed rates of 0.01° and 0.75° per second. A control is provided to reset either offset in either axis to zero.

6.7 *Digital Integrator Offsets*

The ADC output circuits provide a digital integrator for each axis for use by the antenna servo in the spiral scan and autotrack. A digital integration is used to provide a drift-free integrator, and is performed by a simple accumulation technique. The integrators can be shared between the spiral scan and autotrack because these functions are never performed simultaneously. The switching between the two inputs to the integrators is performed in the antenna servo equipment. Thus, when the input is the spiral scan velocities, the integrator yields the spiral scan position offsets to the program command. When the input is the autotrack system instantaneous error, the integrator output is the integrated autotrack corrections, or offsets, to the commanded positions. The digital integrator thus develops and remembers the long-term difference between the predicted track and the actual track of the satellite as determined by the autotrack. When the manual offsets are zero, this long-term difference provides a measure of the accuracy of the track prediction.

The integration is performed by encoding the input provided by the antenna servo and simply adding the encoded quantity to the accumulated sum held in memory. The encoding and summing is performed 128 times per second. The smallest value encoded (the least significant bit) corresponds to $0.0000215°$ ($2^{-24} \times 360°$). However, the smallest value considered in determining the position error is $0.00275°$ ($2^{-17} \times 360°$) and, therefore, the smallest digital integrator offset must persist for 128 encodings, or 1 second, for it to have an effect on the position difference. The maximum encoded input corresponds to $0.00135°$, and this value must persist for only two encodings, or 1/64 second, to be effective. Maximum input errors result in position corrections at a rate of $0.175°$ per second.

6.8 Position Encoding

The ADC output circuits provide the facilities for encoding the horn antenna azimuth and elevation positions. The data pickoff units, which are a part of the antenna servo, produce pulse-position-modulated pulses from a two-speed resolver pickoff on the data gears. The position of the "stop" pulses relative to a reference "start" pulse is proportional to the angular rotation of the data gears and, hence, the position of the antenna. The digitizing of these time intervals is performed by high-speed counting (approx. 2 mc) in two counters, one for fine and one for coarse.[9] The two counts are combined to give a 17-bit binary representation of antenna position. The precision of encoding is $0.00275°$ ($2^{-17} \times 360°$) and the resultant accuracy is $\pm0.005°$.

6.9 Servo Summing Node

One of the most important functions performed by the ADC output circuits is the implementation of the major servo position summing node for the antenna servo. This operation is performed digitally for accuracy reasons 128 times per second for each axis; it is performed with a precision of 1 part in 131,072 (17 bits).

The servo summing node is illustrated diagrammatically in Fig. 5. The first input is the position command from the command selector. Remember that this input may be the program command, PT command, or boresight command. To the position command is added the sum of the two manual position offsets to produce what is called the offset position. To the offset position is added the output of the digital integrator, the digital integrator offset, to produce what is known as the corrected position. Thus, the corrected position is the offset position corrected by the long-term difference determined by the autotrack and
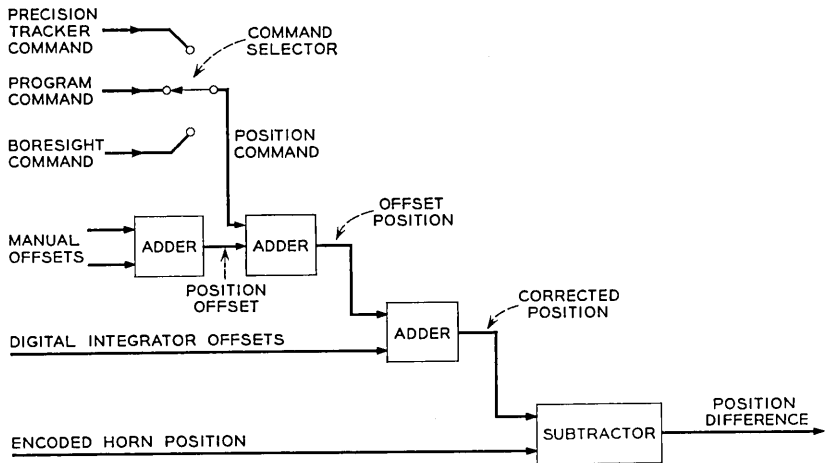
Fig. 5 — Digital servo summing node.

accumulated by the digital integrator. The corrected position, therefore, represents the system's best estimate of the satellite's actual position. Finally, the encoded horn position is subtracted from the corrected position to produce the position difference, the error in the position of the horn. Once the position difference is derived, the need for high precision is removed since the errors are small and they may now be stored and decoded to analog voltages for use by the antenna servo.

6.10 *Velocity Error*

The ADC output circuits determine the velocity error by comparing the actual antenna velocity in each axis with the commanded velocity. The actual velocity is determined by differencing the encoded horn positions 32 times per second, and the velocity error is produced with the same frequency. It is made zero unless the position error is coarse (greater than 0.35°). It is used by the antenna servo to eliminate overshoot as the horn slews to a commanded position.

6.11 *Servo Difference*

Under normal circumstances, if the ephemeris interpolator is working properly, the interpolated commands should agree closely with the new values brought in as each data point is transferred. The difference should not be more than one bit (0.00275°). However, if for some reason several

consecutive data points are rejected, when a new data point is finally accepted a significant difference may exist between the last interpolated point and the new accepted point since the quadratic interpolation may not perfectly describe the actual track. This difference has been termed the servo difference.

If the autotrack is inserted and in phase-lock when this happens, the variation of the interpolated command from the actual track will be compensated by an offset from the digital integrator. It would not be desirable, under these conditions, for the acceptance of a new data point to cause an abrupt jump in the position difference. Therefore, whenever autotrack is inserted and in phase-lock, any difference between the last interpolated point and a new data point is subtracted from the digital integrator contents and the new data point used as the program command. There is no net change in position difference. The result is the same as if the jump were allowed to occur and the autotrack then corrected by making a compensating change in the digital integrator offset. However, the possibility that the step change in position difference would cause the autotrack to drop track is avoided.

6.12 *Error Registers and Digital-to-Analog Conversion*

The ADC outputs to the antenna servo are fine and coarse position differences, and velocity errors in both axes. These signals are delivered as voltages. To produce voltages proportional to these digital quantities, the ADC output circuits provide storage and digital-to-analog conversion circuits. The storage is provided by flip-flop registers. The conversion is performed by constant-current, ladder-type resistance networks which provide a decoding accuracy of 1 per cent. To decode each quantity, two decoding networks, one for positive values and one for negative values, are used to avoid difficulties with zero drift.

6.12.1 *Position Errors*

The fine position error decoders in each axis produce a voltage output of the form shown in Fig. 6(a). As can be seen in this figure, errors less than 0.7° produce a voltage proportional to the error. For errors greater than 0.7°, the output is saturated at 5 volts. As is characteristic of digital-to-analog converters, the voltage produced is actually a staircase where the granularity is 0.02 volt, corresponding to error quanta of 0.00275°.

The coarse decoder output is shown in Fig. 6(b). This output is made zero until the error equals 0.35°. The voltage is then proportional to the
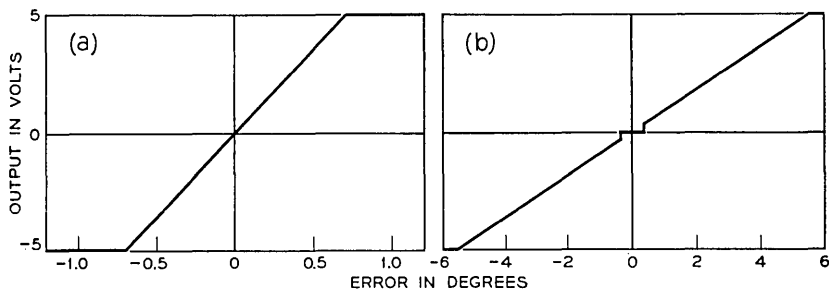
Fig. 6 — (a) Fine position error output; (b) coarse position error output.

error until it saturates at 5 volts for errors greater than 5.6°. In this decoding the 0.02-volt granularity corresponds to steps of 0.02° in error.

6.12.2 *Velocity Errors*

The outputs of the azimuth and elevation velocity error decoders are made zero until the position errors exceed 0.35°. Thereafter, the voltage outputs are proportional to the velocity errors. The maximum voltage of 5 volts corresponds to a velocity error of 2.8° per second. The granularity of decoding is 0.08 volt, corresponding to error quanta of 0.04° per second.

6.12.3 *Range Decoding*

In addition to the outputs to the antenna servo, the ADC output circuits provide a voltage proportional to the range information to the transmitter equipment in the antenna upper room. The range information is proportional to the ratio of the predicted slant range to a fixed range whose value depends on the type of transmission to be used. This output is used to program the transmitted power so that the input signal to the satellite remains essentially constant. The range information is supplied as a part of each data point. The range information is not interpolated but is set into the range register each time a new data point is transferred to the ephemeris interpolator. Thus, in general, the range register is updated once every four seconds.

VII. MONITOR

The function of the monitor is to record on magnetic tape all information on the horn antenna pointing operation that will be useful in orbit

determination and post-run performance analysis. Three types of information are recorded: digital information from the antenna digital control; analog information from the antenna servo, autotrack, and the communication equipment; and telemetry information from the satellite as received and decommutated by the telemetry equipment. The analog information is digitized for recording purposes by an analog-to-digital converter which provides facilities for converting and multiplexing as many as eight channels of analog information.

The digital information recorded includes the time, time offset, and the horn position in both axes. In addition, the acceleration, velocity, and position commands in both axes are included, as are the digital integrator offsets and the two manual offsets. The position differences, the range information, and the checking mode in use by the antenna digital control also are recorded. In other words, everything of interest is recorded.

Eight analog quantities may be recorded. While the quantities to be recorded are easily changed for testing purposes, the autotrack instantaneous errors, the receiver AGC voltage, an indication of autotrack phase-lock status, and the radiometry output (used in star tracking routines) are regularly recorded. The other three channels can be used for test voltages.

The telemetry information from the satellite is received, decommutated, printed, and punched on teletypewriter tape by the telemetry equipment in the control room. This same information is recorded on the monitor tape because the magnetic tape recording provides a more convenient input for computers than does the teletypewriter tape.

In its normal operating mode the monitor samples and records the digital information once per second as a separate tape record. The analog information is sampled seven times per second and the data recorded as two separate tape records. Since there is no synchronization between the monitor operation and the telemetry information, each channel of telemetry data is appropriately tagged and recorded at the end of the next digital or analog record to be recorded.

The monitor has facility for several other modes of operation at different sampling rates that are useful in testing and system checking routines. The monitor equipment is shown in Fig. 3.

VIII. TRACK DIGITAL CONTROL

The track digital control performs functions for the precision tracker similar to those performed by the antenna digital control and monitor
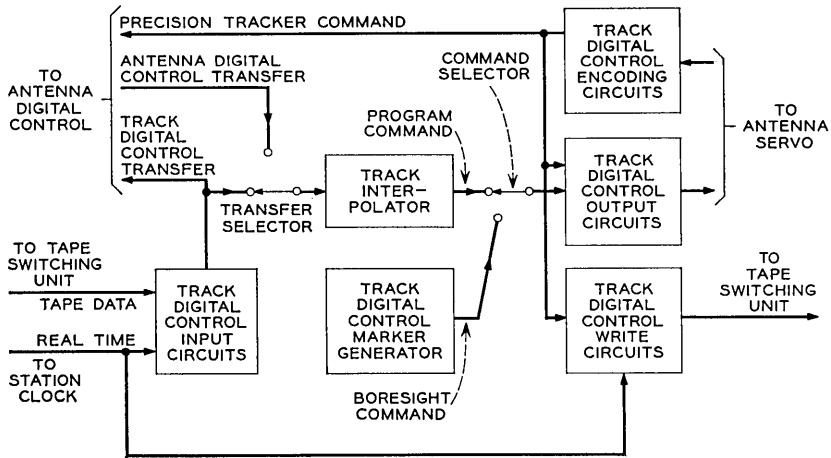
Fig. 7 — Track digital control block diagram.

for the horn antenna. The track digital control is considerably simpler, however, since it serves only as an acquisition aid to the precision tracker.

A block diagram of the track digital control (TDC) is shown in Fig. 7. It is quite similar to the block diagram of the antenna digital control except that the position encoding circuits are shown as a separate entity rather than as part of the output circuits. Also, there is an additional block, the write circuits, which performs a function similar to that of the monitor.

8.1 Data Checking

The TDC input circuits are similar to the antenna digital control input circuits except that the TDC input circuits perform no reasonableness check. The parity and time checks performed are identical to those performed by the antenna digital control input circuits. Similarly, there are two checking modes but, in this case, the second checking operation cancels only the conditional time check since the reasonableness check is never performed in any event.

8.2 Time Synchronization

The TDC input circuits do not make use of the predistortion information in the data points and do not have any provision for adding time offsets. The time synchronization operation, however, is identical to that

performed by the antenna digital control input circuits. Thus, the output of the TDC input circuits is the command data at the tape time specified in the data point. The data are not predistorted and the time of transfer cannot be offset.

Like the antenna digital control, the TDC input circuits output feeds a transfer selector. The other input to the selector is the output of the antenna digital control input circuits.

8.3 *Track Interpolator*

The track digital control interpolator performs a linear interpolation. That is, unlike the ephemeris interpolator, it makes no use of the acceleration information in providing position commands 128 times per second. The track interpolation is performed with a precision of 0.01°.

The output of the track interpolator feeds one input of the command selector.

8.4 *Position Encoding*

The position encoding performed in the TDC is identical with that performed in the antenna digital control. The result is a 17-bit encoding of the position in each axis 128 times per second. The position encoding circuits are shown as a separate block in the TDC block diagram because, in addition to feeding the summing node in the output circuits, the output feeds the write circuits and also is sent to the antenna digital control as the PT command.

8.5 *Summing Node*

One input to the TDC output circuits is the output of the command selector. The TDC command selector has only two positions and may select either the commanded positions from the track interpolator or the precision tracker boresight coordinates from the marker generator. The TDC command selector is under the control of the precision tracker operator.

The TDC output circuits are quite simple compared to the antenna digital control output circuits. No provision is made for manually offsetting the commanded position, and there is no feedback from the precision tracker equivalent to the horn-reflector autotrack. The summing node consists of a single subtractor which subtracts the precision tracker encoded position from the commanded position.

8.6 *Error Registers and Digital-to-Analog Conversion*

The position error output of the summing node is stored and decoded to provide voltage error signals in each axis to the precision tracker. The voltages are proportional to the errors for errors less than 5.6°. For errors greater than 5.6°, the voltage saturates at 5 volts. The granularity of the decoding is 0.02 volt for error quanta of 0.02°.

8.6.1 *Range Decoding*

The TDC output circuits decode the range information in the data points in exactly the same manner as the antenna digital control output circuits. The decoded range information is used by the precision tracker to estimate the signal-to-noise ratio.

8.7 *Track Write Circuits*

The TDC write circuits perform a track recording function for the precision tracker similar to that performed for the horn antenna by the monitor. The write circuits include a tape write control capable of controlling the recording on a magnetic tape unit connected to it by the tape switching unit. Time, azimuth position, and elevation positions are sampled and recorded as a tape record along with four binary control indications. Samples can be taken at 1, 2, or 4 per second with 2 per second being considered the normal rate. Two of the control bits define the precision tracker status by indicating when it is in autotrack and when the signal-to-noise ratio equals or exceeds 5 db. The third indicator is used in precision tracker optical star tracking routines, and the fourth is used as a control in the initial mode operation described in a later section.

IX. TAPE SWITCHING UNIT

The tape switching unit (pictured in Fig. 2) provides the facility for selectively assigning control of any of the eight magnetic tape units to antenna digital control input circuits, track digital control input circuits, monitor, or track digital control write circuits. To make this possible, the tape switching unit also performs the important function of level shifting to make the tape unit signals compatible with the digital control circuit levels and vice versa. The tape switching unit also makes provision for connecting two tape units simultaneously to the antenna digital control input circuits or the track digital control input circuits; one unit is designated as primary source and the other as the alternate source. The input circuits control both units but only the primary source sup-

plies data. Thus, the alternate source is kept in step with the other tape unit, and a source selector switch under control of the ground station control console permits the alternate tape to be selected to supply data if there is evidence of trouble with the primary source.

The tape switching unit also provides the facility for placing the data processors on line in the digital control system. In this operation, the output of the track digital control write circuits is delivered directly to the data processors as well as written on tape. The outputs of the data processors can be sent directly to either of the input circuits. One data processor serves as the primary source and the other as the alternate, and source selection may be used just as with tape units. These connections are used in the initial mode operation to be discussed in a later section.

X. STATION CLOCK

The station clock provides the basic time reference for the antenna pointing system. Its primary output is a digital representation of the hours, minutes, and seconds of Universal Time (UT_2) to a precision of 1/256 second. This output is supplied to the antenna digital control and track digital input circuits for synchronizing the transfer of command data to the interpolators. The pointing operations are thereby synchronized with Universal Time. The time output is also supplied to the monitor and the track digital control write circuits for recording on the track tapes so that the position samples may be accurately correlated with Universal Time.

The heart of the station clock is a pair of crystal-controlled, temperature-stabilized oscillators operating in duplex at a frequency of 2^{23} cycles per second (8.388608 mc). These oscillators have a specified stability of better than 1 part in 10^9 per day (drift rates of 2 parts in 10^{10} per day have been measured). To permit the adjustment of these oscillators and to phase the output, the station clock produces a one pulse per second output which, after allowing for the transmission delay, is compared with the 1-pps VLF signal transmitted by NBA,[10] Canal Zone. Using photographic oscilloscope techniques, the time output can be set with an accuracy of about 1 millisecond.

The station also supplies a number of time displays in the control room and lower room for operator convenience and an encoded time output for use on strip chart timing channels. Many submultiples of the oscillator frequency are supplied in the form of square waves to the other units in the digital control for local timing operations.

XI. OPERATING MODES

Now that the functions performed by the subsystems have been described, the operation of the digital equipment can be discussed. The tape switching features, the transfer selectors, and the command selector permit the system to be operated in a variety of configurations and modes. One form of the normal mode of operation is illustrated in Fig. 8. Prior to the start of the pass, two tape units containing identical mission tapes prepared by the data processors are assigned to the antenna digital control (ADC): one tape as primary and the other as alternate source. The ADC input circuits read the first block of data and, if it checks, store it in memory and begin to compare the tape time with real time. When a comparison is achieved, the command data are transferred to both the ephemeris and track interpolators by way of the transfer selectors. The interpolators begin producing the program commands at a 128 per second
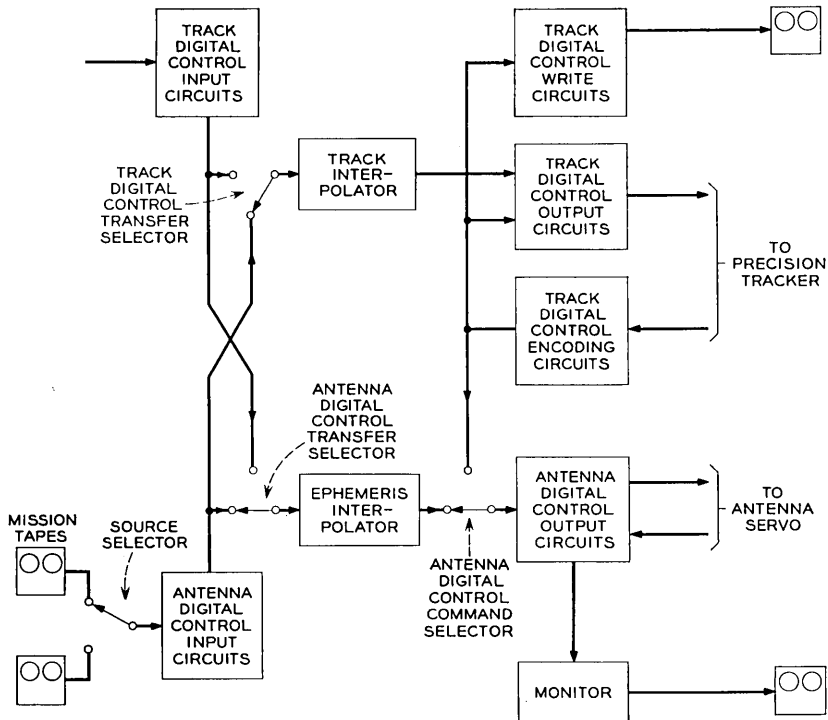

Fig. 8 — Normal mode operation block diagram.

rate and the output circuits cause the horn and precision tracker to come to the proper pointing angle.

At the predicted rise time of the satellite, incoming data points bring in velocity and acceleration commands that cause the horn and precision tracker to begin moving along the satellite's track. If the prediction and pointing accuracy is within ±0.2°, as is usually the case, the autotrack and precision tracker acquire the microwave beacon within seconds after the satellite traveling-wave tube has been turned on by the command tracker. The communications connection is then established. Operation of the antenna servo may then proceed, with the control shared between the program commands and the autotrack; or the control may be placed entirely in the autotrack loop. Throughout the pass the track information is recorded on tapes by the monitor and the track digital control write circuits.

As the pass proceeds, the antenna digital control continues to process data blocks from the mission tape. After a good block is read, the other blocks of that data point are discarded. If a bad block is encountered, it is rejected and the next block inspected. If a number of data blocks are rejected, the ground station control console operator may decide, from observing the history of data point rejections displayed for that purpose, that the alternate source tape should be selected by actuating the source selector switch. Though no data were read from the alternate tape, the tape received control signals from the antenna digital control and was thereby kept in step with the primary tape and ready to assume the task of supplying data points.

If there appears to be difficulty in the ADC input circuits, the mission tapes may be switched by the tape switching unit to the track digital control input circuits and both transfer selectors switched so that the track digital control input circuits transfer the data to both interpolators. The advantage of using the ADC input circuits is that the precision tracker receives data that have been reasonableness checked and that can be offset in time. It has the disadvantage that the track digital control (TDC) receives data that are predistorted with the horn compensation factors. However, these factors are small compared with the precision tracker beamwidth, and the function of the TDC is to provide only an acquisition track. Conversely, the use of the TDC input circuits to provide data to the ephemeris interpolator has the distinct disadvantages that no reasonableness checks are made, the time offset has no effect, and the data cannot be predistorted. This connection is used only in event of equipment failure.

Alternately, one might connect one mission tape to the ADC and the
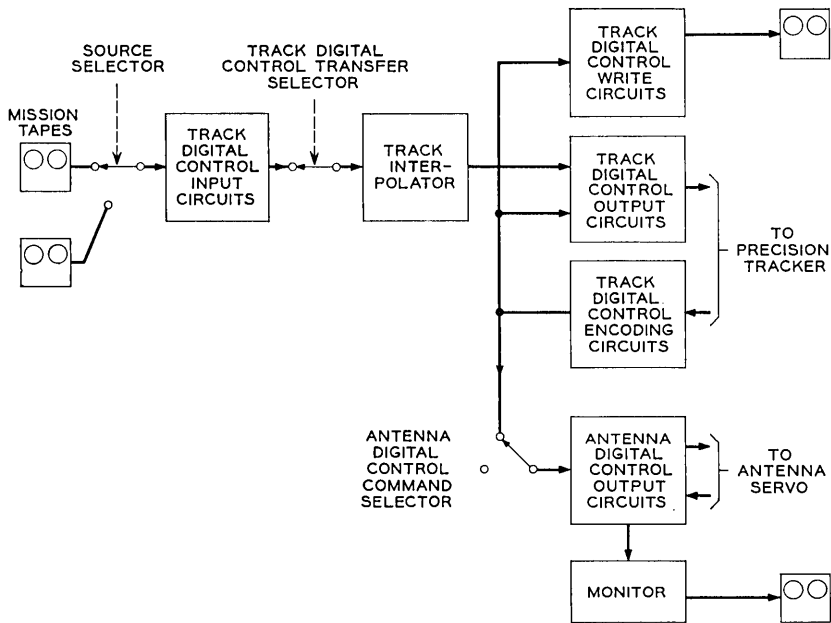
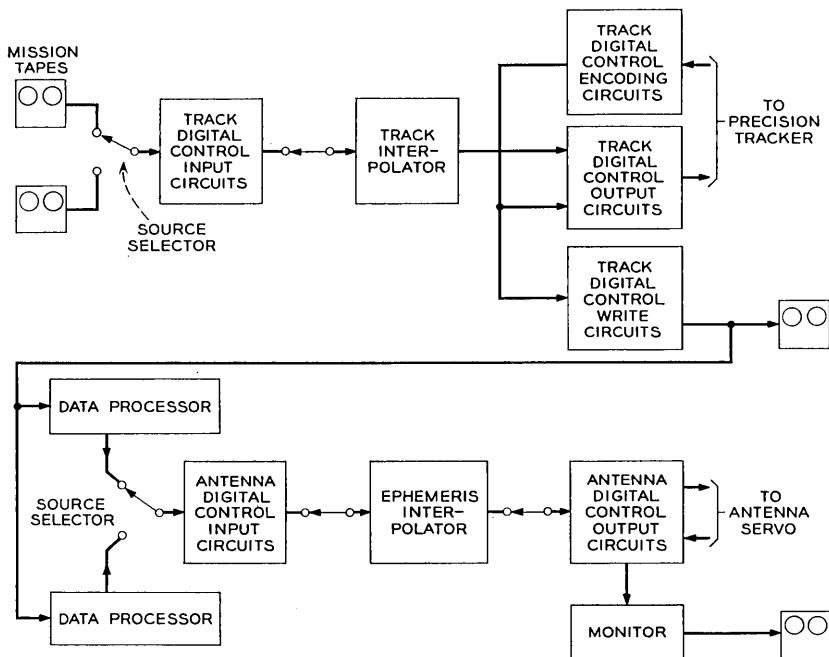Fig. 9 — PT command mode operation block diagram.

Fig. 10 — Initial mode operation block diagram.

other to the TDC. The ADC and TDC would then operate independently and, in event of failure of either input circuit, the equivalent of source selection could be achieved by use of the transfer selectors. This method of operation suffers from the fact that the source selection in the present equipment arrangement cannot be performed from the ground station control console.

In the above discussion it was assumed that the horn and precision tracker were tracking the same satellite. This is usually the case, especially in the present experimental system with only one satellite in orbit. With a number of satellites in orbit there may be frequent occasions when the antennas may track different satellites. This operation is possible and is the reason, of course, that two input circuits are provided.

When the satellite orbit is not accurately known, the system operation is somewhat different. A mission tape containing the best estimate of the pass is used to drive the TDC and point the precision tracker. The command tracker is slaved to the precision tracker by a synchro connection. The precision tracker and command tracker thus are pointed to the best available estimate of the satellite's position. The command tracker begins searching about this track with its 20° beam. When the command tracker acquires, the slave connection is reversed, bringing the precision tracker to the command tracker pointing angles and, after the command tracker has turned on the satellite, the precision tracker can acquire. The digital equipment provides two methods of slaving the horn antenna to the precision tracker so that the autotrack may acquire. The first of these is called the "PT command" mode and is illustrated in Fig. 9. In this mode the ADC command selector is switched to the PT command position and the output of the TDC encoding circuits, the precision tracker azimuth and elevation positions, is supplied as the commanded position input to the ADC output circuits. Thus, the precision tracker positions are supplied directly without smoothing, and the command positions are subject to the precision tracker tracking jitter. Also, no rate information is available to the antenna servo, and the horn antenna pointing is not compensated for distortion.

The second form of the slave mode, called the "initial mode," is designed to yield smoother performance. In this mode, which is illustrated in Fig. 10, the data processors are placed on line in the pointing operation. The output of the TDC write circuits feeds the two data processors as well as the usual tape unit through connections established in the tape switching unit. This input, consisting of time and position information twice a second, is read and smoothed by the data processors. This smoothed information is then used by the data processors as the basis

for a short-term prediction of the next data point. The data processors operate in duplex with the source selector providing the ground station control console operator with the facility of selecting the output of the secondary processor if his displays indicate that the primary processor is producing doubtful results. The output of the selected data processor drives the ADC input circuits through level-shifting circuits provided by the tape switching unit. The form of the data processor's output is identical to the data points normally recorded on the mission tapes and includes position, velocity, acceleration and range information and compensation factors. The ADC, in fact, operates as if it were reading a mission tape. Thus, the operation in this mode can be as smooth as that in the normal mode.

Throughout a PT command or initial mode pass, the monitor and TDC record the horn antenna and precision tracker tracks on tape in the usual manner. These recordings take on added significance in these slave-type modes because this track information can be used to refine the orbit prediction and permit the system operation to graduate to the normal mode on future passes.

XII. EQUIPMENT ASPECTS

The digital control is implemented using solid-state switching techniques for the most part. The majority of the functions are performed by transistor logic circuits. The digit rate required in performing most of the functions is a comfortably low 32 kc. For these speeds, a form of saturating transistor-resistor NOR logic (TRL) is used. In those few functions requiring significantly higher speeds, such as the encoding counting at 2 mc, a form of resistance-capacitor coupled transistor logic (RCTL) is used.

These circuits are mounted in multicircuit plug-in packages. A total of 29 different types of packages are used in the system to provide the various logic functions, cable drivers, and assorted circuit functions required. A typical logic package is shown in Fig. 11. The packages plug into mounting cages which can mount up to 20 packages. Subassemblies may use as many as four of these cages, or a total of 80 packages. The subassemblies are mounted in open-face racks with conventional back panel wiring. Subsystems may contain up to 5 racks. Interconnections between subassemblies within the same subsystem are made with open-wire runs, while interconnections between subsystems are made by coaxial cable. All wiring terminations, both those used in connecting components within the packages and those used in making the interconnections in the back
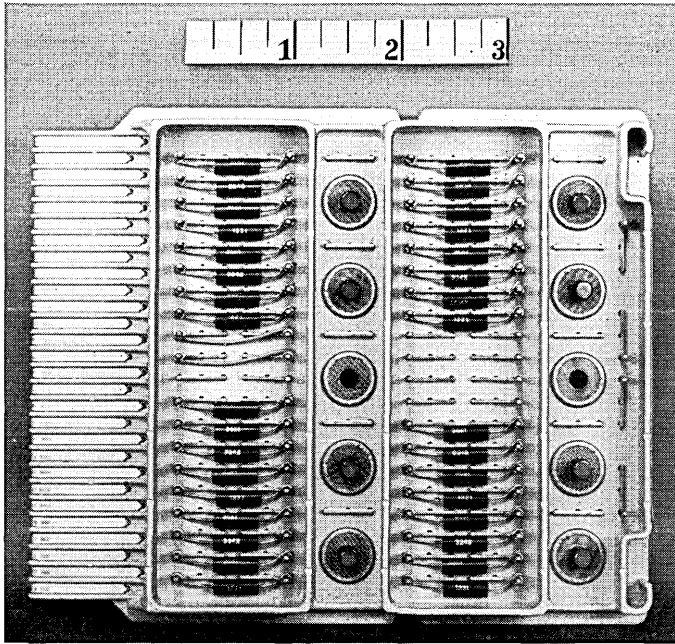
Fig. 11 — Logic package containing eight TRL gates.

panel wiring, are made with solderless-wrap connections for reliability. The racks contain an air ducting arrangement that allows cooling air to be blown over the transistors in each package in a subassembly. Auxiliary equipment, such as power supplies, is mounted in cabinets with swinging door access to both front and back.

With the bulk storage requirements met by magnetic tape units, the requirements for internal storage in the system are modest. Four magnetic core buffer memories are used in the tape read and write control units. These units each have a capacity of 144 characters. In addition, the antenna digital control and track digital control each use a 2048-bit magnetic core memory with sequential access for internal memory requirements.

The information within the digital equipment is handled in serial form, least significant bit first, with negative values represented by two's complement notation. While the use of binary is very convenient for the equipment, the interpretation of binary information by the operators would be difficult. The antenna digital control and track digital control perform the important function of converting the critical position in-

formation from binary to binary-coded-decimal and arranging for its display in decimal form. The antenna digital control provides for the simultaneous display of four two-axis positions selectively chosen from a total of 12 quantities that can be displayed. These quantities are displayed at the antenna control test position with a precision of six digits. Arrangements are made also to display three quantities on the ground station control console with a precision of five digits.

In addition to display functions, the antenna digital control also incorporates a number of features to permit operational control of the horn antenna from the ground station control console. This is not a simple function, because this console is located in the control room of the control building and is 1600 feet from the antenna. The same separation applies to the digital equipment, since the data processors, magnetic tape units, track digital control, station clock, and tape switching unit are in the control room, and the antenna digital control and monitor are in the lower room of the horn antenna. Information between the two areas must be transmitted 1600 feet and pass through the slip-ring assembly which brings all signals and power into and out of the antenna. In general, data signals are transmitted over 75-ohm coaxial cables, and manual control and indication signals are transmitted via a multiplex telegraph system, used to minimize the number of slip rings required. These considerations had considerable influence on the system design.

The dc power for the equipment is supplied by conventional commercially available 60-cycle rectifiers. Since during critical passes the 60-cycle prime power is supplied by diesel powered generators on the site, no precautions against intermittent power failures were taken except in the case of the power supply for the station clock. In this case, even a short power interruption at any time can upset the clock oscillator stability and, by disrupting the countdown process, change the time setting. Therefore, the clock power supply uses duplexed inverters, operating from independent 24-volt battery sources, which supply 60-cycle power to two sets of rectifiers. The outputs of these rectifiers are monitored by an automatic switching circuit which, in event of a failure of one source or one rectifier, switches the load without interruption to the other set of rectifiers. The clock oscillators and the clock countdown chain are thus protected from power failures. For the other parts of the digital control, each voltage also is supplied by two rectifiers which normally share the load but are capable of assuming the entire load. However, in this case, the switching of the loads to the good supply must be performed manually in the event of rectifier failure.

The station clock, track digital control, and tape switching unit oc-

cupy 8 racks, 8 cabinets, and a console in the control room. The antenna digital control and monitor utilize 8 racks and 2 cabinets in the antenna lower room. These racks and cabinets mount a total of 2085 packages and 1000 relays. The packages use over 11,000 transistors.

XIII. OPERATING EXPERIENCE

On the early passes following the July 10, 1962, launch of the satellite, acquisition was achieved using the PT command mode and tracking was performed in the autotrack mode. By the second day, the orbital elements had been refined sufficiently to permit autotrack acquisition from the pointing commands alone. Since that time, the normal mode of acquisition has been from the program command and the use of the precision tracker for acquisition generally has not been necessary. In tracking experiments, all conceivable variations of the acquisition and tracking modes were attempted and, in all cases, operation was satisfactory.[11]

The smoothest tracking performance is achieved with the vernier autotrack in full control. In this mode the antenna follows the autotrack null with peak errors seldom exceeding 0.005°. With the control shared between the program command and the autotrack, these errors can reach 0.008° when the velocities are very low. The program-command-only mode yields tracking performance which meets the design objective. However, the high-quality performance of the autotrack has relegated the program-command-only mode to calibration and testing roles, such as star tracking and measuring the antenna patterns using the satellite.

The operating experience has shown the antenna pointing system to be a very flexible and accurate facility for satellite communications experiments. This operating experience also has demonstrated that the antenna pointing for an operational commercial satellite system can be much simpler and the role of the digital equipment greatly reduced. In such a system, the normal mode of operation would be full autotrack, and the digital equipment would provide acquisition only.

XIV. ACKNOWLEDGMENTS

A system of this size and complexity is not conceived, designed, fabricated and made operational in eighteen months without the full cooperation and extraordinary efforts of many people. The authors are indebted to all these people, and wish to acknowledge in particular the help of M. J. Gilmartin, E. Gomez, and W. T. Hartwell, who contributed heavily to the logical design; G. E. Saltus and W. L. Zweig, who struggled with the circuit problems; and H. Garber and J. O. Whyte, who handled

the equipment design and shepherded the equipment through fabrication, wiring, and installation.

REFERENCES

 1. Githens, J. A., Kelly, H. P., Lozier, J. C., and Lundstrom, A. A., Antenna
    Pointing System: Organization and Performance, B.S.T.J., this issue, p.
    1213.
 2. Anders, J. V., Higgins, E. F., Murray, J. L., and Schaefer, F. J., The Precision
    Tracker, B.S.T.J., this issue, p. 1309.
 3. Dolling, J. C., Blackmore, R. W., Kindermann, W. J., and Woodard, K. B.,
    The Mechanical Design of the Horn-Reflector Antenna and Radome, B.S.-
    T.J., this issue, p. 1137.
 4. Iwama, M., Norton, J. A., and Lozier, J. C., The Servo System for Antenna
    Positioning, B.S.T.J., this issue, p. 1253.
 5. Claus, A. J., Blackman, R. B., Halline, E. G., and Ridgway, W. C., III, Orbit
    Determination and Prediction, and Computer Programs, B.S.T.J., this
    issue, p. 1357.
 6. Cook, J. S. and Lowell, R., The Autotrack System, B.S.T.J., this issue, p.
    1283.
 7. Chapman, R. C., Jr., Critchlow, G. F., and Mann, H., Command and Telem-
    etry Systems, B.S.T.J., this issue, p. 1027.
 8. Westerman, H. R., Padgitt, R D., and Penzias, A. A., Antenna Calibration
    with Radio Stars, to be published.
 9. Kronacher, G., Design, Performance, and Application of the Vernier Resolver
    B.S.T.J., 36, Nov., 1957, p. 1487.
10. Stone, R. R., Jr., Markowitz, W., and Hall, R. G., Time and Frequency Syn-
    chronization of Navy VLF Transmissions, I.R.E. Trans. Instr., I-9, No. 2,
    Sept. 1960, pp. 155-161.
11. Smith, D. H., Carlson, C. P., McCune, R. J., Elicker, R. E., and Sageman, R.
    E., Planning, Operation and External Communications of the Andover
    Earth Station, B.S.T.J., this issue, p. 1383.

The Servo System for Antenna Positioning

By J. C. LOZIER, J. A. NORTON and M. IWAMA

This paper describes the servo system for pointing the horn-reflector antenna. It presents the general considerations which dictated the design and also describes the resulting system in some detail, giving the characteristics of the various parts of the system. Finally, the over-all performance of the servo system is discussed.

I. INTRODUCTION

The needs of broadband satellite communications systems for a high-gain, low-noise antenna led to the choice of the horn type structure. High gain and low noise inherently mean a narrow-beam antenna and, therefore, an antenna with a large reflector which has to be pointed very accurately. In this case, the beamwidth is such that at 4 kmc, the strength of the received signal is 3 db down when the antenna is pointed 0.11° off center. However, in order to conserve signal-to-noise ratio, maximum reduction in received signal strength of 1 db was alloted to errors in pointing.[1] This places an over-all accuracy requirement of 0.06 degree maximum error on the antenna pointing system.

The dynamic requirements on the control system are generated by the orbits of the satellites to be tracked and by the nature of the antenna mount. With an azimuth-elevation mount, it takes a very high azimuth velocity to track a low-altitude satellite passing close to the zenith, and a very low azimuth velocity to track a satellite pass as it comes up over the horizon. The compromise objective set for the system was that it be able to track smoothly and accurately all satellite passes with maximum azimuth velocities up to 0.5 degree per second. For a satellite with a 2500-mile altitude, typical of the first Telstar satellite orbits, the 0.5 degree per second velocity would limit the tracking to passes having maximum angle of elevation less than 81 degrees. However, for satellites with altitudes of 6000 miles and above, the maximum trackable angles of elevation would be 86°.

Two methods of pointing the antenna at the satellite were considered. In one method, the antenna is driven by pointing information derived in advance from the predicted path of the satellite.[2] This is called the "program command" mode. In this mode, pointing information from the digital part of the antenna control system[3] is compared with the encoded outputs of position pick-offs on the mechanical axes to derive the actuating signals for the antenna drive. This mode of operation is subject to errors in prediction and in the calibration of the electrical vs mechanical axes of the antenna, as well as servo errors. A maximum of ±0.2° of the total maximum 0.06° error was allocated to the servo in this mode; this amounts to 0.014° in each axis.

In another method, the antenna is driven by pointing information provided by an autotrack system.[4] In this autotrack mode, the autotrack system generates tracking error signals from a microwave beacon on the satellite, and these signals are used for aligning the electrical axes of the horn antenna with the satellite. The autotrack mode is not subject to the errors of orbital prediction or antenna calibration inherent in the program command mode. However, initial pointing information aid is required, because the acquisition range of the autotrack system is only ±0.02° about the satellite position.

Since the system is experimental and the two methods are compatible, provisions are made so that either of these methods alone or a combination of the two can be used to control antenna pointing. When the two modes are combined, tape commands are used to place the antenna beam on the satellite, and the autotrack is used as a vernier to center the beam precisely. This tracking mode, called the "combined mode," unites the accuracy of the autotrack mode with the acquisition capabilities of the program command mode.

II. GENERAL DESIGN CONSIDERATIONS

For a satellite in a circular orbit with a maximum azimuth velocity of 0.5°/sec, the maximum azimuth acceleration is 0.003°/sec². These maxima define the input signal spectrum that the azimuth axis must follow in tracking a satellite. The spectrum and accuracy requirements determine the open-loop gain and phase requirements for azimuth. A system using two integrations was selected in order to meet the open loop gain requirement. This resulted in the open-loop gain vs frequency characteristic shown in Fig. 1. Shaping near the gain crossover frequency is necessary for stability reasons. To track with a maximum acceleration of 0.003°/sec² with an accuracy of 0.014° means that the gain crossover
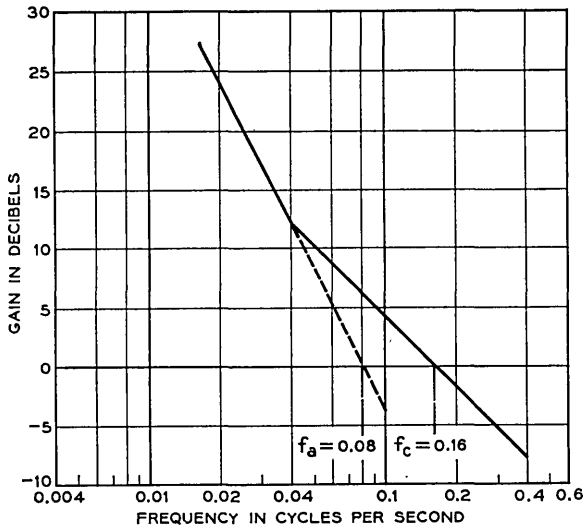
Fig. 1 — Open-loop gain vs frequency characteristic meeting system design objectives.

frequency (f_a) of the projected -12 db per octave asymptote must be at least 0.08 cps, as shown in Fig. 1. In order to realize this frequency with adequate phase margin, the lowest resonant frequency of the combined antenna and drive system must be over 0.64 cps.

Since the antenna and control system were designed and built at one time, it was not clear that the above requirements could be met. Therefore the program command mode was designed to provide and utilize velocity as well as position commands. Velocity command would have been needed if the servo bandwidth could not have been made large enough. However, this proved to be unnecessary, since the primary structural resonance in azimuth was found to be 1.8 cps.[5] Furthermore, the low Q of the antenna structure plus damping at the resonant frequency provided by a pressure feedback loop around the hydraulic motor drives resulted in an effective Q for the system of approximately 3. As a result, an open-loop gain vs frequency characteristic having a gain crossover frequency f_c of 0.4 cps has been achieved, as shown in Fig. 13 of Section 4.1. This gave the ability to track satisfactorily any satellite pass up to the maximum antenna velocity in azimuth of 1.5°/sec.

Other design considerations arise from the need to track accurately at very low speeds. The antenna is supported on rails by four two-

wheeled trucks[5] which develop large discontinuous torques about the azimuth axis at very low turning velocities. Accurate tracking at these speeds requires minimization of the system response to these torques. A peak response of less than 0.014° for a step change of 50,000 ft-lbs applied to the azimuth turntable was the design objective. System responses to these torques are determined by the position feedback loop, antenna inertia, and drive system stiffness. The position feedback loop increases system stiffness at low frequencies; the two integrations in the loop reduce the error due to a constant friction torque to essentially zero. The inertia of the antenna is effective in minimizing the response of the system to the disturbance torques at high frequencies. Hydraulic motor drives were chosen because of their high stiffness, large bandwidth and high acceleration capability. The drive stiffness was further increased by the use of velocity feedback. Compliance of the 15,107:1 gear reduction in azimuth was minimized by the use of a 64-ft diameter bull gear mounted on the antenna foundation and driven by large gear boxes mounted rigidly to the azimuth turntable. The effect of backlash in the gear trains was eliminated by the use in each drive of two opposing hydraulic motors coupled to the bull gear through individual gear trains. As a result of these precautions, a step change in torque of 200,000 ft-lbs rather than 50,000 ft-lbs is required to get a peak error response of 0.014°.

On account of the very large torques that high wind velocities could exert on the horn structure (10^6 ft-lbs at 30 mph), it was clear very early in the project that a radome would be required if the system was to operate reliably under all weather conditions.[5]

Because of the complexity of the servo system and the various nonlinearities present, analog computer simulations have been used extensively for the synthesis and analysis of the proposed configurations. As one of the significant results obtained from the analog computer studies, it was learned that a pressure feedback loop from hydraulic transmissions is not only effective, but essential, for damping out the oscillatory motion of the antenna. The simulations also provided a convenient means for determining the gains of the various minor feedback loops and their effects on the over-all performance. Completely analytical approach would not have been practical because of small as well as large signal nonlinearities present. The final modifications and adjustments of the gains were made on the basis of performance of the actual antenna servo.

III. DRIVE SYSTEM

This section describes the hydraulic transmissions and the associated minor feedback loops, including yoke position, pressure difference, pres-

sure and velocity loops. A functional diagram of the over-all drive system is shown in Fig. 2.

1.3 *Hydraulic Transmission*

Each hydraulic drive system contains a pair of hydraulic transmissions.[5] Each hydraulic transmission is composed of one constant-speed, variable-displacement pump and a pair of constant-displacement motors with output pinions connected to the bull gear through individual gear trains. Pump displacement is controlled by the yoke position.

The two hydraulic transmissions used in the azimuth axis are rated at 25 HP each, and those used in the elevation axis are rated at 10 HP each. The 25-HP unit is capable of developing a maximum output torque of 38 ft-lbs, while a 10-HP unit is capable of delivering 15 ft-lbs. These values correspond to 0.55×10^6 ft-lbs and 0.27×10^6 ft-lbs of torque, respectively, at the bull gear. The actual torques available at the bull gears are reduced by about 10 per cent in overcoming the friction torques. The gear ratios are 15,107:1 for the azimuth axis and 18,344:1 for the elevation axis. Since the inertias (including those of the motors and gear trains) for the two axes are 41×10^6 slug-ft^2 for azimuth and 7.4×10^6 slug-ft^2 for elevation, the maximum accelerations attainable are 1.3 degrees per second squared for the azimuth and 3.0 degrees per second squared for the elevation. The maximum motor velocity is 4200 rpm for both axes. The maximum antenna velocities are 1.5 degrees per second for the azimuth and 1.4 degrees per second for the elevation.
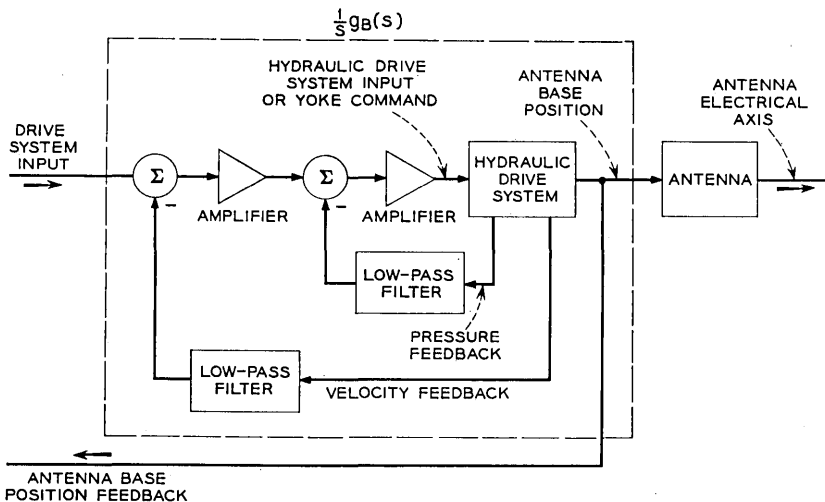

Fig. 2 — Functional diagram of drive system.

A linearized differential equation of the 25-HP unit is:

$$K_L P + K_c(dp/dt) + (d\theta_M/dt) = K_Y Y$$

where

$K_L = 4 \times 10^{-3}$ (radians/second)/(psi)
$K_c = 3.7 \times 10^{-3}$ (radians/second)/(psi/second)
$K_Y = 15$ (radians/second)/(degrees).

Here, Y is the yoke position in degrees, P is the pump pressure in psi, and θ_M is the motor pinion position in radians. The saturation values of Y and P are 30 degrees and 2200 psi respectively. The conversion factor from the pressure to torque is 0.017 ft-lb per psi.

The torque required to overcome friction in the system is a highly nonlinear function of the velocity. This is illustrated in Fig. 3, which shows the average torque required to drive the azimuth axis as a function of velocity.

The friction characteristics in the elevation axis are similar.

This discontinuity of the torque required to overcome friction around zero velocity produces a corresponding nonlinearity in the antenna velocity versus yoke position characteristic shown in Fig. 4. Since the slope of antenna velocity versus yoke position is a measure of the effective gain in the drive system, the small signal gain is highly nonlinear when the average velocity is low.

The hydraulic transmission also has large signal nonlinearities due to such factors as the velocity and amplitude limitations on the motion of the hydraulic yoke, and the hydraulic pressure limitations on the drive motors. However, these large signal nonlinearities are not as difficult to handle as the small signal nonlinearities discussed above.

3.2 Yoke Position Loop

The yoke position loop is the innermost of the minor feedback loops in the drive system, as shown on Fig. 5. As the name implies, this loop is designed to control the position of the pump yoke, which in turn controls the motor velocity.

The yoke mechanism is subject to both velocity and position limitations. Position limiting decreases the loop gain but does not degrade the phase characteristics. However, velocity limiting does introduce an additional phase lag which can be as large as 90 degrees. The closed-loop gain versus frequency response characteristics for three different input

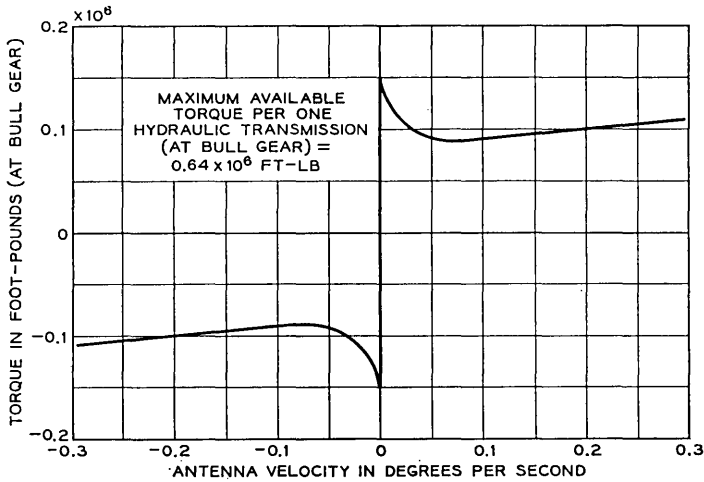Fig. 3 — Average friction torque at constant velocity — azimuth.
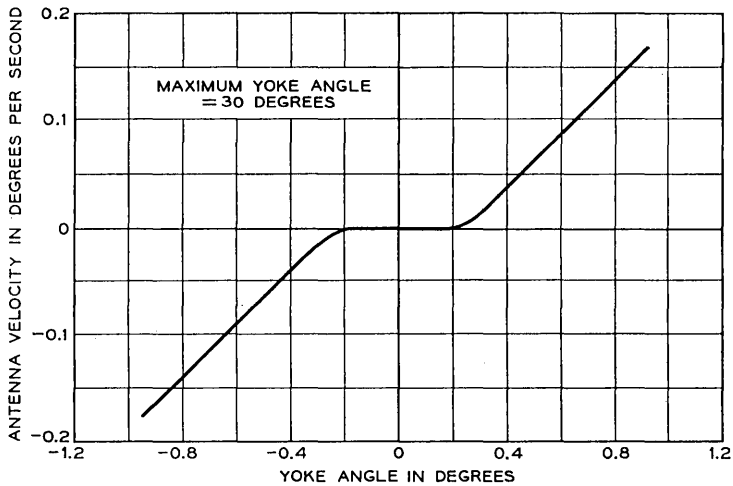
Fig. 4 — Antenna velocity vs yoke position characteristic for one hydraulic transmission — azimuth.

levels are shown on Fig. 6 to illustrate the degradation of the phase characteristic with load.

Allowance was made in designing the rest of the hydraulic drive system for this additional phase shift, so that the system is absolutely stable for large signals.
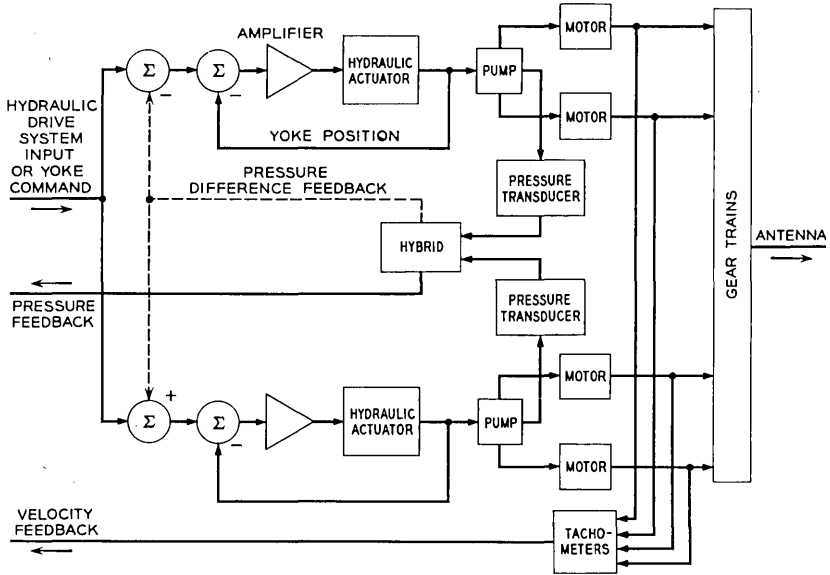
Fig. 5 — Functional diagram of hydraulic drive system.

3.3 *Pressure Difference Loop*

Since two hydraulic transmissions are used per axis to position the antenna, some means for equalizing the load on the two units is necessary. The pressure difference loop performs this function. A voltage proportional to the pressure difference is developed and fed back so as to reduce the yoke position of one unit and increase the other. In this way, the pressures, and consequently the output torques of the two transmissions, are equalized. The pressure difference loop is shown in dashed lines in Fig. 5.

3.4 *Pressure Loop*

It is the function of the pressure feedback loop to minimize the effects of the primary resonance of the combined antenna structure and hydraulic drive system, and this is accomplished by damping the system near its resonant frequency.

The way that the pressure feedback provides damping is easily shown on the electrical analog of the drive system presented in Fig. 7. The equivalent circuit of the antenna is derived from a simplified two-mass-
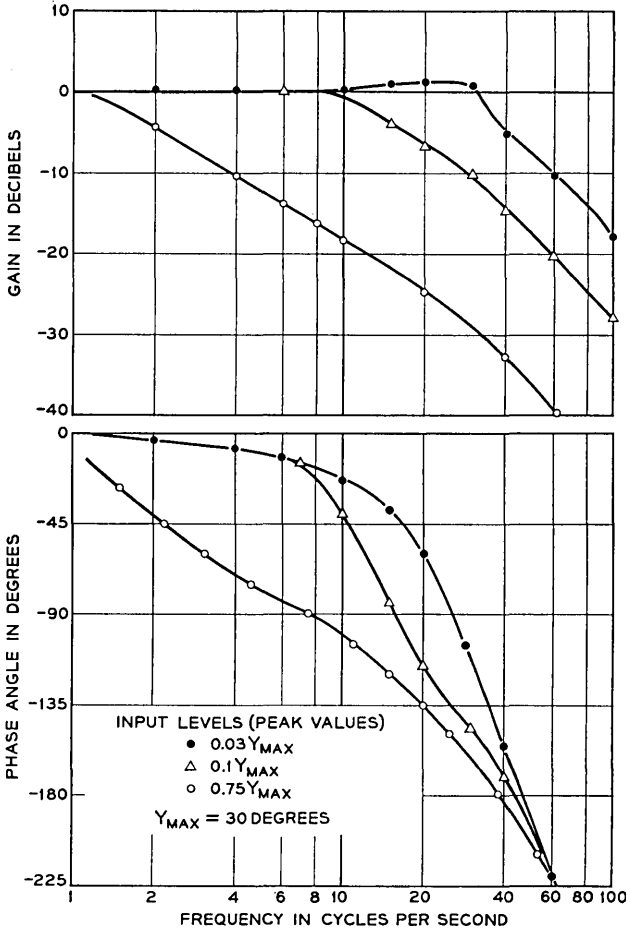
Fig. 6 — Closed-loop frequency response of yoke position — azimuth.

and-spring model, but this simplification does not affect the discussion here. The important point here is that the application of pressure feedback to the system is equivalent to adding a resistance, R_P, in the first mesh of the equivalent circuit. R_P is proportional to the gain of the pressure feedback loop.

It is clear that at resonance the equivalent circuit presents a low impedance to the driving voltage e_Y. R_P will be most effective in reducing the driving current i_M that can flow in the network at resonance
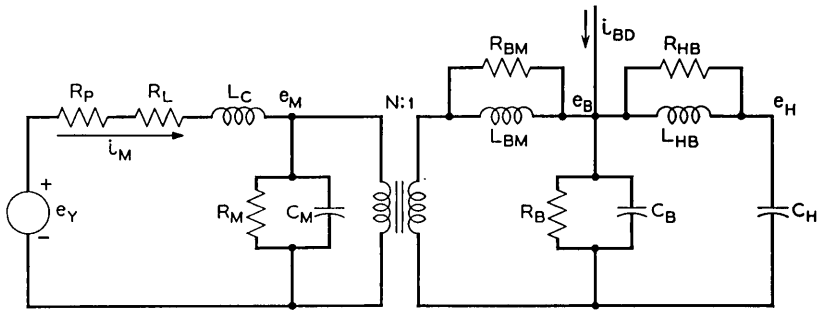
RELATION BETWEEN ORIGINAL AND ANALOGUE QUANTITIES	
ELECTRICAL	MECHANICAL
e_Y	YOKE ANGLE
e_M, e_B, AND e_H	VELOCITIES OF MOTOR, ANTENNA BASE, ANTENNA HORN OR ELECTRICAL AXIS
i_M	HYDRAULIC TORQUE
i_{BD}	TORQUE DISTURBANCE AT BASE
R_L AND L_C	HYDRAULIC TRANSMISSION LEAKAGE AND COMPLIANCE
C_M, C_B AND C_H	INERTIAS OF MOTOR, ANTENNA BASE, AND ANTENNA HORN
L_{BM} AND L_{HB}	COMPLIANCES
R_M, R_{BM}, R_B, AND R_{HB}	MECHANICAL FRICTIONS
N	GEAR RATIO
R_P	EFFECT OF PRESSURE FEEDBACK

Fig. 7 — Electrical analog of hydraulic drive system and antenna.

when the impedance of the load is low. In addition to this, R_P helps to damp out transients that might be set up in the system by the torque disturbance, i_{BD}.

Thus the pressure feedback reduces the driving torques that the hydraulic drive system can deliver to the antenna structure at resonance, and it also helps to damp out transients set up in the system by disturbance torques.

The increase in the driving impedance that the antenna sees as a result of pressure feedback reduces the effective stiffness of the driving system. However, the driving system with pressure feedback allows
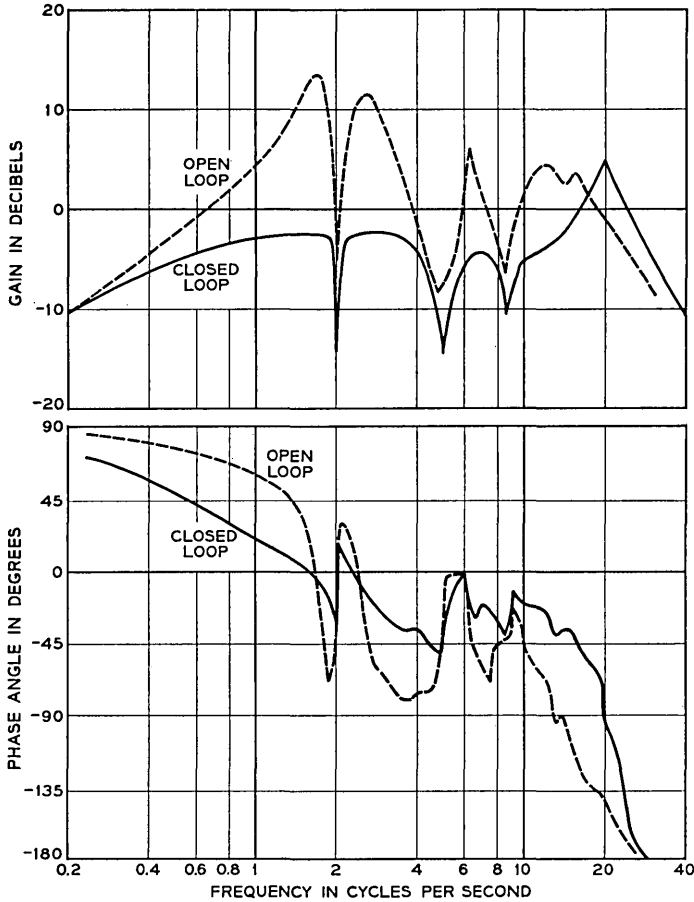
Fig. 8 — Open- and closed-loop frequency response of hydraulic pressure — azimuth.

higher gains in the velocity and position feedback loops at frequencies below resonance so that the effective hydraulic drive system stiffness is maintained at lower frequencies. It is important to keep the hydraulic drive system as stiff as possible to minimize the effects of friction at very low tracking velocities.

The effects of the pressure feedback loop on the characteristics of the combined antenna and hydraulic drive system are shown in Figs. 8 and 9. Here, the input is the driving voltage applied to the hydraulic drive
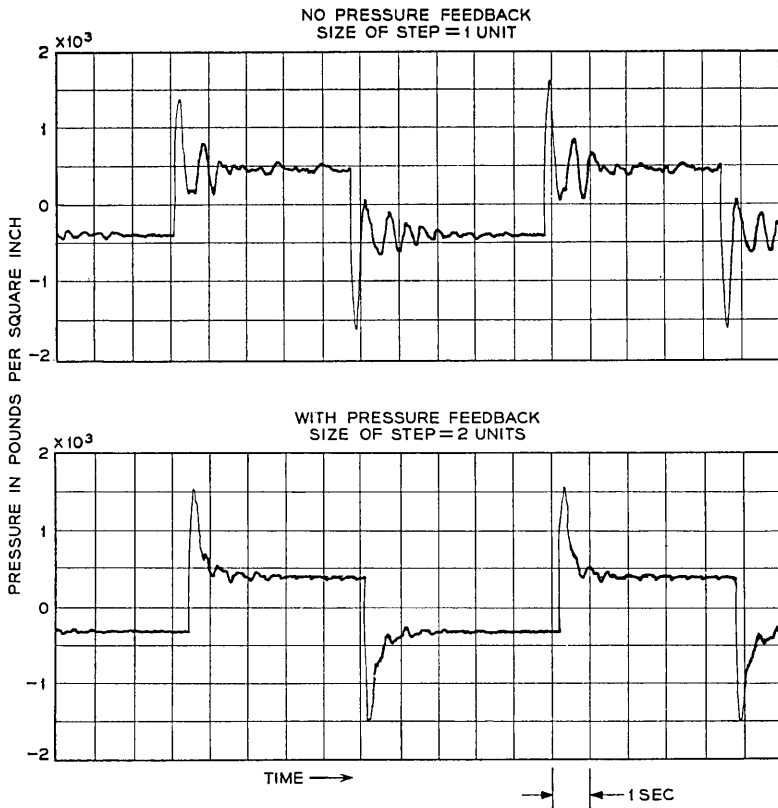
Fig. 9 — Pressure response to a step input with and without pressure feedback — azimuth.

system, and the gain is defined as the ratio of the pressure transducer output to the driving voltage. The gain versus frequency characteristics show that the closing of the pressure loop lowers the driving torque some 16 db at 1.8 cps where the combined antenna and drive system has its primary resonance. The pressure feedback also serves to suppress other resonances in the system all the way out to 15 cps. These curves also show that as far as the gains of the other loops are concerned, the effect of the pressure feedback is negligible at 0.2 cps and below. It should be noted also that the pressure feedback improves the phase versus frequency characteristics at 1 cps. This permits the use of a high-velocity loop gain and ultimately serves to improve the bandwidth and stability of the entire tracking system.

The damping effect is clearly illustrated in the step responses shown in Fig. 9. It is worth noting that two different input step sizes are used, although the peaks in the transient response with and without feedback are comparable in magnitude. It is apparent that the oscillations in pressure are greatly reduced by the use of the pressure feedback. The steady state pressure is equal to the pressure required to overcome the friction torque.

3.5 Velocity Loop

The outermost of the minor feedback loops is the velocity feedback loop. Velocity feedback is effectively shunt feedback, and it lowers the impedance of the driving system, in contrast to the effect of pressure feedback discussed above. Its primary function is consequently to increase the stiffness of the driving system at low frequencies. This is important in minimizing the effects of torque disturbances on the system. The other function of the velocity feedback loop is to reduce the system sensitivity to changes in leakage and compliance of the hydraulic transmissions.

The open- and closed-loop frequency characteristics presented on Fig. 10 show how velocity feedback improves the phase and gain characteristics at frequencies below the primary resonance. The improvement in phase margin in the frequency range between 0.2 and 0.8 cps, where the over-all position control loop will have its gain crossover, is as much as 32°. The reduction in gain is 7 db or more at 0.4 cps and below, thereby increasing the effective stiffness of the system to torque disturbances by some 2 to 1 in this critical frequency range. A low-pass network cuts the high-frequency gain of the velocity loop and makes the effect of velocity feedback negligible at higher frequencies.

The hydraulic drive system with all the minor feedback loops closed will be referred to simply as "the drive system" in subsequent sections. A functional diagram of the drive system is shown in Fig. 2. The transfer function $(1/s)g_B(s)$ relates the antenna base position to the drive input system.

IV. ANTENNA POSITION CONTROLS

Two different methods of pointing the antenna at the satellite are incorporated in the system. From the servo standpoint this means that there are two different ways of deriving error signals for closing the position control loop. One way is to use position pick-offs on the me-
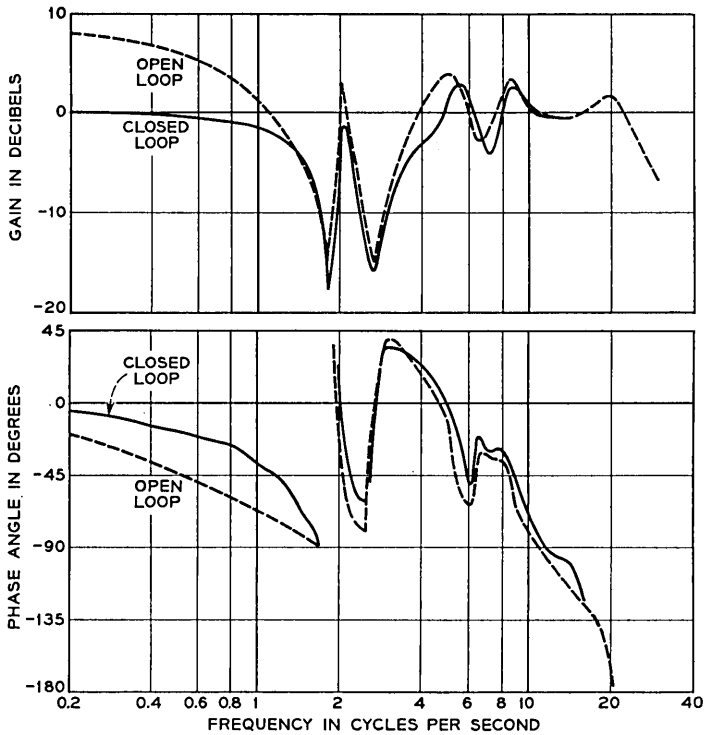
Fig. 10 — Open- and closed-loop frequency response of motor velocity — azimuth.

chanical axes of the antenna structure and compare the measured posi-
tions with program-predicted commands. This is the so-called program
command mode. The other way is to derive the error signal directly
from the 4-kmc beacon signal received from the satellite, using an auto-
track technique. This is called the autotrack mode. A third operating
mode, the so-called combined mode, operates on a combination of the
error signals generated from each of the two methods discussed above.

In order to avoid repetition of the same subject matter, each topic
is discussed just once as it is introduced. As a result, the section on the
program command mode becomes lengthy, while the other two are
relatively short.

A functional diagram of the over-all servo system, showing the inter-
connections of the various individual units and subsystems, is given in
Fig. 11. A brief discussion of the system configuration, responses to test
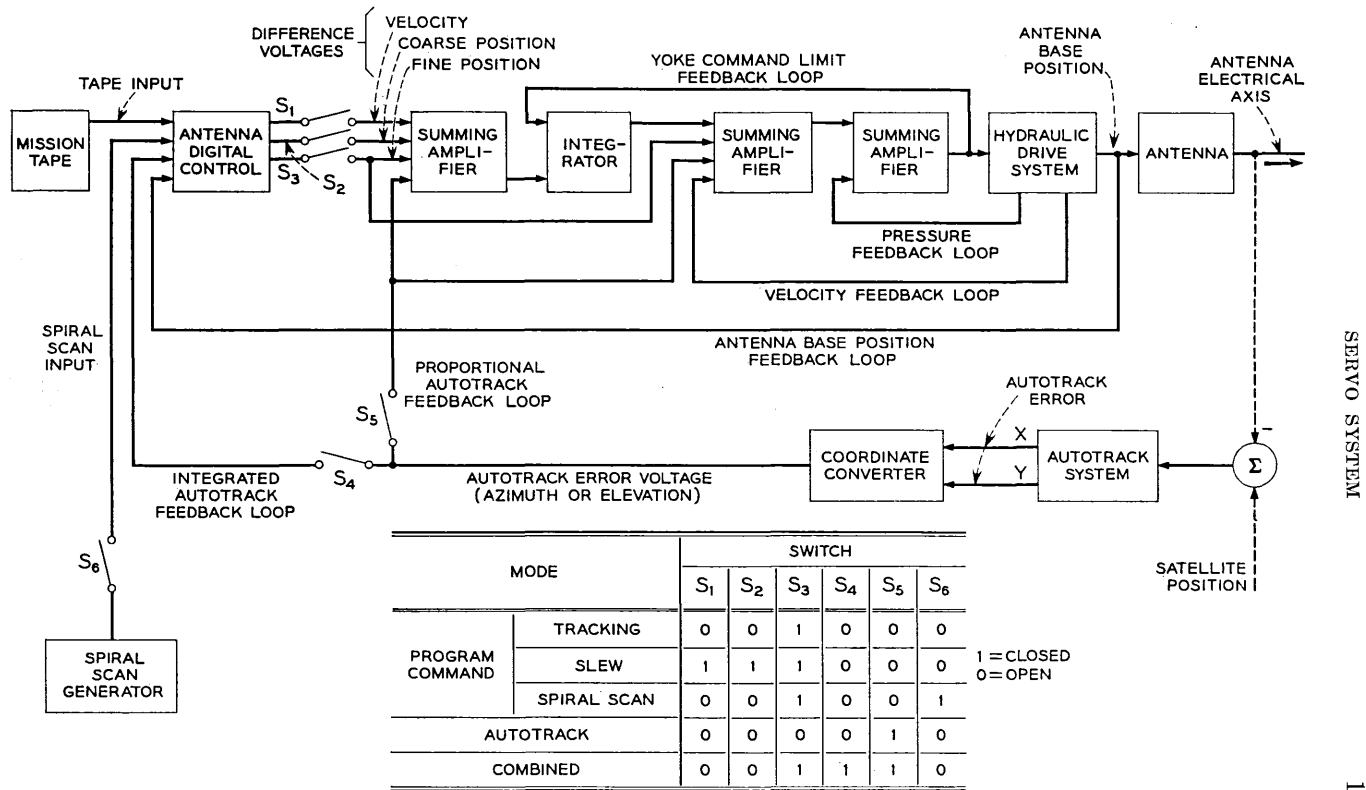
Fig. 11 — Over-all functional diagram of the servo system.

MODE		SWITCH						
		S_1	S_2	S_3	S_4	S_5	S_6	
PROGRAM COMMAND	TRACKING	0	0	1	0	0	0	1 = CLOSED
	SLEW	1	1	1	0	0	0	0 = OPEN
	SPIRAL SCAN	0	0	1	0	0	1	
AUTOTRACK		0	0	0	0	1	0	
COMBINED		0	0	1	1	1	0	

NUMERICAL VALUES

$K_1 = 1.3 \, (\text{DEG/SEC})/(\text{DEG})$

$K_2 = 2.9 \, (\text{DEG/SEC})/(\text{DEG})$
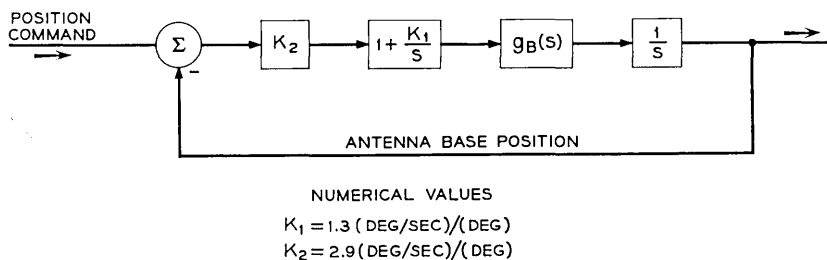
Fig. 12 — Block diagram of servo system in program command mode.

inputs, and the actual tracking performance for each operating mode are presented in the following sections.

4.1 Program Command Mode

In the program command mode of operation, the antenna base position is made to follow the program position command provided by the antenna digital control.[3] The block diagram of the system is shown in Fig. 12.

The antenna digital control receives, for a time increment of four seconds, data points from the tape and constructs the position commands. Each data point contains the predicted satellite position, velocity, acceleration, and the time for which it is valid. The position commands are offset to compensate for the differences between the electrical and mechanical axes of the antenna, as measured by star tracking.

The digital unit interpolates between these calibrated data points to provide new pointing information 128 times per second. The antenna digital control also receives the antenna base position information in digital form, compares it with the position command, and decodes the difference to provide a position difference voltage in analog form to the servo drive system.

The position difference voltage is quantized both in amplitude and time. However, the amplitude quantization is so fine (0.00274 degree) and the time quantization is so frequent (128 times per second) that the position difference analog voltage can be treated as a continuous voltage. The position difference voltage saturates at 0.7 degree.

As Fig. 12 shows, the position difference voltage is precompensated by $[1 + (K_1/s)]$, where s is the Laplace transform variable, before it is fed to the drive system. The transfer function $g_B(s)$ relates the antenna base velocity to the drive system input. For all practical purposes, $g_B(s)$ has unity gain in the low frequency region.

The numerical value of K_1 is 1.3°/sec per degree and that of K_2 is 2.9°/sec per degree. The acceleration constant of the system is K_1K_2, or 3.8°/sec² per degree.

The open-loop gain and phase characteristics for the program command mode are shown by Fig. 13. The gain crossover frequency for this
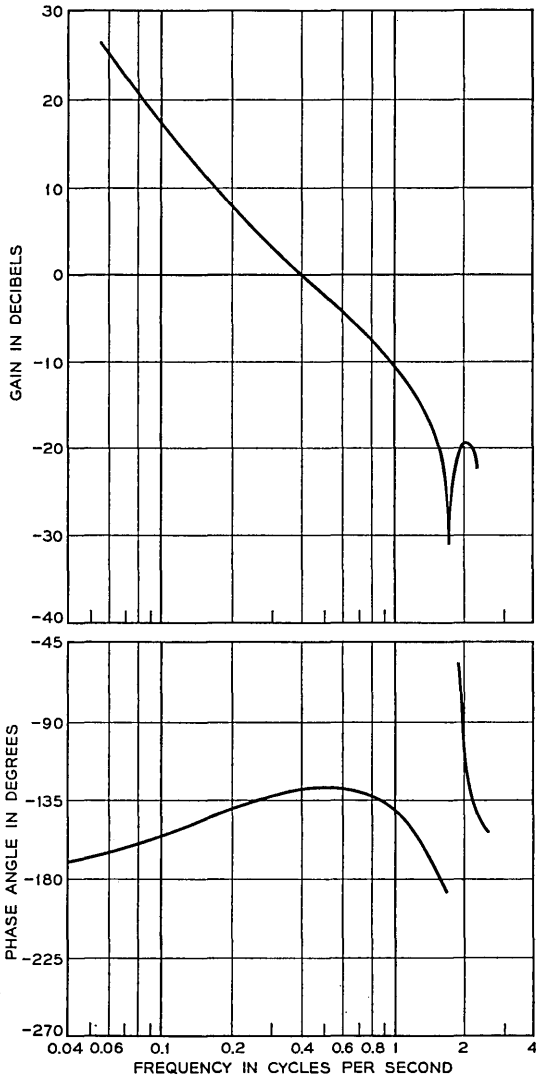
Fig. 13 — Open-loop frequency response of antenna base position — azimuth.

position control loop is 0.4 cps, and the phase margin at gain crossover is 52 degrees. Comparison with the minimum acceptable design objectives illustrated in Fig. 1 shows that the gain versus frequency characteristic realized for the system had the desired shape and that its crossover frequency exceeds the minimum acceptable design objective by 2.5:1. As a direct consequence, it was possible to realize an acceleration constant about 6 times larger than the design objective.

These improvements in loop gain and bandwidth over the minimum acceptable design objectives are due in large part to the increase in fundamental resonant frequency of the antenna structure and drive system from the 0.64 minimum required to the 1.8 cps actually achieved.

The closed-loop frequency response of the system is shown in Fig. 14, and the transient response to a triangular input is presented in Fig. 15. Although these responses are for the azimuth axis only, those for the elevation axis are similar. Input signal magnitudes were chosen to be as
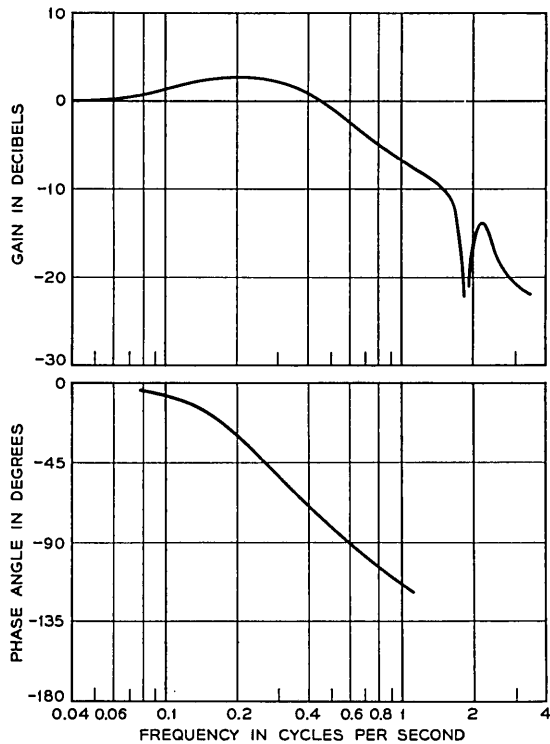
Fig. 14 — Closed-loop frequency response of antenna base position — azimuth.
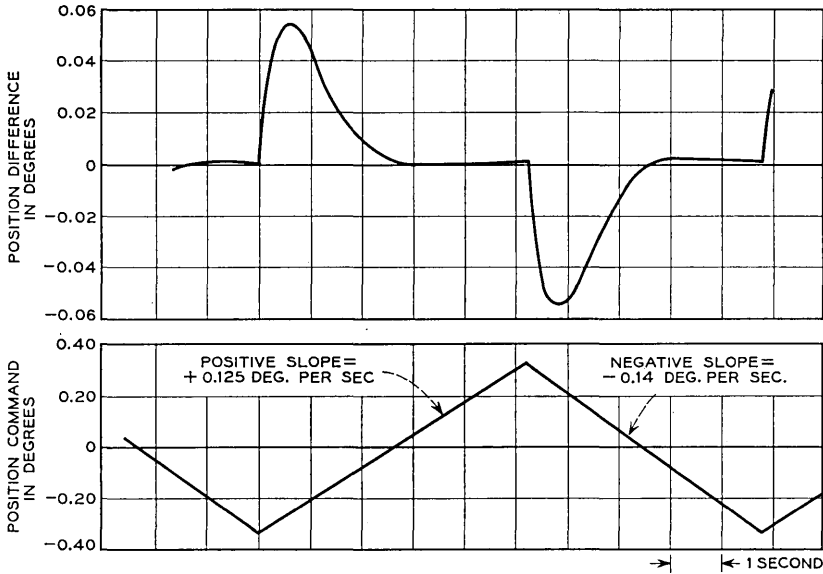
Fig. 15 — Ramp response of program command mode — azimuth.

large as possible but short of saturating the motor torque and velocity. The frequency response curves show that the gain is approximately unity out to 0.4 cps, where the phase lag reaches 60 degrees. Referring to the transient response, the peak position difference in following the position command representing a step velocity change of 0.275 degree per second is 0.055 degree, and the position difference is reduced to zero in less than 3 seconds following each step change in input velocity.

As this is a type 2 servo, the system theoretically follows a constant velocity input with no steady-state error. The acceleration constant for the final system is 3.8°/sec² per degree. This means the position error will not exceed the maximum allowable error of 0.014° for accelerations of less than 0.05°/sec². Since the maximum azimuth acceleration is only 0.026°/sec² for a satellite pass with a maximum velocity of 1.5°/sec, this means that the system can track right up to its maximum slew velocity with an acceleration error of only 0.007°.

The tracking response at low velocities also exceeds the minimum acceptable design objective. The effects of friction have been substantially reduced below the design objectives, since a step in torque of 200,000 ft-lbs applied to the base of the antenna produces a peak position error of less than 0.014°.

SATURATION LEVEL
±2.8 DEGREES
PER SECOND

VELOCITY
DIFFERENCE

YOKE COMMAND LIMIT
FEEDBACK LOOP

YOKE COMMAND

S

K₆

LIMITING VALUE
±30 DEGREES

POSITION
COMMAND

Σ

COARSE POSITION
DIFFERENCE

K₅

PROPORTIONAL
BAND LIMITER

A

−A

Σ

Σ

1/S

Σ

TO
DRIVE
SYSTEM

SATURATION LEVEL
±5.6 DEGREES

FINE POSITION
DIFFERENCE

K₁

SATURATION LEVEL
±0.7 DEGREES

SATURATION LEVEL
±0.56 DEGREES

K₂

ANTENNA BASE POSITION

NUMERICAL VALUES

$K_1 = 3.8 \, (\text{DEG/SEC}^2)/(\text{DEG})$

$K_2 = 2.9 \, (\text{DEG/SEC})/(\text{DEG})$

$K_5 = 0.49 \, (\text{DEG/SEC}^2)/(\text{DEG})$

$K_6 = 2.9 \, (\text{DEG/SEC})/(\text{DEG})$

$A = 2.0 \, (\text{DEG})/(\text{SEC}^2)$

Fig. 16 — Block diagram of the servo system in the program command slew mode.

4.2 *Program Command Slewing*

Program command mode slewing required special attention. Initially, it is necessary to slew the antenna from any arbitrary position to acquire a moving satellite for the start of tracking. The block diagram of the servo system in the program command slew mode shown in Fig. 16 supplements the subsequent discussion.

The tracking servo in the program command mode is actuated by the output of the fine position difference decoder, which produces a proportional difference voltage up to $\pm 0.7°$, but saturates beyond this value. With only this narrow-proportional range the antenna would overshoot several times and suffer rather violent acceleration changes in coming out of slew. These sudden and repeated reversals of drive torque applied to the structure are undesirable because the antenna structure carries both personnel and a large amount of electronic equipment. In order to eliminate this difficulty, the antenna digital control unit also provides a coarse position difference signal with $\pm 5.6°$ proportional range, and a velocity difference signal with $2.8°/\text{sec}$ proportional range. These outputs are both inhibited automatically when the position difference is less than $0.35°$ in order not to interfere with the normal tracking characteristics of this mode. The coarse and fine position difference signals and the velocity difference signals are combined to form an activating signal for the drive system.

At the start of a slew the antenna is accelerated by the maximum motor torque up to the velocity limit of the drives. This phase takes less than 1.2 seconds in azimuth, and about 0.5 second in elevation. The constant-speed portion of slew takes the major part of the slewing time. A 90-degree slew takes one minute in azimuth, and a little longer in elevation. During the deceleration phase the applied torque is always less than one-third of the maximum in order to limit the amount of energy stored in the compliance of the horn support structure. The position and velocity differences are reduced simultaneously; (see Fig. 17). When the position difference decreases to $0.35°$ the control system reverts to a tracking mode of operation; at that time the velocity difference is small enough for the tracking servo to terminate the slew without overshoot (see Fig. 18).

4.3 *Spiral Scan*

The spiral scan facility provides a systematic scan that can be used in conjunction with the program command mode of operation to search for a satellite in an increasing spiral about the commanded position. The pitch of the spiral is 0.2 degree per turn, so that successive scans
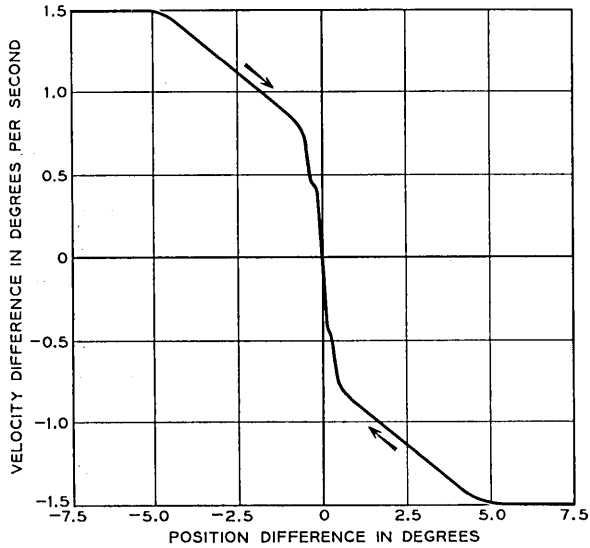
Fig. 17 — Phase plane trajectories of servo system in slew mode — azimuth.
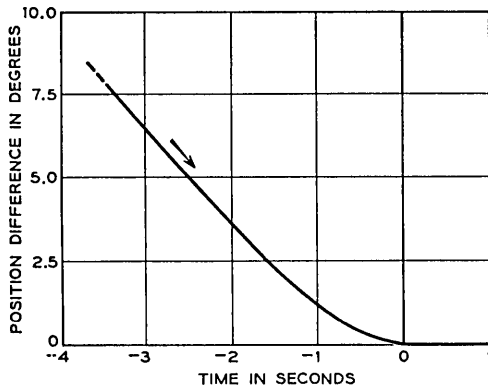
Fig. 18 — Servo system response in slew mode — azimuth.

overlap at the 3-db down point of the antenna beam. In order to scan equal areas in equal times, the angular velocity of the scan is made to decrease as the radius of the scan increases.

Two scanning speeds are provided for fast and slow searching. The fast scan sweeps out a circle with a 1-degree radius in 100 seconds. The slow scan takes 400 seconds to cover the same area. Provisions are made so that the fast scan can be stopped at any time during its scan and a

new slow-speed scan initiated, the center of which is offset from the commanded position by the position of the fast scan at the time the slow scan was initiated.

This spiral scan feature has been used in Telstar tests to search for and acquire the satellite. In a typical test, the high-speed scan was used until indication was received that the antenna had just swept by the satellite. Then the low-speed scan was initiated and the autotrack receiving system was able to achieve phase lock, acquire the satellite, and transfer control to the autotrack mode.

4.4 Autotrack Mode

In the autotrack mode, the autotrack error voltages are used to control the antenna position. In other respects the system configuration is essentially the same as that of the program command mode. The block diagram of the system is shown in Fig. 19. The new transfer function $g_E(s)$ relates the antenna electrical axis velocity to the compensated hydraulic drive system input. Here $g_E(s)$ can be considered unity at frequencies below 1 cps.

The value of K_1 is 1.3°/sec per degree and that of K_2 is 1.9°/sec per degree, for both axes. The value of K_2 has been reduced from that used in the program command mode for two reasons. One is to allow for the additional phase lag between the base position and the electrical axis, and the other is to minimize the system transient at the time the autotrack is engaged. The acceleration constant of the system is 2.5°/sec² per degree.

Fig. 20 shows the relation between the autotrack error voltage and corresponding position error for the azimuth axis. The one for elevation is similar. As Fig. 20 shows, for small position errors the slope of the error voltage is very nearly 65 volts per degree. However, the relation is quite nonlinear and the polarity even reverses for angular errors above
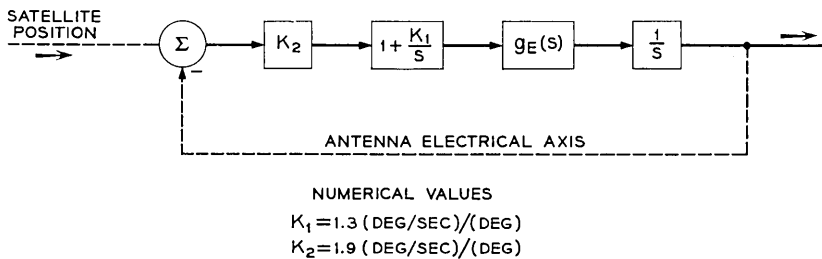
Fig. 19 — Block diagram of servo system in autotrack mode.
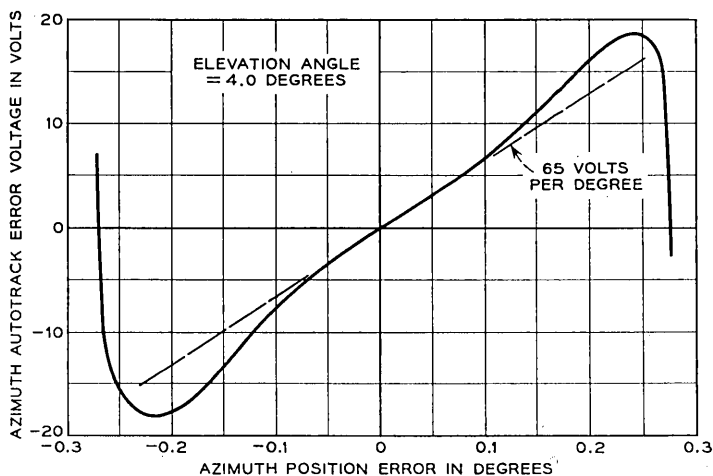
Fig. 20 — Autotrack error voltage versus position error characteristic — azimuth.

0.2 degree. Because of this, the autotrack mode cannot be engaged when the initial pointing error is greater than about 0.15 degree in each axis.

The original autotrack error voltages provided by the autotrack receiving system are in the X and Y coordinate system fixed with respect to the coupler, which does not rotate with the antenna in elevation. These error voltages are converted to elevation and traverse components, and the traverse error voltage is multiplied by the secant of the elevation angle to form the azimuth error voltage.[4]

Fig. 21 shows the transient response characteristics in the autotrack mode when the autotrack loop is closed with an initial error of about 0.1 degree in each axis. These characteristics show that the resulting transients damp out in 4 seconds. Since only the error voltage is available, it is not feasible to measure the open-loop gain and phase characteristics in the autotrack mode.

As in the previous mode, the position error in following a constant velocity is zero, and the position error in following a constant acceleration is proportional to the acceleration. Since the acceleration constant of the system is 2.5 degrees per second squared per degree, this means that the error for the maximum acceleration condition is 0.026 degree per second squared — approximately 0.01 degree.

4.5 *Combined Mode*

The combined mode is a combination of the two previously discussed modes. In this case, the program command and autotrack loops are
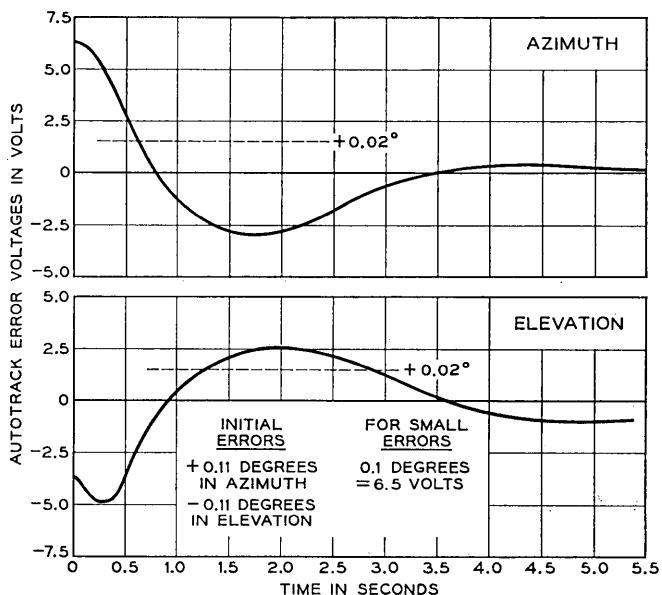
Fig. 21 — Response of servo system in autotrack mode to initial pointing error.

NUMERICAL VALUES

$K_1 = 1.3\ (\text{DEG/SEC}^2)/(\text{DEG/SEC})$
$K_2 = 1.9\ (\text{DEG/SEC})/(\text{DEG})$
$K_3 = 1.0\ (\text{DEG/SEC})/(\text{DEG})$
$K_4 = 1.6\ (\text{DEG/SEC})/(\text{DEG})$
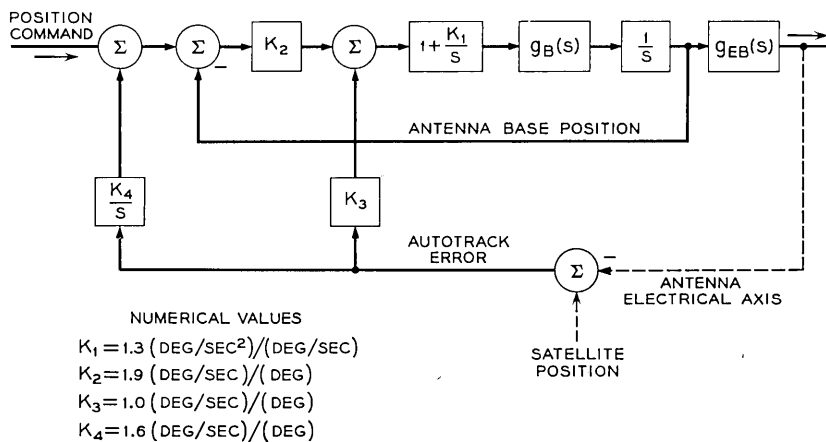
Fig. 22 — Block diagram of servo system in combined mode.

individually closed using the same configurations as before, but with different gains. In addition the autotrack errors are encoded, digitally integrated, and then added to the position command. The configuration is shown on Fig. 22. It is the function of the integrated autotrack error signal to buck out the low-frequency errors in the position command.
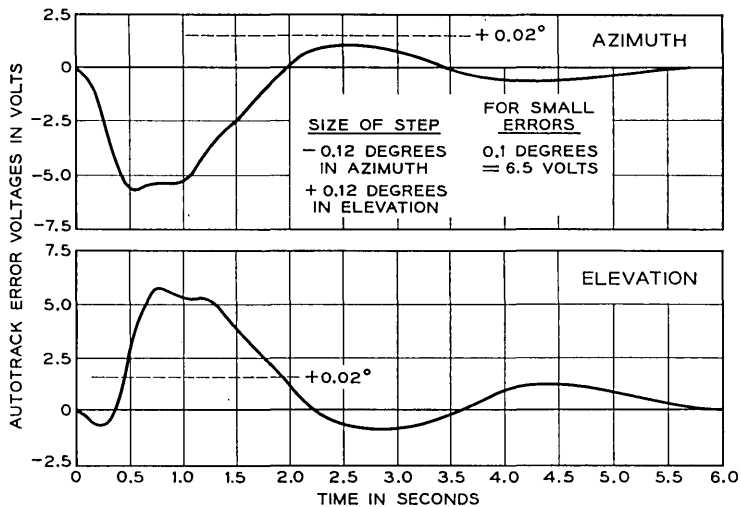
Fig. 23 — Response of servo system in combined mode to step change in program position command.

The relative weights of the program command, proportional autotrack and integrated autotrack loops can be adjusted by changing K_2, K_3, and K_4, respectively. The numerical values of the various gain constants used in the system are 1.3°/sec per degree for K_1, 1.9°/sec per degree for K_2, 1.0°/sec per degree for K_3 and 1.6°/sec per degree for K_4.

In theory, the performance in this combined mode should be comparable to that of the full autotrack mode as long as the errors in the predicted position commands vary slowly as a function of time. However, the higher autotrack loop gain realized in the autotrack mode makes its performance superior to that of the combined mode.

Various step response characteristics for the combined mode are shown in Figs. 23 and 24. Fig. 23 shows the transient response characteristics as measured by the autotrack voltages in response to a step program position command change of 0.12 degree in both axes. The results show that the program position errors are integrated out in less than 6 seconds.

Fig. 24 shows the transients in autotrack error voltages that result from closing the autotrack loop after errors in the program position command had offset the pointing by 0.12 degree both axes. In this case, the pointing errors are reduced to less than 0.01 degree in 5 seconds.

Fig. 25 shows a typical tracking record of the servo system tracking at moderate velocities in the combined mode. Here, the autotrack error
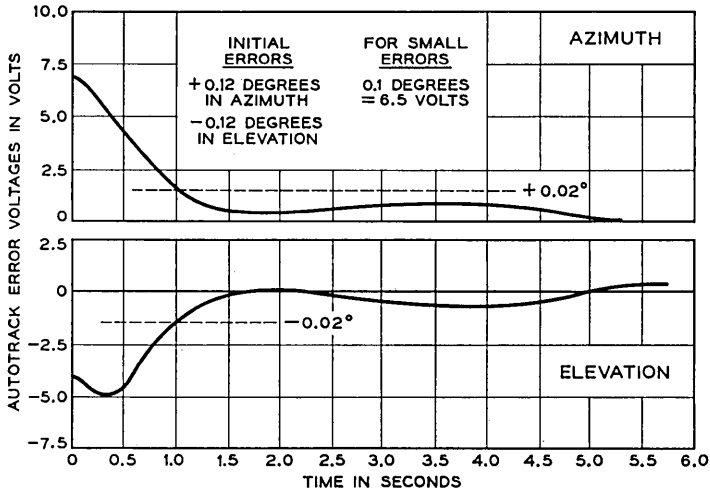
Fig. 24 — Response of servo system in combined mode to initial error in program position command.
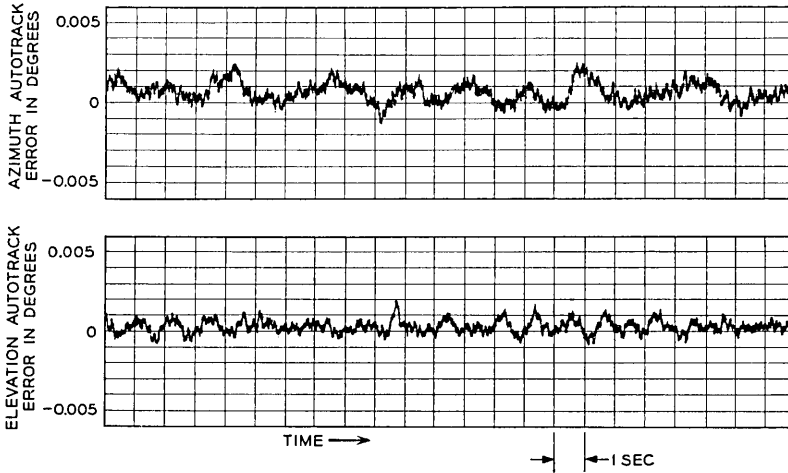
Fig. 25 — Typical tracking record of servo system in combined mode.

voltages are recorded as a function of time. The record shows that the autotrack tracking error voltages in the two axes are less than 0.003 degree. Slowly changing errors in the predicted satellite orbit, distortion of the antenna structure due to gravity, or the effects of quantization
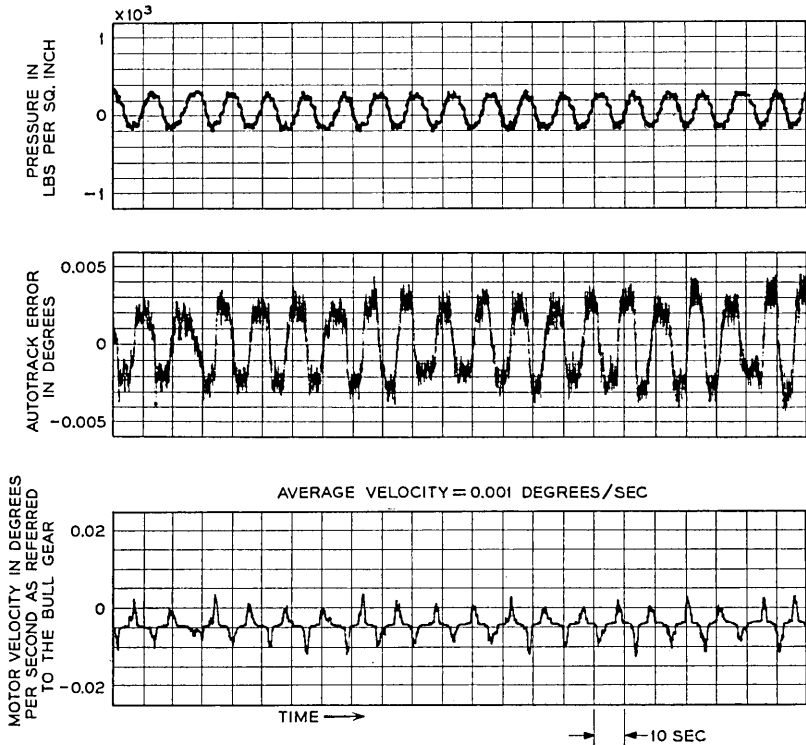
Fig. 26 — Small amplitude hunting in combined mode — azimuth.

in the encoded antenna position do not affect the tracking accuracy in this mode.

The combined mode of operation is subject to a low-amplitude, low-frequency hunting when the tracking velocity in either axis is very low (less than 0.002 degree per second). Hunting about the azimuth axis is shown in Fig. 26. The frequency of the hunting is about 0.17 cps and the corresponding autotrack error can be as large as 0.008 degree.

The hunting phenomenon described above is caused by two factors. One is the extra stage of integration inserted in the autotrack loop to make the autotrack error dominant over the program position command at very low frequencies. The extra integrator makes the combined mode a type 3 servo and, therefore, one which is conditionally stable. The other factor is the reduction in gain of the drive system for small tracking velocities, as discussed previously. This condition is not considered detrimental, because the maximum tracking error is less than 0.008

degree and because the condition disappears when the tracking velocity exceeds 0.002 degree per second.

V. CONCLUSIONS

The design objective called for tracking with a pointing error less than 0.02 degree for all satellite passes where the azimuth velocity is less than 0.5 degree per second. This objective corresponds to tracking a 2500-mile-high satellite up to an elevation angle of 81°.

The relatively high frequency of the first structural resonance and the use of pressure feedback to provide damping of this resonance made it possible to obtain a 2.5:1 increase in bandwidth and a 16-db increase in gain of the position loop over and above the system objectives. The resulting improvement in dynamic performance permits tracking of a 2500-mile satellite up to an elevation angle of 87° rather than the 81° objective.

The servo system has consistently positioned the antenna on the satellite track with an accuracy sufficient to give less than 1-db degradation in antenna gain.

VI. ACKNOWLEDGMENTS

REFERENCES

1. Githens, J. A., Kelly, H. P., Lozier, J. C., and Lundstrom, A. A., Antenna Pointing System: Organization and Performance, B.S.T.J., this issue, p. 1213.
2. Claus, A. J., Blackman, R. B., Halline, E. G., and Ridgway, W. C., III, Orbit Determination and Prediction, and Computer Programs, B.S.T.J., this issue, p. 1357.
3. Githens, J. A., and Peters, T. R., Digital Equipment for the Antenna Pointing System, B.S.T.J., this issue, p. 1223.
4. Cook, J. S., and Lowell, R., The Autotrack System, B.S.T.J., this issue, p. 1283.
5. Dolling, J. C., Blackmore, R. W., Kindermann, W. J., and Woodard, K. B., The Mechanical Design of the Horn-Reflector Antenna and Radome, B.S.T.J., this issue, p. 1137.

The Autotrack System

By J. S. COOK and R. LOWELL

The autotrack system accurately senses the direction of arrival, at the horn-reflector antenna, of the microwave beacon signal from the communications satellite. When this direction does not coincide with the horn-reflector pointing direction, error correcting voltages are automatically generated to enable the antenna direction system to steer the antenna toward the satellite.

This paper presents a simple analysis of error voltage generation, a description of the system, and a brief discussion of system performance. Measurements at Andover, Maine, have shown that an angular pointing error of less than 0.005 degree is maintained by the antenna when using the autotrack system to follow the Telstar communications satellite.

I. GENERAL

The autotrack system (originally designated and often referred to as the "vernier autotrack," or "VAT") is a pointing-error sensing and processing system for the horn-reflector antenna. It receives the circularly polarized 4080-mc CW beacon signal entering the antenna from the satellite, and, by examining the nature of the propagation of this signal through the antenna feed line, determines the discrepancy between the direction the antenna is pointing and the actual direction of the satellite. This discrepancy is reduced to a set of pointing-error signals to be used by the antenna pointing system to provide either a vernier correction of the programmed antenna pointing instructions, or fully automatic tracking, as shown in the block diagram of Fig. 1.

II. PRINCIPLE OF OPERATION

2.1 Received Tracking Signals

As a help to understanding the principle of operation of the autotrack, it is useful to think of the conical horn-reflector antenna as consisting of a conical transition from conventional cylindrical waveguide to a

very large open-end waveguide of circular cross section, having a reflective 90° bend.

Thus, if a particular mode is excited in the feed to the horn reflector, the energy propagated appears in essentially the same modal configuration in the large open cylinder that forms the antenna aperture. Only slight distortion is brought about by the asymmetry of the parabolic reflector which comprises the 90° bend. In all essential characteristics, then, the pattern of radiation from the antenna generated by exciting a particular waveguide mode in the throat of the horn will be like that radiated from a large open-ended circular waveguide excited in the same mode. It is to be recognized that the antenna is a reciprocal device, and that its radiation characteristics hold for transmission and reception alike. Hence, nothing is lost in treating the antenna from a radiating point of view, even though the scheme here described operates on a received CW signal.

In this discussion our interest will be confined to the two lowest-order modes in cylindrical guide: namely the TE_{11}, or dominant, mode and the TM_{01} mode. In fact, the waveguide feed to the horn-reflector antenna at Andover is of such diameter as to cut off all higher modes of propagation at the beacon frequency. The field configurations of the two admitted modes are shown in Fig. 2. Solid lines depict electric fields; dotted lines, magnetic.

Chu[1] has worked out general expressions for the far-field radiation patterns for open-ended circular guides. Though the expressions neglect the discontinuity at the waveguide opening, and are therefore of questionable validity near cutoff frequency, their validity from that point of view is unquestionable for a very large waveguide diameter ≈ 280 λ.
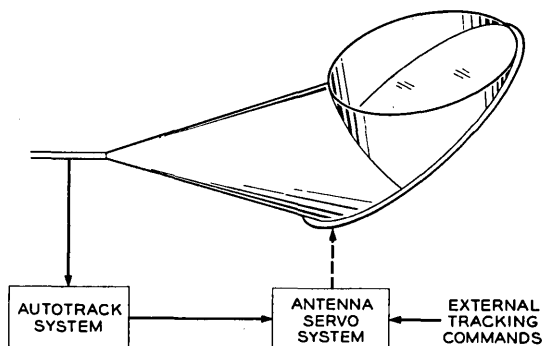
Fig. 1 — Autotrack connection with the antenna servo system.
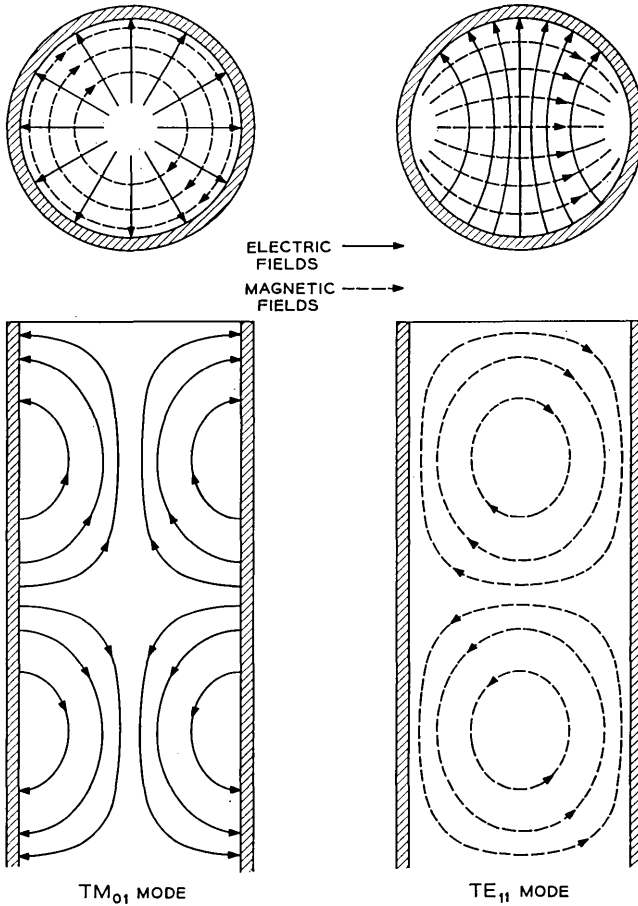
Fig. 2 — Circular waveguide mode field configurations.

The relative amplitude of the far electric fields excited by the radiation of the TM_{01} mode from a large open waveguide is:

$$E_\theta = \frac{E_0}{kR} \frac{J_0(ka\theta)}{\theta\left[\left(\frac{2.405}{ka\theta}\right)^2 - 1\right]}$$

$$E_\phi = 0$$

$$E_R = 0.$$

(1)

For the vertically polarized TE_{11} mode, the far field is characterized by

$$E_\theta = \frac{E_1}{kR} \left[\frac{J_1(ka\theta) \sin \phi}{\theta} \right]$$

$$E_\phi = \frac{E_1 a}{R} \left[\frac{J_1{}'(ka\theta) \cos \phi}{1 - \left(\dfrac{ka\theta}{1.84}\right)^2} \right] \tag{2}$$

$$E_R = 0$$

where k is the free-space propagation constant, J_0 and J_1 are the zero and first-order Bessel functions, a is the waveguide (hence aperture) radius, and E_0 and E_1 are arbitrary field constants which may be rationalized in terms of the total power radiated by each mode. It turns out that $E_0 \approx E_1$. The θ, ϕ, R coordinate system is shown in Fig. 4. Both (1) and (2) assume $\theta \ll 1$; i.e., $\cos \theta \approx 1$, $\sin \theta \approx \theta$. The vertical cross sections of the patterns represented by (1) and (2) are shown in Fig. 3. The actual radiation patterns for both the TM_{01} and TE_{11}
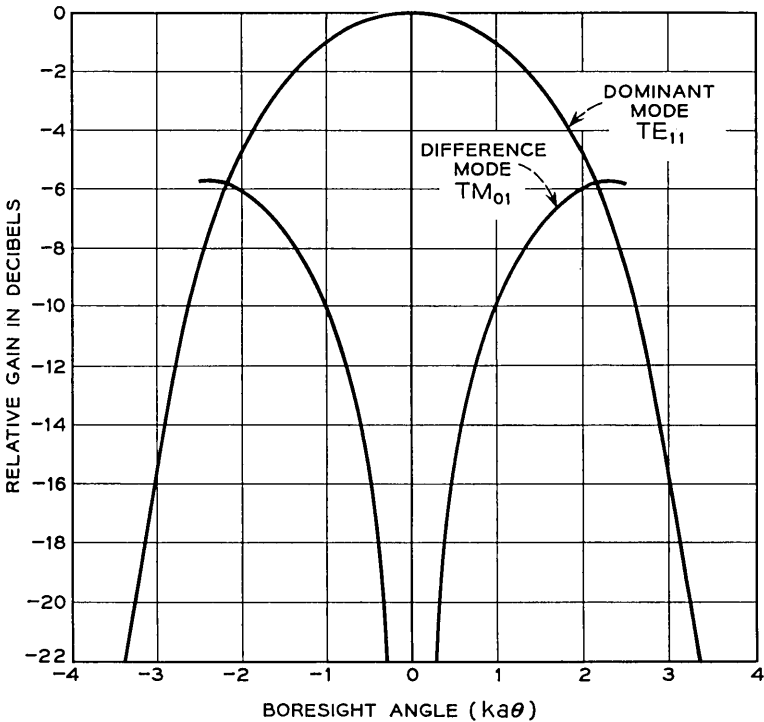
Fig. 3 — Radiation patterns for an open-end circular waveguide.

excitation of the conical horn reflector have been computed by T. G. Li and measured by J. N. Hines[2] and are, indeed, very similar to the corresponding open waveguide patterns.

The significance of the radiation patterns and their associated equations (1) and (2) becomes clear when the reciprocal condition of signal reception is considered. Fig. 4 depicts a source near the waveguide axis at the coordinate position $[\theta, \phi, R]$, where θ and ϕ describe the antenna pointing error. It is assumed that this source is, in general, elliptically polarized. The TM_{01} field-pattern shows that a TM_{01} signal will be excited only by the θ component of incident field, E_θ, and not by the ϕ component. The phase and magnitude of the TM_{01} signal at some reference point in the waveguide will therefore be determined by the phase and magnitude of the E_θ, or ϕ plane component. The magnitude of TM_{01} mode is dependent upon pointing error. For zero error, when the source lies on the waveguide axis, the pattern shows a deep null, indicating that no TM_{01} signal will be excited. However, when the source moves off
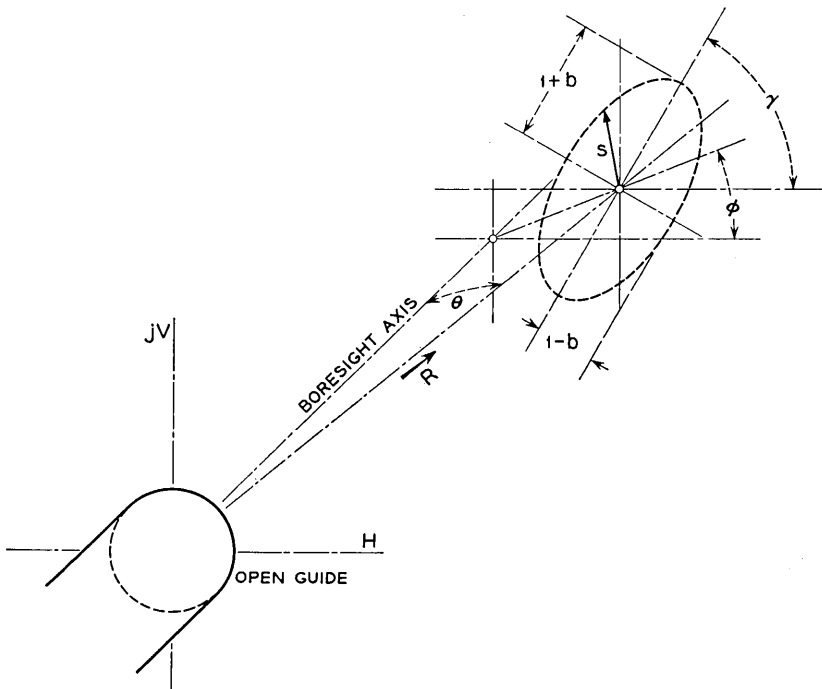
Fig. 4 — Elliptically polarized signal source and space coordinates as used in the analysis.

the waveguide axis, the TM_{01} mode will be strongly excited. When θ is small $(ka\theta < \frac{1}{2})$, (1) may be simplified to

$$E_\theta = \frac{E_0 ka^2 \theta}{2.405R}$$

$$E_\phi = 0 \tag{3}$$

$$E_R = 0$$

which shows that the amplitude of the TM_{01} signal in the waveguide is directly proportional to small pointing error. It will be shown below that these characteristics, an amplitude proportional to pointing error and a phase determined by the θ component of field (that is, the component in the ϕ plane or R-θ plane), allow the TM_{01} signal to be used as an indication of the magnitude (θ) and direction (ϕ) of the pointing error.

The TE_{11} signal provides a reference against which the phase and amplitude of the TM_{01} signal are measured. Its utility for this purpose arises from two properties inherent in (2). First, the magnitude is approximately invariant with pointing error, θ, when θ is small, thus providing a magnitude reference to extract the effects of range. Second, for small θ, the TE_{11} mode is excited by both the θ and ϕ components of field in such a way that the polarization of the incoming signal is preserved; and the measurement of any two orthogonal components of the TE_{11} mode will determine this polarization. This property enables the TE_{11} signal to function as a phase reference.

The TE_{11} and TM_{01} radiation patterns resemble in form and function the "sum" and "difference" patterns, respectively, of conventional simultaneous lobing tracking systems. The conventional designations, "sum" for TE_{11} and "difference" for TM_{01}, will henceforth be used in this paper. The phase and amplitude relationships for these signals will now be derived.

2.2 The Sum and Difference Signals

The beacon wave expected from the satellite will be circularly polarized, though sometimes imperfectly. For generality, it will be assumed that the source, S, generates an elliptically polarized wave. Referring again to Fig. 4 for definitions of coordinates, the rotating field vector thus generated in the aperture can be simply expressed in terms of two counter rotating vectors: a positively rotating vector of amplitude, e_0/R, and a negatively rotating vector of amplitude, $b(e_0/R)$. The constant e_0 represents effective radiated power and propagation factors. The R represents range and accounts for the $1/R$ attenuation

of the wave as it radiates from the source. The two vectors rotate at an angular velocity ω. In order to permit the use of complex vector notation, the H-V plane (transverse to the guide axis) is pictured in Fig. 4 as a complex plane with the vertical axis designated as imaginary. The incident wave can then be expressed as

$$E_S = \frac{e_0}{R} (e^{j\omega t} + b e^{-j\omega t}) e^{j\gamma} \tag{4}$$

where b determines the signal ellipticity, and γ determines the inclination of the major axis of the ellipse in the complex plane. As seen in the figure, the source is located at a small error angle, θ, off the open waveguide axis, and lies in a plane through the axis which is inclined an angle ϕ counterclockwise from the horizontal plane.

In the autotrack system, the horizontal and vertical components of the dominant mode are sampled and amplified separately. These two sum signals, together with the sampled difference mode, constitute the three autotrack signals derived from the elliptically polarized incident wave. As discussed above, the horizontal sum signal, e_H, responds only to the horizontally polarized component of the incident wave, the vertical sum signal, e_V, only to the vertical component, and the difference signal, e_D, only to the ϕ-plane component (E_θ).

For the sum signals, the response is invariant with small error angle, θ. If the conversion of incident field to the sampled sum signals is represented by a determinable constant, c_1, the sum-signals become

$$e_H = c_1 \, \text{Re} \, [E_s]$$
$$e_V = c_1 \, \text{Im} \, [E_s]. \tag{5}$$

For the difference signal, the response is proportional to the ϕ-plane component of E_s, $\text{Re} \, [E_s e^{-j\phi}]$, and to the small error angle, θ. Thus

$$e_D = c_2 \theta \, \text{Re} \, [E_s e^{-j\phi}] \tag{6}$$

where c_2 is the constant of proportionality between the incident field and the sampled difference signal.

Equations (4), (5), and (6) combine to yield

$$e_H = \frac{c_1 e_0}{R} [\cos (wt + \gamma) + b \cos (wt - \gamma)]$$

$$e_V = \frac{c_1 e_0}{R} [\sin (wt + \gamma) - b \sin (wt - \gamma)] \tag{7}$$

$$e_D = \frac{c_2 e_0}{R} \theta [\cos (wt + \gamma - \phi) + b \cos (wt - \gamma + \phi)].$$

These relationships do not contain the fixed differential phase shifts in the system, which will be calibrated out.

If the polarization is indeed circular, $b = 0$, it is evident that the error, θ, and error direction, ϕ, can be extracted from (7) by a straightforward comparison of phase and amplitude between e_D and e_H or e_V. If the polarization is elliptical, these quantities cannot be precisely determined unless the polarization parameters, b and γ, are known. In practice they will not be known, but the polarization will be close to circular. The sum and difference signals will therefore be processed as if polarization were truly circular, and the anomalies introduced by ellipticity will be examined below. The analysis applies only to small error angles for which the assumptions that (a) incident polarization is preserved, and (b) the difference signal is proportional to error angle, are valid. For the 67-foot aperture of the horn-reflector antenna, this linear approximation holds to about 0.035 degree. Large-error performance will be discussed later.

2.3 *Signal Processing*

It is necessary to process the sum and difference signals (7) to produce error signals proportional to the horizontal and vertical pointing errors, ϵ_H and ϵ_V,

$$\epsilon_H = \theta \cos \phi$$
$$\epsilon_V = \theta \sin \phi. \tag{8}$$

The arrangement used is shown in Fig. 5. Techniques similar to simultaneous lobing, such as used in the precision tracker,[3] are involved. Taking each horizontal or vertical coordinate separately, the difference signal is first normalized with respect to the sum signal in automatic-gain-controlled amplifiers to remove common amplitude variations, such as path loss effects. The resulting normalized difference signal is then phase-compared, or multiplied, with the normalized sum signal, and then filtered to remove RF components. The process, which requires four separate IF channels combined in a horizontal-axis pair and a vertical-axis pair, yields angle-error output voltages, E_H and E_V, represented by

$$\begin{bmatrix} E_H \\ E_V \end{bmatrix} = A \begin{bmatrix} 1 & \dfrac{4b \cos \gamma \sin \gamma}{(1 + b)^2 \cos^2 \gamma + (1 - b)^2 \sin^2 \gamma} \\ \dfrac{4b \cos \gamma \sin \gamma}{(1 + b)^2 \sin^2 \gamma + (1 - b)^2 \cos^2 \gamma} & 1 \end{bmatrix} \begin{bmatrix} \epsilon_H \\ \epsilon_V \end{bmatrix} \tag{9}$$

where A is an arbitrary gain constant.
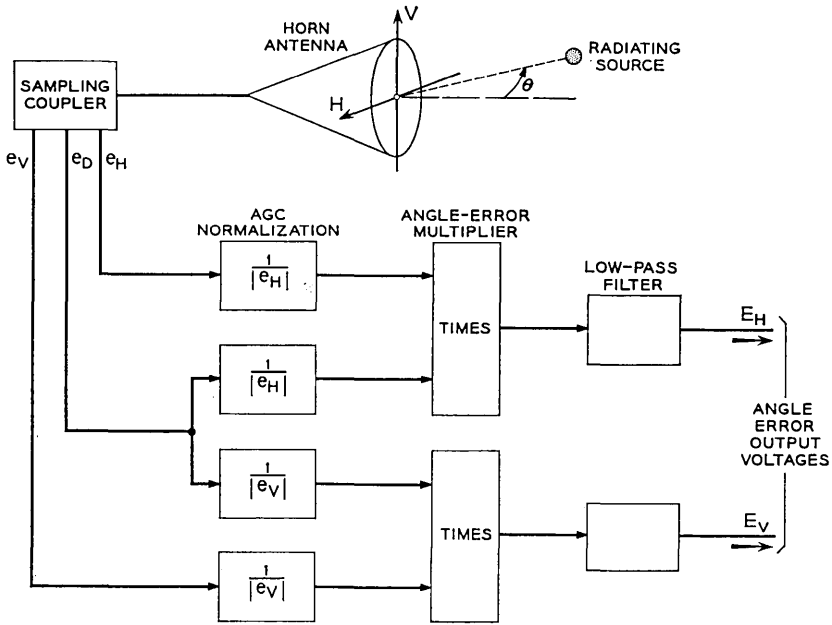
Fig. 5 — Autotrack system block diagram.

This equation shows the existence of cross coupling between the vertical and horizontal axes. The cross coupling is a function of both the ellipticity (determined by b) and the inclination of the major axis. For circular polarization ($b = 0$), the cross coupling vanishes and the error voltages become proportional to the pointing-error angles. Cross coupling also vanishes for any nonlinear polarization ($b \neq 1$) when the major axis of the ellipse coincides with the H or V axes ($\gamma = 0, \pi/2$).

The cross coupling is a consequence of the fact that, with elliptical polarization, the incident field is not a uniformly rotating, constant-amplitude vector. This is reflected in the numerator of the coupling terms, $4b \cos \gamma \sin \gamma$. The denominator results from the particular form of AGC normalization that has been used, and is not fundamental to the basic concept. The AGC system was designed to maintain constant angle-error gain in the diagonal terms of (9). Under conditions of extreme ellipticity, it magnifies the cross coupling terms when γ approaches $n\pi/2$, ($n = 0, 1, 2 \cdots$). It is therefore not the optimum technique for highly elliptical signals.

The cross-coupling coefficients of (9) vary with γ and axial ratio as shown in Fig. 6. For axial ratios less than 3 or 4 db (the maximum expected values for the Telstar satellite) the cross coupling is moderate.
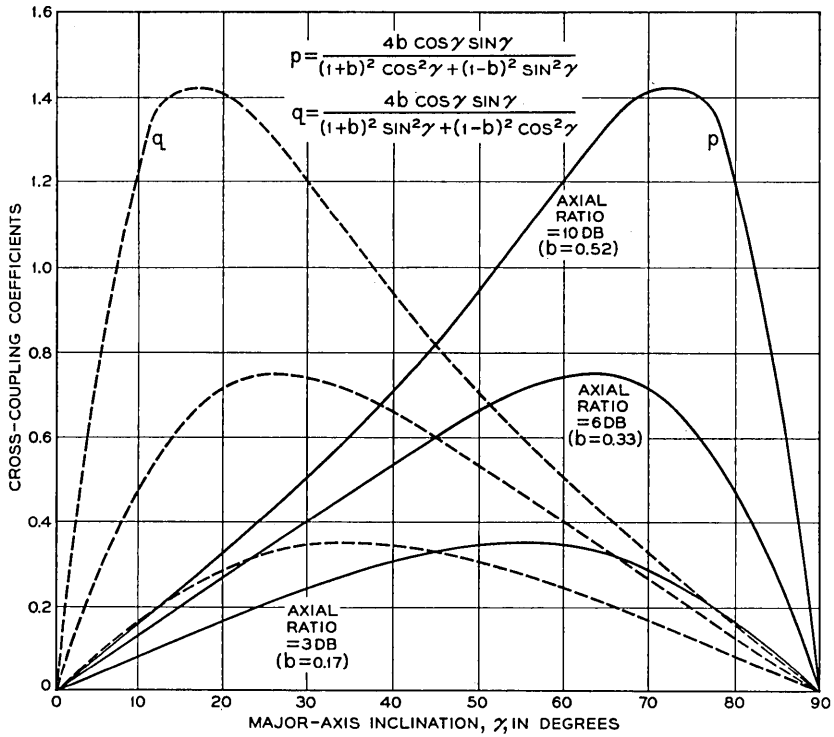
Fig. 6 — Vertical to horizontal pointing error cross coupling due to noncircular polarization of the beacon signal.

To illustrate the effects of cross coupling, (9) was used in a simple iterative error-correcting loop defined by

$$
\begin{bmatrix} \epsilon_H \\ \epsilon_V \end{bmatrix}_n = [I - \delta M]^n \begin{bmatrix} \epsilon_H \\ \epsilon_V \end{bmatrix}_0
\tag{10}
$$

where $[\epsilon_H, \epsilon_V]_0$ is an initial error, $[M]$ is the error-sensing matrix of equation (9), and $[\epsilon_H, \epsilon_V]_n$ is the resulting pointing error after n iterations. The results of applying this process to two cases of different major-axis inclination and axial ratios are shown in Figs. 7 and 8. Here the arbitrary constant, δ, is chosen small enough (0.1) to plot out a smooth curve whose slope is proportional to E_V/E_H, thus illustrating the direction of the corrective influence at each point. These curves show that, in general, noncircular polarization causes correction to occur in a curvilinear path rather than in a straight line. The end-game appears to be asymptotic to
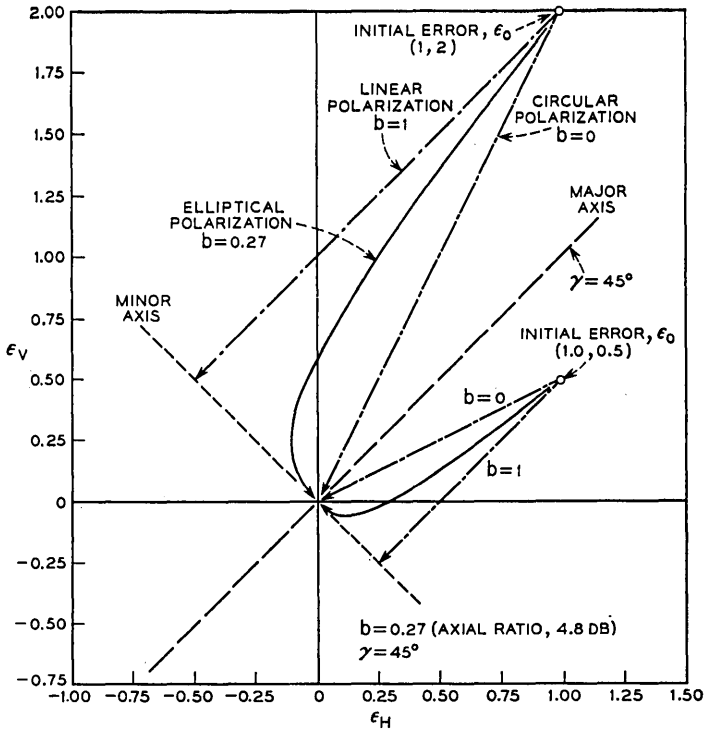
Fig. 7 — Pointing correction path of a weightless antenna in the presence of elliptic cross coupling (b = 0.27, γ = 45°).
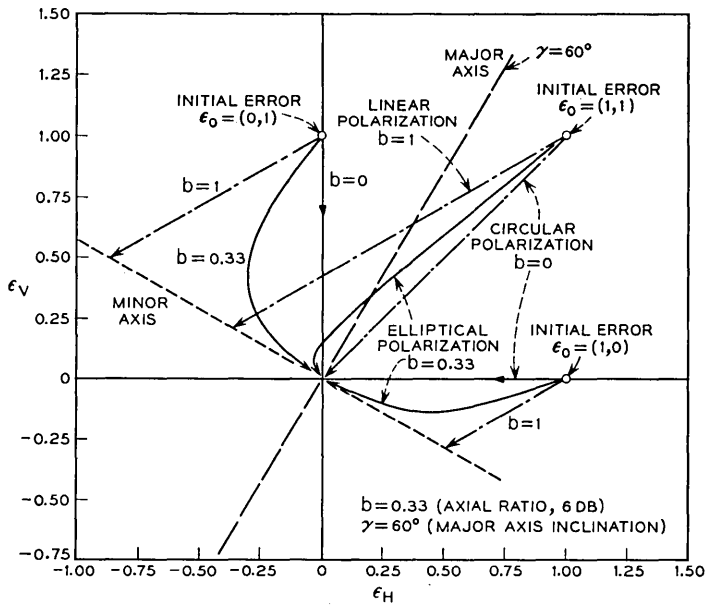
Fig. 8 — Pointing correction path of a weightless antenna in the presence of elliptic cross coupling (b = 0.33, γ = 60°).

the minor axis, implying that the coordinates could perhaps be effectively decoupled along this path. This, however, is strictly true only for $\gamma = 45°$. In general, the cross coupling must be considered in the design of a servo system. The special case of linear polarization is considered in Section 2.4.

The error correcting performance of the actual system in the full autotrack mode is shown in Fig. 9. The tracking target was the Black Mountain boresight antenna,[2] which radiates a slightly elliptically polarized signal of 2 db axial ratio ($b = 0.115$) with a major-axis inclination $\gamma \approx 10°$. A small amount of cross coupling effect is evident in these curves.

2.4 *Linear Polarization*

When the polarization is linear ($b = 1$), an error orthogonal to the plane of polarization will not excite radially symmetric electric fields in
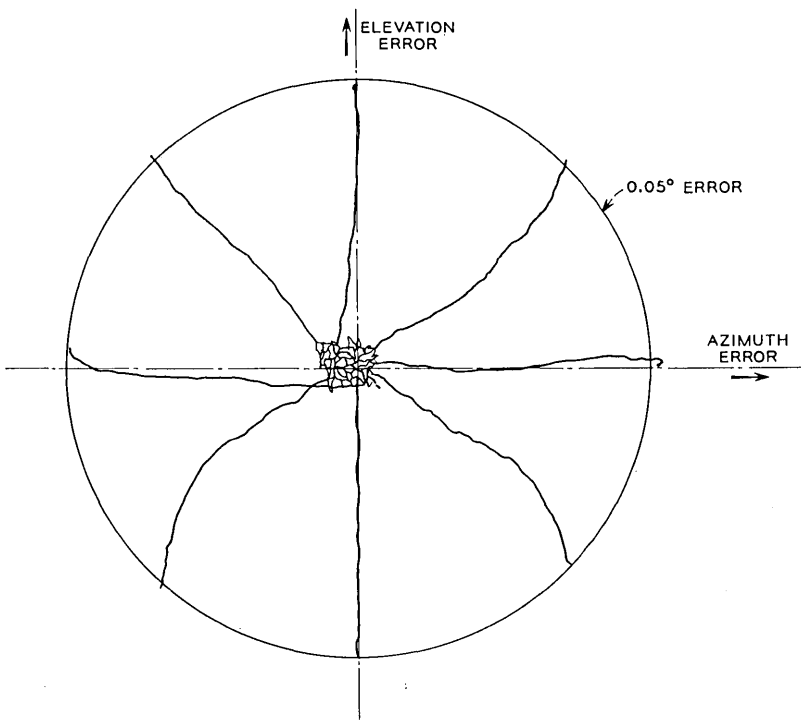
Fig. 9 — Recorded motion of the antenna, using the autotrack system to zero in on the boresight beacon.

the antenna aperture. Hence, the difference mode will not be excited, and no error indication will be generated. This may be seen from (7) and (9) by setting $\phi = \gamma + \pi/2$, to find $e_D = 0$; hence

$$\begin{bmatrix} E_H \\ E_V \end{bmatrix} = 0. \tag{11}$$

Thus, whereas for circular polarization the difference pattern has a null point on the antenna axis, for linear polarization there is a null *plane* orthogonal to the axis of polarization. Fig. 7 shows that attempts at correcting the pointing error with linear polarization result in straight-line motion terminating on the null plane. The target would then tend to slip away along this plane. Target loss of this type has been observed in tracking helicopters equipped with linearly polarized antennas. In theory, however, even a small cross-polarization component will permit full error correction, though with reduced response time.

2.5 *Two-Channel Processing*

For a satellite tracking signal that is near circular in polarization, it is possible to simplify the processing by receiving only one orthogonal component of the TE_{11} mode and generating the other with a $\pi/2$ phase shift. It is presumed here, as before, that the receiving antenna preserves polarization. Two IF channels are required, as shown in Fig. 10. The horizontal error component is obtained using the difference signal, e_D, and the horizontal sum component, e_H. The vertical error component is derived from these, as shown in the figure. The resulting error voltages are

$$\begin{bmatrix} E_H \\ E_V \end{bmatrix} = A \begin{bmatrix} 1 & \dfrac{4b \sin\gamma \cos\gamma}{(1+b)^2 \cos^2\gamma + (1-b)^2 \sin^2\gamma} \\ 0 & \dfrac{1-b^2}{(1+b)^2 \cos^2\gamma + (1-b)^2 \sin^2\gamma} \end{bmatrix} \begin{bmatrix} \epsilon_H \\ \epsilon_V \end{bmatrix}. \tag{12}$$

For circular polarization, $b = 0$, and direct error indications without cross coupling result, as expected. For elliptical polarization with low axial ratio, cross coupling occurs, but the net effect in an error correcting loop is not much different than the four-channel scheme of (9). There is, however, one significant difference. True error sensing in the two-channel system requires prior knowledge of the sense of polarization, while in the four-channel system no prior knowledge is necessary. This may be seen by letting $b \to \infty$. A sign reversal will occur in (12) but not in (9).
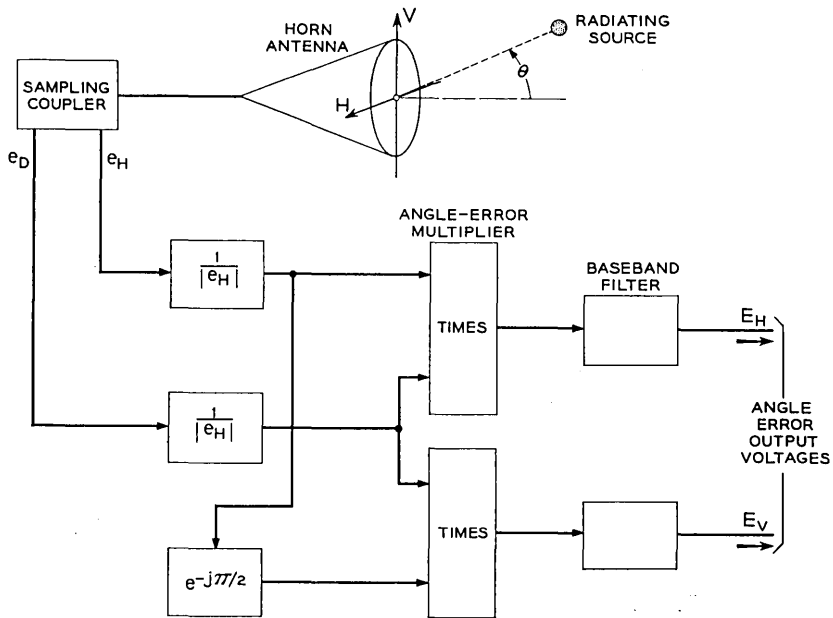
Fig. 10 — Two-channel autotrack arrangement.

The autotrack receiver was implemented for either four- or two-channel processing to permit comparison of the two techniques. The four-channel system offers some advantage in being able to handle signals of either sense of circular polarization. It also permits positive tracking on randomly polarized signals (noise). The two-channel system, on the other hand, requires less equipment.

2.6 Large Pointing-Errors; Pull-In

When the pointing error is large, the error voltage response is non-linear and the receiving antenna introduces cross-polarized signals, so that the foregoing analysis is no longer valid. The resulting distortion in error-indication shows up as additional cross-coupling and effective variation in the tracking loop gain. These anomalies that accompany large error angles affect the pull-in, or angle acquisition limits, of the tracking system. Such behavior does not permit simple analysis, but experimental results show that the pull-in range is almost as large as would theoretically be obtained if circular polarization were preserved. Theoretically, the autotrack system should zero in from error angles up

to the first null in the dominant mode radiation pattern. Reliable acquisition to about 80 per cent of this angle is actually achieved. The pull-in ranges of the four-channel and two-channel systems, furthermore, are about equal.

2.7 *Coordinate Conversion*

Thus far, the analysis has been based on an open waveguide antenna in a simple $H\text{-}V$ coordinate system lying in the aperture plane. In the actual horn-reflector antenna, the mode sampling coupler does not rotate with the horn in elevation. The error signals generated by the autotrack, designated E_x and E_y, refer to the coordinates of the mode coupler, not the aperture. The aperture-plane error signals, E_H and E_V, must be derived from these signals by a simple coordinate rotation.

Let the longitudinal and transverse (elevation) coordinates of the aperture plane be, respectively, H and V; and let the elevation angle be β. The three mode signals, referred to the aperture plane, are as given in (7). E_H and E_V are found by suitable operations on e_H, e_V, and e_D as already shown. These may be expressed in terms of transverse and longitudinally polarized modes whose coordinates are indicated in Fig. 11. Transverse fields are reversed upon reflection from the parabolic
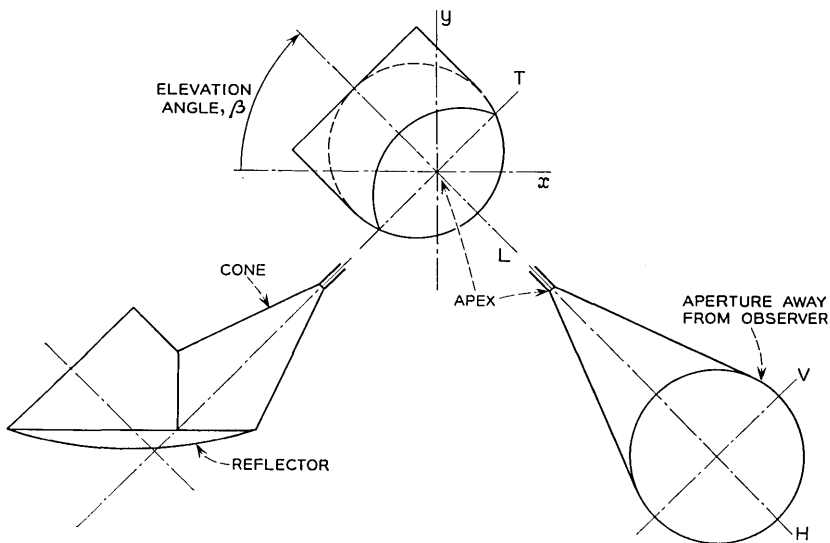
Fig. 11 — Coordinates used in determining the coordinate correction required when the horn rotates in elevation.
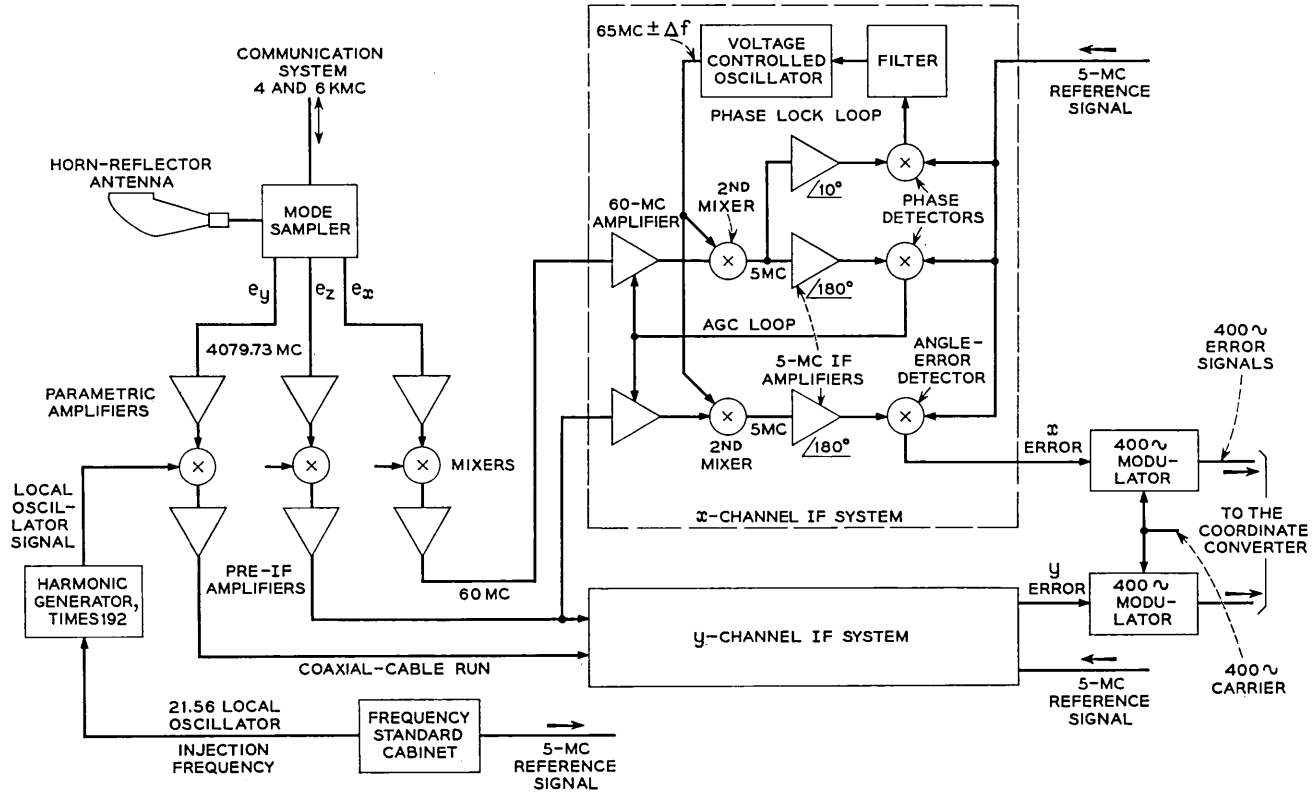
Fig. 12 — Standard four-channel autotrack system arrangement.

surface; longitudinal fields are not. Thus,

$$e_H = e_L \tag{13}$$

$$e_V = -e_T \tag{14}$$

$$e_D = -e_z \tag{15}$$

where e_z is the difference signal propagated in the z-direction.

From the figure,

$$e_L = e_x \cos \beta - e_y \sin \beta \tag{16}$$

$$-e_T = -e_x \sin \beta - e_y \cos \beta. \tag{17}$$

Then

$$e_H = e_x \cos \beta - e_y \sin \beta \tag{18}$$

$$e_V = -e_x \sin \beta - e_y \cos \beta. \tag{19}$$

Since

$$E_n = e_D e_n \tag{20}$$

equations (15), (18), (19) and (20) may now be combined to derive the required coordinate conversion. In doing this, it is necessary to invert the sign of e_x so that, for $\beta = 0$, positive x-coordinate errors will result in positive H-coordinate errors. This is done as a matter of course when the system is calibrated. The resulting transformation from error voltages referred to the mode sampler coordinates to error voltages referred to the aperture coordinates is

$$\begin{bmatrix} E_H \\ E_V \end{bmatrix} = \begin{bmatrix} \cos \beta & \sin \beta \\ -\sin \beta & \cos \beta \end{bmatrix} \begin{bmatrix} E_x \\ E_y \end{bmatrix}. \tag{21}$$

The coordinate conversion is performed on the output signals by the coordinate converter, which is part of the antenna servo system.[4] The necessity for coordinate conversion could have been avoided by rotating the coupler with the antenna in elevation. This, however, would have complicated the mechanical designs of the rotary joint and the autotrack RF circuitry.

III. SYSTEM DESCRIPTION

3.1 *General*

The block diagram of Fig. 12 shows the autotrack system hookup for four-channel signal processing. A special circular waveguide coupler

(the sampling coupler) samples the horizontal and vertical dominant modes and the difference mode excited by the 4079.73-mc beacon signal at the throat of the horn reflector. The resulting signals, e_x, e_y, and e_z, are separately amplified and down-converted in three amplifier chains. Each chain consists of a varactor parametric amplifier, a balanced mixer, and a 60-mc preamplifier. These units are located at the apex of the antenna in close proximity to the mode coupler. The three 60-mc IF signals are then transmitted, via coaxial cables, to the IF signal processing equipment located in the lower equipment room on the antenna structure. It is here that the signals are paired off for four-channel processing. Only one of these pairs, the horizontal error channel, or x channel, is depicted in detail. The other channel is identical. The signal processing for each pair consists first of IF amplification and AGC normalization in a pair of 60-mc main IF amplifiers. The signal is then down-converted to a 5-mc second intermediate frequency. At this point, the sum channel includes a phase-lock loop that works against a stable 5-mc reference signal. The phase-lock loop provides automatic Doppler tracking and permits operation with extremely weak signals. In addition, the phase coherence established by the phase-lock loop is used to advantage by performing AGC and angle-error detection coherently.[6,7] Noncoherent detection, however, is available at the turn of a switch so that the system can track on noise emitting targets such as the sun. After angle-error detection, the resulting dc horizontal and vertical angle-error signals modulate a 400-cycle carrier. They are sent to the coordinate converter in this form.

A comparison of this block diagram and that of the precision tracker[3] reveals a great functional similarity in their circuits. This fact was used to advantage to minimize the over-all development and fabrication effort. Wherever possible, the circuits and equipment were designed to be suitable for both the PT and autotrack systems. The RF and IF amplifiers, and the angle detection and frequency generation circuitry, for instance, are identical to their PT counterparts. Differences exist in the interconnection of these "building block" components to the extent that the autotrack signal processing differs from the PT processing. The autotrack also differs in (a) using dissimilar packaging of the RF "front-end" circuitry; (b) requiring a dc power supply cabinet that operates from 60-cycle, 120-volt, three-phase power; and (c) having a display and control cabinet (in place of a console) to house the 400-cycle angle modulators, status indicators, angle-error indicators, and phase-lock loop tuning controls. For circuit details of common units, the reader is referred to the precision tracker system.[3] The sampling coupler, how-

ever, is unique to the autotrack, and therefore deserves a brief description.

3.2 *Sampling Coupler*

Fig. 13 shows the autotrack RF unit in place at the apex of the horn-reflector. The sampling coupler itself is pictured in Fig. 14. Its function is to separately sample the difference mode and the vertically and horizontally polarized dominant modes excited in the antenna by the satellite microwave beacon. As an energy coupling device, the coupler is not optimum. It was designed to meet the specific needs of the satellite system, including:

(a) minimum attenuation and reflection of the 4-kmc communication signals,

(b) minimum coupling of the transmitted 6-kmc signal into the autotrack paramps, and
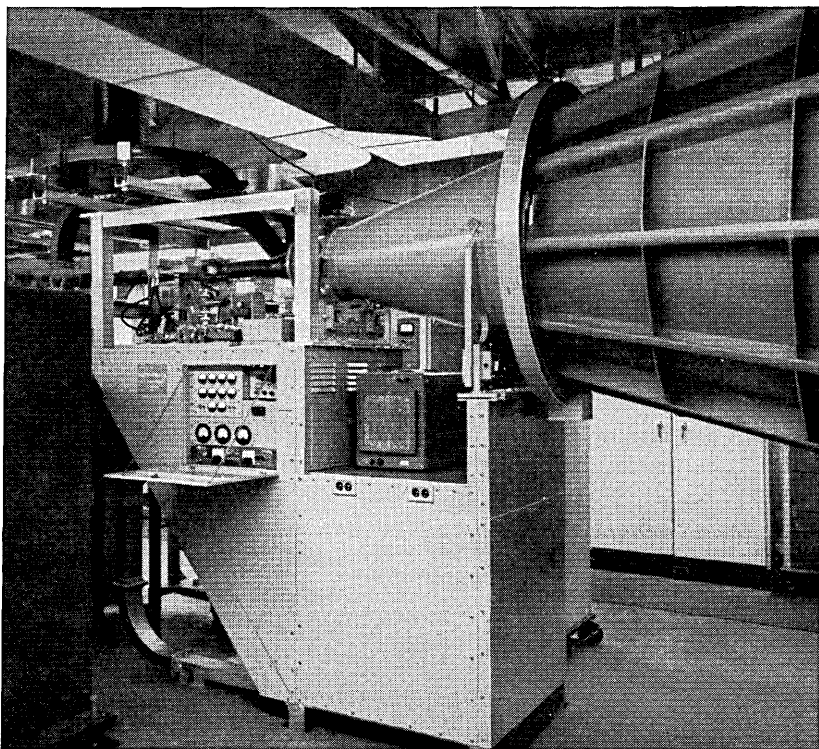
Fig. 13 — Autotrack RF unit in place at the horn apex, Andover, Maine.
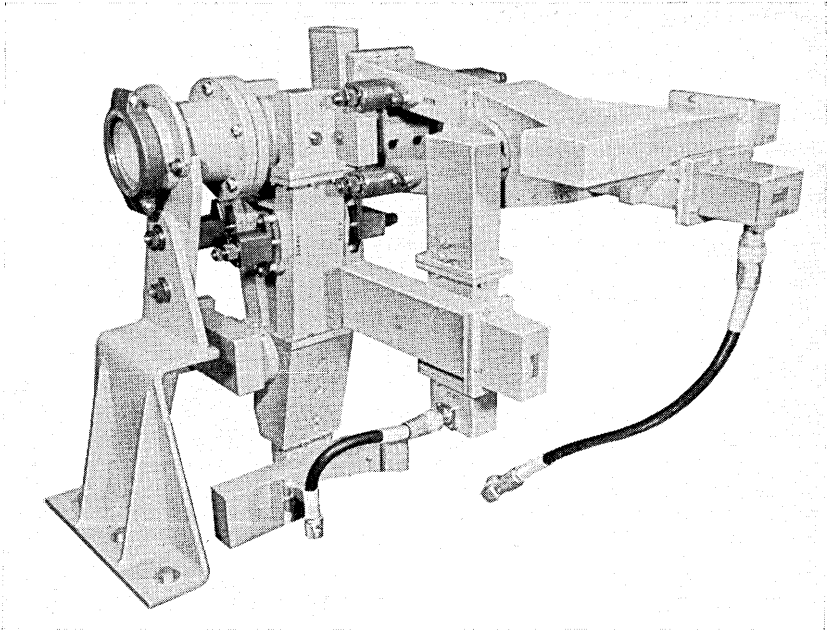
Fig. 14 — Autotrack sampling coupler.

(c) the expeditious use of existing waveguide components where possible.

The coupler takes advantage of the particular symmetry of the circular waveguide modes to separate them from one another. Fig. 2 shows that there exists a circumferential magnetic field at the cylinder walls for both types of mode — at the upper and lower surfaces for the vertically polarized dominant mode, at the side walls for the horizontally polarized mode, and all the way around for the difference mode. Because of the high gain of the large antenna, the ultimate in coupling efficiency is not necessary. It is therefore practical to magnetically couple both modes through the same holes and to separate them after coupling. The magnetic fields for the dominant modes are oppositely directed on opposite guide walls: e.g., clockwise on one side and counterclockwise on the other. By contrast, the difference mode magnetic field is continuous around the guide circumference. If balanced signals are coupled from holes on opposite sides of the guide and combined in a hybrid junction through a balanced filter and waveguide system as shown in Fig. 15, symmetry requires that energy carried by the ap-

propriate dominant mode, and that carried by the difference mode, will be separated in the hybrid.

A two-cavity filter was used to increase the coupling coefficient and provide high rejection of both transmitted and received communication signals.

Since the dominant mode components are geometrically orthogonal, they must be separately sampled using orthogonal sets of coupling holes, and they therefore require the two hybrids seen in Fig. 14. Due to the circular symmetry of the difference mode, it couples out through both sets of holes. To enhance the difference signal, the second hybrid difference arm is shorted at a point that optimizes the difference output of the first hybrid. Coupling of the difference mode is further enhanced by the fact that the waveguide at the coupler output is below cut off for that mode. The signal is reflected from the output transition, and the coupler holes are positioned to take advantage of the resulting standing wave.

The output of the coupler gives a sampling of the dominant mode beacon signal, which is about 7 db down from that received by the horn reflector; the difference mode signal is about 3 db down.

It is important to prevent coupling of the dominant modes into the tracking difference channel. This cross coupling is held about 35 db below the direct coupling level by tuning the filter cavities for a careful
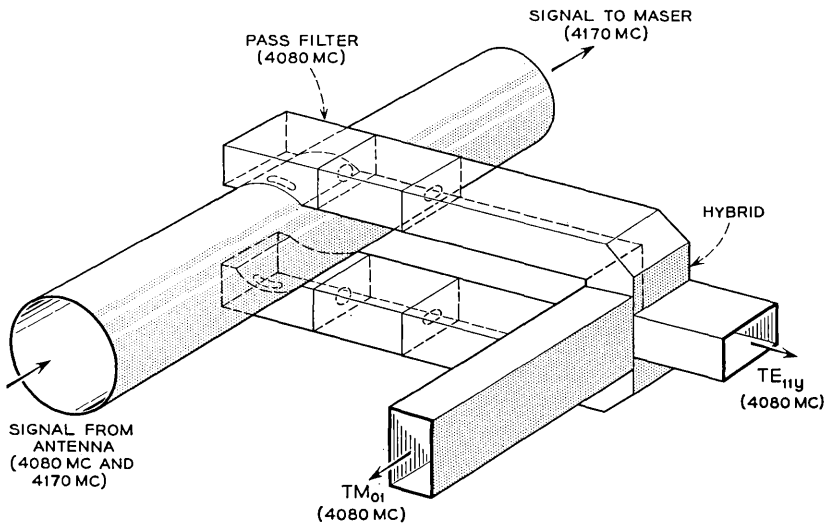
Fig. 15 — Conceptual version of the sampling coupler.

balance coincident with maximum dominant mode sampling. Additional phase and attenuation trimmers in each input arm of the hybrids provide final balance adjustment.

IV. SYSTEM PERFORMANCE

In the design of circuits for common use in both the autotrack and the precision tracker, the system gains, dynamic range, bandwidths and noise thresholds were chosen to meet the requirements of the less sensitive system, the precision tracker. Consequently, the autotrack receiver always operates well above its threshold capabilities. This threshold is determined by the ability of the phase-lock loop to remain locked in phase to the received signal despite the presence of both random phase modulation of the beacon oscillator and thermal noise. The effect of thermal noise is held to a minimum by the use of low-noise parametric amplifiers and a narrow threshold bandwidth phase-lock loop. The random phase noise is kept low by using crystal-controlled devices of high spectral purity for the satellite beacon oscillator and for the receiver beating oscillators. A practical threshold level has been experimentally determined to be about −130 dbm at the input to the sampling coupler for the horizontal and vertical dominant mode signals. Tracking accuracy is adequate for communication purposes for signals of several decibels below this value, but the angle-error gain deteriorates rapidly from its nominal value of about 100 volts/degree. The autotrack signals in normal Telstar system operation range from −90 dbm to −120 dbm.

Closed-loop tracking performance has been measured by Iwama and Norton and is discussed in more detail in their paper.[4] The acquisition angle has been found to be 0.2° in all directions, as shown by the pull-in pattern of Fig. 16. These curves show the paths taken by the antenna in zeroing in on the Black Mountain boresight antenna from an initial error angle of 0.2°. The large-angle coupling factors due to antenna-induced cross-polarization (which are not present in the small-angle pull-in patterns of Fig. 9) are evident here. These are apparent in the circumferential motion that occurs at large initial error angles, particularly in the first and fourth quadrants. The antenna motion is rather complex; it represents the combined effects of the autotrack angle-detection anomalies and the response of the servo system. The major portion of each curve is traced out in about one second.

Iwama's measurements of tracking errors show that the autotrack system maintains the null axis of the antenna within 0.005 degrees of the actual satellite direction, limited only by the tracking rate capa-
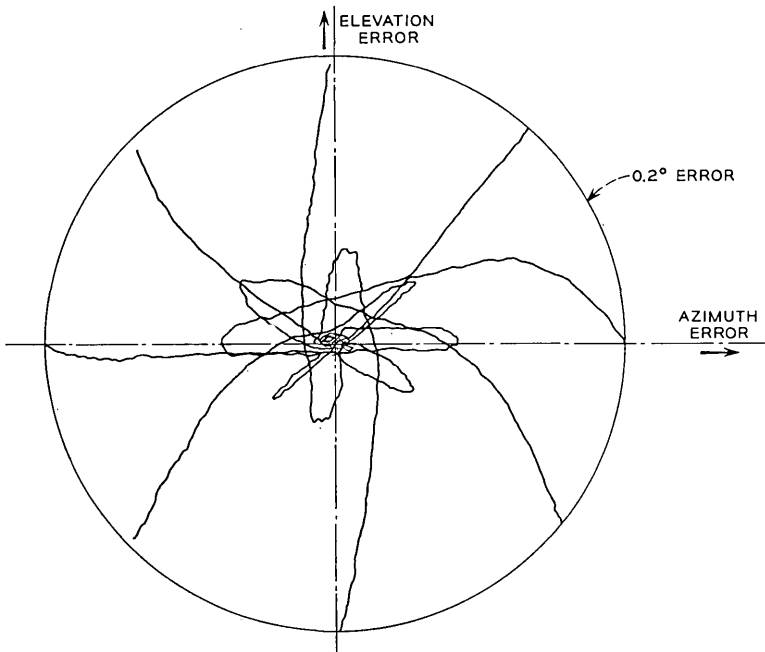
Fig. 16 — Antenna corrective motion from 0.2° initial pointing error.

bilities of the drive motors. The null axis coincides with the geometrical axis of the antenna. In the reception of circularly polarized communication signals, it is possible to obtain a small increase in gain by pointing off-axis in elevation by about 0.02°. Although it is theoretically possible to bias the error signals so as to achieve off-axis tracking by this amount, it is not done, because the gain enhancement is not significant.

The signal levels received in the autotrack system during the first Telstar communication pass are compared with predicted levels in Fig. 17. The received signal data represents points taken from a continuous recording of AGC voltage at about 0.5-minute intervals. The predicted values were based on measured satellite antenna gain patterns (shown as a smoothed curve), predicted range (also plotted), and predicted spin angle (not shown). The spread between the upper and lower predicted signal bounds, S_{MAX} and S_{MIN}, represents two factors: the ellipticity of polarization as a function of spin angle, and a variation in satellite transmitter power from 17 dbm to 19 dbm. This is the maximum power variation expected when the ground transmitter is turned on and off. As may be seen by the 2-db drop in received power at approximately 23:25
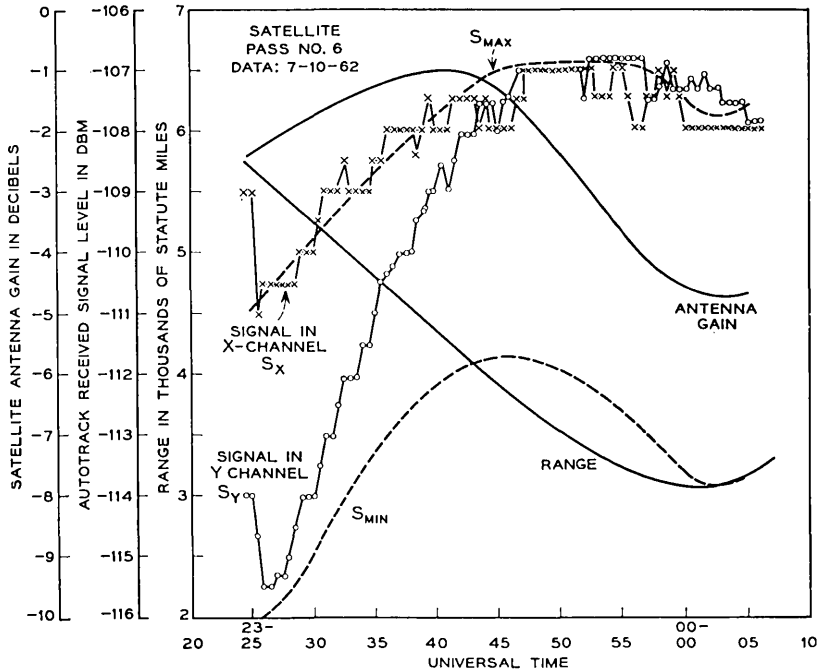
Fig. 17 — Received signal levels for Telstar satellite pass 6.

to 23:26 hours, the ground transmitter was turned on at this time and remained on for most of the pass. The 17-dbm value of satellite transmitter power should therefore have been used for prediction from that time on. Thus, after 23:26 hours, the S_{MAX} curve should have been displaced downward by 2 db in order to represent true conditions. From these considerations, it may be seen that the measured signals differed from predicted values by about $+2$ db. The accuracy of receiver calibration and of prediction are each about ± 1 db.

The high tracking accuracy made possible by the autotrack system eliminates antenna tracking error as a limiting factor in the performance of the ground station. The basic techniques are applicable not only to the horn-reflector antenna, but also to a wide class of more conventional reflector antennas.

V. ACKNOWLEDGMENTS

The multimode sampling technique on which the autotrack system is based was jointly worked out by J. N. Hines and the authors. It was

found to be closely related to S. E. Miller's earlier work.[5] The evolution from first concept to a smoothly operating, reliable system came about through the cooperative efforts and suggestions of many, many people. We feel particularly indebted to R. V. Lohmiller and his department for detailed design and fabrication of a major portion of the equipment; to K. B. Woodard and his group for detailed mechanical design of much of the RF equipment; to E. M. Elam for final design, coordination, assembly, installation, and testing of the complete autotrack RF unit; and to E. C. Snyder, Jr. for coordinating much of the assembly, installation, calibration, testing, and operation of the autotrack system both at Andover, Maine, and Pleumeur-Bodou, France.

REFERENCES

1. Chu, L. J., Calculation of the Radiation Properties of Hollow Pipes and Horns, J. Appl. Phys., **11,** Sept., 1940, p. 603.
2. Hines, J. N., Li, T., and Turrin, R. H., The Electrical Characteristics of the Conical Horn-Reflector Antenna, B.S.T.J., this issue, p. 1187.
3. Anders, J. V., Higgins, E. F., Murray, J. L., and Schaefer, F. J., The Precision Tracker, B.S.T.J., this issue, p. 1309.
4. Lozier, J. C., Norton, J. A., and Iwama, M., The Servo System for Antenna Positioning, B.S.T.J., this issue, p. 1253.
5. Miller, S.E., Multimode Automatic Tracking Antenna System, U.S. Patent 2931033, March 29, 1960. Patent applied for July 19, 1955.
6. Nelson, W. L., Phase-Lock Loop Design for Coherent Angle-Error Detection in the *Telstar* Satellite Tracking System, to be published.
7. Ball, W. H. W., Analysis and Digital Simulation of the *Telstar* Precision Tracker, Paper No. CP-63-368, presented at the IEEE Winter General Meeting, New York, 1963.

The Precision Tracker

By J. V. ANDERS, E. F. HIGGINS, JR., J. L. MURRAY
and F. J. SCHAEFER, JR.

The precision tracker, a simultaneous lobing, amplitude-comparison, passive, continuous-wave tracker based in principle and design upon a monopulse tracking radar, is employed at the Andover, Maine, and Pleumeur-Bodou, France, stations to find the satellite and direct the horn-reflector antennas when required and, at regular intervals during subsequent passes, to provide the precise tracking data required for prediction of future orbital parameters.

I. INTRODUCTION

The Telstar satellite radiates a 4079.73-mc continuous-wave (CW) carrier 90 mc below the frequency of the communications carrier.[1] This signal is designed as a beacon for the processes of tracking and initial acquisition. The design of the precision tracker receiver is thus based on the characteristics of this beacon signal as modified by the dynamic orbital parameters: these are listed briefly in Table I.

The system application — the manner in which the tracker is integrated into the Telstar ground system operations — is described in Ref. 2. Section II of this paper is a brief description of the precision tracker system; sections III through IX cover the several subsystems in greater detail.

II. SYSTEM DESCRIPTION

The precision tracker (hereafter referred to as the PT) is essentially a radio theodolite. From the viewpoint of the over-all Telstar system, it has one simply defined task: to provide the antenna pointing system with the real-time, locally referenced azimuth and elevation angles of the satellite.

TABLE I — NOMINAL DESIGN CHARACTERISTICS OF THE
BEACON AND ORBIT

Apogee	3000 nm
Perigee	600 nm
Inclination	45 deg
Tangential velocity	302 nm/min
Beacon frequency	4079.73 mc
Doppler rate, maximum	575 cps²
Doppler shift, maximum	±65 kc
Precision	±4 kc
Stability	±12 kc/day
Thermal variation	±40 kc
Effective radiated power	+13 dbm

2.1 Data Take-Off

To provide the required angle data, the PT antenna rotates in two axes — azimuth and elevation. A multispeed gear box is associated with each axis; mechanical angle is converted by precision 1-speed and 64-speed resolvers to ac analog voltage, which in turn is converted to pulse time modulation for transmission to the track digital control unit of the antenna pointing system.

2.2 Automatic Tracking

The PT is a *simultaneous lobing, amplitude-comparison, passive, CW* tracker. The antenna, with its four-horn feed system, the microwave comparator, and the three-channel tracking receiver, develops output voltages proportional to the azimuth pointing error and the elevation pointing error. These error signals are passed through equalizers, modulators, and amplifiers to the azimuth and elevation drive motors, thus closing two servo loops that continuously serve to minimize the angular errors between the antenna's boresight axis and the line-of-sight to the satellite.

2.3 Simultaneous Lobing — Amplitude Comparison

The microwave energy received by the four feedhorns is processed by the comparator to develop three different antenna pattern response characteristics: the *sum* pattern, corresponding to a conventional antenna pattern; the *elevation difference* pattern, having two main lobes in the elevation plane with a deep null on the boresight axis; and the *azimuth difference* pattern, having two main lobes in a plane perpendicular to the elevation plane with a deep null on the boresight axis. (Strictly

speaking, this should be called the traverse difference pattern; however, the error signal is applied to the azimuth axis of the mount.)

The difference signals are developed in the comparator by amplitude summations in hybrids. The system is phase-sensitive in that the phase of the error signals relative to the phase of the sum signal is employed as an indication of the sense of the error signals, i.e., left-right and up-down.

The three-channel tracking receiver employs two stages of conversion to bring the sum, azimuth, and elevation signals down to 5 mc prior to demodulation. An AGC voltage is developed from the sum channel and applied to all three channels; thus, the demodulator outputs are proportional to D/S, the difference pattern response divided by the sum pattern response. This has two important effects. First, the angle-error function is linearized with respect to off-axis angle: the two-lobe difference pattern function is converted to a nearly linear function. Second, the output scale factor is rendered insensitive to changes in absolute received signal level within the frequency response of the AGC system and the dynamic range of the receiver.

2.4 *Signal-to-Noise Ratio*

A high probability of detection with a low false-alarm rate is required for the acquisition process; a low standard deviation in tracking error is required by the orbital prediction program. These two requirements imply certain minimum signal-to-noise objectives.

Both the tracking noise (jitter) and bias vary in a complex way with the signal-to-noise ratio (SNR) available to the signal processing circuits. Generally the bias decreases with increased SNR, while tracking jitter increases rapidly as the SNR decreases below values of about $+3$ db at the intermediate frequency output. The available satellite beacon power, the space transmission path, the receiver "front end" design, and the signal-processing equipment all affect the degree to which these objectives are met. The deviation in the radiation pattern of the satellite from isotropic results in variation of about 5 db; the changes in its beacon power due to communication loading result in about 2 db variation. The transmission path length change is the most significant variable, accounting for about 12 db variation over the portion of the orbit tracked. As a result, the dynamic range of input signals is expected to be in the order of 20 db, a relatively small range. Since the SNR and tracking properties vary with path length, the slant path at apogee (about 5700 statute miles) sets the most stringent requirements.

Because orbital tracking requires the tracking antenna to be directed through a wide variety of space regions, the effects of noise sources, both spot and distributed, also contribute to the over-all received signal. The sun, which could contribute some 1500°K additional to the receiver temperature if it were viewed directly, is an example of a potent spot noise source; but the most important noise source in the field of view of the system is the atmosphere. At the receiver frequency of 4079.73 mc, the atmospheric noise contribution for the PT receiver can vary from about 14°K at the zenith to 170°K at the horizon, increasing rapidly for angles below 5 degrees. Normally the system operates over elevation angles of from 7.5 to 82.5 degrees and thus never experiences the maximum noise and SNR degradation condition except during test operations.

The loss effects for the 5700-statute-mile path, including an antenna polarization loss factor, are tabulated in Table II at a reference elevation angle of 10 degrees.

A practical optimum in system noise reduction at the front end of the receiver is attained through the use of room-temperature parametric amplifiers, located in the moving antenna support structure along with the first converters and the 60-mc IF preamplifiers. The resulting system operating noise temperature (about 340° K) and received signal level (as low as −138 dbm) place severe requirements on the signal detection schemes.

2.5 Acquisition Receiver

The PT was designed for rapid acquisition after a few spacecraft orbits. The maximum expected uncertainties in time, angles, and frequency were used as boundary conditions for design.

Enhancement of signal-to-noise ratio by a narrow-bandwidth filter was defeated, for the initial-orbit acquisition process, by *time*: to the

TABLE II — LOSSES

Loss Type	Loss Value (db)
Divergence (path loss)	184.20
Oxygen	0.25
Water vapor	0.15
Ozone and other particles	0.10
Polarization loss, vertically polarized antenna, nearly circularly polarized signal (includes axial ratio effects)	3.00
Total	187.70

finite time required to search the volume of space expected to contain the satellite must be added, for each beamwidth increment, the time per beamwidth necessary to sweep a narrow filter across the frequency band within which the beacon frequency will lie. It was not possible to develop an efficient and simple search strategy in which the necessary search time was compatible with the rate of motion of the search volume. The solution employed in the PT is to reduce the frequency-search time essentially to zero by a stationary search conducted with a comb filter.

The equipment associated with the comb filter has been designated the acquisition receiver. As may be seen from the block diagram (Fig. 1), the acquisition receiver serves as an initial tuning control to preset the frequency of the narrow band tracking receiver. Upon sensing the presence of a signal in the sum channel, it also stops the antenna's angular search at the point where the signal was detected. Thus, at the expense of 300 channels of signal processing, the frequency-search time per unit beamwidth has been reduced from 30 seconds to the $\frac{1}{4}$-second response time of the acquisition receiver's post-detection filters and threshold detectors.

The acquisition receiver was used to advantage on July 10, 1962, at 7:25 p.m. when it set the PT to a condition of fully automatic tracking within 6 seconds after the satellite repeater had been ordered to turn on.
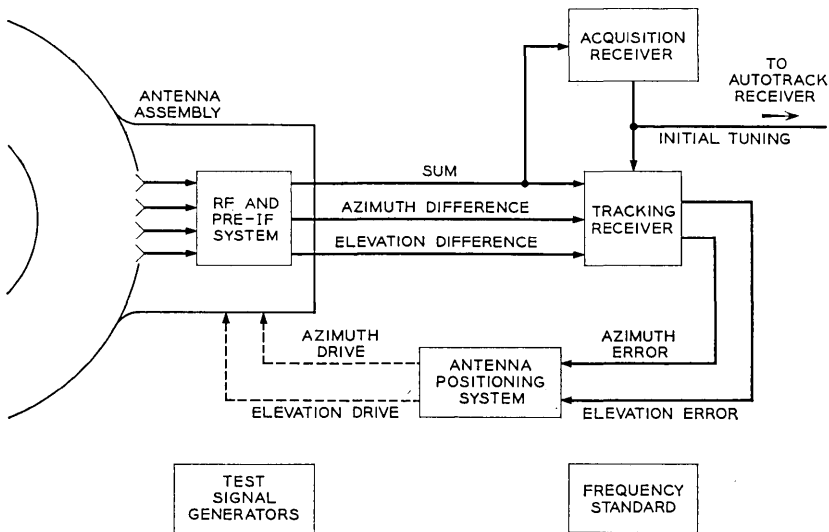
Fig. 1 — Precision tracker, block diagram.

2.6 *Tracking Receiver*

In the tracking receiver, which can develop usable angle-error signals with a signal-to-noise ratio 10 db or more below signal detection threshold, the need for maximizing the signal-to-noise ratio is based on reducing tracking jitter to the levels required by the orbital prediction program. It is also necessary to hold the jitter to levels which will damage neither the horn-reflector antenna and its associated electronic equipment nor the operating personnel when the horn-reflector is slaved to the PT. Since it is essential to recover the phase of the error signals relative to the phase of the sum signal, the demodulation technique offering the greatest noise rejection is coherent detection. The sum signal is kept in phase coherence with a noise-free 5-mc reference by a phase-lock loop or tracking filter discussed in Section IV. The 59.98-mc azimuth difference and elevation difference IF signals are converted to 5 mc by the 64.98-mc local oscillator signal developed in the phase-lock loop; thus, all three channels are maintained in phase coherence with the 5-mc reference, and coherent detection is effected in the angle error and AGC demodulators.

As a test option, the demodulation scheme may be converted to correlation detection for tracking the sun or other sources of wideband, random-phase radiation. To effect this conversion, the 5-mc demodulating reference is replaced by the 5-mc sum signal.

Under normal tracking conditions, when the tracking receiver is employing coherent detection with the phase-lock loop locked to a received CW signal with less than ±10 degrees of phase jitter, the angular tracking jitter of the antenna is controlled by the bandlimiting effect of the servo system upon the effective receiver noise power. The nominal one-sided servo bandwidth varies from 0.2 cps to 1 cps under control of the received signal level. Thus, the narrower bandwidth reduces tracking jitter when the satellite is at longer range and the signal is weaker; the wider bandwidth reduces acceleration lag at shorter ranges where the signal is strong but the angular velocity and acceleration are greater.

The salient characteristics of the PT are listed in Table III. The following sections will describe the various subsystems of the PT in greater detail.

III. ANTENNA, RF PROCESSING, AND PREAMPLIFIERS

3.1 *Introduction*

The RF system used in the PT is composed of a low-noise antenna and comparator,[3] a high-gain, low-noise parametric amplifier, and a

TABLE III — SALIENT PARAMETERS OF THE PRECISION TRACKER

Effective receiver input temperature	315°K
Equivalent noise power in 3-kc bandwidth	−139 dbm
Received signal power at feedhorns for range of 5700 statute miles, satellite beacon power +13 dbm, PT line-of-sight to satellite's equator	−137 dbm
Received signal power at feedhorns for range of 5700 statute miles, satellite beacon power +13 dbm, PT line-of-sight 40 degrees off satellite's equator	−142 dbm
Over-all mechanical precision of antenna assembly, azimuth and elevation (1 sigma), including effects of wind loading and thermal variation on both antenna and boresight tower	0.005 deg
Tracking jitter, azimuth and elevation — standard deviation objective	0.015 deg
Slew rates	45 deg/sec
Servo bandwidth, autotracking mode	0.2, 0.5, and 1.0 cps
Acquisition time	
Angle search	0–24 sec
Acquisition receiver response	0.25 sec
Tracking receiver preset	0.45 sec
Tracking receiver frequency search	0–4 sec
Most probable time lapse from signal presence to autotrack	2.7 sec

well matched mixer-preamplifier transmission system. (See the block diagram in Fig. 2 and associated Table IV.) This arrangement ensures an adequately low receiver noise contribution.

3.2 *Antenna*

The 8-foot Cassegrainian reflector, shown in Fig. 3, provides a 2-degree beamwidth, which represents a nearly optimum compromise between the wide beam needed for acquisition and the antenna gain required for tracking accuracy. The antenna system is a unique embodiment of the Cassegrainian configuration; it consists of a parabolic main reflector, a hyperbolic subreflector, and a four-horn feed system which illuminates the subreflector from the rear through a hole at the axis of the main reflector. It is designed to process an impinging wave front polarized vertically. For any other polarization it may be considered as accepting only the vertical vector component; thus, for the nominally circularly polarized Telstar spacecraft beacon signal, a 3-db effective loss is entailed.

3.2.1 *Reflector Assembly*

Fiberglas honeycomb is the main structural material employed in the reflector assembly, as shown in Fig. 3. The subreflector and its conical support constitute an integral structure of molded Fiberglas honeycomb core overlaid on both sides with a Fiberglas skin. The conducting hyper-
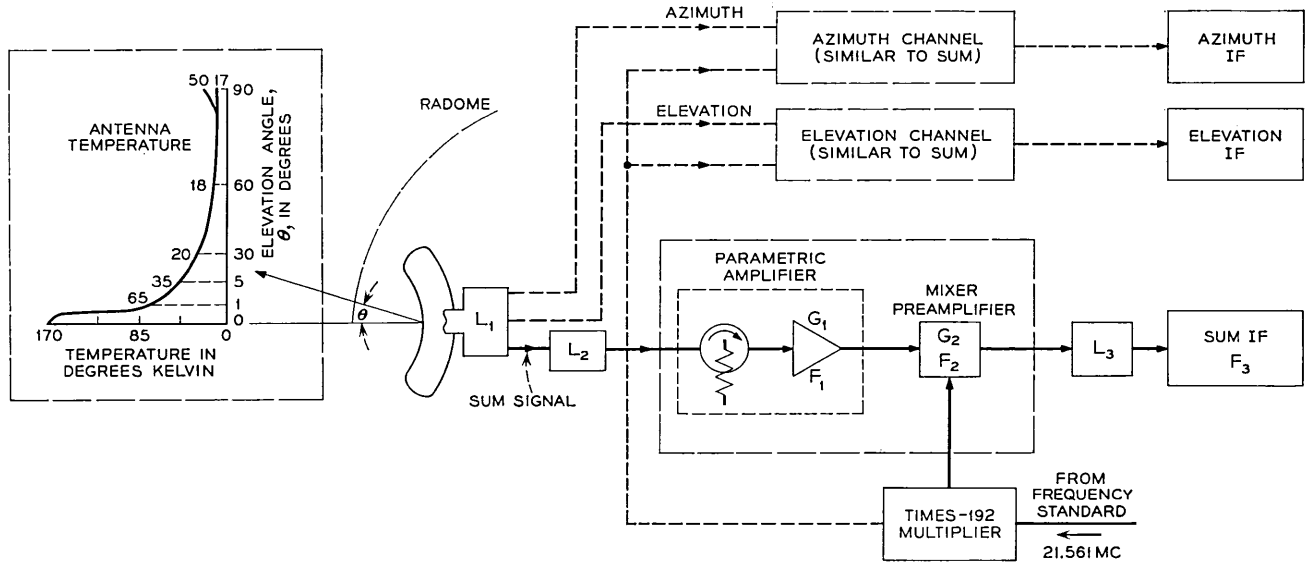
Fig. 2 — Over-all RF block diagram.

TABLE IV

Antenna and Radome Temperature	Comparator Loss	Coupling Losses, Semi-Rigid Line	Parametric Amplifier, Mixer-Preamplifier and Harmonic Multiplier	Slip Rings and Coax Cables	Main IF Amplifier
Radome $\approx 9°K$ System input temperature (T_e) $T_e = \sum\limits_{1}^{n} \dfrac{(T_a)n}{\prod\limits_{n} G(n-1)} = 315°K$ System operating temperature (T_{op}) $\quad T_{op} = T_{ant} + T_e$ $\quad\quad = 340°K$ at $\Theta = 10°$	Dissipative and mismatch loss $\quad L_1 \approx 0.2$ db $T \approx 290°K$ Connector loss = 0.1 db Total $L_1 = 0.3$ db	Rigid cable loss at 4079.73 mc $L_2 = 0.2$ db	Over-all unit noise figure 2.7 db Circulator loss 0.2 db $G_1 = 23$ db, including circulator $G_2 = 25$ db $F_1 = 2.5$ db $F_2 = 9$ db max.	Ring loss 0.4 db Cable loss 4.2 db Connectors 0.2 db Total 4.8 db	$F_3 = 9$ db $T = 290°K$
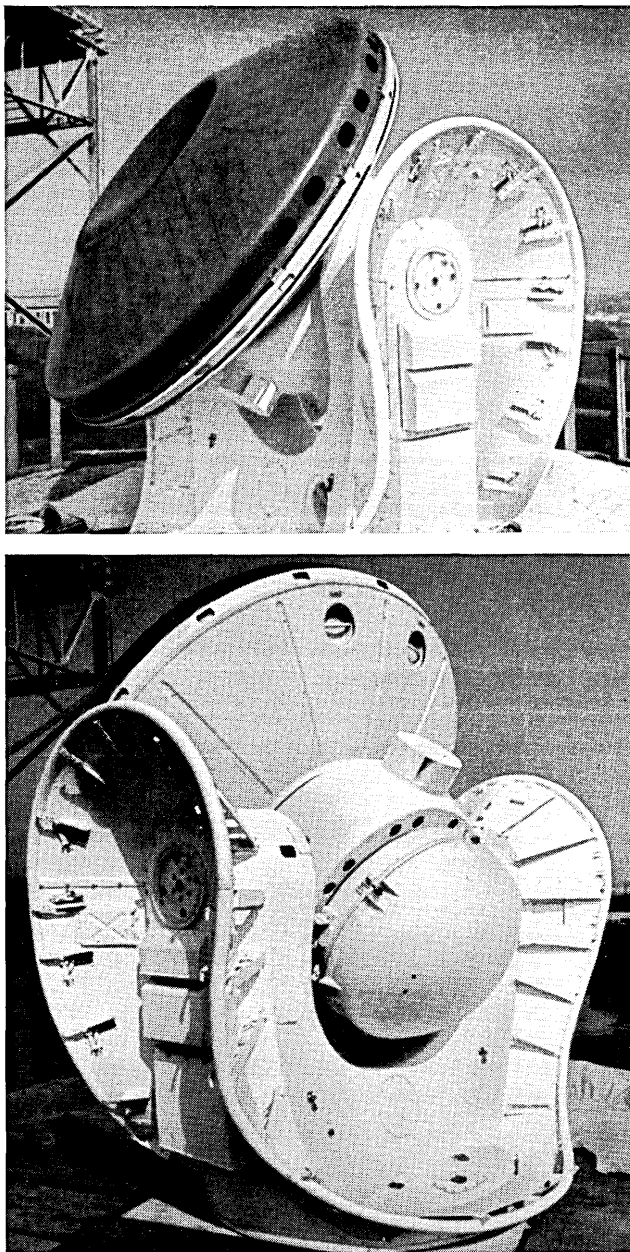
Fig. 3 — Precision tracker antenna, front and rear views.

bolic surface of the 36-inch diameter subreflector is composed of a horizontal array of aluminum wires of 0.01-inch diameter embedded in both the inner and outer skins. The subreflector is transparent to impinging vertically polarized signal components (see Fig. 4). The periphery of the area containing the wires is serrated rather than circular, to cause cancellation of the major effects of diffraction at the wire ends. The subreflector is 26.6 inches in front of the main reflector along the boresight axis.

The 92-inch diameter main reflector is made up of an aluminum parabolic reflector surface on which is overlaid a Fiberglas honeycomb core. The Fiberglas skin affixed to the core contains an aluminum wire grid embedded at an angle of 45 degrees to the vertical. The structure is called a twist-reflector: a vertically polarized signal component impinging upon the surface of the 45-degree wires may be resolved into two vector components, one normal to the wires and the other parallel to the wires. The parallel component is reflected by the wires; the normal component passes through the wires and honeycomb core and is reflected from the aluminum reflector to pass back through the core and the wires. The delay through the core is such that the two components recombine, at the wire surface after reflection, to result in a horizontally polarized signal at the subreflector.

The subreflector, whose wire structure is opaque to horizontal polarization, refocuses the signal to the four feedhorns projecting through the center of the main reflector.
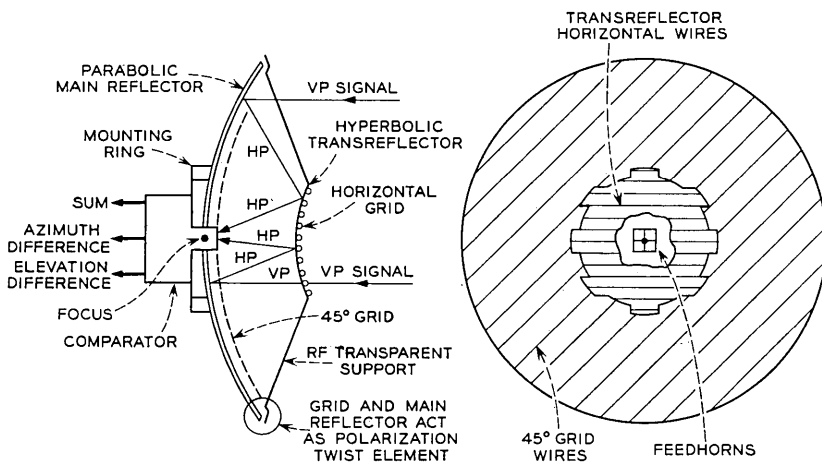
Fig. 4 — Cassegrainian antenna and twist reflector.

3.2.2 Comparator-Feed Assembly

Four individual patterns, each "squinted" symmetrically away from the central boresight axis of the antenna system, are created by the four horns and reflectors. The feedhorns are an integral part of the comparator-feed assembly, illustrated in Fig. 5, which shows the assembly, the microwave absorber ring which surrounds the feed, and the Fiberglas dust cover.

The assembly is made from aluminum stock in which the horns, four waveguide hybrid junctions, and waveguide phasing sections are precisely machined. The signals received by the horns are processed by vector additions and subtractions in the hybrids to form the three antenna response functions[4] required for tracking. The sum pattern is formed by the summation of all signals propagating in the four horns; the azimuth difference and elevation difference patterns are formed by obtaining the difference between the sums of signals in adjacent vertical pairs and horizontal pairs, respectively.

Connections from the signal output ports of the comparator to the parametric amplifiers are made by waveguide-to-coaxial transitions and through semirigid, low-loss coaxial line.

3.2.3 Advantages of the Antenna System

The Cassegrainian antenna as employed in the PT has the following advantages:

(a) It possesses the high gain associated with parabolic structures.

(b) Secondary radiation patterns having excellent sum pattern symmetry and difference patterns with high slope factors and deep boresight nulls are achieved.
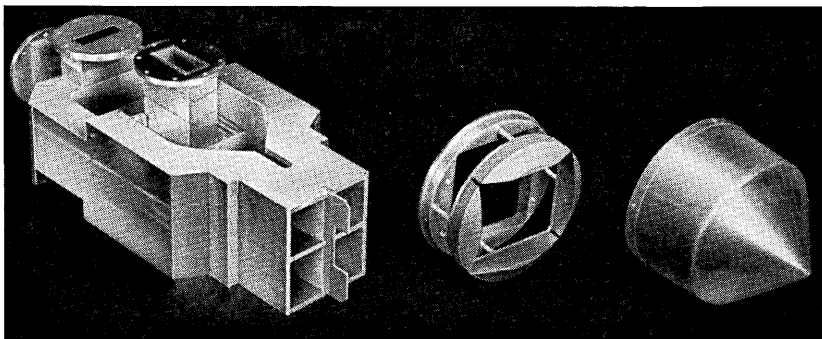
Fig. 5 — Microwave comparator (photo courtesy Wheeler Laboratories, Inc.).

(c) Shadow effects are minimized by the subreflector design, and therefore the effective area is essentially the same as that of an equivalent-sized parabolic system.

(d) Since the focal point is in the parabolic contour, the comparator can be located near the RF amplifier, thus minimizing coupling loss noise; the effective receiver temperature is lowered over that of antenna-receiver types having forward feeds and feed-support schemes.

(e) Since tracking angles are above the horizon, the primary patterns are coupled to the low-temperature sky rather than to the high-temperature earth; therefore, the effect of increased noise due to the primary radiation pattern coupling is lessened.

(f) Side lobes, back radiation, and spillover lobes are well below peak response (see Fig. 6 and associated Table V).

(g) A structure of relatively low moment of inertia is obtained, since the heavy receiving components are located near the rotational axis.

3.3 *Parametric Amplifiers*

Three low-noise parametric amplifiers amplify the sum and difference signals prior to mixing. These amplifiers are of the nondegenerative negative-resistance type. The input signal is fed through an input circulator, an impedance transformer, and a low-pass filter, so as to match the impedance at the varactor element and minimize coupling between the idler, pump, and signal circuits. The varactor element is mounted in a cavity resonant at both the pump frequency (16 kmc) and the idler frequency (12 kmc). The pump signal is produced by a reflex klystron which is immersed in a temperature-controlled oil bath and coupled to the parametric amplifier via K-band waveguide sections. The specifications for the PT parametric amplifiers are given in Table VI.

The parametric amplifier outputs for the three channels are fed to a balanced mixer-preamplifier unit. These units have an over-all gain of 25 db and a maximum noise figure of 9.0 db (double channel). The preamplifier utilizes a cascade circuit to minimize the over-all noise figure of the mixer-preamplifier assembly. The preamplifier has a center frequency of 59.98 mc and a bandwidth, at a -3 db response, of 6 mc.

Local oscillator drive is supplied to all three mixers by a common solid-state harmonic multiplier. This unit produces a minimum of 3 mw of RF power for each mixer at a frequency above the signal input. The output signals from the preamplifier are matched to 50-ohm coaxial cables and supplied to the slip rings for transmission from the rotating portion of the antenna assembly to the stationary tracking mount.
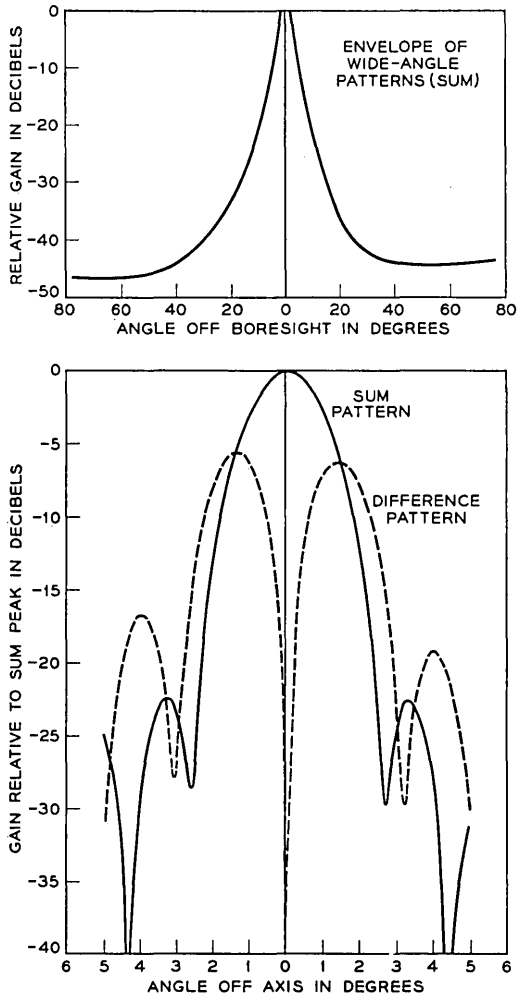
Fig. 6 — Secondary radiation pattern of precision tracker antenna system.

TABLE V — NOTES FOR FIG. 6

Antenna Characteristic	Value
Frequency	4079.73 mc
Polarization	vertical
Sum gain	37.2 db
3-db beamwidth, sum mode	2.1°
Suppression of first side lobe, sum mode	22.3 db
Difference gain, average of EL and AZ	30.6 db
Difference peak separation, average of EL and AZ difference modes	2.8°
Suppression of first difference side lobe, average of EL and AZ difference modes	12.6 db
Difference slope, normalized to an isotropic radiator	43.5v ratio/deg.

TABLE VI — PARAMETRIC AMPLIFIERS

Parameter	Value
Center frequency	4079.73 mc
Gain	23 db nominal
Bandwidth, instantaneous	20 mc nominal
Pump frequency	16,037 ± 2 mc
Pump power	60 mw nominal
Noise figure, excluding coupling losses	2.5 db max.
Gain stability, channel to channel	3 db max. fluctuation
Phase stability, channel to channel	12° max. fluctuation

The 50-ohm coaxial preamplifier lines are matched to the rings by a shorted stub element attached to each of the three signal rings. A 50-ohm double-shielded coaxial cable transmits the IF signals to the main IF amplifier.

3.4 *Signal-to-Noise Ratio*

A determination can be made of the SNR achieved for the system, taking into account the added noise components due to the atmosphere and the properties of the receiver components. The noise producing elements are defined as those up through and including the slip-ring assembly (see the block diagram of the RF system, Fig. 2, and associated Table IV). The receiver's effective input temperature, obtained from the component values shown here, is determined to be 315°K. Adding the antenna temperature to this value gives the system effective operating noise temperature (T_{op}). The effective input noise power ($P_n = KT_{op}B$) can then be obtained for each elevation angle. The results are shown in Fig. 7, together with the expected received signal power (P_S) for the 5700-statute-mile path. The SNR is the difference in ordinates between the two functions. It can be seen that the receiver and antenna noise contribution over the operational range of angles reduces the SNR value, based on the noise power associated with an input termination in thermal contribution over the operational range of angles reduces the SNR value, equilibrium at 290°K, by some 0.7 db. The average SNR over the operational elevations for maximum slant range is +3 db for a beacon signal at +15 dbm, or +5 dbm for a beacon signal power of +17 dbm.

IV. TRACKING RECEIVER

The precision tracker's tracking receiver (fifth bay of Fig. 8) functions to extract azimuth and elevation pointing error information from noise-laden IF signals produced in the tracking antenna and RF assembly by

EFFECTIVE SIGNAL AND NOISE POWER AT PRECISION TRACKER INPUT IN DBM

RECEIVED
SIGNAL POWER
P_s

POSSIBLE VARIATION
IN BEACON POWER
DUE TO COMMUNICATION
LOAD

+15-DBM BEACON
AVERAGE S/N RATIO = 3 DB

NOISE POWER
IN 3-KC
BANDWIDTH
P_n

+17-DBM BEACON
AVERAGE S/N RATIO = 5 DB

DAYTIME

NIGHT

THERMAL NOISE POWER AT
REFERENCE TEMPERATURE K 290° B

NORMAL OPERATING
RANGE

ELEVATION ANGLE IN DEGREES

Fig. 7 — System noise power.

COMB FILTER
CABINETS

LOGIC
CABINET

RECEIVER
CABINET

FREQUENCY RECEIVER
CABINET

FREQUENCY
STANDARD
CABINET

TEST SIGNAL
CABINET

Fig. 8 — PT equipment cabinets.

a 4079.73-mc CW tracking beacon in the satellite. Because of the combined effects of Doppler shift and satellite frequency drift, the received IF signal frequency may differ from a nominal center frequency of 59.98 mc by as much as ±120 kc. A narrow-band adaptive tracking filter provides a phase-locked second local oscillator signal to permit coherent signal detection over a frequency range of ±150 kc.

4.1 *Block Diagram Description*

A simplified block diagram of the complete tracking receiver is shown in Fig. 9. The nominal 59.98-mc IF signals from the three IF preamplifiers in the antenna RF equipment enclosure are transmitted through matched slip rings and 250 feet of triple coaxial cable to the inputs of the sum, azimuth, and elevation main IF amplifiers. These matched amplifiers, under automatic gain control (AGC), provide a large portion of the 151-db receiver gain necessary to amplify the received signals to detector level. Each main IF amplifier is divided into two sections, with a bandpass filter of 1-mc bandwidth located between the sections to reduce the total noise and interference imposed on the amplifiers following.

The signal frequency is reduced to 5 mc at the three second converters by mixing with a nominal 64.98 mc derived from a voltage-controlled crystal oscillator (VCXO) and multiplier chain. The frequency and phase of this oscillator are determined by phase comparison of the 5-mc sum IF signal with a local phase-stable 5-mc reference signal in a somewhat sophisticated phase-lock loop. As shown on the block diagram, this loop also contains 5-mc IF amplifiers, a limiter, a 3-kc bandwidth crystal filter, a phase detector, and the loop filter.

The three remaining 5-mc channels are similar in that they contain 5-mc IF amplifiers, 3-kc bandwidth crystal filters, and phase detectors, all supplied by the same 5-mc reference signal. The phase-lock loop establishes and maintains a constant phase relationship between the received signals and the 5-mc reference signal, and permits coherent detection of the IF signals in these three channels. The detected sum signal provides an indication of phase lock and a measure of the received signal amplitude for operation of the AGC loop. The detected azimuth and elevation signals provide both sense and magnitude of antenna pointing errors for application to the respective antenna-positioning servos.

Biases that might occur in the pointing information because of detector unbalance or dc amplifier drift are eliminated by commutating the phase of the 5-mc IF error signals prior to detection and then synchronously demodulating the ac-coupled detector outputs.
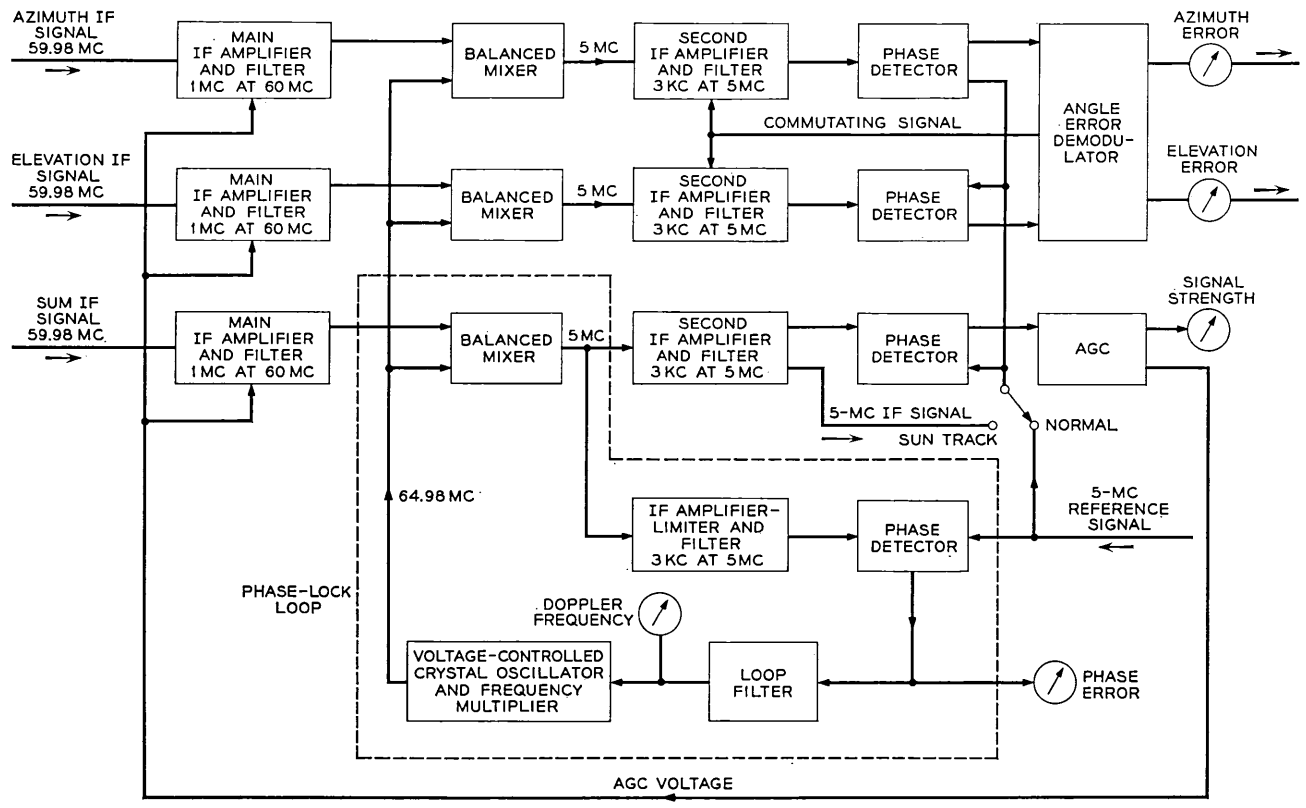
Fig. 9 — Tracking receiver, block diagram.

The mechanism for the correlation detection test option is indicated on the diagram as a "sun track" switch. The switch controls the substitution of a properly phased 5-mc sum IF signal for the 5-mc reference supplying the AGC and angle-error detectors.

A more detailed discussion of the key features of the tracking receiver follows.

4.2 *Main IF Amplifiers*

The two sections of each main IF amplifier include a total of ten transitionally coupled, synchronously tuned amplifier stages utilizing Western Electric 5847 electron tubes at a center frequency of 60 mc and an over-all bandwidth of 8 mc. The first two stages, which employ fixed gain, are followed by an adjustable phase-control network that provides approximately 150 degrees of receiver phasing adjustment per channel. The IF signal for the PT acquisition receiver is tapped off the sum channel at this point. Manual gain adjustment of the first two stages of the azimuth and elevation channels provides ±4 db of receiver gain equalization.

The remaining eight amplifier stages of each channel are gain controlled by the AGC. The stability of the amplifiers is such that the differential gain and phase of the three channels do not exceed 1 db and 3 degrees, respectively, when controlled over a 60-db range of gain from a common gain-control voltage.

A passive LC filter of 1-mc bandwidth separates the two sections of each channel for intermediate reduction of noise bandwidth.

Insertion pads are included at the input of each channel for the connection of a common IF test signal originating in the PT frequency standard and test signal cabinets.

4.3 *Second Converters*

The 59.98-mc IF signals from the three main IF amplifiers are converted to 5 mc by mixing with a common 64.98-mc local oscillator signal in three balanced passive mixers. Each input signal is terminated in a 50-ohm impedance provided by a broadband toroidal transformer hybrid. Mixing is accomplished in a matched pair of 1N35S germanium diodes.

4.4 *5-mc IF Amplifiers*

Conventional single-tuned amplifiers utilizing Western Electric 403B and 404A electron tubes follow mixer impedance matching networks

in the three channels. A 5-mc crystal lattice filter with a 3-kc noise bandwidth and a 180-degree phase delay is located, with appropriate input and output matching networks, between the first and second amplifier stages of the azimuth and elevation channels and the AGC branch of the sum channel. In the third stage of the azimuth and elevation channels, signal impedance is lowered to 50 ohms to drive a phase-commutating transformer, the operation of which will be detailed later. A fourth stage drives the 50-ohm phase-detector transformer. Following the second stage the AGC channel is split into two 50-ohm output stages, one driving the AGC detector transformer and the other providing 5-mc sum IF signals for correlation detection. The net gain of all three channels from mixer input to detector transformer is fixed at 45 db. The level of the signal appearing at all detector transformers is +13 dbm when the azimuth and elevation error signals equal the sum signal.

4.5 Phase-Lock Loop

The phase-lock loop is the heart of the tracking receiver. It embodies a form of adaptive tracking filter that approaches an optimum filter under all conditions of SNR, Doppler change, and rate of change expected in the PT environment.[6]

A block diagram of the phase-lock loop is shown in Fig. 10. The 5-mc IF input signal obtained from the second mixer in the sum channel is amplified approximately 75 db at a bandwidth of 200 kc by three single-tuned amplifier stages and is "hard" limited by a type 6BN6 limiter. The gain is sufficient to ensure at least 20 db of signal limiting at all times. A crystal filter with associated matching networks follows the limiter.
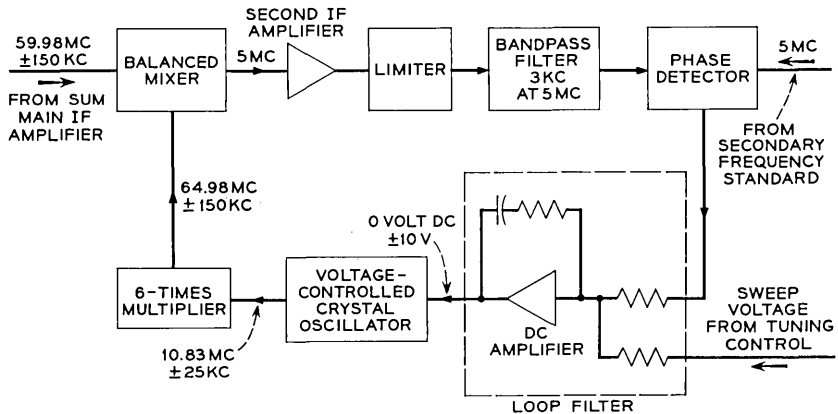
Fig. 10 — Phase-lock loop, block diagram.

This filter is similar to those in the other 5-mc IF channels in that it has a 3-kc bandwidth, but it has only a 90-degree phase delay. The requirement for a 90-degree phase difference between the reference for the phase detector in the phase-lock loop and the reference for all the other phase detectors is thus satisfied by the relative phase delays of the filters used in the 5-mc IF circuits.

A single amplifier stage matches the filter output to the 50-ohm phase-detector transformer. The signal power reaching the detector is a function of the SNR in the limiter. Because the total signal-plus-noise power in the output of the limiter is constant, the signal power at the detector will be suppressed as the direct ratio of noise-to-signal appearing at the limiter input for the ratios above approximately unity in the 200-kc bandwidth at this point. A direct consequence of this action is a reduction of phase-lock loop gain with decreasing received signal strength.

The phase detector (Fig. 11) consists of a carefully balanced and shielded broadband transformer hybrid driving a matched pair of silicon diode detectors. A high-gain dc operational amplifier accepts the two detector outputs in a differential connection to provide a low-impedance, single-ended output. Amplifier gain, and thus the phase detector gain constant, is determined by the ratio between input and feedback resistors. The 5-mc reference signal is applied to the phase detector at a much higher level than the IF signal, resulting in a sinusoidal output

$$e = \alpha K \sin \theta$$

where
α = limiter suppression factor
$K = 5.75$ = detector gain constant
θ = loop phase error.
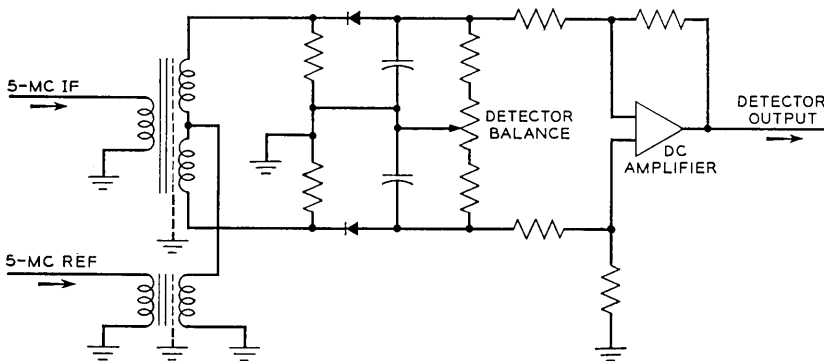
Fig. 11 — Phase detector.

The detector parameters given produce an output of 0.1 volt/degree for $\theta \leq \pm$ 10 degrees and a suppression factor of unity (strong signal).

The phase detectors of the azimuth, elevation, and AGC channels differ from this configuration only in differential amplifier gain.

The loop filter takes a form approaching that of an ideal integrator modified for loop stability. A high-gain, chopper-stabilized, dc operational amplifier with a capacitor in the feedback loop provides a dc gain of 30×10^7, falling off at 6 db/octave above 0.032 cps. This, combined with the inherent 6 db/octave slope of the VCXO/phase-detector combination, causes gain crossover to be approached at 12 db/octave. A resistor in the integrator feedback provides a lead corner at approximately 10 cps to stabilize the phase-lock loop. Because of limiter suppression, with the attendant change of loop gain, both loop bandwith and damping factor change with received SNR in a manner that optimizes the loop characteristics for minimum phase error. A plot of loop bandwidth and damping factor versus SNR is shown in Fig. 12. The use of an integrator as the loop filter results in negligible accumulated phase error at the extremes of the $\pm$150-kc tracking range.
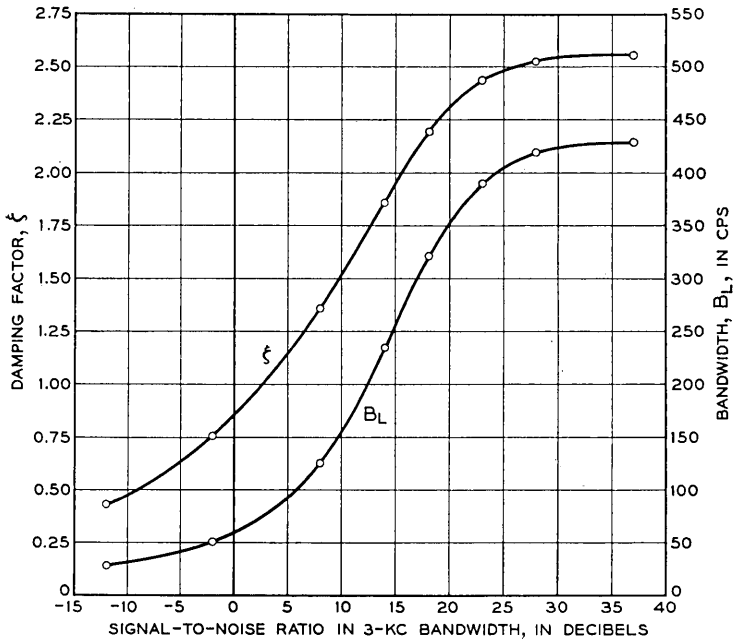
Fig. 12 — Loop bandwidth and damping factor vs signal-to-noise ratio.

During frequency acquisition the integrator is automatically preset to a voltage equivalent of 3 kc below the frequency indicated by the acquisition receiver and swept, by means of a dc voltage applied to the integrator through a separate input resistor, to the equivalent of 3 kc above indicated frequency. When phase lock occurs, the sweep is automatically disabled. The choice of one of four sweep rates is based on predicted signal strength. Manual preset and sweep controls are also provided.

The variable frequency element in the phase-lock loop is a voltage-controlled crystal oscillator (VCXO) with a stable center frequency of 10.83 mc. To permit accurate transfer of frequency acquisition information from an independent source, the voltage-frequency linearity is held to ± 1 per cent of a straight line function having a slope of 2.5 kc/volt over a ± 25-kc range. The unit is a commercially obtained solid-state device packaged in an oven.

The 10.83-mc (± 25 kc) oscillator output is multiplied to 64.98 mc $\pm$ 150 kc by a tripler and a doubler. Three separate output stages are provided to drive the three balanced mixers at $+20$ dbm.

Performance of the phase-lock loop has demonstrated a capability of holding peak phase errors to a level of less than ± 10 degrees over the full dynamic range of tracking conditions encountered in the PT. Good coherent detection of azimuth and elevation error signals, with the associated benefits accrued in the low SNR region, is thus assured.

4.6 Automatic Gain Control

Because of the phase relationships established by the crystal filters in the 5-mc IF amplifiers, the AGC phase detector provides coherent detection of the peak amplitude of the sum IF signal. The gain of the detector differential amplifier is such that a $+13$ dbm IF signal produces $+25$ volts output.

A simplified version of the AGC amplifier and loop filter is shown in Fig. 13. A dc operational amplifier, with current booster, is operated as an integrator. An adjustable limiter is provided to limit the maximum positive output voltage, thus limiting the maximum receiver gain. The $+25$-volt AGC detector output is compared with a nominal -25 volts in the input summing network to provide the necessary error signal for loop operation. The diodes in the capacitor feedback circuit switch an additional capacitor into the loop during signal increase to equalize loop response times for increasing and decreasing signals. Integrator time constants result in a closed-loop cutoff frequency of approximately 3 cps. Because of the extremely high dc loop gain provided by the opera-
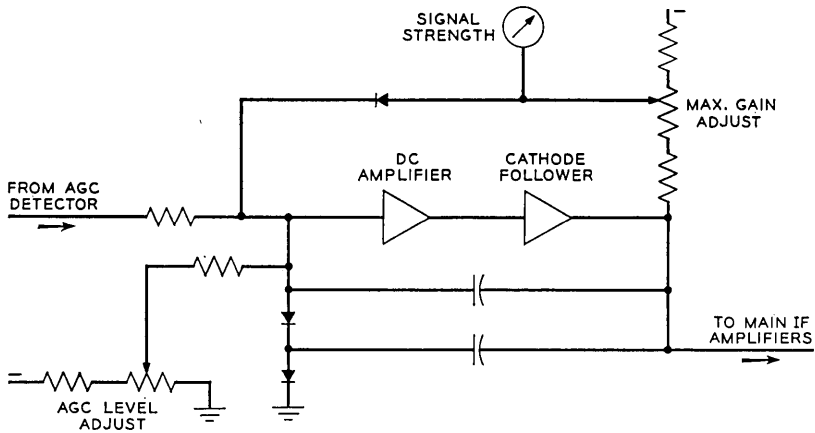
Fig. 13 — AGC amplifier and loop filter.

tional amplifier, there is negligible change in detected signal level over the entire range of gain control.

4.7 Angle-Error Detectors

As in the AGC detector, the azimuth and elevation phase detectors provide coherent amplitude detection of the 5-mc IF signals. The polarity of the detector output depends upon the direction of the antenna pointing error.

The prediction program, which employs the PT data, is particularly sensitive to bias errors in the angular position data obtained in the process of tracking. Bias errors of large magnitude could occur in angle-error detectors and dc circuits associated with the detectors. A commutation technique used in the tracking receiver to eliminate these errors is shown in Fig. 14. The phase of the 5-mc IF error signal is periodically reversed by the switching action of diodes in the secondary of a balanced transformer, initiated by a square wave generated at about 50 cps. As a result, the detector output becomes a square wave containing the angle error information in its amplitude. A capacitor blocks any dc bias content and couples the square wave for amplification and synchronous demodulation in a carefully balanced ring demodulator, using the same switching square wave as reference.

Detector and demodulator gain constants, together with the antenna difference pattern slope factor, result in a nominal 7.14-volt/degree pointing error scale factor at the antenna servo input. Some gain adjust-
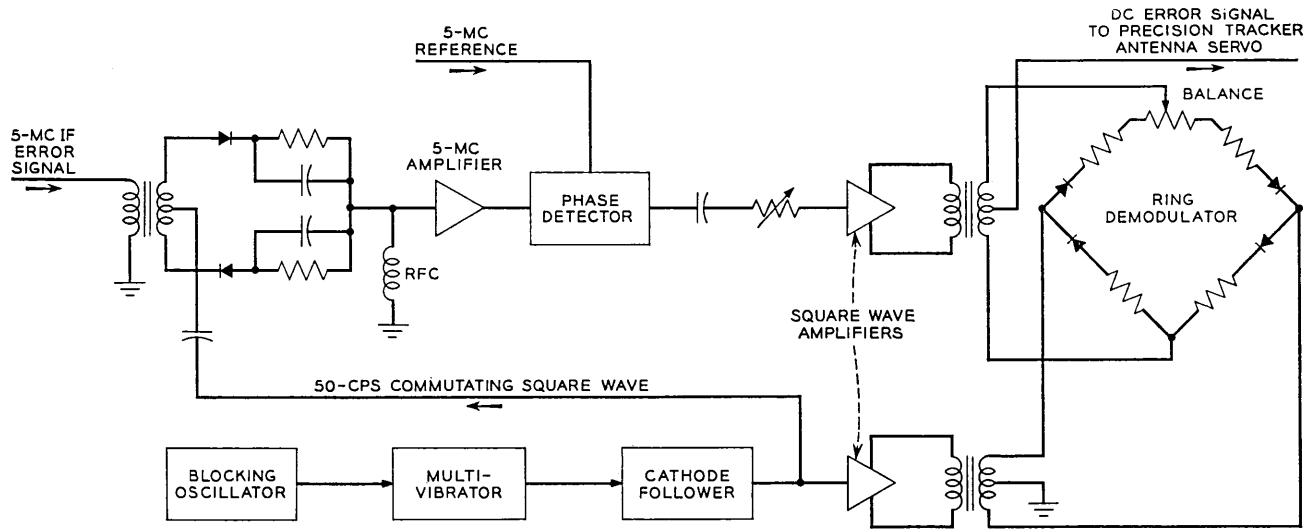
Fig. 14 — Angle-error detector commutation.

ment is provided at the demodulator input for over-all antenna servo loop gain adjustment.

V. ANTENNA POSITIONING SYSTEM

5.1 *General Description*

The antenna positioning circuits permit automatic, manual, or test control of the PT antenna. The positioning circuits consist basically of similar azimuth and elevation servo loops, which operate antenna drive motors.

In the automatic tracking mode of the precision tracker, antenna positioning data for the servo loops are in the form of azimuth and elevation error signals from the tracking receiver. Before these signals can be generated, however, the precision tracker must acquire the 4079.73-mc beacon signals from the Telstar spacecraft. To do this, input data from the track digital control or the command tracker drive the antenna positioning circuits.

During the initial stage of satellite acquisition, azimuth and elevation error signals from the track digital control point the PT antenna to the predicted position of the satellite, as described in Ref. 2. When the 4079.73-mc beacon signal is acquired by the precision tracker, the scan program is automatically stopped, the antenna positioning circuits of the precision tracker switch to the automatic tracking mode, and pointing signals from the command tracker are automatically removed.

During its acquisition and tracking operations, the precision tracker uses data on the predicted range of the satellite to optimize the frequency search rate in the tracking receiver and the bandwidths in the antenna positioning circuits. Normally, the range data are supplied in printed form by the on-site data processing system prior to the pass.

Once the 4079.73-mc beacon signal from the satellite has been acquired and the antenna positioning circuits are operating in the automatic tracking mode, the precision tracker can supply precise azimuth and elevation data to the antenna pointing system and to the data processors via the track digital control.

If because of some external or local disturbance, the precision tracker should lose autotrack, the 4079.73-mc signals may be reacquired in several ways. The precision tracker again may be slaved to the command tracker (if the CT itself is still in autotrack); the PT antenna may be repointed with predicted satellite position data from the track digital control; or the precision tracker may be placed in the manual tracking

mode. During reacquisition by any of the above means, manual or automatic scanning may be employed.

The antenna positioning circuits can be operated in any one of the following six modes:

(1) manual (test and backup acquisition mode)
(2) aided (test mode)
(3) track digital control (acquisition mode)
(4) autotrack (operational mode)
(5) command tracker (acquisition mode)
(6) remote (test and maintenance mode).

5.2 Servo Drive Circuits

Basically, each of the antenna positioning circuits comprises a main servo drive circuit and several servo control circuits, as shown in Fig. 15. Since the antenna positioning circuits for azimuth and elevation are electrically similar, Fig. 15 is applicable to both circuits. The main servo drive circuit is shown outlined in heavy brackets. All other circuits, outlined in light brackets, are a part of the servo control circuits.

The main servo drive circuit amplifies relatively low-level control signals to the higher power levels required to position the PT antenna mechanically. The circuit consists essentially of an input network, preamplifier, four magnetic amplifiers, four drive motors, and four tachometers.

The input network consists of three low-pass filters. One of these 0-6-0-6 db/octave filters is selected for insertion in the track loop, depending upon the range between the tracker and satellite. The widest bandwidth filter is used for the low-range, fast-moving portion of the pass, while the lowest bandwidth is used during the early, long-range portion of the pass. An additional 6-db/octave roll-off is present because of the servo closed-loop motor-tachometer combination. The 6-db/octave roll-off causes the servo to be of the velocity type 1 variety. Table VII shows a plot of open-loop gain versus frequency, and lists some of the associated parameters of the servo system.

5.3 Manual and Aided Modes

The manner in which the control signals are generated depends on the PT mode of operation. During either the manual or the aided mode, the control signal is generated by means of a handwheel mounted on the PT control console. During the manual mode, rotation of the handwheel generates a drive signal, which represents desired speed and direction
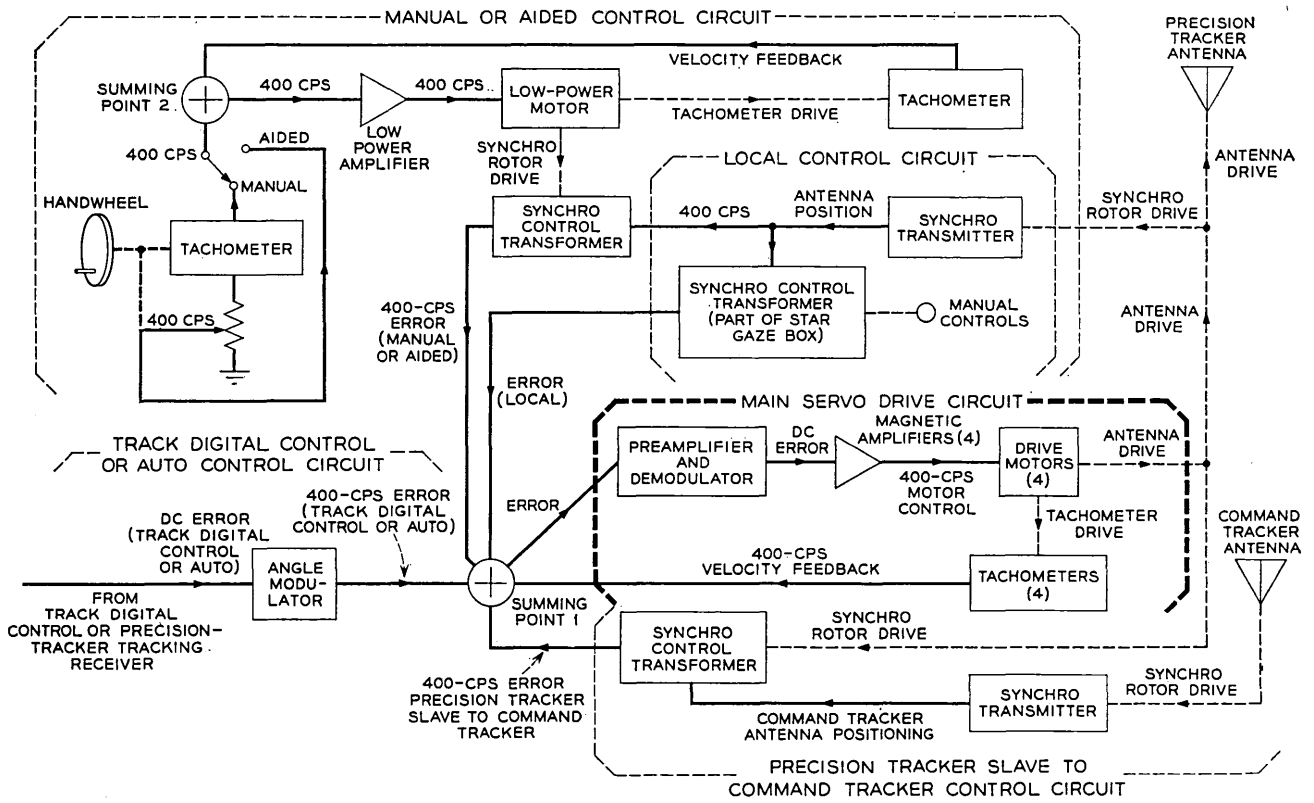
Fig. 15 — Antenna positioning circuits, azimuth or elevation.

TABLE VII — SERVO TRANSFER FUNCTION AND CONSTANTS

Open-Loop Transfer Function

$$G = \frac{\left(\dfrac{S}{\omega_2} + 1\right)}{\left(\dfrac{S}{\omega_0}\right)\left(\dfrac{S}{\omega_1} + 1\right)\left(\dfrac{S}{\omega_3} + 1\right)}$$

Closed-Loop Transfer Function

$$K = \frac{\left(\dfrac{S}{\omega_2} + 1\right)}{\left(\dfrac{S}{\omega_2} + 1\right) + \dfrac{S}{\omega_0}\left(\dfrac{S}{\omega_1} + 1\right)\left(\dfrac{S}{\omega_3} + 1\right)}$$

GAIN IN DECIBELS — 6 DB PER OCTAVE — 12 — 6 — 0 — 12 — ω_1 ω_2 ω_c ω_3 ω_0 — FREQUENCY IN RADIANS
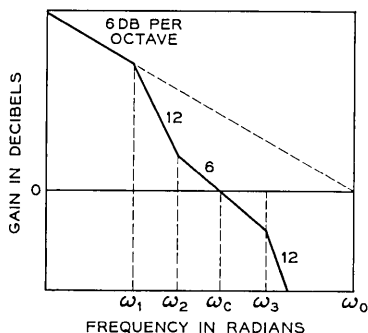
Constants

	Range (miles)			
	400–800	800–1700	1700–3500	3500–7000
Scan Rate (sec/revolution)	2	3	4	6
ω_1	0.046	0.012	0.0021	0.0021
ω_2	1.5	0.76	0.31	0.31
ω_3	150	150	150	150
ω_0	200	200	200	200

Scan Radii

Step	Degrees
0	0
1	1.4
2	2.8
3	4.2

of antenna movement. During the aided mode, an angular displacement of the same handwheel generates a constant-rate signal, which represents desired rate and direction of antenna movement. Either signal (depending on the selected mode) is amplified and applied to a low-power motor. The motor, in turn, physically positions the rotor of a synchro transformer. The position of the rotor of the control transformer represents desired antenna position. A second input to the same control transformer is an electrical input to its stator, representing actual antenna position as sensed and transmitted by a synchro transmitter that is geared to the PT antenna. The output of the control transformer represents an error between the desired antenna position and the actual

antenna position. This error signal, called "error (manual or aided)" on Fig. 15, is injected into summing point 1, where it becomes the error signal in the main servo drive circuit.

5.4 *Track Digital Control and Autotrack Modes*

During either the track digital control or the autotrack mode, the control signal is generated by circuits external to the antenna positioning circuits. The track digital control signal originates in the track digital control portion of the antenna direction system, and the autotrack signal is developed within the PT tracking receiver. Each is a dc voltage representing an error in desired antenna position. The dc voltage is converted into ac voltage by the angle modulator and is inserted into summing point 1, where it becomes the error signal within the main servo drive circuit.

5.5 *Command Tracker Mode*

During the command tracker mode, a synchro link between the precision tracker and the command tracker is used to control the main servo drive circuit of the PT. A synchro transmitter within the command tracker senses the position of the command tracker antenna and transmits this information to a synchro control transformer within the PT. The output of the synchro control transformer, representing the error between the PT and command tracker antenna shafts, is injected into summing point 1 as the error signal within the main servo drive circuit.

5.6 *Remote Control Mode*

In the remote mode, the antenna can be positioned by use of a portable control unit called the "star gaze box," which is connected by cable to the antenna base. Manual controls mounted on the star gaze box enable the operator to choose two types of control: (a) He can rapidly slew the antenna by means of switches that introduce a constant error signal into the main servo drive circuit via summing point 1. The error persists as long as the slew switch is depressed. (b) He can gently position the antenna by means of a control knob that controls the rotor of a synchro control transformer mounted in the star gaze box. A second input to the same control transformer senses actual antenna position as given by a synchro transmitter geared to the antenna. Any difference between desired antenna position, as represented by the position of the manually controlled rotor of this control transformer, and actual antenna position,

as received from the synchro transmitter, generates an error, which is fed into summing point 1 and then into the main servo drive circuit. The error persists until the antenna moves to the desired position.

5.7 *Search Scan*

In order to enhance the satellite acquisition capability of the precision tracker, the PT antenna beam can be caused to search about the mean azimuth and elevation angle to which it is pointed. The search is the result of a circular motion of the PT antenna and is controlled (either manually or automatically) by the scan control circuits located in the PT control console.

The PT antenna, as mentioned above, is positioned by two independent servo systems, one for the azimuth angle and one for the elevation angle. A separate error signal within each servo system controls antenna position in each angle. Since the PT antenna is a two-axis system, simultaneous motion in both axes is necessary if a circular pattern is to be traced about the mean angle. This is achieved by the superimposing of small offset (or bias) errors onto the main error signal in each servo system. The biasing errors are developed by the rotating rotor of a resolver, which is the key component in the scan control circuits.

Both the radius and the frequency (or period) of the circular search must also be controlled. The radius is controlled by the amplitude of the bias signals applied to the two servo systems. A choice of one of four different preset radii is available to the console operator. The desired radius is selected by means of the scan step control indicator mounted on the console. The period is established by the rate of rotation of the rotor of the resolver, which depends on the scan mode of operation.

During manual scan, the period of the PT antenna circular search is controlled by the scan handwheel drive (refer to Fig. 16). Rotation of the handwheel causes a generator to produce a voltage proportional to the speed of rotation of the handwheel. This voltage is combined with velocity feedback voltage and sent to the low-power amplifier as a motor control voltage. The motor drives the rotor of resolver B_2 at a speed proportional to the original speed of handwheel rotation and thus establishes the period of circular search. The two quadrature voltages taken from the rotor of the resolver are sent to the switch assembly, where their amplitude is regulated by the radius of scan selected by the console operator.

During the automatic scan mode, the period of the PT antenna's circular search is controlled as a function of range to ensure a good probability of beacon signal detection. At short ranges, when the satellite
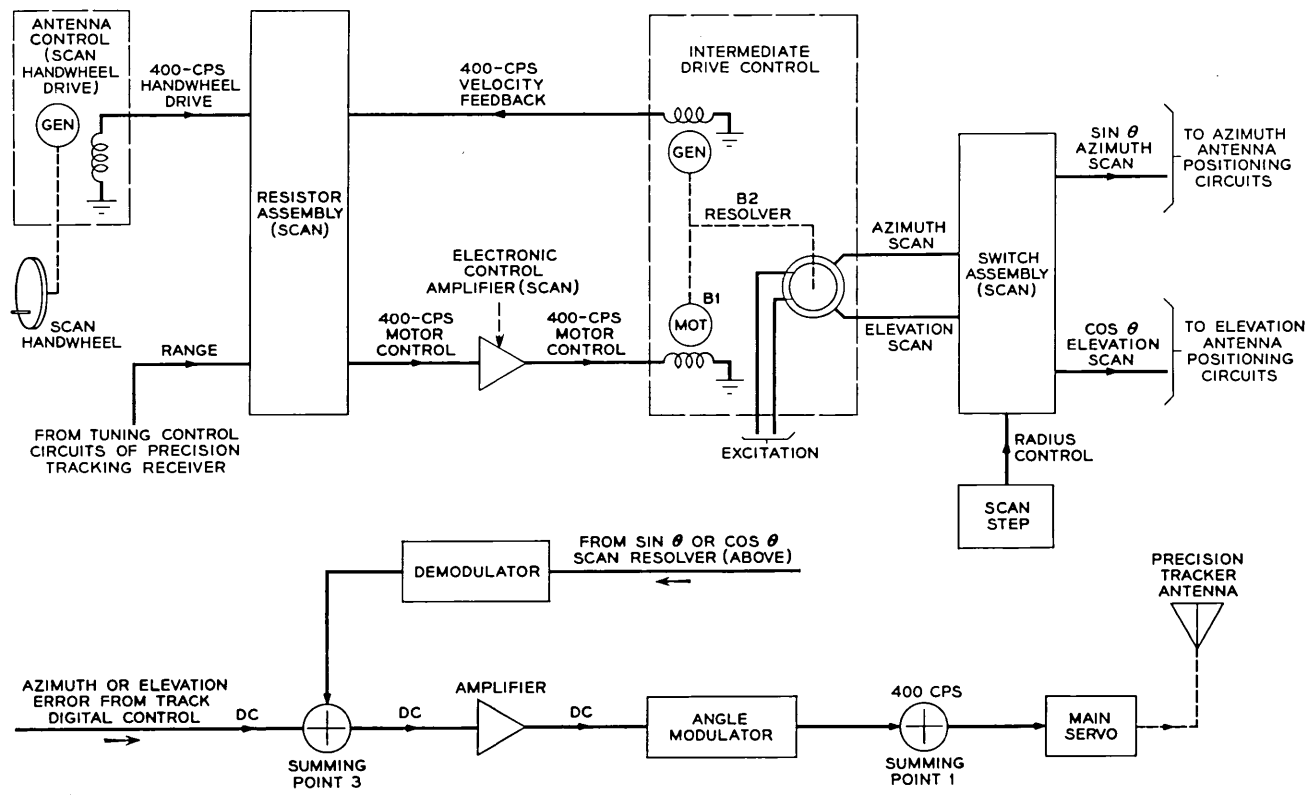
Fig. 16 — Scan control circuits.

has a high angular velocity, the antenna scans rapidly in order to search the area around the satellite. However, at longer ranges, when the angular velocity of the satellite is slower but the beacon signal strength is weaker, the antenna must search more slowly to ensure the same probability of detection.

When the track digital control mode is utilized, the orthogonal resolver rotor outputs are sent to a demodulator for conversion to a dc voltage. The automatic scan signal is then combined at summing point 3 with the track digital control error signal and converted to an ac signal in the angle modulator. This error signal is sent to the main servo drive circuit for use in positioning the antenna.

If the manual or command tracker mode has been selected, the resolver rotor output is sent directly to azimuth and elevation summing point 1.

5.8 *Data Take-Off*

The precise readout of PT azimuth and elevation angles is accomplished by 1-speed and 64-speed resolvers and analog-to-digital encoders contained in data transmitter gear boxes geared to the PT's precision data gears. These resolvers and encoders are essentially a remote extension of the track digital control and are described in another paper.[7]

VI. ACQUISITION RECEIVER

6.1 *General Description*

Owing to such factors as Doppler frequency shift and satellite oscillator drift, the frequency of the beacon signals from the Telstar spacecraft may deviate by as much as ± 150 kc about the 4079.73-mc design center frequency. The acquisition receiver (bays 1, 2, 3, 4, and 6 of Fig. 8) is employed to detect the actual received frequency and to provide an analog of this frequency for initial tuning of the phase-lock tracking receiver.

The requirement of tuning to the Doppler shifting received frequency within the period of time that the narrow antenna beam is crossing the satellite demands a rapid determination of received frequency. This is accomplished with a stationary search by use of a comb filter bank conducting a parallel observation of the frequency spectrum.

In the acquisition receiver, the sum IF signal is amplified, converted to 2.15 mc, and applied to a comb filter bank. This frequency-detection circuit consists of 300 channels housed in three cabinets, 100 in each
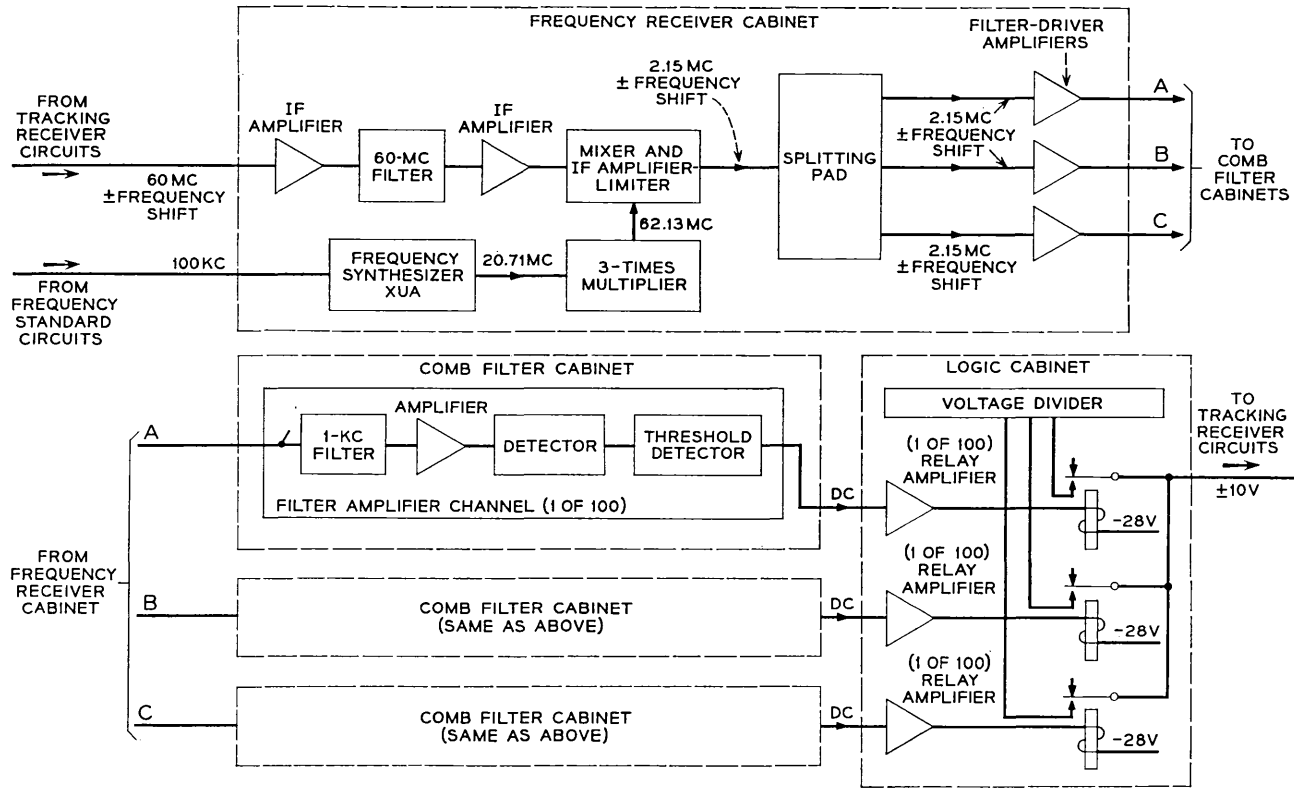
Fig. 17 — Acquisition receiver, block diagram.

cabinet. Each channel includes a narrow-band (1 kc at −1 db) crystal filter, an amplifier, a detector, a low-pass filter and a threshold circuit. All 300 detection channels are identical except that the crystal filters are cut to different center frequencies. (Filters are arranged to give a continuous coverage across the band.)

An incoming signal at the PT antenna that is within the range of 4079.73 mc ± 150 kc and is equal to or greater than noise in a 1-kc band will activate one of the comb filter channels. Overlap of the filter band-pass characteristics may cause two adjacent channels simultaneously to energize the associated threshold indicators. Normally, no more than two channels will pass a signal simultaneously. The operated channel will feed a signal to an associated relay amplifier located in the logic cabinet.

Logic circuitry determines which channel contains the received signal, disables all channels except this one and the two adjacent, and provides an analog output voltage proportional to signal frequency deviation. This voltage is supplied to the tuning control operational amplifier in the tracking receiver in order to bring a voltage-controlled crystal oscillator within the pull-in range of an automatic phase-lock loop. Once the phase-lock loop of the tracking receiver is locked, the logic input is disconnected and the frequency acquisition receiver performs no active function in the tracking. However, the acquisition circuitry is still active and can be utilized if tracking is lost. The output voltage from the acquisition receiver circuits also is sent, as an indication of received frequency, to the autotrack equipment.

6.2 *59.98-mc Amplification and Conversion*

Fig. 17 is a block diagram of the acquisition receiver. The acquisition receiver accepts 59.98-mc intermediate frequency signals and noise from the tracking receiver circuits. The two 59.98-mc IF amplifiers amplify the IF signal and noise from the sum IF amplifier in the tracking receiver circuit. The 59.98-mc narrow-band filter band limits noise to prevent overloading of the second IF amplifier.

The frequency synthesizer, synchronized to the 100-kc frequency standard, produces a signal of 20.71 mc. This signal is tripled by the 3× multiplier, which feeds a 62.13-mc signal to the mixer. The mixer produces a nominal frequency difference signal of 2.15 mc. Because of the Doppler shift in the beacon signal, the 2.15-mc signal will shift by a like amount. However, this shift will not exceed ±150 kc, which defines the limits of the comb filters.

TABLE VIII — ACQUISITION RECEIVER LEVELS

Unit	Gain (db)	Nominal Band-width (mc)	Minimum Signal Level (dbm)
Parametric amplifier	+18	20	−139
Mixer preamplifier	+25	8	−119
Cable	−5		−94
59.98-mc IF amplifier	+70	10	−99
59.98-mc filter with pads	−15	1	−29
59.98-mc IF amplifier	+45	10	−44
Mixer, amplifier, limiter	+50	600 kc	+1
Driver			3v rms
Comb filter			22v rms

6.3 *2.15-mc Amplification and Limiting*

The mixer output is amplified to a power level sufficient to "hard" limit the noise. In effect, the zero crossings are preserved but the peaks are clipped. The limiter output, consisting of signal plus noise, is fed to three filter driver amplifiers, which, in turn, drive the remainder of the acquisition receiver circuits.

The limiter is incorporated to establish a uniform noise threshold across the 300-kc filter bank, resulting in a constant false-alarm rate. This permits signal detection close to threshold in all channels, thus improving detection probability and simplifying logic design. After limiting, additional amplification is necessary to provide a suitable level of output to the filter driver amplifiers. A noise level set potentiometer sets the gain between the limiter and output to the comb filters. The bandwidth of each stage between the mixer and limiter is 1 mc with an over-all bandwidth of 600 kc at 3 db.

Further amplification is necessary to supply noise at the proper level for the comb filters. This is accomplished by the three filter driver amplifiers, each of which feeds the 100 filters contained in one cabinet.

6.4 *Comb Filter Channels*

Each filter-amplifier channel in the system contains a crystal filter, a two-stage amplifier, a detector, a post-detection filter, an amplifier, and a threshold circuit. The signal plus noise is filtered, amplified, and sent to the envelope detector. At this point the signal plus noise enters a 10-cps post-detection filter, after which it is amplified and compared with the threshold voltage. If its level exceeds that of the threshold voltage, the detected and amplified signal drives saturated solid-state amplifiers to provide a "signal present" dc output of −10 volts.

6.5 *Logic Circuits*

Each of the 300 comb filter channels terminates in the logic cabinet at a relay channel consisting of a transistor amplifier and relay. The relays, when operated, provide a contact closure which ties the precision voltage divider to the phase-lock loop in the track receivers of both the PT and the autotrack. In addition, the logic cabinet locks out all comb filter channels except the channel indicating a signal present and those adjacent to it. The logic circuits will follow a Doppler shifting signal and progressively lock out past adjacent channels and unlock new adjacent channels. A third feature provides a scan freeze indication to the servo scan circuits when a signal is present, in order to stop angular search.

Tests have indicated a reliable detection threshold better than −143 dbm, with a usable limit around −147 dbm, as observed during a moon bounce experiment between Holmdel and Andover.

VII. FREQUENCY STANDARD AND TEST SIGNAL

7.1 *General Description*

The frequency standard cabinet (bay 7, Fig. 8) contains circuits designed to provide stable frequencies to the precision tracker for use as local oscillator injection and testing signals. In addition, this cabinet generates the primary and secondary frequency and time references used throughout the satellite communications ground station. These references are used to adjust the station clock to the Naval Research Laboratory cesium standard at Bethesda, Maryland.

7.2 *Basic Standard*

The basic 100-kc frequency is generated in a standard master oscillator, which is in turn referenced to the VLF 18-kc Naval Station NBA. A VLF phase comparator (see Fig. 18) accepts the standard master oscillator 100-kc output and compares this frequency with an 18-kc signal received from NBA. The resultant phase difference is recorded on a strip-chart recorder. The VLF receiver also develops an audio 1-second time tick for use in the station clock. The standard master oscillator uses a highly accurate, comparator-controlled, quartz oscillator to generate a 1-mc signal. Other circuitry within the standard master oscillator utilizes the 1-mc signal in the generation of the standard 100-kc and 5-mc signals. These two signals are applied to the dis-
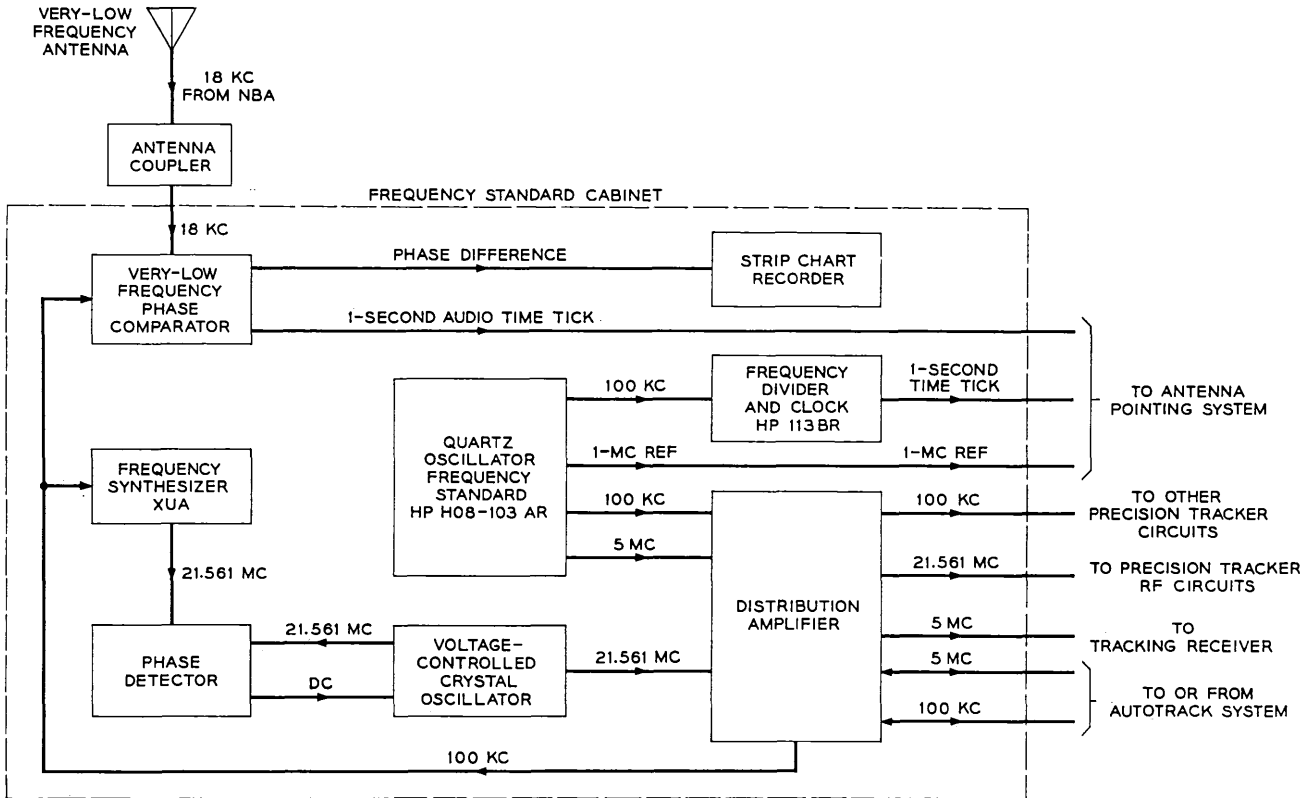
Fig. 18 — Frequency standard circuits, block diagram.

tribution amplifier, which provides amplification necessary to distribute the standard frequencies as needed throughout the PT. The 100-kc signal is also applied directly to the frequency divider and clock.

The frequency divider and clock utilizes the 100-kc signal from the standard master oscillator in the generation of a 1-second time tick. This signal is fed out of the precision tracker to the antenna pointing system along with the 1-second time tick from the VLF phase comparator for comparison purposes. An adjustment within the frequency divider and clock corrects any time deviations from NBA time. A time read-out located in the unit is also driven by the 100-kc input signal.

7.3 *Local Oscillator Signals*

A 21.561-mc signal from the frequency standard cabinet is sent to a harmonic generator, which multiplies this signal 192 times to give a 4139.71-mc local oscillator frequency for use in mixing the incoming beacon frequency (4079.73 mc), to give an IF frequency of 59.98 mc. Any variation in the initial 21.561-mc signal will be multiplied 192 times, directly affecting the stability of the track and frequency acquisition receivers. A phase-lock loop is used to minimize the variation; it consists of a frequency synthesizer, a phase detector, and a short-term, stable voltage-controlled crystal oscillator (VCXO). The frequency synthesizer derives a 21.561-mc signal from the basic standard master oscillator 100-kc output. This 21.561-mc signal is compared in the phase detector circuit with the 21.561-mc output of the VCXO.

The frequency multiplier which converts the 21.561-mc signal to 4139.71 mc is a solid-state harmonic generator consisting of two 2× multipliers, a power amplifier, a low-frequency 4× multiplier using a varactor diode in shunt configuration, a quadrupler using a self-biased diode operated in a series configuration, and a microwave tripler. The harmonic generator is designed for an input from a 50-ohm source of from 3 to 5 mw at 21.561 mc and delivers 15 mw at 4139.71 mc into a 50-ohm load.

The frequency receiver cabinet receives the 100-kc standard master oscillator signal for use in deriving the frequency acquisition receiver local oscillator injection signal. A frequency synthesizer receives the 100-kc signal and develops a 20.71-mc signal. The 20.71-mc signal is tripled to a frequency of 62.13 mc and then inserted in the local oscillator port of the frequency acquisition mixer.

Table IX shows the output levels and accuracy of each frequency discussed above.

TABLE IX — FREQUENCY GENERATION

Frequency (mc)	Cabinet	Level	Accuracy	Application
18 kc	Frequency standard	>0.1 μv	1:10^{11}	NBA reference
100 kc	Frequency standard	1v rms	5 10^{10}	Second LO injection frequency acquisition IF test
5	Frequency standard	1v rms	⎫	Coherent phase detection
20	Test signal	0–1v rms (0.4v nom)	Short term 1:10^{10} Long term 5:10^{10}	IF test
20.71	Frequency receiver	0–1v rms (0.4v nom)	⎭	Second LO injection for frequency acquisition
21.561	Frequency standard	50 mw in 50 ohms	Long term 5:10^{10} Short term 1:10^{7}	First LO injection for track receiver
60	Receiver	1–2.8v rms in 50 ohms	⎫ Long term 5:10^{10}	IF test
62.13	Frequency receiver	1–2.8v rms in 50 ohms	Short term 1:10^{10} ⎭	Second LO injection for frequency acquisition
4079.73	Test signal	0 dbm	±0.001%/day	RF test
4139.71	RF assembly	5 mv in 50 ohms	Long term 5:10^{10} Short term 1:10^{7}	First LO injection for track receiver
Time				
1-sec audio tick	Frequency standard	1v in 600 ohms 450 msec	Same as NBA	Coarse time for station clock
1-sec tick	Frequency standard	2v in 50 ohms 200 μsec	Same as NBA	Reference time for station clock

7.4 RF Test Signals

The test signal cabinet contains circuits designed to provide a 4079.73-mc frequency for use as a simulated satellite beacon signal. This signal is sent through a pressurized semirigid Heliax coaxial cable to a bore-sight tower test horn antenna located 300 feet from the PT track mount and 600 feet from the test signal cabinet. A TD2 harmonic generator is used to generate the microwave CW test signal. The generator may be turned on and off locally at the test signal cabinet or remotely at the PT control console. A directional coupler (see Fig. 19) provides a sampling take-off for a power meter. This measurement is made to validate receiver sensitivity checks made by use of the test tower.

A phase-coherent 20-mc test signal is also developed in the test signal cabinet (Fig. 20). A 100-kc input from the standard master oscillator is
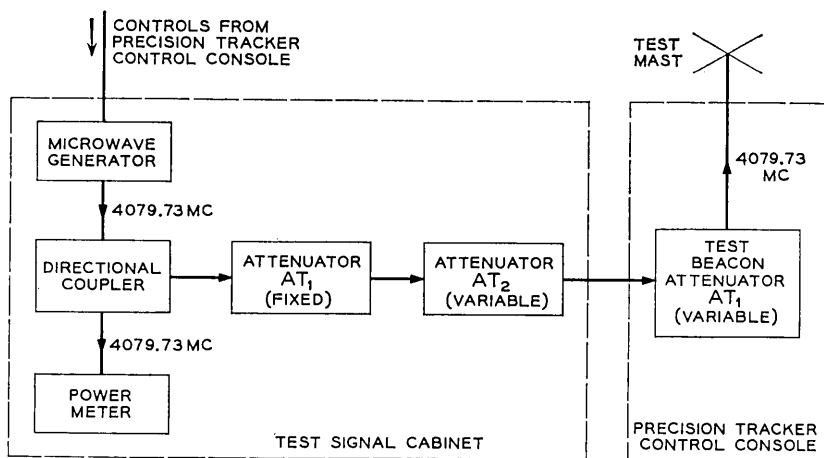
Fig. 19 — 4-kmc test signal circuits, block diagram.

multiplied to 20 mc in a frequency synthesizer. The 20-mc signal is fed to the track receiver cabinet and frequency tripled for use as a 60-mc IF test signal. A motor-driven chain drive is coupled to the frequency synthesizer to simulate Doppler shift for testing purposes.
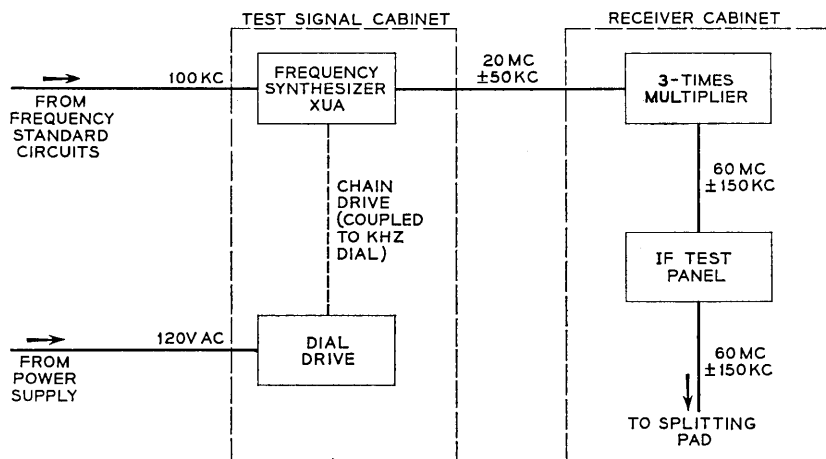
Fig. 20 — 60-mc IF test signal circuits, block diagram.

VIII. CONTROL CONSOLE

8.1 *Controls and Indicators*

Operating controls and indicators for the precision tracker are mounted on the PT control console (Fig. 21). Among the controls on the console are switches used to select mode of operation and input data source, handwheels used to point the antenna and scan the beam manually, and controls used to search in frequency. Indicators on the console include lamps showing PT and system status; meters showing azimuth error, elevation error, range, signal strength, and frequency deviation; and decimal readouts of station time and PT antenna angle data. In addition, an array of test function switching controls is located behind the upper right-hand door.

The various acquisition modes, discussed in Section V, are controlled at the console. The three operational groupings include elevation at the left, azimuth in the center, and frequency at the right. Experience has shown that only one operator, seated centrally before the azimuth position, is required. His duties are mainly to precondition the system before a pass and monitor the acquisition and tracking processes during the
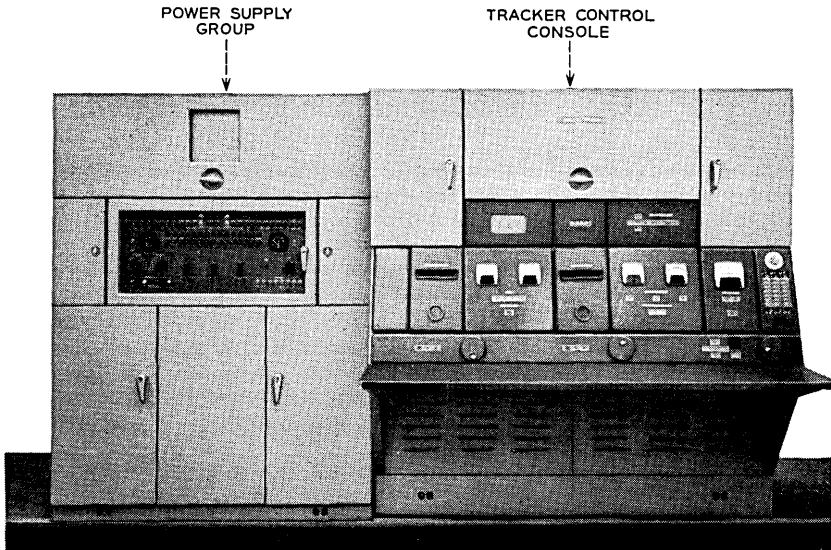
Fig. 21 — Console and power supply group.

pass. He can intervene to change modes or manually search in angle and frequency. The operator can read out Doppler shift, received signal strength, and tracking perturbations if requested by the tracking director.

8.2 Power System

The precision tracker uses both 120/208-volt, 400-cycle, 3-phase power and 120-volt, 60-cycle, single-phase power in its operation. The 400-cycle power is fed directly to the PT power control cabinet (Fig. 22) for operation of power supplies in the cabinet and for distribution to the antenna positioning circuits. "Technical" 60-cycle power is distributed from a wall panel to the acquisition and tracking receivers and to the frequency standard, VLF, and test circuits. "Utility" 60-cycle power is distributed from another wall panel to outlets in the PT equipment cabinets.

IX. ANTENNA ASSEMBLY AND TOWER

The physical specifications associated with the major structures of the precision tracker system are listed below.

(1) Antenna Assembly
    Weight   7000 pounds
    Height, jack pads to elevation axis   11 feet 9 inches
    Torques:
        Overturning, 60-mph wind   8700 ft-lbs
        Overturning, 120-mph wind   27,200 ft-lbs
        Rotational in horizontal plane   650 ft-lbs max.
(2) Antenna Tower (Fig. 22)
    Concrete with hexagonal cross section
    Height, base to elevation axis   35 feet 8 inches
    Twist at 650 ft-lbs torque   0.05 milliradian max.
    Sway   0.05 milliradian max.
    Settling:
        Per day   0.03 milliradian max.
        Limit   45 milliradians, total
(3) Test Tower
    Distance from antenna tower   300 feet
    Height   60 feet
    Twist in 40-mph wind   ±3 minutes max.
    Sway at top in 40-mph wind   ±0.06 inch max.
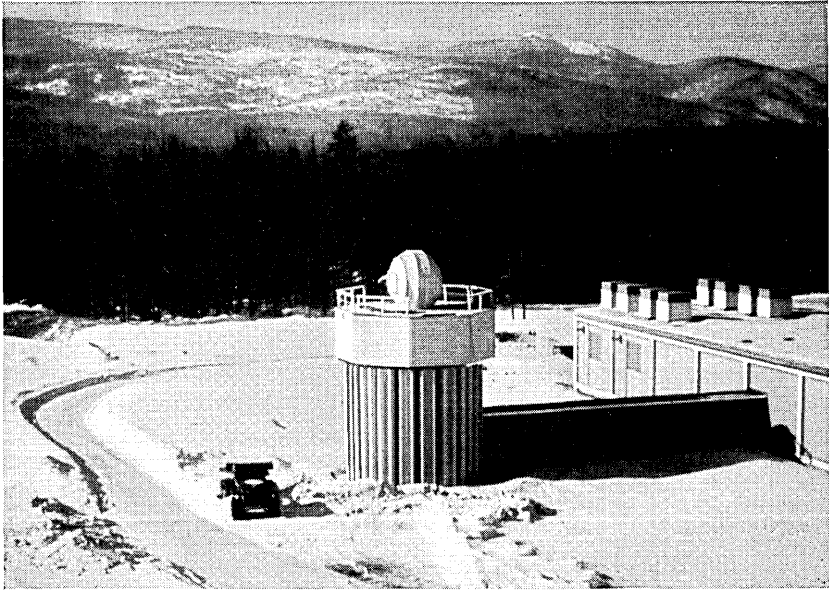
Fig. 22 — PT antenna tower at Andover, Maine, radome deflated.

X. TEST DATA AND OPERATING EXPERIENCE

10.1 *Operating Noise Temperature*

The input noise power from all sources including antenna, sky, and radome as measured by the CW signal substitution method is −138 dbm at an elevation of 0 degree. The measurement was made in the 3-kc bandwidth of the tracking receiver's sum channel to an accuracy of 0.9 db. The receiver noise figure, which was also measured, was found to be 3.1 db corresponding to a noise temperature of 315°K. The total effective noise temperature, for an elevation angle of 10 degrees, is estimated as follows:

Sky	13.5°K
Side lobes	2.5°K
Radome	9°K
Input temperature of receiver including comparator and fittings	315°K
Total at 10° elevation	340°K

The variation in system noise with elevation angle was also meas-

ured. This is shown in Fig. 7. The slight increase at the zenith is typical of a daytime measurement and is caused by coupling to the sun. Similar measurements made at night reveal the expected minimum at the zenith. −139 dbm is taken as a receiver signal power reference for a 0-db signal-to-noise ratio in the 3-kc bandwidth of the sum channel.

A careful measurement was made of the degradation in sensitivity with the parametric amplifiers bypassed. The increase in effective system input noise was measured as 7 db. This figure was obtained by relation of the signal-to-noise ratios obtained in each condition for the same fixed input signal level.

10.2 *Received Signal Levels*

Received signal levels for six typical passes of the Telstar spacecraft are plotted in Fig. 23. In this figure, signal level is plotted as a function of slant range, a technique adopted during the first days of tracking to enable on-the-spot checks of beacon transmitter and PT performance. The reference line is plotted as a 6-db per octave slope to account for variation in path loss with range; it assumes +17 dbm radiated beacon power and a truly isotropic antenna on the satellite. The 0-db SNR is based on the −139 dbm effective input noise power of the PT. The data were plotted point by point during each pass, taking slant range from the mission printout at the time of measurement; SNR was read from the calibrated signal strength meter on the PT console.

The measured SNR may generally be expected to fall below the reference slope. Variations in communications power from none to maximum may cause the beacon power to vary from the nominal +17 dbm to +15 dbm with full power in the communication channel. These variations appear on the measured SNR curves as the minor fluctuations departing from the generally smooth curve; they were correlated in time with the changing power levels indicated by the accompanying communication experiments during the first several passes.

The general trend of departure from the 6 db/octave slope is a function of the satellite's antenna pattern and the changing spin angle. Reference to the spin angle predictions and the antenna pattern showed a correlation within 1 db.

10.3 *Tracking Jitter*

The variation of angle tracking jitter with signal-to-noise ratio is shown in Fig. 24. The test consisted of tracking the RF test signal from the boresight tower. The data shown are for the azimuth coordi-

NOTE: REFERENCE LINE IS BASED ON +17-DBM BEACON SIGNAL, ISOTROPIC
       SATELLITE ANTENNA, AND PRECISION-TRACKER RECEIVER SENSITIVITY
       OF -139 DBM FOR 0-DB SIGNAL-TO-NOISE RATIO
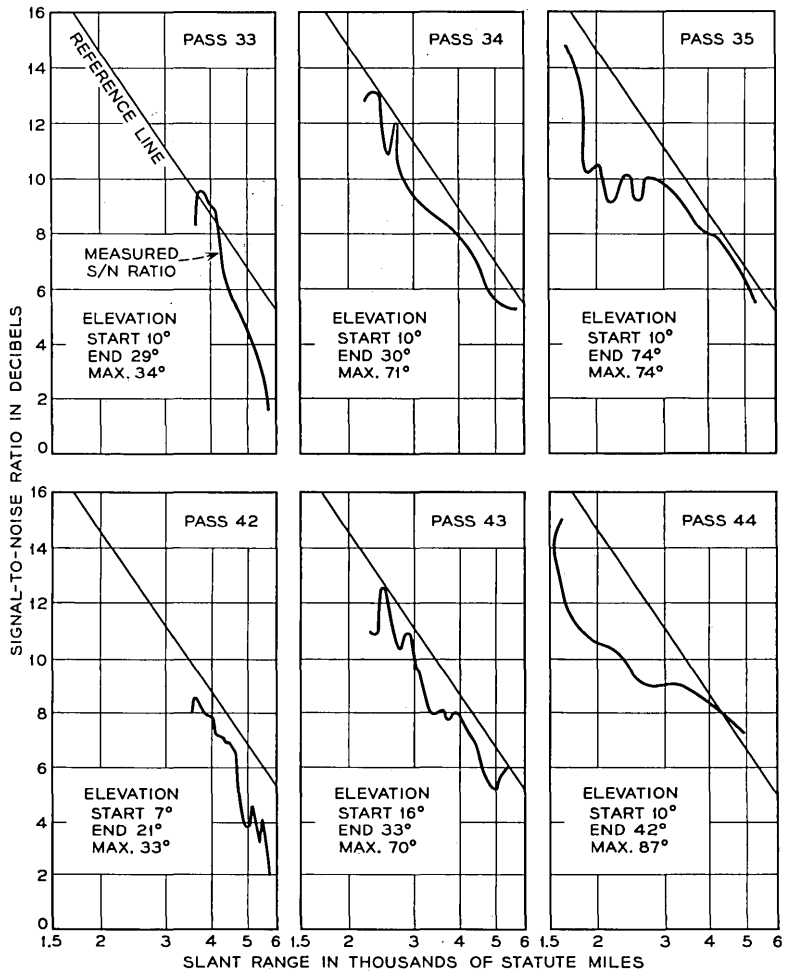
Fig. 23 — Received signal levels.

nate; the elevation data agreed more closely with the theoretical per-
formance.[8]

10.4 *Phase Jitter and Frequency Measurements*

The coherence time, or phase jitter, of the beacon signal is a critical
parameter in the performance of the PT and the autotrack. The phase-
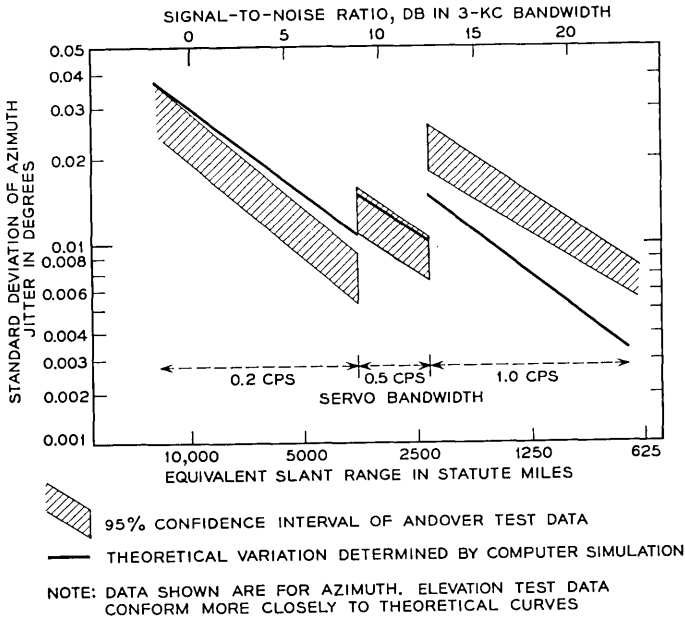
Fig. 24 — Angle tracking jitter.

lock loop of the PT tracking receiver has been employed to measure this parameter of different beacon sources, including models of the Relay and Telstar satellites and the Holmdel, N.J., 4079.73-mc transmitter employed to illuminate Echo I for tracking tests. In all cases, the jitter of the beacon signals made a negligible contribution to the total jitter in the phase-lock loop.

XI. ACKNOWLEDGMENTS

Credit for the successful completion of the precision tracker is due to many individuals and organizations. The staff of Wheeler Laboratories, Incorporated, designed and tested the Cassegrainian twist-reflector antenna and the microwave comparator/feedhorn assembly and provided valuable consultation throughout the program. Itek Corporation designed and produced the 300-channel comb filter. Mr. K. B. Woodard and members of his group were responsible for the mechanical design of the antenna, the RF assembly, and data units, and for testing the mechanical accuracy of the antenna assembly. Messrs. W. L. Nelson, R. W. Hatch, R. Lowell, L. H. Enloe, and R. H. Turrin made important

analysis and design contributions in the development of the phase-lock loop and coherent angle-error detectors.

REFERENCES

1. Davis, C. G., Hutchison, P. T., Witt, F. J., and Maunsell, H. I., The Spacecraft Communications Repeater, B.S.T.J., this issue, p. 831.
2. Githens, J. A., Kelly, H. P., Lozier, J. C., and Lundstrom, A. A., Antenna Pointing System: Organization and Performance, B.S.T.J., this issue, p. 1213.
3. Hannan, P. W., Optimum Feeds for All Three Modes of a Monopulse Antenna I and II, Trans., I.R.E., AP-9, 1961.
4. Rhodes, D. R., *Introduction to Monopulse*, McGraw-Hill, New York, 1959.
5. Reed, E. D., Diode Parametric Amplifiers — Principles and Experiments, Semiconductor Products, 4, Jan., 1961, pp. 25–30, and Feb., 1961, pp. 35–42.
6. Nelson, W. L., Analysis of the Angle-Error Detection System for Automatic Tracking of *Telstar* Satellites, to be published.
7. Githens, J. A., and Peters, T. R., Digital Equipment for the Antenna Pointing System, B.S.T.J., this issue, p. 1223.
8. Ball, W. H. W., Analysis and Digital Simulation of the *Telstar* Precision Tracker, Paper No. CP-63-368, presented at the IEEE Winter General Meeting, New York, 1963.

Orbit Determination and Prediction, and Computer Programs

By A. J. CLAUS, R. B. BLACKMAN, E. G. HALLINE and W. C. RIDGWAY, III

Orbit determination and prediction programs are needed to generate ephemerides for the satellite. Orbit determination is from tracking data consisting of angles only, and is based on a modified version of a method by R. E. Briggs and J. W. Slowey of the Smithsonian Institution. Trends in the data due to perturbations from a Keplerian orbit are removed before this process, and estimates of the orbital elements from individual passes are combined statistically to produce refined estimates. Ephemeris calculation is by a semi-analytic method in which deviations from a Keplerian orbit are obtained by integrating the perturbing forces. The programs to implement these procedures have been written for both the IBM 7090 and the IBM 1620 computers.

I. INTRODUCTION

The following paper describes the methods and programs used in the Telstar project for the purposes of orbit determination and ephemeris calculation. The orbit determination process involves the computation of orbital elements from tracking data obtained during each pass, and subsequent refinement by combining such single-pass estimates. The tracking data are in terms of angular observations only. The ephemeris calculations involve standard procedures for computation of Keplerian orbits and perturbations due to the earth's oblateness.

It is well known that in the problem of orbit determination from angular data only, three observations (each observation consisting of two angles and a time) are not sufficient to determine an orbit if the three sightlines are coplanar. If the three sightlines are nearly coplanar, the computed orbital elements may reflect large uncertainties which are not necessarily due to observational errors. Hence, the method used is based on the determination of a set of orbital elements from four observations.

This method is a modified form of the method described in Ref. 1. In the modified form, initial estimates of the orbital elements are computed from the first and last of the four observations, supplemented by estimates of the ranges corresponding to them (Section 2.1). By a method of successive approximations the two ranges are adjusted until an agreement with the second and third observations is secured in a least-squares sense (Section 2.2).

With typically many more than four observations in one pass through the visibility zone of an angular tracker, the observations are divided into four nonoverlapping blocks, each block containing the same number of observations, N. Taking one observation at a time from each block, in serial order, N sets of orbital elements are computed. These N sets are combined into a single set of intrapass average orbital elements and an associated covariance matrix (Section III).

Trends in the data due to perturbations induced by the earth's oblateness are removed by a method which is essentially the same as that described in Ref. 2 (Section IV).

Sets of intrapass average orbital elements, and their associated covariance matrices, from two or more passes, are combined into a set of interpass average orbital elements and an associated covariance matrix (Section V). The method used is similar to the method described in Refs. 3 and 4, inasmuch as it was motivated by the desire to avoid the necessity of pooling all of the observational data from two or more passes in order to derive refined estimates of the orbital elements, as would have to be done in the classical "differential corrections" method commonly ascribed to K. F. Gauss (1777–1855). However, the method used differs from the referenced method in two respects, viz., (a) the covariance matrix associated with each set of intrapass average orbital elements is related to the actual observational data for the pass, and (b) the necessity of computing the partial derivatives of all of the observed angles (numbering $8N$ in each pass) with respect to each of the orbital elements is avoided. On the other hand, this method gives single-pass estimates of the orbital elements which are biased even when the observational errors are not biased. These biases may be appreciable for short passes associated with low altitudes of the satellite near perigee. Methods for removing or reducing these biases have been under study but were not ready for use before the launching of the Telstar satellite on July 10, 1962.

This orbit determination method was designed to permit effective antenna pointing operations with the use of a modest computing facility. The program implementation (Section VI) consists of two major

program subsystems. The first of these is the orbit determination program (Section VIII), which determines the characteristics of the satellite orbit from tracking information. The second program (Section IX) computes orbit predictions from a knowledge of these orbit characteristics. The operational results obtained in using these methods and programs are discussed (Section X).

II. ORBIT DETERMINATION FROM ANGLE-ONLY DATA

2.1 *Orbit Determination from Two Observations and Estimated Ranges*

Two observations (each observation consisting of two angles and a time) and estimates of the ranges (i.e., topocentric distances) along the two sightlines are sufficient to establish two points P_1 and P_2 through which an orbit can be passed at the times of observation by only one set of orbital elements. Denoting the geocentric distances by r_1 and r_2, and the geocentric angular difference by θ_{12}, we have

$$r_1 = \frac{a(1 - l^2 - m^2)}{1 + l}, \tag{1}$$

$$r_2 = \frac{a(1 - l^2 - m^2)}{1 + l \cos \theta_{12} + m \sin \theta_{12}}, \tag{2}$$

where

$$\begin{aligned} l &= e \cos \omega, \\ m &= e \sin \omega, \end{aligned} \tag{3}$$

a is the semi-major axis, e is the eccentricity, and ω is the argument of perigee referred to the first sightline. From (1) and (2), we have

$$\alpha_1 l + \alpha_2 m = \alpha_3 \tag{4}$$

where

$$\alpha_1 = \cos \theta_{12} - \frac{r_1}{r_2},$$

$$\alpha_2 = \sin \theta_{12},$$

$$\alpha_3 = \frac{r_1 - r_2}{r_2}.$$

It is convenient to regard either l or m as an independent variable. Actually, in order to avoid an indeterminacy and to improve accuracy,

preference is given to l if $|\alpha_1| \leqq |\alpha_2|$, and to m if $|\alpha_1| > |\alpha_2|$. In either case, the other two of the three quantities l, m, and a are determined by (1) and (4). These, in turn, through Kepler's equation, determine a travel time between P_1 and P_2. A search is then made for the value of l which gives the observed travel time. For bounded orbits (the only ones of interest for ground-to-ground communications) the search is confined to the interval (l_-, l_+), where

$$l_\pm = \frac{1}{\alpha_1^2 + \alpha_2^2} (\alpha_1\alpha_3 \pm |\alpha_2| \sqrt{\alpha_1^2 + \alpha_2^2 - \alpha_3^2}).$$

With a, l, m (hence also e and ω) determined, the time of perigee passage, τ, is determined through Kepler's equation.

2.2 Orbit Determination from Four Observations

The two observations involved in the procedure described in the preceding section are the first and last of a set of four observations. Subsequent to that procedure, the four angles corresponding to the times of the second and third observations are computed and compared with the observed angles. The sum, Φ, of the squares of the differences between the computed and observed angles is regarded as a function of the estimated ranges D_1 and D_4 associated with the first and last of the four observations. The quantity Φ is next minimized with respect to D_1 and D_4 by a method which is analogous to the classical "differential corrections" method. (With only three observations corresponding to coplanar sightlines there would be only one angular difference, and therefore D_1 and D_3 would be indeterminate.) This method involves the solution of two simultaneous equations which are linear in the corrections to D_1 and D_4, with coefficients which are quadratic in the first-order partial derivatives of the computed angles with respect to D_1 and D_4. The terms which do not involve the corrections to D_1 and D_4 are products of the first-order partial derivatives and the angular differences. Since the partial derivatives are functions of D_1 and D_4, the minimization of Φ is an iterative procedure which is terminated when the values of a, e, ω, and τ are sufficiently stabilized. Detailed formulas are given in Ref. 5.

With a, e, ω, and τ determined, the orientation of the plane through P_1, P_2, and the center of the earth gives the values of Ω and i, where Ω is the longitude of the ascending node and i is the inclination of the orbital plane.

III. ORBIT DETERMINATION FROM $4N$ OBSERVATIONS IN ONE PASS

The combined procedures described in Sections 2.1 and 2.2 are applied to as many sets of four observations as may be drawn from all of the reliable observations for each pass in accordance with the method of selection indicated in the third paragraph of Section I. The N sets of orbital elements are then combined into a single set of intrapass average orbital elements. In addition, an associated covariance matrix (an estimate of the variability of the mean in a sample of size N drawn from a correlated multivariate population) is computed in accordance with the standard formulas

$$\tilde{C}_{\overline{\alpha\alpha}} = \frac{\sum_{i=1}^{N} (\alpha_i - \bar{\alpha})^2}{N(N-1)}, \qquad \tilde{C}_{\overline{\alpha\beta}} = \frac{\sum_{i=1}^{N} (\alpha_i - \bar{\alpha})(\beta_i - \bar{\beta})}{N(N-1)},$$

where α stands for each of the six orbital elements (with average $\bar{\alpha}$), and β for each of the other five (with average $\bar{\beta}$).

A typical result of the single-pass routine, as described up to this point, is shown in Tables I and II. The orbital elements listed as "exact value" were used to generate tracking angles. These angles, combined with random errors from a normal population with a standard deviation of 0.2 milliradian, were processed. It may be noted that were it not for the strong correlation between some of the orbital elements, errors in

TABLE I

	Ω, degrees	i, degrees	a, feet	e	ω, degrees	τ, seconds
Exact value	144.4462	46.9190	31,567,194	0.240764	171.6756	47,953.227
Sample mean	144.4455	46.9184	31,573,342	0.240688	171.6349	47,950.120
Standard deviation of sample mean	0.0018	0.0018	6,212	0.000120	0.0374	2.852

TABLE II — CORRELATION COEFFICIENTS

	Ω	i	a	e	ω	τ
Ω	1	0.13189	0.64082	−0.57898	−0.67162	−0.64998
i	0.13189	1	−0.49292	0.52030	0.44004	0.47260
a	0.64082	−0.49292	1	−0.96559	−0.99058	−0.99680
e	−0.57898	0.52030	−0.96559	1	0.92798	0.94376
ω	−0.67162	0.44004	−0.99058	0.92798	1	0.99797
τ	−0.64998	0.47260	−0.99680	0.94376	0.99797	1

the elements of the order of the standard deviations shown could result in pointing angles for the same pass with errors as large as 10 times the standard deviation of the original tracking errors.

A caveat should also be noted with respect to the precision of computation of the covariance matrix. Any matrix which purports to be a covariance matrix must have a nonnegative determinant. Due to the high correlation among the elements a, e, ω, and τ, however, values of 10^{-8} for the determinant of the correlation matrix are common. Errors of the order of 0.1 per cent in some covariances could result in a matrix with a negative determinant. Such a matrix can still serve as a guide in judging the reliability of the orbital elements obtained, but the use of this matrix for interpass orbit refinement would very likely lead to absurd results, such as negative variances.

IV. TREND REMOVAL

Since the procedures described in Sections 2.1 and 2.2 are based on the assumption that the orbit is Keplerian, it is important to determine the extent to which it is necessary and sufficient to correct for deviations from that assumption. Such deviations, usually called perturbations, are induced by the asphericity of the earth, drag, radiation pressure, etc. Preliminary computations, confirmed by tests with artificial data, indicated that for the orbit and satellite under consideration here it would be necessary and sufficient to correct only for the earth's oblateness. The corrections are made to the observational data. Detailed formulas for the corrections are given in Ref. 5. These formulas involve the orbital elements which, however, do not need to be known to high accuracy for the purposes of trend removal. If sufficiently accurate values of the orbital elements are not available for trend removal, they may be obtained by including trend removal in the iterative routine of Sections 2.1 and 2.2 after the first values of the orbital elements have been obtained without trend removal.

Table III shows the importance of trend removal for the effects of oblateness. The same input data, which included the effects of oblateness, were used in both runs. The errors in the second run (without trend removal) are not acceptable. In particular, the error in the semi-major axis could lead to an error in predicted pointing angles of as much as 1.5° after only one period.

Table IV shows the speed of convergence, with trend removal, in the absence of initial estimates of the orbital elements. After only one iteration (one-half minute additional computing time for 200 observa-

TABLE III

	Ω, degrees	i, degrees	a, feet	e	ω, degrees	τ, seconds
Exact osculating elements at the center of the pass	144.4439	46.9170	31,566,742	0.240879	171.6124	47,950.421
Results of run no. 1 (with trend removal)	144.4439	46.9169	31,566,884	0.240875	171.6118	47,950.365
Results of run no. 2 (without trend removal)	144.4372	46.9152	31,542,821	0.241313	171.7500	47,961.173

TABLE IV

	Ω, degrees	i, degrees	a, feet	e	ω, degrees	τ, seconds
Exact osculating elements at the center of the pass	144.4439	46.9170	31,566,742	0.240879	171.6124	47,950.421
Results of run no. 1	144.4377	46.9149	31,543,423	0.241311	171.7487	47,960.978
Results of run no. 2	144.4439	46.9169	31,566,909	0.240874	171.6117	47,950.352
Results of run no. 3	144.4439	46.9169	31,566,886	0.240875	171.6118	47,950.362

tions, on an IBM-7090 computer), acceptable orbital elements were obtained.

V. COMBINATION OF SINGLE-PASS ORBITAL ELEMENTS

The method of combining single-pass estimates of the orbital elements is based on a matrix formula derived briefly as follows. Let $\bar{x}$ be a vector (i.e. a one-column matrix) estimate of the vector z, with ave $\{\bar{x} - z\} = 0$ and cov $\{\bar{x} - z\} = A$, where A is a covariance matrix. Similarly, let $\bar{y}$ be another estimate of z, with ave $\{\bar{y} - z\} = 0$ and cov $\{\bar{y} - z\} = B$. If $\bar{x}$ and $\bar{y}$ obey independent multivariate normal probability distributions, the "maximum likelihood" estimate of z is the $\bar{z}$ which minimizes the quadratic form

$$\bar{Q} = (\bar{z} - \bar{x})' \cdot A^{-1} \cdot (\bar{z} - \bar{x}) + (\bar{z} - \bar{y})' \cdot B^{-1} \cdot (\bar{z} - \bar{y})$$

where the primes denote transposition. Thus,

$$A^{-1} \cdot (\bar{z} - \bar{x}) + B^{-1} \cdot (\bar{z} - \bar{y}) = 0,$$

whence,

$$\bar{z} = (A^{-1} + B^{-1})^{-1} \cdot (A^{-1}\bar{x} + B^{-1}\bar{y}) \tag{5}$$

with covariance matrix

$$C = (A^{-1} + B^{-1})^{-1}. \tag{6}$$

In fact, it may be easily verified that

$$\bar{Q} = [\bar{z} - C \cdot (A^{-1}\bar{x} + B^{-1}\bar{y})]' \cdot C^{-1} \cdot [\bar{z} - C \cdot (A^{-1}\bar{x} + B^{-1}\bar{y})]$$

$$+ \text{ terms independent of } \bar{z}.$$

A somewhat longer derivation without the normality assumption, in which the main diagonal (variance) elements of C are minimized, leads to the same results.

Formulas (5) and (6) require three matrix inversions which result in an intolerable loss of accuracy in cases of highly correlated estimates of the orbital elements. This difficulty is relieved to a very large extent by using the equivalent formulas

$$\bar{z} = w_1\bar{x} + w_2\bar{y} - (w_1P - w_2Q)(P + Q)^{-1}(\bar{x} - \bar{y}), \tag{7}$$

$$C = \tfrac{1}{2}[w_1A + w_2B - (w_1P - w_2Q)(P + Q)^{-1}(A - B)] \tag{8}$$

where $P = AG$, $Q = BG$, G is an arbitrary six-by-six matrix, and w_1, w_2 are any two six by six matrices whose sum is a unity matrix (see Appendix A). Formulas (7) and (8) require only one matrix inversion. The matrix G can be constructed so that the matrix $(P + Q)$ is well suited for inversion.

As a matter of additional necessity, formulas (7) and (8) were further transformed by the introduction of matrices U, V, defined by $U = SAS$, $V = SBS$, where S is a diagonal matrix whose elements are

$$S_{ii} = (A_{ii} + B_{ii})^{-\frac{1}{2}},$$

so that the diagonal elements of the matrix $(U + V)$ are unity. Restricting w_1, w_2 to diagonal matrices, then,

$$\bar{z} = w_1\bar{x} + w_2\bar{y} - R(\bar{x} - \bar{y}), \tag{9}$$

$$C = \tfrac{1}{2}[w_1A + w_2B - R(A - B)], \tag{10}$$

where

$$R = S^{-1}(w_1\hat{P} - w_2\hat{Q})(\hat{P} + \hat{Q})^{-1}S, \tag{11}$$

$\hat{P} = UH$, $\hat{Q} = VH$, and $H = S^{-1}G$. The formal construction of the arbitrary matrix H is not necessary. The matrices $\hat{P}$, $\hat{Q}$, and $\hat{P} + \hat{Q}$ are obtained by linear combinations of rows and/or of columns of the matrices U, V, and $U + V$ according to rules which are easily programmed for a digital computer.

Two details must be noted in the use of these formulas for combining

sets of orbital elements. The first detail is that the orbital elements are actually "osculatory" orbital elements which vary with time; therefore, each set is necessarily referred to a specific "epoch." Hence, before combining two sets, the set referred to the earlier epoch must be "updated" to the later epoch. In updating a set of orbital elements, it must also be noted that the "time of perigee passage" is actually the "time of mth perigee passage," where m is a specific number, usually different from the one for the set referred to the later epoch. The second detail to be noted is that the covariance matrix for the set referred to the earlier epoch must also be updated.

If $\tilde{C}_1$ is the covariance matrix to be updated, the updated covariance matrix is given by the formula

$$C_1 = J\tilde{C}_1 J',$$

where J is the Jacobian of the updated orbital elements with respect to the orbital elements from which they were predicted. Even in the hypothetical case of Keplerian orbits, in which all of the orbital elements, with the possible exception of τ, are constants, the Jacobian may differ from a unity matrix. For example, if the updating is through m times the period $2\pi\sqrt{\tilde{a}_1^3/k}$, so that

$$\tau_1 = \tilde{\tau}_1 + 2\pi m\sqrt{\tilde{a}_1^3/k},$$

then,

$$\partial\tau_1/\partial\tilde{a}_1 = 3\pi m\sqrt{\tilde{a}_1/k}.$$

The results of a test problem of this hypothetical sort are shown in Table V, in which the updating was through one period. The standard deviation of the improved estimate of the semi-major axis is approximately $\frac{1}{150}$ times the average of the corresponding standard deviations for the two runs. The improved estimate is in error by only 52 feet.

Table VI shows the results of a more realistic test problem in which the input data included perturbations due to the earth's oblateness. With "no updating" of the orbital elements and the covariance matrix from the earlier pass, except only to the extent required in the hypothetical case of Keplerian orbits, the "improved" semi-major axis is in error by 5094 feet, which is inconsistent with the standard deviation of only 73 feet. However, with updating of the orbital elements, taking account of the effects of the earth's oblateness, the error is only 72 feet.

VI. PROGRAM DESCRIPTION

The computer program system required to track a satellite and generate steering information for the communications antenna is divided into

TABLE V

		Ω, degrees	i, degrees	a, feet	e	ω, degrees	τ, seconds
Exact Values		144.5662	47.5190	32,107,194	0.253364	175.2756	49,218.920 or 58,853.603
Pass No. 1	Single-pass estimates	144.5638	47.5181	32,102,870	0.253387	175.3081	49,221.250
	Standard deviations	0.0017	0.0014	5,884	0.000124	0.0318	2.609
Pass No. 2	Single-pass estimates	144.5688	47.5196	32,116,970	0.253228	175.2114	58,848.774
	Standard deviations	0.0017	0.0006	8,683	0.000100	0.0543	4.325
Combination of passes No. 1 and No. 2	Combined estimates	144.5667	47.5193	32,107,246	0.253340	175.2741	58,853.608
	Standard deviations	0.0010	0.0005	46	0.000023	0.0026	0.128

TABLE VI

		Ω, degrees	i, degrees	a, feet	e	ω, degrees	τ, seconds
Exact values at $t = 54,046$ sec.		144.4439	46.9170	31,566,742	0.240879	171.6124	47,950.422
Exact values at $t = 64,081$ sec.		144.2383	46.9111	31,562,512	0.241047	171.8311	57,341.533
Pass No. 1 (center of the pass $\approx$ 54,046 sec.)	Single-pass estimates ($t = 54,046$ sec.)	144.4461	46.9183	31,562,047	0.241027	171.6318	47,952.202
	Standard deviations	0.0038	0.0024	11,077	0.000227	0.0638	4.936
Pass No. 2 (center of the pass $\approx$ 64,081 sec.)	Single-pass estimates ($t = 64,081$ sec.)	144.2410	46.9111	31,557,704	0.241211	171.8561	57,343.464
	Standard deviations	0.0025	0.0014	13,931	0.000176	0.0932	6.946
Combination of the passes No. 1 and No. 2; no updating	Combined estimates	144.3523	46.9400	31,557,418	0.240653	171.7592	57,344.864
	Standard deviations	0.0018	0.0010	73	0.000030	0.0044	0.186
Combination of the passes No. 1 and No. 2; updating included	Combined estimates ($t = 64,081$ sec.)	144.2412	46.9110	31,562,440	0.241105	171.8262	57,341.304
	Standard deviations	0.0018	0.0010	73	0.000030	0.0044	0.186

two major subsystems. The first of these is the orbit determination program, TELETRACK, which determines the characteristics of the satellite orbit from tracking information. The second major program, TELEPATH, computes orbit predictions from a knowledge of these orbital characteristics.

The division of the program system into these two parts is not only natural, but is also dictated by systems considerations. One of the requirements on the system was to minimize the amount of data transmissions. Ephemeris data to steer the communications antenna can be generated from the six orbital elements, and a division of the program system into two components linked together only by these six numbers achieves this requirement if each ground station is provided with suitable computational facilities. Stations having communications antennas require the program TELEPATH and updated sets of the orbital parameters. Stations having tracking antennas process the tracking data with TELETRACK and broadcast the updated elements to other stations as they become available.

The IBM 1620 computer was chosen to provide on-site computations. The IBM 7090 computer was used, however, for the initial development of the program systems. This was done for two reasons. First of all it was desirable to take advantage of the more powerful facilities and speed of the larger computer to facilitate the development and testing of the methods employed in the program system. Secondly, it was desirable to have the complete program system available at the Whippany, N. J., location of Bell Telephone Laboratories as a back-up to the on-site computer centers. Experience has shown that it is absolutely essential to have these duplicate programs available for testing and checking of the on-site operations.

By the nature of the 7090 and 1620 computers, different operating philosophies are required for each. The speed of the 7090 and turn-around times inherent in a large computation center are such that the programs must be as automatic as possible. However, they must also be flexible enough to allow selected programs from the system to be performed when necessary. Towards this end the following system evolved. The entire set of 7090 programs can be run consecutively as a single automatic chain job. Each program communicates to the following program through a magnetic tape, but as far as the computation center is concerned each program is a separate job. As a consequence, each program can also be run independently (with input provided by cards) since it is an entity in itself. The hidden gain in this system is the fact that there is only the one flexible version of each program, thus eliminating confusion and mistakes.

For the 1620, which is devoted entirely to this problem, and which is a slower machine, such completely automatic operation is not necessary. The system can be run automatically, but is usually run with more direct operator intervention. This allows greater flexibility and the ability to monitor intermediate results. On the 1620 the two major program systems are broken down conveniently into several program components. Each of these programs runs independently of the others, receiving input data generated by one of them and preparing output data for another. Operation of the program systems is achieved by loading and running one of the program components at a time. The various program components are stored on magnetic tape, and each program in the system loads the next program into the computer from this tape. Transfer of data between the programs is accomplished by punched cards, magnetic tapes and common memory storage. The method of data transfer in a particular instance depends upon the nature and quantity of the data.

Numerous error conditions were anticipated while the programs were being written. Many of these are handled automatically by the programs themselves. Some must be taken care of by manual intervention.

VII. INERTIAL COORDINATES AND ORBITAL ELEMENTS

All orbital calculations must, of course, be referenced to an inertial (or near inertial) coordinate system. The basic system used in these programs is the usual earth-centered, right-handed rectangular system. The X-Y plane coincides with the earth's equatorial plane, the X-axis is parallel with the line of equinoxes, and the Z-axis passes through the North pole. The orientation of the earth in this system at the time of an observation is obtained from UT_2 at time of observation and the Greenwich Mean Sidereal Time at 0 hours UT of date. Conversion from Mean Sidereal Time to Apparent Sidereal Time is made using the Equation of Equinoxes at 0 hours UT of date; interpolation of this number to the time of observation was deemed unnecessary.

The satellite orbit is described by means of the osculating orbital elements, consisting of
  (a) semi-major axis
  (b) eccentricity
  (c) right ascension of ascending mode
  (d) inclination angle
  (e) argument of perigee, and
  (f) time of perigee passage.

These elements specify the ellipse osculatory to the satellite orbit at some instant in time. These six numbers are therefore accompanied by an epoch specifying the time of osculation. The time of perigee passage specifies the perigee passage immediately preceding the epoch and is stated in seconds relative to the epoch.

The following paragraphs describe in some detail the two program systems, TELETRACK and TELEPATH.

VIII. TELETRACK PROGRAM SYSTEM

The TELETRACK program system processes tracking data in terms of azimuth and elevation to produce estimates of the six orbital elements describing the satellite orbit. It processes tracking data from one pass over the tracking station at a time to produce a "single-pass estimate." Single-pass estimates are combined to provide "combined estimates." The combining of several single-pass estimates provides a statistical averaging of the several independent estimates and a refinement based on the separation in time of the various independent estimates.

A flow chart of TELETRACK is shown in Fig. 1. Each of the major program components and the modes of data transfer between them are shown. A few of the program switches which control the mode of operation of the system are also shown.

8.1 *TELED*

TELED is the input/edit section of TELETRACK. Inputs to this program are

(a) tracking data consisting of time, azimuth and elevation for one pass, and

(b) data cards containing date and number of pass, identification of the tracking station and satellite, meteorological conditions during the pass, GMST at 0^h of date, estimates of the orbital elements, number of data sets to be selected (N), and values of the mode control switches for TELETRACK.

TELED reads the tracking data from tape and performs format and units conversion. Data points for which the precision tracker was not in autotrack or for which the signal-to-noise ratio level was not above a predetermined level (usually 4 or 5 db) are rejected. Furthermore, data points for which the elevation is below 7.5° or above 82.5° are rejected. The specified number ($4N$) of data points is selected from the group satisfying these criteria. The set of data so selected is distributed as uniformly as possible over the available set.
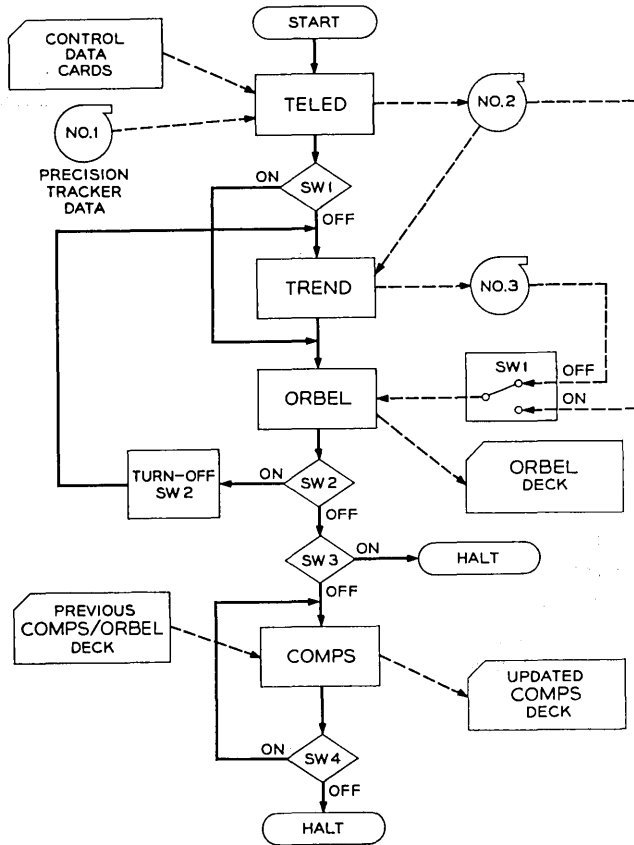
Fig. 1 — TELETRACK flow chart.

Boresight and refraction corrections are then applied to the selected data points. Following this, coordinate conversions are performed to transform the data from the topocentric azimuth-elevation system to the inertial coordinate system. Deviations of the vertical from the normal to the geodetic spheroid are accounted for in this process. Since range data are not available, the results of the coordinate conversion are in terms of the direction cosines relative to the inertial system of the observed sight lines. Also computed are the coordinates in inertial space of the tracker at the time of each observation.

Outputs from TELED are stored on magnetic tape for subsequent

programs. The primary output consists of $4N$ data points. Each data point contains time of observation, the three direction cosines of the observed sight line, sine and cosine of the right ascension of the tracker at the time of the observation, and the inertial coordinates of the tracker at the time of the observation. Various other data are also stored on this tape for subsequent programs.

8.2 *TREND*

The direction cosines produced by TELED are adjusted by TREND to produce the set which would have been obtained had the satellite been moving in an unperturbed, elliptical orbit throughout the pass. These adjustments are described in detail in Section IV above. The time of osculation (t_c) between the perturbed and unperturbed orbits was selected by TELED to correspond to the center of the pass and is passed on to TREND via tape.

As noted above, an estimate of the orbital elements at time t_c is needed. These are obtained by updating to time t_c the elements supplied on the input cards to TELED. Program ORBFIX is used for this purpose, details of which are given below.

The output from TREND consists primarily of the adjusted direction cosines for each observation. These are stored on a tape which is identical in format with the TELED output tape. By making these formats identical it is possible under one of the modes of operation to bypass TREND if estimates of the orbital parameters are not available.

8.3 *ORBFIX*

As mentioned above, ORBFIX updates a set of osculating orbital elements valid at one epoch to another epoch. The program essentially makes use of the subroutine OBLATE with only minor additional bookkeeping operations. The subroutine OBLATE is a numerical integration routine in true anomaly which integrates in steps of 0.08 radian the first-order oblateness perturbation equations to provide the desired corrections. The equations also include sufficient second-order terms to allow taking steps of 2π, so that in actual use steps of 2π are taken until a value π or closer to the desired point is reached. The program then integrates either forward or backward in small steps to reach the desired point exactly. It is also possible to go only in 2π steps in cases where only limited accuracy is required. This results in a large time saving.

8.4 *ORBEL*

Calculation of the orbital parameters is performed by the program ORBEL. The input data normally consist of the adjusted direction cosines from TREND. In the absence of initial estimates of the orbital elements, however, ORBEL can process the unadjusted data from TELED. The $4N$ observations are divided into four nonoverlapping groups. A set of four observations is obtained by selecting one observation from each group. N independent estimates of the orbital elements are calculated from the resultant N sets of observations. Averages, variances and covariances of the six elements for one pass are calculated from these. Details on the methods are given in Sections II and III.

The estimates of the ranges required in producing the first set of elements are normally produced by TREND during the trend removal procedure. In the absence of trend removal these estimates must be supplied on the input data cards to TELED. Subsequent estimates of range are derived by ORBEL itself from its previous estimates of the elements.

The output from ORBEL consists of a set of cards (an "ORBEL deck") containing the single-pass estimates of the orbital elements, the standard deviations of those elements, and the correlation coefficient matrix. Pass number and the corresponding epoch are also stored on these cards. These cards are filed away for possible future use.

The information on these cards is also retained in memory for use by the combination of passes program, COMPS.

8.5 *COMPS*

Combination of the estimates from the various passes is accomplished by the program COMPS. The method employed is described in Section V above. The inputs consist of two sets of orbital elements, standard deviations and correlation coefficient matrices. The first set, obtained from input cards, is either from a single ORBEL run or from an earlier COMPS run. The second set is from the current ORBEL run and is usually supplied directly by ORBEL through common memory storage. Under some modes of operation, however, the second set is supplied by cards.

The output from COMPS is a set of cards (the "COMPS deck") identical in content and format with the ORBEL deck. These cards are filed to maintain a permanent record of the combined orbital elements. The output data also replace the data from the first input set in memory in case certain operating modes are selected.

8.6 *Modes of Operation*

Several mode-control switches are provided to permit selection of one of a number of possible operating modes. The more significant of these switches are shown in Fig. 1. Each switch is identified by a number and consists of a one-bit variable which is read from an input data card and stored in memory.

In the normal mode of operation it is assumed that some estimate of the orbital elements is available for trend removal and that a combination of the ORBEL output with an earlier COMPS output is wanted. All switches are set in the "off" condition and the sequence of operations is TELED, TREND, ORBEL and COMPS in that order. The first set of inputs to COMPS is determined by the operator, who selects the proper COMPS deck, and the second set is supplied directly by ORBEL.

An alternative mode of operation is to stop the program after the single-pass estimate is produced by ORBEL and then combine a number of such estimates in a "batch combination" at a later time. This is accomplished by turning switches 3 and 4 on and accumulating a number of ORBEL decks. These decks are fed to COMPS in order by time, with the earliest deck first. COMPS reads the first two decks and combines them, producing a combined estimate valid at the time of the second set. This in turn is combined with the third set to produce a combination of the first three decks valid at the time of the third. This process continues until all decks have been combined into a single estimate valid at the time of the last set.

Another mode of operation is available in case estimates of the orbital elements are poor or unavailable. By turning switch 1 on, trend removal is skipped initially, and ORBEL is given unadjusted data with which to estimate the elements. If switch 2 is also on, ORBEL will call on TREND after computing this initial estimate of the orbital elements. This estimate is passed on to TREND for use in adjusting the data. Switch 2 is turned off, the data are adjusted, and then ORBEL is called upon a second time, this time to process data with trend due to perturbations removed.

IX. TELEPATH PROGRAM SYSTEM

The ephemeris generation for the Telstar satellite is carried out by a trio of programs collectively known as the TELEPATH program. The three individual programs are called MUVIS, COKE, and ACEXP, and are complete entities in themselves, solving distinctly separate

portions of the problem. The MUVIS program is solely concerned with finding times of future visibility or mutual visibility and updating the orbital elements to these time periods. Its output is a listing of future passes which is in itself useful, and a set of cards which serves as input to the COKE program. The COKE program generates a theoretical ephemeris for each pass as determined by the input cards, and outputs it on tape. The COKE program can also be used by itself to re-create any pass for which orbital elements are available. Both programs exist in almost identical form both for the IBM 7090 and the IBM 1620. The only differences in the programs are due to storage limitations in the 1620. This results in some extra tape manipulations in the 1620 programs which are unnecessary on the 7090. The final program, ACEXP, exists only on the 1620 and is used for adding predistortion and refraction corrections to the theoretical ephemeris.

Fig. 2 shows the flow chart of the 1620 program with its various operating options. A more detailed description of the program follows, without reference to machine.

9.1 *MUVIS*

This program takes a set of osculating orbital elements at an epoch and using them predicts when the satellite will be visible at a designated site, and when it will be mutually visible with a second designated site. The emphasis in this program is speed with only a limited amount of accuracy. It is envisaged that this program will be used for planning and general information, and thus the methods used were chosen with this in mind.

Basically, the program steps time by some increment, predicts the satellite's position in inertial coordinates for the new time, checks for visibility and mutual visibility, and continues. There is naturally a fair amount of bookkeeping associated with executing these steps, but they are essentially the heart of the program.

Since the program consists of many iterations through the basic loop outlined above, it was felt worthwhile to streamline it as much as was possible. Towards this end the following steps were taken.

(*i*) The program takes variable time steps. A coarse step is used until visibility is determined, and at this point a finer step is used for a more refined estimate. This feature is carried one step further by permitting a time step of close to a full period after visibility ends, or when the satellite appears to be moving away from visibility.

(*ii*) When the satellite's position is calculated at some time, osculat-
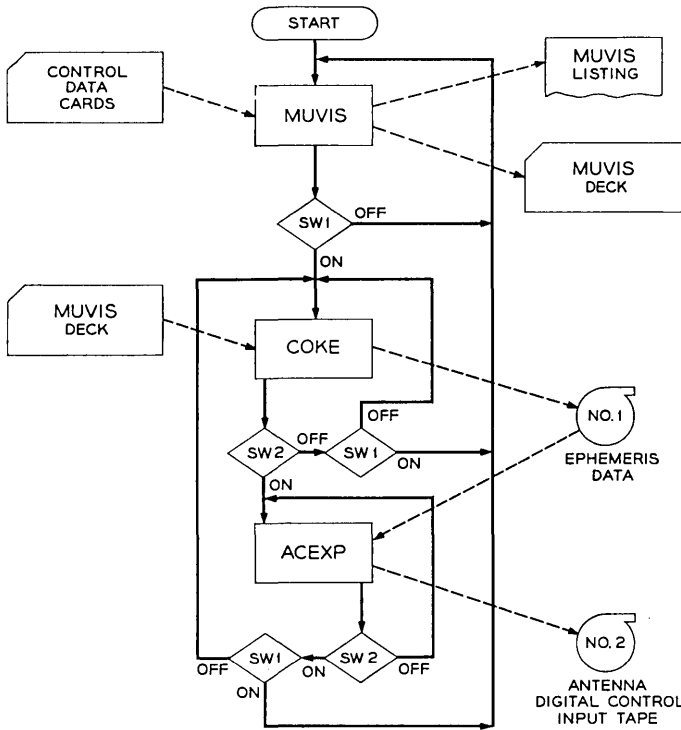
Fig. 2 — TELEPATH flow chart.

ing orbital elements are used which are valid at most one-half a period away. This enables the program to update the elements in steps of 2π, which results in a large time saving. The errors introduced by not completely updating the orbital elements are far less than the accuracy desired.

(*iii*) The determination of visibility at a site is not done by the obvious method of computing elevation and checking for a positive angle. The reason for this is that once the satellite's coordinates have been obtained, this method requires at least a square root, an arc tangent, and approximately thirteen multiplications. The method used instead requires only seven multiplications with the resultant saving in time. Instead of computing elevation, the program passes a plane through the site tangent to the earth. This plane, which can be considered a ground plane at the site, has the equation

$$\alpha X_s + \beta Y_s + \gamma Z_s - R_e = 0$$

where X_s, Y_s, Z_s are the inertial coordinates of the site, and R_e is the distance from the center of the earth to the site. If, however, the coordinates of the satellite are substituted in the equation, then a value other than zero is usually obtained. If this value is minus, then the satellite lies on the same side of plane as the center of the earth and is therefore below the horizon, but if the value is positive, then the satellite is on the opposite side of the plane which is above the horizon and is therefore visible. The determination of visibility is thus reduced to evaluating α and β, which are time varying due to the rotation of the earth, evaluating the four-term expression, and testing the sign of the result. The evaluation of α and β can be done using the previous values of α and β with only four multiplications. It should again be noted that the price for this increase of speed is the loss of some accuracy. This method does not fully take into account the earth's oblateness. The result is that the plane is not exactly tangent to the earth, and a small amount of inaccuracy is to be expected. (About 140 feet of error in placing the site.) This method is also limited in that it cannot predict rise and set at any angle other than $0°$, but this information can always be obtained later from the COKE program.

When the program has determined a period of visibility, it updates the orbital elements to either the center of the mutual visibility if any exists or otherwise simply the center of visibility, and punches out the elements plus other pertinent data on the pass. The program also prints out the pass number, rise and set times at the ground station, start and end of mutual visibility, and the maximum elevation seen at the site.

This procedure is continued until a final time is reached. At this point the program finishes any pass it may be working on and then stops.

9.2 *COKE*

The COKE program uses the MUVIS results to generate an ephemeris that is exact but omits physical effects such as refraction and antenna distortion. Thus the tape can be generated ahead of time and just before the pass corrected for both meteorological conditions and the boresight corrections of the antenna to be used (there is only one antenna at each site at present).

The program uses an Encke type method (see Ref. 6, p. 176) to solve for the satellite's position at four-second intervals. These are computed both forward and backward from the center of the pass or the center of mutual visibility, whichever the orbital elements have been updated to. Thus some rearrangement of data must be done to output the

ephemeris in time order. The heart of the program is the same integration program used in the trend-removal portion of TELETRACK. Therefore only the peripheral programming needed to convert the results to pointing angles, to rearrange and output the results, and to control the direction and length of integration had to be written from scratch.

9.3 *ACEXP3*

The ephemeris tape required as input to the antenna digital control during a pass is generated by the expander program, ACEXP. In addition to generating this tape, this program also produces the "mission printout," a listing of pertinent data regarding a pass over the ground station. The main input to this program is the data tape from COKE, containing time, azimuth, elevation and range at four-second intervals.

One data point on the ephemeris tape contains the following information:

(a) time
(b) azimuth and elevation positions
(c) azimuth and elevation first differences
(d) azimuth and elevation second differences
(e) azimuth and elevation predistortions, and
(f) gain factor.

Azimuth and elevation first differences for the ith data point are computed according to

$$D^1 = \tfrac{1}{2}(P_{i+1} - P_{i-1})$$

where P_i represents azimuth or elevation position. The second differences are computed according to

$$D^2 = P_{i+1} - 2P_i + P_{i-1} .$$

Azimuth and elevation predistortions, which are discussed in Ref. 7, are estimated to be functions of elevation only and to be of the form

$$PD_A = (a + bE)/\cos E$$

$$PD_E = c + dE.$$

Current values for the parameters are

$a = 0.015$ degree
$b = -0.000786$
$c = 0.057$ degree
$d = -0.000712.$

The ground station transmitter gain factor, discussed more fully in Ref. 8, is computed as a function of range as follows

$$\gamma = \frac{127}{128} \alpha[1 + 0.0791(\alpha - 1)]$$

where $\alpha = \log_{10} S/S_{min}$ for $S_{min} < S < 10\ S_{min}$

$\qquad\quad = 0$ for $S \leqq S_{min}$

$\qquad\quad = 1$ for $10\ S_{min} < S.$

S_{min} is chosen according to the characteristics of the pass over the site.

Elevations are corrected for refraction as follows. Index of refraction is computed according to

$$n - 1 = (0.776 \times 10^{-4}\ p + 0.372\ e/T)/T$$

where T is temperature in degrees K, p is air pressure in millibars, and e is water vapor pressure in millibars (Ref. 9, pp. 13–15). The correction

$$\Delta E = (n - 1) \cot E$$

is added to the elevation, E, before putting it on the ephemeris tape.

The mission printout is generated to aid the operating personnel during a satellite pass. Tabular data at one-minute intervals specify time, azimuth, elevation, range, one-second increments in azimuth, elevation and range, and Doppler shift. From a knowledge of the azimuth rates the program predicts when (if at all) the horn antenna will lose autotrack due to excessive azimuth rates. The angular distances between the satellite and the sun are also computed, and if they come within 2° of each other an appropriate warning is included in the mission printout.

X. OPERATIONAL RESULTS

These programs have been a part of the Bell System satellite communications ground station operational system since the July 10, 1962, launch. Initial predictions were based on the launch and injection data, corrected by the few observations possible in the first six orbits. From the sixth orbit on, predictions were based entirely on track data acquired at the Andover site. By the seventeenth orbit (the second day), the orbital elements had been refined sufficiently so that the horn-reflector antenna autotrack could acquire the satellite using the predicted angles. From that point on the normal mode of acquisition was from the

predicted angles, and the use of the auxiliary antennas as acquisition aids was generally not required. This means that predictions have generally been within ±0.2°, at least at the horizon where acquisition is usually achieved.

The launch of the Telstar satellite was carefully planned to put the apogee in the northern hemisphere to maximize the periods of mutual visibility in the early phases of the experiment. During the first few weeks following the launch, the prediction accuracy was very good. Samples of the results of orbit determination and prediction during this period are shown in Table VII. The predicted angles, extending five days ahead, were generated from orbital elements computed from precision angular tracking data obtained during the preceding five days. The observed angles were obtained from the precision tracker. It should be noted that errors in azimuth should be multiplied by the cosine of the elevation in order to convert them to errors in sightline angle on a par with the errors in elevation.

With apogee in the northern hemisphere, the tracking periods were long (over 30 minutes). As perigee precessed toward the northern hemisphere and the tracking periods became shorter, a gradual degradation in prediction accuracy was noted. While the prediction accuracies were sufficient for the daily antenna pointing operations at Andover, they proved inadequate for providing pointing information for the optical experiment at Holmdel[10] and for determining satellite positions for the radiation effects study.[11] These uses of the predictions require accuracies of 0.1° and both require that the satellite positions be related to geographical sites other than that at which the track data are acquired.

This prompted a renewed study of the orbit determination method and the program implementation. This investigation revealed that this method is quite sensitive to observational bias, particularly when the track data are obtained from short passes rising to high elevations. This sensitivity can be reduced by using only tracking passes of 30 minutes or more in which the maximum elevations do not exceed 50°. However, that is a severe restriction to place on a single tracking site with a highly eccentric orbit such as that under consideration here. In addition, it was found that the approximate methods used to account for the perturbations due to the earth's oblateness were inadequate except when the line of apsides is nearly parallel (as in July, 1962) or nearly perpendicular to the line of the nodes. Programs providing more complete perturbation calculations have been written and are presently undergoing tests.

From this study it was concluded that to achieve prediction accura-

TABLE VII

Date and Pass Number	Time (hrs-min, UT)		Azimuth (degrees)		Elevation (degrees)	
			Observed	Predicted	Observed	Predicted
7/23	21	35	195.16	195.20	20.50	20.48
⚹124	21	41	188.83	188.86	29.37	29.38
	21	47	179.58	179.60	38.28	38.29
	21	53	165.12	165.14	46.35	46.37
	21	59	142.81	142.80	51.28	51.29
	22	05	115.18	115.21	49.24	49.22
	22	11	92.13	92.15	39.03	39.04
	22	17	77.19	77.19	24.08	24.08
7/24	21	17	187.80	187.81	25.73	25.72
⚹133	21	23	179.40	179.40	34.40	34.40
	21	29	166.95	166.97	42.47	42.44
	21	35	148.30	148.32	48.26	48.26
	21	41	123.75	123.75	48.91	48.88
	21	47	99.92	99.93	42.22	42.20
	21	53	82.60	82.60	29.77	29.77
7/25	23	43	238.23	238.24	22.01	22.03
⚹143	23	49	237.62	237.61	32.26	32.29
	23	55	235.99	236.00	44.29	44.29
7/26	00	01	231.28	231.31	58.89	58.94
⚹143	00	07	207.91	207.83	76.43	76.44
	00	13	99.76	99.82	72.91	72.91
	00	19	80.65	80.65	46.23	46.22
7/26	20	31	183.69	183.68	21.11	21.12
⚹151	20	37	175.55	175.59	29.39	29.42
	20	43	164.51	164.54	37.05	37.04
	20	49	149.13	149.17	42.90	42.91
	20	55	129.16	129.21	45.17	45.18
	21	01	107.72	107.77	41.98	42.02
	21	07	89.57	89.59	33.43	33.44
	21	13	76.29	76.29	21.36	21.35
7/27	20	08	181.81	181.84	18.66	18.67
⚹160	20	14	173.80	173.85	26.84	26.84
	20	20	163.25	163.30	34.25	34.31
	20	26	149.03	149.11	40.15	40.19
	20	32	130.89	130.95	42.99	42.98
	20	38	110.85	110.93	41.09	41.09
	20	44	92.90	92.93	34.18	34.20
	20	50	78.98	79.01	23.62	23.63

cies of 0.1° or better, the angular observations must be taken from more than one geographical point or, if from a single tracking site, the angular observations must be supplemented by an additional independent track measurement, such as slant range to the satellite. A program system avoiding the shortcomings of the present method is now under active development. This system uses a modified method of combining

passes and improved perturbation calculations, and has the ability of including slant range measurements and data from several tracker sites.

The orbit determination method described meets the objective of minimizing the computer requirements by eliminating the mass storage requirements and time-consuming iterative procedures inherent in the classical differential corrections technique. As described, the method and programs are adequate for providing acquisition information for autotracking communications antennas if the tracking restrictions can be met. For a single tracking site, these restrictions imply a perigee of 1000 nautical miles or more. If lower orbits must be handled or greater accuracies are required, the improvements mentioned above should be considered.

APPENDIX A

Derivation of Equations (7) and (8)

Since $A^{-1}\bar{x} = (A^{-1} + B^{-1})\bar{x} - B^{-1}\bar{x}$, (5) may be written in the form

$$\bar{z} = \bar{x} - (A^{-1} + B^{-1})^{-1} B^{-1}(\bar{x} - \bar{y}).$$

Now,

$$\begin{aligned}
(A^{-1} + B^{-1})^{-1} B^{-1} &= [B(A^{-1} + B^{-1})]^{-1} \\
&= [1 + BA^{-1}]^{-1} \\
&= [(A + B)A^{-1}]^{-1} \\
&= A(A + B)^{-1}.
\end{aligned}$$

Hence,

$$\bar{z} = \bar{x} - A(A + B)^{-1} (\bar{x} - \bar{y}).$$

Since, by (5), we may interchange $\bar{x}$ and $\bar{y}$ provided that A and B are also interchanged, we have

$$\bar{z} = \bar{y} + B(A + B)^{-1} (\bar{x} - \bar{y}).$$

Thus, if w_1 and w_2 are any two six-by-six matrices whose sum is a unity matrix,

$$\bar{z} = w_1\bar{x} + w_2\bar{y} - (w_1A - w_2B) (A + B)^{-1} (\bar{x} - \bar{y}).$$

Substituting $A = PG^{-1}$ and $B = QG^{-1}$, and noting that

$$(A + B)^{-1} = G(P + Q)^{-1}$$

$$w_1A - w_2B = (w_1P - w_2Q)\ G^{-1}$$

we get (7).

Noting that the right-hand member of (6) is a half of that of (5) if we replace $\bar{x}$ by A and $\bar{y}$ by B, (8) follows from (7).

REFERENCES

 1. Briggs, R. E., and Slowey, J. W., An Iterative Method of Orbit Determination from Three Observations of a Nearby Satellite, Special Report No. 27, Astrophysical Observatory, Smithsonian Institute, June 30, 1959.
 2. Shapiro, I. I., *The Prediction of Ballistic Missile Trajectories from Radar Observations*, New York, McGraw-Hill Book Company, Inc., 1959, Part III, Chapter IV.
 3. Swerling, P., A Proposed Stagewise Differential Correction Procedure for Satellite Tracking and Prediction, Rand Corporation Report P-1292, January 8, 1958.
 4. Swerling, P., First Order Error Propagation in a Stagewise Smoothing Procedure for Satellite Observations, Journal of Astronautical Sciences, **6**, No. 3, Autumn, 1959.
 5. Claus, A. J., Orbit Determination for Communication Satellites from Angular Data Only, to be published.
 6. Brouwer, D., and Clemence, G. M., *Methods of Celestial Mechanics*, New York, Academic Press, 1961.
 7. Githens, J. A., and Peters, T. R., Digital Equipment for the Antenna Pointing System, B.S.T.J., this issue, p. 1213.
 8. Giger, A. J., Wickliffe, P. R., Jr., and Pardee, S., Jr., The Ground Transmitter and Receiver, B.S.T.J., this issue, p. 1063.
 9. *Handbook of Geophysics for 1960*, U.S. Air Force Air Research and Development Command.
10. Jakes, W. C., Jr., Participation of the Holmdel Station in the *Telstar* Project, B.S.T.J., this issue, p. 1421.
11. Brown, W. L., Gabbe, J., and Rosenzweig, W., Results of the *Telstar* Radiation Experiments, B.S.T.J., this issue.

Planning, Operation and External Communications of the Andover Earth Station

By D. H. SMITH, C. P. CARLSON, R. J. McCUNE,
R. E. ELICKER and R. E. SAGEMAN

This paper relates some of the considerations in the planning of the Andover, Maine, earth station. It describes the station layout, the operating plan and the Long Lines interconnections. Power facilities, air conditioning, heating and dehumidification arrangements are also covered.

I. INTRODUCTION

The purpose of this paper is to describe the layout, operation, and external communications links of the Andover, Maine, earth station. This station was designed to provide the terminal facilities required for communications via artificial earth satellites. Complete facilities for orbit determination, tracking, and broadband microwave communications were included in order to obtain data which would be useful in the evaluation of designs for future operational systems. Experimental verification of the feasibility of communicating via satellites was, however, the primary goal.

In this paper, various aspects of the Andover station are described in detail under the following headings: II. Site Planning, III. Operating Plan, IV. Power Facilities, V. Air Conditioning and Heating, VI. External Communications Requirements, and VII. Experimental Demonstrations

II. SITE PLANNING

The Andover ground station is situated in a 1000-acre tract surrounded by mountains. The site is nearly ideal since the mountains are high enough to protect against interference from overland microwave systems but low enough to permit proper operation when the satellite is near the horizon.
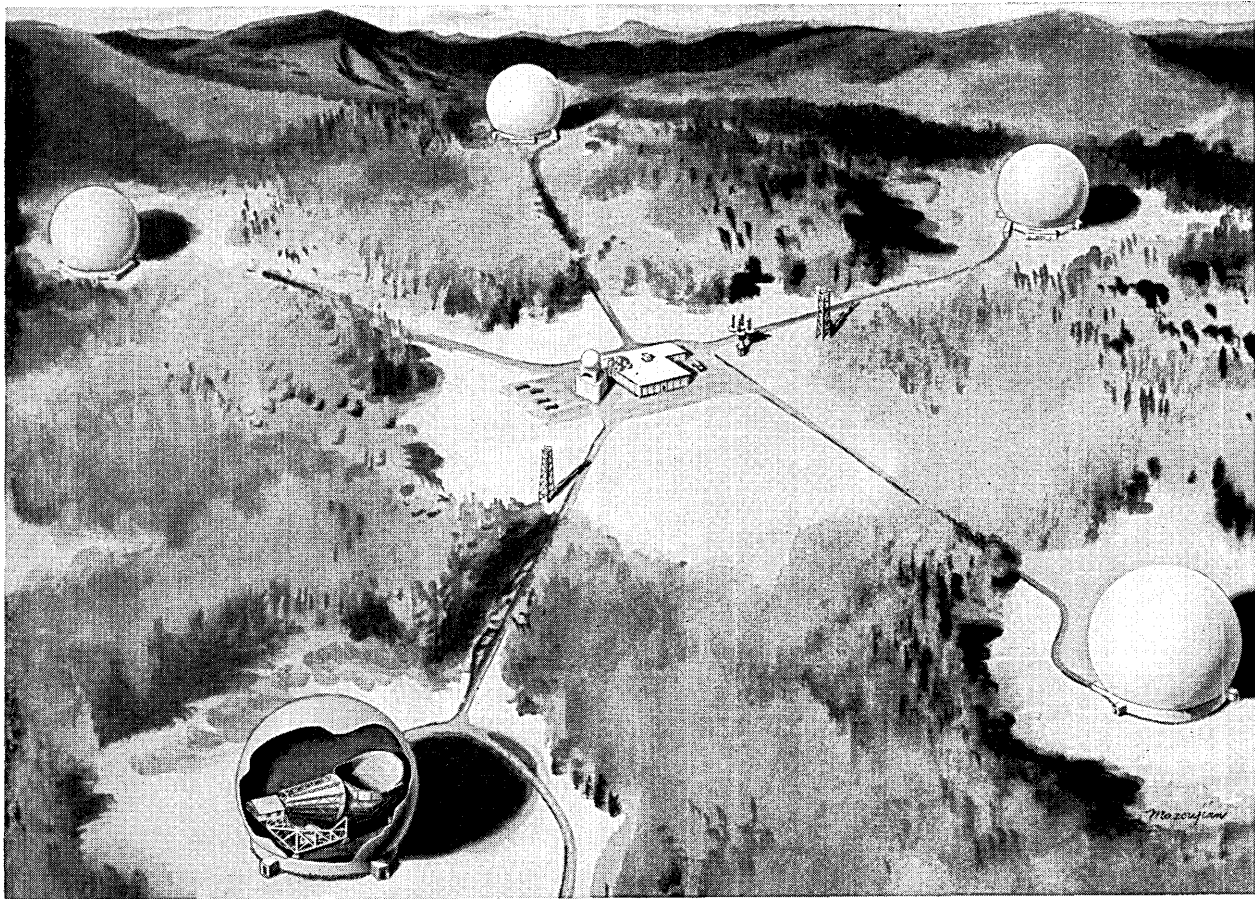
Fig. 1 — Site plan for Andover.

Aerial surveys of the site were used to assist in locating the control building, antennas and boresight towers. Anticipating the possibility of more extensive experimentation or of eventual commercial systems, a sufficiently large site was obtained such that a control building could be located on relatively high ground, surrounded by five horn antennas. One possible commercial system would require a multiplicity of satellites and a minimum of two antennas at each terminal for efficient operation. One antenna at each terminal point would follow a satellite as long as that satellite is mutually visible. As the end of a period of mutual visibility is approached, continuity of service could be provided by switching to a second, or handover, antenna which would be tracking another satellite in the early part of its period of mutual visibility. A third antenna might be provided as an active spare. On this basis, it was estimated that five antennas would be sufficient to provide three broadband radio channels, with one antenna always available for handover and another as a spare.

2.1 *Antenna Spacings*

On the Andover site, five antennas could be located, as shown in Fig. 1, in such a manner as to prevent masking of the microwave signals by each other at elevation angles above 7.5 degrees. The most practical arrangement would be to cluster the antennas about the control building. At the potential locations the antennas would be at varying distances from the control building and from each other because of the contours of the land. The antenna location for the Telstar experiment was selected because of its proximity to the approach highway.

Trees were cleared to avoid interference at low angles. For the same reason the commercial power line was placed underground as it approached the control building. Masking of the precision tracker and command tracker antennas by the control building was avoided by elevating them on concrete pedestals and locating them at opposite sides of the control building so that their beams would clear the building and each other for elevation angles above 7.5 degrees.

2.2 *Control Building*

A cutaway view of the control building and its facilities is shown in Fig. 2. The building is a windowless one-story structure, and it may be considered as being made up of three areas. One area contains the heating, power and utility equipment, not only for the control building itself but also for the horn antenna and its radome. Another area contains
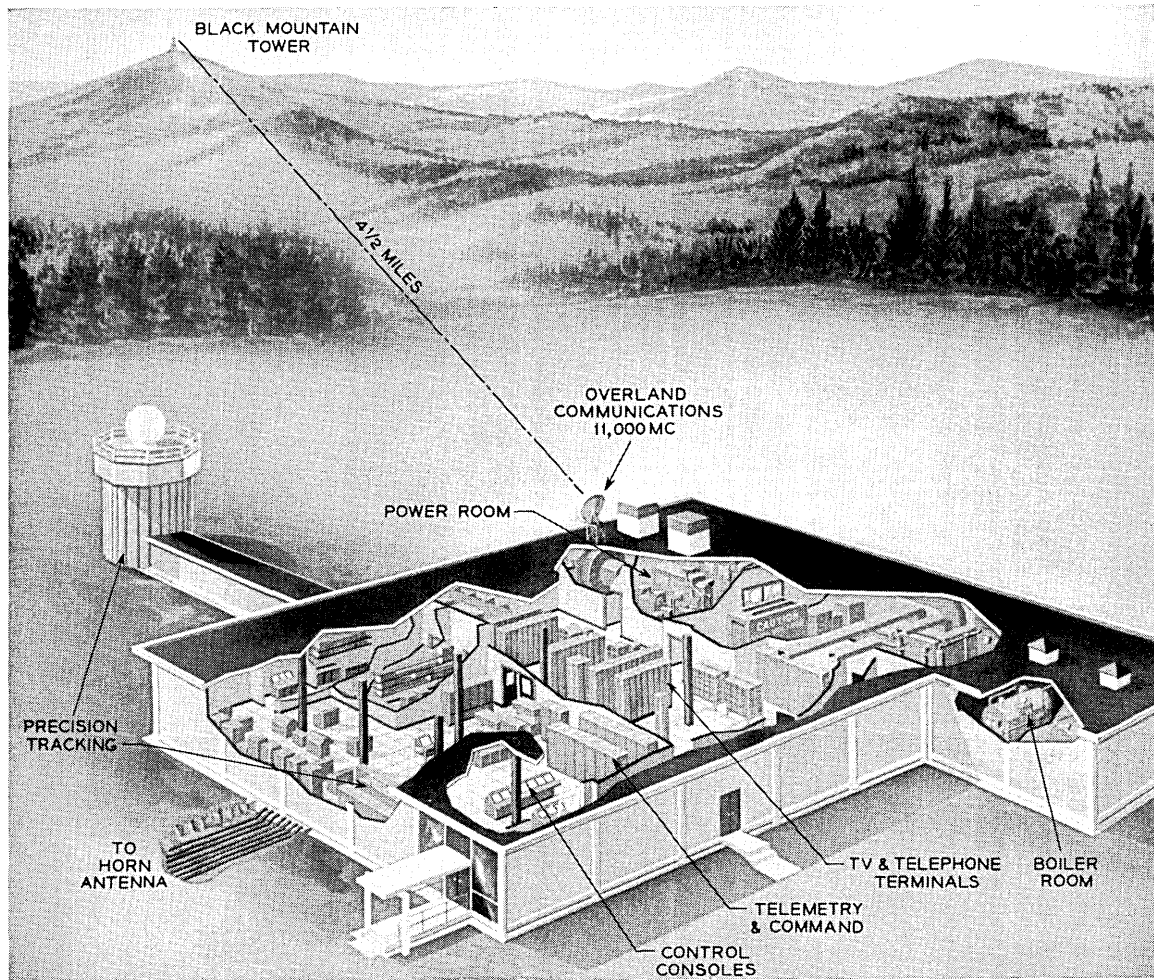
Fig. 2 — Control building.

the telephone terminal equipment, microwave terminal, television operating center and distributing frames. Most of the equipment in this area is made up of standard Bell System items.

The third area contains equipment quite special for the Telstar project. This consists of the ground station control and other consoles, antenna pointing equipment, computers, precision tracker, command, telemetry and sundry testing equipment.

2.3 *Main Antenna Building*

It was considered desirable to concentrate as much of the transmission and antenna guidance equipment as possible in the control building. This would obviate dispersal of maintenance personnel and equipment. However, to avoid expenditure of considerable development time, it was necessary to locate much of this equipment on the horn-reflector antenna structure or in the utility building at the periphery of its radome. The horn antenna structure design included two rooms for equipment and personnel. One room, located at and behind the apex of the horn feed, is called the "upper" room. The other room, located on the floor of the azimuth near the pintle area, is called the "lower" room. The apportionment of equipment among the utility building and the lower and upper rooms of the rotating antenna structure was given serious consideration. In order to achieve optimum servo performance it was essential that the nonstructural weight on the movable structure be minimized. It was not only the weight of the equipment that had to be considered, but also the flooring and housing for it. Furthermore, of the equipment that was to be placed on the antenna structure, as much as possible was located in the lower room close to the center of rotation. Figs. 3 and 4 show the arrangement of equipment in the upper and lower rooms, respectively.

In the interest of weight saving, the cabinets, unit frameworks and overhead cable rack and framing supports were made of aluminum. Closed cabinets permitted the use of local air cooling as required. The air for cooling equipment in some of the cabinets is provided from outside the room and is exhausted outside the room through a closed system over a chilled water heat exchanger. In other cabinets where the heat generated is moderate, room air is used for cooling.

2.4 *Slip Ring Assembly*

Electrical connections between the equipment on the moving part of the antenna and the remainder of the system are made through slip
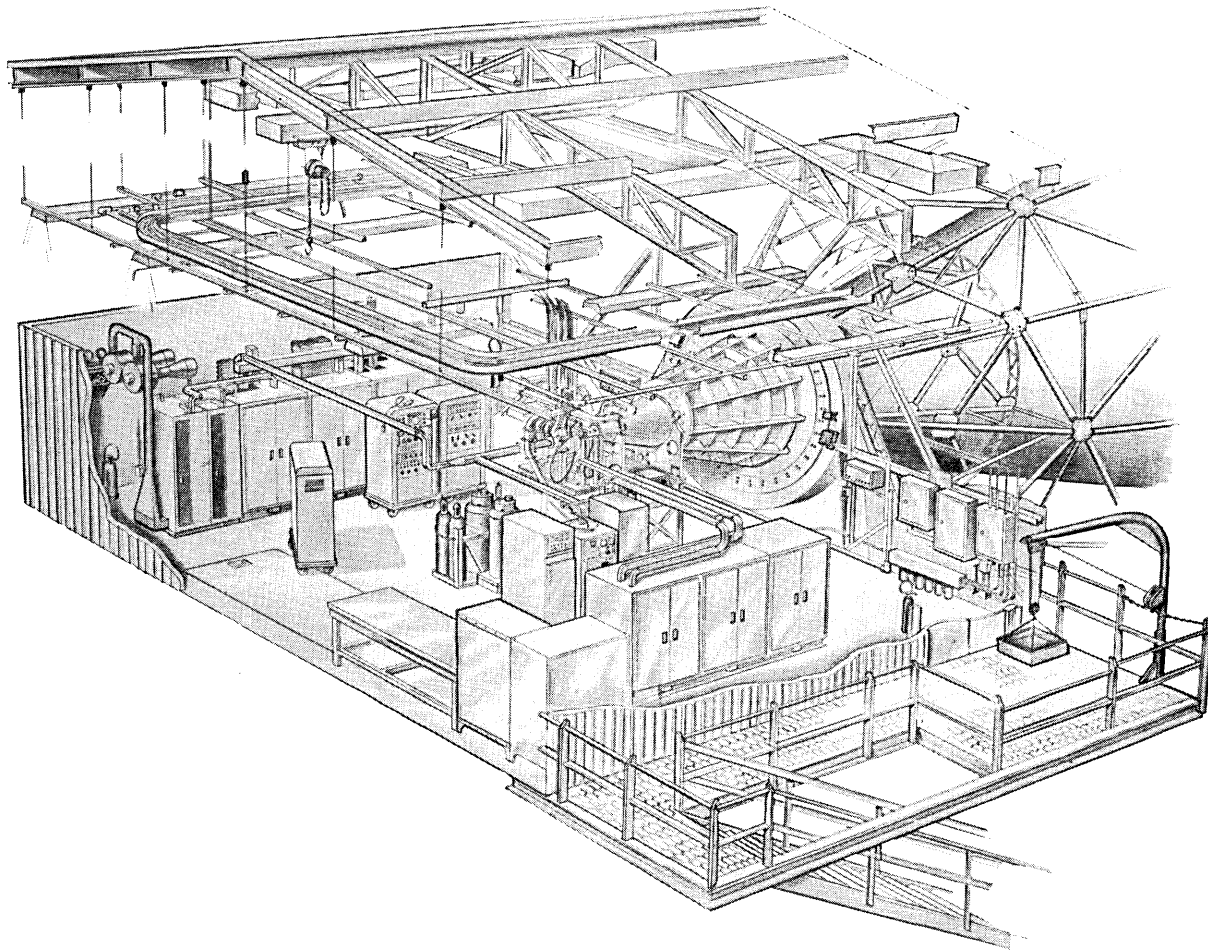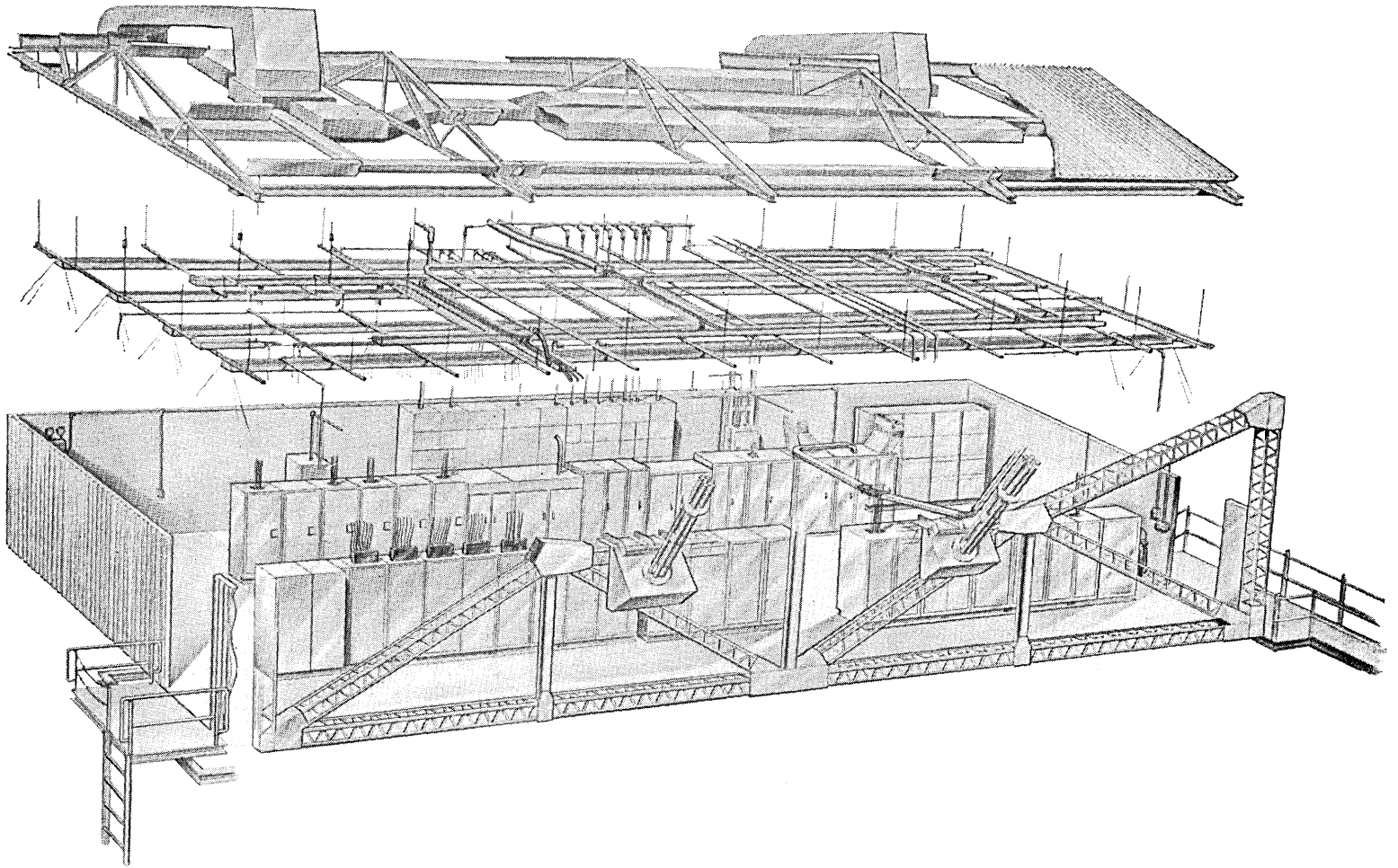
Fig. 3 — Upper room of antenna structure.

Fig. 4 — Lower room of antenna structure.

rings. A slip ring assembly previously designed for another project was modified to satisfy the requirements of the Telstar installation. The previous design was for 12 power rings, 300 general-purpose rings and seven unbalanced video circuits. The modifications permitted 28 power rings, 246 general-purpose rings and three balanced video circuits of very good quality.

The bulk of the power requirements for the rotating structure are satisfied by 340 KVA 440-volts 3-phase 60-cycles. It was deemed desirable to bring 440 volts instead of lower voltages into the rotating structure in order to minimize the current requirements for the slip rings. Where 208/120-volt power is needed, this is obtained from transformers on the antenna structure.

It is now believed that a cable-wrap system would be more practical than a slip ring assembly. The slip ring assembly would be essential for an antenna that has to revolve continually but is not of great value for a communications satellite ground station antenna that requires only a partial revolution for any one pass. With a cable-wrap system a fair amount of equipment would be eliminated.

III. OPERATING PLAN

An early step in system planning for the Andover ground station was the development of an operating philosophy. Analytic studies were made to determine the sequence of activities that could occur during the interval commencing with preparation for a satellite pass and ending with release of all systems at the termination of a mission. From these studies, operator decision points were defined and assigned as functional responsibilities at logical operator positions. Control and display requirements were then established and incorporated in the design of operating consoles. Also, an operations plan was prepared to set forth the specific procedures that would be used when operating various systems in concert. Training exercises and evaluation tests were carried out for the system as a whole to: (a) calibrate the interconnecting equipments, (b) determine system response times and other necessary operations data, (c) verify operations procedures, and (d) develop an efficient operator team. The last step in operations "prove-in" came through the experience obtained once the Telstar satellite was in orbit.

3.1 *Concept of Operations*

Centralized control was considered essential for coordinated operations involving many interrelated but independent subsystems—particularly

in view of the experimental nature of the project, the time constraints imposed upon design and installation, and the objective of insuring highest probability of success. Of secondary importance, but still significant, was a desire to minimize manpower requirements once standardized routines were validated.

The central control functions for ground operations very naturally group into two areas of responsibility: (*i*) satellite acquisition and tracking, and (*ii*) broadband experimental communication. The purpose of the first area is to establish and maintain a usable broadband communication path, while that of the latter is to carry out the various transmission experiments and obtain resulting test data. The two areas are assigned, respectively, to a ground station controller and a communications controller. Over-all supervision of operations during a mission is accomplished by a mission director or by one of the two controllers, dependent upon the complexity of the scheduled experiments and degree of external coordination required. Operating positions for the two controllers are adjacent to each other, with the director's monitoring position located behind the controllers as shown in Fig. 5.

The ground station controller has specific responsibility for:

1. Coordinating the pre-mission calibration and testing activities.

2. Verifying operability of the tracking and command complex before each pass.

3. Locating the satellite.

4. Activating the satellite in an appropriate sequence.

5. Positioning the horn-reflector communication antenna to excite the satellite repeater with broadband signals from the ground, and to receive its 4-kmc signal outputs.

6. Keeping the horn-reflector antenna properly positioned throughout the satellite pass so that experiments can be conducted.

7. Deactivating the satellite functions in an appropriate sequence before the satellite goes outside of command coverage.

The communications controller has specific responsibility for:

1. Calibrating the communication transmitter and receiver systems before and after each pass.

2. Setting up and verifying readiness of all scheduled communications experiments.

3. Carrying out such experiments and coordinating with external participating sites so that valid useful data are obtained.

Assisting the controllers are operators at a few vital equipment positions. Their duties are: (*i*) to monitor the performance of a subsystem or major equipment group, (*ii*) to make operating adjustments or con-
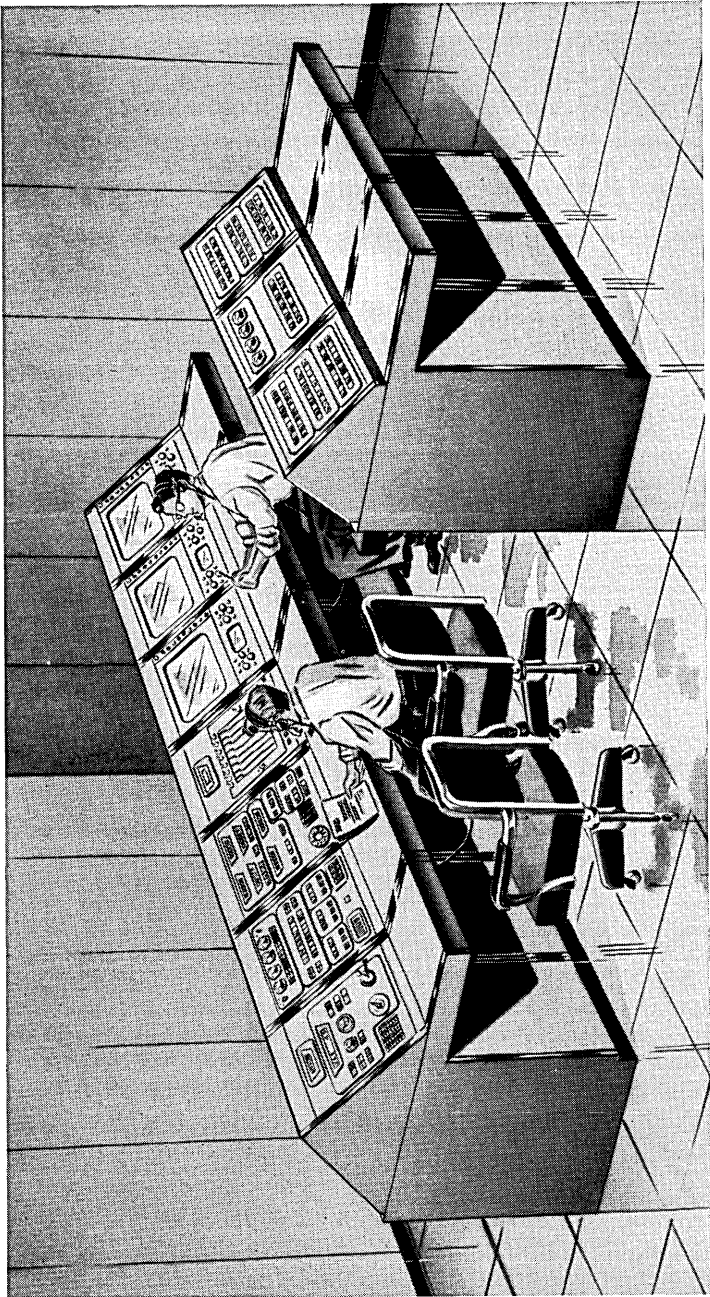
Fig. 5 — Director and control consoles.

TABLE I — BASIC OPERATIONS MANNING

Mission Operator Designation	Operator Position
Director	Director console
Ground controller	Ground station control console
Communication controller	Communication console
Command operator	Command encoder cabinet
Command track (1)	Command tracker equipment
Data operator	Tape switching console
ACE	Antenna digital control group
SERVO (2)	Antenna servo group
VAT	(Vernier) autotrack equipment
Receiver	4-kmc receiver equipment
Transmitter	6-kmc transmitter equipment
Test operator	Communications test center
TEG (3)	Track digital control group
Precision track (4)	Precision tracker console
Recorder (5)	Intercom and video recorders
Satellite (6)	Telemetry equipment bay

Notes:
(1) Manned only for initial operations, usually covered by command operator.
(2) Manned separately when needed, otherwise covered by ACE.
(3) Manned only when ranging data are scheduled.
(4) Manned separately when needed for orbit determination data.
(5) Manned only when video recordings are scheduled.
(6) Manned during first weeks of operation, for real-time assessment of satellite operating performance.

figuration changes when directed, and/or (*iii*) to perform manual control actions assigned to the local position. Table I presents the positional manning that was used during the first three weeks of operation after launching of the Telstar satellite. As indicated on the table, several of the positions are not manned during normal, routine missions.

Fig. 6 shows the basic control configuration of the ground station and the primary flow of status and control signals during a satellite pass. Briefly stated, normal operations proceed according to the general plan outlined below, assuming that the horn-reflector, command tracker and precision tracker antennas are all active. The plan is simplified for approximately 50 per cent of the passes by the deletion of the precision tracker and associated track digital control group when data for orbit determination are not required.

All systems are activated, tested and calibrated individually; they are then turned over to the two controllers who establish the integrated configuration and verify its operability by use of the satellite replica located on the test tower several miles from the station. The mission tape, with the pointing ephemeris and related data for the satellite pass, includes a set pattern of pointing and ranging data necessary for dynamic verification using the test tower. This tape is generated and

SATELLITE

123-MC
COMMANDS

6390-MC
COMMUNICATIONS

136-MC BEACON
AND TELEMETRY

4170-MC
COMMUNICATIONS

—4080-MC BEACON—

HORN-REFLECTOR
COMMUNICATION ANTENNA

COMMAND TRACKER

PRECISION
TRACKER
ANTENNA

TAPE
UNITS

ANTENNA
SERVO
GROUP

TAPE
SWITCHING
UNIT

MONITOR
GROUP

COMMAND
TRANSMITTER

GROUND
TELEMETRY

RECEIVER
AND
CONSOLE

TRACK
DIGITAL
CONTROL
(ENCODER)
GROUP

ANTENNA
DIGITAL
CONTROL GROUP

(VERNIER)
AUTOTRACK
SYSTEM

COMMAND
ENCODER

FREQUENCY
STANDARD

DATA
PROCESSORS
(COMPUTERS)

ANTENNA
CONTROL
EQUIPMENT (ACE)

COMMUNI-
CATION
TRANSMITTER

COMMUNI-
CATION
RECEIVER

COMMAND-TELEMETRY
SYSTEM

PRECISION
TRACKER
SYSTEM

STATION CLOCK

ANTENNA
DIRECTION SYSTEM

GROUND STATION
CONTROL CONSOLE

DIRECTORS
CONSOLE

COMMUNICATION
(VIDEO MONITOR)
CONSOLE

VIDEO
RECORDERS

COMMUNICATION
TEST CENTER

TO TJ/TD-2
COMMUNICATION
SYSTEM

DIRECTS ACQUISITION,
TRACKING, AND
TERMINATION PHASES

SUPERVISES MISSION
OPERATIONS

DIRECTS
COMMUNICATION
PHASE

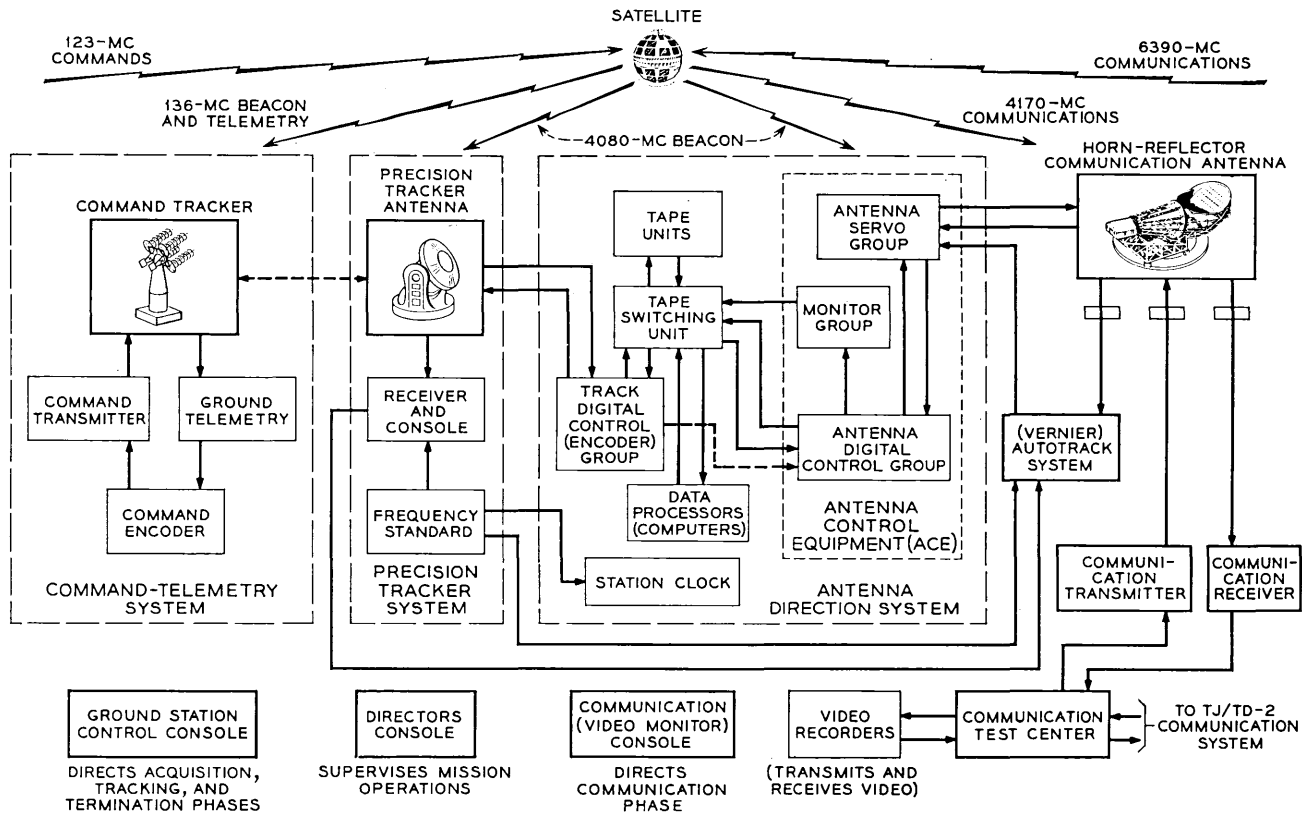(TRANSMITS AND
RECEIVES VIDEO)

Fig. 6 — Basic control configuration.

checked by one of the local computers prior to the system testing interval. Concurrent with generating the tape data points, the computer produces a print-out of information about the pass for use by the operators; this print-out includes, among other things, pointing angles and rates for every whole minute during the passage. The print-out provides the operations team with a convenient reference for anticipating actions that will be necessary during the pass; it also serves as a back-up, for manually positioning any of the antennas to acquire the satellite, in case of loss of the automatic pointing data coming from the mission tape or other antennas.

Upon completion of the verification tests, and several minutes prior to expected satellite rise time, all three antennas are positioned to the angles for expected acquisition, using the mission tape as a common pointing source. When the command tracker begins receiving 136-mc beacon signals from the satellite and obtains a frequency phase-lock, its autotracking mode is selected. As soon as the strength of the received signal permits, commands are transmitted in a prescribed sequence to energize operating circuits in the satellite that activate telemetry and later turn on the broadband repeater. During this interval of several minutes, all vital conditions for safe operation of the satellite are verified by the received telemetry data. The mission tape keeps the horn-reflector communication antenna and the precision tracker pointed toward the satellite as it rises, or, optionally, the precision tracker can be slaved to the command tracker if desired.

As soon as the satellite repeater is ON, its 4080-mc beacon signal is radiated. At that time, both the autotrack system (sometimes referred to as vernier autotrack or VAT) and the precision tracker commence frequency search and obtain phase-lock for tracking. Concurrently, the communication transmitter may radiate 6390-mc carrier at normal power, and the broadband FM signals from the satellite repeater will usually be detected through the communication receiver, confirming satisfactory pointing by the horn-reflector antenna. When phase-lock is established, the autotrack system outputs are inserted into the tracking loop for the main antenna; similarly, the precision tracker begins auto-tracking. If difficulties are experienced in acquisition by either antenna, outputs from the other system may be used to assist in completing the process.

When the autotrack system error loop has been completed and the signal strengths in the 6390-mc and 4170-mc paths have been confirmed to be at expected levels, the communications controller uses the link for scheduled experimental transmissions. At a predetermined time during

satellite descent, or if a critical condition should occur in its operation, the ground station controller sends a sequence of commands that shut down the satellite repeater and restore other operating circuits to their secured state. Tracking is terminated at this time, and any necessary post-mission calibration data are obtained prior to release of the ground systems.

3.2 *Operational Performance*

The first several days of operation after the Telstar satellite launching established that command tracking acquisition normally can be accomplished slightly before the satellite rises to the optical horizon, that command of the satellite is reliable as soon as the acquisition is completed, and that usable telemetry data can be obtained before 5 degrees elevation except in the presence of severe noise from electrical storms or man-made interference. Acquisition by the horn-reflector antenna was found to be considerably more rapid than had been anticipated, usually being completed in less than ten seconds after full activation of the satellite repeater. Similarly, precision tracker acquisition was usually swift and was no problem. Some of the contingency capabilities that had been provided in the tracking systems were therefore of lesser importance than had been expected. These capabilities did give a great deal of flexibility for handling any troubles that might arise, and for probing for the marginal performance limits of tracking — quite appropriate characteristics for an experimental facility. During the first three weeks after the launch, all possible acquisition and tracking modes and configurations were attempted and all were successful. This even extended to slaving the horn-reflector antenna to the command tracker for acquisition. Of particular interest was the capability for manual acquisition by the horn-reflector antenna — that is, manually positioning to angles in advance of the satellite along its expected path and then achieving a full autotrack state during the interval that the satellite moved through the 0.22-degree beamwidth of the antenna's main receiving lobe. It was found that this technique could be used even at high elevation angles: At a satellite angular rate of movement of 0.3 degree/sec or less, the acquisition was relatively easy; at an angular rate of 0.45 degree/sec the acquisition required good operators, particularly at the autotrack position, but could be effected. Also of interest was the capability for minimizing disruptions of the communications link when the satellite passed very close to the site's zenith. By alert operation at the ground station control console, the link outage could be kept to within 10 seconds of the calculated interval for azimuth slew at the maximum rate

of 1.5 degrees/sec. Finally, horn-reflector antenna tracking up to eleva-
tion angles of 85 degrees was eminently satisfactory: The autotrack
system nearly always held the pointing to within 0.005 degree of its null
when its servo-loop was closed, or with the autotrack loop open the
indicated pointing error could be kept under 0.01 degree by manually
inserted offsets. Even with the autotrack system outputs turned off, a
usable communications link could be maintained by keeping the 4170-mc
received carrier AGC maximized through manual offset insertions, ad-
mittedly an arduous monitoring task for the ground station controller.

3.3 *Console Design Considerations*

3.3.1 *Ground Station Control Console (GSCC)*

An important objective in designing the operating position for the
ground station controller was to achieve a minimum over-all manpower
requirement for supervision, operation and maintenance at the ground
station; consequently, design philosophy was based on performing as
much of the acquisition and tracking control from this one console as
was practical. This meant that the ground station control console or
GSCC would interconnect with nearly all systems on the station (see
Fig. 7). At the same time, the experimental nature of the project dictated
that the design be flexible enough to accommodate development changes.
Therefore, displays and controls were organized so that console activities
could be handled by a single operator or apportioned between two, or
even three, operators if necessary during training and early experiments.
Also, features were included in the mechanical and wiring design so that
functional changes could be made quickly after the console was installed,
with minimum interference to its operational use.

Controls for the entire tracking and command complex were provided
in the GSCC except for the precision tracker, data processors and their
associated equipments. These were excluded for three reasons:

1. The primary real-time tracking complex does not require control
changes involving these subsystems during normal operations.

2. If operating controls for these subsystems were included, the GSCC
size and complexity would be such that a single operator, or possibly
even two operators, might not handle the work load.

3. The excluded subsystem might be used for other operations during
certain active passes in which they were not a part of the real-time
horn-reflector antenna pointing complex. In particular, the data proces-
sors would be used for data reduction or generation of future predictions,
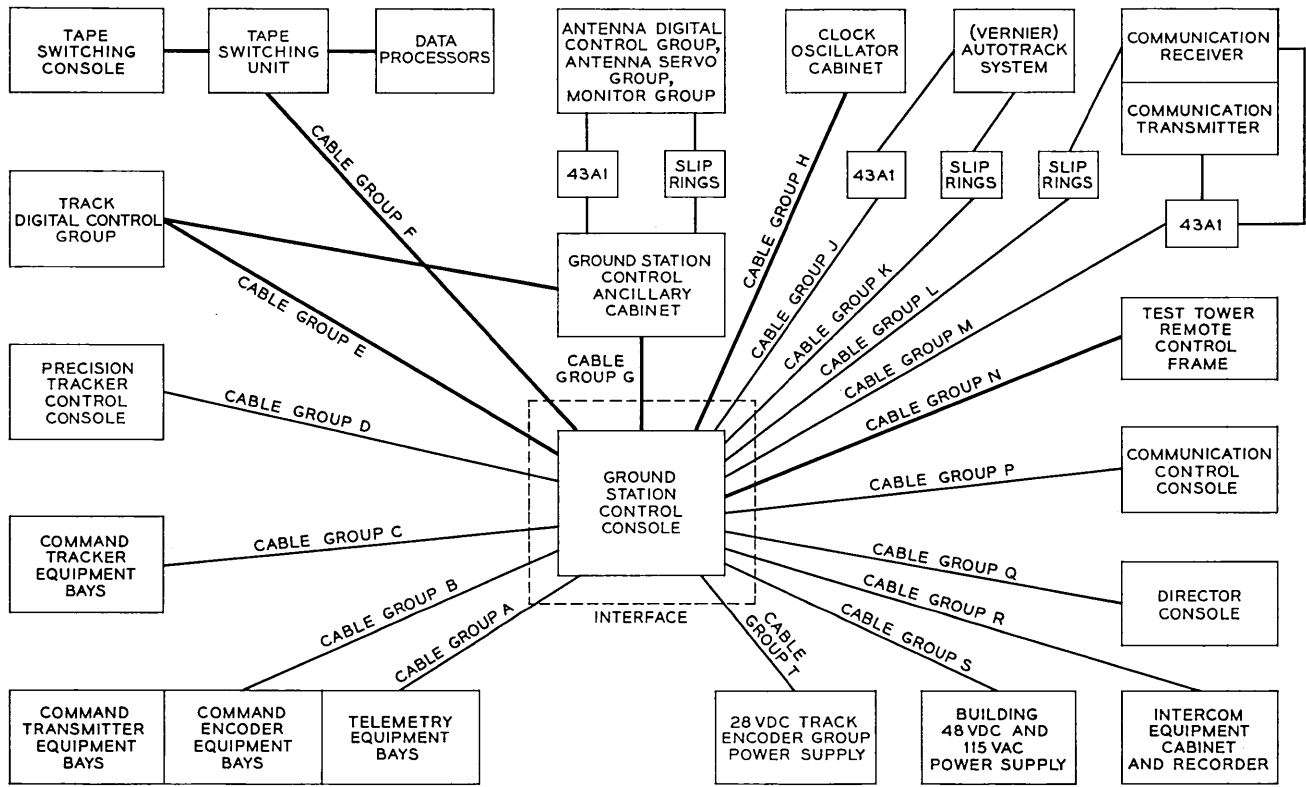
Fig. 7 — Connections to ground station control console (GSCC).

and the precision tracker might eventually be used for concurrent tracking of a second satellite.

Several of the GSCC controls and displays were included to allow full manual operation if required or desired during early experiments. In some instances, this capability was essentially a back-up for a mechanized feature or a hedge against operating problems that could but probably wouldn't arise; in others, it was an interim measure used for operations procedures that might eventually be automated after experience was gained with the first satellite. Thus, it was anticipated that the console and the operator's job would simplify as the system evolved after first experiments.

Fig. 8 shows the front panel layout of the console. Controls and displays were arranged in logical functional groupings and were located in the general order that the groupings are needed during acquisition and tracking; thus, operator activities start from the left and proceed to the right, going from top to bottom of each section. In so far as was practicable, the usual human engineering rules of uniformity, legibility, compatibility and operability were followed in the over-all design.

Components for display of magnitude quantities were selected on the basis of the dimensionality of the quantity and total range or precision required. Unidimensional quantities were presented on meter movements if no better than 2 per cent of full-scale accuracy was required; when greater precision was needed for such quantities, co-planar, projection-type decimal-digital displays were used. Important quantities whose history of variation over an interval of time was significant were presented on an eight-channel strip chart recorder in the section furthest to the right.

The digital nature of a substantial portion of the circuits in the tracking systems required that magnitude controls be in a digital form. An exception to this was the manual pointing control for the command tracker, which was in analog form. For uniformity in control and display configurations, magnitude inputs were decimal-digital wherever practicable. For quantities whose rate of change had to be limited, control from the GSCC was effected through increase/decrease switches associated with a decimal-digital display feeding back the present magnitude of the quantity stored in the associated subsystem.

Self-illuminated placard displays were used for binary event and for status information displays. Labels were engraved directly on the placards so that they would be visible even when the placard was dark. If a display was associated with a binary control function, the control and status displays were combined in a single pushbutton placard assembly.
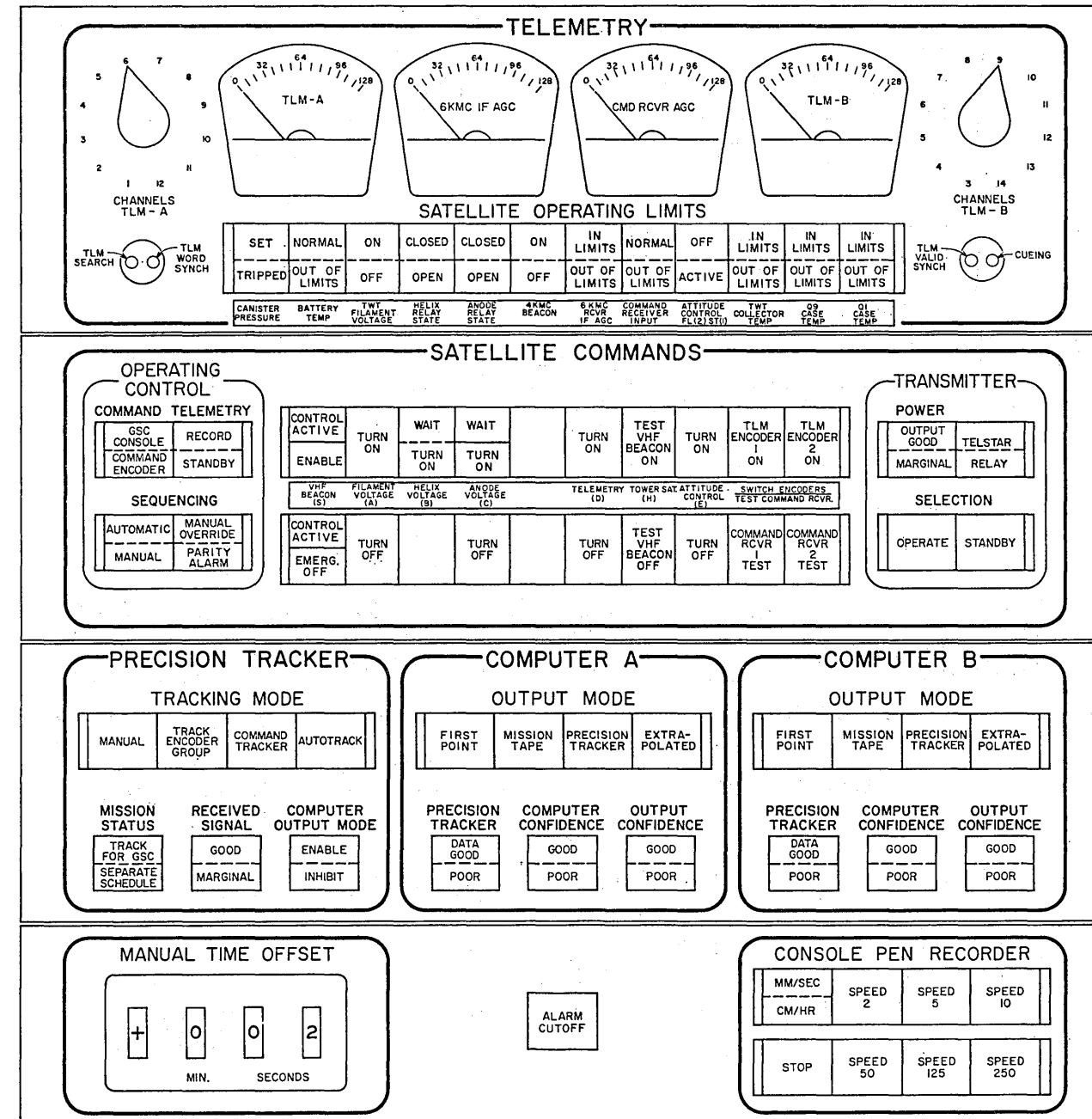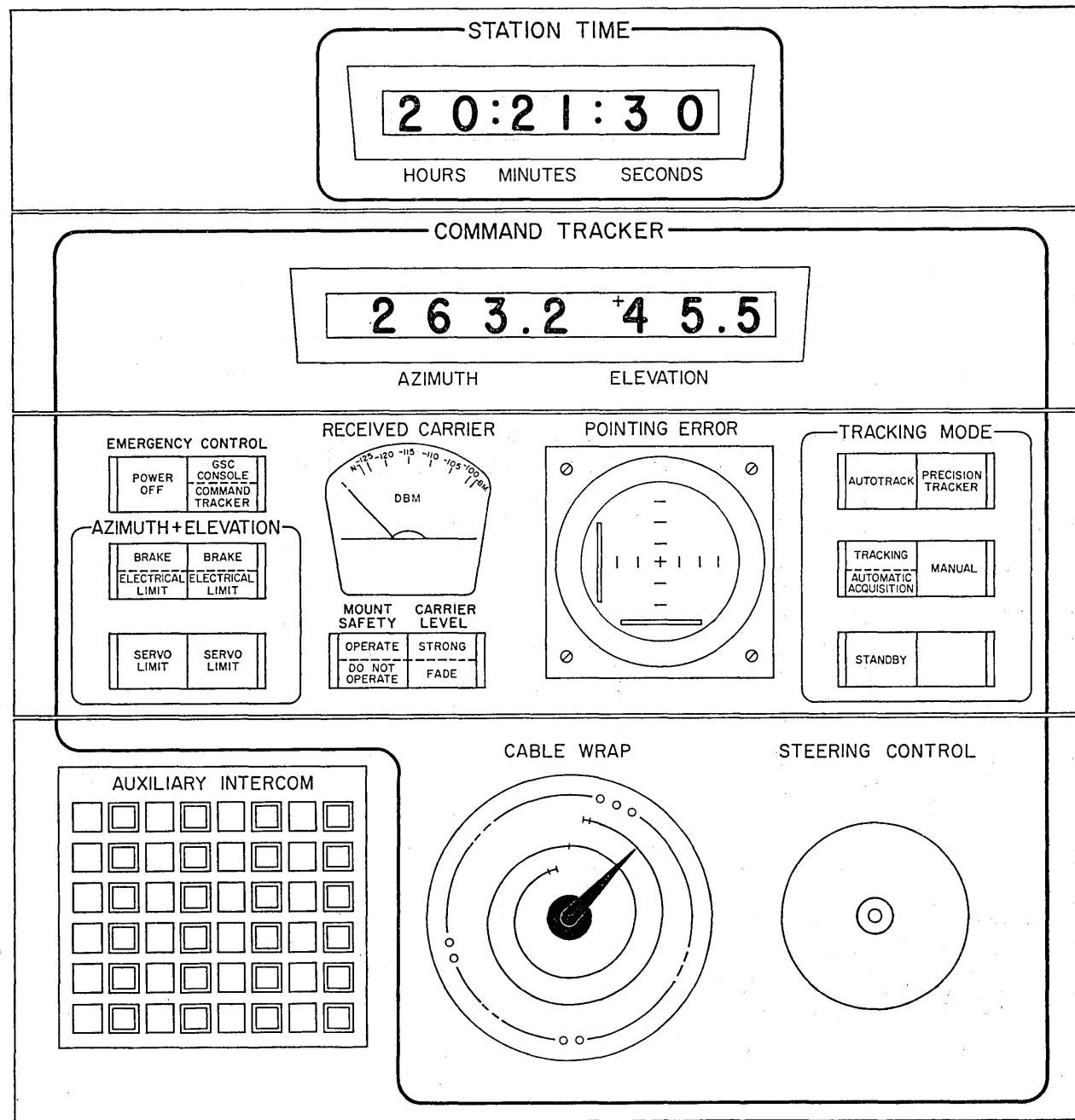
STATION TIME

2 0 : 2 1 : 3 0

HOURS   MINUTES   SECONDS

COMMAND TRACKER

2 6 3 . 2   +4 5 . 5

AZIMUTH   ELEVATION

EMERGENCY CONTROL

POWER OFF	GSC CONSOLE
	COMMAND TRACKER

AZIMUTH + ELEVATION

BRAKE	BRAKE
ELECTRICAL LIMIT	ELECTRICAL LIMIT
SERVO LIMIT	SERVO LIMIT

RECEIVED CARRIER

DBM

MOUNT SAFETY   CARRIER LEVEL

OPERATE	STRONG
DO NOT OPERATE	FADE

POINTING ERROR

| | + | | |

TRACKING MODE

AUTOTRACK	PRECISION TRACKER
TRACKING AUTOMATIC ACQUISITION	MANUAL
STANDBY	

AUXILIARY INTERCOM

CABLE WRAP

STEERING CONTROL

TELEMETRY

5 6 7
4
3
2 1 12
CHANNELS TLM-A

TLM-A   6KMC IF AGC   CMD RCVR AGC   TLM-B

8 9
10
11
5 13
3 14
CHANNELS TLM-B

TLM SEARCH   TLM WORD SYNCH   TLM VALID SYNCH   CUEING

SATELLITE OPERATING LIMITS

SET	NORMAL	ON	CLOSED	CLOSED	ON	IN LIMITS	NORMAL	OFF	IN LIMITS	IN LIMITS	IN LIMITS
TRIPPED	OUT OF LIMITS	OFF	OPEN	OPEN	OFF	OUT OF LIMITS	OUT OF LIMITS	ACTIVE	OUT OF LIMITS	OUT OF LIMITS	OUT OF LIMITS
CANISTER PRESSURE	BATTERY TEMP	TWT FILAMENT VOLTAGE	HELIX RELAY STATE	ANODE RELAY STATE	4KMC BEACON	6 KMC RCVR IF AGC	COMMAND RECEIVER INPUT	ATTITUDE CONTROL FL(2)ST(1)	TWT COLLECTOR TEMP	09 CASE TEMP	01 CASE TEMP

SATELLITE COMMANDS

OPERATING CONTROL

COMMAND TELEMETRY

GSC CONSOLE	RECORD
COMMAND ENCODER	STANDBY

SEQUENCING

AUTOMATIC	MANUAL OVERRIDE
MANUAL	PARITY ALARM

CONTROL ACTIVE	TURN ON	WAIT TURN ON	WAIT TURN ON		TURN ON	TEST VHF BEACON ON	TURN ON	TLM ENCODER 1 ON	TLM ENCODER 2 ON
ENABLE									

| | VHF BEACON (S) | FILAMENT VOLTAGE (A) | HELIX VOLTAGE (B) | ANODE VOLTAGE (C) | | TELEMETRY (D) | TOWER (F) | SAT ATTITUDE CONTROL (E) | SWITCH ENCODERS TEST COMMAND RCVR. |

CONTROL ACTIVE	TURN OFF	TURN OFF	TURN OFF	TEST VHF BEACON OFF	TURN OFF	COMMAND RCVR 1 TEST	COMMAND RCVR 2 TEST
EMERG. OFF							

TRANSMITTER

POWER

OUTPUT GOOD	TELSTAR
MARGINAL	RELAY

SELECTION

OPERATE	STANDBY

PRECISION TRACKER

TRACKING MODE

MANUAL	TRACK ENCODER GROUP	COMMAND TRACKER	AUTOTRACK

MISSION STATUS	RECEIVED SIGNAL	COMPUTER OUTPUT MODE
TRACK FOR GSC	GOOD	ENABLE
SEPARATE SCHEDULE	MARGINAL	INHIBIT

COMPUTER A

OUTPUT MODE

FIRST POINT	MISSION TAPE	PRECISION TRACKER	EXTRA-POLATED

PRECISION TRACKER	COMPUTER CONFIDENCE	OUTPUT CONFIDENCE
DATA GOOD	GOOD	GOOD
POOR	POOR	POOR

COMPUTER B

OUTPUT MODE

FIRST POINT	MISSION TAPE	PRECISION TRACKER	EXTRA-POLATED

PRECISION TRACKER	COMPUTER CONFIDENCE	OUTPUT CONFIDENCE
DATA GOOD	GOOD	GOOD
POOR	POOR	POOR

MANUAL TIME OFFSET

+ 0 0 2

MIN.   SECONDS

ALARM CUTOFF

CONSOLE PEN RECORDER

MM/SEC	SPEED 2	SPEED 5	SPEED 10
CM/HR			
STOP	SPEED 50	SPEED 125	SPEED 250

Fig. 8 (This page and overleaf)—Front panel layout of ground station control console.

COMMUNICATION ANTENNA

```
2 6 3 . 5 9          0 4 4 . 3 2
```
AZIMUTH POSITION   ELEVATION POSITION

```
0 0 0 . 0 2          +0 0 0 . 0 4
```
MANUAL AZIMUTH OFFSET   MANUAL ELEVATION OFFSET

| -- | - | + | ++ |

| AZIMUTH RESET | ELEVATION RESET |

| -- | - | + | ++ |

VERNIER AUTOTRACK

```
0 0 0 . 0 3          +0 0 0 . 3 2
```
AZIMUTH CORRECTION   ELEVATION CORRECTION

FREQUENCY CONTROL

| VERNIER AUTOTRACK |
| PRECISION TRACKER |

INTEGRATED CORRECTIONS

| VAT III INSERT | VAT I INSERT | HOLD | RESET |

RECEIVER STATUS

| PHASE-LOCK |
| FREQUENCY SEARCH |

ERROR SIGNAL

| SAFE RANGE |
| LIMIT WARNING |

COMMUNICATION

POINTING ALARM

| SAFE |
| UNSAFE TO TRANSMIT |

TRANSMITTER

| CARRIER ON | STANDBY | CARRIER OFF |
| | | OUT OF SERVICE |

RECEIVED CARRIER

| GOOD |
| MARGINAL |

ANTENNA CONTROL

MAIN INTERCOM

SPIRAL SCAN

| INITIATE FAST | INITIATE SLOW | RESET |
| HOLD | HOLD | |

DATA INPUT

| ACCEPT | NORMAL SOURCE |
| REJECT | ALTERNATE SOURCE |

ACE OPERATION

| GSC CONSOLE HORN CRADLE | ACTIVE | STANDBY |

MONITOR

| RECORD | STANDBY |

| 28V FUSE A |
| 28V FUSE B |

| 48V FUSE | CONSOLE POWER |

| ACE MODE PROGRAMMED | INTERCOM RECORD |
| ACE MODE PT DRIVE | INTERCOM STANDBY |

STATION TIME

```
2 0 : 2 1 : 3 0
```
HOURS   MINUTES   SECONDS

EVENTS CHANNEL 1   EVENTS CHANNEL 2

| VAT X (DB) | VAT Y (DB) | VAT Z (DEG) | GR AGC (DB) | TRAVS Δ (DEG) | ELEV Δ (DEG) | CT AGC (DB) | CT FREQ Δ (KC) |

| CHANNEL 1 | CHANNEL 2 | CHANNEL 3 | CHANNEL 4 | CHANNEL 5 | CHANNEL 6 | CHANNEL 7 | CHANNEL 8 |

LOCAL
STANDBY
REMOTE

TEST MAST

| 136 MC BEACON | TIMER ACTIVATED | TOWER SATELLITE ACTIVE | AUX 4 KMC BEACON ON |
| | | | BORESIGHT BEACON ON |

| MISSION STATE | ACE SLEWED TO TOWER | ORDER WIRE CONTROL | RADIO LINK DISABLED |
| TEST STATE | | | DECODER LOCKED |

LAMP TEST

OP   OP

	A, B1		-		1
	B2		+		2
	B3, B4				3
DIGITS   4
FLASHER   C   9 8 7 6 5

This afforded visual confirmation by illumination of the control when an action was effected. All status indicators were arranged to be lighted by contact closures at the applicable system so that only confirmed status would be displayed. Wherever possible, a satisfactory condition would be shown by positive information (a lighted indicator), rather than by the lack of a warning signal.

Color coding for indicators was assigned on the following bases:

1. *White* was used for display of active equipment status or to confirm the execution of a simple, mutually exclusive GSCC command.

2. *Green* was used to signify that operation is normal and within limits or, on a control, that a binary command which is necessary in the acquisition-tracking process has been executed by the interconnected subsystem.

3. *Amber* was used to indicate that a function necessary to the acquisition-tracking process remains to be executed or requires attention by the controller. When flashing, the amber indicator was to denote a mild warning that a function of some urgency requires attention.

4. *Red*, when steady, was used to warn the operator that a control action is prohibited or that a vital function is in an unsatisfactory, nearly critical condition. Flashing red was reserved for emergency and alarm situations that required immediate action by the controller. Flashing red indicators were arranged also to trigger an audible alarm and to remain ON until acknowledged by the controller. When warranted, steady red controls were provided automatic interlocks to prevent effecting the prohibited action until the improper status had been cleared.

The color-coded status displays were selected so that they (*i*) prevented overlooking any essential steps in the acquisition, activation and tracking processes and (*ii*) gave the ground station controller confirmation at a glance (only green and white displays showing) that all conditions were normal once the communications link was established. This made it possible for the controller to direct primary attention during transmission experiments to the recorded traces on the strip chart or to specific satellite operating parameters.

Operational experience, after the Telstar launch, confirmed that for normal passes all necessary ground station controller responsibilities could be carried out by a single competent operator at the GSCC. Two operators could adequately handle the position under even the most unusual command or tracking experiments that were scheduled. It was also demonstrated that the position could be shared by three operators in a quite satisfactory manner, which was very convenient for collecting specific data on tracking performance during early operations and for training new controllers.

3.3.2 *Communication and Director Consoles*

In conducting transmission experiments via the satellite, it is nec-
essary that close coordination be maintained with the ground controller
and with participating external stations while concurrently monitoring
the test signals sent and received. The communication console was there-
fore located adjacent to the GSCC so that key displays could be shared
and critical interactions could be accomplished expeditiously and effi-
ciently. A separate test center was provided as well, instrumented
essentially as both a television operating center and a toll test board.
Duplicate facilities were provided so that either the communication
console or the test center could control, through a video and an audio
crossbar switch, the connection of baseband inputs to the communication
transmitter and outputs from the communication receiver.

For dynamic evaluation of the working outputs at the video switch,
the communication console was instrumented with three commercial-
type picture and waveform video monitors. One of these displays the
selected outputs for transmission on the satellite up-path, another the
received picture on the satellite down-path, and the third any available
picture input such as that received over land-line circuits from the
Holmdel station. For control of the video, a pushbutton matrix was
installed on the console whereby any one of 10 transmission and test
input signal channels may be applied to any one of 10 output channels.
Associated audio, where applicable, was made available to the operator's
headphones via a separate group of 10 pushbuttons on the console. In
addition, several auxiliary control and status features were provided,
such as those for interposition and external communication and those
for selecting between the three available video standards for display
generation.

The director console was designed to give a general view of the prog-
ress of operations and to provide flexibility in communicating with
external participating stations prior to, during, and upon completion of
a mutual experiment. For convenience, many of the individual status
displays at the GSCC were provided to the director console in multiple.
The only controls provided to this position were those associated with
the intercom system and a mission time counter. This counter provided
a display of time relative to the expected rise of the satellite, in minutes,
from up to 99 minutes before the epoch until 99 minutes after the epoch
had occurred. This display was used by the controllers and operators
as the main reference for cueing during operations in that it was a more
convenient display for the purpose than conventional station time.

The consoles for the controllers and the director were each provided

with direct access to the voice telephone circuits interconnecting ex-
ternal participating stations for operational coordination purposes. Also,
the consoles were given access to the local PBX, intercom and paging
systems. This arrangement allowed nearly complete freedom among the
three positions for exercising supervisory responsibilities and for pre-
venting overloads or coordination delays. The local intercom was de-
signed to include two conference loops with appearances at all operating
positions, and four maintenance loops with appearances at certain
operating and related maintenance points. The conference loops were
engineered for monitoring by each operator at all times desired, with
freedom to talk simultaneously over this or another selected circuit.
During operational missions, one conference loop is normally monitored
by all operators as the primary coordination channel, and the other is
used to handle any lengthy interchanges that may become necessary
between two or three positions during the mission. Standardized station
designations, push-to-talk, and a modest set of rules are imposed as
circuit discipline for the conference loops.

IV. POWER FACILITIES

The Andover earth station, fully equipped with several communica-
tion systems, would require about 1000 kw of 60-cycle alternating current
to energize rectifiers in the technical equipment and loads such as motors,
lights and other utilities. Present load at the station is about one half
the anticipated maximum load. There are two sources of this current.
One source is commercial service from the local public utility company.
The second source is a self-contained prime power plant equipped with
diesel engine-generator sets.

The earth station loads are divided into the categories of technical
loads and utility loads. Among the technical loads, examples include
power for electronic equipment: rectifiers for tracking equipment, an-
tenna control equipment, computers, receivers, transmitters, video
monitors, tape recorders, and 60-cycle servomechanisms; and for pri-
mary essential services: motors for the main antenna drive, motor gener-
ators for 400-cycle servomechanisms, compressors for the maser cryostat,
air conditioning and lighting for movable rooms on the main antenna
structure, and blowers for equipment cabinets. Among the utility loads,
examples include power for various secondary essential services: lighting
circuits and convenience outlets in the control building and for stationary
rooms in the main radome, motors and controls for building heating and
air conditioning equipment, blowers for pressurizing the main radome

(see below), and dc power plants with battery stand-by for alarms and carrier telephone facilities.

The general plan for distribution of current to these loads is shown in Fig. 9. The service reliability criterion influenced greatly the choice of power switching circuits, the choice of the engines, the plant operating procedures, and the switchgear operating sequences.

The Andover plant is presently operated as a hybrid prime power installation with commercial service used for both the technical and utility busses during stand-by periods. During an experiment, even a brief interruption on the technical bus is unacceptable. A short interruption on the utility bus is undesirable, but tolerable.

The power-plan circuit in Fig. 9 is shown in the normal operating condition which obtains during a satellite communications experiment. Generators A and B are in parallel, delivering energy through the generator circuit breakers A and B, and the tie breaker AB to the technical bus. The utility bus is energized from the commercial service through circuit breaker K1B. When an interruption occurs in the commercial service, breaker K1B is opened and breaker 2B is closed, so that the engines feed both busses. If one engine fails during normal operations, the other engine can carry the load on the technical bus. If an engine
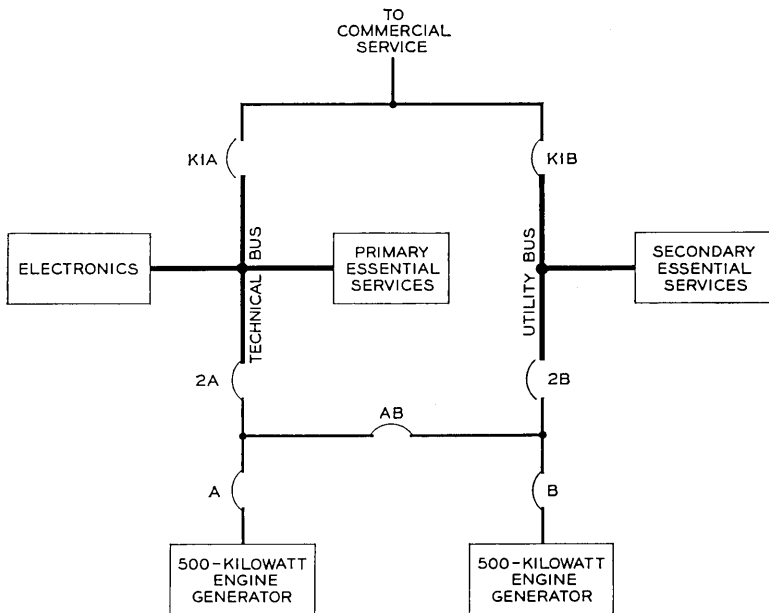
Fig. 9 — General plan for distribution of power.

fails during a commercial failure, the remaining engine will carry the entire load on the technical bus plus part of the load on the utility bus.

The engine-generators are rated at 500 kilowatts, 900 rpm, and are of the type procured by the Bell System for stand-by service in central and toll offices. The choice of this particular machine was dictated primarily by load demand, although a single larger engine could have been used to carry the total station load. The use of two 500-kilowatt machines gives greater flexibility for growth, and for higher reliability than would be obtainable with a single machine. Also, a considerable backlog of experience has been built up with this particular set, and its proven performance in other prime power applications makes it a preferred choice.

An axiom derived from Bell System power plant experience is that the probability of occurrence of operator error is highest during the first few minutes of an emergency such as a power failure. Therefore, power plant operator procedures are arranged so that most failures of the types expected to be encountered do not require immediate action on the part of the operator. Thus, if commercial service fails, the operator is relieved of pressure to restore utility bus voltage by the fact that immediate restoration is not necessary, by definition, on the utility bus. Similarly, if one of the engines fails, the operator is relieved from pressure by the fact that one engine can carry the technical bus load indefinitely. Of course, engine circuit breakers are depended upon to clear overloads due to faults or current reversals.

It will be noted that the blowers for pressurizing the main radome are fed from the utility bus. This is the one load on the utility bus for which a power failure of a few minutes duration could be a hazard. Consequently, the motor control center for the blowers can be energized from a small 30-kilowatt, automatic-start diesel generator, located at the radome, as well as from the utility bus. This arrangement gives protection against failure of the utility bus or any of the switchgear associated with the bus, for more than a few minutes.

The reliability features in the power system have proved to be well worth-while. Operating records show that there were six interruptions in the commercial service in 1962, four of which occurred after the Telstar satellite was launched. One of these interruptions caused a loss of system power long enough to disturb seriously a communications experiment. In addition, there have been partial and full power failures due to operator errors and training sequences, but these failures were anticipated as an unescapable part of the installation and familiarization program. Analysis of the causes of these failures has confirmed the sound-

ness of the plan to minimize pressure on the operator during an emergency.

V. AIR CONDITIONING AND HEATING

The Andover site, located in a remote section of Maine, experiences some of the most severe environmental conditions in the United States. In order to communicate with a satellite orbiting in space, precise control of the 380-ton antenna[1] is essential at all times. To reduce mechanical deviations which might be expected from snow, ice, wind and large fluctuations in temperature, the entire antenna is housed in a large air-inflated plastic radome. The inside of the radome requires heating to prevent the accumulation of ice and snow on the outside surface of the radome. It also requires dehumidification to avoid damage to equipment through rain, fog or condensation within the radome.

In addition to the radome, the two rooms which house transmitting, receiving and tracking equipment are part of the rotating antenna structure and require heating and cooling for both equipment and personnel.

Heating and cooling for the utility building adjacent to the radome foundation and the control building presented no unusual problems and will not be discussed in this paper.

5.1 Radome Heating and Deicing

The use of a protective radome created a number of engineering problems. Controlled heating of the inside air is needed to prevent ice and snow accumulation on the radome which might impair system transmission. The heating system must be capable of maintaining temperatures suitable for both personnel and equipment.

Fig. 10 is a schematic diagram of the closed hot water system used to heat the utility building and to heat and deice the radome. This system originates at the control building where two oil-fired boilers, each with an output rating of 10 million BTU per hour, supply 200°-225°F hot water. The complete output of these boilers is not used at the radome, however, since some 4 million BTU per hour are used at the control building itself. The hot water is piped one quarter mile underground to the radome and utility building where it is distributed by branch piping to the heating coil, room space heaters, and the radome heating-deicing units. The discharge water from these units is directed into return water lines which eventually return the water to the boilers for reheating.

Radome heating and deicing represent two different heat problems.
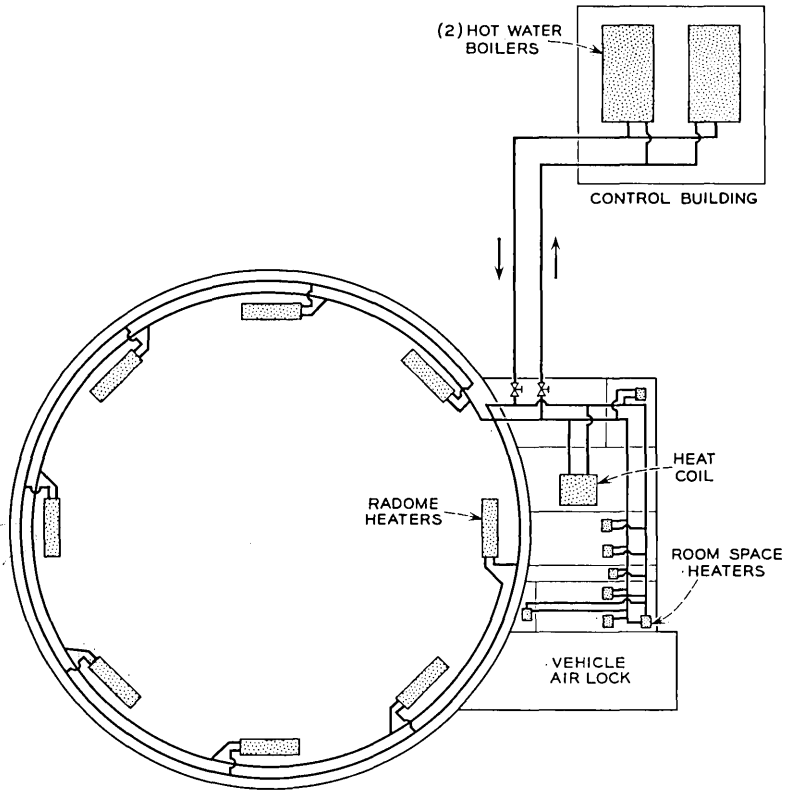
Fig. 10 — Schematic diagram of closed hot water system.

For interior heating it is desirable to direct the bulk of the heat near the equipment and working areas and to minimize heat losses through the plastic type radome. For snow melting and deicing, heat concentration should be at the top and sides of the radome with a maximum heat flow through the radome material being desirable.

In order to design an adequate heating-deicing system for the radome, it was necessary to calculate heating requirements for both heating and deicing. Calculations indicate that 13,551,000 BTU/hr is required for radome heating and that 10,250,000 BTU/hr is required to melt the snow and any ice film on the outside surface. Therefore, radome heating determines the maximum amount of heat to be supplied to the radome.

Although heating is the governing criterion in determining the amount of heat to be supplied to the radome, the distribution of heat is another

problem. The air temperature in the upper portion of the radome must be 107°F to melt snow, and an air temperature of 62°F is required to keep water from freezing on the lower portion. To accomplish this heat distribution, eight radome deicers spaced 45 degrees apart discharge warm air into a plenum chamber through a transition section and into flexible plastic wall ducts. Tap-off ducts, with damper-controlled flow, were designed for scrubbing the lower radome wall. Eight circular plastic ducts were provided; four were designed to extend 50 feet above the radome heaters and four designed to extend eighty feet. The duct openings are directed to provide a scrubbing action over the inner radome surface.

5.2 *Radome Dehumidification*

In addition to radome heating, another problem encountered in using a protective enclosure was radome dehumidification. Provisions for this had to be made in order to avoid damage to equipment through rain, fog or flooding of the concrete base by condensation. Condensation occurs when saturated air is cooled. During the cooling process, the heat losses of the saturated air represent the sum of sensible heat of air and the latent heat of the condensed water.

Considering the radome conditions, if it is assumed that the outside dry bulb temperature is less than the inside dew point temperature, the following conditions can occur:

1. When the inner radome surface temperature is greater than the inside dew point temperature, no condensation will occur.

2. When the inner radome surface temperature is less than the inside dew point temperature, condensation will occur on the radome skin.

3. When the inside dry bulb temperature is equal to the inside dew point temperature, the air will be saturated and condensation in the form of fog or rain will occur within the radome.

In order to prevent the formation of condensation within the radome enclosure, it is necessary to keep the dew point temperature lower than the dry bulb temperature. This can be accomplished by using a dehumidifying coil. The coil can be placed in the incoming air stream and by circulating cold water through the coil, most of the moisture contained in the incoming air can be condensed out. With a chilled water system supplying 40°F water, incoming air can easily be cooled to 45°F. 38.7 tons of refrigeration are required to maintain the proper conditions during the summer.

For winter operation, a thermostatically controlled heat coil, located on the input side of the dehumidifying coil, is used to heat incoming air

above freezing. The heat coil selected is a 2-row Aerofin Coil having the required heat capacity when circulating 13 GPM of 225°F water.

5.3 *Temperature Control in the Equipment Rooms*

The two house-sized rooms, built as part of the rotating structure, require heating and cooling for both equipment and personnel. The upper room, measuring approximately 26 feet by 34 feet by 9 feet high at the walls, is located about 60 feet above the radome floor. This room contains the radio transmitting and receiving equipment. The lower room, located about 10 feet above the floor of the radome, is approximately 24 feet by 68 feet by 9 feet high at the walls. This room contains the antenna drive and control equipment and the power distribution equipment.

Electronic equipment, transistorized and otherwise, operates very efficiently in a stabilized ambient of 60° to 85°F with a relatively low humidity; the majority of people are comfortable at 70°F and approximately 50 per cent relative humidity.   Fortunately, these conditions are not contradictory, and the latter condition was established as the ambient design condition inside both rooms on the antenna structure.

Chilled air is transmitted through a system of ducts for both equipment and personnel cooling. The duct system is split into two parts, one for distributing chilled air to plenum chambers running under each row of equipment cabinets for equipment cooling, and the second for supplying chilled air to outlets in the head space of the room for personnel cooling. Resistance heaters in the personnel supply ducts permit the use of these ducts for heating purposes. Air-handling units mounted beneath the floor of each room, upper and lower, contain the blowers and chilled water cooling units required to supply chilled air to the duct systems.

A source of chilled water was required for the air-handling units and for the water-cooled traveling-wave tube in the transmitter for the Telstar satellite, and also for the klystron used in the transmitter used for experiments with the Relay satellite.

5.3.1. *Equipment Cooling and Personnel Air Conditioning*

The first step in the solution of the equipment cooling and personnel air conditioning problem was to determine the expected climatic conditions from synoptic meteorological records. Expected heat loads and their distribution were established and were categorized as to whether they were sensible or latent. Finally, it was necessary to determine the most

efficient means to dissipate the heat, i.e., by forced cooled air or chilled water, and whether the equipment and personnel cooling systems should be in series, parallel or a combination of both.

Investigation indicated that one of the following three systems for providing over-all cooling and heating would be feasible.

1. A chilled water system for water cooling plus radome air-cooled, self-contained air conditioning units for forced air cooling plus electrical resistance heating.

2. A chilled water system for water cooling plus chilled water air handling units for air cooling plus electrical resistance heating.

3. A chilled water system for water cooling plus water-cooled, self-contained air conditioning units for air cooling plus electrical resistance heating.

Using as an evaluation criterion the basic philosophy of requiring (i) the least weight on the rotating structure, (ii) the least power required, and (iii) the least expense from the standpoint of maintenance as well as first cost, system No. 2 was selected for the Telstar project.

To insure that the heat-transfer surfaces of the traveling-wave tube in the 6-kmc transmitter[2] did not suffer degradation from contamination, the water used in the chilled water system had to be very pure. Copper piping, which has a tendency to kill bacteria and does not add impurities such as rust to the water, was selected for use in the chilled water system. To further insure that the water passing over these heat transfer surfaces was pure, all minerals found in ordinary drinking water in the form of ions and cations had to be removed. This was accomplished by installing a deionizer with a bed of nuclear grade resin in series with a microfilter. The microfilter is capable of removing particles as small as 1 micron. The water obtained by using the copper piping, the microfilter and the deionizer is purer and cleaner than normal drinking water and has an electrical resistance of between 12 and 20 million ohm-centimeters.

Specifying the size and physical requirements of the equipment to be designed or modified requires that a summation of the heat gains and losses be determined for all equipment and personnel locations. Using established design criteria, the heat gains and losses had to be correlated with the existing outside ambient conditions for Andover, as well as for the predicted inside ambient radome conditions. After accumulating this information, a heat balance was made to determine the amount of refrigeration required in the summer and the heating required in conjunction with cooling during the winter. The requirements for refrigeration are summarized in Table II.

TABLE II — REFRIGERATION AND CHILLED WATER FOR UPPER AND
LOWER ROOMS

	Gal/min Water	Tons
Lower room		
Air handler	35	25.2
Klystron for Project Relay	25	11.44
Upper room		
Air handler	24	17
TWT tube	25	7.10
	109	60.74
Dehumidification	60	38
Total	169	98.74

Air handlers having the following characteristics based on the use of 42°F cooling water were selected:

	Lower Room	Upper Room
Cooling capacity	25.2 tons	17 tons
Quantity chilled water required	25 gal/min	24 gal/min
Air temperature drop	20°F	20°F
Air flow capacity	14,000 CF/M	10,000 CF/M

5.3.2 *Refrigeration System*

To insure reliability in this system, multiple smaller-sized refrigeration components are used instead of one large unit. The main components of the water system are two chillers, each having four compressors, two centrifugal water pumps, four condensers, a deionizing unit, two air handlers, four receivers, and a dehumidifying coil. The majority of these components are installed in the utility rooms at the base of the radome, external to the pressurized area.

The refrigeration system uses four refrigeration circuits. If one circuit fails, maintenance can be completed without affecting the other three circuits. Each refrigeration circuit consists of two compressors, one air-cooled condenser, a liquid freon receiver, and associated refrigerant valves. The nominal capacity of the four circuits is 100 tons of refrigeration.

Integral with each refrigeration circuit is an air-cooled condenser located on the roof of the utility building. Again reliability was a contributing factor in the selection of this type condenser. The severe winter

conditions in the Andover area made it necessary to pick a unit with simple controls requiring a minimum of maintenance. The air-cooled condenser is preferred over the evaporative type of condenser or cooling tower because air instead of water is used to dissipate heat.

5.3.3 Chilled Water System

The requirement for reliability indicated the need for more than one high-pressure pump for circulating chilled water. Failure of the operating pump requires that the standby pump must start automatically and immediately. As a result, the pumps were supplied with automatic back-flow check valves at the supply end of each pump. This insured no loss of pressure due to flow through the idle pump but of course increased the flow pressure on the output of the other pump. The requirement that the traveling-wave tube, inherently a high-flow resistance device, be used in parallel with a low-flow resistance unit such as an air handler, required special valves in conjunction with regular valves, which increased the over-all flow resistance of the system.

Two high-pressure pumps, each having a flow capacity of 230 gallons per minute when pumping against a head pressure of 231 feet of water (93 psi), were installed. The chilled water flow path starts at the operating pump and passes through the two chillers operating in parallel. These chillers cool the return water to 40°F. The water is then forced through a 4-inch, cork-insulated copper pipe. At the center of the antenna, the pipe size is reduced to 2 inches prior to passing through the rotary joint. (Water flowing from a stationary component onto a rotating structure, such as the antenna, requires a leakproof rotary joint, illustrated in Fig. 11.) The chilled water then passes through one cavity of the rotary joint onto the antenna, where it is diverted to several branches of fiberglass insulated pipe which carry it to the upper and lower rooms. At these rooms the chilled water is distributed to the TWT, klystron tube and air-handling units.

The requirement for very pure water also dictated that the chilled water system be a closed one. Therefore, the return water passes through the second cavity of the rotary joint and back to the pumps. A portion of the chilled water is used to dehumidify the air used to inflate the radome.

The selection of a deionizer was based upon an established standard that a deionizer have sufficient capacity to handle at least one per cent per minute of the total gallonage in the system. A deionizer with a capacity of 6 to 20 gallons per minute was selected.
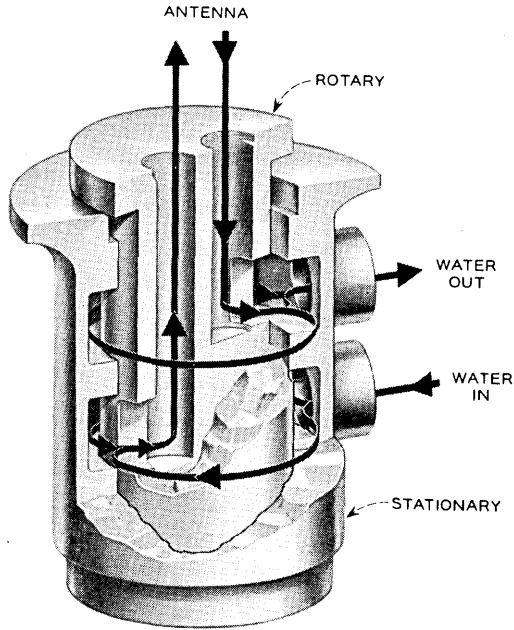
Fig. 11 — Rotary joint for chilled water system.

5.3.4 *Heating of Equipment and Personnel Areas*

To establish a stabilized air conditioned area for personnel in both the upper and lower room requires that heat be added when the radome temperature is between 40° and 50°F. Since both the rooms are on the rotating structure, a great advantage can be derived in using an electrical resistance type of heat, as no storage tanks are required and the heat is "clean." Assuming that the radome temperature surrounding the lower equipment rooms is 45° and knowing that the personnel area is to be maintained at 70°F, there will be a loss of heat from the room to the radome. Part of this heat loss is offset by warm air discharged from the equipment and by heat radiated from the lights and personnel. Additional heat, however, must be added to the air being supplied directly to the personnel area in order to maintain the desired 70°F room temperature. A summary of the heat losses indicates that 19.7 kw is required in the lower room and 15 kw is required in the upper room to maintain design temperature of 70°F.

5.3.5 Duct and Control System for Equipment Rooms

The duct system used for both upper and lower rooms is made of aluminum. In these rooms, it was desirable to keep background noise levels as low as possible. In order to achieve this with the air flow required, the ducts had to be not only thermally insulated but also insulated acoustically with all ninety-degree duct turns vaned. This was accomplished by using a 1-inch fiberglass thermal insulation in conjunction with a simulated horse hair acoustical absorbing material, both of which were attached to the inside of the ducts. Control of the air distribution was accomplished by using strategically located manual dampers, along with adjustable air diffusers and registers. Due to the limited space available in both the upper and lower equipment rooms, the associated air handlers were suspended in a centrally located area under each room. This also helped to reduce the noise level inside the rooms. A system of catwalks and platforms provides access to the air handlers for maintenance purposes. Transmission of vibration to the antenna structure and rooms was reduced by mounting the air handler units on vibration isolators. To further reduce noise and vibration transmission through the ducts, canvas boots were used to attach both supply and return ducts to the air-handling units.

The duct system was designed so that the air handler associated with a specific room cools both the personnel area and equipment. This meant that the unit had a common return and supply duct. The supply duct was branched under the room floor to feed cool air to distribution ducts and equipment plenum chambers running under each row of equipment cabinets.

The personnel area branch duct feeds a portion of the cooled air to the distribution duct system located in the head space of the rooms. The temperature of all cool air leaving the air conditioning unit is controlled by a by-pass damper box. This box is located on the return side of the air handler and is controlled by a thermostat in the supply duct in front of the unit. This adjustable thermostat, usually set for 60°F air, modulates the flow of air across the cooling coil of the unit. If the outgoing air is too warm, the dampers direct more return air across the coil; if the air is too cold, most of the air by-passes the cooling coil.

The air temperature in the personnel space is controlled by a thermostat. This instrument is located in the personnel return air duct in the room just prior to the point where the equipment and personnel return air ducts combine into a common return duct. The thermostat controls the resistance heaters, which can add heat in increments of 2.5 kw in the

upper room and 3.3 kw in the lower room up to totals of 15 kw and 20 kw, respectively.

VI. EXTERNAL COMMUNICATIONS REQUIREMENTS

An extensive communications network involving some 86 circuits was provided between the Andover earth station and various U. S. and European locations by the Long Lines Department of the American Telephone and Telegraph Company. Its purpose is to provide operations control and coordination, tracking and telemetry data exchange, and interconnection for remotely originated tests and demonstrations. The facilities used include voice, teletypewriter, data and video channels.

Access by the Andover station to the nationwide radio relay network was attained by the construction of four links of microwave radio relay between Andover and Portland, Maine. In addition, a 150-pair cable was placed between Andover and Rumford, Maine, where it connected with existing cable facilities.

On July 10, 1962, all connecting circuits with Andover were involved in the initial tests and demonstrations. For the first four months after launch, these facilities were used regularly for nearly 400 demonstrations and remote tests.

6.1 Support Communications

Control and information circuits were provided to coordinate station operations and to exchange tracking and telemetry data between Andover and other Bell Laboratories, NASA, A.T.&T. Co., and overseas locations. Figs. 12 and 13 show these circuits, consisting of 7 full-period voice circuits, 5 order wires, 3 DATA-PHONE and 5 teletypewriter circuits.

The voice circuits interconnect Andover with the several Bell Laboratories locations in New Jersey and at Cape Canaveral, as well as with the French and British earth stations at Pleumeur-Bodou and Goonhilly. The order wires interconnect with A.T.&T. Co. Long Lines Department plant operating centers for the coordination of carrier telephone, radio relay and television channel usage to and from Andover.

DATA-PHONE circuits between Andover and the Murray Hill and Whippany Laboratories and the French station were established to transmit antenna pointing data to Andover and Pleumeur-Bodou and to return satellite telemetry information from Andover. These circuits transmit digital data at 1200 bits per second between commercial magnetic tape data terminals.
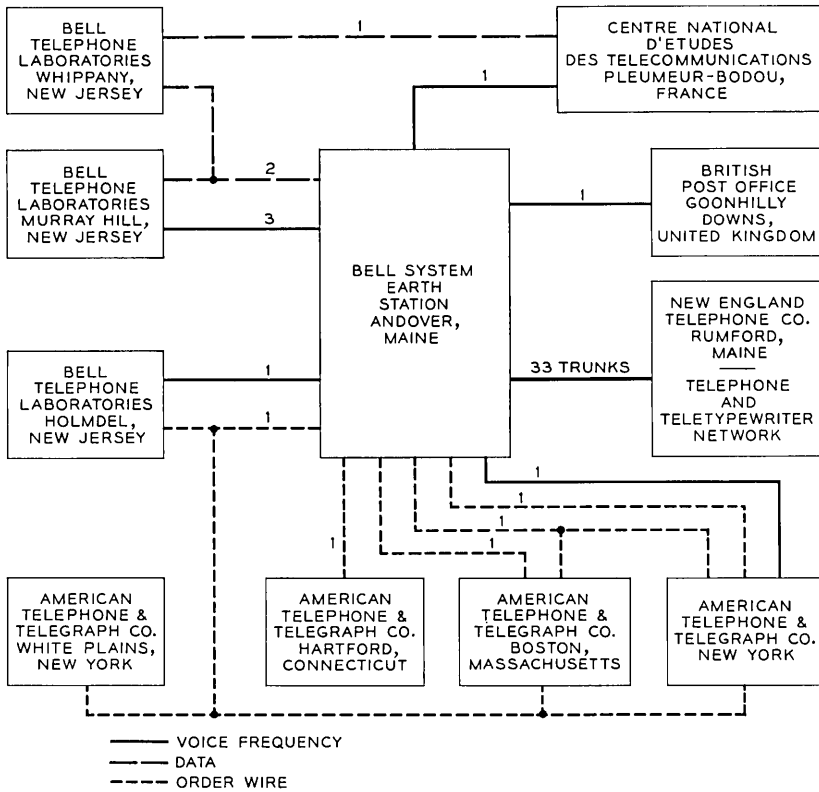
Fig. 12 — Voice-frequency, data and order wire connections with Andover.

Teletypewriter circuits to carry scheduling information, operations messages, orbital tracking data and administrative traffic were installed between the Andover station and NASA Goddard Space Flight Center, Bell Laboratories computing center and operations offices in New Jersey, and the British and French stations.

As shown in Fig. 12, local trunks from the Andover station interconnect with the message telephone network at Rumford, Maine. These serve the local administrative needs of the station and include 10 inward and 10 outward dial trunks through the station PBX, a TWX trunk, 2 public coin box lines and 10 miscellaneous local trunks.

The basic test and demonstration network, consisting of 24 voice-grade channels, 2 telephoto circuits and 2 video channels in each direction, is shown in Fig. 14. These facilities were used for demonstrations
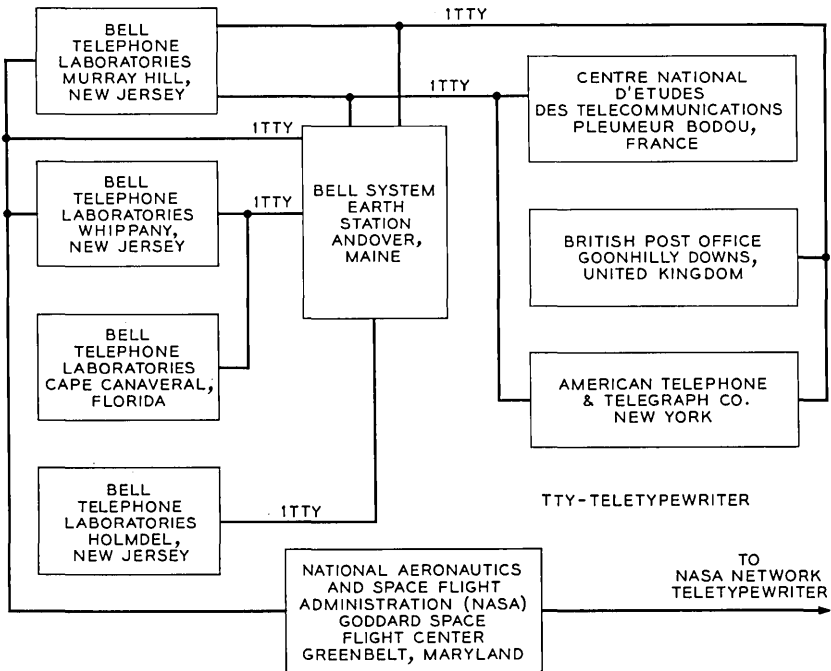
Fig. 13 — Teletypewriter connections with Andover.

and for conducting data transmission tests at the A.T.&T. Co. Long
Lines Department headquarters in New York City. In addition, a pair
of video channels and a telephoto circuit were provided from the Bell
Laboratories Holmdel, New Jersey, receiving station to New York for
test and demonstration use.

6.2 Radio Relay and Cable Access Links

New broadband facilities were required to link the Andover station
with the existing Bell System radio relay network to handle video and
multiplex telephone channels. The nearest junction point was Portland,
Maine, approximately 90 miles south of Andover. Microwave radio
relay links of TD2 (4 kmc) and TJ (11 kmc) were constructed in tandem
between Portland and Andover. Since the satellite-to-ground signal is
at 4170 mc and the ground-to-satellite signal is at 6390 mc, it was de-
cided not to employ either TD2 (4 kmc) or TH (6 kmc) systems for the
first external microwave links out of Andover. Therefore, a TJ (11 kmc)
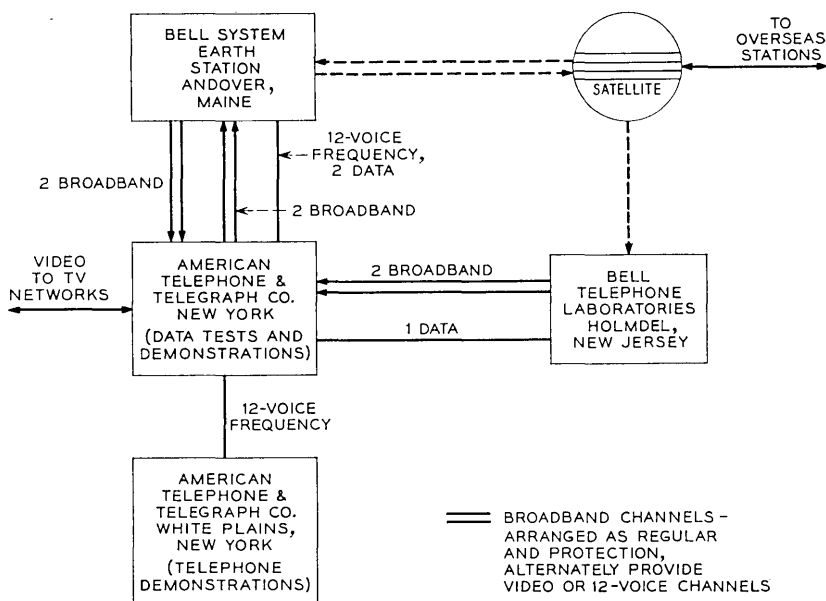
Fig. 14 — Test and demonstration network.

system was selected for the first two links. A coaxial cable system would have been free of interference but was economically impractical because of the mountainous terrain. The first microwave repeater station was located 4.5 miles south of the Andover station atop Black Mountain, on the rim of the "Andover bowl." Beyond the second link a TD2 system was used. The combination of the ring of mountains forming the bowl, the physical distance, and the bearing of the paths reduce to inconsequential levels any stray signals between the repeater stations and the Andover site. From this point to Portland, Maine, where connection was made to the existing TD2 microwave network, normal engineering criteria were used. The over-all route is shown in Fig. 15.

Two radio channels, one regular and one protection in each direction, were provided between Andover and Portland. They were each equipped to handle a 4-mc video signal with the corresponding audio signal provided by a diplexing arrangement using a subcarrier inserted above the video band. Channelizing equipment to permit transmission of 12 two-way telephone circuits instead of the video signals was also installed.

In addition to wideband facilities, voice-frequency cable circuits were provided to handle the support communications requirements. Sixty-one
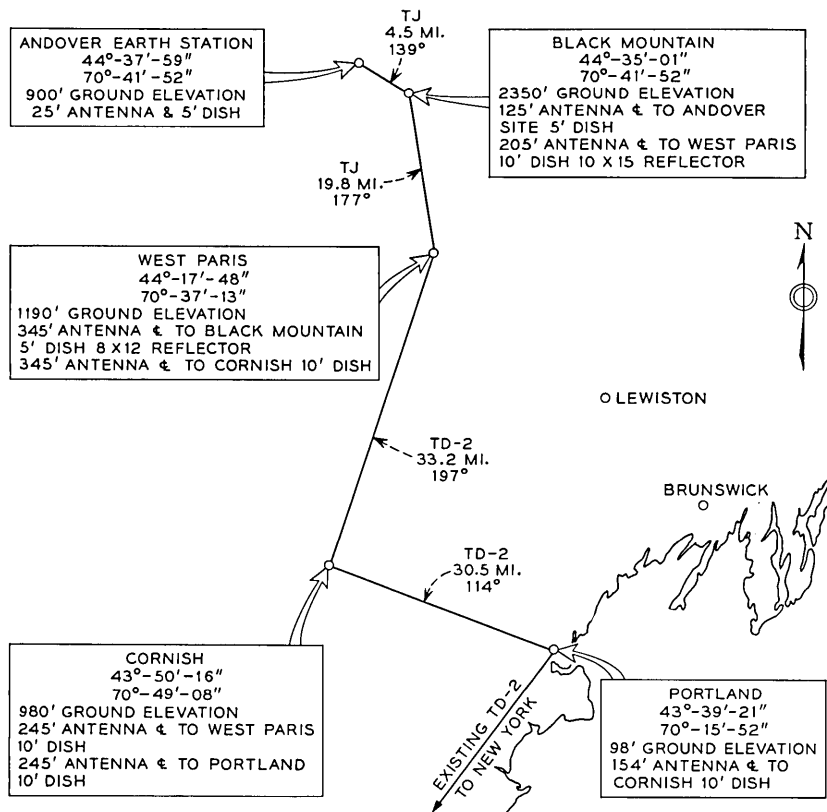
Fig. 15 — Overland route to Portland.

pairs of a 150-pair 19-gauge cable, planned to serve the area north of Rumford, Maine, were extended into the Andover site by the New England Telephone and Telegraph Company. Voice-frequency circuits over this cable were interconnected at Rumford with existing ON carrier circuits to Portland. Later, the ON carrier system was extended directly to Andover to provide 24 direct Andover-Portland circuits.

VII. EXPERIMENTAL DEMONSTRATIONS

Eight special networks were established for the first demonstrations on July 10, 1962, using the support communication facilities shown in Fig. 14.

A closed-circuit video network was established between Andover, Boston, New York, Holmdel and Washington. The pickup equipment

located at Andover and Washington was provided by Theatre Network Television, Inc., monitors provided in the Andover, Boston, Washington and New York areas made it possible for several thousand people to view the closed-circuit program. In addition, a feed was provided from Andover to New York to feed the program to the ABC, CBS, and NBC television networks.

Vice President Lyndon B. Johnson and Mr. F. R. Kappel, Chairman of the Board of the A.T.&T. Co., spoke between Washington and Andover on the first telephone call using the Telstar satellite. Mr. Kappel spoke via the satellite and the diplexed audio channel. Special program facilities were used to transmit Vice President Johnson's voice to Andover.

Special facsimile, data and telephone circuits also were established for the several initial transmissions. The first facsimile test, a picture of the Telstar satellite, was transmitted during the latter portion of the first usable pass (during the 6th orbit) from the auditorium of the Long Lines

TABLE III — SUMMARY OF *Telstar* DEMONSTRATIONS AND TESTS:
July 10, 1962, to November 22, 1962

Telephone calls		117
Black-and-white TV (to and from Europe) including simultaneous 2-way TV, Andover/France		42
Color TV		5
Facsimile		9
International carriers (6)		126
Telegraph	68	
Data	26	
Facsimile	31	
Telephone	1	
Data		66
42,000 bits/sec (52,000 wpm)	1	
62,500 char/sec computer to computer	1	
875,000 bits/sec (1.4 million wpm)	1	
1,000 wpm—punched tape	3	
Data speed—magnetic tape (1,200 bits/sec)	1	
1,000 wpm—teletypesetter	3	
Clock synchronization to UK	3	
66 wpm—teletypewriter to UK	9	
EKG—recording over DATA-PHONE	1	
Other data tests	43	
Business machine manufacturers (11)		14
Radio broadcast programs		6
Satellite light-route equipment tests and demonstrations— Holmdel/Andover and Holmdel/Holmdel		5
Total		390

headquarters building in New York via the satellite to press locations in New York, Andover, Holmdel and Washington. A press release was prepared on punched paper tape and transmitted at 1050 words per minute during the second usable pass (the 7th orbit) from the visitors' building at Andover via the satellite to the Long Lines headquarters in New York using Bell System DATA-PHONE sets. The message was converted to page copy by a tape reader and printer in New York. Six telephone channels were also established via the satellite during this pass, including circuits connecting via the regular message telephone network to points throughout the United States. Calls were made by government and Bell System officials and members of the press.

Between July 10, 1962, and November 22, 1962, some 390 demonstrations and tests were conducted using the connecting communications facilities to Andover. A summary of the demonstrations is shown in Table III.

VIII. ACKNOWLEDGMENTS

The authors acknowledge with thanks the contributions of Mr. J. L. White and Mr. D. L. Schwemmer of the Long Lines Department of the American Telephone and Telegraph Company and of Mr. W. E. Peterson, Mr. Dona Cauchon, Mr. John Sturm, and Mr. John Cloutier of Bell Telephone Laboratories in the preparation of this paper.

REFERENCES

1. Dolling, J. C., Blackmore, R. W., Kinderman, W. J., and Woodward, K. B., The Mechanical Design of the Horn-Reflector Antenna and Radome, B.S.T.J., this issue p. 1137.
2. Giger, A. J., Pardee, S., Jr., and Wickliffe, P. R., Jr., The Ground Transmitter and Receiver, B.S.T.J., this issue, p. 1063.

Participation of the Holmdel Station in the *Telstar* Project

By WILLIAM C. JAKES, JR.

(Manuscript received January 21, 1963)

The facility for satellite communication studies at Holmdel, New Jersey, was originally established to take part in Project Echo. This paper describes the modifications required to participate in the Telstar experiments and the results obtained during operations from July 10 to November 9, 1962. Reception of television from the satellite was successfully accomplished, studies were made of the signal levels, and the changes with time of the satellite spin rate and spin axis orientation were determined.

I. INTRODUCTION

1.1 *Objectives*

The Holmdel station was originally established in 1959–1960 to carry out communication tests with the passive earth satellite Echo I. A complete description of the station and results obtained during Project Echo are given in Ref. 1. In the summer of 1961 it was decided to take part in the Project Telstar program, and the necessary modifications to the station were begun at that time.

The main objective for Holmdel was to receive an acceptable television picture from the Telstar satellite and relay it back to Andover by land routes for comparison with the original picture transmitted from Andover. The Andover station was also expected to receive a television signal, but it was felt that a demonstration of transmission between two separated points would be meaningful. It was not anticipated at the time that the European stations would be ready by the expected launch date. In addition, having two receiving stations would increase the probability of successful operation.

Secondary objectives for Holmdel operation were:
(a) Measure the 4-gc signal levels to check the satellite transmitted power.

(b) Determine the location of the spin axis of the satellite and the spin rate.

(c) Carry out any other scientific experiments of value.

1.2 *Preliminary Tests*

Before the Telstar launch a number of transmissions were made at 4079.73 mc from Holmdel to Andover via reflections from Echo I and the moon. A 200-watt transmitter was connected to the Holmdel horn-reflector antenna for this purpose. These tests made it possible for Andover to check their tracking capabilities under actual operating conditions. The 961-mc "Project Echo" radar system was used to point the Holmdel horn at the target.

II. SYSTEM DESCRIPTION

The facilities used in Project Telstar were essentially those used for receiving in the Project Echo experiment. The 20-foot horn-reflector antenna was used for reception and modifications were made in the receiving equipment for use at 4170 mc instead of the 2390 mc used in Project Echo. The 18-foot tracking antenna from the radar system was also modified to permit operation with the 4080-mc beacon signal from the satellite. A simplified block diagram of the system is shown in Fig. 1, and the system is briefly described in the following four sections, covering the functions of reception, tracking, optics, and data recording.

2.1 *Receiving System*

2.1.1 *Antenna and Waveguide*

The properties of the horn-reflector antenna are described in detail in Ref. 1. Additional tests were made at 4170 mc before the spacecraft launch, and the resulting characteristics are:

Gain	48.0 db
3-db beamwidth	0.78° (circular polarization)
Projected area	380 square feet
Effective area	274 square feet

As anticipated,[1] a difference in elevation boresighting was noted for CW and CCW circular polarization. The measured value was 0.09°, which compares favorably with the calculated value of 0.10°. Final boresighting was done with CCW polarization, which would actually be transmitted by the satellite.
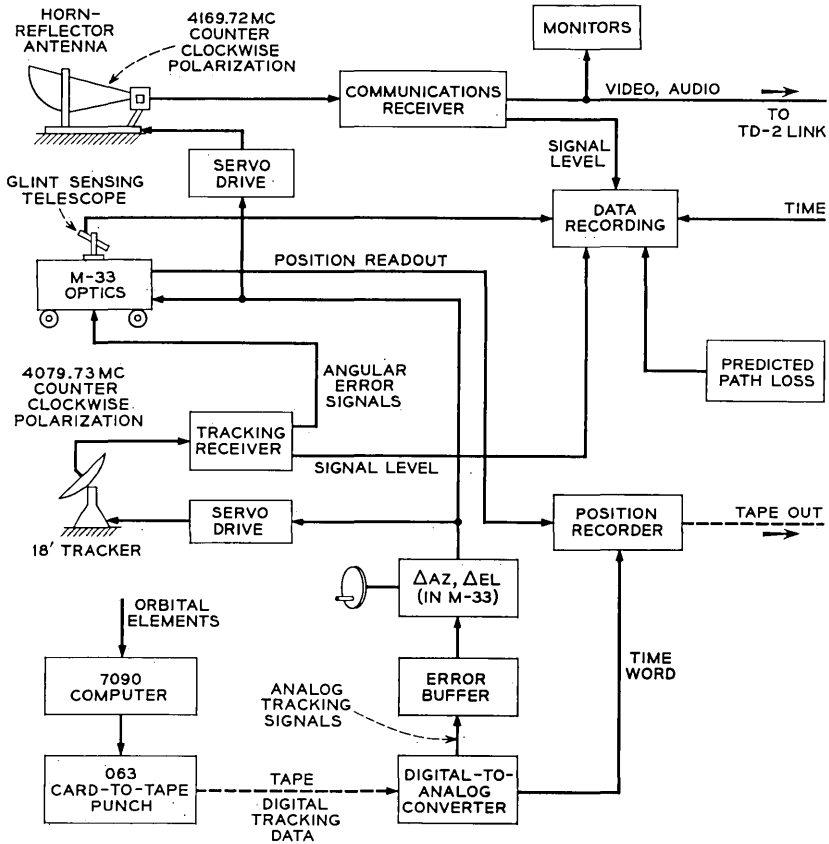
Fig. 1 — General block diagram of Holmdel facilities for Telstar satellite communications experiment.

The horn throat tapered down to round waveguide inside the antenna cab. A low-loss rotating joint was provided between the horn and the waveguide system, which included a 90° phase shifter to convert to linear polarization, a transducer to couple to the maser, and a directional coupler for the introduction of either a noise source or signal source for calibration purposes.

2.1.2 Low-Noise Amplifiers

The first stage of RF amplification was a maser operating at 4.2°K in liquid helium. This was followed by a parametric amplifier cooled with liquid nitrogen, and then by a traveling-wave tube amplifier. The maser

would operate for about 20 hours on one filling of liquid helium, and the paramp for about 10 days on one filling of liquid nitrogen. A certain amount of equalization was provided between the paramp and TWT amplifier to achieve an RF band flat to within ±1 db over 20 mc. This rather elaborate array of low-noise amplifiers was felt necessary in order to achieve a system with the lowest possible noise temperature and capable of operating over the wide band necessary for television reception. Calculations indicated that if all system objectives were realized a good quality picture could be obtained from the satellite out to a range of 5,000 statute miles. In addition, a certain amount of flexibility was provided in that operations could still be carried on at reduced ranges in the event of failure of any one amplifier. The characteristics of the amplifiers are listed in Table I.

The over-all system noise temperature was measured to be somewhat less than 17°K pointing at the zenith, which included about 4.5°K for waveguide losses, 2.5°K sky noise, 2.5°K for antenna side lobes and heat losses, and 5°K for the maser.

The TWT amplifier was followed by a filter to remove the undesired noise sideband, and then a balanced crystal mixer with 70-mc cascode IF preamplifier. The mixer-preamp noise figure was about 11 db. The IF signal was then brought from the antenna to the main control building via a wrap-around coaxial cable for distribution to the various receivers located there.

2.1.3 Television Receiver

The heart of the television receiver was the frequency compression demodulator which was used to obtain an improvement in the S/N threshold. This unit and underlying design principles are described in detail in Refs. 2 and 3 and will be only briefly discussed here. As shown by the block diagram in Fig. 2, the incoming 70-mc IF was up-converted to 263 mc and then mixed with a voltage-controlled oscillator (VCO) to give a 70-mc IF. This signal was then amplified, filtered, limited, and demodulated in a frequency discriminator. The baseband signal was

TABLE I

	Maser	Paramp	TWT
Gain, db	27	31	20
3-db bandwidth, mc	20	30	>50
Noise temperature, °K	≈5	70	625
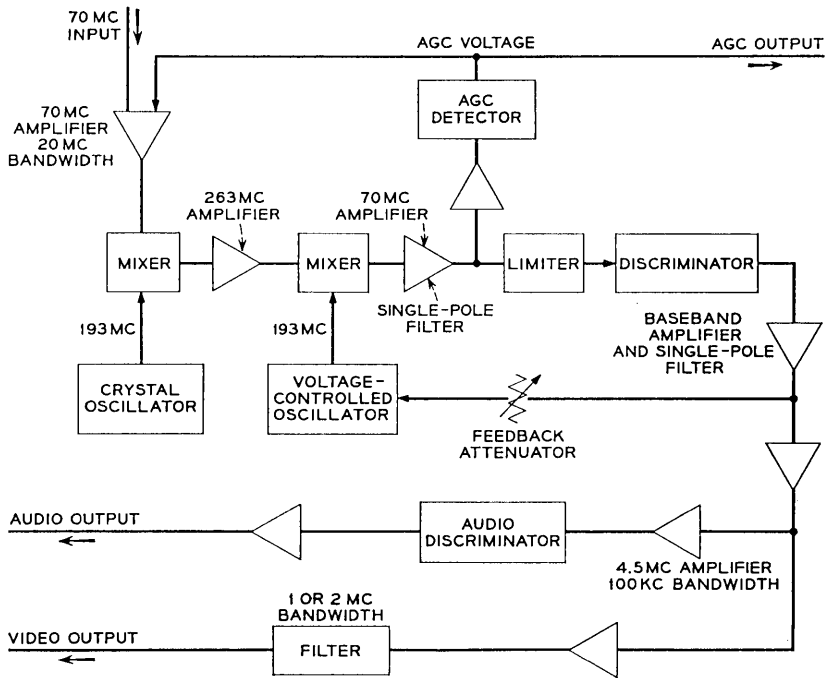
Fig. 2 — Block diagram of frequency compression demodulator.

then amplified, filtered, and applied to the VCO in the proper sense to cause a reduction in the FM index. The baseband signal was also passed on to television monitors for local viewing and to the Bell System microwave relay terminal for transmission to New York City and Andover. The audio portion of the signal was carried on a 4.5-mc FM subcarrier in the baseband, and was separated from the video signal by a filter of 100-kc bandwidth. AGC was supplied by a separate amplifier and detector, and also made available for recording signal strength. The system specifications were:

Video frequency deviation	±7 mc
Audio channel deviation	±0.7 mc
Audio subcarrier deviation	±0.05 mc
Open loop bandwidth	1.0 mc
Closed loop bandwidth	6.7 mc
Feedback factor	12 db
Threshold improvement	5–6 db.
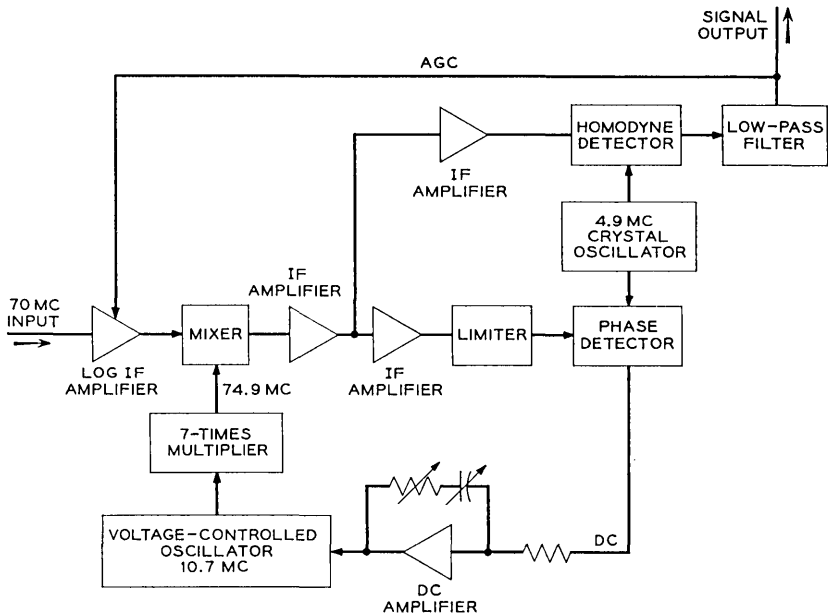
Fig. 3 — Block diagram of phase-locked loop.

2.1.4 *Phase-Lock Receiver*

In order to obtain signal level measurements at times when the signal might be below the threshold of the frequency compression demodulator, a phase-lock receiver was provided with a much narrower bandwidth. Because of the narrow band it was expected that for these tests it would be necessary for Andover to transmit a crystal-controlled, unmodulated carrier.

A block diagram of the receiver is shown in Fig. 3. The 70-mc input was passed through a logarithmic IF amplifier, and then converted to 4.9 mc by mixing with a 74.9-mc signal from the VCO. This IF was amplified, limited, and then phase-detected by comparison with a 4.9-mc crystal oscillator. The output of the phase detector was then passed through a filter to the VCO in the proper sense to cause the VCO frequency to lock in to the incoming frequency. The 4.9-mc IF was also separately detected in a homodyne detector with a low-pass output filter. The output voltage was then recorded for signal level determinations.

Receiver characteristics:

Closed-loop bandwidth   ≈100 cps

Maximum tracking rate   20 kc/sec² for large signal
Signal channel bandwidth   2 kc
Tuning range   ±200 kc.

2.1.5 *Video Relay*

The video baseband signals were connected to standard Bell System video relay equipment in the control building, passed by cable to a microwave relay transmitter connected to a small paraboloid antenna, and transmitted to a nearby TD-2 microwave relay tower for transmission to New York City. The audio portion of the signal was sent by regular land-line circuits.

2.1.6 *Expected Signal Levels*

Ignoring effects such as atmospheric attenuation and tracking errors, the received signal level may be calculated from

$$P_r = P_t G_t G_r \left(\frac{\lambda}{4\pi r} \right)^2$$

where P_t = satellite transmitted power
G_t = satellite transmitting antenna gain
G_r = receiving antenna gain
λ = wavelength
r = slant range.

Two cases were of importance at Holmdel: reception of the 4079.73-mc beacon signal on the tracking antenna, and reception of the 4169.72-mc communications signal on the horn-reflector antenna. For the nominal transmitted power, the expected received levels and S/N ratios are summarized in Table II for a maximum practical operating range of 5,000 statute miles. The receiving system temperature is specified at an antenna elevation of 15°.

The values of S/N ratio given are the worst that would be encountered, since at higher elevation angles the system temperature and slant range both decrease. Taking into account the acceptable operational

TABLE II

Frequency mc	G_t db	G_r db	P_t dbm	P_r dbm	Bandwidth kc	Rec. Temp. °K	S/N Ratio db
4079.73	0	38.9*	13	−130.9	0.1	≈420	21
4169.72	0	48.0	33	−102.0	2000	≈30	19

* Includes cable and scanning loss.

S/N thresholds of 14 db for the television receiver and 6 db for the tracker it is evident that both systems would operate satisfactorily over the major portion of every satellite pass with some margin.

2.2 Tracking at Holmdel

As shown in Fig. 4, the tracking information was principally derived from the predicted satellite trajectory. Corrections were then manually applied during the pass by using the angular error information provided by the beacon tracker. At times when the satellite was close enough to be seen optically the corrections could also be provided by means of the tracking telescope. As a last resort the corrections could be determined by scanning the horn-reflector antenna manually in azimuth and elevation to maximize the signal.

2.2.1 Determination of Predicted Position

The local azimuth, elevation, and corresponding rates of change of these quantities as a function of time were computed from the "modified orbital elements" of the Telstar satellite orbit for each pass. Details of the
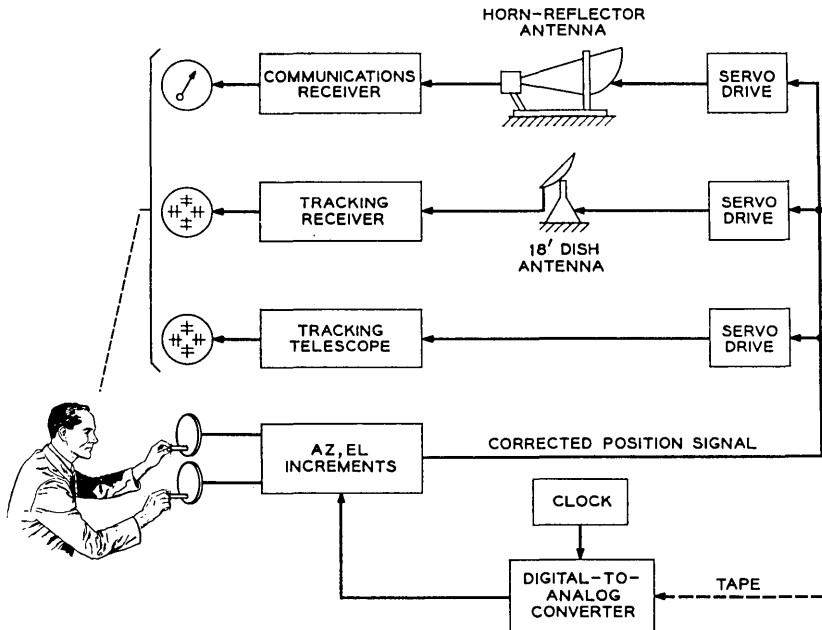
Fig. 4 — Block diagram of tracking modes at Holmdel.

method are given in Ref. 4, and hence will be only briefly summarized here. It was assumed that the orbit could be defined at a given time (epoch), T_0, by six parameters unchanging with time: eccentricity, e, and focal distance, f (perigee), of the ellipse and its inclination, i, to the earth's equator; the angle of perigee ω_0 (measured from the equator in the plane of the ellipse), the ascending node longitude, Ω_0, (determined by the intersection of the orbital plane with the equator), and the perigee-perigee period, P_0. In addition, the two main precessions, apsidal and nodal, were assumed to vary linearly with time. From this description of the orbit it was possible to calculate local "look-angles" by first solving Kepler's equation and then using simple geometric transformations. The Telstar satellite orbit proved to be so stable that predictions accurate to a few tenths of a degree for more than a month could be made using this method and an accurate set of orbital parameters.

Following determination of the azimuth and elevation of the satellite referred to the Holmdel station for a given pass by the 7090 computer, the data were transferred to a standard five-hole paper tape along with the corresponding time for each point. The tape was then read automatically in real time by the digital-to-analog converter[1] (DAC) which provided appropriate analog output signals for positioning the various elements of the system. An error buffer unit, which stored the current azimuth rate, was also provided in the azimuth channel. If an obvious error occurred in the azimuth signal from the DAC (caused possibly by an erroneous punch in the tape) the error buffer sensed the fact and switched the drives to the stored rate, which would then keep the antennas moving along an approximately correct path until remedial steps could be taken. It was the intent to provide a similar unit for the elevation channel, but time did not permit.

Before the analog position signals were transmitted to the antennas and optics, they were finally passed through the manually controlled device for inserting differential corrections in azimuth and elevation.

2.2.2 Beacon Tracker

The beacon tracker was essentially a modification of the Echo radar receiver.[1] Briefly, the original 961-mc receiver consisted of an 18-foot diameter paraboloid with a conically scanned beam for angular error determination, a low-noise RF amplifier and down-converter, AFC and gated narrow-band IF amplifier circuitry, quadrature phase detectors for extracting voltages proportional to azimuth and elevation errors, and appropriate error displays. The 4-cps conical scanning feature was preserved for angular error determination, but gating the receiver off and

on was no longer necessary since the tracker worked on the CW signal from the Telstar spacecraft beacon.

The RF portion of the system had to be converted from 961 mc to 4080 mc, and for this purpose a new circularly polarized turnstile feed for the 18-foot paraboloid was provided, along with a parametric amplifier for the new frequency. The dish surface was lined with window screening to render it more opaque to the higher frequency. As shown in Fig. 4 the angular error was presented to the operator by the position of the spot on a CR tube, and by introducing offsets he could zero the indicated errors. Since the horn-reflector antenna and the tracking antenna had been previously boresighted together, the horn antenna would then also point at the target.

In order to measure the received signal level at 4080 mc the tracker AGC voltage was calibrated in terms of input signal power and recorded. A determination of the apparent beacon power output from the satellite could then be made. The beacon tracker system parameters were:

Antenna gain	42.4 db
Cable loss	1.2 db
Radius of conical scan	0.4°
Scanning loss	2.3 db
Antenna 3-db beamwidth	0.8° × 1.0°
System noise figure	4 db
System threshold	−145 dbm
System pointing sensitivity	±0.03°
Tracking IF bandwidth	500 cps.

2.2.3 *Optical Tracking*

The telescope used on Project Echo[1] was also used for Project Telstar. It was part of an M-33 surplus fire-control radar, and was characterized more by convenience of operation than by high sensitivity. The field of view was 6° with a magnification of 8x and a 2-inch diameter objective lens. On a clear night stars of magnitude +6 to +7 could be seen, comparable to the magnitude of Telstar when it approached to 1000 miles or less.

In addition to the M-33 telescope a spotting telescope, mounted on the glint telescope, was available for checking the tracking optically. It had a 3-inch diameter objective lens and thus could see much fainter objects than the M-33 telescope. On the few occasions when the satellite was observed, the spotting telescope was used to check on the beacon tracker.

2.3 *Glint Telescope*

In order to maintain a favorable aspect of the satellite antenna patterns with respect to the earth and to insure that all solar cells received an equal amount of sunlight the satellite was given an initial spin of 178 rpm about an axis normal to the ecliptic plane. The interaction of a spinning conductor with the earth's magnetic field, however, introduced a force which tended to move the spin axis away from its preferred orientation. To follow this motion, and to check on the effectiveness of corrective measures when they were applied, three mirrors were mounted on the satellite's surface in order to reflect flashes ("glints") of sunlight to earth. Two mirrors were mounted tangent to the sphere at an angle of 95° from the spin axis spaced 120° apart in longitude, and a third mirror at 68°. For a given location of the spin axis there was then a unique time during a given pass when the sun-satellite-observer angle was such that the observer could see a glint from one of the two sets of mirrors. Conversely, knowing the time of the glint and the satellite position (given by the orbital parameters), a cone could be determined on which the spin axis must lie. Another such observation determined a second cone, and the spin axis must then lie along one of the two intersection lines of these two cones. A third glint observation, of course, would remove the ambiguity; however, solar aspect information from solar cells on the satellite was generally available at the same time, and was sufficiently accurate to eliminate the wrong intersection line. The position of the spin axis was usually specified in terms of the right ascension and declination of the intersection of the axis with the celestial sphere.

The glint telescope itself was a 12-inch Cassegrain with a 0.5° field of view seen by a photomultiplier at the focus. Sensitivity was such that the glints could be detected out to a slant range of 3,000 miles or more, depending on viewing conditions. (Of course, the glints could only be seen at night.) The telescope was mounted on the M-33 optical tracker, and was pointed at the target by the methods described above to an accuracy well within the angular field of view. Because of the finite size of the sun, a glint event usually consisted of a train of flashes occurring at the spin rate of the satellite and lasting from ten to thirty seconds. The mid-point of the train was taken as the time of the glint. By using a precise crystal oscillator for time comparison it was also possible to determine the spin rate of the satellite by measuring the interval between successive flashes. A more detailed description of the telescope and associated electronics is given in Ref. 5.

2.4 *Data Recording*

A variety of recording means was provided in order to insure that no significant information during a Telstar satellite pass was lost. The areas of interest may be grouped as follows:

(a) Signal levels
(b) Glint telescope
(c) Spin rate
(d) Audio portion of the television signal
(e) Comments of operating personnel during a pass
(f) Tracking data
(g) Time synchronization of all recordings.

A block diagram of the recording system is shown in Fig. 5.
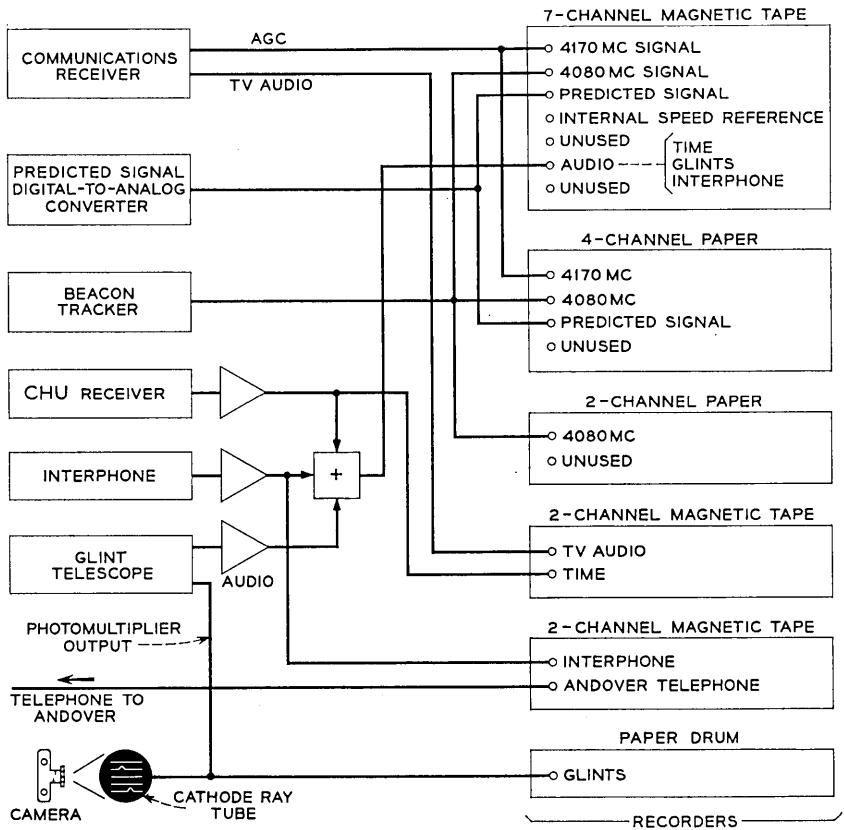
Fig. 5 — Block diagram of data recording facilities.

2.4.1 *Signal Level Recording*

The AGC voltage from the beacon tracker receiver was recorded on a paper recorder at the tracker location, and also in the main control building on the 7-channel magnetic tape recorder and the 4-channel paper recorder. This voltage was calibrated in terms of signal level before and after every pass.

A voltage from the communications receiver was also recorded by the magnetic and paper recorders in the control building. This voltage was obtained either from the frequency compression demodulator AGC during video transmission, or from the phase-lock receiver when a crystal-controlled carrier was transmitted. Signal level calibrations were also made before and after every pass.

Knowing the slant range to the satellite, frequency, and gain of the antennas, it was possible to calculate the received power as a function of time for a given transmitter power. This calculation was included in the computer program used for making the tracking tapes, making it possible to provide another punched paper tape containing the predicted received power level at four-second intervals. This tape was fed into a fairly simple digital-to-analog converter and read in real time during a Telstar satellite pass. The output voltage was proportional to the received signal in dbm, and was recorded in the control building on the magnetic and paper recorders. It was thus possible to compare predicted signal levels with those actually being observed during the pass.

2.4.2 *Glint Telescope Recording*

The pulses of light incident on the glint telescope photomultiplier during a glint event were recorded in three ways:
  (a) Photographs of a CR tube with the pulses on the vertical plates and a linear time raster on the horizontal plates.
  (b) Pen deflections of a paper drum recorder.
  (c) Tone bursts on the audio recording channel of the 7-channel magnetic recorder. Audio time signals from radio station CHU were also recorded on this channel.
This variety of methods for glint recording facilitated the determination of the exact time of the glints and the flash spacing for spin rate determination.

2.4.3 *Spin Rate Recording*

The signal level voltage from the communications receiver contained a number of Fourier components due to the satellite rotation and the

slight nonuniformity of the azimuthal antenna radiation pattern. The fundamental component occurred at the spin rate, approximately 3 cps, and was selectively amplified by a high-Q (≈ 25) amplifier tuned to the actual spin frequency. The amplifier output was a close approximation to a sine wave whose period was then measured with a standard counting instrument by manually recording the time required for ten periods. An average of 500 periods was actually used to determine the spin rate, achieving an accuracy of about ± 0.05 rpm.

The spin rate was also independently determined on passes when the glints were observed by comparing the time between glints to the period of an accurate, crystal-controlled oscillator. An accuracy of about ± 0.02 rpm could be achieved.

2.4.4 *Audio Recording*

The audio portion of the television signal was recorded on one channel of a 2-channel magnetic tape recorder, with time signals recorded on the other channel.

2.4.5 *Personnel Comments*

All operating personnel at Holmdel were in communication with each other by a common telephone circuit. This circuit was recorded on one channel of another 2-channel magnetic recorder. The comments obtained in this way occasionally proved very helpful in subsequent data reduction, since it was impossible to keep a written log of all the last-minute changes in system performance or operation that occurred on various passes.

The Holmdel station was also in constant communication with Andover by means of a private telephone circuit for purposes of coordinating operations. This circuit was recorded on the other channel of the 2-channel recorder mentioned above, and served the same purpose as the local interphone recording.

2.4.6 *Recording of Tracking Data*

During a pass the azimuth and elevation offsets required to track the satellite accurately were recorded at approximately one-minute intervals in a written log. The true azimuth and elevation could then be determined later by adding the offsets to the predicted positions during the pass. The true angles were used to make slight corrections in the orbital

elements so that more accurate determination of the satellite position could be made for use in other studies concerned with the satellite.

Towards the end of the Holmdel experiments with the Telstar satellite an analog-digital converter unit was acquired which encoded the true azimuth-elevation angles into punched paper tape, along with time, at selectable intervals of 1, 2, 4, or 8 seconds. This unit made the task of improving the orbital elements considerably easier.

2.4.7 *Time Synchronization of Recordings*

The station clocks were generally set to the correct time by referring to the time signals broadcast by the Canadian station CHU on 3.33 mc, 7.335 mc, or 14.670 mc. As mentioned above, the magnetic tapes were time referenced by actually recording CHU on one audio channel. The 4-channel paper recorder included an auxiliary time marking pen which was actuated by a pulse every 10 seconds from the clock chain in the DAC. The paper recorder for the beacon tracker also contained a time marking pen which was supplied with 1-second and 1-minute pulses generated locally by synchronous motors. These were initially synchronized with the station clocks. The paper drum recorder for the glint telescope was manually time-tagged by referring to the station clocks.

III. EXPERIMENTAL RESULTS

3.1 *Preliminary Tests*

During the period from April 11–July 6, 1962, transmissions were attempted to Andover via reflection from Echo I on 36 passes, with increasingly successful results culminating in the demonstration of satisfactory operation at Andover of all the various tracking modes. These tests helped to confirm, among other things, that it was possible to predict a satellite trajectory for Andover and have the horn properly follow the predictions, that the sense of polarization of the microwave signals was correct, and that the system thresholds at Andover were as expected. The Echo tests were challenging, since the signal levels were marginal and had large, rapid fluctuations due to the wrinkled nature of the balloon.

During the same period of time mentioned above, transmissions were made to Andover via reflections from the moon at 4080 mc on a total of five separate occasions, again with increasing success. Although these tests were not as demanding as the Echo tests, they did serve a useful purpose in checking system performance. The average value of signal

received from the moon indicated its scattering cross-section at this frequency to be about 20 db below a perfect sphere of the same size.

3.2 *Television Reception*

Starting with the first possible pass (No. 6) television was received at Holmdel on a total of 23 passes with excellent results. A brief summary of the more noteworthy demonstrations seen at Holmdel is given in Table III.

Fig. 6 shows pictures of the Holmdel monitor during scenes from the earlier passes. These are reproductions of selected frames from a 16-mm movie camera using a high-speed film, which accounts for a certain amount of graininess in the photographs. The streaks of light are reflections of room lights in the monitor glass surface. Also shown is a photograph of the picture seen at Andover after being relayed from Holmdel by land routes. The 1.0-mc filter was in the output circuit of the Holmdel receiver when these pictures were taken. The general impression was that a 1-mc bandwidth provided a picture of quite acceptable quality. On a few occasions the 2.0-mc filter was tried, and resulted in somewhat improved definition. It is evident from the photograph of the multiburst test pattern that the 1.0-mc filter had a fairly slow cutoff characteristic, which probably accounts for the qualitative appraisal of picture mentioned above.

The predicted threshold of the television receiving system was verified during operations with the Telstar satellite, as the picture showed essentially no noise out to maximum range. On a few occasions, however, a signal from a nearby microwave relay transmitter operating at 4165 and 4175 mc produced interference either by direct propagation or by scatter from thunderstorms. This caused a noticeable deterioration in the S/N ratio.

The audio portion of the television signal was received with acceptable quality.

TABLE III

Date	Pass	Test
July 10	6	First transmission from satellite
July 11	15	First television from France
July 12	16	First television from England
July 23	123	Special program to Europe
	124	Special program from Europe
July 24	133	Special program from France
	134	Special program from England
July 31	196	Special program from Sweden

FIRST PICTURE RECEIVED AT HOLMDEL
PASS NO. 6, JULY 10, 1962
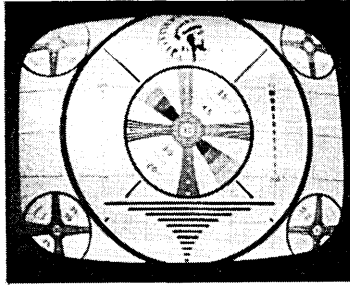
INDIAN HEAD TEST PATTERN

LIVE VIDEO ON PASS NO.6
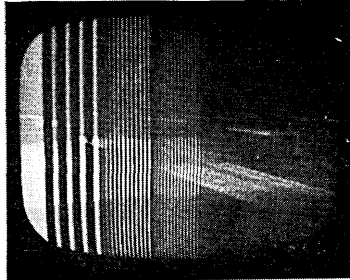
|◄———►|◄———►|◄———►|◄———►|
0.5 MC 1.5 MC 2.0 MC 3.2 MC
MULTIBURST TEST PATTERN
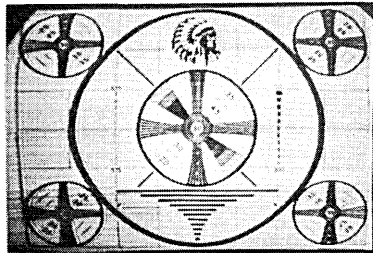
PICTURE SEEN AT ANDOVER AFTER
RELAY FROM HOLMDEL

Fig. 6 — Television received at Holmdel from Telstar spacecraft repeater.

3.3 *Data Reception*

On pass 270, August 8, 1962, transmission of high-speed data was demonstrated at Holmdel. The data were sent at a rate of approximately 40 kilobits/sec from a computer at the Murray Hill, New Jersey, location of the Bell Laboratories to Andover for transmission to the Telstar satellite. From the satellite it was relayed to the Holmdel station, and then

sent by microwave relay to the computer in the new laboratory building at Holmdel, some 2 miles from Crawford Hill. The accuracy of data transmission was found to be as good as that obtained over the usual land line route from Murray Hill to Holmdel.

3.4 *Received Signal Levels*

Using the expression for received power given in Section 2.1.6, a comparison between predicted level and observed level was made for one point on every pass worked for both the beacon signal and communication signal. The point used on each pass was chosen to fulfill the following conditions as nearly as possible:

(a) Angle between the spin axis and observer-satellite line within $90° \pm 30°$. This insured that the gain of the spacecraft transmitting antenna could be assumed to be 0 ± 1 db

(b) Tracking satisfactory at the time

(c) System operation normal.

Assuming the system parameters given in Section 2.1.6, the following expressions were used to calculate signal levels:

$$\text{Beacon signal:} \ P_r = -116.9 - 20 \log \left(\frac{r}{1000} \right), \text{dbm}$$

$$\text{Communications signal:} \ P_r = -88.0 - 20 \log \left(\frac{r}{1000} \right), \text{dbm,}$$

where r is the slant range in miles.

Any differences between calculated and observed signal levels may be interpreted in terms of departures of the satellite communications repeater transmitted power from nominal values. Points calculated on this basis are plotted in Fig. 7. The gap in the data for the beacon signal between pass 198 and 762 is due to the use of the tracker antenna in the skinny route terminal project (see Section 3.8). After pass 606 the horn antenna receiver was used for measuring the beacon signal and reception at 4170 mc was discontinued.

The data show that the power transmitted by the Telstar satellite repeater was 2 watts at 4170 mc within a measurement accuracy of ± 2 db and at least 20 mw at the beacon frequency. These were the design objective values for the satellite. No significant changes with time were observed.
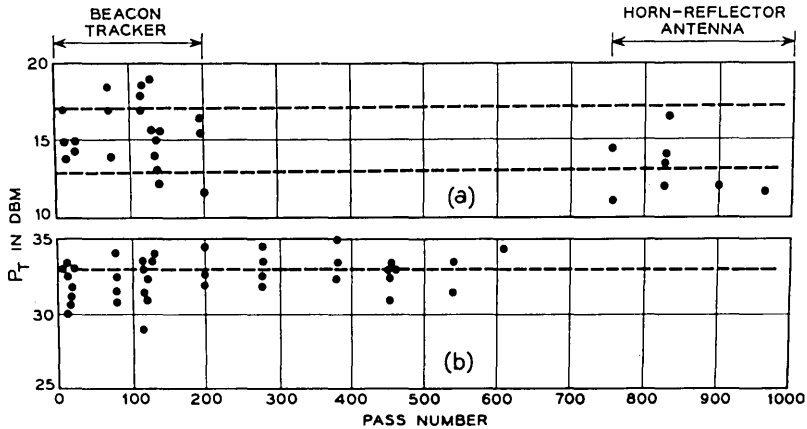
Fig. 7 — Telstar spacecraft radiated power inferred from signal level measurements at Holmdel. (a) Apparent beacon power radiated at 4080 mc. The dashed lines define the nominal tolerance of +13 to +17 dbm. (b) Apparent power radiated on the communications channel at 4170 mc. The dashed line represents the nominal power of 2 watts. Reception on horn-reflector antenna.

3.5 *Tracking*

The beacon tracker was operated on 29 passes of the Telstar satellite, and was able to acquire and hold the beacon signal through the Doppler shift of as much as ±100 kc with no difficulty. The achieved tracking accuracy was on the order of ±0.05°, shown by comparison with the 3-inch spotting telescope on a few passes.

The satellite was seen optically in the M-33 tracking telescope on four passes out to a maximum range of 1700 miles. With care, a tracking accuracy of about ±0.05° could be achieved.

Scanning the receiving horn antenna in azimuth and elevation proved to be a surprisingly accurate method of correcting errors in prediction, with tracking accuracies of ±0.1° being typically obtained. There were certain drawbacks to this method, however, which made a more sophisticated system desirable. For example, during the time that the antenna was being scanned the signal level data were essentially useless. A typical scanning procedure took about 15 seconds and was usually repeated every one or two minutes, depending on the accuracy of the predictions. Thus for predictions seriously in error the method would become increasingly poor due to the necessity of more frequent scanning, whereas the beacon tracker did not have this limitation. It was also essential to have a predicted drive tape to use this method, whereas the tracker could follow the satellite by manually steering the antenna to zero the error, as demonstrated on a few passes.

3.6 *Spin Rate*

The spin rate was measured on almost every pass worked, using either signal analysis or the optical "glints". It was found that an exponential function could be determined which agreed with the measured data to within ±0.5 rpm from pass 6 to 1114 (or 122 days after launch):

$$R = 178.2 \exp\,(-t/333),\ \mathrm{rpm}$$

where t is the number of days since launch. The spin has a "half-life" of 333 days, which is in the range of 300–400 days estimated by a rough calculation prior to launch by E. Y. Yu of Bell Laboratories. If this expression continues to be valid, the spin will be reduced to a minimum useful value of 20 rpm in two years. A plot of the spin decay is given in Fig. 8.
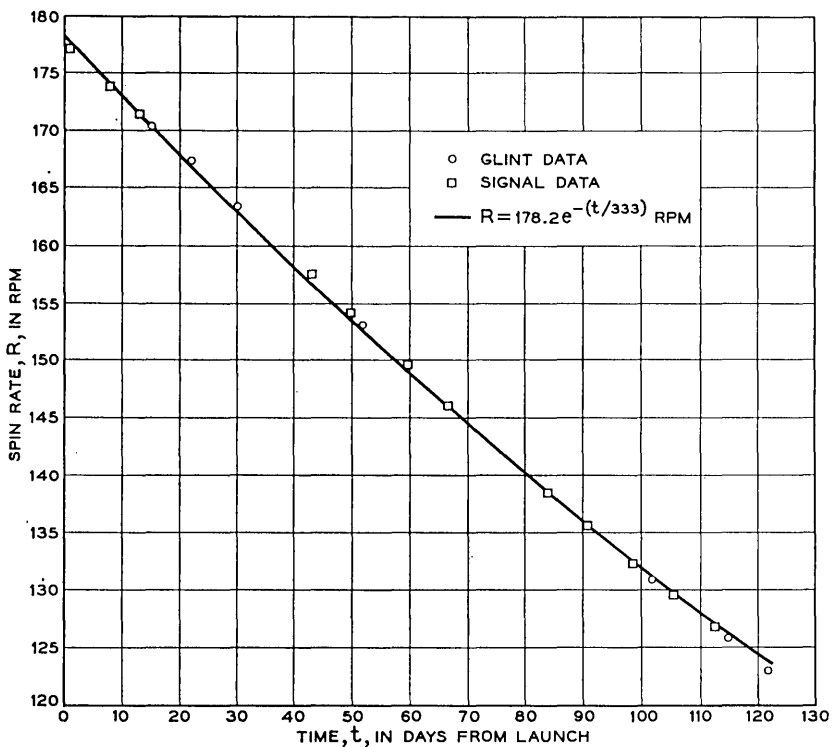
Fig. 8 — Change of satellite spin rate with time.

3.7 *Spin Axis Orientation*

3.7.1 *Determination of the Axis Using Glint Data*

During the period from the launch on July 10, 1962, to November 9, 1962, a total of 17 separate glint events were observed at Holmdel. These made it possible* to determine 11 different locations of the spin axis, as summarized in Table IV.

These points are plotted in Fig. 9, along with a theoretical curve derived by L. C. Thomas for an assumed satellite magnetic dipole moment of -1.0 ampere-turn-meter^2. From pass 16 to 472 the agreement is quite good, but pass 931 falls more closely on a -1.1 ampere-turn-meter^2 curve. Some discrepancies were expected, of course, due to lack of complete knowledge of the earth's magnetic field and to the elliptical shape of the satellite orbit. In order to test the effectiveness of the torque coil in the satellite it was turned on in the positive sense for 18 hours between passes 1052 and 1069, and in the negative sense for about the same length of time between passes 1069 and 1114. The changes caused by these tests were apparent, and demonstrated the ability to take corrective action whenever necessary.

Also shown in Fig. 9 is the design objective location of the spin axis, corresponding to a line normal to the ecliptic plane. The achieved orientation was well within tolerance.

TABLE IV

Pass	Date	Mirror Observed	Right Ascension	Declination
7	7/11	68°		
7	7/11	68°		
8	7/11	68°	These passes were averaged together to give one fix:	
8	7/11	68°	81.96°	−65.57°
9	7/11	68°		
9	7/11	95°		
16	7/12	68°	84.39°	−65.81°
72	7/18	68°	86.86°	−66.10°
135	7/25	68°	91.22°	−65.86°
136	7/25	68°		
199	8/1	68°	95.4°	−65.4°
272	8/9	68°	100.08°	−64.51°
472	8/31	68°	104.44°	−59.92°
931	10/20	95°	98.04°	−50.69°
1051	11/2	95°	95.8°	−50.3°
1069	11/4	95°	98.48°	−49.36°
1114	11/9	95°	94.05°	−51.91°

* The data reduction was carried out by D. W. Hill[6] and L. C. Thomas of Bell Laboratories along lines laid out by the former.
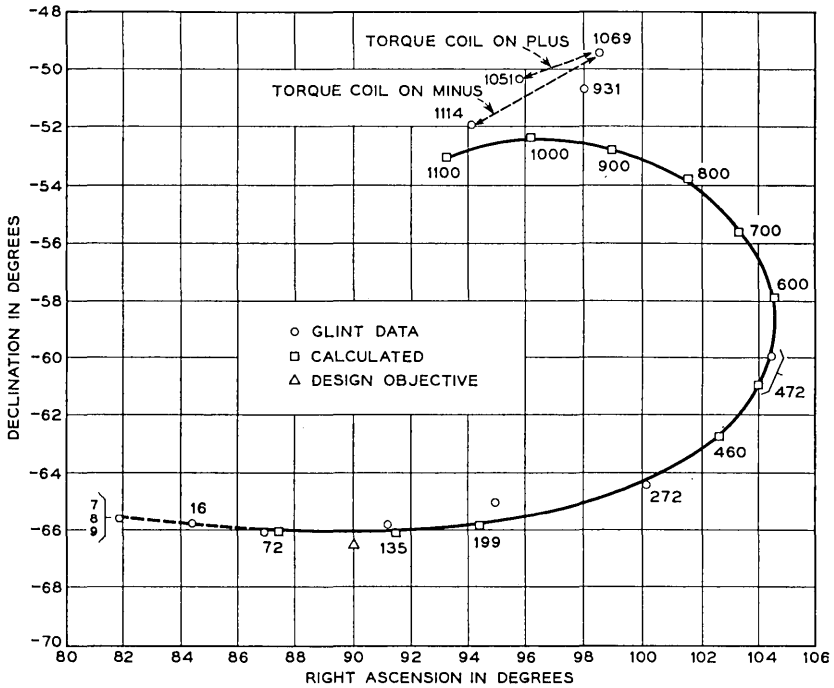
Fig. 9 — Change of spin axis location as determined by glint data; numbers refer to pass number.

3.7.2 *Determination of the Axis Using Signal Level Data*

The transmitting antenna pattern of the satellite at 4 gc was very nearly uniform in longitude,* and also in latitude* for angles within ±30° of the equator. (The satellite transmitting antenna belt was approximately on the equator, and the satellite spun about an axis normal to its equatorial plane.) For values of latitude progressively nearer the poles, however, the pattern contained maxima and minima of increasing range. Thus during a pass when the observer-satellite line made an angle of about 45° or less with respect to the spin axis the received signal level showed corresponding fluctuations with time. If the angular location of the maxima and minima of the satellite latitude pattern were known with respect to the spin axis, it would be possible to determine values of the spin angle (defined as the latitude of the observer, measured in the satellite co-ordinates) as a function of time during a pass. Two such values

---

* These are satellite-centered coordinates.

would then be enough to determine a "fix" on the spin axis location. In order to determine the satellite pattern, the process was reversed on one or two passes for which the spin axis location had been determined from the glint data. Knowing the axis orientation it was a simple matter to compute the spin angle for a number of times during the pass corresponding to the observed maxima and minima, and thus obtain a pattern calibration. Curves obtained by this method are shown in Fig. 10 for the two frequencies of measurement, 4080 mc and 4170 mc. As one would expect, the minima are somewhat closer together in angle at the higher frequency. In the plots the maxima have all been set to the same level, revealing that all minima have different values so that there is the possibility of unambiguously determining spin angles from the received signal level variations. An expanded replica of the signals received during pass 117 is shown in Fig. 11, including both the 4170-mc and 4080-mc signals. By measuring the depth of a minimum referred to the midpoint of a line joining two adjacent maxima for all minima, a list of minima depths was determined. This list was then compared to that given by the appropriate reference pattern calibration (Fig. 10) and correspondence of minima and maxima thereby established. Knowing the times associated with the minima and maxima it was then possible to determine the apparent variation of spin angle with time during the pass. Such a plot for pass 117 is shown in Fig. 12, where data determined from both frequencies are included. It can be seen that the points for both frequencies lie on the same curve, as they should.

In order to determine the orientation of the spin axis from the spin
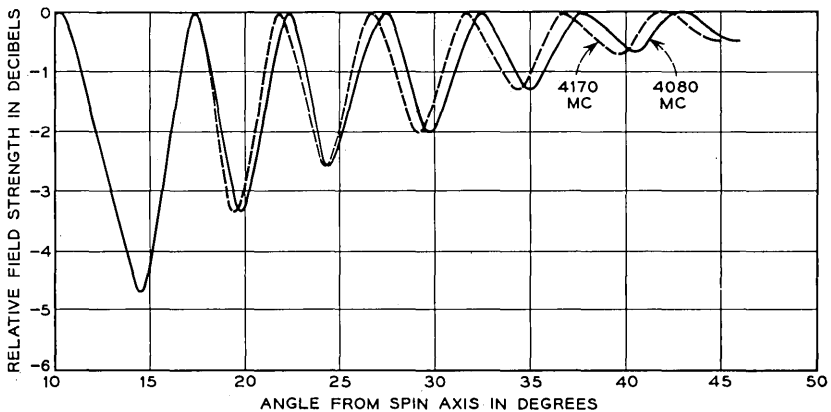
Fig. 10 — Measured latitude radiation patterns of spacecraft while in orbit.
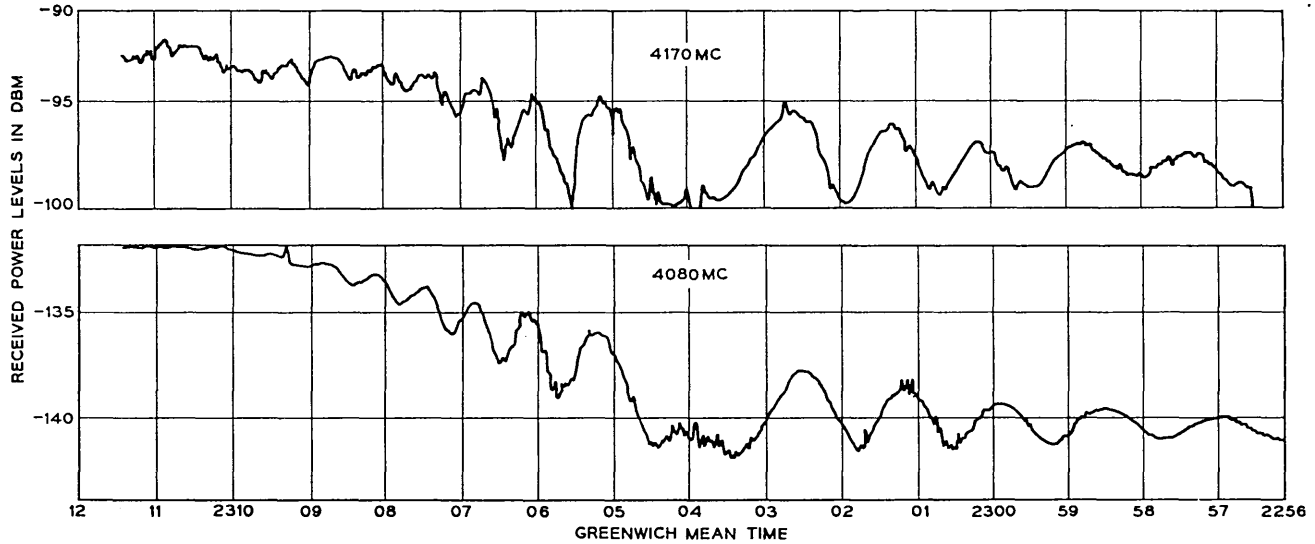
Fig. 11 — Expanded replica of received signal recordings at 4080 mc and 4170 mc showing variations caused by Telstar spacecraft antenna pattern lobes on pass 117, July 23, 1962.
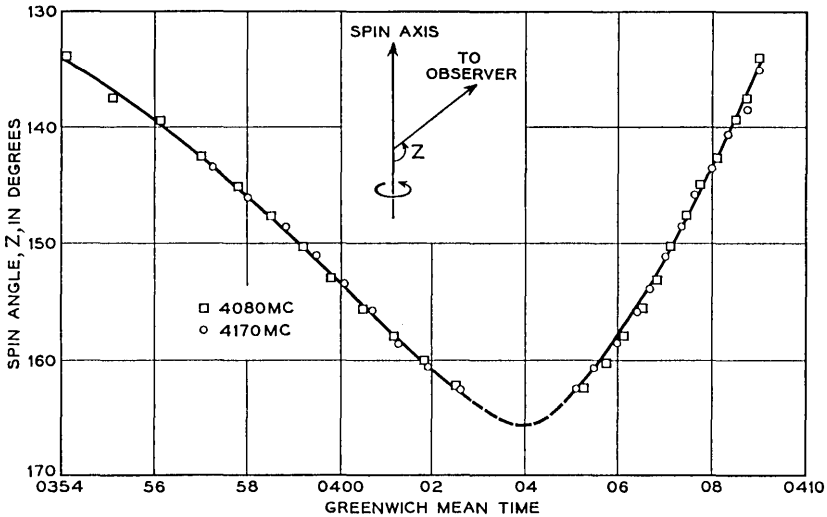
Fig. 12 — Measured variation of spin angle with time for pass 117 on July 23, 1962.

angle information, a computer program was prepared which computed the axis location from two selected data points from the set of given spin angles and corresponding times, and then computed spin angles from this value of spin axis location and compared them to the remaining given data points. Examination of the differences then revealed any gross errors, such as a slip of one adjacent minimum in achieving a correspondence between the pattern calibration and measured signal variations. Generally the spin angle differences did not exceed 1°. It was found that in choosing the two points from which to compute the axis, it was better to use two with the largest difference in spin angle, rather than the largest difference in time.

A more elegant approach, of course, would be to utilize all of the data points (spin angles with their corresponding times) and make a least-squares fit to determine the best value of spin axis orientation. It was felt, however, that the accuracy of measurement was insufficient to warrant this approach.

The coordinates of the spin axis determined from the pattern data are plotted in Fig. 13 for passes 7-271 and the agreement is seen to be within ±1° of the values determined from the glint data. After pass 271 the line-of-sight to the satellite did not come close enough to the spin axis to yield any more data, due to a combination of orbital precessions and movement of the spin axis.

3.8 *Skinny Route Terminal*

After the Telstar spacecraft was successfully launched and proved to be operating as planned, it seemed desirable to demonstrate a minimal-type ground station that would provide one voice channel over the satellite. An inexpensive, compact station would be useful for remote locations in the world. It was decided to adapt the 18-foot tracker antenna at Holmdel for both transmission and reception, and modify the tracking mode to make it independent of a predicted drive tape. The effort was started on a crash basis in late July, 1962, by members of the Military Research Laboratory at Whippany, and culminated in successful demonstrations of a two-way voice circuit to Andover less than three weeks later. A description of the system and tests conducted may be found in Ref. 7.

IV. CONCLUSIONS

The general objectives outlined in Section 1.1 were accomplished during the Telstar experiments. In addition, it was clearly demonstrated that a relatively modest ground station utilizing a 20-foot horn-reflector antenna can do a creditable job of receiving a television picture across the Atlantic Ocean from an active satellite.
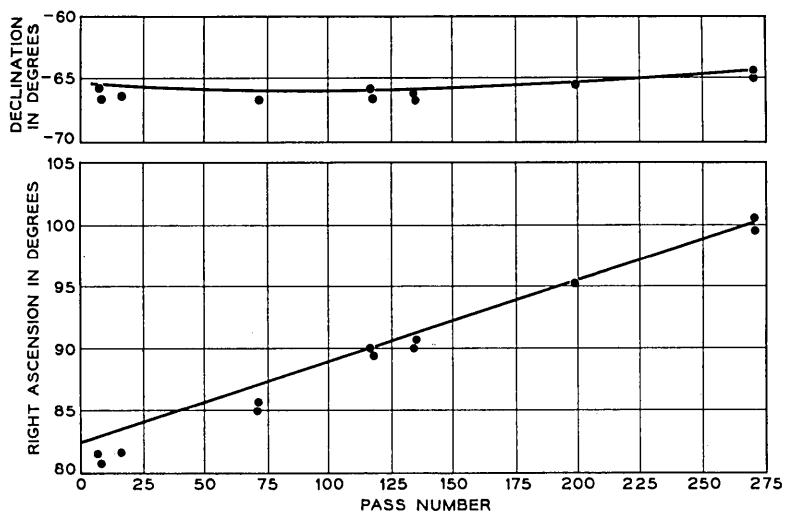
Fig. 13 — Plotted points: spin axis determination from signal level analysis. Solid curve: average of glint data.

REFERENCES

1. B.S.T.J., Project Echo Issue, **40,** July, 1961.
2. Ruthroff, C. L., and Bodtmann, W. F., Design and Performance of a Broad-band FM Demodulator with Frequency Compression, Proc. I.R.E., **50,** December, 1962, p. 2436.
3. Enloe, L. H., The Synthesis of Frequency Feedback Demodulators, Proc. Nat. Elec. Conf., Vol. **18,** 1962, p. 477.
4. Ossanna, J. F., Jr., The Generation of Look-Angles from Regularly Available Mean Orbital Elements for 1960 Iota One, Photographic Science and Eng., Nov.–Dec., 1962.
5. Courtney-Pratt, J. S., McLaughlin, J. W., and Hett, J. H., Optical Measurements on the *Telestar* satellite to Determine the Orientation of the Spin Axis and the Spin Rate, to be published.
6. Hill, D. W., Optical Attitude Determination for the *Telestar* satellite, to be published.
7. Two-Way Voice Channel via Telstar Established with Compact Ground Station, Bell Labs. Record, **40,** October, 1962, p. 342.

Launching of the *Telstar* Satellite

By H. N. UPTHEGROVE, J. B. D'ALBORA, JR.,
A. R. KOLDING and B. A. McLEOD

The launching of the Telstar satellite from Cape Canaveral is described, with emphasis on the pre-launch testing and test facilities.

I. INTRODUCTION

The Telstar satellite was launched on July 10, 1962, from Cape Canaveral by a Delta launch vehicle. The pre-launch and launch operations were carried out jointly by the National Aeronautics and Space Administration (NASA) and Bell Telephone Laboratories. NASA had responsibility for procurement, checkout, and launch of the Delta vehicle and for mating of the Telstar spacecraft with the launch vehicle. Bell Telephone Laboratories was responsible for delivery, checkout and monitoring of the spacecraft, and observed and participated in the launch vehicle preparation and spacecraft-to-vehicle mating operation. Bell Telephone Laboratories provided radio command guidance for the Telstar launch, as for all Delta launches.

At Cape Canaveral the principal test locations for the Telstar launch operations are:

(1) Launch Complex 17, consisting of two launch pads, 17A and 17B, and supporting facilities; the Telstar satellite was launched from 17B.

(2) Guided Missile Control Facility No. 3, the Laboratories-operated command guidance ground station; Telstar launch operations facilities were located here.

(3) Spin Test Building, operated by Douglas Aircraft Company for NASA; here, the Telstar spacecraft was mated to the Delta third-stage motor and the combination was spin-balanced prior to installation on the launch vehicle.

II. LAUNCH PREPARATIONS AND FACILITIES

2.1 *Summary*

Following the final tests and inspections at the Hillside, N. J., Bell Telephone Laboratories, the spacecraft used in the launch operations
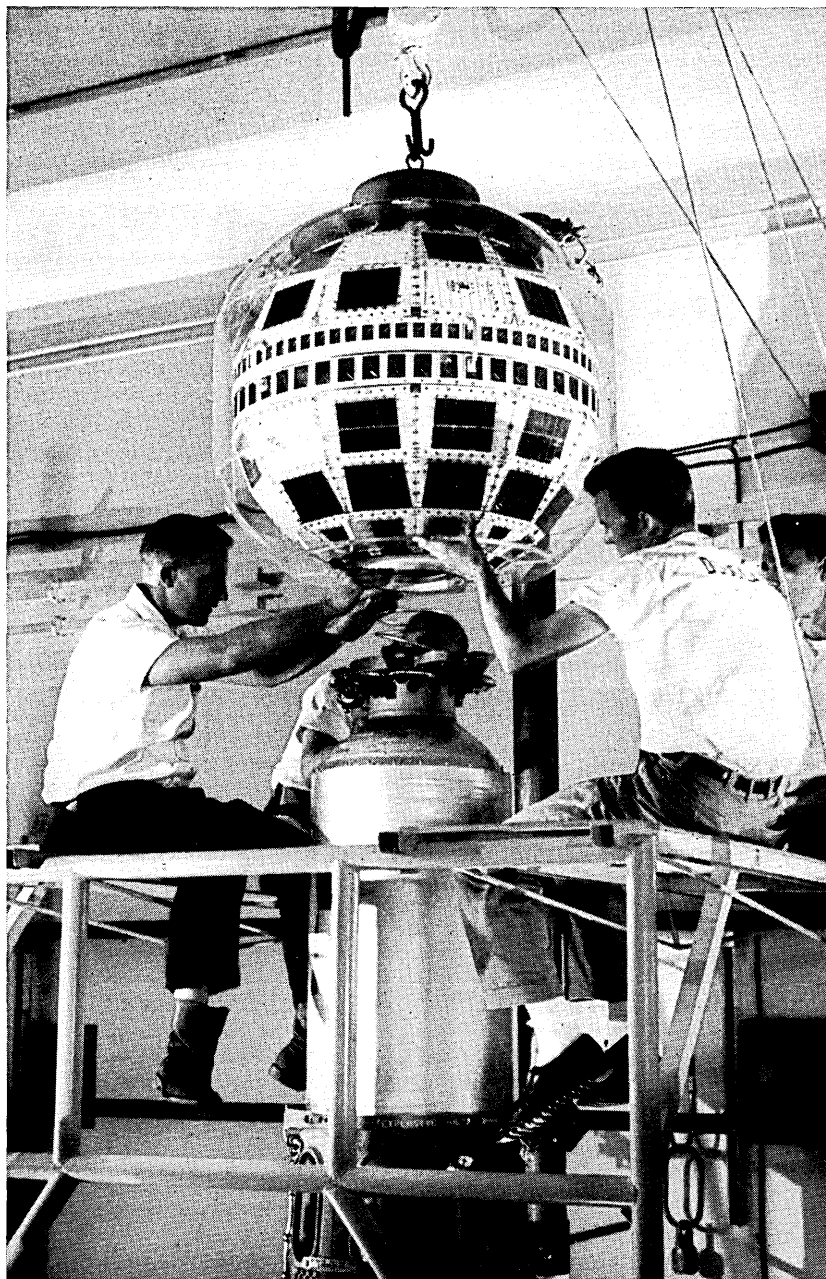
Fig. 1 — Mating the spacecraft to the Delta third stage.

were shipped by special truck to Cape Canaveral for the subsequent series of pre-launch tests and the mechanical operations involved in mating the satellite to the Delta launch vehicle.

The electrical testing required the establishment of new facilities at Cape Canaveral in three locations. The base location at the Laboratories' missile guidance area provides test equipment and spacecraft storage facilities in three air-conditioned 40-foot vans. In addition, there are an autotracking VHF antenna system for command and telemetry and several microwave antennas used for tests when the spacecraft is at either of the other two locations.

A second test location is in the spin test building. In this building, the spacecraft is mated to the third stage of the rocket as shown on Fig. 1, and the combination is dynamically balanced at spin rates it will have in flight. The special installation for the Telstar project consists primarily of three antennas mounted on a tower outside the building and coupled to the satellite to permit remote testing from the base location.

The third test location is the launch stand, where test equipment was installed in an existing test room on the seventh level. This was used together with the test equipment at the base location for tests of the satellite.

Before the flight models were available, the prototype model of the spacecraft was sent to Cape Canaveral and used to check out all of the testing and handling procedures at the three locations. It was also used in the radio-frequency compatibility test which is required by the missile range. Two spacecraft were provided to serve as the flight model and the back-up model. These were designated Fly 2 and Fly 3; Fly 2 was to be launched unless trouble developed requiring the substitution of Fly 3.

The first operation with the Fly 2 spacecraft after arrival at the Cape was the comprehensive arrival check to verify that all of its systems were intact after the trip from Hillside. Subsequent to this, the spacecraft was given a daily routine check during the period of time it remained in the satellite van prior to delivery to the spin building. The back-up spacecraft, Fly 3, was tested in the same way and then remained in the spacecraft van receiving daily checks until it was shipped back to Hillside after the launch.

On F − 9 day (9 days before launch), Fly 2 was moved from the spacecraft van to the spin building for mating to the live third stage.* This operation consists of coupling the spacecraft to the third stage. The combination of spacecraft and third stage was tested for eccentricity before the dynamic spin balancing operation. A remote electrical performance

---

* Discussed later in this paper. The live stage contained approximately 500 pounds of solid propellant.

test was then made from the vans at the base location to make sure that the spacecraft had not been damaged.

Following this test, the spacecraft and third-stage assembly was moved to the spin test fixture. In the balancing operation, the assembly was rotated at its flight rate and the imbalance measured with accelerometers. Following the balancing operation, another remote check was made to verify that no damage was done during the spin operation.

The mated third stage and spacecraft were then transported to the launch stand in a special carrying canister on F − 4 day. After attachment to the second stage of the rocket, the spacecraft and the live third stage were encased in a clear plastic enclosure which was continuously supplied with dust-free, dry, cool air.

Prior to roll-back of the gantry, the spacecraft was tested daily using test consoles on the seventh level of the gantry. After the gantry was rolled back the testing was done by direct radio coupling from the Telstar spacecraft antennas to the base location antennas. In the final minutes of the terminal count immediately preceding the launch, the spacecraft microwave repeater was again tested. Telemetry monitoring was continued through lift-off and until the satellite disappeared below the horizon.

2.2 Transportation to Cape Canaveral

A one-ton truck equipped for the special requirements of spacecraft transportation was procured. The body is insulated and contains a heater (independent of the cab heater) and a cooling device which uses solid carbon dioxide. The spacecraft carrying case contained a shock mounting to which the spacecraft was clamped. Additional shock suspension of the carrying case within the truck was found to be undesirable.

Road tests with a dummy spacecraft load verified that the truck and carrying case would provide safe transportation for the actual spacecraft.

The carrying case was filled with dry nitrogen before it left the Hillside Laboratories, and a small positive pressure was provided by a low-pressure feed of nitrogen from tanks in the truck.

2.3 Satellite Test Facilities at Base Location

The base location at the Bell Laboratories guidance area, GMCF-3, is far removed from the industrial area and vehicle traffic. Because of the unobstructed radio paths from this location to the spin building and to launch area 17, antennas could be mounted on low supporting structures. The arrangement of the vans and antennas at the base location is shown in Fig. 2.
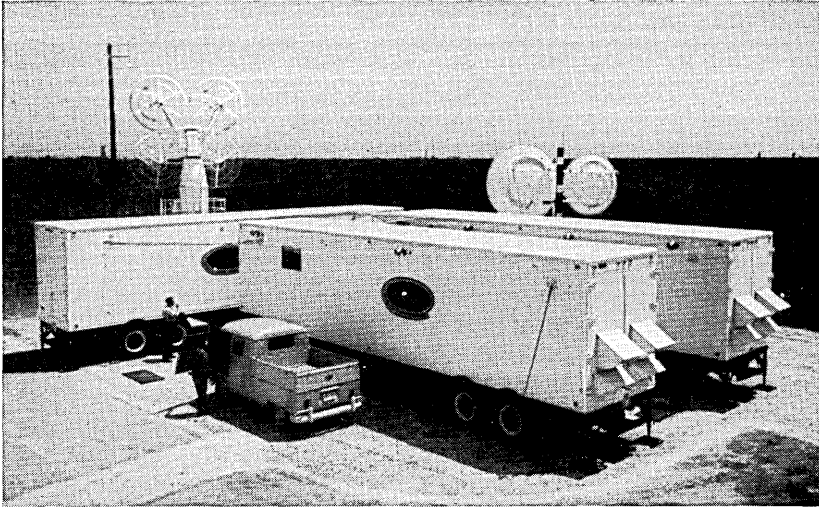
Fig. 2 — Launch operations — base location.

2.3.1 Description of Vans

The vans were designed for the particular requirements of the Telstar base location. The three vans are designated "spacecraft van," "telemetry van" and "command tracker van," where the names are those of the principal function of the van. Each van is 40 feet long and 8 feet wide and has about 7 feet of head room. All features required for long-distance road travel were provided to permit relocating the base.

The air-conditioning system provides air filtering and limits the maximum relative humidity. The spacecraft van has additional dust filtering which removes particles larger than 2 microns. The ac power is taken from the power supply of the missile guidance system. For launch operations and other critical operations, the power circuit is switched to two large diesel-driven generators.

The interior arrangements of the three vans are illustrated in Fig. 3. The spacecraft van is divided into three compartments. The central area contains mounting pedestals for two spacecraft. The end compartment is an unpacking area where the spacecraft in its carrying case is unloaded from the truck. In this area, the three-piece carrying case is removed and the spacecraft lifted off the base with a traveling electric hoist which carries the spacecraft to the mounting pedestal. After the arrival tests on each spacecraft, the daily routine tests were conducted remotely through cables to the telemetry van.

The limitation of traffic by the provision of a separate van for the

SPACECRAFT RECEIVING AREA

SPACECRAFT TEST STANDS

SPACECRAFT VAN

TELEMETRY VAN

A/C

A/C

TELETYPEWRITER

TABLE CABINET

TELEMETRY STATION

TEST EQUIPMENT

COMMAND ENCODER

FILE DESK

DESK

EXTERNAL JUNCTION BOX

PLATFORM

POWER ROOM

TRACKER VAN

A/C

A/C

COMMAND TRANSMITTER

TRACKER CONSOLE

RECORDER

BENCH

FILE DESK

BENCH CABINET

DESK

FILE

A/C A/C
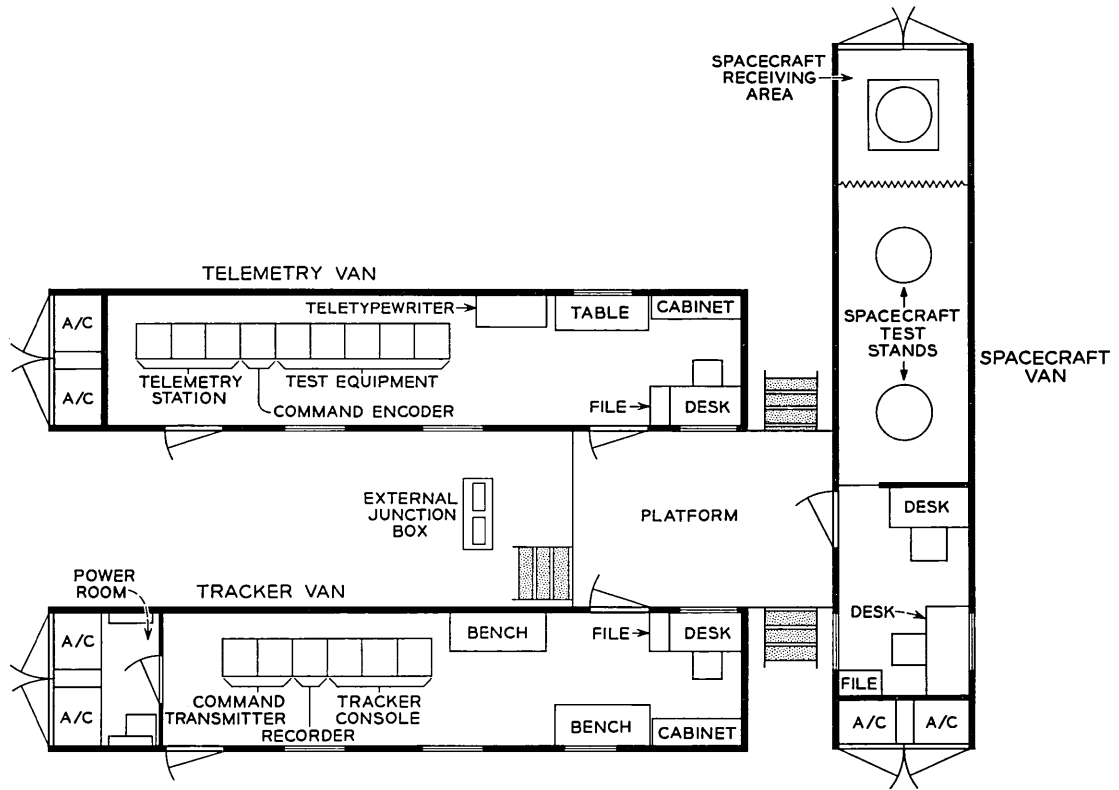
Fig. 3 — Van layout — base location.
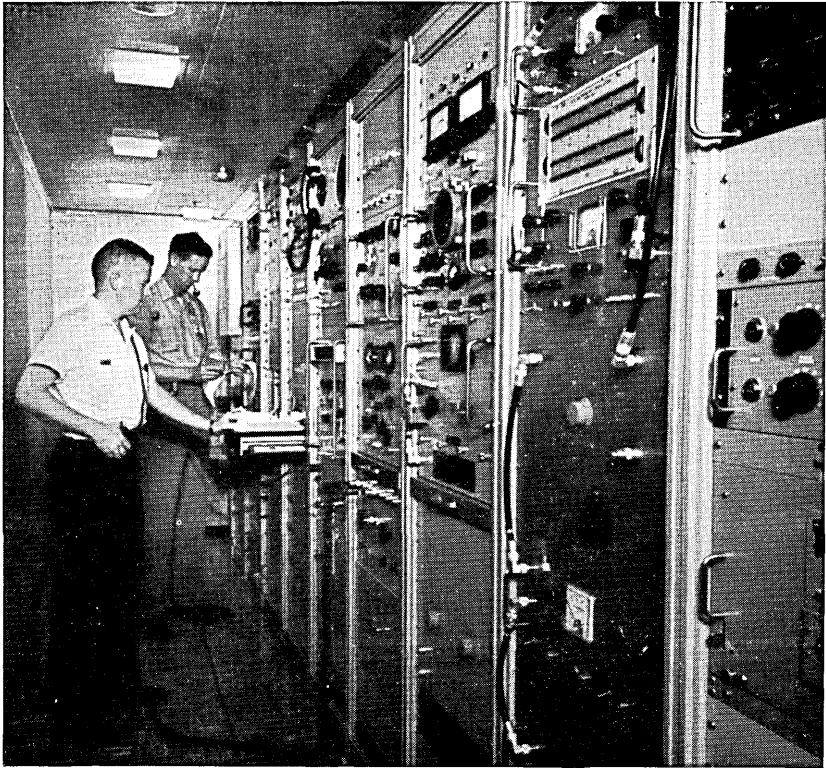
Fig. 4 — Interior view of telemetry van.

spacecraft minimizes exposure to contamination, humidity, and fluctuations in temperature.

The telemetry van provides the principal working area for pre-launch testing, countdown tests at launch, and telemetry and command activities in post-launch orbits.

This van contains a lineup of 9 cabinets, as shown in Fig. 4. Three of these house the telemetry receiver and decommutating circuits. The next cabinet contains the command encoder, whose output modulates either a low-power 123-mc* command transmitter for pre-launch testing or the 200-watt transmitter in the command tracker van. The remaining five cabinets contain a variety of test equipment. This van also contains an arrangement of teletypewriter instruments, primarily for the transmis-

* This value, as well as all other frequencies given in this paper, is approximate, but is within 1 per cent of actual.

sion of telemetry information from the Cape to Andover, Murray Hill, and Hillside. The telemetry decommutating system provides a punched tape for sending the data to other locations.

Provisions were made to use the identical telemetry reduction systems at the Cape and at the Hillside Laboratories as back-ups for each other. This allowed tests on two spacecraft to be conducted at the same time at the Hillside Laboratories during periods when the Cape telemetry was not in use. It also provided a back-up during critical operations against failure of the Cape telemetry system. The means for doing this required only the addition of a two-way audio-frequency data channel between the two locations to carry the 3-kc telemetry subcarrier and its sidebands. The teletypewriter circuit returned the output to the distant station in either case. Since the 136-mc receiver of the telemetry system was not included in the back-up, the 136-mc receiver of the command tracking antenna system was arranged to be used as a spare.

A full-period telephone line from the telemetry van to the Andover earth station was used to coordinate activities during launch and in subsequent tracking operations.

Telephone communication among all locations involved in launch and pre-launch operations was provided at Cape Canaveral by the Missile Operations Phone System (MOPS).

The command tracker van contains the equipment used for all tracking operations, sending of commands, and receiving telemetry. The 200-watt command transmitter and the control console for the command tracking antenna system are the principal items.

2.3.2 Antennas

Antennas at the base location were needed for remote testing by radio coupling to the spacecraft at the spin building, for terminal countdown tests on the launch stand and for the monitoring of telemetry during the ascent trajectory and subsequent orbits.

The same type quad-helix autotracking antenna designed for use at the Andover earth station was provided for command and telemetry. This antenna system provides autotracking of the 136-mc beacon to a precision of about $\pm 1°$ in both azimuth and elevation. The 136-mc signal received by the antenna is amplified and sent to the telemetry receiver for detection and decommutation.

The 123-mc command signal from either the 200-watt or the 2-mw transmitter may be multiplexed to the antenna.

A boresight antenna for periodic alignment of the command tracker is located 100 feet away on a 50-foot wood pole. A low-level 136-mc signal

is sent from the command tracker van to this antenna over a coaxial cable.

Two parabolic dish antennas were installed at the base location for remote testing of the spacecraft at the spin building and on the gantry. The 6390-mc transmitting antenna is 8 feet in diameter, and the 4170-mc receiving antenna is 10 feet in diameter. Both antennas were attached to a rigid framework mounted on a 25-foot telephone pole embedded in concrete and well braced with guy wires. The framework is manually steerable to permit aiming at either of the two remote locations. A low-power optical telescope is used to aim the antenna.

2.4 *Test Facilities at the Spin Building*

At the spin building, two 4-foot diameter parabolic antennas were mounted facing the base location on a 40-foot steel tower. Waveguide runs connect these antennas to one port of each of the spacecraft's antennas. The same tower also supports a VHF corner reflector antenna for telemetry and command use. The only other test equipment at the spin building is a rectifier for supplying power to the spacecraft during electrical tests.

2.5 *Spacecraft Facilities on the Launch Stand*

Upon completion of spin balancing, the spacecraft–third-stage combination was enclosed in a carrying canister for transportation to the launch stand. The carrying canister was lifted up to the top level of the service tower and lowered to mate with the Delta second stage. After removal of the canister, the spacecraft and the third stage of the rocket were each enclosed in plastic shrouds continuously supplied with dry, cool air. The working area on this level was also enclosed in an air-conditioned tent.

Because of the presence of the live third stage, it was decided to put the test equipment consoles in an existing room on a lower level and connect to the spacecraft through waveguide and coaxial cable runs. Thus, the testing prior to removal of the gantry was done in a manner similar to the testing at the base location.

III. SPACECRAFT TESTING

3.1 *Summary*

Two types of tests were made on the spacecraft. The first was a comprehensive test which was made three times — after the spacecraft was

received from Hillside, again after mating to the third stage and balancing, and again after the spacecraft was moved into launch position. The second type of test was a daily routine which determined that all major systems continued to function properly.

The comprehensive test included: physical inspection; checks on the radiation package, microwave antennas, solar cells, and two-year timer; and the complete daily routine. The daily routine included VHF beacon measurements, telemetry encoder comparisons, and checks on the command receiver, command decoder, power plant, microwave repeater, transistor damage experiment, and temperature and pressure sensors.

The spacecraft was tested at the base of operations, at the spin building and at the gantry tower, using the test arrangements previously described. During the final hours of the terminal countdown, testing and monitoring continued via radio through the fairing to the antennas at the base location.

During the launch the command tracking antenna tracked the satellite to the horizon, so continuous communication was maintained until that time. Telemetry was closely watched during this period, so that in the event that any relays should change state due to shock, they could be corrected by sending the appropriate command.

3.2 Specific Test Procedures

In preparation for all tests in the vans the spacecraft circuits were coupled to the test equipment in the following manner:

(1) The spacecraft helical antenna was disconnected near the canister and was replaced by a cable to the test equipment. This connection made possible precise measurements on the VHF systems without having to use the spacecraft antenna. It also permitted testing of the satellite without radiating power at the VHF beacon frequency or at the command frequency. The latter consideration is especially important at Cape Canaveral, where all radio-frequency radiation is carefully scrutinized and frequently prohibited for the sake of range safety.

(2) A single port of each microwave antenna was connected through a special coupling device to the equipment in the telemetry van. The remainder of the ports were girded by RF absorbing bands which reduced radiation and provided a termination for the antennas.

(3) A rectifier which supplied current required by the circuitry plus a small amount required for charging of the nickel-cadmium cells was connected through the battery jack.

The command and telemetry connections are shown in Fig. 5. A 20-db
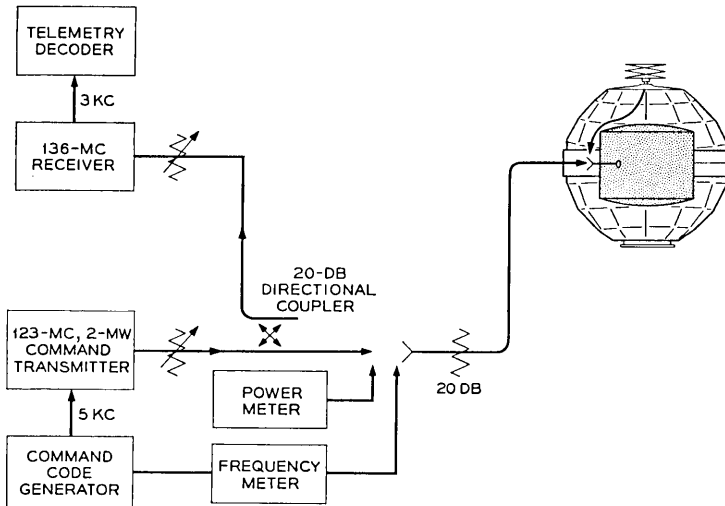
Fig. 5 — Command and telemetry test connections.

directional coupler was used to pick off the 136-mc signal for telemetry and to minimize the 123-mc command signal at the telemetry receiver input. The 20-db fixed pad was introduced to prevent the spacecraft from ever being subjected to the full power of the small command transmitter. It also attenuated the 136-mc signal down to the range of the power meter. The variable attenuators were used to set independently the desired power levels for both the 123-mc command and 136-mc beacon.

The microwave test connections are shown in Fig. 6. The 6-gc path contains only a variable attenuator. The 4-gc path has switching and filtering so that the composite 4-gc signal could be viewed on the spectrum analyzer and the 4170 and 4080-mc signals could be measured separately.

Figs. 7 and 8 show connections used to communicate with the spacecraft after it has left the van area. The test procedures in these locations were nearly the same as the van tests.

A description of each part of the daily test routine is given below.

3.2.1 *VHF Beacon*

The power output and frequency of the unmodulated 136-mc beacon were measured.
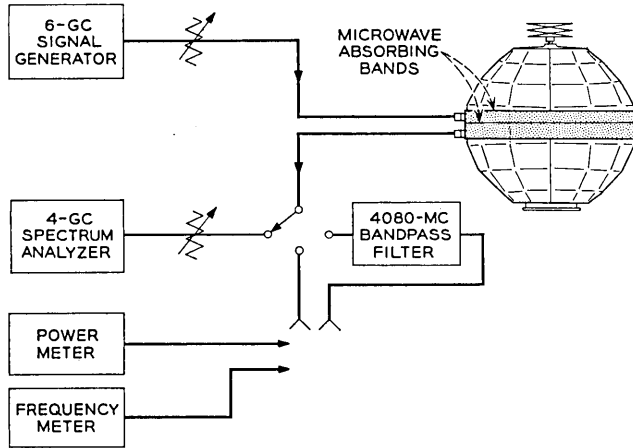
Fig. 6 — Microwave test connections.
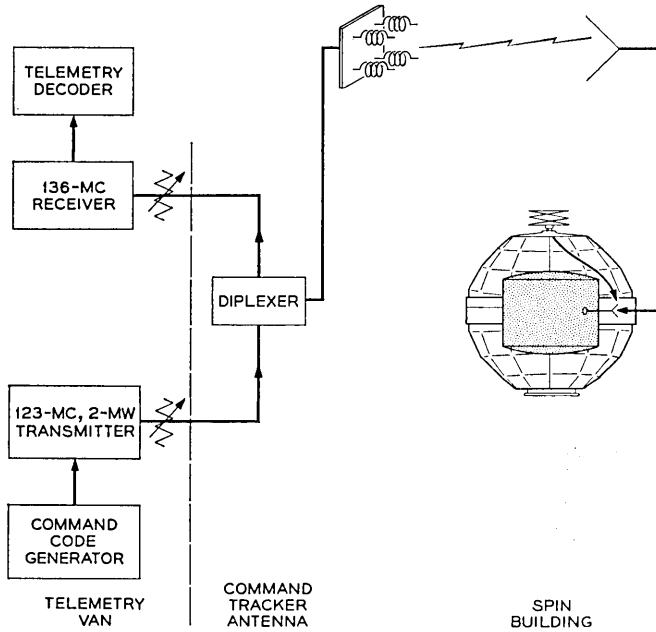
Fig. 7 — Command and telemetry connections for testing spacecraft in spin building.
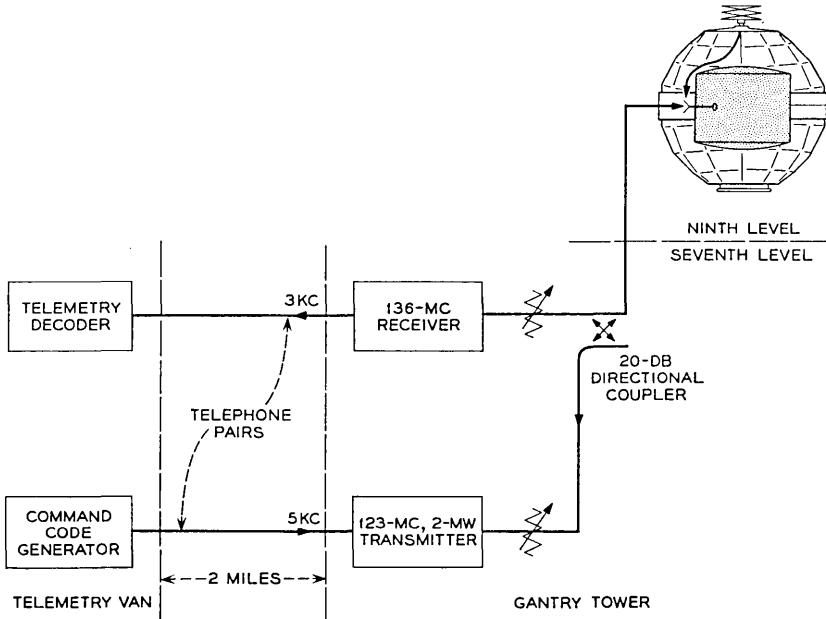
Fig. 8 — Command and telemetry connections from F − 5 day to F − 0 day.

3.2.2 *Telemetry Encoder Comparisons*

One complete frame of telemetry was taken from each of the two telemetry encoders and the readings compared.

3.2.3 *Command Systems*

The sensitivities of the two command receivers were checked with unmodulated signals. Following this, the commandability of each command receiver was verified.

3.2.4 *Power Plant*

The power plant test was an observation of 22 telemetered values of voltages, currents, and temperatures. Included were voltages and temperatures of the nickel-cadmium batteries and temperatures of key transistors in the regulators and dc-to-dc converters.

3.2.5 *Temperatures and Pressures*

Telemetry reads out 40 temperatures and 2 pressures. All values were checked and where possible were compared with external thermometers.

3.2.6 Transistor Damage Experiment

Six transistors with various degrees of shielding were placed in circuits which measured common-base short-circuit current gain. The values were checked via telemetry and compared with the known value of gain.

3.2.7 Microwave Repeater

The microwave repeater was checked using the following steps:
(a) check all related telemetry channels,
(b) with no signal input, measure 4-gc noise output,
(c) with no signal input, measure 4080-mc beacon frequency and power,
(d) with midrange signal input, measure beacon power,
(e) with midrange signal input, measure signal output power,
(f) view the spectrum of output signal for spurious sidebands, and
(g) measure point-by-point frequency characteristic of repeater.

The following tests were made in addition to the daily routine for the comprehensive test:

3.2.8 Microwave Antenna

As a check of the 4-gc transmitting antenna, a power measurement was made at each of the 48 ports. This test was made in lieu of a pattern measurement, which could not be made with the existing facilities. As a check of the 6-gc receiving antenna, a low-level 6390-mc signal was sent separately to each of the 72 antenna ports while the 4170-mc signal was observed at a single 4-gc port. The level was chosen to be below the automatic gain control range of the repeater so that amplitude differences in 6390-mc signal reaching the repeater would cause differences in level of the 4170-mc output.

3.2.9 Solar Cell Check

The output of all 50 banks of solar cells in the power plant and all of the individual cells in the solar aspect circuit was read as each cell or bank of cells was illuminated with a low-intensity light source. For the solar power plant, short circuit current was read with a milliammeter, and the solar aspect circuits outputs were read by telemetry.

3.2.10 Radiation Package Checks

Each of the four radiation sensing circuits was tested by bypassing the actual sensing element and delivering pulses directly to the inputs of

the preamplifier circuits. The thresholds of all of the detectors were verified by changing the pulse amplitudes once per minute and observing the telemetered data.

3.2.11 *Two-year Timer Check*

This test involved temporary powering of the two-year timer, applying a start signal, and verifying that the timer had started. After verification, the timer was stopped by removing power.

3.3 *Testing of the Spacecraft at Remote Locations*

All testing of the spacecraft in the spin building was done remotely by radio from the base location. All of the tests described above were made, but some techniques had to be changed to accommodate the lower signal levels available over the radio link to the base location.

When the spacecraft was at the launch stand, daily tests continued. To reduce radiation at all working frequencies and to eliminate the variability of the path losses in the measurements, all of the spacecraft radio systems were terminated in test equipment on the seventh level of the gantry tower. From that point to the base location, telephone pairs were used to carry the 3-kc telemetry and the 5-kc command subcarriers. Microwave tests were made on the seventh level. All tests made on the gantry were under the direction of the test conductor in the telemetry van, so voice communication was maintained at all times.

IV. FROM F − 15 DAY TO F − 0 DAY

On F − 15 day (15 working days before launch) the prototype spacecraft was taken from the van to the spin building, where it was mated to a dummy third stage. This event was in preparation for the RF compatibility test on F − 11 day, but it also gave personnel of the Douglas Aircraft Company and of the Laboratories an opportunity to rehearse their procedures a few days in advance of the arrival of the flight model at the spin building.

On F − 12 day the prototype and dummy third stage were transferred to the launch stand and were attached to the second stage of the Delta vehicle. The RF compatibility test on F − 11 day showed that all the range radars, the guidance system, the destruct system, vehicle beacons, and the spacecraft systems were mutually compatible.

On F − 9 day the Fly 2 spacecraft was transferred to the spin building to be mated to the live third stage. Daily checks continued at the

spin building until F − 5 day, when the spacecraft was transferred to the launch stand.

From F − 5 to F − 1, daily checks continued on the spacecraft and the Delta vehicle.

The F − 0 countdown was started at 5:40 p.m., July 9, on the evening before the launch. The first check of the day, ending at 7:00 p.m., was a complete daily routine. After completion of the routine, telemetry was left on and the spacecraft battery was charged until 8:15 p.m. At approximately 10 p.m. preparation for fairing installation began. For this it was necessary to: (1) disconnect all test cables, (2) remove air-conditioning and shroud, (3) remove the plastic protective cover, (4) remove microwave absorption bands, (5) remove spacecraft access panel, (6) connect helix antenna, (7) verify two-year timer operation, (8) install access panel, (9) remove protective covers from radiation sensors and mirrors, and (10) inspect. After these preparations were made, the fairing was installed, leaving one access hole open for insertion of the umbilical plug, which was the final link between the spacecraft battery plant and the rectifier in the blockhouse.

By midnight the fairing was installed and all umbilical connections were made and checked. Once again, before the gantry tower was rolled away, the spacecraft was turned on for the purpose of making a test with commands going through the fairing to the helical antenna, as they would during the early part of the ascent trajectory. This task was completed successfully by 30 minutes after midnight, and the spacecraft was turned off again as a period of "no radiation — no switching" began.

At 1:10 a.m. checks of the van equipment were started as the gantry tower removal began. The command tracker was aligned with the boresight; the command transmitter was measured for proper VSWR, modulation percentage, and power output. Another command routine was made and completed at 2:10 a.m. For the next 50 minutes, batteries were charged and telemetry was watched very closely.

At the end of the 50 minutes, the time was 3 a.m. or T − 35 minutes. The terminal count began. Between T − 35 and T − 10 a brief command routine test was performed, and the microwave repeater was given a last test. At T − 10 all commandable circuits were in launch condition: i.e., all were turned off except for the 136-mc beacon and the telemetry modulating the beacon.

Lift-off occurred at 3:35 a.m. (0835 GMT) on schedule. The command tracking antenna autotracked the VHF beacon from lift-off to horizon. Small variations appeared in the signal level due to ground reflections and attenuation, but otherwise the track was routine. Until the satellite dropped below the radio horizon, telemetry was watched very closely

with particular emphasis on relay states, battery temperature and volt-age, solar plant current, AGC level from command receivers and the low-level calibration channel.

To ensure that good command capability was maintained during the launch, the telemetered AGC levels of the spacecraft command receivers were watched, and at a predetermined level, the 123-mc carrier power was increased 20 db to the full 200 watts.

Other telemetry channels bore interesting information on several aspects of the ascent. Fig. 9 shows skin temperatures on two different facets of the satellite. One of the two was illuminated by the sun continu-ally for approximately 10 minutes — from the time the spacecraft emerged from the earth's shadow until the spin rockets were fired, caus-ing the satellite to spin and thereby putting the facet into the shadow of the satellite part of the time. The other facet shown was in complete darkness until spin-up, when it began to receive some solar radiation.

Fig. 10 shows on one trace the amount of current supplied to the satel-lite either by the blockhouse rectifier or by the solar plant. Between 0840 GMT and 0849 GMT the current showed a steady decrease because that part of the solar plant which was delivering the current was being warmed (see Fig. 9) and was becoming less efficient. After spin-up some of the cooler portions came into sunlight and the average current in-creased.
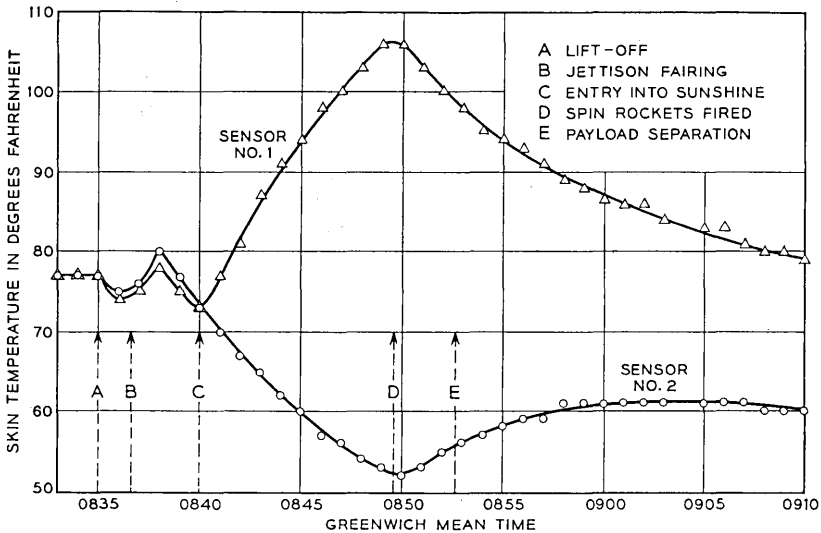
Fig. 9 — Skin temperature variation after lift-off
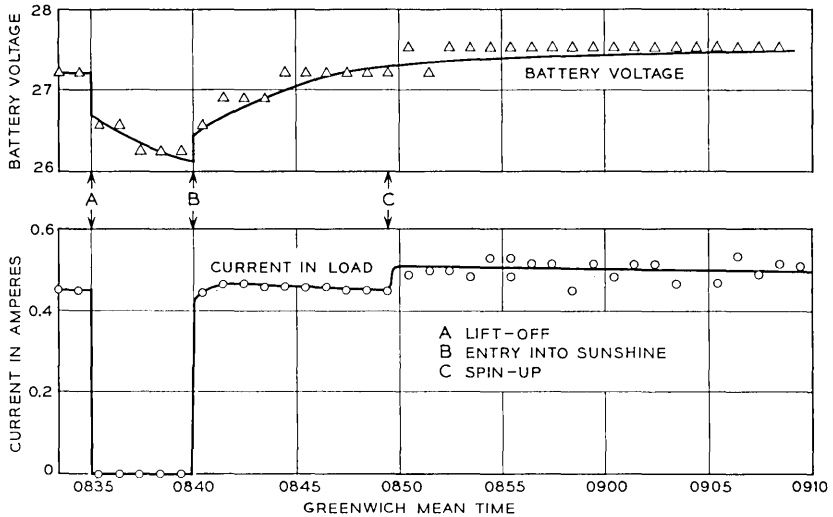
Fig. 10 — Ni-Cd battery voltage and current delivered to canister during launch.

The voltage of the battery plant is shown in the other trace of Fig. 10. The abrupt drop in the battery voltage at lift-off is attributable to the fact that when the rectifier in the blockhouse was disconnected, the current in the battery changed from a 0.3-ampere charge to a 0.2-ampere discharge. The battery continued to discharge until the satellite emerged into the sunlight, at which time the voltage began to increase.

The spacecraft went below the Cape Canaveral radio horizon at 0848 GMT (0348 EST), so all information shown beyond this time was taken from magnetic tape recordings made by the NASA Minitrack stations. Coverage by Cape Canaveral and by these stations was as follows:

> Cape Canaveral from lift-off to 0848 GMT
> Antigua from 0839 to 0853 GMT
> Ascension from 0845 to 0902 GMT
> Johannesburg from 0904 to 0917 GMT.

V. LAUNCH VEHICLE AND ORBIT

5.1 Description of the Delta Launch Vehicle

Fig. 11 is a cutaway view of the Delta vehicle as used for the Telstar launch. It is a three-stage rocket, with ground-guided, liquid-fueled first

TELSTAR SPACECRAFT

SOLID PROPELLANT MOTOR

SPIN TABLE

BTL GUIDANCE

2ND STAGE FLIGHT CONTROLLER

FUEL TANK

HELIUM SPHERE

FAIRING

SPIN ROCKETS

2 ND STAGE
TELEMETRY ANTENNA

GUIDANCE ANTENNA

OXIDIZER TANK

2 ND STAGE ENGINE

1ST STAGE AUTOPILOT

FUEL TANK

TELEMETRY ANTENNA

TURBO PUMP

1ST STAGE TELEMETRY

OXIDIZER TANK

STABILIZING FINS

1ST STAGE ENGINE
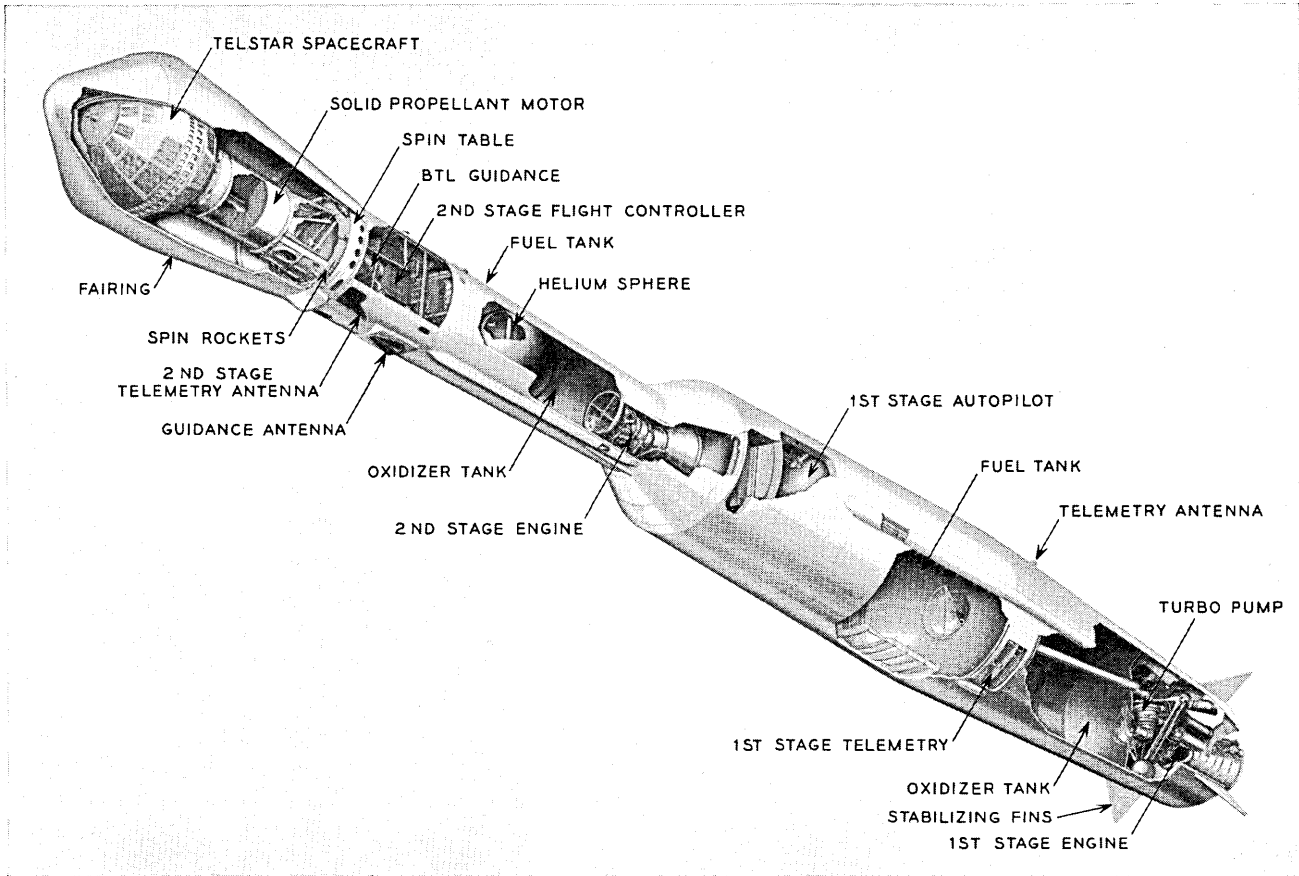
Fig. 11 — Delta vehicle-Telstar spacecraft.
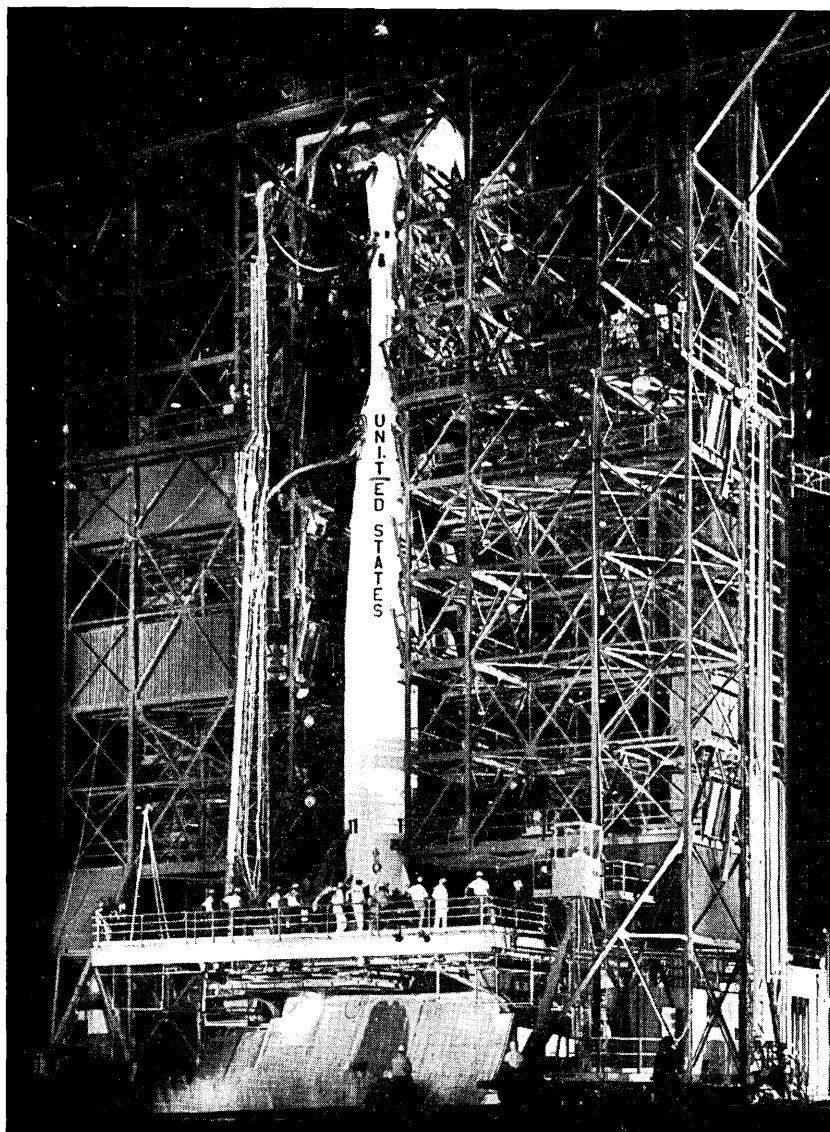
Fig. 12 — Delta vehicle and Telstar spacecraft in gantry.

and second stages, and a spin-stabilized, solid propellant third stage. A bulbous fiber glass fairing surrounds the third stage and the Telstar spacecraft mounted on it in the launch configuration. Fig. 12 shows Delta No. 11 in the service tower about three hours before launch. It is approximately 90 feet high and weighs about 57 tons, fueled and ready for launch.

The first stage is an operational-type Thor missile modified for the Delta use. Its engine uses RP-1 (kerosene) fuel with liquid oxygen (lox) as the oxidizer. Vehicle performance is based on use of at least 99 per cent of the propellants. A flight controller employing three integrating gyros, three rate gyros, and a programmer is used to provide open-loop control until the ground guidance system takes control at about 90 seconds after lift-off. Control is achieved by a combination of the gimballed main engine nozzle and two small vernier engines.

The second stage is a propulsion system which uses unsymmetrical dimethyl hydrazene fuel (UDMH) and inhibited white-fuming nitric acid as the oxidizer. A gaseous nitrogen retro system is used on the second stage to provide reverse thrust to get the required separation distance between the second and third stages at third-stage ignition.

Second-stage in-flight steering control is achieved by hydraulic gimballing of the second stage engine thrust chamber. Roll control is accomplished by discharging helium gas through four roll jets, two of which react in a clockwise direction, and two of which react in a counterclockwise direction. Both pitch and yaw control systems respond to commands from the Laboratories guidance system.

During the coast period, starting at second-stage burnout and ending at second/third-stage separation, the vehicle was turned to its proper spatial orientation by means of a second-stage coast phase control system. The gyros used to control the second stage during the powered portion of flight supply the attitude reference used to control the gas jet system during the coast phase. An on-off type of gas jet operation was used. To provide range safety destruct capability, the Delta vehicle carries radio receivers in the first and second stages. The flight termination system in each stage consists of the receiver and decoder, antenna system, safety and arming mechanism, detonating cord strand to rupture propellant tanks, and a power supply independent of vehicle power. Prior to first/second-stage separation, either system would destruct both stages. A large-diameter (approximately 22 inches) ball bearing mounted at the forward end of the second stage supports the spin table, which in turn supports the third-stage motor and spacecraft. Prior to third-stage ignition, the third stage and spacecraft were spin stabilized at approximately

180 rpm by small rocket motors attached to the spin table. The third-stage propulsion system had a solid propellant motor.

The separation of the third stage was delayed approximately 2 minutes after nominal fuel depletion to allow time for afterburning and outgassing of the third-stage motor and thus prevent contamination of the satellite. The third-stage motor was tumbled by an asymmetrical weight after separation to prevent impact with the satellite.

A bulbous fairing was provided to decrease aerodynamic drag and to protect the spacecraft and third-stage motor from aerodynamic heating during flight through the atmosphere. This fairing was jettisoned at an altitude of 85 nautical miles, where protection from aerodynamic heating was no longer required.

5.2 *Spacecraft/Launch Vehicle Integration*

The Delta vehicle for the Telstar project placed limits and require-ments on the spacecraft to ensure compatibility. The dimensions of the standard bulbous fairing fixed the maximum diameter of a spherical spacecraft at slightly over 35 inches. A standard Delta payload attach fitting was incorporated as an integral part of the spacecraft structure, to mate with the corresponding fitting on the Delta. The compatibility of the spacecraft design was confirmed at a fit-check mating at Douglas Aircraft Company, Santa Monica, California, in December, 1961, when a full-scale, accurate mockup of the spacecraft was assembled with the ap-propriate launch vehicle components. The Fly 2 spacecraft weight, when delivered to Cape Canaveral, was 170.325 pounds. General environmental capabilities for temperature, humidity, shock, vibration, acceleration and thermal vacuum were established by qualification and acceptance tests at the Laboratories. Possible contamination from fairing outgassing due to aerodynamic heating was investigated and found to be of no concern.

5.3 *Orbit Determination and Guidance*

The desired Telstar satellite orbit resulted from a sequence of activities taking more than a year and involving several organizations. In 1960 and 1961, the Laboratories made parametric studies to relate Telstar trans-mission requirements to Delta capabilities in terms of achievable orbits and spacecraft weight and size. When the weight had been set at ap-proximately 170 pounds, more detailed studies were made to precisely define the desired orbit. This study indicated that the Delta vehicle could place 170 pounds in an orbit of the following characteristics:

Apogee: 3000 nautical miles

Perigee: 500 nautical miles

Inclination of orbit to the earth's equator: 45°

Spin-axis azimuth at injection: $\geq 155°$

A Delta trajectory to achieve this orbit was generated and its feasibility confirmed. This trajectory became part of the detailed test objectives (DTO) for Delta No. 11. The necessary guidance equations to represent the desired trajectory were developed. After translation into a punched guidance tape, these results were checked by simulation testing in the command guidance system at Cape Canaveral.

Because of range safety considerations, when a Delta vehicle is launched from Cape Canaveral the launch azimuth may not exceed 108°. This establishes a path which crosses the equator at an angle of about 33°. The orbital inclination will have this value if all three stages are fixed in the initial flight plane, as they would be for maximum energy use. The desired higher inclination of 45° was attained by yawing the second and third stages to the south of the initially established ascent trajectory plane when the vehicle had arrived at a point where the range was clear to the south. Since the energy imparted to a spacecraft is reduced by such yawing, the final apogee or perigee or both will be reduced.

In developing the ascent trajectory it is necessary to ensure that the command guidance system at the launch site maintains contact with the vehicle during first and second-stage burning. The vehicle must stay well above the launch site horizon, and certain limitations are imposed on the orientation of the axis of the vehicle so that its antenna pattern will properly receive guidance signals from the launch site. Several calculations are required for the determination of the optimum ascent trajectory.

After the second-stage engine cutoff (SECO), the vehicle is allowed to coast upward, losing speed, until finally it reaches the apogee of the ascent trajectory established by the first and second stages. At this point the third stage is ignited. The third-stage axis is maintained in the local horizontal plane at the time of firing, in order that no more energy be wasted than necessary, and so that the final perigee position will coincide with the ascent trajectory apogee. For the final Telstar satellite orbit, perigee was about 5° latitude north of the equator and apogee about 5° south.

Within this framework, various possible orbits were calculated. First, a particular spacecraft weight and perigee height were selected and a series of ascent trajectories was calculated with the object of finding ones

whose ascent trajectory apogees were equal to the specified final perigee height. One was chosen which had the maximum velocity at ascent trajectory apogee and still met the requirements that command guidance contact be maintained during the burning of first and second stages and that a certain amount of yawing to the south be accomplished during second-stage burning in order to increase inclination. When such an optimum ascent trajectory had been determined, possible final orbits were calculated, assuming the third stage to be yawed southward by increasing amounts, resulting in increasing inclinations and decreasing apogee heights. The result was a family of orbits where apogee height is a function of inclination. Iteration of this process produced a family of feasible orbits from which one was selected for the Telstar satellite.

The Telstar launch vehicle was guided by the command guidance system designed by the Laboratories. The command guidance system consists of a precision tracking ground radar, a digital computer and a missile-borne system in the second stage of the rocket, consisting of a radio receiver, decoder and transmitter. The ground guidance facility, GMCF-3, which is located about two miles from the launch pad, houses the radar and the computer. In the command guidance system the launch vehicle position is continuously determined by the precise ground-based automatic tracking radar. The computer accepts the position data and derives appropriate vehicle velocities. The missile position and velocity data are compared with precalculated values, representing the desired trajectory, which have been stored in the computer prior to flight. Coded steering commands, based on deviations between the actual and desired values, are transmitted to the missile on the radar beam.

An engine cutoff command is sent to the vehicle when the ground-based computer is satisfied that appropriate terminal conditions have been met. The high degree of accuracy of the command guidance system results primarily from the combination of reliable communications to the vehicle, precise radar tracking, and a unique computation process involving radio inertial guidance principles for determination of velocity.

TABLE I — *Telstar* ORBIT PARAMETERS

	Orbit Computed Preflight	Orbit Predicted From Burn-Out Parameters	Actual Orbit (NASA Minitrack)
Apogee (nm)	3000	2990	3043.2
Perigee (nm)	503	513.14	511.9
Period (min)	156.48	156.55	157.6
Inclination to equator (deg)	44.97	44.99	44.78

5.4 *Actual Orbit Achieved*

The Delta No. 11 second-stage burnout parameters obtained from the guidance computer at the conclusion of the second-stage guidance were used to predict the final orbit. The predicted orbit parameters obtained are shown on Table I, with the preflight computed orbit and the actual orbit obtained by tracking shown for comparison. Differences among the three are small.

VI. CONCLUSION

The testing methods and facilities developed by the Laboratories for the pre-launch and launch operations at Cape Canaveral were used successfully on the first Telstar launch, and only minor changes will be made for the second Telstar launch.

The excellent cooperation between all of the people of the Laboratories involved in the launch and the members of the National Aeronautics and Space Administration and its supporting agencies at Cape Canaveral contributed immeasurably to the successful launch.

Results of the *Telstar* Satellite Space Experiments

By P. T. HUTCHISON and R. A. SWIFT

This paper describes how the Telstar satellite has performed in space. Included is information on changes in the temperature, spin rate, spin-axis precession, orbital parameters and power levels of the satellite signals, and comments on the behavior of the electrical circuits in the space environment.

I. INTRODUCTION

This paper describes the initial performance and changes in the electrical characteristics of the communications repeater, command system, and telemetry system and changes in the temperatures, spin rate, spin-axis precession, and other physical phenomena occurring in the Telstar spacecraft during the first months of operation.

One of the objectives of the Telstar experiment was to obtain information on the performance of an active communications satellite repeater over an extended time interval and to obtain data that would be applicable in the design of a commercial communications satellite. To this end, the Telstar spacecraft has been closely monitored since it was launched. The satellite is monitored by measurements of signals received at the ground stations and by telemetry. Observations at ground stations give orbital, satellite-orientation, antenna-pattern, and signal-level data. Telemetry gives satellite orientation, solar plant output, satellite temperature, and electrical performance data.

The spacecraft was spin-stabilized and injected into orbit with its spin axis nearly perpendicular to the ecliptic plane. This insured the most favorable coverage of the earth by the Telstar antennas, the maximum output power of its solar cells, and the most favorable skin temperature distribution. The value of the spacecraft as a communications satellite is a function of how well it retains this orientation as it orbits the earth. Measurements of the changes in this orientation indicate an average precessional torque of 3×10^{-6} pound foot due to the residual

magnetic moment of the satellite. This type of information is helpful in developing orientation schemes for future satellites.

The spacecraft was designed and tested to withstand the environmental conditions it would see throughout launch and its life in orbit, based on the known and assumed aspects of its environment. By placing the spacecraft in orbit, the assumptions made could be evaluated.

The most meaningful test of a communications satellite is the test of how well its electronics circuitry operates under actual space conditions. The results of the successful communications experiments are discussed in a separate paper[1] in this issue. In this paper, the emphasis is placed on changes that may have occurred since launch on July 10, 1962.

When the Telstar satellite was launched, it was injected in the predicted orbit with the spin axis favorably orientated with respect to the sun at a time of day which resulted in 14 full sunlit days before the satellite entered periods of eclipse. The initial orbit parameters were as follows:

Apogee	3047 nautical miles
Perigee	515 nautical miles
Inclination	44.79 degrees
Spin rate	177.7 rpm
Solar aspect	90.5 degrees

During the period from launch on July 10, 1962, to the time of interruption of the VHF command system on November 23, 1962, there were only minor variations in the power levels and the operating characteristics of the communications repeater in the satellite. The satellite temperature, attitude, visibility times, and eclipse times have varied as anticipated. It is the purpose of this paper to discuss qualitatively the causes and effects of the expected and unexpected variations in satellite performance.

II. SOLAR ASPECT

Solar aspect is defined as the angle between the sun-satellite line and the satellite spin axis, measured from the telemetry antenna. This angle is determined by sampling the currents from (each of) six solar cells mounted at the ends of three mutually perpendicular axes on the satellite skin. The output currents of the six cells, together with their known geometric arrangements, uniquely define the solar aspect angle[2] with an accuracy of ±0.5°. The curve shown in Fig. 1 indicates the spacecraft orientation for the twelve-week period following launch.

The reasons for the shape of this curve are twofold. First, the satellite spin axis at injection was not quite normal to the plane of the ecliptic.
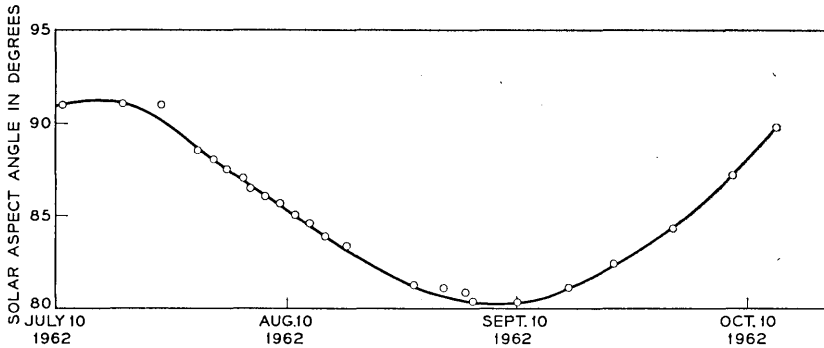
Fig. 1 — Telstar spacecraft — solar aspect angle versus time.

As both the earth and the orbit rotate with respect to the sun, the spin-axis projection alternately decreases and increases. Second, the attitude of the spin axis in inertial space is varying due to a precessional torque. This will be discussed later. The main effects of solar aspect deviations from 90° on the satellite's performance are to reduce the available power from the solar cells and to change the skin temperature distribution. This occurs because the solar-cell distribution is not isotropic over the satellite surface; however, the small deviations noted to date have not resulted in a significant change in output from the power supply.

III. ATTITUDE

Changes in the solar aspect angle are due in part to attitude changes in inertial space. Attitude is expressed in the spatial coordinates of declination and right ascension. In terms of an infinite sphere with the earth's lines of latitude and longitude projected upon it, declination corresponds to the latitude and right ascension to the longitude measured eastward from the vernal equinox. The coordinates of the attitude indicate the intersection of a line coinciding with the spin axis that starts at the center of the satellite and goes through the telemetry antenna and the infinite sphere.

The analysis of three sets of data serves to determine the attitude of the satellite. As previously mentioned, solar sensors indicate the angle between the satellite spin axis and the sun. Another angle is obtained from a series of light flashes observed from mirrors mounted on the satellite.[3] The time of the flash occurrence yields an indication of the angle between the spin axis and the satellite-ground station line, some-times denoted as the earth aspect angle of the satellite. These two angles form tangent cones with a common apex. The intersection is a straight

line whose direction is determined from the knowledge of initial launch conditions. Fig. 2 is a plot of satellite attitude during the first three months, equivalent to approximately 800 orbits.

Changes in satellite attitude are caused by a torque generated by the interaction of the satellite magnetic moment and the earth's magnetic field. Prior to launch, a compensating magnet was mounted on the satellite to reduce the effect of the TWT magnetic field. However, a residual moment causing torques on the order of 10^{-6} pound feet remained. Owing to the nodal regression of the Telstar satellite orbit, the precessional torque rotates with respect to the satellite. The torque induces a continuously changing attitude of the satellite moment of momentum and a rapid precession about the momentum vector. Precession dampers within the satellite effectively eliminate this rapid precessional motion. As seen in Fig. 2, attitude changes increase from orbit to orbit as the satellite spin decreases; that is, the satellite tendency to rotate due to torques increases with spin decay.

The satellite is equipped with a coil of wire around its equator and a direct-current supply which, when activated, either reinforces or reverses the axial magnetic moment, thereby providing a means for attitude correction.

IV. SPIN RATE

The effect of the precessional torque is heightened by the steady decrease in the satellite spin rate. The major retarding torque causing this
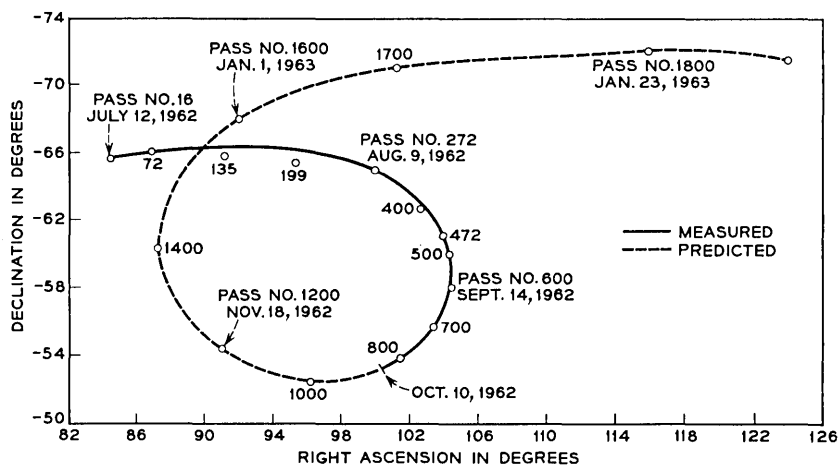
Fig. 2 — Telstar satellite attitude.

spin decay is produced by eddy currents generated in the satellite as it rotates in the earth's magnetic field. Since the instantaneous torque is dependent on the spin rate, the satellite would undergo a pure exponential decay if it were rotating in a uniform field. However, the effective magnetic vector, which is the component normal to the spin axis, is a function of both satellite attitude and altitude, geomagnetic field along the orbit, the regression of the orbit plane, and the advance of perigee. Satellite attitude and nodal regression are considered to be secondary effects. Fig. 3 is a sketch of field variation and satellite latitude versus orbital period. The dashed line indicates the satellite latitude. Shortly after injection, the perigee occurred near the equator. As the orbit precessed, the perigee moved toward the region of higher field strength. The net effect is to continuously alter the slope of the exponential decay curve, resulting in an initial decay that was almost linear, as shown in Fig. 4.

On the basis of this curve, it is calculated that the spin rate will be
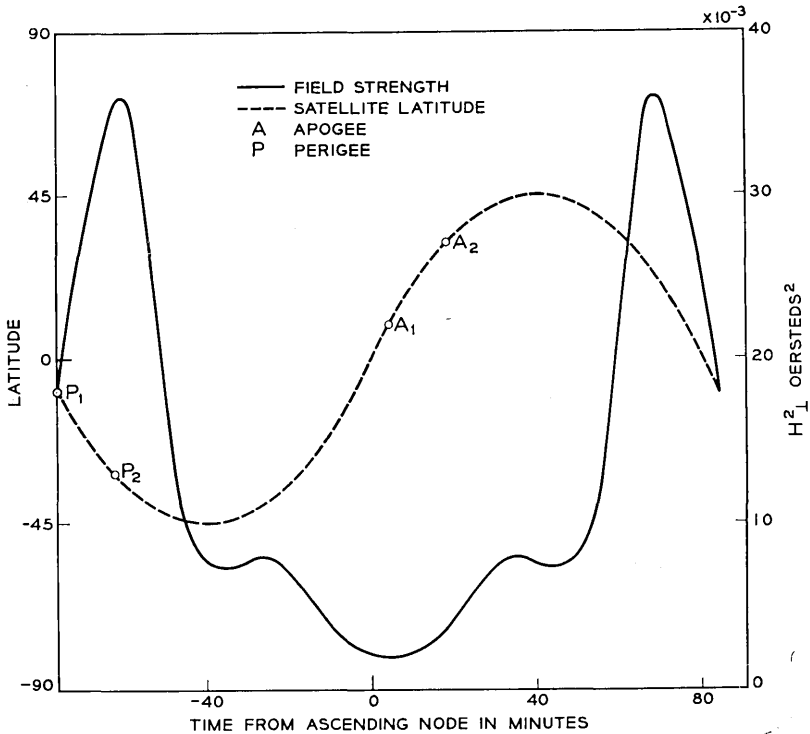
Fig. 3 — Field strength and satellite latitude versus time from ascending node.
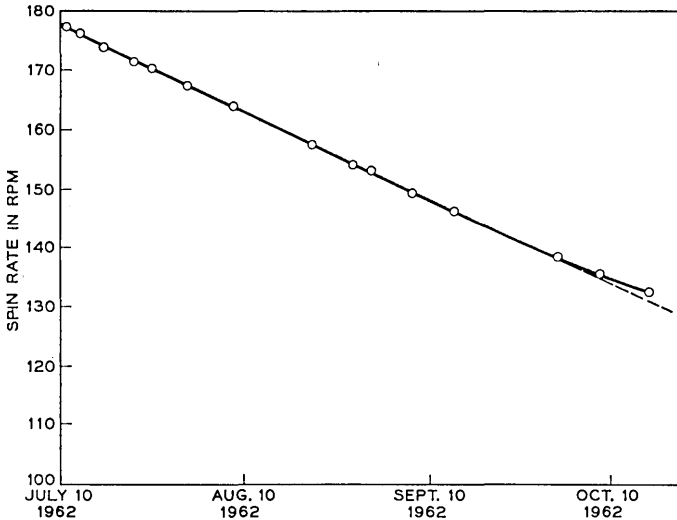
Fig. 4 — Telstar satellite — spin rate versus time.

reduced from an initial rate of 177.7 rpm to 66 rpm in about 330 days,[4] and the spin rate will therefore stabilize the Telstar satellite for about two years.

V. VISIBILITY TIME

It has been shown that the motion of the perigee within the orbit plane affects the satellite spin rate and attitude. Owing to the ellipticity of the orbit, the perigee motion also affects the minimum usable time per day. Usable time is defined as the time the satellite remains at least 7.5° above the horizon. The higher the satellite is during a pass, the longer it will be visible to a particular ground station. As the perigee moves to its most southern latitude (−45°), the apogee is almost over the Maine ground station; and as shown in Fig. 5, the usable time reaches a maximum. Maximum visibility occurs when apogee is over the ground station for two reasons. This is the time when the greatest portion of the orbit is visible and also the time in orbit when the satellite velocity is a minimum.

VI. ECLIPSE DURATION

Satellite eclipse duration is important insofar as it affects the satellite temperatures and the ability of the solar cells to recharge the batteries. A curve of satellite eclipse time per orbit is shown in Fig. 6.
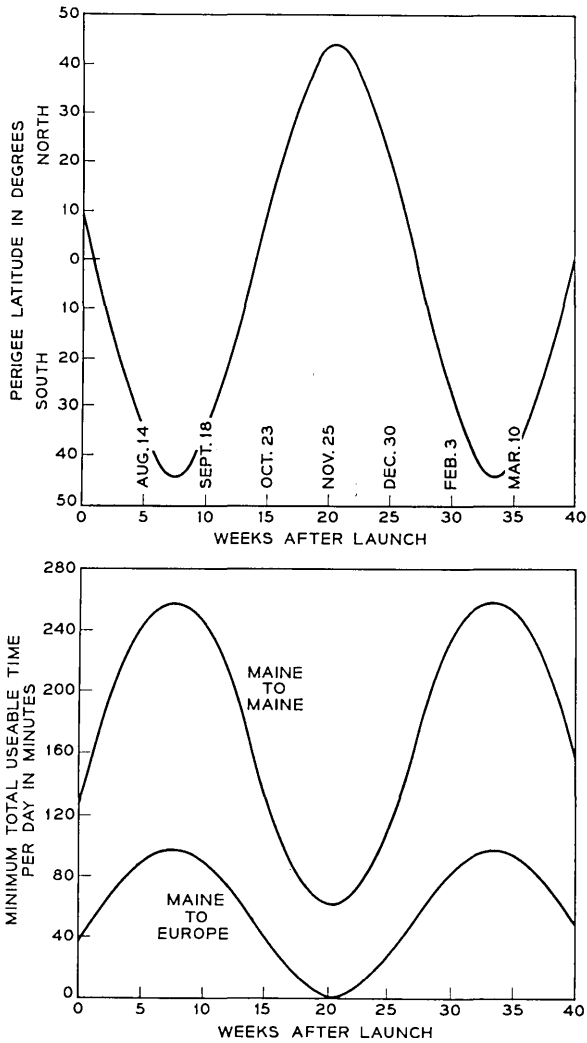
Fig. 5 — Telstar satellite — perigee latitude and minimum usable time per day.

Between July 21, 1962, and January 8, 1963, the satellite was to be in shadow for a period of about 30 minutes per orbit on the average. The shape of this curve is principally a result of three motions·

(1) The motion of the earth and the orbital plane about the sun.

(2) The regression of the orbital plane.

(3) The advance of the apogee and perigee within the orbital plane.

The effect of these motions on the orbit-earth-sun orientation is shown
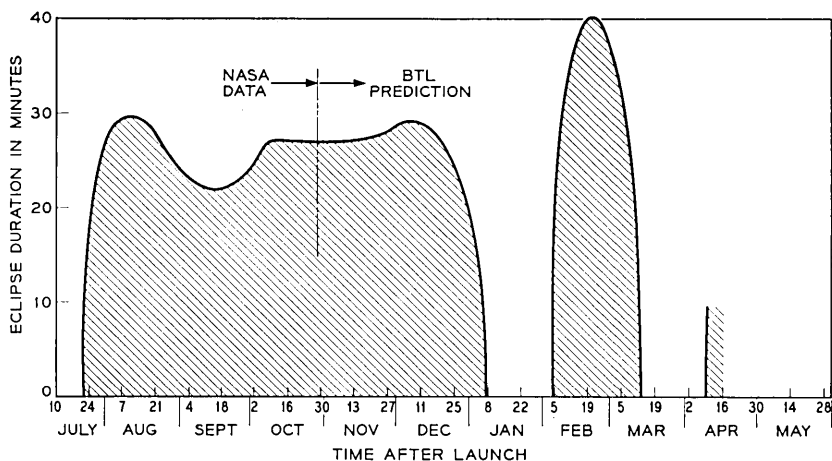
Fig. 6 — Predicted satellite eclipse duration.

pictorially in Fig. 7. It is seen that the orbit rotates clockwise in the direction opposite to the earth's spin as the earth moves counterclockwise about the sun. The perigee moves in the direction of the satellite motion within the plane of the orbit. The perturbing influence causing these motions is due principally to the attractive forces associated with the earth's equatorial bulge.

Shortly after the Telstar satellite first went into eclipse, July 21, 1962, the perigee was in shadow. Each day the satellite goes into eclipse approximately two minutes later than on the previous day. This is shown in Fig. 8, where eclipse occurrence time after ascending mode is plotted against calendar time and orbit number. The vertical height of the gray area on any particular day represents the eclipse time. This curve was made for passes occurring near midnight EDT.

VII. SATELLITE TEMPERATURES

The satellite temperatures of major interest are those of the electronics canister and the solar cells. The energy transfer paths determining these temperatures are shown schematically in Fig. 9.

It is important that the solar-cell temperatures be kept low for two reasons: first, the conversion efficiency of the solar cell plant decreases with increasing temperature; second, the solar cell life decreases with sustained high temperatures. Temperatures within the canister must be kept within certain ranges to ensure optimum system operation.* It will

---

* In the satellite, the nickel-cadmium battery is the component most sensitive to temperature variations.
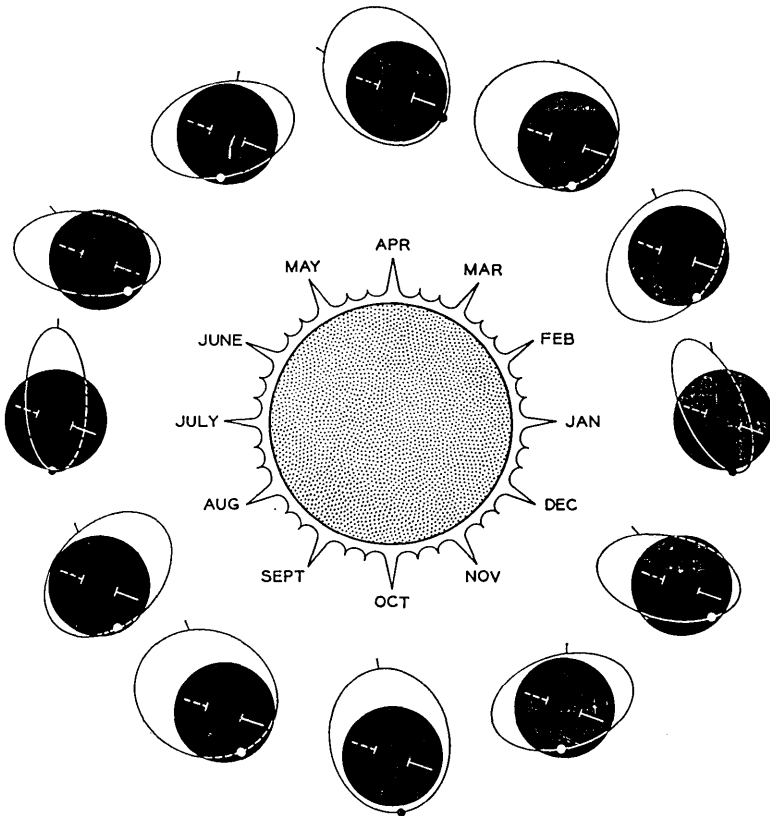
Fig. 7 — Orbital motion of spacecraft.

be seen in the following how solar aspect, in addition to periods of eclipse, influences satellite temperatures and power-plant efficiency.

The Telstar spacecraft geometry and the near isotropic distribution of solar cells makes the total energy absorbed nearly insensitive to the satellite orientation or attitude. Therefore, the mean radiant temperature, T,* depends chiefly on the energy incident on the satellite and the

---

* The mean radiant temperature, T, is determined by equating the incident energy to the radiated energy.

$$\text{heat in} = \text{heat out}$$

$$\pi R^2 \alpha (S + A + I) = 4\pi R^2 \epsilon \sigma T^4$$

$$T^4 = \frac{1}{4} \frac{\alpha}{\epsilon} \frac{1}{\sigma} (S + A + I)$$

where
  α = absorptivity
  ϵ = emissivity
  σ = Stefan Boltzmann constant
  R = radius.
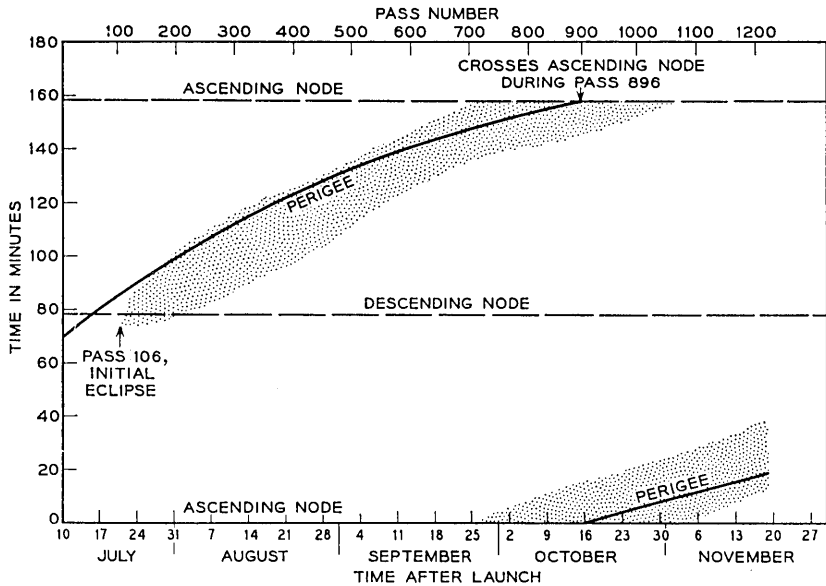
Fig. 8 — Telstar spacecraft orbital events.

satellite's surface characteristics. Both the skin temperature distribution and the temperatures within the electronics canister are related to the mean radiant temperature and the energy dissipated within the chassis, Q. However, the nature of the skin temperature distribution affects the solar plant; large temperature extremes over the satellite surface result in lower net power.

Since the spacecraft is spinning, the most favorable skin temperature distribution occurs when the sun rays are normal to the spin axis.

7.1 *Satellite Skin Temperatures versus Time*

Typical satellite skin temperatures for the first three months after launch are plotted in Fig. 10. During this period the solar aspect has varied over a range of 10°. The effect of the changing aspect has been to increase the temperature of the pole inclined toward the sun. The period of temperature variation closely corresponds to that of the variation in solar aspect. The difference is accounted for by the effects of secondary radiation, infrared energy radiated from the earth, and solar energy reflected from the earth. These data were recorded when the satellite was well out of eclipse. It is evident that the average of these skin tempera-
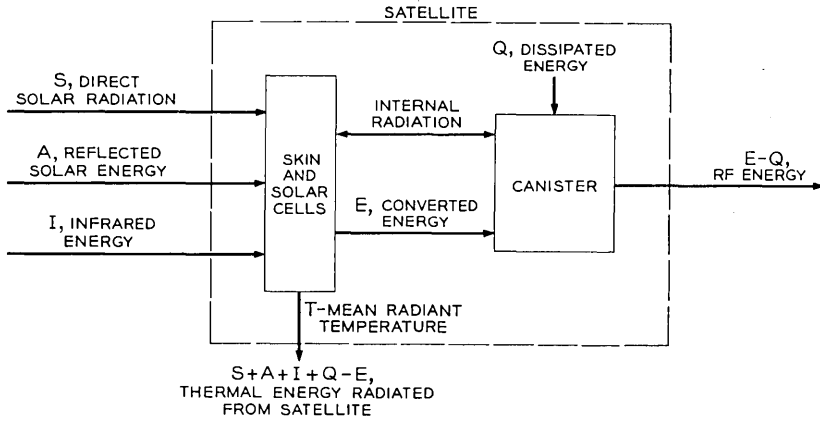
Fig. 9 — Spacecraft energy transfer.

tures has decreased, even though the solar flux density is increasing as the earth moves closer to the sun. This indicates that the effect of eclipse is greater than the effect of the increasing solar flux density.

7.1.1 Skin Temperatures During a Typical Orbit

Fig. 11 indicates how the skin temperatures vary as a function of time from perigee. These data were recorded August 16, 1962, and are repre-
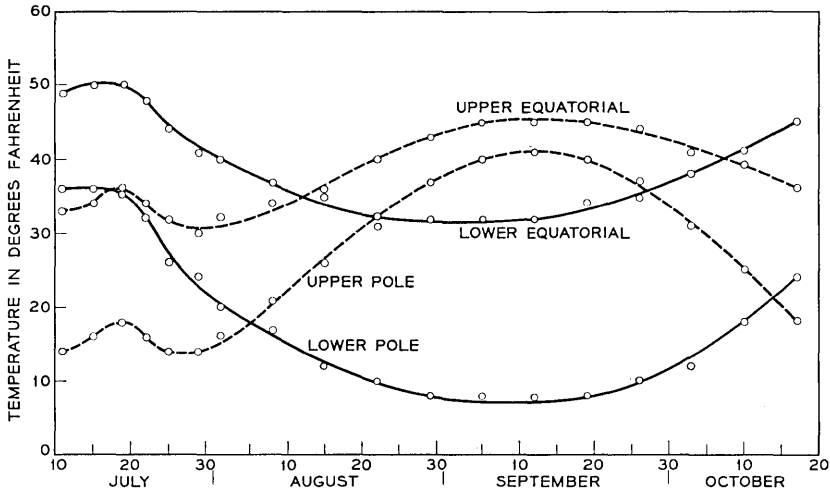
Fig. 10 — Skin temperature versus time.

sentative of a few orbits on that day. The effect of solar aspect is clearly seen during the period 60 minutes to 130 minutes. After 130 minutes the satellite went into eclipse. During eclipse the upper pole temperature was lower than the lower pole temperature. This temperature difference is a result of energy reflected and energy radiated from the earth. While in eclipse, the lower hemisphere was favorably inclined with respect to the earth for heat transfer from these secondary sources.

7.1.2 *Skin Temperatures During Eclipse*

The Telstar satellite first went into eclipse on July 21, 1962, and by August 16, 1962, the perigee was in shadow for 30 minutes. As shown in
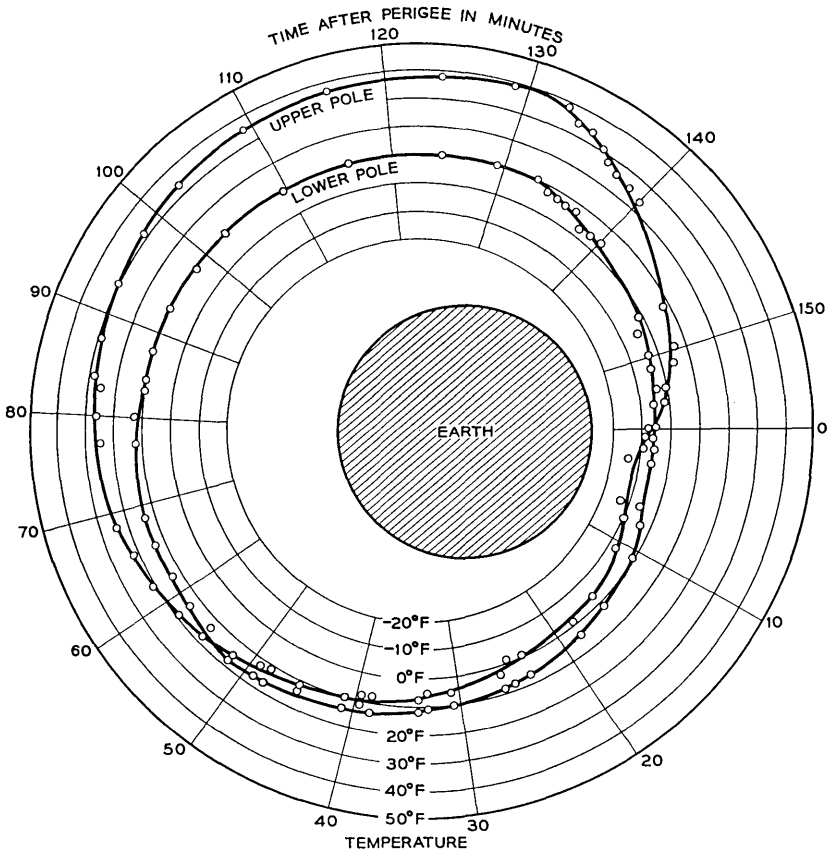
Fig. 11 — Skin temperature versus orbital position.

Fig. 12, the skin temperatures dropped sharply as the satellite went into eclipse, but were slow to return as the satellite emerged from shadow. This is best explained in terms of the skin surface properties. Since the average value of the absorptivity to emissivity ratio, α/ϵ, is about 0.65, the spacecraft emits energy faster than it will absorb.

7.1.3 *Skin Temperatures During Launch*

The satellite was designed to operate satisfactorily over wide temperature variations during both orbit and launch. During the launch
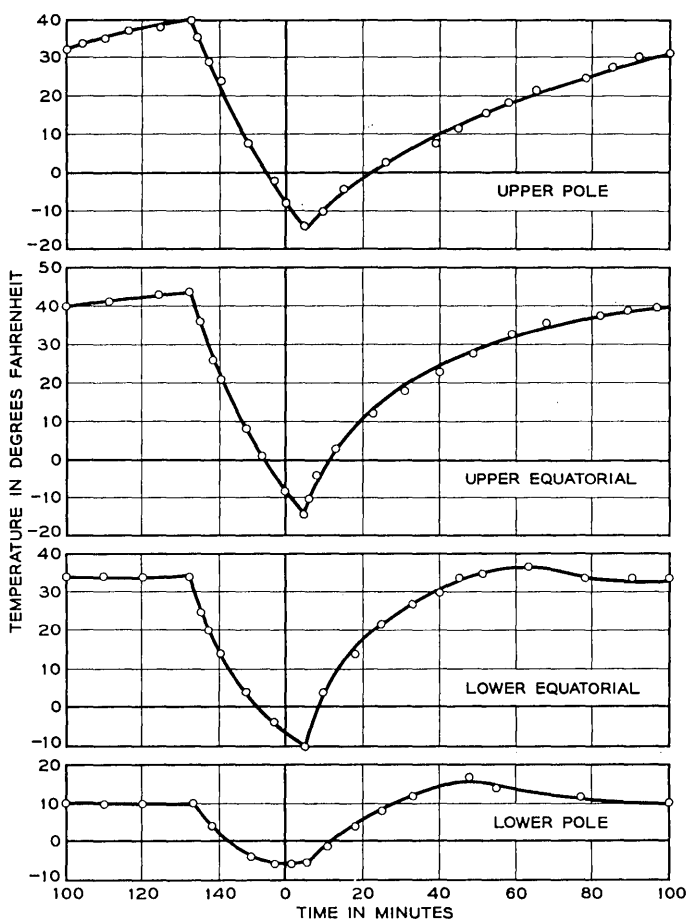
Fig. 12 — Satellite skin temperature during typical orbit with eclipse.
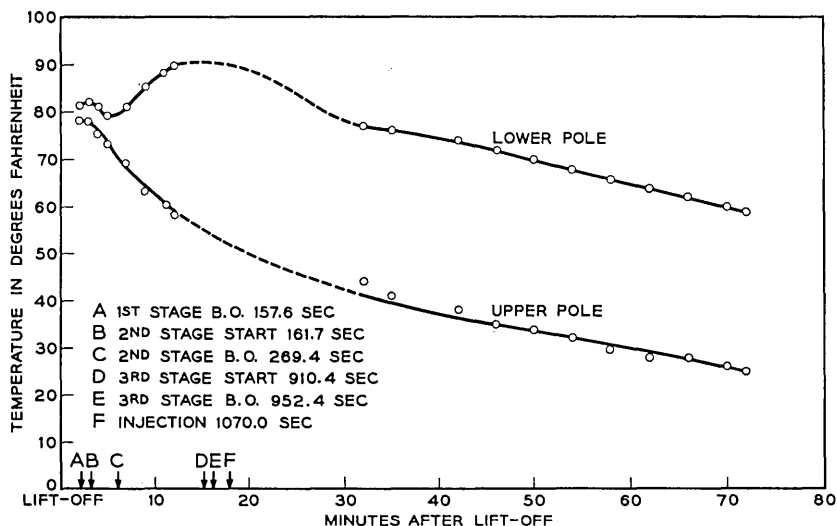
Fig. 13 — Skin temperature during launch.

phase, the satellite was protected from aerodynamic heating by a fiber-glass shroud which separated from the second stage prior to third-stage ignition. As seen in Fig. 13, the shroud was effective in maintaining reasonable skin temperatures on the satellite. Initially, the lower pole temperature rose slightly; it is believed that energy conducted from the missile was responsible for this temperature increase.

7.2 Temperatures Inside the Electronics Canister

The electronics canister is a hermetically sealed unit which houses 95 per cent of the electronics circuitry of the satellite. The canister is completely covered with an aluminized Mylar "blanket" when the bellows-actuated shutters, which cover the upper and lower domes, are closed.[5] When the shutters are open, the emissivity of the domes is increased, so the shutters control the canister temperatures. The solar plant furnishes, when new, a power of about 14 watts continuously except when the satellite is in eclipse. This primary source of power energizes the electronics equipment, charges the battery, and heats the canister.

Telemetry information from 21 thermistors located inside the electronics canister gives the temperatures of various components and sub-

assemblies from which rough temperature gradients can be found. Nine of these sensors are located in the switching regulator, in the dc-to-dc converter, and near the collector of the traveling-wave tube (TWT). These sensors are located at expected local hot spots, so the TWT can be turned off before the temperature exceeds the safe limit at these points. The remaining 12 sensors are located on various subassemblies where the temperature affects the calibration of a telemetry channel, or near points of special interest such as the Ni-Cd cells.

The temperature of the Ni-Cd cells is important, so this temperature is one of two chosen as representative for discussion. Maximum and minimum telemetry readings of the Ni-Cd cells are plotted as a function of time in Fig. 14(a). The general wavy nature of these curves does not mean that the temperature extremes vary this much from week to week, but is a result of the fact that telemetry data are taken only during certain times in each orbit and the temperatures of all parts of the satellite are dependent on satellite position as shown in Fig. 11. Also, the variation of temperature over one day depends partially on how much the TWT is used. During the time the TWT is used, the battery is discharging, so stored energy is furnished by the battery to the tube and other circuits which convert most of the electrical energy to heat energy. After long use of the TWT, the battery is discharged, and energy from the solar plant goes into chemical energy in the battery instead of going into heat energy, as it does when the battery is fully charged. Thus, there is a short time after TWT use when there is a slight drop in battery temperature. The TWT was operated more in August than at other times because of longer visibility from Andover, Maine, during this period.

The temperature of the waveguide used as part of the up converter is plotted as a function of time in Fig. 14(b). This plot shows much less temperature variation than the plot of battery temperature because the waveguide is a good heat sink.

VIII. RADIO-FREQUENCY POWER LEVELS

In this section, telemetry readings are presented to show that there have been no appreciable changes in the power levels of the three signals radiated from the satellite, the local oscillator signals used for the modulators in the satellite, or the signals associated with the microwave carrier supply (MCS). In order to prove the invariance of some of these power levels, it is necessary to show that the characteristics of the TWT and the beat-oscillator (BO) modulator have not changed. Microwave
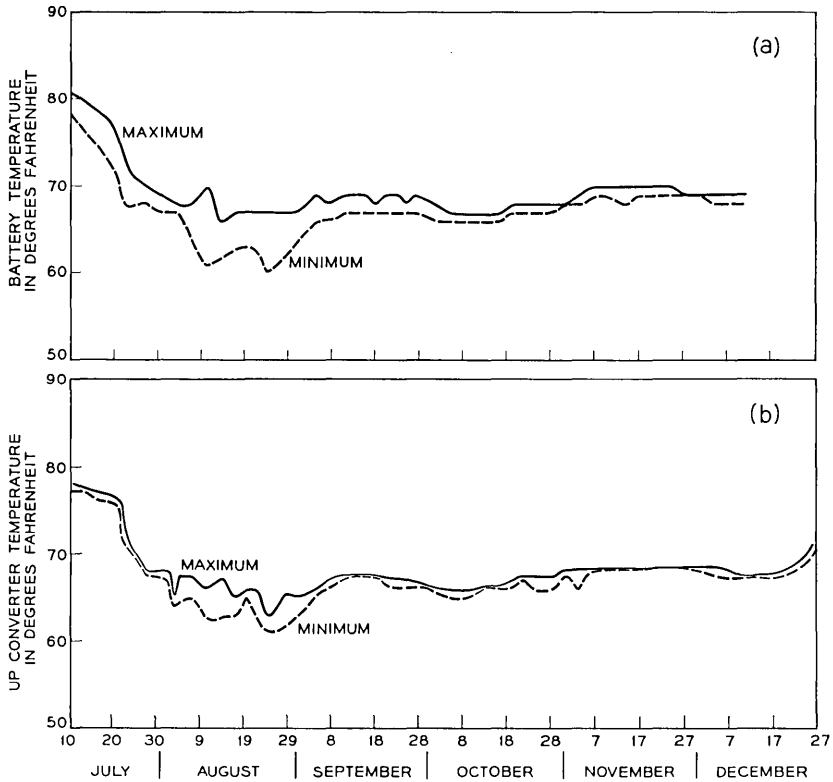
Fig. 14 — (a) Battery temperatures since launch; (b) up-converter temperature since launch.

power levels and their associated telemetry channels are shown in Fig. 15, which gives a simplified block diagram of the communications repeater. Fig. 16 is a block diagram which shows the VHF beacon and other VHF circuitry. Both figures show frequencies accurate to two decimal places, but for simplicity approximate values will be used in the discussion. Throughout this and the following sections, reference is made to Table I, which gives voltages, currents, powers, and temperatures for important telemetry channels. The purpose of these representative data is to show changes in these quantities, and not the actual values. In particular, some of the power monitors are inaccurate in determining absolute values, but changes in readings are significant. The telemetry channel numbers used in the discussion are for conven-
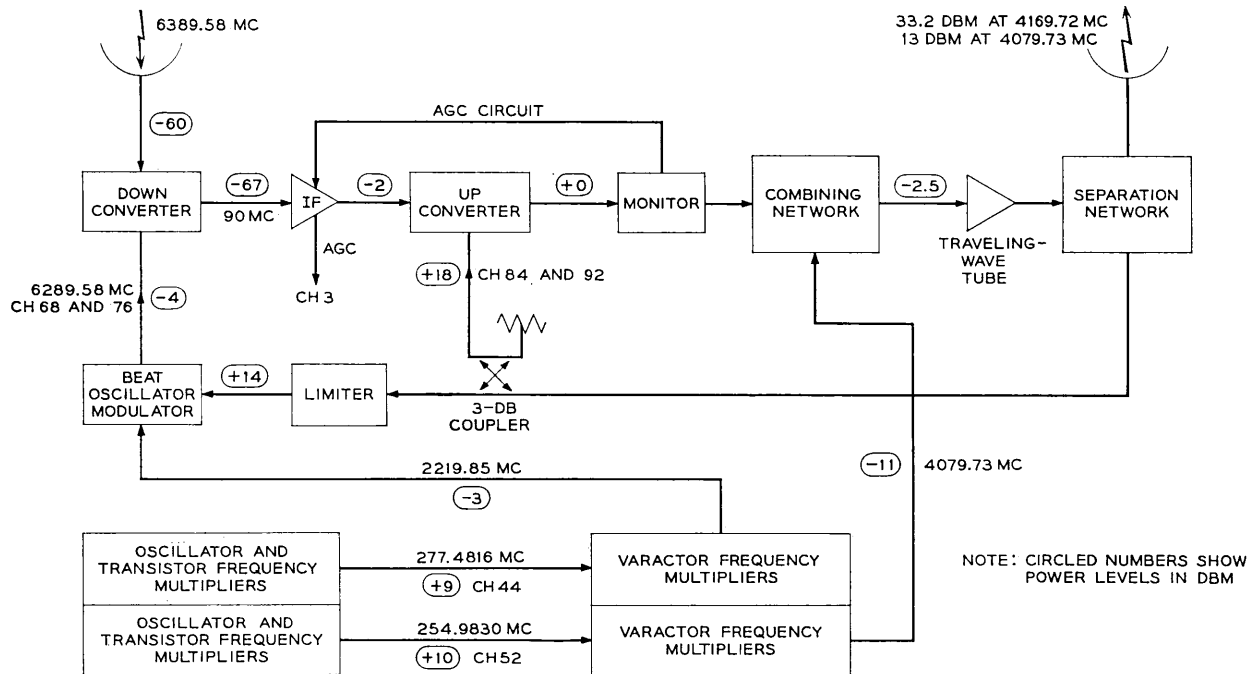
Fig. 15 — Communications repeater.
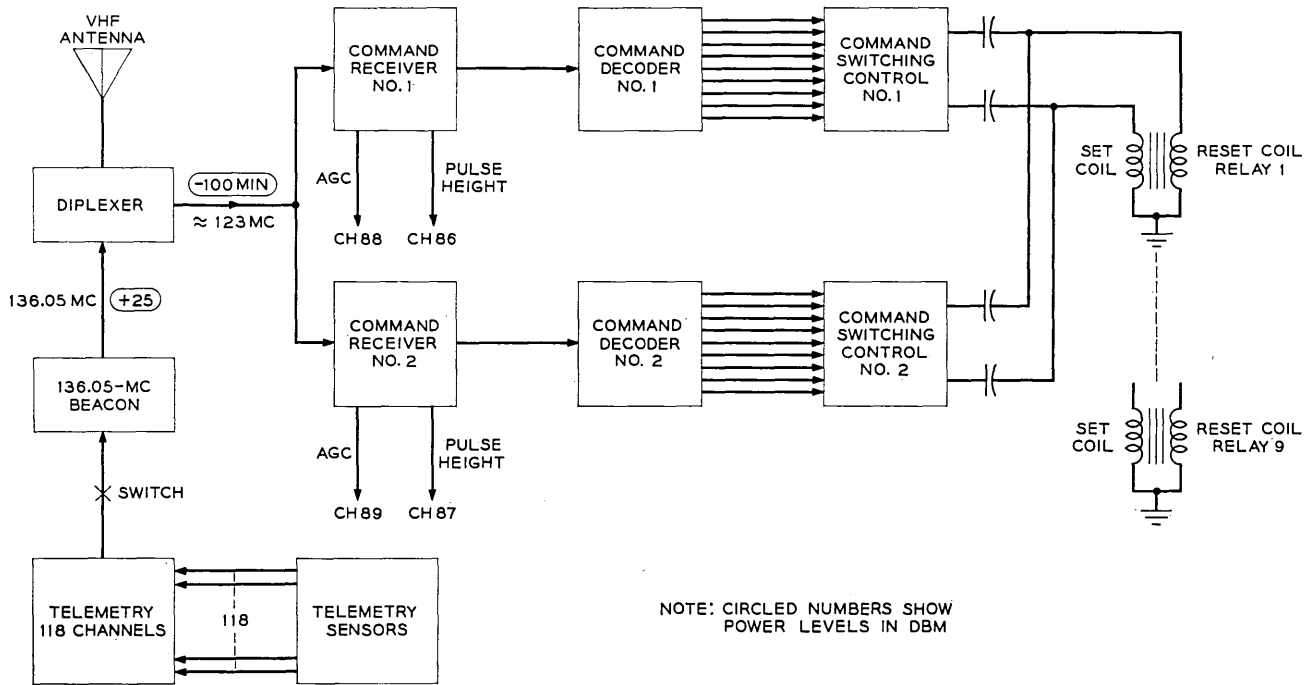
Fig. 16 — Command and telemetry systems.

ience only; the assignment of the actual channel numbers was to a large degree arbitrary.

8.1 *Microwave Beacon*

As Fig. 15 shows, the same 4080-mc frequency is used to provide the microwave beacon signal and to pump the varactor diodes in the up converter and BO modulator. The reflex circuit which provides sufficient power at this frequency is discussed by another paper[6] in this issue. Since the insertion losses of all the filters in the satellite are known, the 4080-mc power levels at any point can easily be calculated if the level at one point is known. The 4080-mc signal is used to pump the self-biased varactor diodes in the up converter, so the bias voltages on these diodes, monitored by telemetry channels 84 and 92, are used to measure the power levels at this part of the circuit. The IF signal level into the up converter is small (-2 dbm) so the bias voltages on these diodes are due almost entirely to the 18-dbm pump at 4080 mc. Figs. 17(a) and 17(b) show the relationships between the bias voltages and the pump
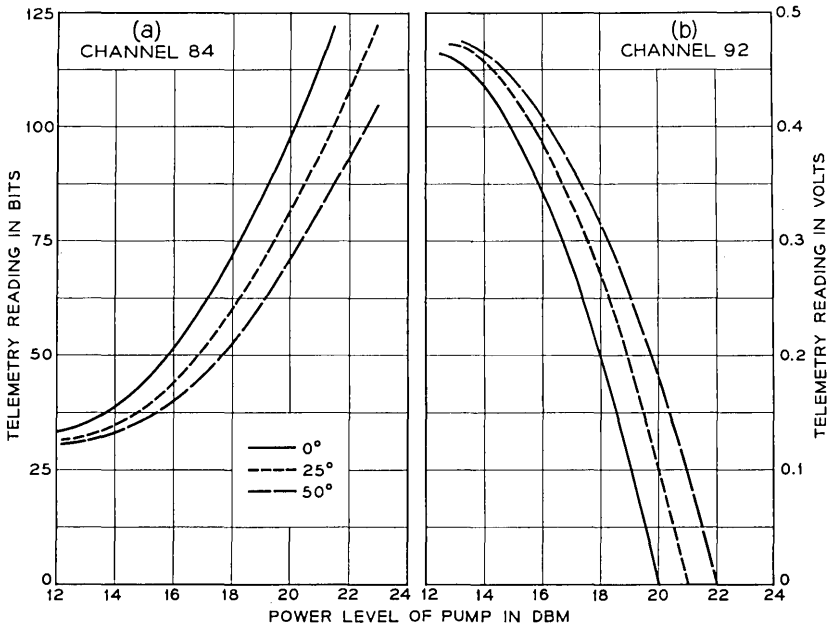
Fig. 17 — Telemetry readings versus pump level for the up converter.

input.* A normal power level of 18 dbm at the input to the up converter corresponds to a power of 18.6 dbm to the antenna feed system. Insertion loss of the antenna and feed is approximately 1.6 db, so the normal radiated microwave beacon power is 17 dbm.† The exact insertion loss of the antenna and feed system is not known over the temperature range experienced by the satellite, but the variation is known to be less than 0.1 db.

The data for channels 84 and 92 in Table I show about a ½-db disagreement in the measured pump level, but the change in power since launch, as shown by both channels, is very small. Powers are calculated to three significant figures in an effort to show changes in level, but obviously no such absolute accuracy is claimed by this method of monitoring the power.

When no power at 6390 mc is transmitted to the satellite, only noise (about −6 dbm) drives the TWT, and the power output of the tube at 4080 mc increases[6] about 2 db, as shown in Fig. 18. This results in an increase in the radiated power at 4080 mc, but this is normal circuit behavior and does not represent any change in the satellite circuitry.

8.2 *The Communications Signal*

The power output of the satellite in the 4170-mc band is not monitored, but the approximate output can be calculated by using known values of satellite antenna gain and path loss and the measured values of received signals on the ground. However, changes in the power output can be more accurately determined by another method. As Fig. 15 shows, the TWT in the satellite amplifies signals at both 4080 and 4170 mc. Because the tube is driven into partial saturation by the signal at 4170 mc (see Fig. 18), changes in the output level at this frequency are accompanied by greater changes in the level of the signal at 4080 mc. The power at 4080 mc is monitored, so changes in the power level at 4170 mc can be measured indirectly if the characteristics of the TWT do not change and if the input signal to the TWT is constant. The drive to the TWT is constant when the signal at 6390 mc is within the AGC range. The data in Table I show that the helix and accelerator currents have increased from 135 and 115 microamperes prior to launch to 185 and 155 microamperes, respectively, in four months. However, the tube charac-

---

* The output of the diode monitored by channel 92 is positive, so its output is combined with a fixed negative voltage to give a net negative voltage needed by the telemetry circuit.

† The required radiated power at this frequency is only +13 dbm.

TABLE I—CURRENTS, VOLTAGES, POWERS AND TEMPERATURES
IN THE ELECTRONICS CANISTER

Channel No.	Function	Universal Time of Telemetry Readings				
		18:11 July 9, 1962	23:03* July 11, 1962	23:15 July 11, 1962	11:51* Nov. 6, 1962	12:03 Nov. 6, 1962
		Readings in bits and units				
1	TWT heater	50 bits	50	50	49	50
		4.7 volts	4.7	4.7	4.75	4.7
3	6390-mc input power	21 bits	11	16	33	11
		−62 dbm	−66.5	−64.5	−60	−66.5
41	IF amplifier temperature	70 bits	64	65	57	59
		86°F	79	81	71	74
4	TWT accelerator	24 bits	24	22	34	32
		115 μa	115	110	163	155
12	TWT collector current	86 bits	85	85	85	85
		17.8 ma	17.6	17.6	17.6	17.6
60	TWT helix current	14 bits	17	16	21	19
		135μa	165	155	200	185
36	Calibration voltage	69 bits	69	70	69	70
		0.23 volt/ bit				
44	277-mc power	102 bits	103	102	104	104
52	255-mc power	109 bits	110	109	112	111
68	Down converter bias 1	43 bits	44	43	43	43
		−4 dbm	−4.1	−4	−4	−4
76	Down converter bias 2	66 bits	66	66	66	66
		−3.9 dbm	−3.9	−3.9	−3.9	−3.9
13	Down converter temperature	74 bits	70	70	64	64
		80°F	77	77	70	70
84	Up converter bias 1	50 bits	55	54	56	55
		17 dbm	+17.45	+17.4	17.45	17.4
92	Up converter bias 2	79 bits	70	70	68	68
		+17.4 dbm	+17.9	+17.9	+17.9	+17.9
29	Up converter temperature	68 bits	64	64	57	57
		82°F	77	77	69	69
99	Reference diode	105 bits	105	105	105	105
		8.4	8.4	8.4	8.4	8.4

* Time when the TWT was turned on. Launch time was 08:35 Universal Time, July 10, 1962.

teristics do not change even when these currents increase to 500 microamperes. The input signals for comparative power measurements must be within the AGC range of −70 to −55 dbm or the 4170-mc drive to the tube will not be the same, and obviously this will cause a change in output at both 4080 and 4170 mc. Since launch there has been almost no change in the 4080-mc output of the tube, so the change in output at 4170 mc from the normal output of 35 dbm has been negligible. The insertion loss of the antenna and feed system is 1.6 db at room temperature, and this loss decreases less than 0.1 db at the low temperatures
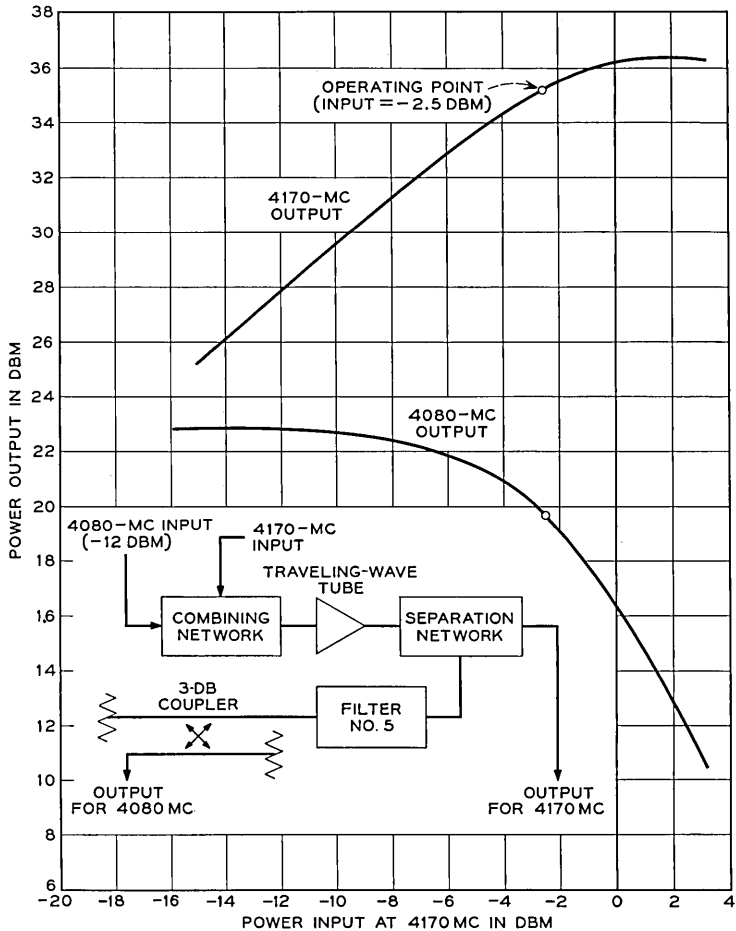
Fig. 18 — Operating characteristics of the traveling-wave amplifier.

encountered in space. At 4170 mc the uncertainty of the antenna insertion loss and the inaccuracies of monitoring 4080 mc by telemetry may give a combined error of $\frac{1}{4}$ db when calculating the power level, but the radiated power at 4170 mc (33.2 dbm) has not changed appreciably since the satellite was assembled.

8.3 The Local Oscillator for the Down Converter

The 6300-mc local oscillator signal for the down converter is obtained from the BO modulator, which combines a signal at 2220 mc from the
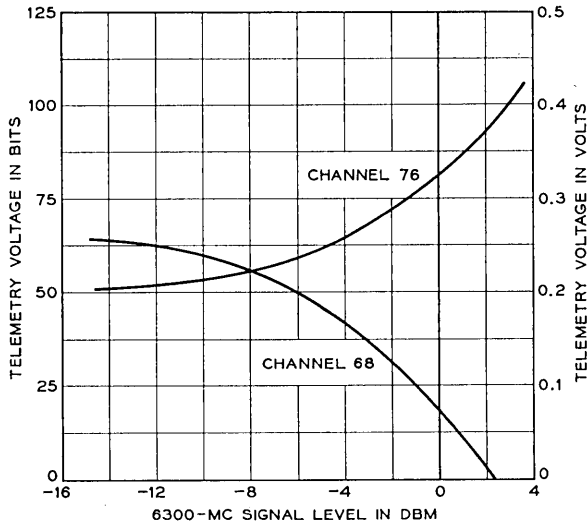
Fig. 19 — Telemetry readings versus local oscillation level for the down converter.

MCS with a portion of the pump signal at 4080 mc. The direct currents in the silicon diodes in the down converter are caused by the RF signal at 6300 mc and by small external dc voltages that forward bias the diodes. Fig. 19 shows the relationship between the telemetry readings of channels 68 and 76 and the level of the local oscillator signal. As is the case with channel 92, used to monitor one of the up-converter currents, the positive output voltage from the down converter is added to an external negative voltage to give a net negative voltage for telemetry. The data in Table I show that the 6300-mc signal has since pre-launch measurements changed only one bit according to channel 68 and no bits according to channel 76. At the operating point, a change of one bit on telemetry corresponds to a change in 6300-mc power level of less than $\frac{1}{4}$ dbm, so this power has remained almost constant for four months.

8.4 *Power Levels in the Microwave Carrier Supply*

The microwave carrier supply furnishes signals at 2220 and 4080 mc which are used to provide the local oscillator signals for the up and down converters. Each signal is obtained by feeding the output of a crystal oscillator into a transistor frequency multiplier section, which in turn feeds a varactor frequency multiplier section.

8.4.1 The Transistor Sections

Each transistor frequency multiplier section in the MCS contains a pseudo AGC system which in all tests prior to installation in the Telstar spacecraft held the VHF power drive to the varactor section constant to within ±0.15 db over a temperature range from 25 to 125°F. The telemetry readings, channels 44 and 52, associated with these powers do not give an accurate measure of power output because changes in transistor characteristics change the calibration. However, if the telemetry reading at a known temperature corresponds to a value taken during bench tests when the power was measured, there is a strong indication that the power is normal. The readings of channels 44 and 52, as shown in Table I, have since launch varied only 3 and 2 bits, respectively. Pre-launch measurements on the completed satellite showed that the readings of these two channels increased with a decrease in temperature. On November 6 the average canister temperature was 7°F below the temperature the day after launch, so the slight increase in the readings of channels 44 and 52 on this date is normal and indicates that the transistor sections of the MCS were normal.

8.4.2 The Varactor Sections

The output powers of the varactor multipler sections are not monitored, but these powers can be checked indirectly.

The output power at 2220 mc can be checked indirectly by noting the changes in channels 68 and 76, which measure the level of the power at 6300 mc. A change of 1 db in the 2220-mc signal into the BO modulator, when operating normally, changes the output at 6300 mc by $\frac{3}{4}$ db, and the BO modulator conversion gain does not change rapidly with temperature. Since the level of the 6300-mc signal has remained essentially constant, the level of the 2220-mc signal could not have changed appreciably.

As is the case with the output of the 2220-mc varactor section, the output of the 4080-mc varactor section is checked indirectly. The 4080-mc power from the MCS is amplified by the TWT and is fed to the pump arm of the up converter. Since any change in the output of the MCS at 4080 mc is translated as an equal change in power to the up converter, channels 84 and 92 indirectly give a measure of the power from the MCS if the tube characteristics and RF power drive are unchanged, as discussed earlier. The measurements made since launch do not show the actual power level of the 4080-mc output of the MCS, but they do show that this power level has not changed appreciably.

8.5 *The VHF Beacon*

Under normal conditions the satellite radiates continuously a 23-dbm signal at 136 mc, used for tracking purposes by the command tracker on the ground. This tracker is completely separate from the tracking equipment associated with the microwave beacon, which is radiated only when the TWT is turned on. When telemetry is turned on, the 136-mc signal is amplitude modulated. This VHF beacon is not monitored by telemetry, so the only check on this power is made by measuring the received ground power and by calculating the transmitted power from known values of path loss and known gains of the satellite and ground antennas. This method is accurate to within ±1 db when many readings are averaged. Accurate measurements can be made only when the weather is clear and the satellite is above elevation angles of 10°. At low elevation angles, this signal is subject to selective fading.

Measurements of the 136-mc beacon made on the ground prior to launch and in orbit on a weekly basis since launch show that the power has not changed, but day-by-day fluctuations of 1 db, if they existed, could not be detected by these measurements.

IX. CIRCUIT PERFORMANCE CHANGES

In the preceding section, telemetry readings were used to show that power levels of the 255, 277.5, 2220, 4080, 4170, and 6300-mc signals inside the electronics canister had not changed appreciably since launch. Also the method of calculating the transmitted power levels at 136, 4080, and 4170 mc using antenna gains, path loss, and received signal level was discussed. In order to show the invariance of 6300 and 4170-mc signals, it was necessary to show by telemetry that the characteristics of the TWT, MCS, and BO modulator have not changed. In this section, the remaining parts of the satellite circuitry, excluding the radiation experiment circuits, will be discussed from the viewpoint of changes in their operating characteristics.

9.1 *The Down Converter, IF Amplifier, and Up Converter*

In Section 8.2 the methods of checking the output of the tube at 4170 mc were described. The conclusion of this section is that the output power of the TWT, and thus the input power to the TWT at 4170 mc, has remained essentially constant when the input at 6390 mc falls in the AGC range. However, the conversion loss of the down converter, the gain of some stage in the IF amplifier, or the conversion gain of the up

converter could change, and the power drive at 4170 mc to the TWT would remain constant, because the AGC system keeps the power input to the TWT constant by changing the gain of the IF amplifier. If changes occur in the up or down converters or in some part of the IF amplifier, the current through variolossers in the IF amplifier changes to keep the TWT input constant. Channel 3 in the telemetry circuit gives the vario-losser current as a function of the input signal to the satellite. Calculations using ground transmitted power, antenna gains, and path loss show that channel 3 readings in space are consistent with readings made before launch. However, the accuracy of this method is no better than 2 db, so the gain of some unit between the input and the TWT could have changed by this amount and it would not have been detected.

9.2 *Nickel-Cadmium Cells*

Since (1) there is no simple way of telling when the Ni-Cd cells are fully charged, (2) the cells may be damaged by excessive discharge and (3) the charging efficiency is a function of state-of-charge, charging current, temperature and past history of the cells, the operating procedure for the Telstar satellite has been very conservative. Graphs are plotted daily showing the state-of-charge of the battery on the basis of a conservative 60 per cent average charging efficiency. Each time the TWT is used, a continuous plot is kept of battery voltage versus time. These plots are compared in an attempt to find changes in the battery, either gradual or otherwise. Two battery discharge curves will be the same only if the battery temperature, the solar-plant current, TWT operate time, and initial battery charge are the same for the two passes compared. The aging of the solar plant due to radiation damage and the variation of eclipse period and its time relative to visibility from An-dover, Maine, make exact duplication of conditions for battery comparisons at widely separated intervals impossible. Since these conditions cannot be duplicated, corrections are made in order to get a meaning-ful comparison. The corrected discharge curves are so similar that they indicate no measurable change in the battery.

9.3 *The Solar Cells*

The solar power plant consists of 50 parallel-connected groups of 72 series-connected silicon n-on-p solar cells covered with sapphire shields 32 mils thick. Fig. 20 shows the average solar plant current from the time the satellite was launched until early January, 1963. These data were taken while the TWT was on, so there is a period of about a month
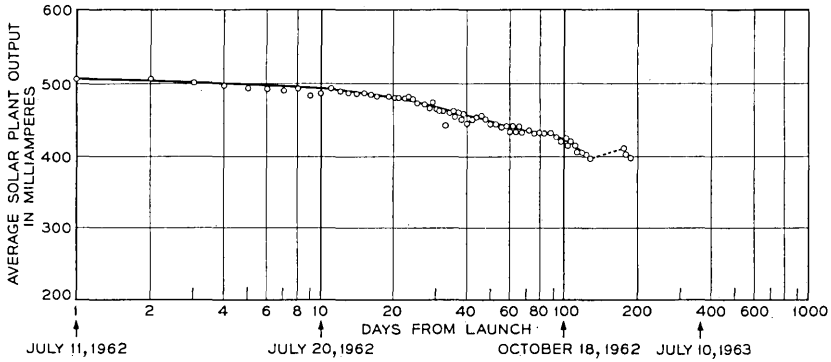
Fig. 20 — Solar plant output.

(December, 1962) when data were not available because of the command malfunction. The points on this graph do not give a perfectly smooth curve because there are, at different times, temperature differences in the solar cells which affect their output. The general shape of the curve shows a degradation due to radiation which by July, 1964, should result in a 32 per cent reduction in capacity.[2]

9.4 *The Voltage Regulator and the dc-to-dc Converter*

The voltage regulator receives power at a varying voltage from the Ni-Cd battery and provides a regulated output of negative 16 volts to power all the transistor circuits and the dc-to-dc converter. When the regulator was first installed in the electronics package, the output voltage of the regulator, as measured by telemetry, remained constant at 96 bits as the load current changed from 0.3 ampere to 1.5 amperes. One telemetry bit corresponds to 0.167 volt. After approximately five months in orbit, the regulated output for all load currents has changed only one bit. It was estimated before launch that radiation damage plus aging might cause the output voltage of the regulator to vary as much as ±3 per cent, although present data indicate this prediction was pessimistic.

The dc-to-dc converter chops the 16-volt direct voltage from the regulator and steps up the resulting ac voltage with transformers to higher voltages which can be rectified, filtered and applied to the helix, accelerator, and collector electrodes of the TWT. The TWT heater voltage is also obtained by transformer action, but it is only about 4.5 volts. Telemetry is used to monitor the heater voltage and the helix, accelerator, and collector currents for the TWT. Since launch, as Table I

shows, the heater voltage after transients have died out has varied only one bit or 0.08 volt. Increases in accelerator and helix currents shown in Table I result from aging and a slight defocusing of the electron beam in the tube, and are not necessarily caused by increases in voltages. The best proof of the constancy of the TWT voltages is the measure of the output power at 4080 mc, a point discussed earlier. Changes of only 10 volts in the helix voltage (1520 volts is normal) will cause a change of about $\frac{1}{2}$ db in the output of the TWT at 4080 mc. Telemetry readings which monitor this 4080-mc power level indicate a change much less than $\frac{1}{4}$ db, so the helix voltage has changed very little. The accelerator and collector voltages are derived from the same source as the helix voltage, so they should not have changed either, but there is no direct proof of these voltages remaining constant.

9.5 *Pressure Switches*

The electronics package is hermetically sealed to keep the pressure inside the package at a level of 10 psia. In the event of a leak, the high voltages associated with the TWT would cause corona at critical pressures. One 5-pound and one 1-pound pressure switch (monitored by telemetry) are inside the electronics canister to show the presence of leaks. Since neither pressure switch has operated after six months of operation, even if a small leak exists, no corona problems would exist for several years.

9.6 *The Telemetry System*

While the telemetry does not have a self-check, there are ways to tell something about the unit if some readings are suspicious. The power supply has a reference diode which is monitored by telemetry channel 99, and the telemetry circuit has its own reference diode. Any general error in telemetry readings would show up in channel 99 unless both reference diodes change the same amount. Also, the 16-volt regulated supply is monitored in two places, so differences in these channels could show telemetry troubles. Troubles in the telemetry would probably be first detected by bad readings on many channels. There have been isolated telemetry errors due to external noise pulses in the telemetry receiver on the ground, but in each case an error that occurs in a particular channel on one frame of telemetry information has been corrected on the following frame.

Channels 119 and 120 are used to send out a Barker code[7] and its complement to synchronize the ground telemetry system. It has been

found that when the telemetry is first turned on, the synchronizing signals on channels 119 and 120 are incorrect during the first minute. After one minute, the synchronizing information on these channels is correct.

9.7 *The Command System*

The Telstar command system, as shown in Fig. 16, has redundancy from the diplexer to the relay driver circuits. The output pulse heights of the command receivers are monitored by telemetry channels 86 and 87, and the AGC voltages of the receivers, calibrated to give received RF power levels, are monitored by channels 88 and 89. The receivers can be tested by comparing the output voltages as measured on channels 86 and 87 with similar data taken prior to launch and by comparing the received power levels. The tests on the receiver have been made on a daily basis since launch, and they indicate that there has been no apparent damage to the command receivers.

The T1 and T2 commands are used to test the command receivers and decoders. The T1 command disables decoder 2 for 15 seconds so that command receiver 1 and decoder 1 can be tested; T2 is a similar command which disables decoder 1 for 15 seconds. It was decoder 2 that first gave trouble in the Telstar satellite. This decoder became intermittent on August 8, 1962, became inoperative a few days later, and except for one short intermittent period in mid-October was inoperative until December 21, 1962. On November 23, 1962, after five days of sluggish operation, decoder 1 became inoperative. The cause of the malfunction of the command systems and the measures taken to correct the problem are discussed in a separate paper in this issue.[8]

X. CONCLUSIONS

The launch of the Telstar satellite was highly successful, so the initial orbit, attitude, solar aspect, and spin rate agreed very closely with the predicted values. Most of the data in this report cover the first three months of operation. Subsequent information obtained through January 4, 1963 proves that, except for the command system, the satellite behavior has been normal and predictable. The temperature sensors on the shell show that these temperatures have not exceeded 79°F, which is slightly less than the predicted value. While the electronics equipment operates satisfactorily over a wide temperature range, it is important to see that the average canister temperature has been held at near 70°F throughout the first 1400 orbits. Data from telemetry and from ground

measurements give no indication of any deterioration of the communications repeater or the telemetry system. The command system has obviously been damaged by radiation, but the extent of the present damage after the recovery is not known. The pressure in the electronics canister, as proved by the pressure switches, is at least 5 psi; even if a very small leak does exist, no corona problem associated with the TWT high voltages will exist for several years.

REFERENCES

1. Hatch, R. W., Bennett, S. B., and Kinzer, J. P., Results of the *Telstar* System Communication Tests, B.S.T.J., this issue, p. 1561.
2. Brown, W. L., Buck, T. M., Medford, L., Thomas, E. W., Gummel, H. K., Miller, G. L., and Smits, F. M., The Spacecraft Radiation Experiments, B.S.T.J., this issue, p. 899.
3. Courtney-Pratt, J. S., Hett, J. H., and McLaughlin, J. W., Optical Measurements on *Telstar* Satellite to Determine the Orientation of the Spin Axis and the Spin Rate, to be published.
4. Yu, E. Y., Spin Decay, Spin Precession Damping, and Spin-Axis Drift of the *Telstar* Satellite, to be published.
5. Hrycak, P., Koontz, D. E., Maggs, C., Stafford, J. W., Unger, B. A., and Wittenberg, A. M., Spacecraft Structure and Thermal Design Considerations, B.S.T.J., this issue, p. 973.
6. Davis, C. G., Hutchison, P. T., Witt, F. J., and Maunsell, H. I., The Spacecraft Communications Repeater, B.S.T.J., this issue, p. 831.
7. Chapmann, R. C., Critchlow, G. F., and Mann, H., Command and Telemetry System, B.S.T.J., this issue, p. 1027.
8. Mayo, J. S., Mann, H., Witt, F. J., Peck, D. S., Gummel, H. K., and Brown, W. L., The Command System Malfunction of the *Telstar* Satellite, B.S.T.J., this issue, p. 1631.

Results of the *Telstar* Radiation Experiments

By W. L. BROWN, J. D. GABBE and W. ROSENZWEIG

The data from the particle experiments of the Telstar satellite have been analyzed to provide maps of the distribution of electrons and protons as measured in three of the Telstar detectors during the period from July through October, 1962. For the protons between 26 and 34 Mev and >50 Mev, the particle distributions are stable in time, but for the electron distribution there is a time decay of the electron flux over most of the region explored by the Telstar orbit. The connection of these observations to the high-altitude nuclear explosion of July 9, 1962, is discussed. The introduction of additional electrons by Russian tests at the end of October was also observed. The particle maps have been used to derive the integral particle exposure of the satellite, which is found to account quantitatively quite well for the radiation damage observed in the main solar power plant and in the radiation damage experiments on solar cells and special damage transistors carried by the satellite. In the main power plant the proton and electron contributions to damage are found to be equal. The integral particle exposure has also been used to compute the level of ionization in different depths of material in order to evaluate the degradation of semiconductor devices in the Telstar canister.

I. INTRODUCTION

This article presents some of the results obtained from the radiation experiments on the Telstar satellite. It describes the distribution of several classes of energetic charged particles mapped out by these experiments, and the integral radiation exposure of the satellite in orbit which has been calculated from these distributions. It also describes the radiation damage effects observed directly on semiconductor devices carried by the satellite and compares the damage with that to be expected on the basis of the orbital integrals.

1.1 *Charged Particle Experiment*

As described in detail in an accompanying article,[1] there are four silicon p-n junction charged particle detectors on the Telstar satellite, three that measure the distribution of protons in space at different energies and one that measures the electron distribution and some simple properties of the electron energy spectrum. All four detectors are energy proportional devices, giving an electrical pulse-height response proportional to the energy deposited by a charged particle in the active volume of the detector. By adjustment of the active volume, the levels of pulse height examined, and the amount of absorbing material which must be penetrated by a particle in reaching the detector, it is possible to distinguish protons from electrons and put bounds on the particle energies.

In the electron detector, particle pulses are sorted into four channels corresponding to deposition of different amounts of energy between 250 and 1000 Kev in the detector. Because of the nature of the energy loss processes for electrons, this detector primarily responds to electrons below 1 Mev but also responds to electrons of much higher energy with decreasing sensitivity. The efficiency of the four pulse-height channels of this detector for monoenergetic electrons in the region of primary sensitivity is shown in Fig. 1. The time and spatial variations of the electrons as observed by this detector will be discussed in considerable detail in Section 2.2. Electrons are of major importance in the radiation surface effects observed in the Telstar command decoder and also contribute about half of the radiation damage in the main solar power plant.

The highest-energy proton detector of the three carried by the satellite measures protons above 50 Mev. The medium-energy detector measures in a well defined energy interval between 26 and 34 Mev. The results for these two detectors are simpler than the electron case because of the relative time stability of the proton distributions that they measure and the simplicity of their detection sensitivity. The spatial distribution of these protons and the energy spectrum that can be derived from them will be discussed in Section 2.3. The remaining half of the damage to the Telstar solar power plant is caused by protons. The fourth detector in the satellite measures low-energy protons between 2.5 and 25 Mev and provides rather detailed information on the spectrum, particularly below 12 Mev. The analysis of these data is not yet complete and the results from this detector are not included in this paper.

The period between July 10, when the Telstar spacecraft was launched, and the end of October, 1962, has been of special interest. This period begins just after the United States high-altitude nuclear test (Starfish)
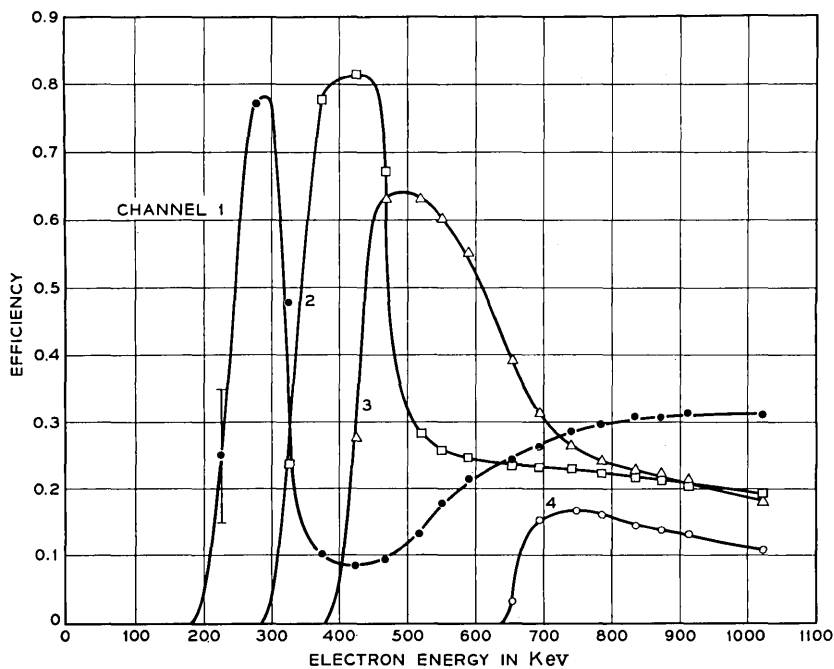
Fig. 1 — Electron detection efficiency as a function of incident electron energy.

of July 9 and ends with the first two Russian high-altitude nuclear tests on October 22 and 28. During most of this time, the Telstar satellite was the only intermediate-altitude radiation monitor in space. In these months, 770 hours of usable telemetry was acquired by the NASA tracking network and the Bell System telemetry stations at Andover, Maine, and Cape Canaveral, Florida. Although some later data are used, it is the 180,000 data points which represent the output of the electron and the two higher-energy proton detectors for the first 104 days in orbit that form the basis of the charged particle distributions that follow.

1.2 *Radiation Damage Experiments*

Radiation damage effects on the bulk properties of silicon are directly observed in the short-circuit current of four solar cells and in the common-base direct current gain of six specially fabricated silicon transistors. The details of these devices and the type of information they provide are described in an accompanying paper.[1] In addition to these special experiments, the main solar power plant provides a large statistical study of damage to several thousand essentially identical devices

measured together. The present paper will describe the results from all three of these sources and will relate the damage observed to the radiation exposure of the satellite as calculated from the particle experiments. Particular attention will be centered on the first 104 days in orbit because the particle distribution has been studied in detail during this time.

II. PARTICLE EXPERIMENTS

2.1 General

2.1.1 Motion of Geomagnetically Trapped Particles

The basic motion of a charged particle trapped in the earth's magnetic field is a spiral around a magnetic line of force; see Fig. 2. As the
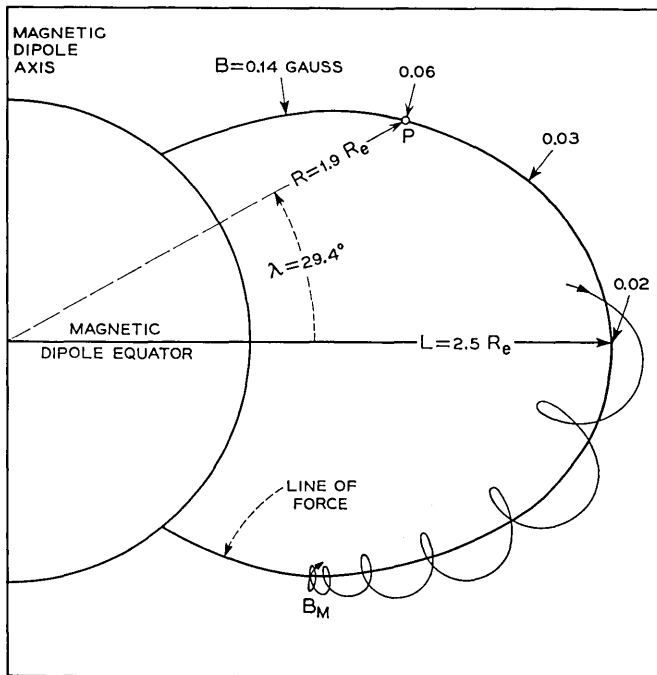
Fig. 2 — The motion of a charged particle trapped in a dipole magnetic field. The particle is confined near the magnetic shell $L = 2.5\ R_e$ and is mirroring at field strength B_m. The B-L coordinates of the point P are $B = 0.06$ gauss and $L = 2.5\ R_e$. The R-λ coordinates of the point P are $R = 1.9\ R_e$ and $\lambda = 29.4°$. Distances are measured in units of earth radii, R_e.

particle gets nearer to the earth and into regions of higher magnetic field strength, the spiral becomes flatter until eventually the particle is reflected and goes back out along the line of force. A given particle is always reflected at the same value of the field strength, B_m (B_{mirror}). The mirror point depends upon the angle between the particle velocity vector and the magnetic field vector at the magnetic equator. Particles moving very nearly parallel to the field line at the equator mirror close to the earth, at large values of B_m, while particles moving nearly perpendicular to the field line at the equator mirror close to the equator, at nearly equatorial values of the field. Superimposed on the back and forth motion in the magnetic field is a small but important longitudinal drift, westward for protons and eastward for electrons. These motions, their stability and various injection and loss mechanisms have been treated in considerable detail in the literature.[2-14] The longitudinal drift shifts the particles so that they spiral about longitudinally adjacent lines of force which are equivalent. The set of equivalent lines of force is called a magnetic shell. Thus, a particle is constrained to move so that the locus of the center of its spiral always lies near the same magnetic shell, and is confined to regions on the shell with magnetic fields equal to or less than B_m. A natural coordinate system in which to consider this motion is one which identifies the magnetic shell appropriate to the particle and then measures position in the shell in terms of the magnetic field strength. Such a coordinate system has been developed and is described below.

2.1.2 Coordinate Systems

A transformation developed by McIlwain[15] maps the earth's magnetic field onto a dipole field having the same first moment. In the axially symmetric dipole field, a magnetic shell is defined simply as the surface generated by rotating a line of force about the dipole axis. The magnetic shell is labeled by L, the distance from the dipole axis in the equatorial plane of the dipole. Position in the magnetic shell is given by the field strength, B, Fig. 2. Because of the additional symmetry of the dipole field, a quarter of a meridian plane is a complete representation. The B-L coordinate system is well suited to many theoretical calculations, and we have done most calculations and present some results in this system. However, the geometrical distortions inherent in the transformations make it difficult to get an intuitive picture of the spatial distribution of the particles in B-L coordinates. For this reason, we present many results in the magnetic dipole polar coordinates R and λ,

Fig. 2, which give a pseudo-geographic representation. Both R and L will be measured in units of earth radii, R_e, in what follows. As a result of the anomalies in the real field, the surface of the earth is very wrinkled in R-λ coordinates. Some of the wrinkles exceed 0.1 R_e in extent.

The magnetic field used to calculate the coordinates is a 48-term spherical harmonic expansion with the Jensen and Cain[16] coefficients for 1960. The coordinates are only as good as the expression for the magnetic field, $\pm \approx 2$ per cent.[53] In addition, the magnetic field is assumed to remain fixed, whereas the field in space is known to vary as a result of fluctuations in the earth's magnetization, currents in the ionosphere, currents due to circulating magnetically trapped particles, and other perturbations connected with solar activity. The coordinate system as used here acts as a fixed grid against which changes in both the magnetic field and the particle population are measured. The two effects are not separable, but in the part of the magnetosphere covered by the Telstar satellite the magnetic variations are small compared to the changes in the particle population.

2.1.3 *Treatment of the Data*

The counting rates of the various channels of particle information are deduced from readings of the 14-bit binary register in the telemetry,[17] modified in the case of register overflow in accordance with analog readings of log ratemeters in those channels to which the ratemeter information applies.[1] It is convenient to report the distribution of a particular class of particles in space in terms of its omnidirectional flux, defined as the number of particles passing through a sphere of unit cross-sectional area per unit time. Deducing this quantity requires a knowledge of the efficiency of the detector, which in turn depends on the energy spectrum of the particles being measured. To obtain a number which expresses the data more directly, we have chosen to define an omnidirectional counting rate (OCR) which contains all the geometrical factors required to specify an omnidirectional flux, but which does not contain a factor for the detector efficiency. The efficiency can be specified for an assumed particle spectrum by integration over curves of the type shown in Fig. 1. For example, if the electron spectrum is that corresponding to equilibrium beta decay from fission fragments, channel 3 of the electron detector has an efficiency of 0.2, and a flux can be deduced from its OCR by multiplying by 5. In principle, several parameters of an approximate spectrum and the corresponding detector efficiency can both be deduced by iteration, using the efficiency curves for monoenergetic particles. This process has not yet been carried out in detail.

The angular distribution of particles at any particular point in space is far from isotropic, and the omnidirectional flux (or omnidirectional counting rate) is the average over all directions. The two proton detectors whose results will be described in Section 2.3 are essentially omnidirectional detectors in their construction; that is, they measure an approximately equally weighted average of the proton flux from all directions. The electron detector, however, is highly directional. Its axis is normal to the spin axis of the satellite and hence, over a number of satellite rotations, it measures an average directional intensity that depends on the angle between the satellite spin axis and the local magnetic field. The average directional counting rate has been converted to an omnidirectional counting rate (OCR), using an approximate expression for the influence of the aspect of the satellite.

$$OCR = \frac{C/G}{1 + 0.4 \cos 2A}, \tag{1}$$

where C is the average directional counting rate, G is the geometrical factor of the detector, and A is the angle between the spin axis and the local magnetic field. A more exact expression would take into account the anisotropy of the angular distribution of the particles at the particular location at which the measurement is being made and hence would vary from one place to another in space. Expression (1), however, is a good approximation over most of the space investigated. For the omnidirectional proton detectors, the OCR involves only the counting rate and the geometrical factor of the detector. Note that the OCR has the same units as omnidirectional flux $(1/cm^2 \ sec)$ throughout the paper. The OCR has been written most conveniently in terms of the variable Φ defined by

$$\Phi \equiv \log_{10}(OCR). \tag{2}$$

From a knowledge of the satellite ephemeris and the orientation of the satellite spin axis, the coordinates B-L or R-λ and the angle A are calculated and associated with the OCR as defined above. The data have then been machine plotted in a number of different forms:

Plot 1. *Constant* OCR *contours in* R-λ *space.* The plotting coordinates are R and λ. For a given detector, a point is plotted if Φ and the time, T, at which the datum point was taken fall within specified intervals. Fig. 3 is a plot of all the points for which data are available in electron channel 3 between days 263 and 267, 1962. Fig. 4 is a plot of all the points in Fig. 3 for Φ-range 2 (contour 2), Table I. The inner-belt contour stands out clearly. These plots give the flux distributions in space.
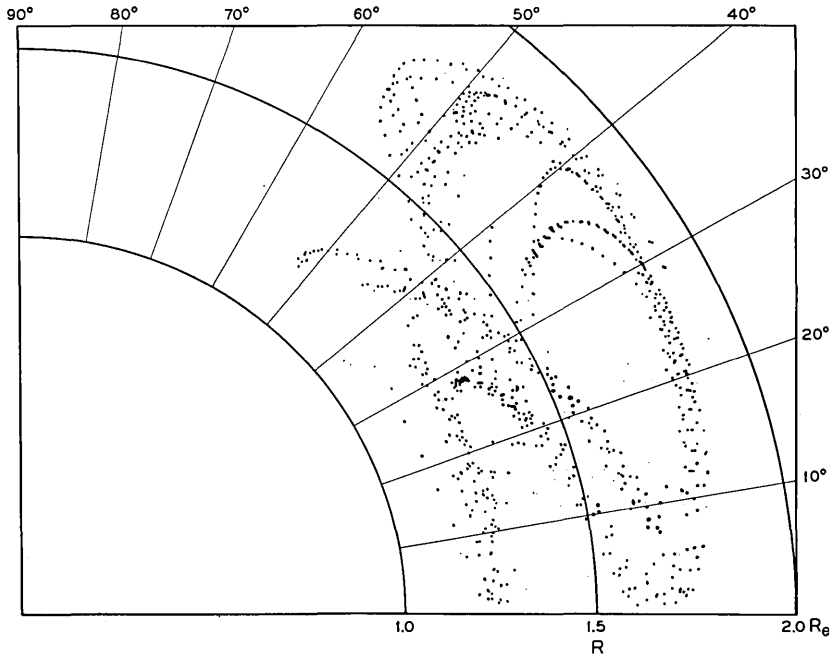
Fig. 3 — Points at which data were acquired in electron channel 3 for days 263 to 267, 1962, plotted in R-λ coordinates. The surface of the earth occurs at $R = 1.0 \pm 0.1\ R_e$.

Plot 2. *Constant* OCR *ratios in* R-λ *space*. These plots are analogous to plot 1, except that a range of $\Phi_a - \Phi_b$, where a and b indicate different channels, is selected instead of a range of Φ_a. These plots give an indication of the energy spectrum.

Plot 3. *Constant* OCR *contours in* B-L *space*. The difference between plots 1 and 3 is that B and L are used as plotting coordinates for plot 3 instead of R and λ. The geometry of the two coordinate systems is very different and they are appropriate to different calculations.

Plot 4. *Constant* OCR *ratios in* B-L *space*. The remarks under plot 3 apply.

Plot 5. Φ *vs* T. Under strict constraints, Φ values separated in time by not more than two minutes are interpolated to find Φ at given values of L. Φ is then plotted against T in days for the given value of L and a small range of B. The resultant plots give a time history of the radiation in almost 200 limited regions of space.

Plot 6. Φ *vs* B. Φ is interpolated to specific values of L, as in plot 5,
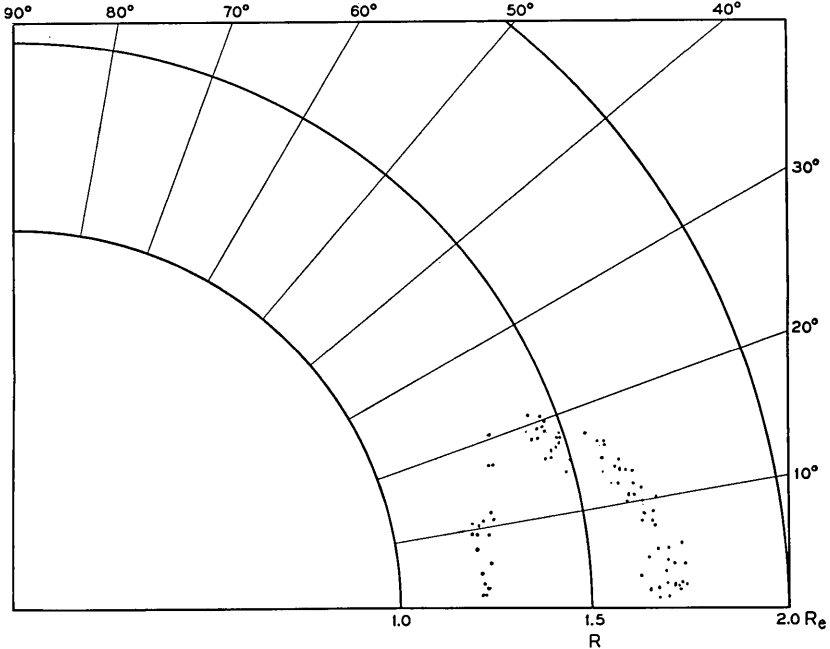
Fig. 4 — Points in Φ-range 2 (contour 2), electron channel 3, days 263 to 267, 1962, plotted in R-λ coordinates. The inner-belt contour is well defined. Φ ranges are defined in Table I.

TABLE I — VALUES FOR THE ELECTRON CONTOURS [OCR has the units counts/cm^2 sec; $\Phi \equiv \log_{10} (OCR)$]

Contour	Φ min	Φ max	Average OCR
1	8.0	≈ 8.4	1.5×10^8
2	7.5	8.0	6.6×10^7
3	7.0	7.5	2.1×10^7
4	6.5	7.0	6.6×10^6
5	6.0	6.5	2.1×10^6
6	5.5	6.0	6.6×10^5
7	5.0	5.5	2.1×10^5
8	4.5	5.0	6.6×10^4
9	4.0	4.5	2.1×10^4
10	3.5	4.0	6.6×10^3
11	3.0	3.5	2.1×10^3
12	2.5	3.0	6.6×10^2
13	$-\infty$	2.5	$<10^2$

and plotted against B. Only data taken within a given interval of days are included. These plots indicate the distribution of mirror points within a given magnetic shell.

Plot 7. Φ *vs* T. Φ is plotted against T in minutes for each pass. A pass is a single passage within range of a telemetry station. By examining the data in this context, spurious points may be identified. This is most important when the data are sparse.

The material presented in the next section has been selected and synthesized from the seven kinds of cross-referenced plots just described.

2.2 *Results of the Electron Measurements*

2.2.1 *Flux Maps*

Contours of constant *OCR* for electron channel 3 have been drawn through collections of points like those of Fig. 4. Data from the other electron channels have been treated as spectral rather than intensity information. Five of the contour maps thus produced in R-λ space are presented in Figs. 5 through 9. In four cases, the maps cover five-day
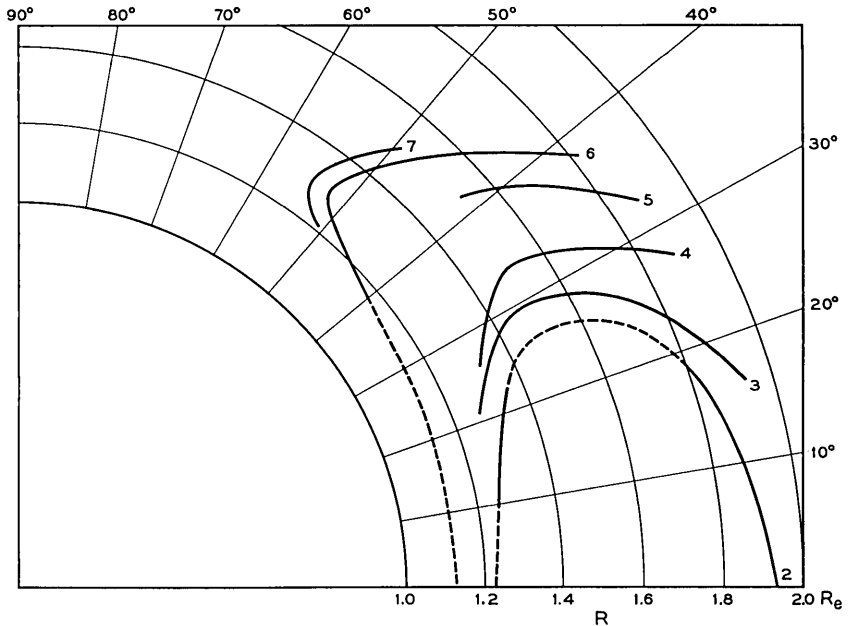
Fig. 5 — Contours of constant *OCR*, electron channel 3, days 193 to 197, 1962, plotted in R-λ coordinates. Dashed lines indicate interpolations and extrapolations. Φ ranges are defined in Table I.
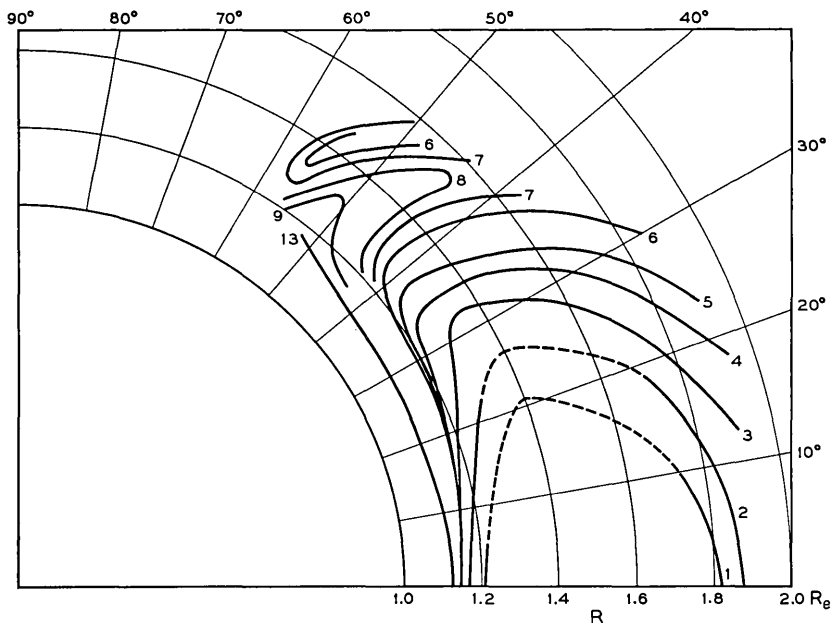
Fig. 6 — Contours of constant OCR, electron channel 3, days 203 to 207, 1962, plotted in R-λ coordinates. Dashed lines indicate interpolations and extrapolations. Φ ranges are defined in Table I.
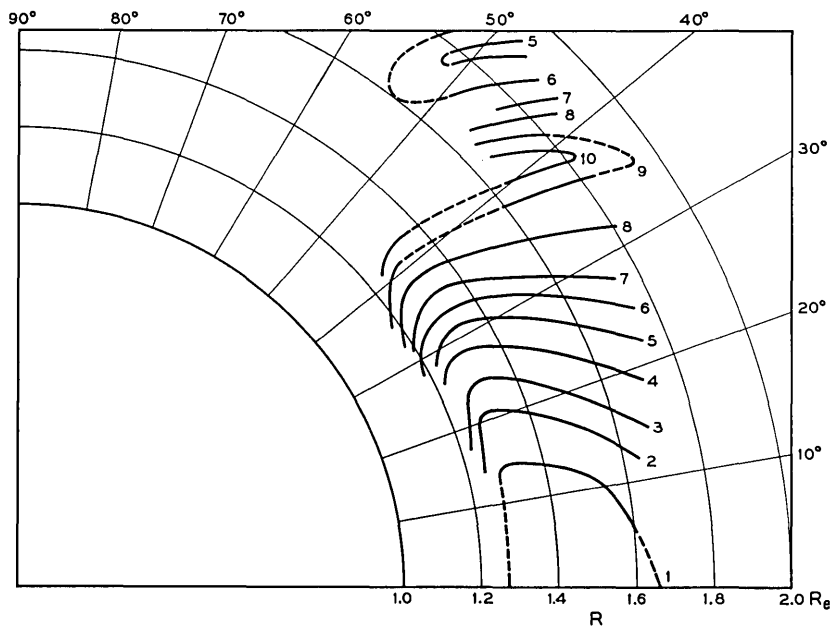
Fig. 7 — Contours of constant OCR, electron channel 3, days 238 to 242, 1962, plotted in R-λ coordinates. Dashed lines indicate interpolations and extrapolations. Φ ranges are defined in Table I.
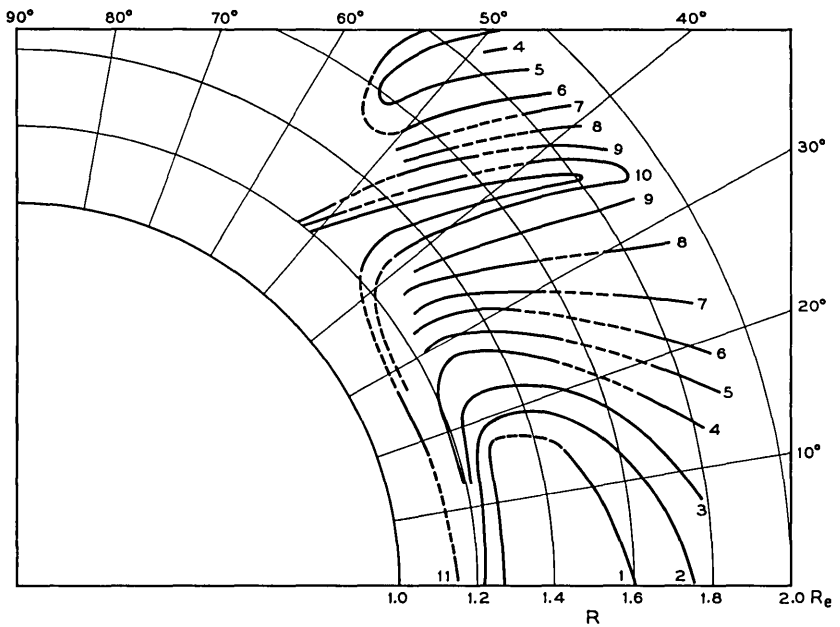
Fig. 8 — Contours of constant OCR, electron channel 3, days 263 to 267, 1962, plotted in R-λ coordinates. Dashed lines indicate interpolations and extrapolations. Φ ranges are defined in Table I.
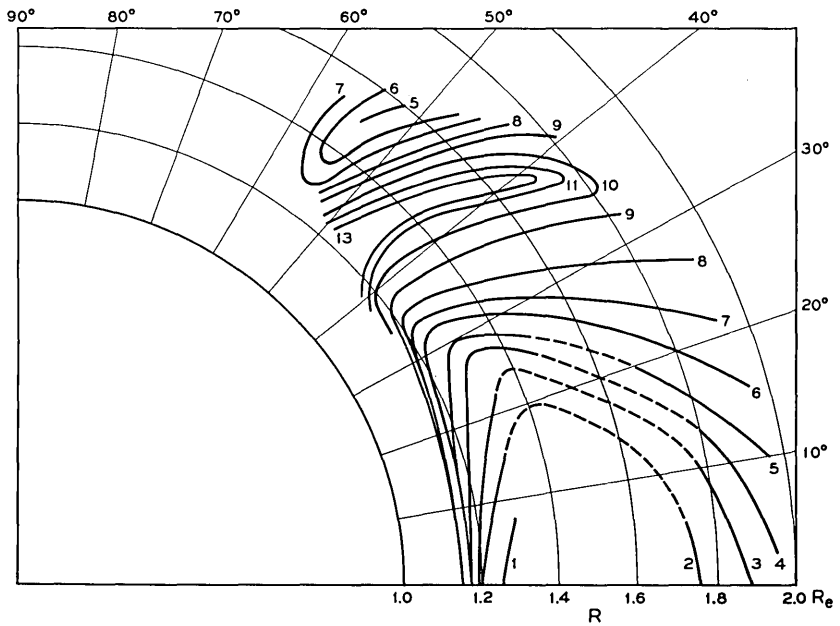
Fig. 9 — Contours of constant OCR, electron channel 3, days 288 to 294, 1962, plotted in R-λ coordinates. Dashed lines indicate interpolations and extrapolations. Φ ranges are defined in Table I.

intervals, the earliest containing the data for days 193–197, start-
ing two days after the Telstar launch and three days after the Star-
fish nuclear test. The latest map, covering the seven-day period,
days 288–294, is for the week immediately preceding the first of the
Russian high-altitude nuclear tests on October 22. The counting rates
of adjacent contours on these plots are separated by $\sqrt{10}$ in OCR or
by 0.5 in Φ, as indicated in Table I. An exception is contour 1, for which
the actual data do not uniformly cover the half decade counting rate
range that would be assigned to this contour in the normal progression.
A second exception is contour 13, which indicates the limit beyond which
the counting rate is not measurably different from 0. The contour maps
for each five-day interval have been drawn by hand essentially inde-
pendent of one another, and there are minor changes in contour shapes
and positions which do not represent the optimum contour fitting to the
data taken as a whole. A more comprehensive processing of the data
is in progress. Dashed lines on the contour maps indicate extensions of
the contours into regions devoid of data. Such regions shift with time
as the orbit of the satellite precesses, a feature which will be discussed
more fully in Section 2.4.1.

The highest electron fluxes lie on the equator in a region centered at a
radial distance of about 1.45 R_e . This is the general region of the inner
Van Allen belt. The contours lie increasingly close together as one pro-
ceeds to lower altitudes from this maximum because of the removal of
particles from trapped orbits by the increasingly dense atmosphere. In
Figs. 6 through 9 the tip or horn of the outer Van Allen belt is also
clearly evident in the secondary maximum at $\lambda \approx 50°$ and $R \approx 1.5 \; R_e$.
The separation into two belts is not apparent on days 193-197, partly
because the orbit stops short of the outer belt maximum, but even more
importantly, because the region between the two belts on those early
days is filled with electrons, presumably from the Starfish explosion.
Through the sequence of five figures a minimum-intensity slot between
the inner and outer belts continually develops until on days 288-294 it
contains a counting rate immeasurably different from 0 in the Telstar
electron detector. During this period, all the contours around the inner
belt peak are contracting. This occurs more rapidly on the lower-intensity
contours and at larger values of R and λ than in the low-R nearly equa-
torial region, but nowhere as dramatically as in the region of the slot.
This time decay will be discussed in more detail in Section 2.2.3.

Figs. 10 and 11 show contours of constant OCR in the B-L representa-
tion, corresponding to the contours in R-λ space shown in Figs. 6 and 9,
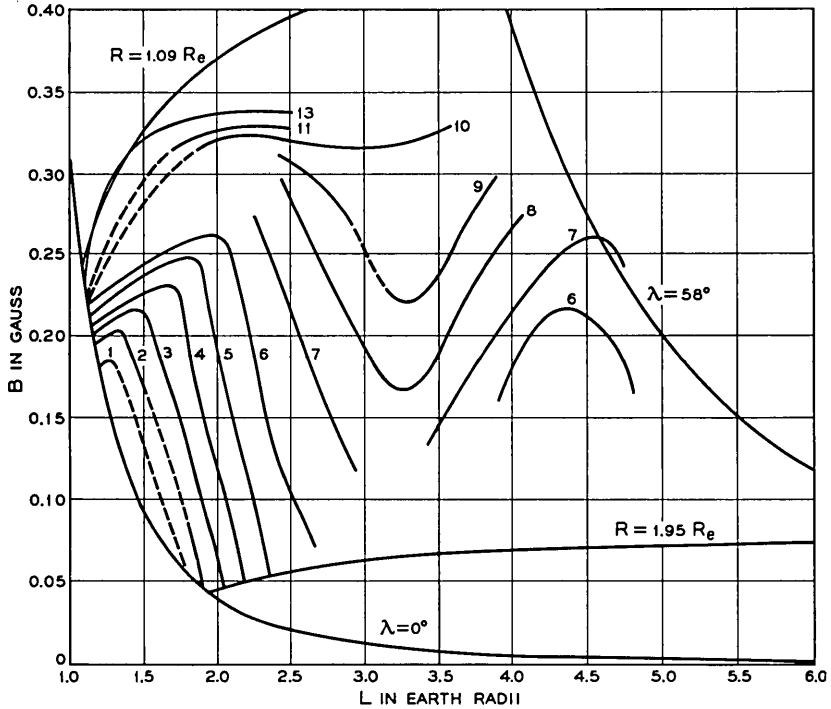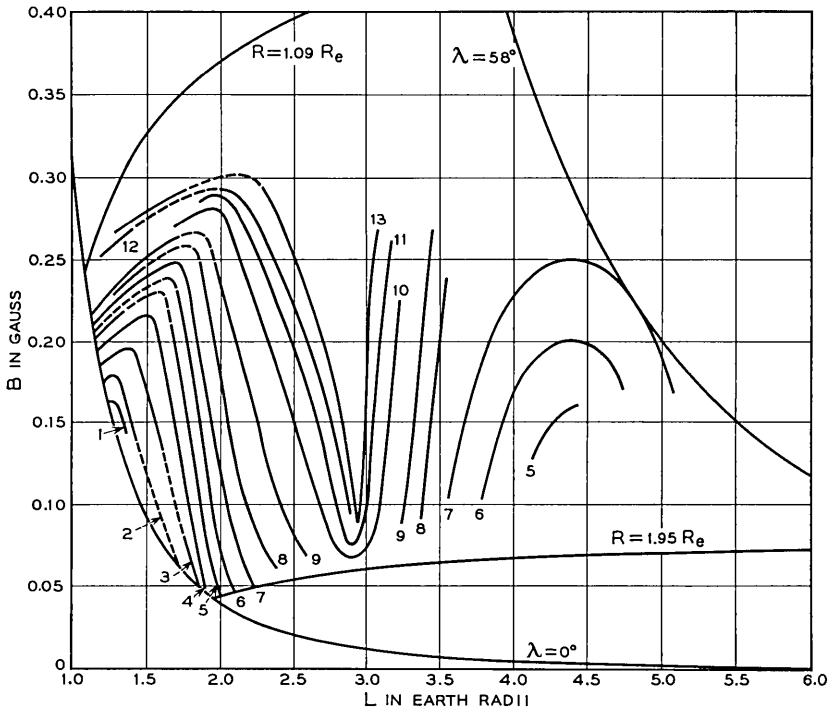respectively. The distortions introduced by the B-L coordinates show

Fig. 10 — Contours of constant OCR, electron channel 3, days 203 to 207, 1962, plotted in B-L coordinates. Dashed lines indicate extrapolations and interpolations. The lines $R = 1.09\ R_e$, $R = 1.95\ R_e$ and $\lambda = 58°$ define the approximate boundaries of the space swept out by the Telstar orbit. Φ ranges are defined in Table I.

graphically in contour 1 and in the appearance of the horn of the outer belt. The B-L diagrams contain three lines that approximately bound the Telstar orbit: $R = 1.09\ R_e$, the lowest altitude limit; $\lambda = 58°$, its extreme in equivalent dipole latitude; and $R = 1.95\ R_e$, the upper altitude extreme. All of the space more distant from the earth than the Telstar satellite can observe is compressed between the $R = 1.95\ R_e$ line and the $\lambda = 0°$ line, the trace of the equatorial plane of the magnetic dipole in this space. The orbital integrals which will be described in Section 2.4 have been conveniently carried out in B-L space.

2.2.2 The Energy Spectrum

As discussed in Section 1.1, the major sensitivity of the electron detector is to electron energies between 0.25 and 1 Mev. The detector

Fig. 11 — Contours of constant OCR, electron channel 3, days 288 to 294, 1962, plotted in B-L coordinates. Dashed lines indicate extrapolations and interpolations. The lines $R = 1.09\ R_e$, $R = 1.95\ R_e$, and $\lambda = 58°$ define the approximate boundaries of the space swept out by the Telstar orbit. Φ ranges are defined in Table I.

gives only an indirect indication of the spectrum above 1 Mev, an energy region which contributes heavily to radiation effects. The ratios, ρ_{34}, of channels 3 to 4 for two five-day periods are indicated in Figs. 12 and 13. Unfortunately, channel 4 has no log ratemeter and ratios cannot be taken in the high-intensity region inside contour 3, where the register begins to overflow. During mid-July, ρ_{34} had a value of approximately 3 over much of the space accessible to the instruments. This is exemplified by the region marked C in Fig. 12. A ratio of 3 is consistent with an electron spectrum appropriate to fission fragment beta decay.[18,19] Such consistency does not, however, constitute a unique determination of such a spectrum. Without postulating an extremely complex spectrum with a maximum intensity at about 700 Kev, a ρ_{34} equal to 3 cannot be produced unless there is a significant population of electrons in excess of 1 Mev. It is not possible, however, to assert that the fraction of electrons
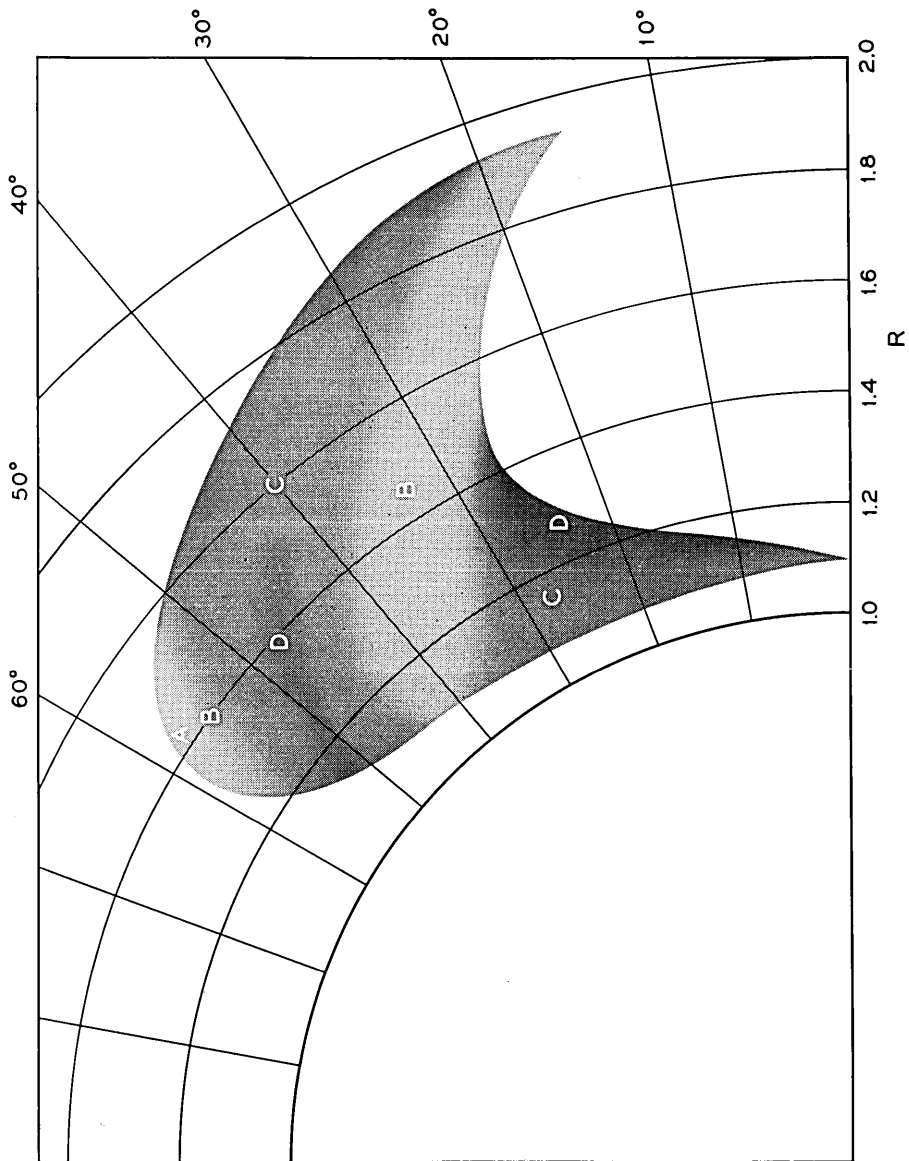
Fig. 12 — Ratio of *OCR* electron channel 3 to *OCR* electron channel 4 (ρ_{34}), days 203 to 207, 1962, displayed in R-λ coordinates.

Label	Range of ρ_{34}	Comment
A	>8	very soft
B	4–8	soft
C	2–4	fission-like
D	1–2	hard
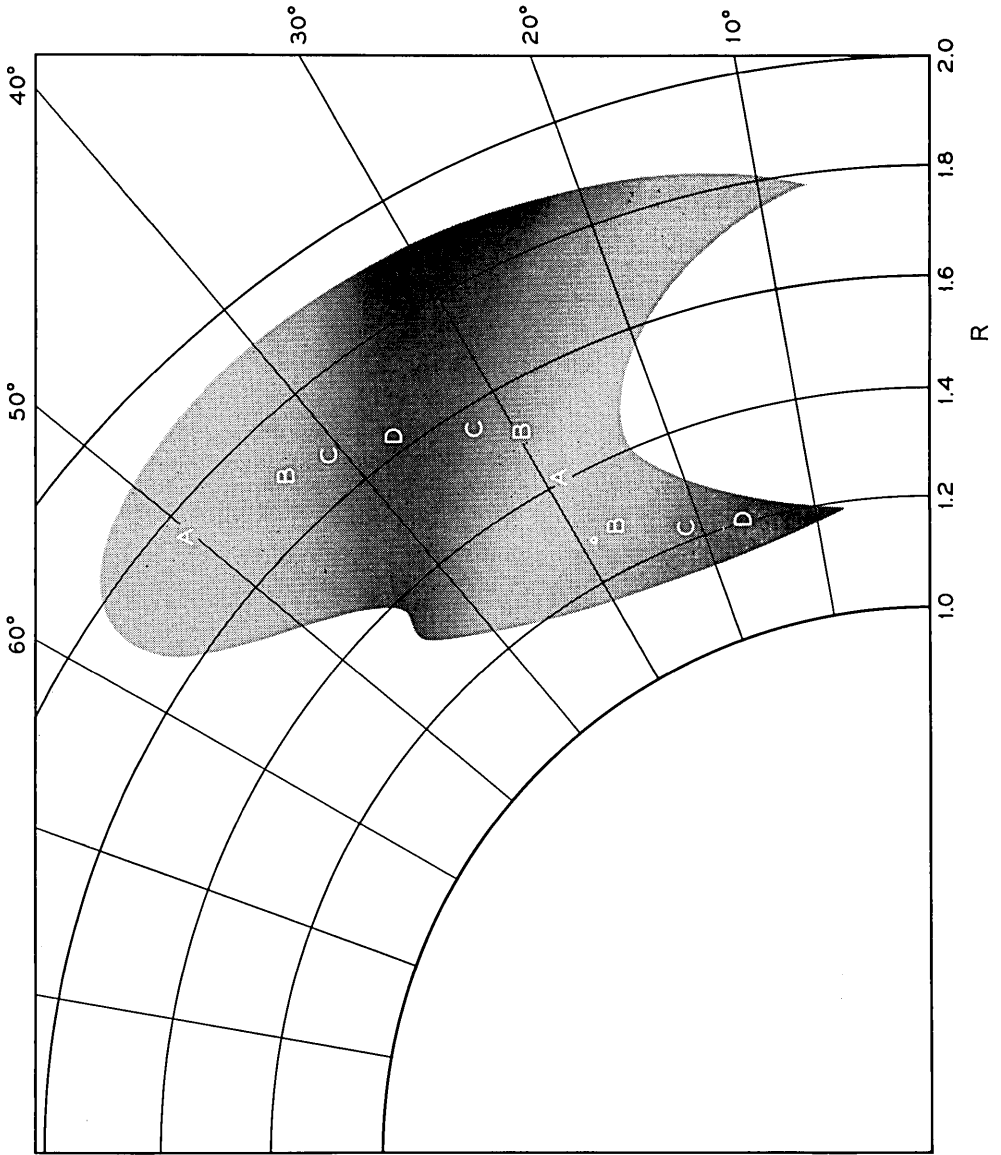
Fig. 13 — Ratio of *OCR* electron channel 3 to *OCR* electron channel 4 (ρ_{34}), days 263 to 267, 1962, displayed in R-λ coordinates. Labels are identified in the legend of Fig. 12.

above about 1.5 Mev is 0.2 of the total electron spectrum, as would be the case in the fission spectrum.[19]

Van Allen, Frank, and O'Brien[20] have reported on measurements from an instrument in the Injun I satellite that effectively measures electrons above 1.5 Mev.[21] They have concluded that the spatial distribution of the energetic electrons injected by Starfish had a maximum at $L \approx 1.2$ R_e, and they have inferred that the flux is 10 per cent of this maximum at an equatorial L of about 1.8 R_e. From the Telstar data shown in Fig. 6, the electron flux at $L = 1.8$ R_e on the equator is essentially the same as that at $L = 1.2$ R_e, and contour 3, which is 10 per cent of the maximum measured value, apparently has an upper crossing of the equator at $L \approx 2.1$ R_e. When these two sets of observations are translated into R-λ space, they give high-intensity regions very different in extent and will, if one asserts that the electrons seen by the Telstar detector are a result of Starfish, give rise to quite different values of the total number of electrons injected into trapped orbits by that explosion. Since the two detectors measure electrons at quite different energies, the apparent conflict between these two sets of results is easily resolved by proper treatment of the electron energy spectrum. The higher flux of electrons for $L > 1.6$ R_e as seen by the Telstar detector do not have associated with them the proportion of high-energy electrons to be expected in a fission electron spectrum. The possibility has been considered that most of the lower-energy electrons (the Telstar data) on these higher-L lines may be of natural origin. However, the time-dependence of the measured flux, which will be discussed in Section 2.2.3, strongly suggests that a major fraction of these electrons was connected with the explosion. A mechanism is thus required by which a high-altitude explosion can introduce a spectrum of electrons which varies in space and can be appreciably different from that of fission beta decay. Although the details of such a process are not yet understood,[22] direct observation of this effect on a less extensive scale was made by Explorer XV[23,24] on electrons injected by the second Russian high-altitude explosion on October 28. Several mechanisms for degrading the electron energy spectrum from a fission electron source have been suggested.[25,26] It also seems possible that low-energy electrons (<0.25 Mev) normally present in space might be accelerated as a result of the shock front of the expanding bomb debris to energies where they would be counted by the Telstar electron detector. A quantitative determination of the spatial variation in the electron spectrum which will satisfy the July measurements of the Telstar and Injun satellites has not yet been made, but with recognition of a softer spectrum on higher-L lines there seems

little doubt that a large part of all the electrons measured by the Telstar satellite in July were a result of the Starfish test.

In the tip of the outer belt, region A of Fig. 12, the spectrum softens appreciably, $\rho_{34} > 8$, and a similar but less pronounced softening occurs in region B. In the small regions D, the spectrum was apparently harder, $2 > \rho_{34} > 1$, than a fission beta spectrum. It is very difficult to see how a ratio smaller than 2 can be obtained for any electron spectrum in the light of the efficiency curves of Fig. 1, and the low ratios seem to arise from two other effects. In the lower-intensity of the two regions marked D (at high λ), ratios of <2 arise from statistical fluctuations in the number of counts in the register. In the high-intensity D region, these anomalous ratios arise from fluctuations in the log ratemeter measurement of the counting rate of channel 3, which is modulated as the spin of the satellite sweeps the acceptance cone of the detector through the nonisotropic particle distribution.

The temporal changes in the electron belts are heavily energy dependent. By late September, Fig. 13, the configuration is still fissionlike, as indicated by ρ_{34} only in the areas marked C. The spectrum is soft on the high-altitude slope of the inner belt, very hard in the slot, and soft again in the tip of the outer belt. The higher-energy electrons appear (surprisingly) to decay faster on the high-altitude slope of the inner zone, while the lower-energy electrons seem to disappear more rapidly in the center of the slot, at $L = 3\ R_e$.

Until about September 23, the ratio, ρ_{13}, of channel 1 to channel 3 on the Telstar detector indicates that between 0.25 and 0.6 Mev the spectrum is very soft, $\rho_{13} > 8$, in the slot and contains appreciably more low-energy electrons than a fission beta-decay spectrum except at very low altitudes and the center of the inner belt. Beginning on September 23, there is a very extensive and complex change in the electron population for $L > 1.8\ R_e$ and particularly for lower-energy electrons. The changes are small in channels 3 and 4, but are sufficiently large in channels 1 and 2 to have a profound influence on the ρ_{13} ratio in some places. These effects are apparently of natural origin. They have not yet been studied in sufficient detail to permit discussion in this paper.

2.2.3 Time Variation

The time variation of the electron flux will be discussed in terms of the omnidirectional counting rates of channel 3. The other channels show generally similar time decays, but there are differences in detail which give rise to the changes in the spectrum discussed above. Figs. 14
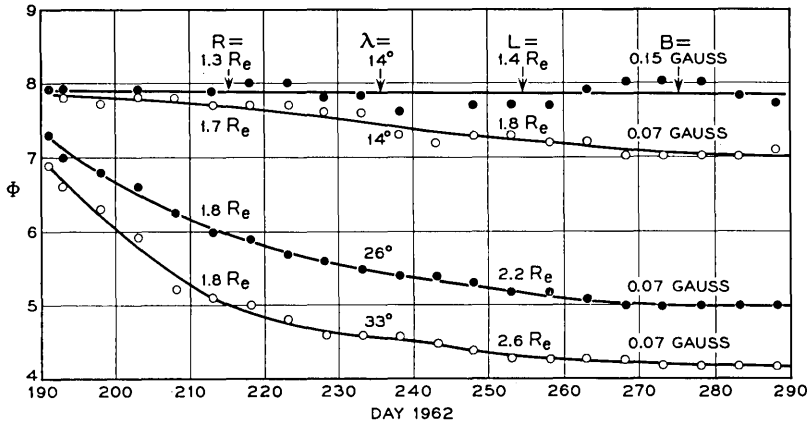
Fig. 14 — Temporal behavior of Φ for electron channel 3 at various positions in the radiation belts.

and 15 have been constructed from type 5 and 6 plots and show the long-term time dependence in representative regions of the belts.

The *OCR* in the high-intensity zone of the inner belt, typified by the point $L = 1.4\ R_e$ and $B = 0.15$ gauss ($R = 1.3\ R_e$, $\lambda = 14°$), shows no net long-term variation. There is some scatter in the points which may be real but which seems more likely to be a result of systematic differences introduced by the interpolations required to remove the B, L, and A dependence of the data. At $L = 1.8\ R_e$ and $B = 0.07$ gauss ($R = 1.7\ R_e$, $\lambda = 14°$) the *OCR* has decayed by somewhat less than a factor of 10 between July and the middle of October, and the rate of
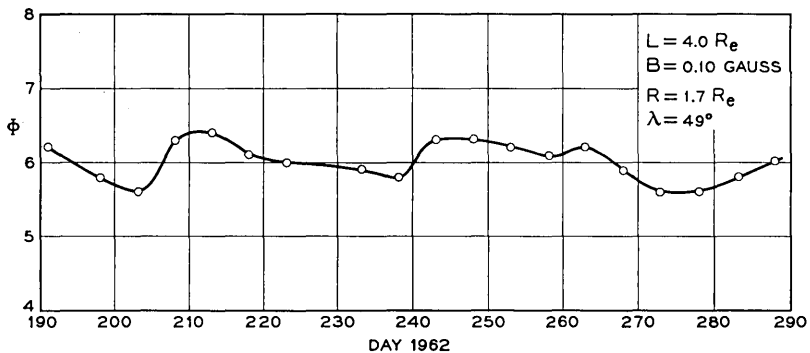
Fig. 15 — Typical temporal behavior of Φ for electron channel 3 in the tip of the outer belt.

decay seems to be slowing. Closer to the center of the slot $B = 0.07$ gauss and $L = 2.2$ and $2.6\ R_e$ ($R \approx 1.8\ R_e$ and $\lambda = 26°$ and $33°$) the decay is faster and greater, and the OCR levels off after day 260 at a value 50 times less than it had in early July. The outer-belt horn is characterized by the fluctuations apparent in Fig. 15, at $L = 4.0\ R_e$, $B = 0.10$ gauss ($R = 1.7\ R_e$ and $\lambda = 49°$). The short-term fluctuations are much sharper than those shown in Fig. 15, which have been smoothed over five-day intervals. There is no doubt that the variations here are real, but in these data there appears to be no trend.

In the region below $L = 1.4\ R_e$ there is general agreement that the bulk of the electrons present were injected by Starfish. This was directly observed as a sudden change by Injun I[20] and TRAAC,[27] both of which had a record of the high-energy electron distribution in this region for many months prior to July. Furthermore, Telstar and Injun measurements in this region have subsequently been verified by other satellites — Explorer XIV,[21] Explorer XV,[23,24] and several Air Force satellites[28-31] — that show the spectra in this region are far too hard to be of natural origin. Since the Telstar satellite was launched a day after Starfish, such a direct statement cannot be made for near equatorial regions with $L > 1.4\ R_e$. However, the observation of continuous monotonic decay over the months from July to October, and verification of the absolute intensities observed by the Telstar satellite with measurements by Explorer XV, make it almost impossible to conclude that electrons beyond $L = 1.4\ R_e$ were not also a result of that test. Electrons were introduced by Starfish even as far out as $L = 3.5$ or $4\ R_e$. If one adds up the electrons in space as shown on days 203-207, and if the detector efficiency of channel 3 were unity above the threshold, approximately 1.2×10^{25} electrons must have been introduced with energies above 440 Kev. Using the average efficiency (0.38) between 440 Kev and 1 Mev as shown in Fig. 1, the data require at least 3×10^{25} electrons with energies between 440 Kev and 1 Mev. If one uses an efficiency for a fission electron spectrum of 0.2, the number of electrons of all energies was 6×10^{25}. This is something like 10 per cent of all the fission electrons produced in the explosion, although some nonfission source associated with the bomb cannot yet be ruled out.

Fig. 16 presents some preliminary results of observations made during the Russian high-altitude test series. The first two tests, days 295 and 301, injected electrons into the slot region between L values of about 1.8 and $4.0\ R_e$. After the initial surge we again observe a rapid decay near the center of the slot, and a slow decay near the slopes of the inner and outer belts.
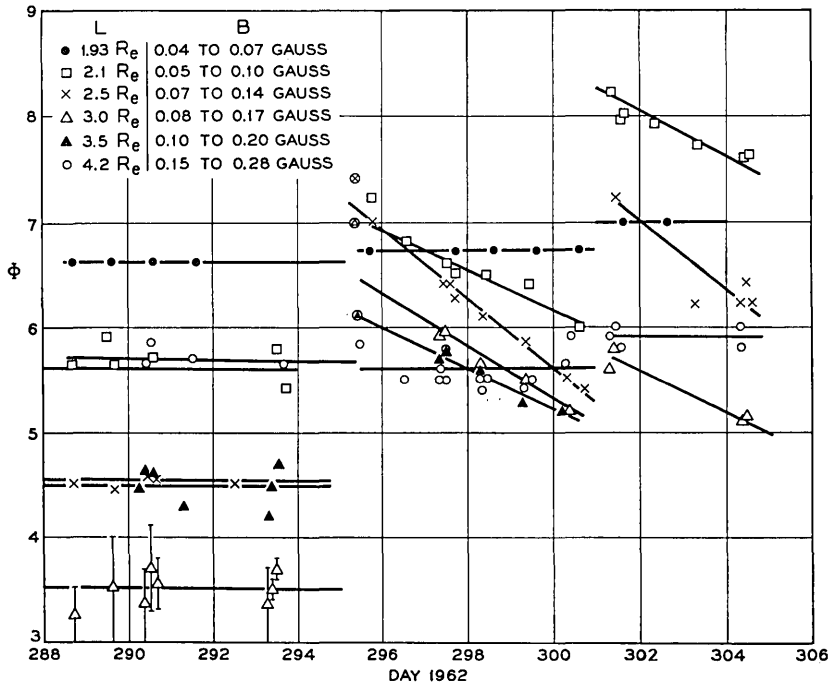
Fig. 16 — Temporal behavior of Φ for electron channel 3 during the first two Russian high-altitude nuclear tests. Circled points on day 295 are probably initial transients.

2.3 *Results of the Proton Measurements*

The *OCR* of the omnidirectional proton detectors have proven very stable in time. This stability has greatly simplified the analysis of the results. Figs. 17 and 18 are maps of the *OCR*, which apply to the entire 15-week period covered. There are five contours per decade in the proton plots, rather than two as in the electron maps previously described. No shift of as much as half a contour (25 per cent) has been observed. The measurements agree well with previous measurements in the inner zone,[32,33] and it seems unlikely that the Starfish test had any appreciable effect on protons in these energy ranges. The maximum intensity occurs at a lower altitude for the higher-energy protons in agreement with theory[10] and other observations.[23,24,34] Both detectors exhibit a well-defined cutoff, beyond which no counts are recorded in the region accessible to the spacecraft. The efficiency of the detectors is high, and
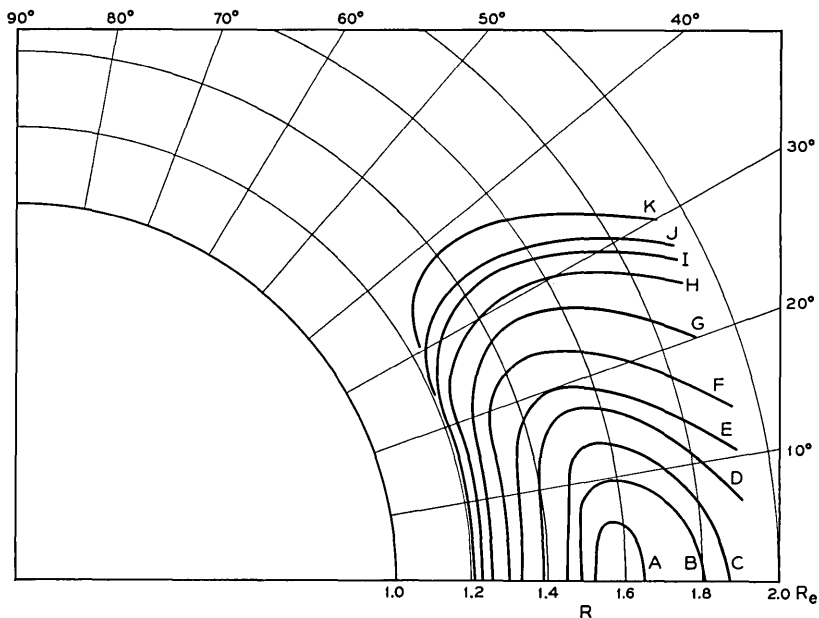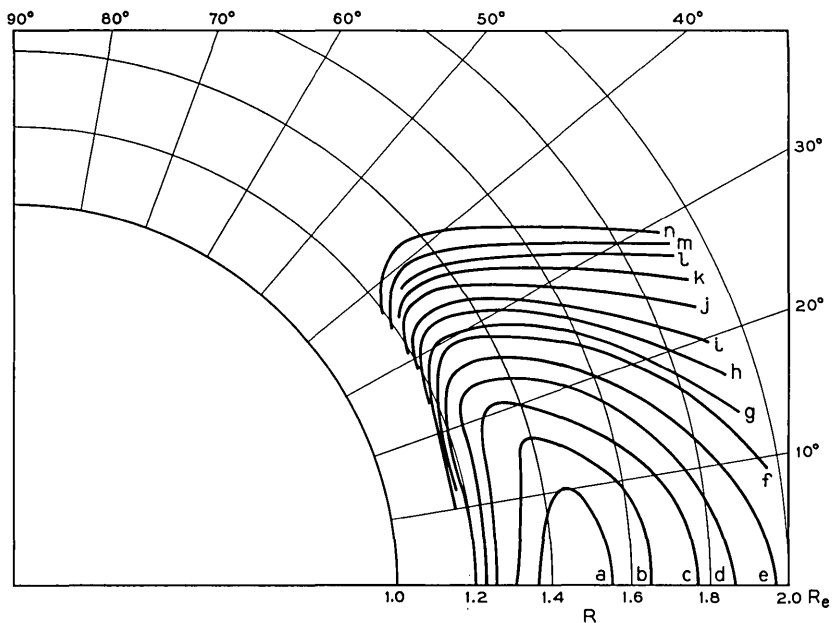
Fig. 17 — Contours of constant OCR, protons in the energy range 26 to 34 Mev, days 191 to 294, 1962, plotted in R-λ coordinates. To convert OCR to omnidirectional flux (1/cm² sec), add 0.32 to Φ. The range of Φ associated with the contours is: A, 4.0-4.2; B, 3.8-4.0; C, 3.6-3.8; D, 3.4-3.6; E, 3.2-3.4; F, 3.0-3.2; G, 2.8-3.0; H, 2.6-2.8; I, 2.4-2.6; J, 2.2-2.4; K, 2.0-2.2.

using the average efficiency in their regions of sensitivity, the flux is approximately 2.1 OCR for the 26 to 34 Mev detector, and 2.6 OCR for the > 50 Mev detector.

2.3.2 Energy Spectrum

The contours for the two detectors have different shapes, which show that the energy spectrum in this range of energies is not constant with position. This is clearly indicated in the equatorial flux plot of Fig. 19. The equatorial omnidirectional *fluxes* for the two detectors are graphed as a function of L. (On the dipole equator $L = R$.) Plotted in the same figure are the quantities N_{26} and n from the expression for the differential spectrum

$$N(E) = N_{26}(E/E_0)^{-n}, \tag{3}$$

where $N(E)$ is the flux of electrons in the energy range dE at E, and

Fig. 18 — Contours of contant OCR, protons with energies >50 Mev, days 191 to 294, 1962, plotted in R-λ coordinates. To convert OCR to omnidirectional flux (1/cm² sec), add 0.42 to Φ. The range of Φ associated with the contours is: a, 3.2-3.4; b, 3.0-3.2; c, 2.8-3.0; d, 2.6-2.8; e, 2.4-2.6; f, 2.2-2.4; g, 2.0-2.2; h, 1.8-2.0; i, 1.6-1.8; j, 1.4-1.6; k, 1.2-1.4; l, 1.0-1.2; m, 0.8-1.0; n, 0.4-0.6.

$E_0 = 26$ Mev. A fit to the data could have been made with an exponential spectrum of the form[33]

$$N(E) = N_0 \exp(-E/E_c), \tag{4}$$

where N_0 and E_c are constants. However, such a spectrum extrapolates in a very unreasonable way to lower energies, giving far fewer low-energy protons than observed either by the Telstar low-energy proton detector or by detectors on Explorer XV.[24]

With the power law spectrum the value of $n \approx 4.5$ applies over a considerable part of the region beyond the 50-Mev proton maximum, but at smaller L values the spectrum is very much harder and n decreases to a value of about 2. Such a power law variation at low equatorial altitudes seems to be in reasonable agreement with the observations of Freden and White[35] and Naugle and Kniffen.[36]

Using the constants of the spectra as given in Fig. 19, the maximum integral flux of protons with energies >40 Mev is found to be approxi-
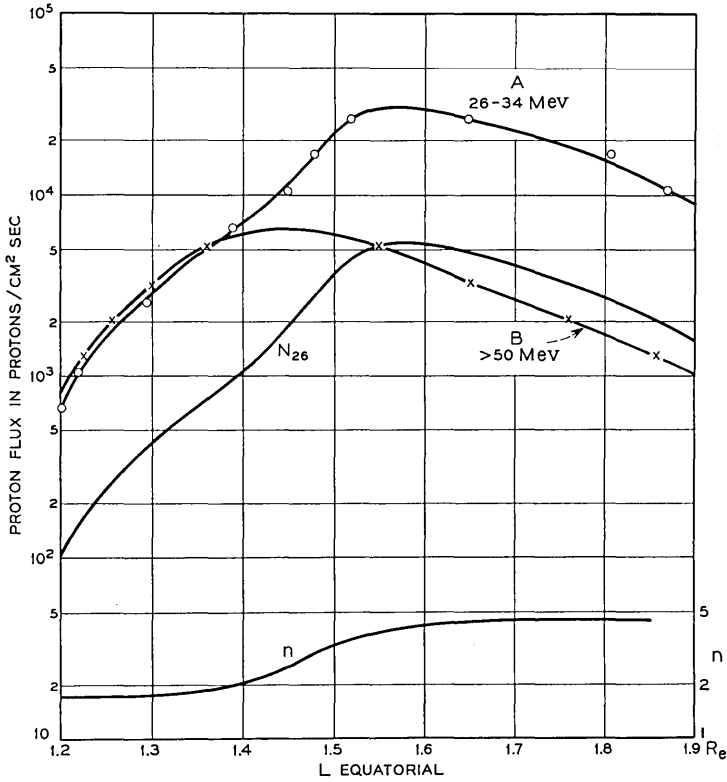
Fig. 19 — Equatorial proton flux. Curve A is for protons in the energy range 26 to 34 Mev, and curve B for protons with energies >50 Mev. n and N_{26} are defined in the text.

mately 1.5×10^4 protons/cm^2 sec, quite close to the historical value of 2×10^4 quoted by Van Allen in 1958[32] for the peak flux in the inner belt.

2.4 *Radiation Exposure of the Satellite*

2.4.1 *Orbital Effects and Method of Calculation*

The radiation exposure of a satellite is an integral along the satellite orbit of the particle flux weighted in accordance with its energy spectrum. The Telstar satellite spends a considerable part of its time in the inner Van Allen belt and thus experiences an unusually rigorous radiation environment. The radiation exposure is far from constant in time, however. The instantaneous exposure varies enormously as the
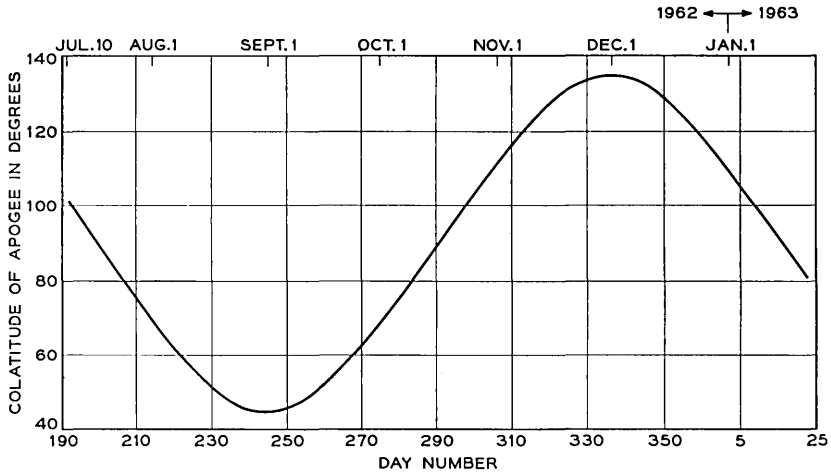
Fig. 20 — The position of apogee colatitude for the Telstar satellite as a function of time.

satellite enters and leaves the region of high intensity in the inner belt. Furthermore, the average exposure over an orbit varies throughout a day because of the geographical asymmetry of the magnetic field that controls the trapped particle distribution. And finally, the average exposure over a period of several days varies as the position of apogee in the orbit precesses. This latter orbital change is shown in Fig. 20, which is a plot of the colatitude of apogee, θ_A, of the Telstar orbit as a function of time. The period of this precession is 181 days, and the maximum and minimum colatitudes are 45 and 135 degrees, corresponding to the 45-degree inclination of the orbit.

To illustrate the wide differences between orbits on a single day, orbits 1 and 6 for day 205 are shown in Fig. 21 in the R-λ space used in displaying the electron and proton distributions. The particles by definition have north-south symmetry in this equivalent dipole representation, but the northern and southern parts of the satellite orbit are far from the same. The differences between the two orbits of the figure near $\lambda = \pm 45°$ are caused primarily by the 11-degree offset of the earth's geomagnetic axis. Near $\lambda = 0°$ and especially at low altitudes, the differences arise from the Brazilian magnetic anomaly. On day 205 of Fig. 21, apogee is near the equator, $\theta_A = 81°$. In contrast, two orbits for day 335, when apogee is at its most southern point, $\theta_A = 135°$, are shown in Fig. 22. These orbital variations from week to week were
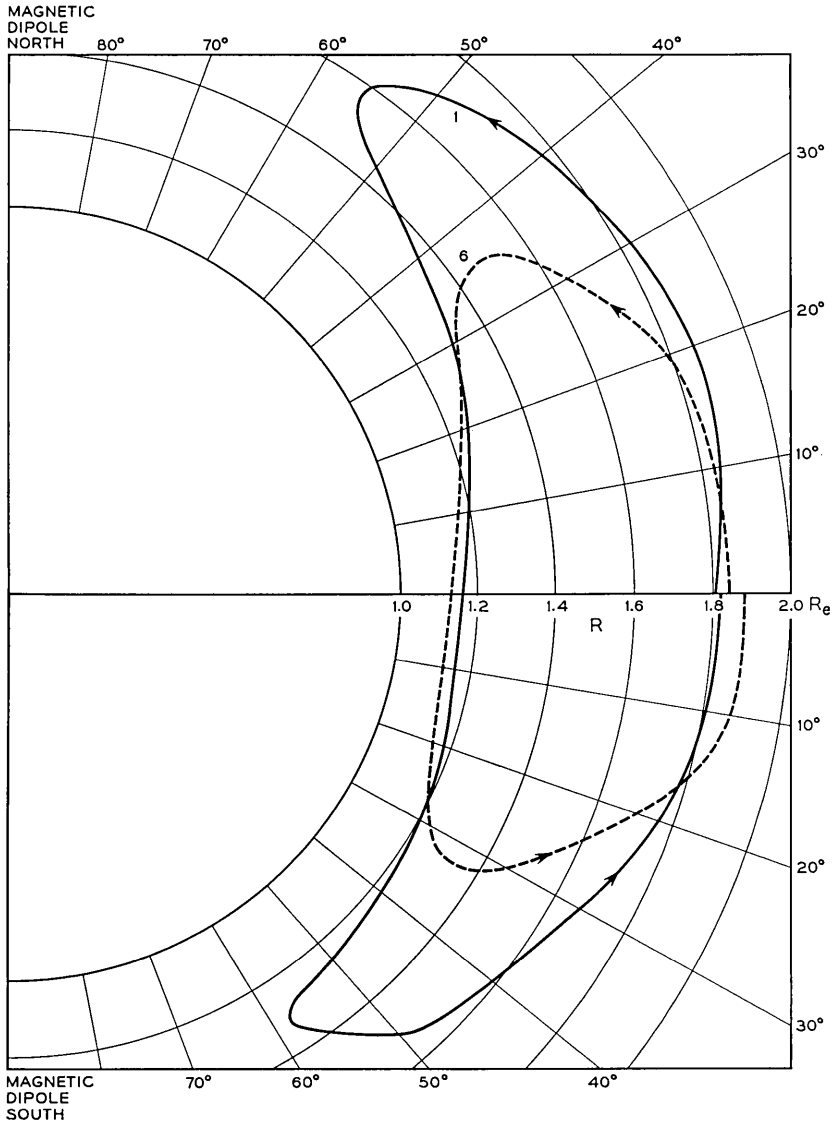
Fig. 21 — Orbits 1 and 6 for day 205, 1962, plotted in R-λ coordinates. Apogee is near the geographic equator.
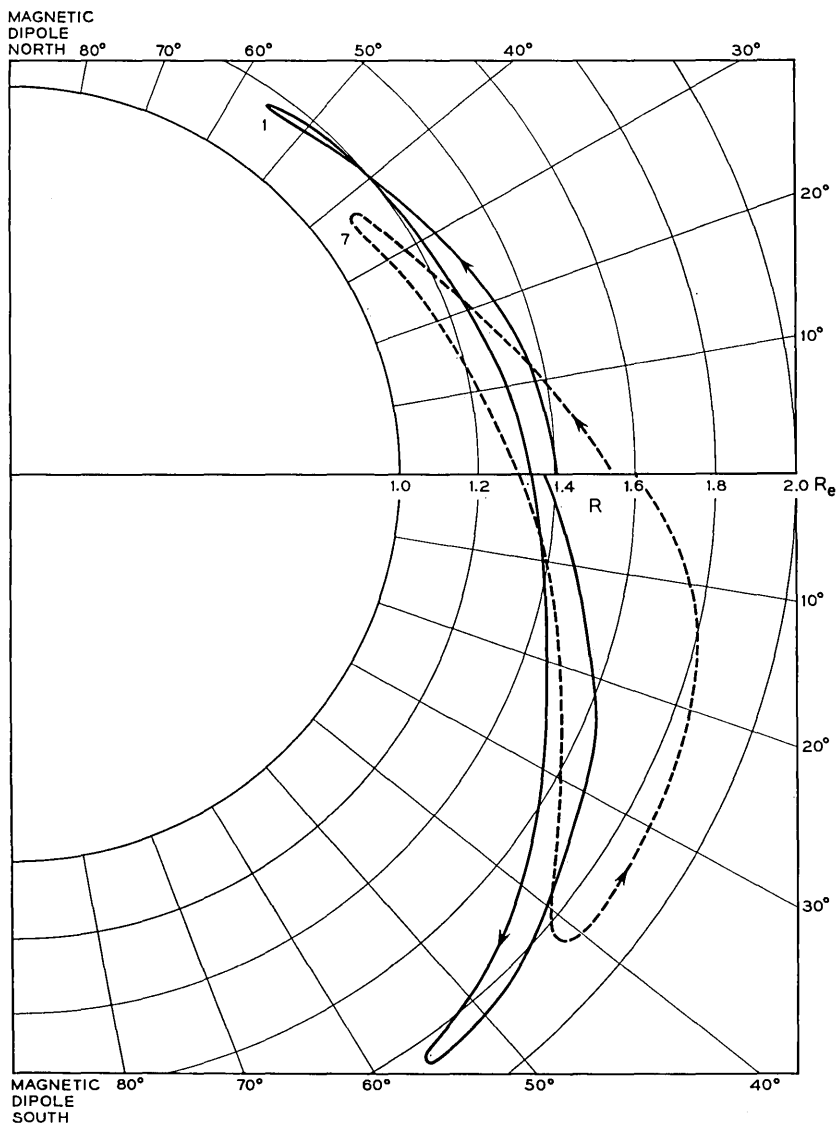
Fig. 22 — Orbits 1 and 7 for day 335, 1962, plotted in R-λ coordinates. Geographically, apogee is at the most southern point in the orbit.

previously noted in connection with regions in B-L space for which data are missing; see Figs. 5-9. The orbital picture is further complicated in computing an integral radiation exposure by the variation in satellite speed along the orbital path, a factor not shown in Figs.

21 and 22. The vehicle spends much more time close to apogee than to perigee. The complex motion of the satellite with respect to the trapped particles makes it necessary to undertake fairly detailed calculations, including transformations to a magnetic coordinate system, in order to find the integrated radiation exposure of the satellite.

The following method has been used. The part of B-L space to which the Telstar satellite is confined has been divided into 620 areas by a grid that is spaced so that the areas are small in the important regions. Thirteen colatitudes of apogee, at 7.5-day intervals, have been selected. For each position of apogee, eighteen equally spaced ascending-node longitudes have been chosen. The fraction of time, T_{ik}, spent in each B-L box has been computed and averaged over the eighteen nodal positions associated with each apogee position, using a Keplerian orbit very close to the Telstar orbit. The step size along the orbit is varied so that the computation is done most accurately in the most critical places. The results of the calculation for $\theta_A = 79.48°$ are shown in Table II. By examining the OCR maps in B-L space, values, OCR_{ik}, appropriate to the days when θ_A had a given value are assigned to the B-L boxes. When necessary a similar procedure is followed for the spectrum, S_{ik}. The operation

$$F = \sum_{i,k} T_{ik} OCR_{ik} S_{ik} \qquad (5)$$

is performed. F is now approximately the average flux of all electrons incident on the spacecraft during a one-day period. The calculation is approximate in the sense that the actual orbit, with its continuously varying apogee colatitude and with ascending node longitudes that do not shift by a simple fraction of 360°, has been replaced by a set of closely spaced but discrete orbits. One does not calculate in this way an instantaneous radiation intensity but only an intensity that is very nearly correct over a period of a day or several days. Actually, a more serious inaccuracy is contributed by a lack of detailed knowledge of the particle energy spectrum. This will be described in more detail in connection with specific applications in Sections 3.2 and 3.3.

2.4.2 Integrated Electron Flux

Using the method outlined above, the average and cumulative omnidirectional electron flux to which the Telstar spacecraft was exposed have been calculated. The electron flux is obtained from the OCR contours for channel 3 of the electron detector, e.g., those shown in Figs. 10 and 11. These counting rates are multiplied by a factor of 5 to yield the total flux (above 0 energy) under the assumption that the

TABLE II — AVERAGE TIME SPENT BY THE *TELSTAR* SATELLITE IN VARIOUS B-L REGIONS FOR AN APOGEE COLATITUDE OF 79.48°

| B_{MIN} gauss | | .04 | .06 | .08 | .10 | .12 | .13 | .14 | .15 | .16 | .17 | .18 | .19 | .20 | .22 | .24 | .26 | .28 | .32 | .36 | .40 |
| B_{MAX} gauss | | .06 | .08 | .10 | .12 | .13 | .14 | .15 | .16 | .17 | .18 | .19 | .20 | .22 | .24 | .26 | .28 | .32 | .36 | .40 | .50 |
L_{MIN} R_e	L_{MAX} R_e										(Entries are in 0.1 Per cent)										
1.00	1.05	0	0	0	0	0	0	0	0	0	0	0	0	0	0	0	0	0	0	0	0
1.05	1.10	0	0	0	0	0	0	0	0	0	0	0	0	0	1	2	0	0	0	0	0
1.10	1.15	0	0	0	0	0	0	0	0	0	0	0	0	6	9	3	1	0	0	0	0
1.15	1.20	0	0	0	0	0	0	0	0	0	0	2	3	13	4	1	2	1	0	0	0
1.20	1.25	0	0	0	0	0	0	0	0	1	3	5	3	7	3	1	1	1	0	0	0
1.25	1.30	0	0	0	0	0	0	0	0	1	1	1	4	4	2	1	0	2	0	0	0
1.30	1.35	0	0	0	0	0	0	0	0	1	1	0	3	5	2	0	1	1	0	0	0
1.35	1.40	0	0	0	0	0	0	0	0	1	0	0	3	2	2	1	1	1	0	0	0
1.40	1.45	0	0	0	0	0	0	0	0	1	0	0	3	4	2	0	0	2	1	0	0
1.45	1.50	0	0	0	0	0	0	0	0	1	0	1	2	4	2	0	0	1	0	0	0
1.50	1.60	0	0	0	0	0	0	0	0	1	0	3	3	2	3	1	1	2	1	0	0
1.60	1.70	0	0	0	0	0	0	0	1	1	1	2	1	6	2	2	0	1	2	0	0
1.70	1.80	0	7	0	0	0	0	0	2	1	1	3	3	2	2	0	2	1	0	0	0
1.80	1.90	102	17	5	0	0	1	2	1	0	2	3	3	2	1	1	0	0	0	0	0
1.90	2.00	65	27	5	4	3	2	2	0	1	3	3	0	3	0	1	1	0	2	0	0
2.00	2.10	26	29	4	3	1	1	0	1	4	5	1	1	2	2	3	0	2	1	0	0
2.10	2.20	12	18	12	3	1	1	0	2	4	2	1	0	0	0	0	0	0	1	0	0
2.20	2.30	3	17	16	1	1	1	4	4	2	1	1	1	1	2	1	0	0	0	0	0
2.30	2.40	6	8	9	9	5	4	2	4	1	0	0	1	2	1	1	0	1	0	0	0
2.40	2.50	3	11	7	4	3	2	1	1	0	0	0	0	0	0	0	0	0	0	0	0
2.50	2.70	0	7	10	20	3	7	1	2	3	2	1	1	1	4	0	1	0	3	0	0
2.70	2.90	0	10	8	6	3	0	1	1	1	1	0	0	4	2	0	1	1	1	0	0
2.90	3.10	0	3	0	4	3	8	1	3	1	1	2	2	0	1	0	0	2	0	0	0
3.10	3.30	0	4	0	5	0	3	0	1	1	0	2	0	2	0	0	0	0	0	0	0
3.30	3.50	0	0	3	2	2	0	5	2	2	0	1	0	1	2	0	0	2	0	0	0
3.50	3.80	0	0	3	0	0	0	0	2	7	1	0	4	0	0	1	2	0	0	0	0
3.80	4.10	0	0	7	6	0	2	0	0	0	2	0	2	4	0	2	0	4	0	0	0
4.10	4.40	0	0	0	0	2	0	2	0	0	2	2	4	0	2	0	0	0	0	0	0
4.40	4.70	0	0	0	3	0	0	0	0	0	0	0	0	0	1	3	0	0	0	0	0
4.70	5.00	0	0	0	0	3	2	4	0	0	2	0	0	0	0	0	0	0	0	0	0
5.00	9.99	0	0	0	0	0	0	0	2	0	0	0	0	0	0	0	0	0	0	0	0
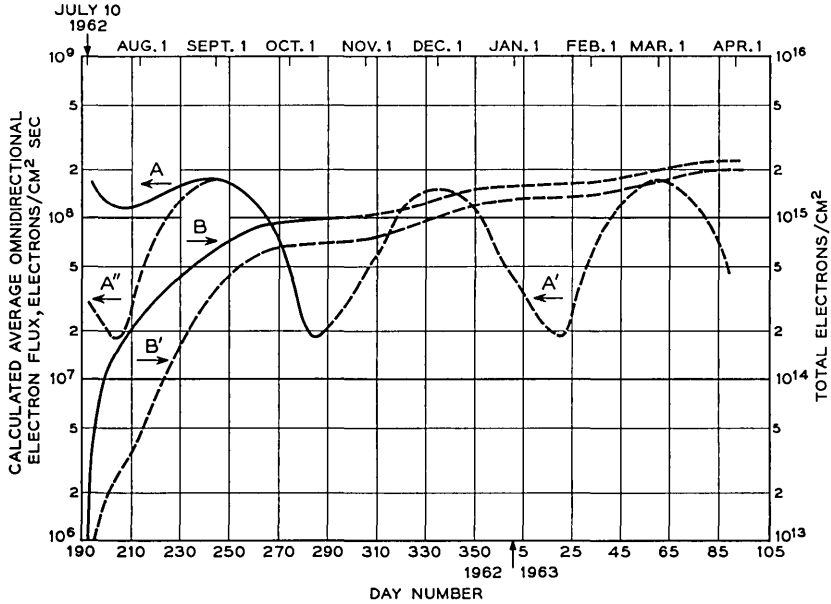
Fig. 23 — The exposure of the Telstar satellite to electrons. A fission beta-decay spectrum is assumed throughout space. The various curves are discussed in Section 2.4.2.

spectrum is everywhere that of fission fragment beta decay. The results are plotted in Fig. 23. When apogee is near the equator, the principal contribution comes from the high-intensity zone above $R = 1.7\ R_e$ and within 15 degrees of the magnetic dipole equator. When apogee is far north and south, the principal contribution comes from the higher-altitude portion of the passage through the equatorial region. In both cases, major contributions are made by regions on the high-altitude slope-off of the inner belt, where the spectrum definitely is softer than a fission spectrum, at least in later months. The total electron exposure as calculated is not substantially in error as far as electrons of 0.5 to 1 Mev are concerned. The total as plotted is probably too low to represent all electrons above 0 energy (or even 100 Kev) because of extra lower-energy electrons that are not shown in channel 3, but on the other hand it overestimates the flux of 1.5- or 2-Mev electrons if one applies to Fig. 23 the fraction of the fission beta spectrum that is appropriate to these higher energies.

The curves A and B represent the observed data from channel 3 with the assumed spectrum. From curve B we deduce that the Telstar

satellite experienced an average omnidirectional flux of 1.2×10^8 electron/cm^2 sec during its first 104 days in orbit. However, we point out that the instantaneous peak flux was 1.2×10^9 electrons/cm^2 sec and that the minimum instantaneous flux was substantially zero.

The curves A', A'', and B' make the additional assumption that the situation in mid-October prevailed between launch and March, 1963. The difference between curves A and A'' is due to those electrons which were observed to decay between July and October and hence seem certainly associated with the Starfish test. A large but still ill determined part of the remaining exposure, shown as curves A', A'' and B', is also attributable to Starfish electrons which are decaying much more slowly than those on the high-altitude side of the inner belt or in the slot between the inner and outer belts.

Substantial perturbations of the electron distribution were produced by a series of three Russian high-altitude nuclear tests on October 22, 28 and November 1. These additional electrons contributed significantly to the exposure of the satellite during late October and early November, when the exposure due to the natural electrons and those residual from Starfish, as indicated by curve A', is relatively small. However, the effects of these electrons soon after they were produced were small in comparison with the peak exposure, such as shown by curve A' for December 1. Furthermore, the Russian electrons disappeared relatively rapidly. The study of the detailed time dependence of the contributions of these three tests has not yet been completed.

2.4.3 Integrated Proton Flux

The OCR of the omnidirectional proton detectors have also been integrated. The results for protons between 26 and 34 Mev are presented in Fig. 24. Because the proton fluxes displayed so little temporal variation, the extrapolation to April, 1963, is more likely to be valid for protons than for electrons. The average OCR for this detector is 1.1×10^3 counts/cm^2 sec. The instantaneous OCR has a peak value of 1.5×10^4 counts/cm^2 sec and a minimum of zero. The curve A in this figure best displays the effect of the Brazilian anomaly. When apogee gets sufficiently far north, the orbit begins to go under the most intense region inside contour A of Fig. 17; this causes the dip in the average OCR centered at day 244. Owing to the Brazilian anomaly, the average position of the magnetic dipole equator is somewhat south of the geographic equator, and apogee does not get far enough south to make the dip pronounced on day 331. The asymmetry in the curve for the >50-
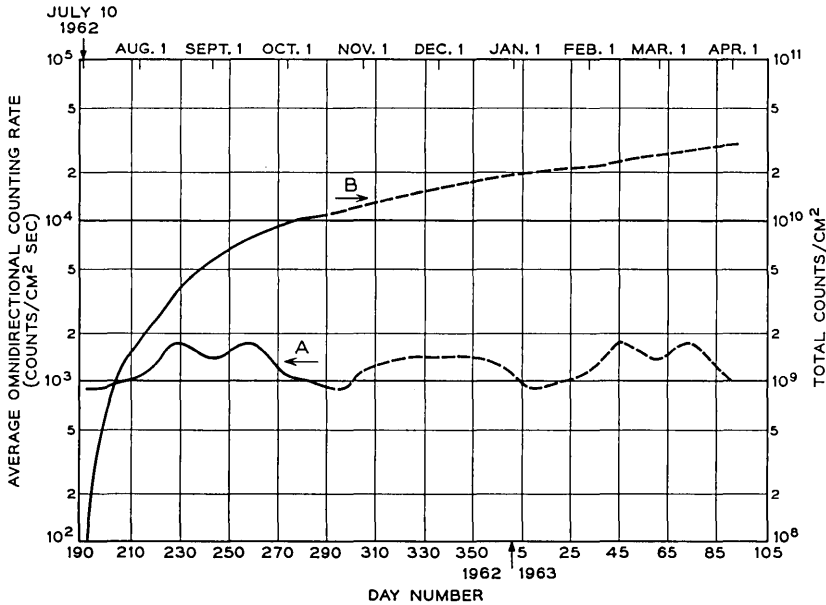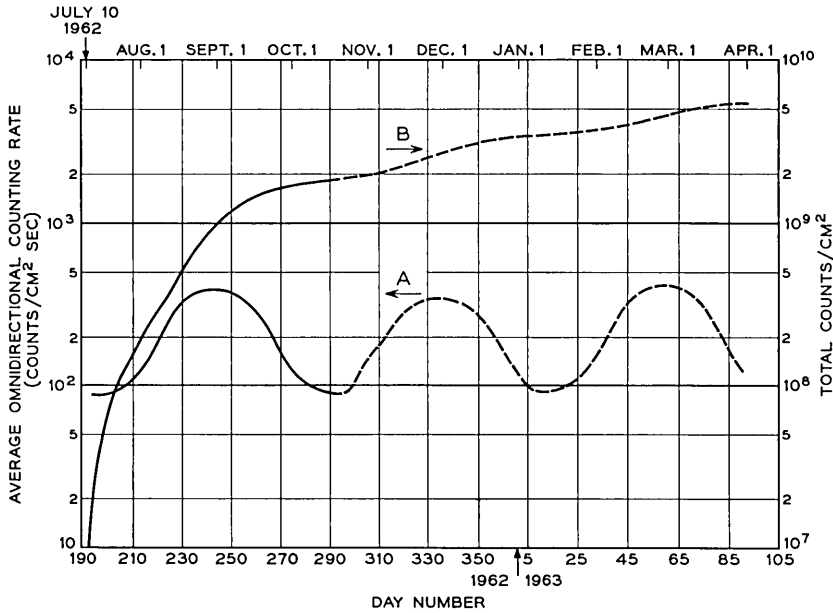
Fig. 24 — The exposure of the Telstar satellite to protons in the energy range 26 to 34 Mev. To convert to flux, multiply scales by 2.1. The curves are discussed in Section 2.4.3.

Mev proton detector is not as noticeable because here, as in the electron case, the central OCR contour extends to lower altitudes. The average OCR for protons above 50 Mev is 190 counts/cm^2 sec, as may be seen in Fig. 25. The range of observed instantaneous OCR is from 0 to 2500 counts/cm^2 sec. The conversion from OCR to flux is given in Section 2.3.

III. RADIATION DAMAGE AND SATELLITE COMPONENT EXPOSURE

The effects of radiation on the satellite fall into two broad classes. First, there are effects which arise from collisions of high-energy particles with the atoms of a solid in which sufficient energy may be transferred to create defects in the bulk of the solid. Immediately after a collision, the defects consist of vacancies where atoms are missing from normally occupied positions in the crystal and of interstitial atoms which occupy positions between the normal lattice sites. These defects are often highly mobile in the crystal and may recombine to restore the local crystal perfection or may become associated with one another or with other chemical or structural imperfections in the crystal. It is these combined

Fig. 25 — The exposure of the Telstar satellite to protons with energies above 50 Mev. To convert to flux, multiply scales by 2.6. The curves are discussed in Section 2.4.3.

centers that are in general stable at room temperature and give rise to radiation damage effects on the electrical, optical and structural properties of the material.[37,38] Such effects are produced in all solids. However, for semiconductor devices to operate, a high degree of perfection is required of semiconductor materials, and therefore radiation damage is usually much more important in semiconductor than in other solid-state materials.

The second broad class of radiation effects is produced by ionization due to high-energy charged particles. The ionization may be in the bulk of a solid and give rise to transient currents or provide electrons or holes that may be trapped at existing chemical or structural defects. The latter case is responsible for much of the coloration of transparent solids by radiation, an effect of negligible importance in the sapphire chosen for shielding the solar cells on the Telstar satellite. The ionization may cause chemical changes in organic plastics with resultant changes in their electrical and mechanical properties, and in the oil of capacitors with a resultant pressure build-up. By choice of materials, these effects have

been reduced to minor significance in the Telstar satellite. The ionization may also occur in gases, where it has been found to be of substantial importance if the gases are closely associated with semiconductor surfaces, as is often the case in encapsulated semiconductor devices. This latter effect, ionization damage to semiconductor devices, was recognized[39] and has proven to be of major importance in the performance of the satellite in space.

In this section of the paper, radiation damage (bulk effects) as observed in the semiconductor devices of the Telstar satellite will be considered in detail. The last parts of this section will discuss ionization to be expected at components in the canister of the satellite. The effects of this ionization on the component performance of the Telstar command decoder are discussed in another paper.[40]

3.1 *Measurements of Radiation Damage in the Satellite*

Radiation damage is measured directly in the solar power plant of the satellite, and in solar cells and specially fabricated transistors carried by the satellite for this experimental purpose. Solar cell results all depend upon the orientation of the sun with respect to the satellite, and thus the measurements of damage will be preceded by a description of the solar aspect determination made by the satellite.

3.1.1 *Solar Aspect*

As described in detail in a preceding paper,[1] the sun's orientation with respect to the satellite is determined by essentially simultaneous measurement of the output of six pre-irradiated silicon solar cells placed with their normals mutually perpendicular. The orientation can be described in terms of two angles: φ, the rotational angle or longitude of the sun in the coordinates of the satellite, and α, the colatitude of the sun measured with respect to the spin axis. Fig. 26 shows a sequence of measurements with the six aspect cells during an orbit on July 17, 1962. Because the spin rate of the satellite is not in general commensurate with the frame time of the telemetry, the particular cells which see the sun most directly change from frame to frame of the telemetry. In the case shown in Fig. 26, during each telemetry frame (approximately one minute), the satellite rotated by a number of complete rotations plus approximately 36 degrees. Thus, from frame to frame the readings gradually work through a sequence of rotational angles. Since the spin rate of the satellite gradually decreases (from its initial rate of approximately 180
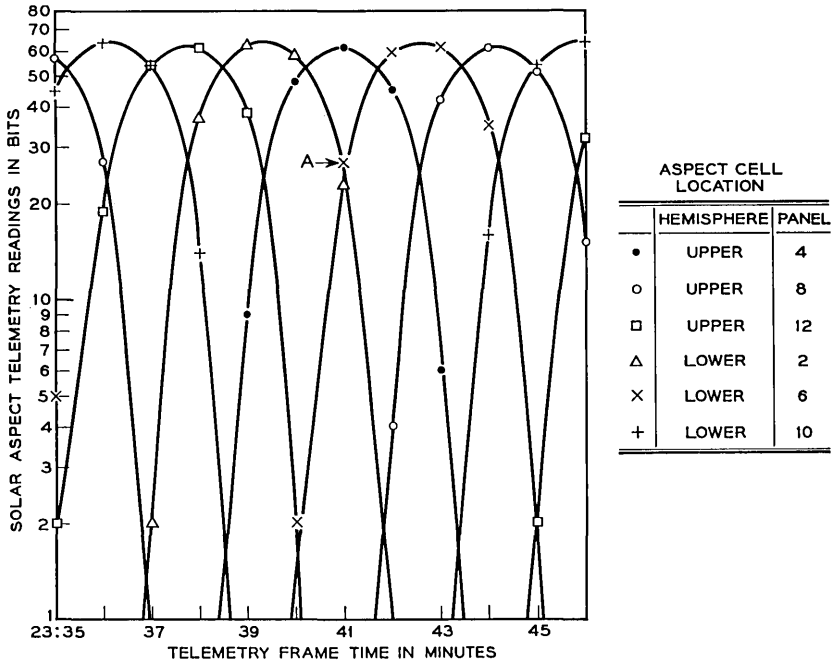
Fig. 26 — Telemetry bit readings of the six solar aspect cells on twelve successive frames of pass 70, July 17, 1962.

rpm at launch), this change in φ from frame to frame also changes. Furthermore, since this change in φ is measured at the end of a large number of complete rotations, the strobing of the solar aspect measurement gives a vernier measure on the rate of decay of the spin of the satellite. The accuracy of the measurement is limited by the accuracy of the telemetry frame time and by the accuracy of the determination of φ in a particular sequence of frames. No further discussion of this facet of the measurement will be included in the present paper.

The accuracy of the determination of the sun's position varies as the satellite rotates. At points such as A in Fig. 26, where three cells are prominently illuminated, α and φ can both readily be determined to within ±0.5 degree. The data of the figure indicate that the sun is nearly on the equator of the satellite, since the peak outputs of the cells on the upper and lower hemispheres are nearly equal. The lower-hemisphere cells are reproducibly higher, however, and when calculated from these data, α is found to be 91.5 ± 0.5 degrees, measuring from the telemetry antenna end of the satellite.
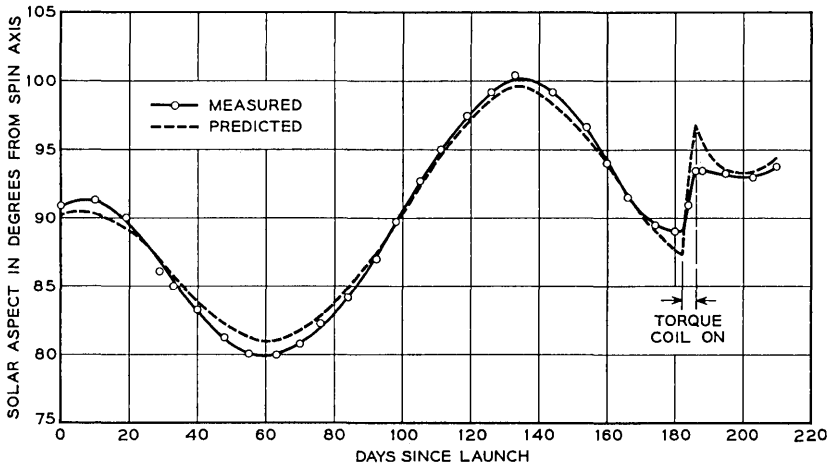
Fig. 27 — The time variation of α, the angle between the spin axis of the satellite and the satellite-sun line, from launch until February 5, 1963. The angle is measured from the telemetry antenna end of the satellite.

The history of the solar aspect of the satellite from launch to February, 1963, is shown in Fig. 27. The sun has been within ± 10 degrees of the equator at all times, a desirable position from the standpoint of temperature uniformity of the satellite and maximum capability of the solar power plant. The predicted curve illustrated here is discussed in an accompanying paper[41] dealing in more detail with satellite performance.

3.1.2 Solar Power Plant

Fig. 28 shows the output of the solar power plant of the satellite.[42] Since the distribution of solar cells is not uniform over the surface of the satellite, the telemetry reading which gives a momentary snapshot of the current from the power plant varies with φ and α. The data points of Fig. 28 have been derived from averages over a sequence of readings which, judging from the solar aspect measurements described in Section 3.1.1, represent a complete sampling over all values of φ. In cases for which the spin rate and telemetry frame rate are more nearly commensurate than in Fig. 26, a long sequence of readings will produce a cluster of points near some one or some several rotational angles. These cases have not been used in Fig. 28. Because small changes in the spin rate are reflected as large changes in φ at one-minute intervals, successive passes on the same day will exhibit quite different sampling characteristics. Data have also been selected for a particular battery voltage,
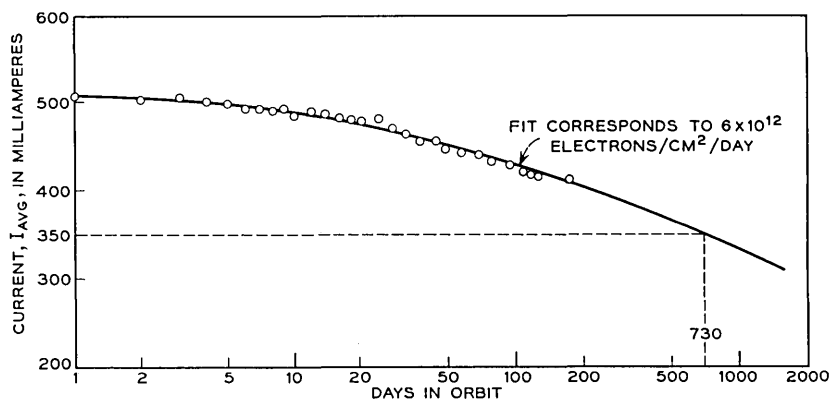
Fig. 28 — The average over the angle φ of the output current of the solar power plant from launch until February, 1963. Corrections have been made for mean solar distance. No detailed temperature corrections or corrections for solar aspect angle have been made in these data. Such corrections are expected to reduce the scatter of the points.

since the current which the power plant supplies depends on the load into which it is working. The chosen voltage corresponds to 0.36 volt/cell in the series solar-cell strings. The solar power plant current, selected in this way and averaged over φ, has been corrected for mean solar distance to give the points plotted.*

The solar power plant output will decrease due to radiation damage of silicon by energetic particles capable of penetrating the 0.3 gram/cm² sapphire shielding which covers the solar cells. The observed damage can be expressed in terms of an equivalent flux of 1-Mev electrons which would have produced this damage in the laboratory under conditions of normal incidence and zero shielding. The term "1-Mev equivalent flux" will be used for this measure of damage. The curve fitted through the points of Fig. 28 corresponds to a 1-Mev equivalent flux of 6×10^{12}/cm² day. This fitting implies that the damage flux encountered by the satellite is constant in time, in contrast to the oscillatory radiation exposure of the satellite discussed in Section 2.4. The accuracy of the solar cell data does not permit such a conclusion to be drawn, however, and the fit of Fig. 28 represents an equivalent flux averaged over 100 or more days in orbit. The choice of 6×10^{12} in this fit is at least accurate to within a factor of 1.5. The extrapolation of the curve indicates, as shown in the figure, that after two years the solar power plant will have degraded to 68 per cent of its initial performance.

* These considerations are discussed in more detail in Ref. 42.

3.1.3 *Solar Cell Damage*

Three solar cells with different shielding thicknesses were flown to measure radiation damage. Their outputs are sampled at the same time as the outputs of the solar aspect cells, Section 3.1.1, and the damage cells have the same orientation with respect to the sun as the aspect cell on panel 12 of the upper hemisphere of the satellite. Thus, no corrections for angle of illumination are required in recognizing the presence of damage. The ratio of the output currents of the damage-measuring cells to that of the pre-irradiated aspect cell on panel U-12 are shown in Fig. 29. The initial ratios are within ±2 per cent of those anticipated from laboratory calibrations of the spectral response of the cells and calculation of their performance under outer space illumination.

The currents of the initially unirradiated cells degrade with time in orbit and after a few days are ordered in accordance with their shielding thicknesses. The lack of order in the earliest days is due entirely to the slightly different initial outputs of the three individual devices. The shapes of the three curves are very similar, although there is some scatter in the data due in large measure to the approximately ±1 per cent digitizing accuracy of the telemetry. The shapes of the curves are not what would be expected from a constant particle exposure and indicate a minimum in the damage rate between approximately 70 and 110 days after launch. This corresponds reasonably well with the minima in radiation exposure shown on Figs. 23 to 25. The damage sensitivity
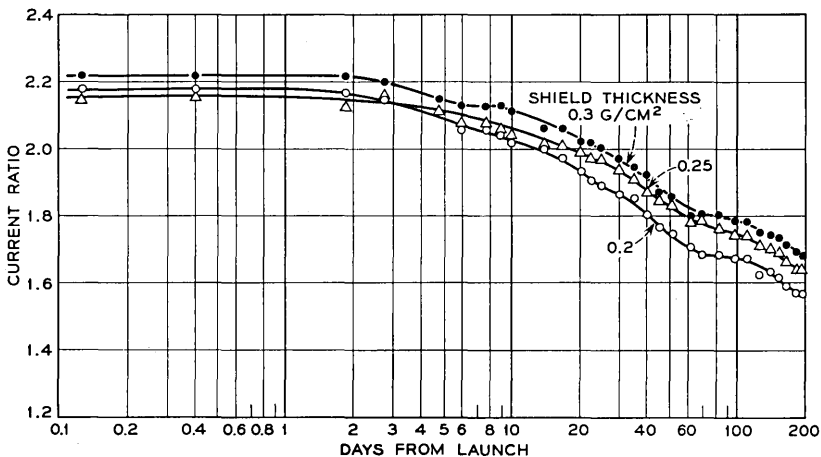
Fig. 29 — The ratios of the output currents of the radiation damage solar cells to the pre-irradiated aspect cell on satellite panel upper 12.
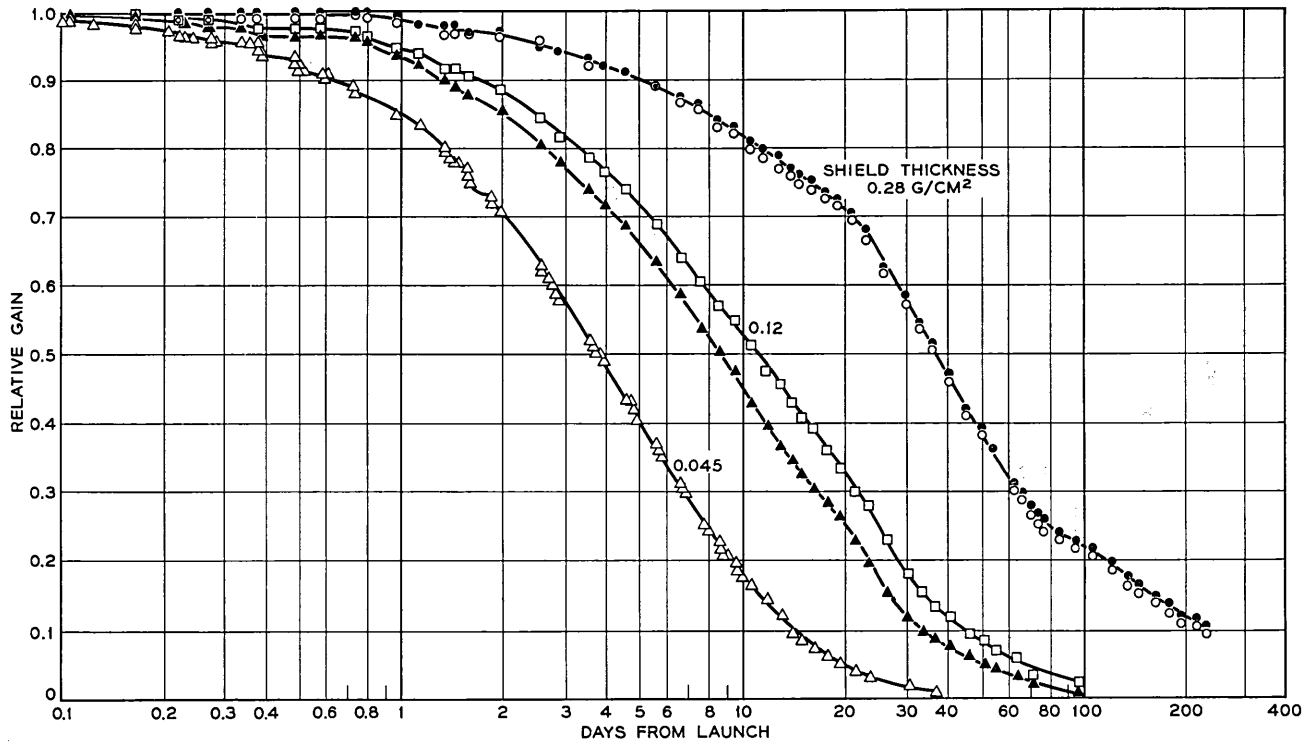
Fig. 30 — The relative gains of the radiation damage transistors as a function of time.

of the 0.20 and 0.30 gram/cm^2 shielded devices differs by approximately a factor of 2, with the 0.25 gram/cm^2 shielded cell falling between these extremes.

3.1.4 *Damage Transistors*

A group of specially fabricated n-p-n transistors with unusually wide base regions provides an independent measure of radiation damage to silicon with advantages in comparison to solar cells that light is non-essential and that sensitivity to damage is quite high. These devices are described in a previous paper.[1] The common-base current gain of these transistors is directly related to the lifetime of holes in the p-type base region and thus to the additional recombination centers added by radiation damage. This is the same property which is of major importance to damage in solar cells.

Fig. 30 shows the current gain of the transistors, normalized by their initial gain values. The initial gain ranged for this group of devices between 0.40 and 0.48, but examination of the theory indicates that a normalized gain scale retains very little sensitivity to the actual initial gain values. Five devices provide the essential data of Fig. 30, two each at two shield thicknesses and one at a third. The shield of these transistors is made up partly (and in the most lightly shielded case, totally) of the 3-mil Kovar lid of an encapsulating can and partly of additional aluminum. The thickness indicated on the curves is the aluminum shielding which would be equivalent to the sum of these, taking into account the relative mass stopping power of the two materials for protons.

All of the curves of Fig. 30 have similar S-shapes. If the devices followed a simple form of the theory, the curves should be closely related to the hyperbolic secant of the square root of the damaging flux, or if the flux is constant in time, to the square root of the abscissa of Fig. 30. This is only very roughly the case. In the 0.045 gram/cm^2 shielded device, the decrease observed during the first two days in orbit exhibits some clear downward steps. These steps are larger than those to be expected from changes of the telemetry reading by a single bit. They are associated with passages of the satellite through the inner radiation belt. The separation of the steps is a minimum of about 0.1 day, or approximately the orbital period of the satellite. Similar changes cannot be discerned beyond two days in orbit for this transistor or at any time for the more heavily shielded devices. This is a result in both cases of too low a sensitivity to detect such behavior, although it must occur. On the most heavily shielded pair of transistors there is a definite indica-

tion that the damage rate increases in the region between 25 and 70 days, decreases between 80 and 110 days, and increases again at longer times. This is suggestive of the oscillations in radiation exposure illustrated in Figs. 23 to 25. The more lightly shielded devices have been so severely degraded by these times that it is not possible to draw similar conclusions from their data. The relative damage sensitivity of the devices, as represented by their separation on the log time scale, varies only a small amount for relative gains between 0.9 and 0.2. Comparing the least and most heavily shielded devices, these ratios range from approximately 9 to 12, with the larger number being clearly too high because of the jog in the curve between 80 and 110 days. The average response of the intermediate-shielded transistors, compared with the heavily shielded pair, shows a relative sensitivity to radiation of between a factor of 3.5 and 4.5 over this same range in normalized gain. The effective damaging flux versus time could be deduced for each of the devices essentially by differentiation of the plotted curves. The data do not seem to be capable of providing this detailed a result, however, and although the variations in slope of the curves are evident as noted above, the magnitude of these variations cannot be deduced with any significant accuracy. The data have been used to specify the relative effectiveness of shielding or the relative sensitivity of differently shielded devices to radiation damage in the Telstar orbit.

3.1.5 Composite Damage vs Shielding

The results of the solar cell damage and transistor damage experiments have been combined in Fig. 31. The damage rate for the 0.30 gram/cm² shielded solar cell has been selected as unity and the other solar cells referred to it. The most heavily shielded transistors (0.28 gram/cm²) have been placed at an ordinate interpolated between the 0.30 and 0.25 gram/cm² solar cell results. The other transistors have been placed by reference to the most heavily shielded pair. The increase in damage rate with decreasing shielding in the Telstar orbit is more than a factor of 10 over the range examined. This range extends from the sapphire shield of the Telstar power plant to shielding approximately equivalent to the 6-mil glass microsheet often used in the solar power supplies of lower-altitude satellites. If very thin solar cell shields had been used on the Telstar satellite, the two-year extrapolated performance of the power plant would have been realized in about 2.5 months. Furthermore, if p-on-n rather than n-on-p solar cells had been used in the power plant, this extrapolated end-of-life power would have been reached
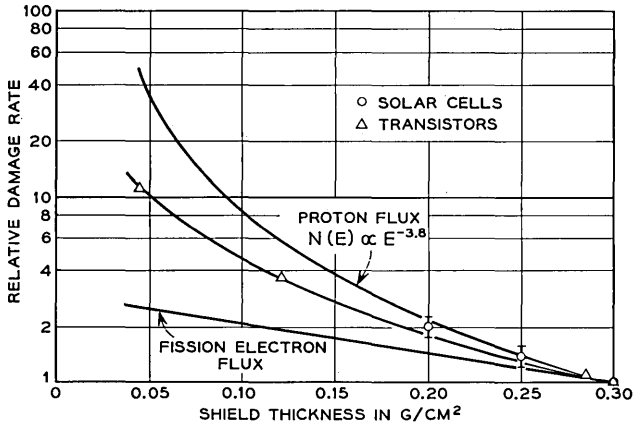
Fig. 31 — The composite results for radiation damage rate vs shielding thickness as determined from the solar cell and transistor damage experiments.

after about two or three weeks in space. The increase in damage with decrease in shielding can arise from either the proton or the electron component of the radiation environment. The two remaining curves of Fig. 31 bear on this question and will be discussed in detail in Section 3.2.3.

3.2 Correlation of Particle Exposure and Observed Damage

In this section the effects of the Van Allen belt particles on damaging n-on-p silicon solar cells will be considered, first in general and finally specifically in terms of the radiation exposure of the Telstar satellite as mapped out by its particle detectors and computed by integrating over the satellite orbit.

3.2.1 Proton Damage vs Energy and Shielding

A great deal of experimental data has been obtained on the changes in characteristics of n-on-p solar cells under bombardment by electrons and protons of different energies.[43-46] The experiments have generally been carried out with particles brought in at normal incidence to un-shielded solar cells. These data, together with an understanding of the penetration characteristics of particles through shield materials, provide the basis for constructing the equivalent damage flux in the sense of Section 3.1.2 for any particle energy distribution and shielding con-figuration of a solar cell array.
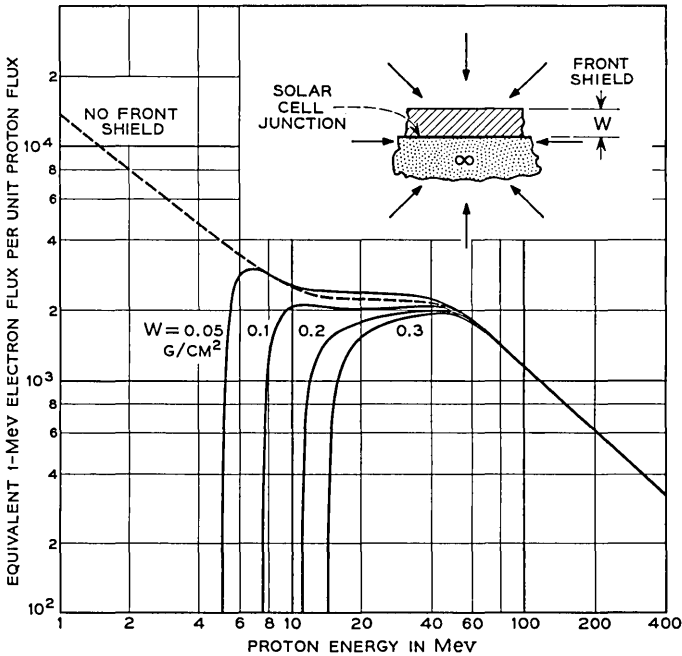
Fig. 32 — The damage-equivalent 1-Mev electron flux as a function of the energy of a monoenergetic isotropic flux of protons incident on n-on-p solar cells with various front shielding. The back shield is assumed to be infinitely thick.

Fig. 32 shows the 1-Mev electron flux equivalent in damage to a monoenergetic isotropic proton flux at different energies and for different shielding thicknesses. The curve for "no front shield" is a smooth curve with a shape determined by data obtained at four different proton particle accelerators and at seventeen different energies over the energy range between 1.4 and 135 Mev. It has been extrapolated with only minor uncertainty at both ends, although particles in the extrapolated extremes have a negligible effect on damage in the Telstar satellite case. The absolute ordinate scale for this curve differs from the data by exactly a factor of 2. As noted in the inset to the figure, the incident flux is assumed to be omnidirectional and uniform, and in all cases the solar cell is considered to have effectively infinite shielding on the back. This represents the actual situation in the Telstar solar power plant quite well. In this case, only one-half of all the protons in the incident flux can reach the solar cell, hence the factor of 2. The simplicity of this factor involves another approximation. Particles arriving at non-normal

incidence have longer paths in the solar cell and as a result create proportionately more defects in the radiation-sensitive thickness of the device. This introduces a $1/\cos \theta$ factor, where θ is the angle of particle incidence, which just cancels the $\cos \theta$ factor that reduces the proton flux because of the change in projected area of the device at an angle θ. As long as the sensitive thickness, t, is small enough so that $t/\cos \theta$ is small compared with the proton range, this approximation is good. At very low proton energies and at large angles of incidence, however, this approximation breaks down. For the sensitive thickness of the n-on-p solar cells used in the Telstar power plant, this approximation begins to be poor below about 5 Mev. One final reservation needs to be made concerning these data. The solar cell property that is being affected by the radiation damage in these experiments is the diffusion length for electrons in the p-type silicon base of the solar cell. This property controls the efficiency with which hole-electron pairs created by light in the base material can reach the p-n junction and contribute current to an external load.[44] This property change exhibits itself directly in a decrease in the short-circuit current of solar cells as a result of radiation. This effect is the primary cause of degradation in solar cell performance in the Telstar satellite. It is not, however, the only effect that occurs. There is a change in junction impedance that shows up as a decrease in open-circuit voltage, and there is a change in the temperature coefficient of the solar cell because of the introduction of new recombination centers. Although these are of minor importance in the Telstar case, they are not always of minor importance for other solar power plant designs. In particular, recent experiments have shown very severe damage to the junction impedance by very low energy, <1-Mev protons.[46] For unshielded solar power plants and possibly for very lightly shielded cases as well, this effect could be of major significance. Furthermore, if the power plant has not been designed for maximum power after radiation damage, including the modified temperature coefficient of the solar cells, the particular operating point may emphasize the changes in junction voltage.[42]

The shape of the basic proton energy dependence of damage, as illustrated by the upper curve of Fig. 32, is still not quantitatively understood. The straight line portions at low and high energies have slopes that agree very well with the theory of atomic displacements[47] by heavy charged particles. The offset in these two line segments, produced by the nearly energy-independent portion between about 10 and 40 Mev is, however, still a subject of discussion.[45,48,49] The same energy dependence, but with a difference in absolute magnitude, is also found for

proton damage in p-on-n solar cells. The shape seems most likely to be determined by details of the short-range interaction of energetic protons with atoms of the silicon lattice.

Starting with the upper curve of Fig. 32, the other curves in the figure have been generated by machine computation, taking into account the penetration properties of protons. For each shield thickness, the equivalent damage flux rises sharply with increasing proton energy as the protons are capable of penetrating the shield. The curves then join with the unshielded curve at higher energies. One might expect that because lower-energy protons are more damaging, the introduction of shielding, which would reduce the proton energy for those protons capable of penetrating the shield, might increase rather than decrease the damage. However, because the protons are incident over all angles, the very severe limitation of the solid angle available to protons that go through the shield and have a small residual energy reduces what must be a real effect to relative unimportance. The effect does appear as a small crossing of the equivalent flux curves for the unshielded and most lightly shielded cases. The Telstar radiation damage experiments discussed in Section 3.1 covered just the range of shields illustrated in Fig. 32. The main solar power plant with 0.3 gram/cm² sapphire shielding is sensitive only to protons of more than 15 Mev. The most lightly shielded damage transistors respond to protons of more than 5 Mev. Because the damage per particle is high at lower energy, and because there are more protons in the Telstar orbit with lower energies, a reduction in shielding is expected to effect a large increase in damage.

3.2.2 Electron Damage vs Energy and Shielding

Fig. 33 shows a set of curves for electron damage having the same significance as those for protons of Fig. 32. These curves are based on measurements made of damage at different angles of incidence and thickness of shielding with electrons up to 3 Mev.[50] The uniformity in variation of the results with the extrapolated range of electrons has permitted extension of the shielding calculations to higher energies. In all cases the damage increases with increasing electron energy in contrast to the decrease with increasing proton energy. For the "no front shield" curve, the rapid fall-off below 1 Mev reflects the fact that electrons are relatively inefficient in moving atoms in the silicon crystal to produce damaging defects and at low energies become nearly incapable of transferring enough energy to the atoms for them to be displaced. The shape of the curve is very roughly in accord with theoretical expectation below
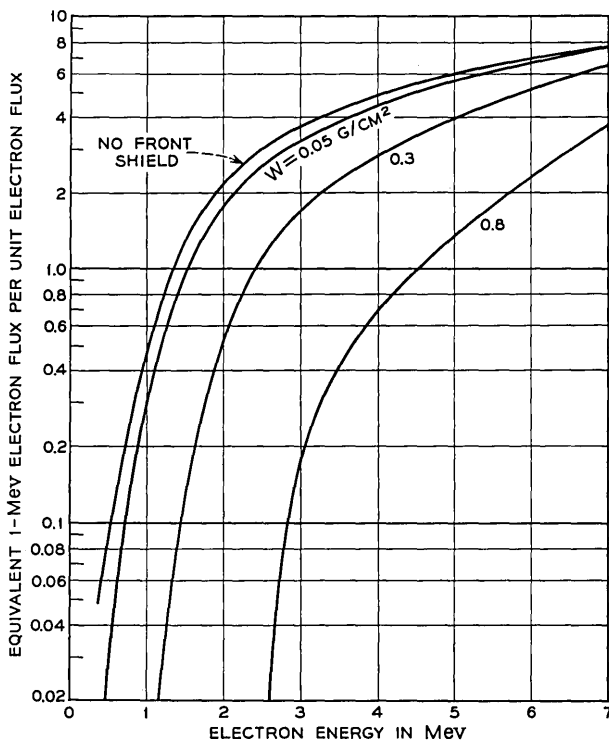
Fig. 33 — The damage-equivalent 1-Mev electron flux as a function of the energy of a monoenergetic isotropic flux of electrons incident on n-on-p solar cells with various front shielding. The back shield is assumed to be infinitely thick.

1 Mev. Above 1 Mev the simple theory of atomic displacement predicts that the curve should flatten out without much further increase at higher energies.[47] The experimental data from which the curve was drawn, however, show more than a factor of 10 increase between 1 and 7 Mev.* The situation for p-on-n solar cell damage is quite different in this respect, the increase above 1 Mev being much more nearly in accord with the simple theory. Apparently the high damage efficiency for high-energy electrons in p-type silicon is due to the formation of a different type of damage defect in the crystal which is very efficient as a recombination center. It is plausible that this new defect is a divacancy.[52]

The equivalent 1-Mev damage flux for 1-Mev electrons is 0.5 in Fig.

_____

* The data above 3 Mev for no front shield are due to J. M. Denney and R. G. Downing, Ref. 51.

33 because of rejection of half of the electrons in an omnidirectional flux by the assumed infinite back shielding. There is an additional effect of reflection of electrons (back scattering) from the surface of the silicon for high angles of incidence that tends to reduce the value to less than 0.5, but this effect is quite small. The Telstar solar power plant, with 0.3 gram/cm² shielding, begins to be severely damaged by electrons in the 1- to 2-Mev region, while transistors shielded by 0.045 gram/cm² are similarly damaged by electrons of 0.5 to 1.0 Mev energy. Even for these lightest shields, electrons below 0.5 Mev become rapidly insignificant.

3.2.3 *Composite Damage from the Satellite Exposure*

Two factors in the Telstar radiation damage results will be considered in this section: first the damage vs shielding thickness of Fig. 31, and second the absolute magnitude of the damage to the solar power plant as described in Section 3.1.2. It is evident from the curves of Figs. 32 and 33 that the energy spectra of the protons and electrons encountered by the satellite are of enormous importance in both of these respects.

The proton spectrum varies with position in space as discussed in Section 2.3.2, and this spectrum change could have been included in carrying out the initial orbital integrals. However, from the 100-day average exposure of the 26 to 34 Mev protons, Fig. 24, and the >50-Mev protons, Fig. 25, we have instead deduced an average spectrum for the exposure. This average spectrum has the same significance as the spectrum derived for any single point in space. It is characterized by (1) in Section 2.3.2 with $n = 3.8$, a value which is intermediate between the $n \approx 2$ for the heart of the inner belt and $n \approx 4.5$ for the outer side of the inner belt. The average spectrum has been derived over approximately half a period of the precession of the line of apsides, Fig. 20; and since the proton flux is essentially constant in time, the average should reflect the situation for longer times as well.

The spectrum above has been folded through the curves of Fig. 32 to obtain the dependence of the proton damage on shielding thickness. The result is the upper curve of Fig. 31, which has been normalized to the 0.3 gram/cm² point. This curve asserts that if the damage at 0.3 gram/cm² shielding is due entirely to protons, then the damage should increase at thinner shields as shown. The actual observations lie everywhere below this computed curve, suggesting tentatively that protons may not be responsible for all the damage at 0.3 gram/cm². Because of the extrapolation involved in including protons as low as 5 Mev in energy, the calculation for lower shield thicknesses becomes increasingly

uncertain. However, from an as yet incomplete analysis of Telstar and Explorer XV low-energy proton data, the 5-Mev proton exposure derived from the average spectrum seems to be correct to within approximately a factor of 2.

Because of the very important contribution of high-energy electrons to the damage and the inability of the Telstar electron detector to specify their spectrum above 1 Mev, the electron case is more difficult. There is no doubt that a substantial part of the Telstar electron exposure came from regions where the electron spectrum was characteristic of fission beta decay (Section 2.2.2). However, a substantial part of its exposure also came from regions in which there is little doubt that the spectrum contained a smaller fraction of high-energy electrons than the fission spectrum. For lack of more complete knowledge, we have assumed the spectrum is fission-like throughout and recognize that this over-estimates the high-energy part of the average electron spectrum. Folding this spectrum through the curve of Fig. 33, the lowest curve of Fig. 31 is obtained. This curve is fitted, as in the proton case above, at the 0.3 gram/cm^2 point under the assumption that at that point all the damage is due to electrons with a fission spectrum. In this case the calculation falls everywhere below the observations. The calculated curve is relatively flat because fission electrons are so energetic. The electron spectrum could, of course, be adjusted to fit the actual observations by adding electrons between 0.5 and 1.0 Mev. However, this is the energy range in which the Telstar electron detector is measuring the flux of particles, and there are altogether too few electrons under the assumption of such a soft spectrum to allow electrons to contribute in a major way to the damage at any thickness of shielding.

The fact that the observations fall between the electron and proton predictions suggests that the actual situation contains important contributions from both types of particles. A half-and-half sharing of the damage at 0.3 gram/cm^2 nearly accounts for the points at lesser shielding. For the thinnest shield, such a computation gives a result a factor of approximately 2 above the point; however, this is the region in which the proton damage is subject to an uncertainty of about this magnitude.

Using the same spectral assumptions discussed above and the computed average of the particle exposure of the satellite, Figs. 23 to 25, the absolute damage to be expected in the solar power plant can be obtained. The damage from the proton exposure averaged over 100 days in orbit is found to be equivalent to that which would be produced by 3×10^{12} 1-Mev electrons/cm^2 day at normal incidence on bare n-on-p solar cells. A similar calculation for electrons gives the same results, although in this case the spectral assumption is such as to overestimate
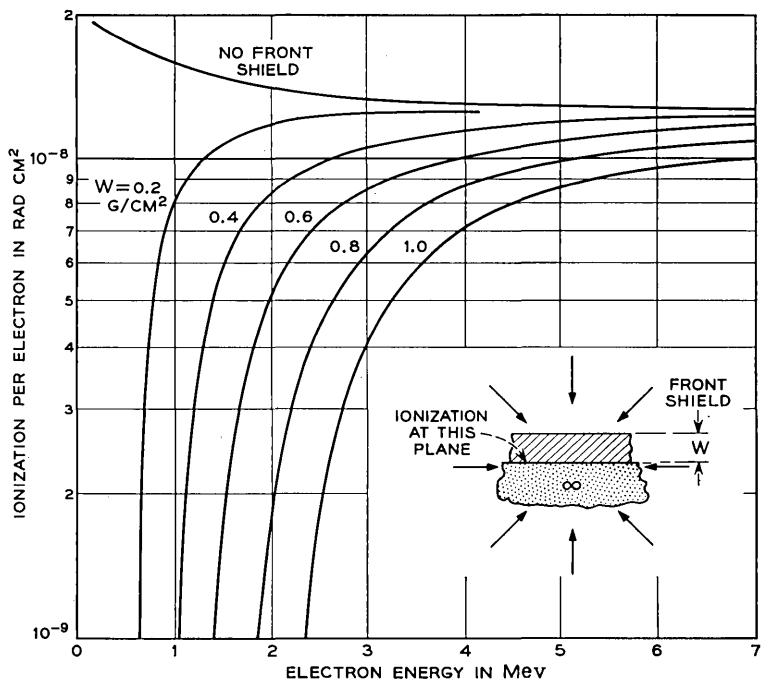
Fig. 34 — Ionization produced by a monoenergetic isotropic flux of electrons behind various thicknesses of front shielding. The back shield is assumed to be infinitely thick.
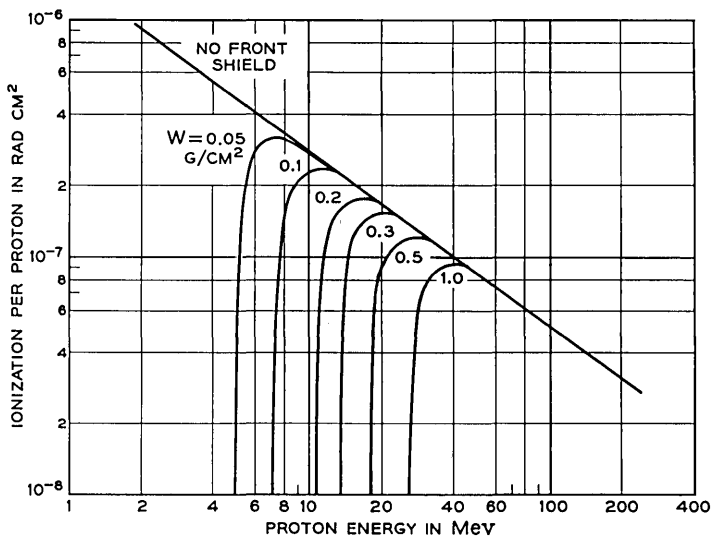

Fig. 35 — Ionization produced by a monoenergetic isotropic flux of protons behind various thicknessess of front shielding. The back shield is assumed to be infinitely thick.

the electron damage. To the accuracy with which this calculation has presently been carried out, it is possible to account for the observed damage by an equivalent 1-Mev electron flux of $6 \times 10^{12}/cm^2$ day, half of which is produced by protons and half by electrons. This composite also provides a satisfactory fit to the dependence of damage on shielding thickness. The electron contribution in this calculation is higher than that quoted in an earlier paper[18] because recently measured damage by high-energy electrons to n-on-p solar cells is considerably greater than had been anticipated from measurements at lower energies which were used in the earlier computation.

3.3 *Radiation of Circuit Components in the Satellite Canister*

The calculation of the radiation exposure of the satellite has made it possible to explain the changes in characteristics that have been observed in the silicon solar cells and the closely related damage transistors. In this section we will examine the exposure from the standpoint of the ionization (rather than the bulk semiconductor damage) it produces under different thicknesses of shielding. The results are applicable, for example, to ionization damage in the transistors of the Telstar command decoder.

3.3.1 *Ionization Due to Electrons and Protons*

Fig. 34 shows the ionization as a function of electron energy in an isotropic monoenergetic electron flux. The geometry of the case considered is indicated in the inset to the figure. A typical point on this set of curves is to be interpreted as follows. In an omnidirectional flux of 10^7 2-Mev electrons/cm^2 sec incident on a semi-infinite slab of material, the ionization level would be $5 \times 10^{-9} \times 10^7$ rads/sec or 1.8×10^2 rads/hr at a depth of 0.6 gram/cm^2.

Fig. 35 shows a similar set of curves for protons. There is more ionization per particle in this case because the protons are not minimum-ionizing. Beyond the right-hand extreme of the proton curves, the ionization converges to the same value per particle as for the electrons, the protons now being relativistic in velocity and minimum-ionizing in their interaction with materials.

3.3.2 *Composite Ionization from the Integrated Satellite Exposure*

With the same average particle spectra as used in Section 3.2.3 to compute the radiation damage to solar cells, the ionization due to elec-
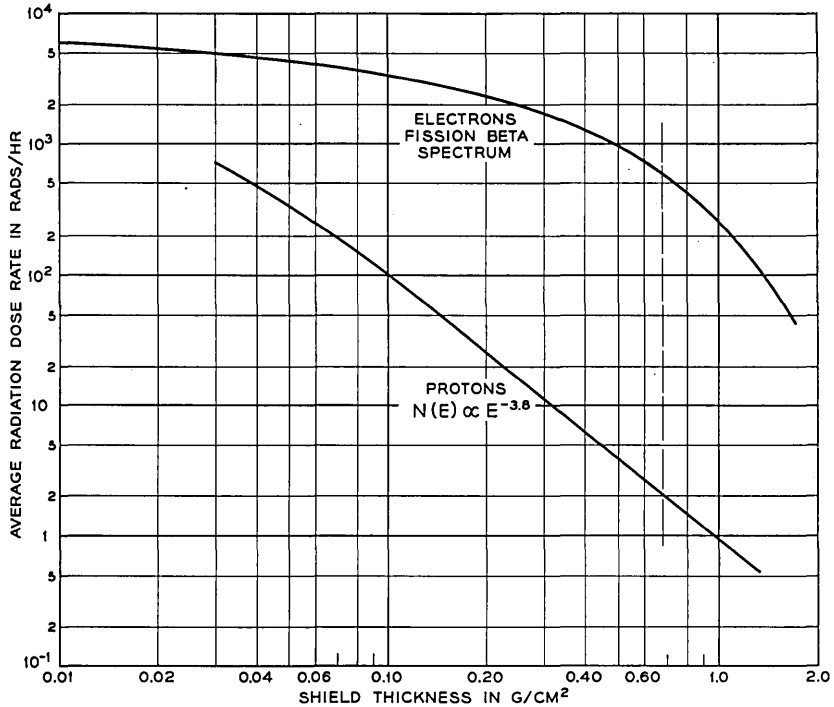
Fig. 36 — Average radiation dose rate vs shielding thickness for the average proton and electron exposure of the satellite.

trons and protons has been derived from the curves of Figs. 34 and 35. The results are shown in Fig. 36. At a shielding thickness of 0.68 gram/ cm² (0.1 inch of aluminum, the approximate location of the Telstar decoder transistors) only protons of >20 Mev and electrons of >1.5 Mev are important. At this thickness the electron contribution to the radiation is about 600 rads/hr compared with 2 rads/hr from the protons. The proton-produced intensity is nearly what had been expected before launch, but the more than two orders of magnitude additional ionization contributed by the penetrating electrons were totally unexpected and were responsible for the failure of the Telstar command decoder.[40]

IV. ACKNOWLEDGMENT

We are deeply appreciative of the efforts of many people who have contributed greatly to this work. In particular we are grateful to Miss

E. M. Engert, who had a major role in the data reduction; Mrs. M. F. Robbins, who wrote many of the plot programs; R. L. Stickle, who decommutated the telemetry data, and Mrs. P. L. Gibbs, who edited it; L. C. Thomas, who supplied the satellite spin axis orientation and most of the ephemeris, and F. T. Geyling and G. J. Miron, who supplied the remainder; D. B. Cuttriss, who reduced the solar power plant data; D. W. Hill, who organized the program for reduction of solar aspect data; and L. V. Medford, who carried out this reduction as well as that for the radiation damage solar cells and transistors.

We especially acknowledge the participation of the NASA worldwide tracking network which recorded more than half of the telemetry acquired from the Telstar satellite.

REFERENCES

1. Brown, W. L., Buck, T. M., Medford, L. V., Thomas, E. W., Gummel, H. K., Miller, G. L., and Smits, F. M. The Spacecraft Radiation Experiment, B.S.T.J., this issue, p. 899.
2. Welch, J. A., Jr., and Whitaker, W. A., Theory of Geomagnetically Trapped Electrons from an Artificial Source, J. Geophys. Res., 64, 1959, p. 909.
3. Northrop, T. G., and Teller, E., Stability of the Adiabatic Motion of Charged Particles in the Earth's Field, Phys. Rev., 117, 1960, p. 215.
4. Northrop, T. G., The Guiding Center Approximation to Charged Particle Motion, Ann. Phys., 15, 1961, p. 79, and references therein.
5. Hess, W. N., Canfield, E. H., and Lingenfelter, R. E., Cosmic Ray Neutron Demography, J. Geophys. Res., 66, 1961, p. 665.
6. Dessler, A. J., and Karplus, R., Some Properties of the Van Allen Radiation, Phys. Rev. Letters, 4, 1960, p. 271.
7. Walt, M., and MacDonald, W. M., Diffusion of Electrons in the Van Allen Radiation Belt, J. Geophys. Res., 67, 1962, p. 5013.
8. Welch, J. A., Jr., Kaufmann, R. L., and Hess, W. N., Trapped Electron Time Histories for $L = 1.18$ to $L = 1.30$, J. Geophys. Res., 68, 1963, p. 685.
9. Ray, E. C., On the Theory of Protons Trapped in the Earth's Magnetic Field, J. Geophys. Res., 65, 1960, p. 1125.
10. Lenchek, A. M., and Singer, S. F., Geomagnetically Trapped Protons from Cosmic-Ray Albedo Neutrons, J. Geophys. Res., 67, 1962, p. 1263.
11. Pizzella, G., McIlwain, C. E., and Van Allen, J. A., Time Variations of Intensity in the Earth's Inner Radiation Zone, October 1959 through December 1960, J. Geophys. Res., 67, 1962, p. 1235.
12. Kaufmann, R., Experimental Tests for the Acceleration of Trapped Particles, J. Geophys. Res., 68, 1963, p. 371.
13. O'Brien, B. J., A Large Diurnal Variation of the Geomagnetically Trapped Radiation, J. Geophys. Res., 68, 1963, p. 989.
14. O'Brien, B. J., Direct Observations of Dumping of Electrons at 1000 Kilometer Altitude and High Latitudes, J. Geophys. Res., 67, 1962, p. 1227.
15. McIlwain, C. E., Coordinates for Mapping the Distribution of Magnetically Trapped Particles, J. Geophys. Res., 66, 1961, p. 3681.
16. McIlwain, C. E., private communication, June, 1962.
17. Chapman, R. C., Jr., Critchlow, G. F., and Mann, H., Command and Telemetry Systems, B.S.T.J., this issue, p. 1027.
18. Brown, W. L., and Gabbe, J. D., The Electron Distribution in the Earth's Radiation Belts during July 1962 as Measured by Telstar, J. Geophys. Res., 68, 1963, p. 607.
19. Carter, R. E., Reines, F., Wagner, J. J., and Wyman, M. E., Free Antineutrino

Absorption Cross Section, Expected Cross Section from Measurements of Fission Fragment Electron Spectrum, Phys. Rev., **113**, 1959, p. 280.

20. Van Allen, J. A., Frank, L. A., and O'Brien, B. J., Satellite Observations of the Artificial Radiation Belt of July 1962, J. Geophys. Res., **68**, 1963, p. 619.

21. Van Allen, J. A., Absolute Intensity, Spatial Distribution and Time Decay of Intensities of Artificially Injected Electrons Based on Observations with Injun I, Explorer XIV, Injun 3, and DOD Satellites, Program of the 44th Annual Meeting of the American Geophysical Union (April 17, 1963), p. 76.

22. Brown, W. L., Hess, W. N., and Van Allen, J. A., Collected Papers on the Artificial Radiation Belt from the July 9, 1962 Nuclear Detonation. Introduction, J. Geophys. Res., **68**, 1963, p. 605.

23. McIlwain, C. E., Trapped Electron-Proton Intensities as Functions of Energy, B, L, and Time, Program of the 44th Annual Meeting of the American Geophysical Union (April 17, 1963), p. 76.

24. Brown, W. L., Trapped Particle Population from Telstar and Explorer XV Observations, Program of the 44th Annual Meeting of the American Geophysical Union (April 17, 1963), p. 76.

25. Hess, W. N., Injection and Loss Problems, Program of the 44th Annual Meeting of the American Geophysical Union (April 17, 1963), p. 76.

26. Whitaker, W. A., private communication, April 1963.

27. Pieper, G. F., Williams, D. J., and Frank, L. A., TRAAC Observations of the Artificial Radiation Belt from the July 9, 1962 Nuclear Detonation, J. Geophys. Res., **68**, 1963, p. 635.

28. West, H. I., Jr., Mann, L. G., and Bloom, S. D., Spectra and Fluxes of Electrons Trapped in the Earth's Magnetic Field Following Recent High-Altitude Nuclear Bursts, Program of the 44th Annual Meeting of the American Geophysical Union (April 17, 1963), p. 77.

29. Giacconi, R., Paolini, F. R., and Katz, L., Measurements of Trapped Particles Injected by Nuclear Detonations, Program of the 44th Annual Meeting of the American Geophysical Union (April 17, 1963), p. 77.

30. White, R. S., Freden, S. C., Mihalov, J. D., Mozer, F. S., and Paulikas, G. A., The Artificial Radiation Belts at Low Altitudes, Program of the 44th Annual Meeting of the American Geophysical Union (April 17, 1963), p. 77.

31. Smith, R., Electron Flux Measurements from DOD Satellites During the Period July to November 1962, Program of the 44th Annual Meeting of the American Geophysical Union (April 17, 1963), p. 76.

32. Van Allen, J. A., The Geomagnetically Trapped Corpuscular Radiation, J. Geophys. Res., **64**, 1959, p. 1683.

33. McIlwain, C. E., and Pizzella, G., On the Energy Spectrum of Protons Trapped in the Earth's Inner Van Allen Zone, J. Geophys. Res., **68**, 1963, p. 1811.

34. Davis, L. R., and Williamson, J. M., *Low Energy Trapped Protons*, Space Research, vol. III, edited by W. Priester, Interscience Publishers, Inc., New York, 1963.

35. Freden, S. C., and White, R. S., Particle Fluxes in the Inner Radiation Belt, J. Geophys. Res., **65**, 1960, p. 1377.

36. Naugle, J. E., and Kniffen, D. A., Flux and Energy Spectra of the Protons in the Inner Van Allen Belt, Phys. Rev. Letters, **7**, 1961, p. 3.

37. Conference on Radiation Effects in Semiconductors, J. Appl. Phys. **30**, 1959, p. 1117.

38. Watkins, G. D., and Corbett, J. W., Electron Paramagnetic Resonance of Defects in Irradiated Silicon, Disc. Faraday Soc., **31**, 1961, p. 86.

39. Peck, D. S., Blair, R. R., Brown, W. L., and Smits, F. M., Surface Effects of Radiation on Transistors, B.S.T.J. **42**, January, 1963, p. 95.

40. Mayo, J. S., Mann, H., Witt, F. J., Peck, D. S., Gummel, H. K., and Brown, W. L., The Command System Malfunction of the *Telstar* Satellite, B.S.T.J., this issue, p. 1631.

41. Hutchison, P. T., and Swift, R. A., Results of the *Telstar* Space Experiment, B.S.T.J., this issue, p. 1475.

42. Smith, K. D., Gummel, H. K., Bode, J. D., Cuttriss, D. B., Nielsen, R. J., and Rosenzweig, W., The Solar Power Plant, B.S.T.J., this issue, part 3.

43. Loferski, J. J., and Rappaport, P., The Effect of Radiation on Silicon Solar Energy Converters, RCA Review, **19**, 1958, p. 536.
44. Rosenzweig, W., Gummel, H. K., and Smits, F. M., Solar Cell Degradation under 1-Mev Electron Bombardment, B.S.T.J., **42**, March, 1963, p. 399.
45. Rosenzweig, W., Smits, F. M., and Brown, W. L., Energy Dependence of Proton Irradiation Damage in Silicon, Bull. Am. Phys. Soc., Series II, **7**, 1962.
46. Lodi, E. A., and Crowther, D. L., Some New Results from Low Energy Proton Irradiation of Silicon, Appl. Phys. Letters, **2**, 1963, p. 22.
47. Seitz, T., and Koehler, J. S., *Displacement of Atoms During Irradiation*, Solid State Physics, vol. 2, Academic Press, 1956.
48. Baicker, J. A., Flicker, H., and Vilms, J., Proton Induced Displacement in Silicon, Appl. Phys. Letters, **2**, 1963, p. 104.
49. Denney, J. M., and Downing, R. G., private communication, May, 1962.
50. Rosenzweig, W., Augustyniak, W. M., and Wright, K. A., to be published.
51. Denney, J. M., and Downing, R. G., IEEE-AIAA Photovoltaic Specialists Conference, April 1963.
52. Bemski, G., Szymanski, B., and Wright, K. A., A New Paramagnetic Center in Electron Irradiated Silicon, J. Phys. Chem. Solids, **24**, 1963, p. 1.
53. Heppner, J. P., *The World Magnetic Survey*, Space Science Reviews, D. Reidel Publishing Company, Dordrecht, to be published.

Results of the *Telstar* System Communications Tests

By R. W. HATCH, S. B. BENNETT and J. P. KINZER

(Manuscript received February 29, 1963)

The results of the communications tests on the Telstar satellite system which have been conducted at the Andover earth station are presented. These tests have included successful transmissions of telephone, television, and data signals. In addition, measurements of received carrier power, noise, transmission characteristics, linearity, data system errors, absolute delay, and Doppler shift have been made. The results are in good agreement with the expected performance.

I. INTRODUCTION

Since the launch of the Telstar satellite on July 10, 1962, a large number of communications tests have been conducted at the A.T.&T. earth station at Andover, Maine. These tests have consisted of numerous successful transmissions of monochrome and color television signals, two-way telephone signals, and a variety of data signals. In addition, communications test signals of many types have been transmitted. Most of the television and telephone transmission tests have been conducted between the Andover station and the British Post Office (GPO) and French National Center for Telecommunications Studies (CNET) stations. These stations are respectively located at Goonhilly Downs, England and Pleumeur-Bodou, France. In addition, a number of one-way transmissions were made from the Andover station to the Bell Telephone Laboratories station at Holmdel, New Jersey, described in a companion paper.[1] Communications tests, most of which have been made on a loop basis to the satellite and back to the Andover station, have included measurements of received carrier power, noise, transmission gain and stability, system linearity, data system errors, absolute delay and Doppler shift. A large amount of valuable data has already been obtained; and, as this is written, system tests continue. This paper summarizes the more significant communication test results, most of which have been gathered during the period from July to November, 1962.

Although the companion papers provide detailed descriptions of the various subsystems which make up the Andover-Telstar communications system, it seems advisable to devote a small portion of this paper to a short over-all description. This has been provided in Section II, which also includes a communications system block diagram that will be useful in understanding and interpreting the test results to which most of this paper is devoted.

Section III provides a brief summary of the modulation methods, baseband signals, and the frequency allocation used for both the one-way and two-way tests.

Section IV is devoted to a description of the experiment plan. This section includes a list of the principal experiments which have been conducted and are herein reported. As such it serves as a table of contents for the remainder of the paper, which is devoted almost completely to documentation of test results.

II. COMMUNICATIONS SYSTEM

An over-all block diagram of the Andover communications system is shown in Fig. 1. The major part of the communications equipment, including the ground transmitter and ground receiver, is located on the horn antenna structure. A video transmission system interconnects this communications equipment and the test area, which is located in the control building 1600 feet away. Most of the communications test equipment is located in the test area. The Andover station is connected to the Bell System network via a microwave radio system from Boston which also terminates at the test area.

The over-all layout permits a large amount of flexibility in the way tests are conducted, as indicated in Fig. 1. Most of the tests described in this paper are RF loop tests. In this case, the communications path is from the test area, through the ground transmitter to the satellite, back through the ground receiver, finally terminating in the test area. Transmission to the satellite and back can also be simulated by transmitting to a boresight repeater located on Black Mountain about 4.5 miles from the ground station. This repeater is a bay-mounted duplicate of the Telstar communications repeater and uses waveguide feeds to small tower-mounted horn antennas. Adjustable attenuators are provided in the feeds so that the received power at both the repeater and ground receiver can be adjusted to simulate those in the actual satellite system.

In addition to these two RF loops, provision is also made for IF and baseband loops as shown. In this paper those test results which were
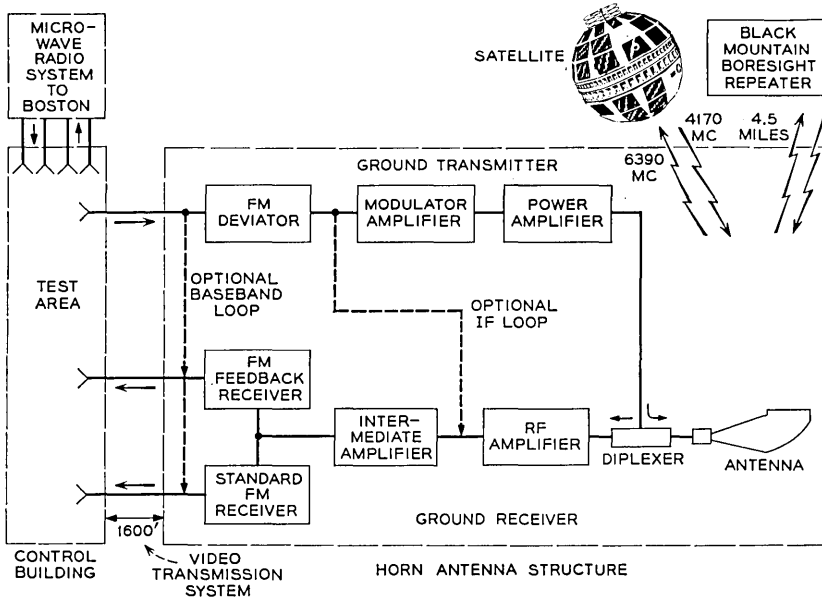
Fig. 1 — Telstar communications system.

taken on loops which do not include the Telstar satellite are identified as boresight, IF, or baseband loop test results.

The baseband transmission characteristic for a loop from the test area to the satellite and back depends on which FM receiver is used. As some of the later data will show, the transmission is essentially flat to well beyond 5 mc with the standard receiver and is flat to about 3 mc with the FM feedback receiver. Additional design and performance information for the individual parts of the communications system are included in the various companion papers.

III. MODULATION METHODS AND BASEBAND SIGNALS

Many of the test signals can be applied directly at baseband in the test area and similarly measured there. Typical examples are baseband transmission measurements such as gain-frequency characteristics and baseband noise spectra. However, other signals such as the combined video and audio signals for television transmission and the frequency-multiplexed telephone signal require additional equipment. In this section the special arrangements used for these signals will be described.

Fig. 2 is a simplified block diagram showing the optional patching arrangements for television and two-way message transmission. For television transmission, the audio signal is applied to the transmitting diplexer, which frequency-modulates the audio signal onto a 4.5-mc subcarrier. The video signal is band-limited by a 2-mc low-pass (roll-off) filter and combined with the 4.5-mc aural subcarrier. The combined signal is then transmitted to the ground transmitter via the video transmission system.

At the receiving end of the system the reverse procedure takes place. The combined signal is received at the ground receiver and transmitted to the control building via the video system, where it is applied to the receiving diplexer. Here, the 4.5-mc aural subcarrier is separated from the video signal and demodulated by a frequency discriminator centered at 4.5 mc. Separate video and audio outputs are provided from the diplexer.

For two-way message operation, standard telephone channel bank equipment replaces the diplexers, as shown in Fig. 2. In this arrangement, 12 individual telephone channels are frequency-multiplexed into the 60 to 108-kc band as shown. However, there is an additional difference between
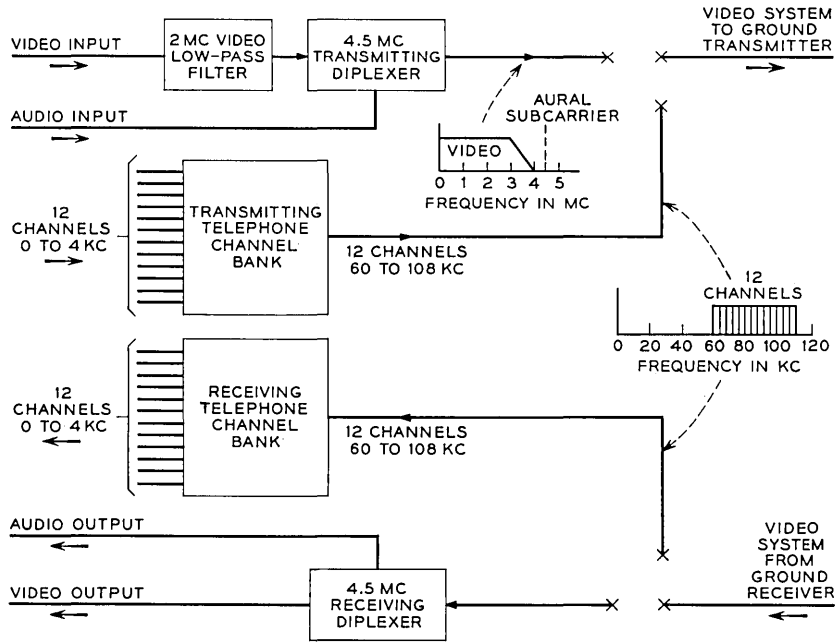
Fig. 2 — Arrangements for television and two-way message transmission.

the television and two-way telephone tests; the television tests are one-way tests which normally use the entire RF bandwidth of the system, whereas the two-way message tests involve simultaneous transmission and reception by two ground stations. This is accomplished by simultaneously using two separate bands for the two directions of transmission. In this case, the individual ground transmitters and receivers are offset by 5 mc from their normal center frequencies, as shown in Fig. 3. Typically, the Andover transmitter and the European receiver are tuned 5 mc above the nominal center band frequency. Similarly, the European transmitter and the Andover receiver are tuned 5 mc below the center of the band. Both signals, separated 10 mc in frequency, are simultaneously received and amplified by the satellite repeater. Since the repeater has only a single wideband channel and a single automatic gain control circuit, the two amplified signals at the satellite output will be unequal in power unless the two input signals are equal. In fact, due to the compression in the traveling-wave tube, any difference in signal power at the input is exaggerated at the output. In order to prevent vastly different signal powers, and hence unequal noise performance for the two directions of transmission, it has been customary for the two participating ground stations to coordinate and control their transmitter power so that approximately equal signals are received at the satellite repeater input.
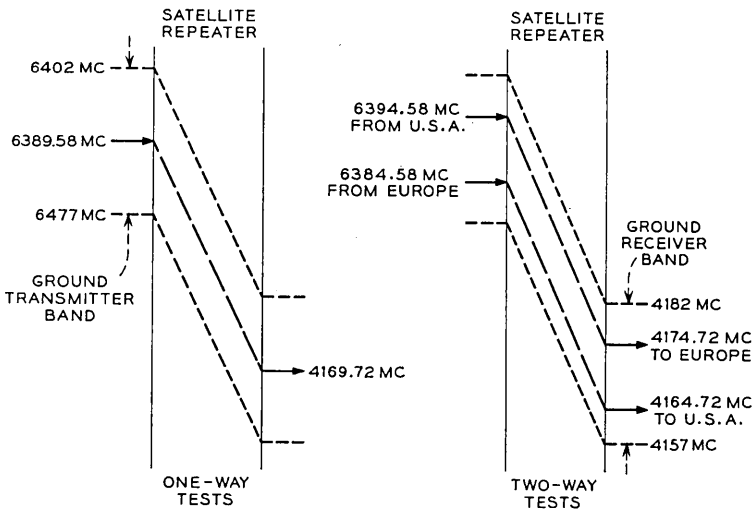
Fig. 3 — Frequency allocation plan.

When two ground stations are conducting two-way tests, both signals are received at a particular ground receiver input. Narrow bandpass filters (3 mc wide at Andover) are inserted at IF to pass the desired signal and reject the unwanted one.

Normal frequency deviations for both television and two-way message transmission are presented in Table I. Television transmission tests have been made both with and without the standard 525-line television pre-emphasis and de-emphasis prescribed by the CCIR.[2] The respective networks, when used, are inserted directly in front of the FM deviator and immediately following the FM receiver. These networks have the effect of increasing the frequency deviation for the high video frequencies by about 3 db and reducing the deviation for the low video frequencies by about 9 db. No pre-emphasis was used for the 12-channel two-way telephone tests.

Table I also shows the nominal frequency deviation used for one-way noise loading tests which simulate 600-channel loading.

TABLE I — NORMAL FREQUENCY DEVIATIONS

Television	
Peak-to-peak deviation by video	14 mc
Peak-to-peak deviation by aural subcarrier	2.8 mc
Nominal peak-to-peak deviation of aural subcarrier by audio signal	100 kc
Two-way message	
Nominal peak-to-peak deviation by 12-channel telephone signal	2 mc
Full load sine wave power at 0 db TL	+16 dbm
One-way message (600-channel noise loading)	
Nominal peak-to-peak deviation by 600-channel telephone signal	20 mc
Full load sine wave power at 0 db TL	+23 dbm

IV. EXPERIMENT PLAN

Prior to the launch of the Telstar satellite it was apparent that special consideration would have to be given to the test procedures because:

(a) the time per day available for tests would be small

(b) significant variations in the system signal-to-noise ratios would occur because the satellite range would change rapidly with time

(c) there would be a time variation in the apparent gain of the satellite antenna due to change in the "spin angle," defined as the angle between spin axis of the satellite* and the line of sight to the satellite from the earth station

(d) Doppler shift might affect some of the tests

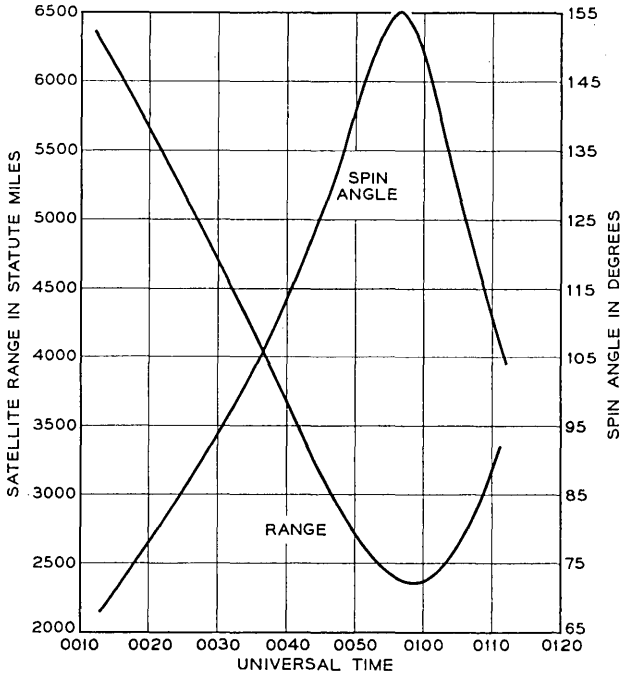* Measured from the south pole (opposite the telemetry antenna) of the satellite.

Fig. 4 — Range and spin angle vs time; pass 125, July 24, 1962.

(e) the life of the satellite might be shorter than expected, and it would therefore be essential to gather as much data as possible during the first few weeks.

Of the above considerations, the small amount of available test time has probably been the most important. With a total of about four thirty-minute passes per day and six operating days per week, there is a total of only two hours per day or twelve hours per week to be shared by several earth stations conducting a variety of tests, demonstrations, and special transmissions. This, plus the rapid variation in range and spin angle due to satellite orbital motion (Fig. 4 shows the variation in range and spin angle for a typical pass), made it very important to plan the individual tests to insure rapid and accurate completion. Several steps were taken to make this possible. An experiment plan was developed describing each of the proposed tests in detail, including test equipment requirements, patching arrangements, prepass calibration procedures, data to be recorded, and the recording method. Where possible, several individual tests were combined so that they could be per-

formed simultaneously. In addition, the station itself was arranged so that as many tests as possible could be made from a single test area in the control building. Finally, a video switch was provided so that input and output signals to the satellite system could be rapidly switched during a pass without the need for patch cords.* A portion of the test area is shown in Fig. 5.

The principal experiments described in this paper are listed in Table II. The section numbers are included, so that this table also serves as an index to the experimental results reported in the remainder of the paper.

No tests were made of correction techniques for the effect of Doppler shift on transmission, or on the problem of transferring transmission from one satellite to another without interruption.

V. RECEIVED CARRIER POWER

Received carrier power in the communications channel centered at 4170 mc was continuously measured at the ground receiver by monitoring the voltage in the main IF amplifier's automatic gain control circuit. Similarly, the 6390-mc received carrier power at the satellite was measured by monitoring the automatic gain control voltage in the satellite's IF amplifier; in the latter case, the measurements were taken at one-minute intervals and the quantized readings transmitted to the ground via the telemetry system. The over-all accuracies in these measurements are estimated to be approximately ±0.5 db at the ground receiver and ±1 db at the satellite receiver. Large amounts of these data have been obtained and analyzed in various ways. In general, the measured values of received carrier power agree with the predicted values when both range and spin angle effects are included.

5.1 Received Carrier Power as a Function of Time

A typical pen recording of the 4170-mc received carrier power at the ground receiver is shown in Fig. 6. This trace, taken with a recorder speed of about 50 cm/hour, covers a period of about 20 minutes during pass 125. The relatively broad width (1 to 3 db) of the trace is due to a rapid jitter of the pen following the variations in the antenna pattern due to the spin of the satellite. The slower variations which are more clearly visible are caused primarily by the variation in the spin angle at the satellite and to a lesser extent by range variations.

---

* Even with these precautions, it has been difficult to obtain completely consistent sets of data; a critical reader can undoubtedly find some evidence of this in the paper.
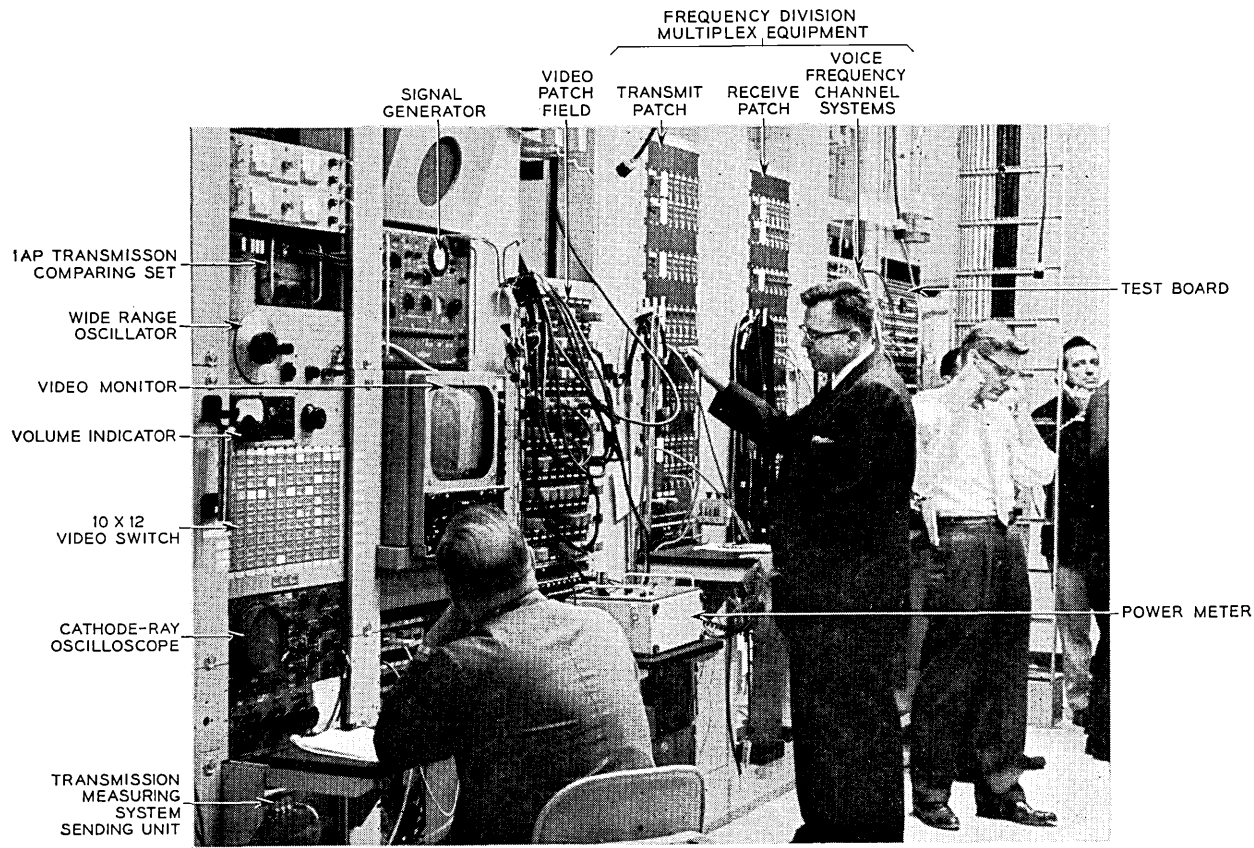
FREQUENCY DIVISION
MULTIPLEX EQUIPMENT

VOICE
FREQUENCY
VIDEO
PATCH   TRANSMIT   RECEIVE CHANNEL
SIGNAL   FIELD   PATCH   PATCH   SYSTEMS
GENERATOR

1AP TRANSMISSON
COMPARING SET

WIDE RANGE
OSCILLATOR

VIDEO MONITOR

VOLUME INDICATOR

10 X 12
VIDEO SWITCH

CATHODE-RAY
OSCILLOSCOPE

TRANSMISSION
MEASURING
SYSTEM
SENDING UNIT

TEST BOARD

POWER METER

Fig. 5 — Portion of Andover test area.

TABLE II — EXPERIMENT RESULTS INCLUDED IN THIS PAPER

Type of Test	Section
Received Carrier Power	5.0
Received Carrier Power as a Function of Time	5.1
Received Carrier Power vs Range	5.2
Antenna Patterns	5.3
Radio Frequency Transmission Stability	5.4
Linear Transmission	6.0
Baseband Transmission	6.1
IF-RF Transmission	6.2
Baseband Stability	6.3
Noise	7.0
Baseband Noise Spectrum	7.1
Noise at 6 mc	7.2
Television Noise	7.3
Telephone Noise	7.4
Impulse Noise	7.5
IF Noise Spectrum	7.6
Nonlinearity and Cross-Modulation	8.0
Envelope Delay Distortion	8.1
Differential Gain and Phase	8.2
Noise Loading	8.3
Intermodulation: Video to Audio	8.4
Television	9.0
Early Transmissions	9.1
Color Television	9.2
Two-Way Television	9.3
Two-Way Telephony	10.0
Early Transmissions	10.1
Channel Noise	10.2
Crosstalk	10.3
Data Transmission	11.0
Digital Data	11.1
Facsimile	11.2
Miscellaneous	12.0
Doppler Shift	12.1
Absolute Delay	12.2
Time Synchronization	12.3
Interference	12.4

The symmetry of the pattern around 00:57:00 Universal Time occurs at the point of maximum spin angle. This point can be quite accurately determined and, therefore, serves as a check against computer-produced spin angle data.

In Fig. 7, similar but higher-speed pen recordings are shown of the 4170-mc received carrier power. Here, the details of the previously mentioned pen jitter become apparent and show the variations in received carrier as the satellite rotates. These variations correspond to the constant-latitude antenna patterns of the satellite for the three values of spin angle shown. The spin rate of 159 rpm was determined from the periodic nature of the patterns.
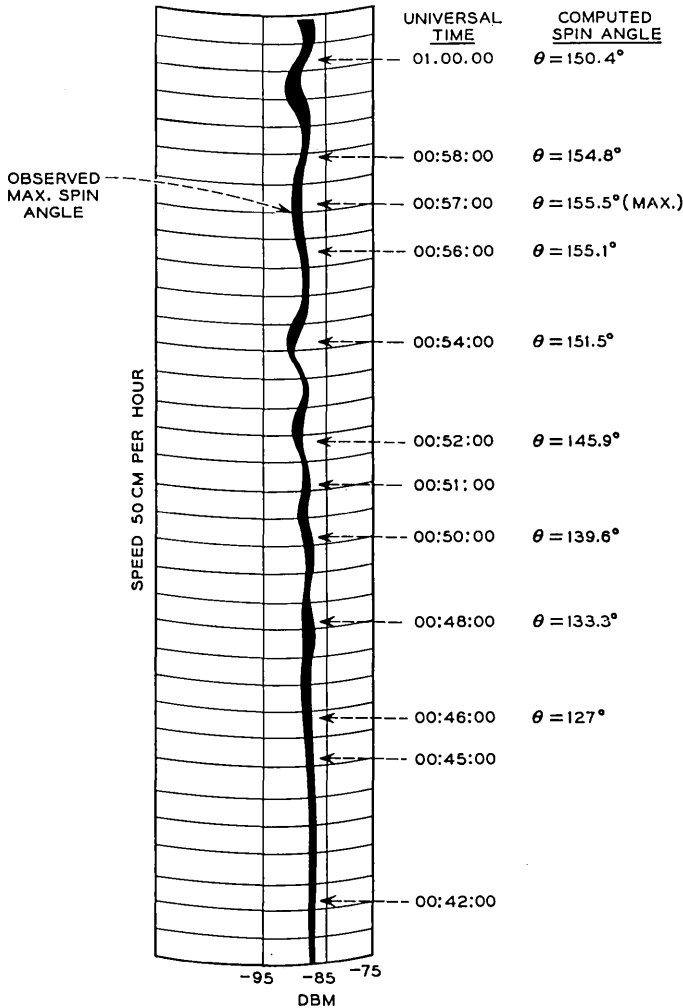
Fig. 6 — Recording of received signal power; pass 125.

Transmission phenomena at low elevation angles are not normally observed at the Andover station because the satellite is commanded on and off well above the horizon. However, on pass 470 the Bell Laboratories command system at Cape Canaveral was instructed to command on the satellite as it rose above the horizon at Andover so that low-elevation effects could be observed. The pen recording shown in Fig. 8 was obtained during this pass. For this test, the horn antenna was slaved

1910 UNIVERSAL TIME
SPIN ANGLE = 73.36°

1918 UNIVERSAL TIME
SPIN ANGLE = 90.18°

1922 UNIVERSAL TIME
SPIN ANGLE = 99.05°

1 CM

20 MM/SEC

1 MM/SEC

MAX. Δ
1.74 DB

MAX. Δ
1.85 DB

MAX. Δ
1.85 DB

-95   -90   -85
            DBM

-95   -90   -85
            DBM

-95   -90   -85
            DBM
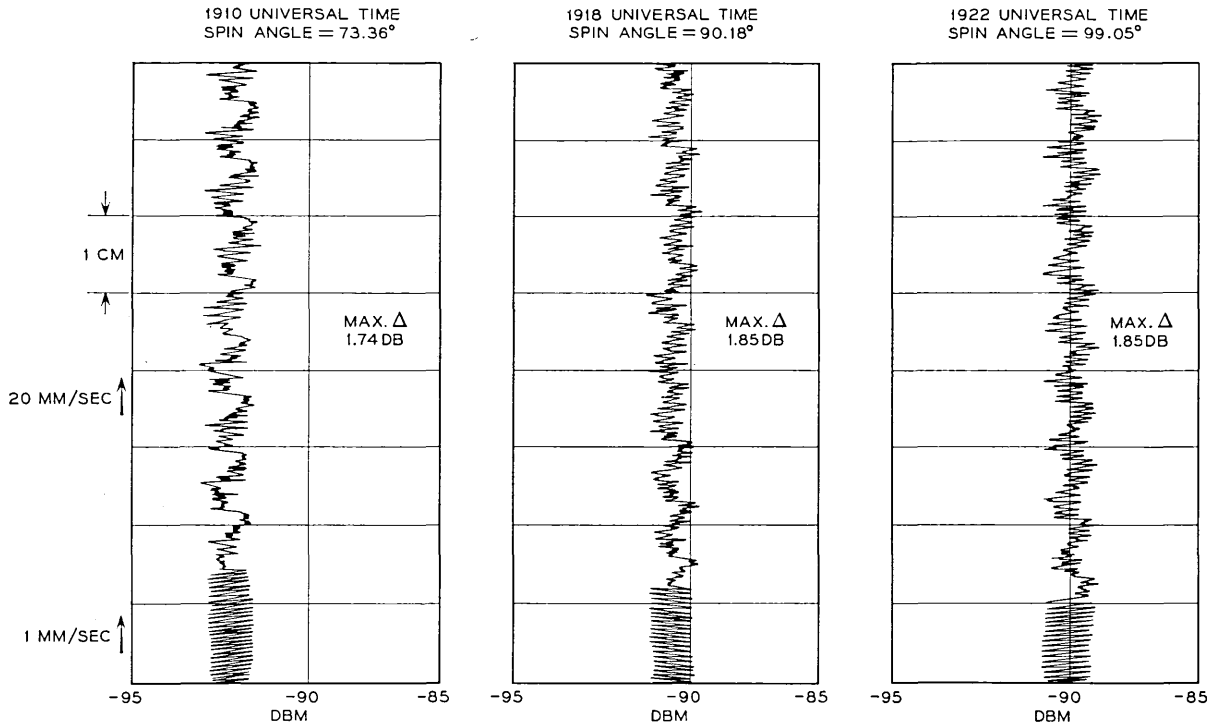
Fig. 7 — Received carrier power recordings showing constant-latitude satellite antenna patterns at 4 kmc; spin rate = 159 rpm; pass 397, Aug. 22, 1962.
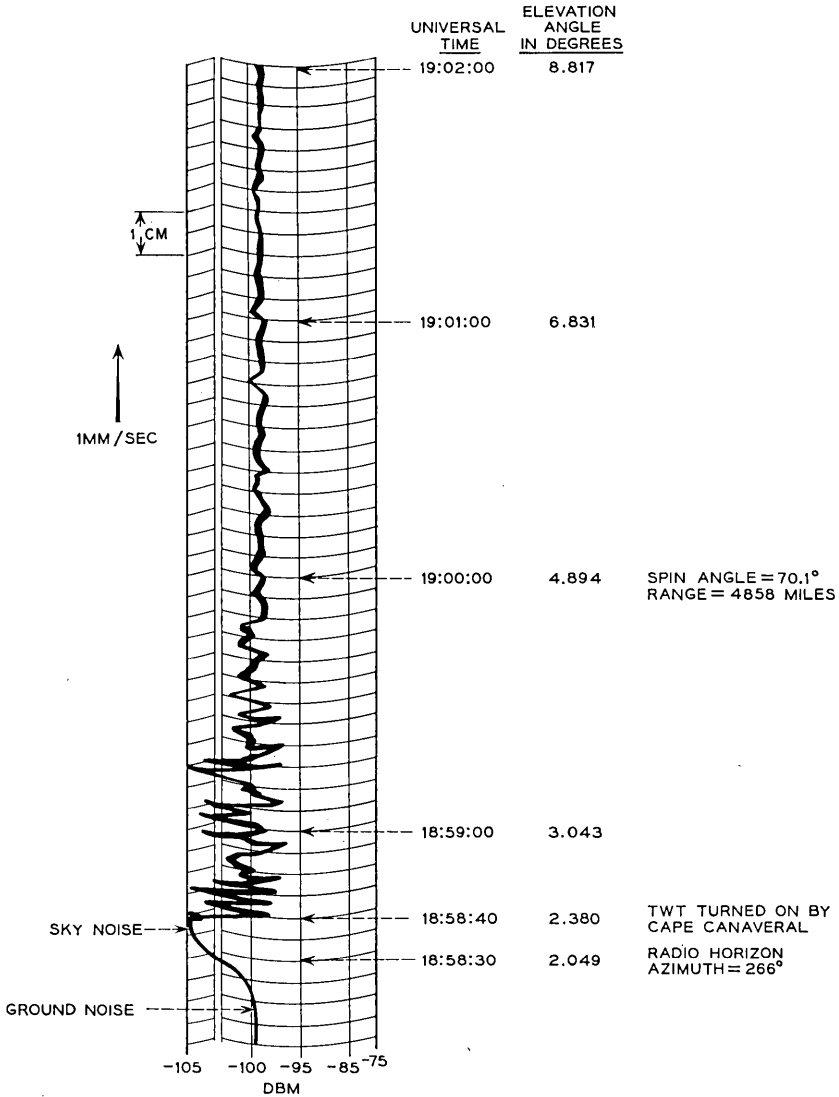
Fig. 8 — Low-angle fading at 4170 mc; pass 470, Aug. 30, 1962.

to a magnetic tape drive with an estimated accuracy of ±0.02° (well within the 4-kmc antenna beamwidth). A ground noise level of −99.5 dbm was observed (bottom of Fig. 8) while the horn antenna was pointed below the radio horizon. At 18:58:30 UT the antenna was driven

above the radio horizon at 2.04° elevation (optical horizon 1.95°) and the noise dropped to a level of about −104 dbm. A few seconds later, at 18:58:40 UT, the satellite was commanded on from Cape Canaveral. For a period of about one minute large variations in the signal were observed. Some of these appear to be almost complete fades or cancellations of the signal. Reliable transmission was not attained until an elevation angle of about 4° was reached.

5.2 *Received Carrier Power vs Range*

The received carrier power in db plotted against range is shown in Fig. 9 on a logarithmic scale for pass 125. If range were the only variable
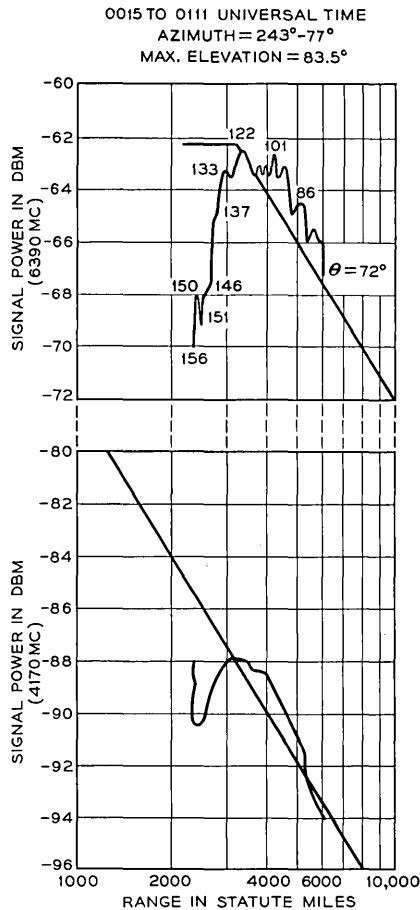
Fig. 9 — Received carrier power vs range; pass 125.

affecting received carrier power, the curves would be straight lines. The straight lines appearing on the graph represent the theoretical results under the assumptions shown in Table III.

5.3 Antenna Patterns

At elevation angles well above the horizon, the variation in received carrier power has been found to be primarily a function of range and spin angle. Thus, it is possible to take received carrier power measurements such as those in Fig. 6, compensate them for range variations, and plot them against accurate spin angle data to display the polar patterns of the 4-kmc satellite antenna. Fig. 10 illustrates the received carrier power measurements obtained during pass 125, compensated for range and plotted against spin angle. The resulting curve agrees very well with antenna pattern measurements made in the laboratory prior to launch.[3]

Fig. 11 shows a similar curve for the 6-kmc antenna. In this case, the received carrier power measurements were only obtained once per minute from telemetry, and it is not possible to get the same accuracy and fine detail as is possible for the 4-kmc antenna.

The pointing accuracy of the horn antenna has also been checked by means of the satellite. This has resulted in determination of the 4- and 6-kmc horn reflector antenna patterns shown in Figs. 12 and 13. Known offsets were added to the programmed horn antenna drive tape, and the changes in carrier power were measured and plotted after correction for range and spin angle. In order to obtain the 4-kmc measurements, the French station at Pleumeur-Bodou transmitted a 6-kmc signal to the satellite during pass 132 to insure a constant output as the Andover horn was offset. The 6-kmc pattern was taken during pass 105 and the received carrier measurements were made at the satellite. The measurements confirmed that there was no offset between the 4- and 6-kmc communications patterns or between the patterns and the drive tape. The patterns themselves were comparable to those obtained earlier by means of the boresight tower.

TABLE III — ASSUMED SYSTEM CONSTANTS

	6390 mc	4170 mc
Radiated power	62 dbm	33.5 dbm
Satellite antenna gain at 90° spin angle	1 db	0 db
Earth station antenna gain	60 db	58 db
Loss in satellite antenna cable	2 db	
Radome loss		0.4 db
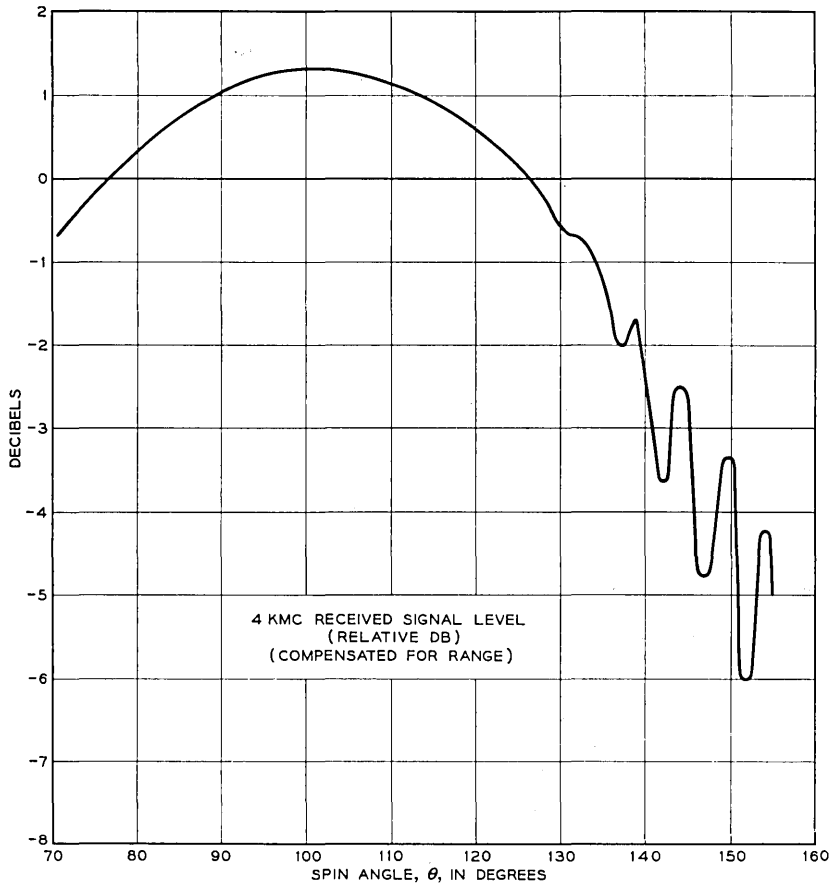
Fig. 10 — 4-kmc satellite antenna pattern; pass 125.

5.4 Radio Frequency Transmission Stability

Fading is a common phenomenon in 4- and 6-kmc overland microwave radio systems. In fact, this problem is so severe that in systems where high reliability is required, it is customary to provide spare radio channels and automatic switching equipment to protect the working channels. A fading problem was not anticipated in satellite systems except at very low elevation angles. The performance thus far achieved tends to confirm this expectation.

To study the system stability, received carrier power measurements from a number of passes were compensated for range and plotted against
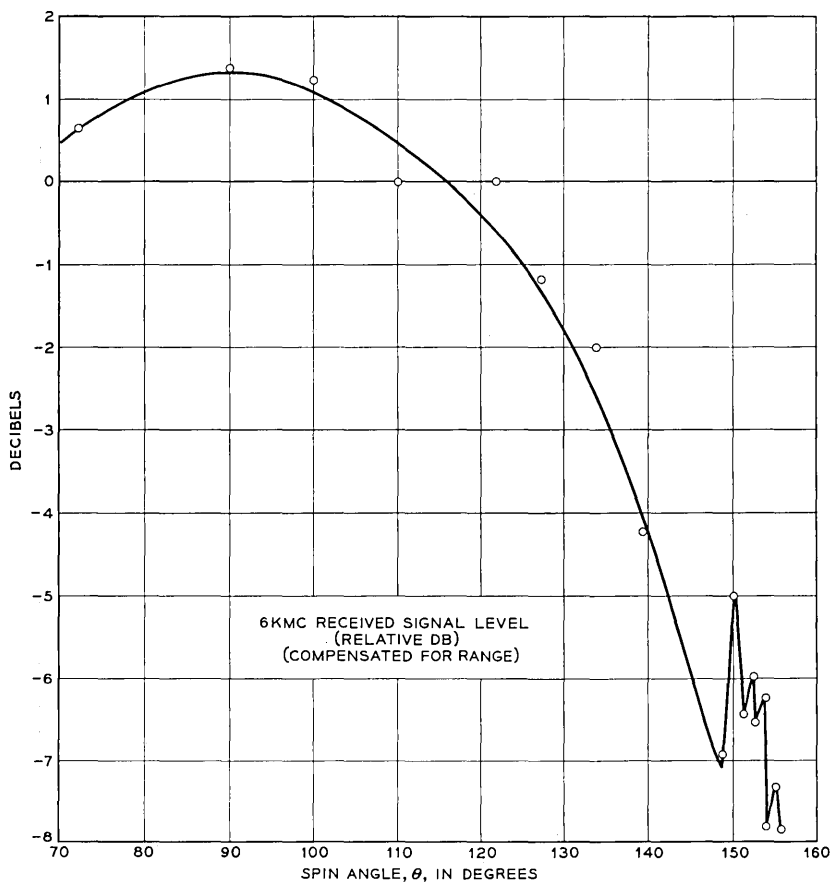
Fig. 11 — 6-kmc satellite antenna pattern; pass 125.

the computed spin angle of the satellite. The scatter diagram which is thus obtained provides a basis for estimating the system stability and the predictability of received carrier power. Two such scatter diagrams are shown here as Figs. 14 and 15.

VI. LINEAR TRANSMISSION

The linear transmission tests define the baseband and IF gain vs frequency characteristics. Due to the many varying parameters, e.g., range, spin angle, and satellite antenna patterns, the stability of these characteristics is of prime concern and is included as part of these tests. The accuracy of the baseband transmission tests is estimated at ±0.1 db and
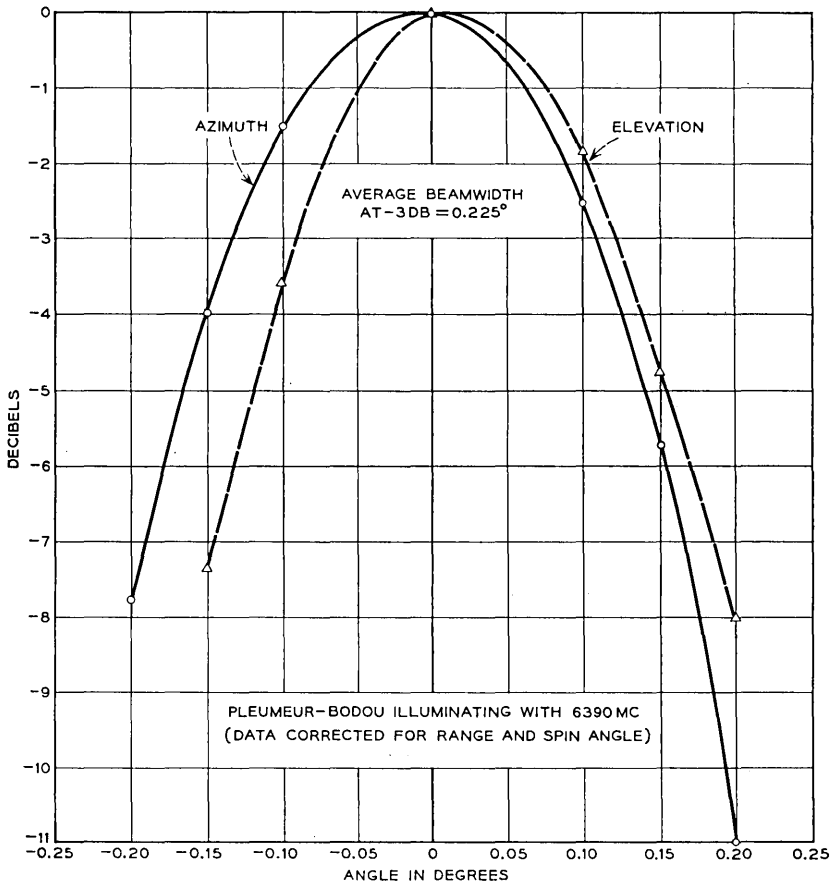
Fig. 12 — 4-kmc horn antenna pattern; pass 132, July 24, 1962.

that of the stability measurements at ±0.05 db. In general, the results of these tests with the Telstar satellite show that the transmission shapes are primarily due to the ground equipment, as expected, and that the baseband transmission is not a function of the varying satellite parameters.

6.1 Baseband Transmission

The baseband gain vs frequency characteristic for various transmission loops is shown on Figs. 16 and 17. Fig. 16 shows the baseband frequency response for the baseband loop (A), the IF loop (B), and the
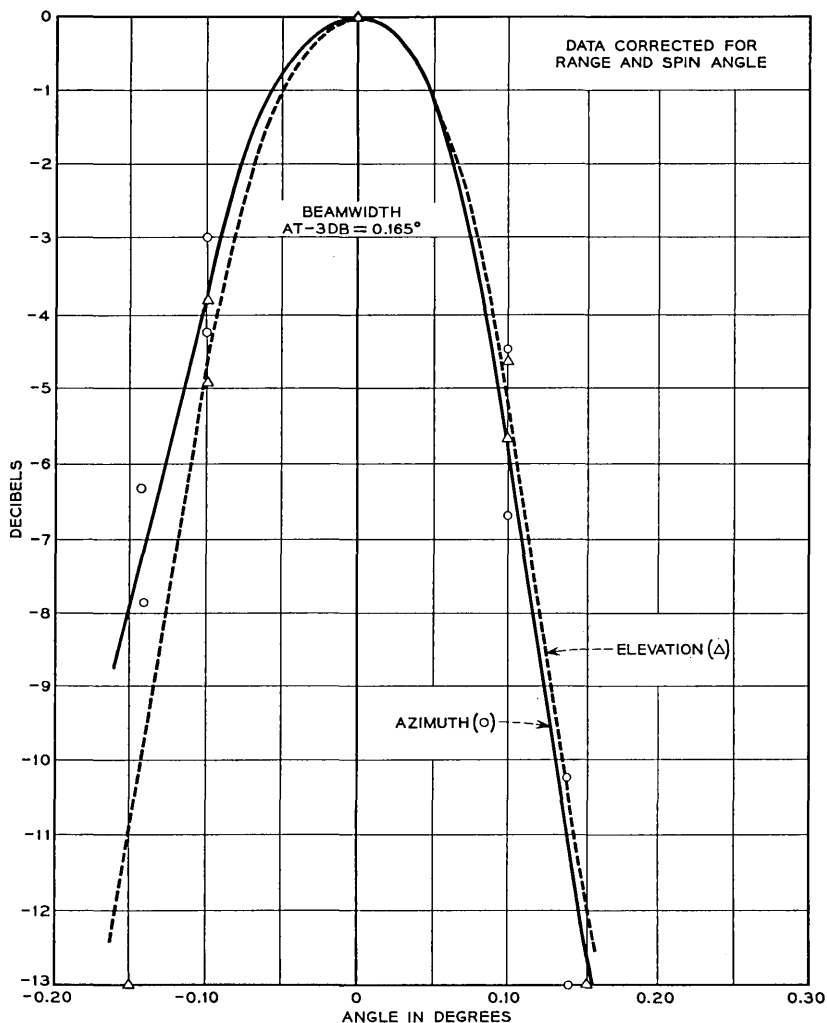
Fig. 13 — 6-kmc horn antenna pattern; pass 105, July 21, 1962.

satellite loop (C). The standard FM receiver was used in determining (B) and (C); no diplexers or roll-off filters were used for any of the three curves.

The gain of the baseband loop appears to be about 0.5 db higher than that of the other loops. However, the baseband loop was measured on a different day than the others, and the difference is probably due to a
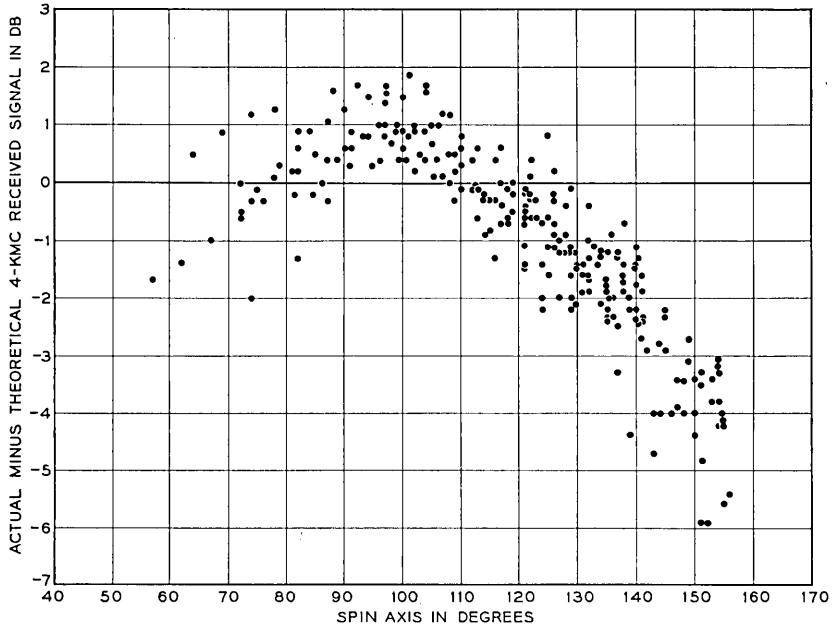
Fig. 14 — 4-kmc received carrier: difference between actual and theoretical power vs spin angle.

slightly different gain adjustment for the various video amplifiers in the transmission path.

The principal difference between the IF and the satellite loops, (B) and (C) of Fig. 16, is the peak of about 0.5 db at 1.7 mc. This is a characteristic of this particular satellite, and was first discovered during pre-launch tests. No noticeable degradation of transmission is caused by this irregularity. It is clear from Fig. 16 that the transmission is essentially flat, up to at least 5 mc, when the standard FM receiver is used. Color television signals were transmitted across the Atlantic, as described in Section 9.2, using such an arrangement.

The effect of the FM feedback receiver (FMFB) on the baseband transmission characteristic is shown on Fig. 17. Curves (A) and (B) show that there is little difference in baseband frequency response between the IF and the satellite loops;* the response is essentially flat to within ±0.5 db to about 3 mc and approximately 3 db down at 4 mc. Adding the 2-mc roll-off filter and diplexers for video transmissions results in the characteristic shown by curve (C). This transmission shape

---

* The peak at 1.7 mc is not shown due to the coarseness of this measurement.
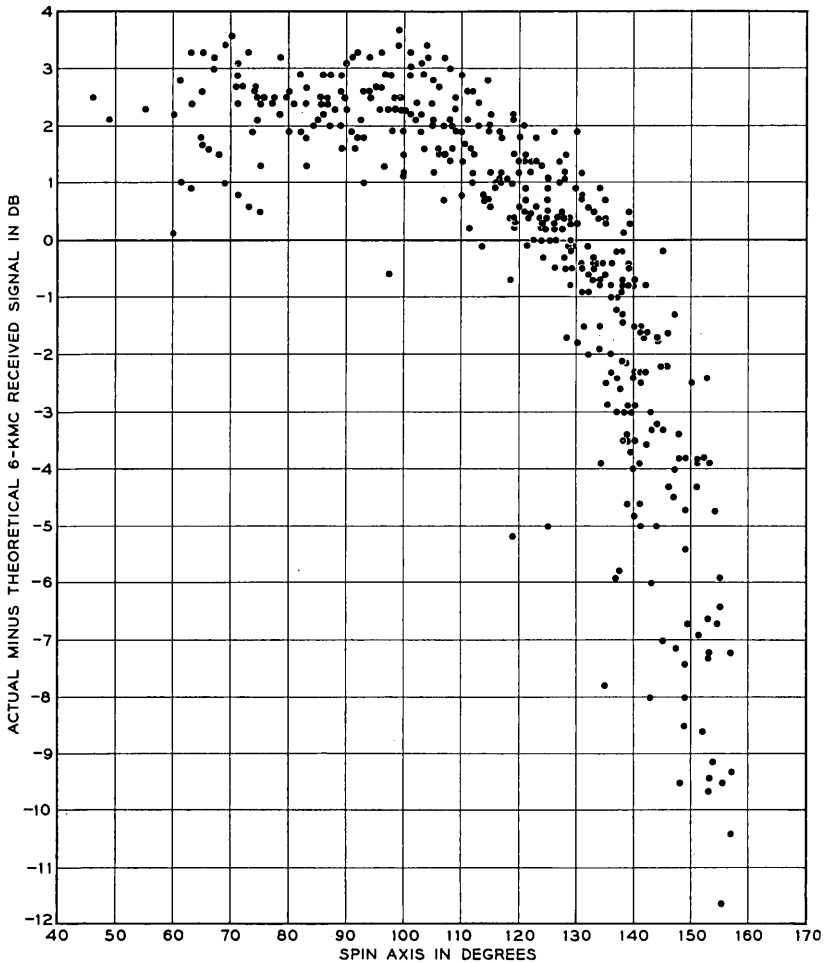
Fig. 15 — 6-kmc received carrier: difference between actual and theoretical power vs spin angle.

is the product of a preliminary design and has been used with satisfactory results for many of the television demonstrations. A substantial improvement is possible by a redesign of the diplexers and the roll-off filter.*

The baseband transmission characteristics, shown in Figs. 16 and 17,

---

* A roll-off filter is desirable to limit the video spectrum at the aural subcarrier frequency and also to restrict the amount of high-frequency energy entering the FMFB receiver.
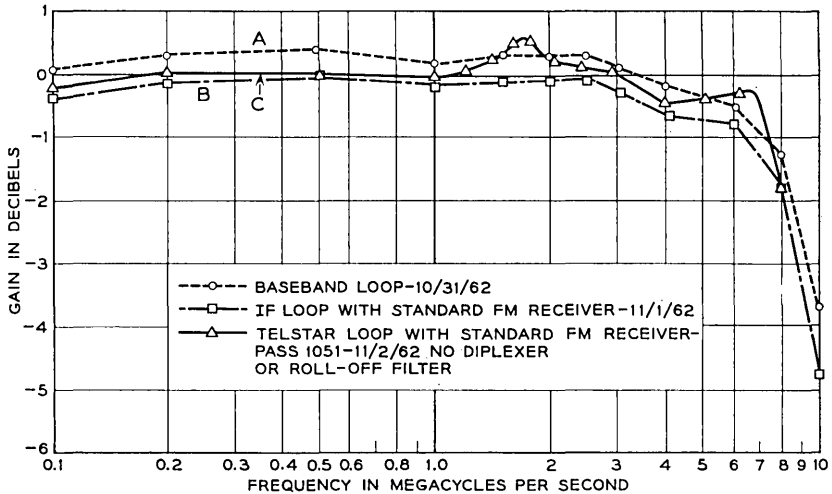
Fig. 16 — Baseband frequency response (standard FM receiver).

determine to a large extent the quality with which black-and-white television pictures are transmitted over the system. The effect of the system with a characteristic as shown on (C) of Fig. 17 on various patterns and signals is illustrated in Fig. 18. The reduction in the high-frequency content is obvious from the "after" pictures.

6.2 *IF-RF Transmission*

A gain-frequency characteristic of the IF and RF equipment, including the satellite repeater, determined during pass 188, is shown in Fig. 19. Before each pass the maser is adjusted to produce a transmission curve similar to the center curve of Fig. 19. When the satellite first appeared on pass 188, the transmission characteristic was that shown at the left of the figure; it then changed gradually over to the middle curve and finally to that shown on the right. The phenomenon can be explained by the interaction of the earth's magnetic field with the field of the maser. The earth's field either adds to or subtracts from the maser field, and thereby shifts the maser frequency at the rate of 2.4 mc per gauss. This shift, superimposed on the maser equalizer characteristic, then introduces the transmission slopes shown. The tilt in the transmission characteristic has not caused any detrimental effects to the system performance. However, this characteristic must be taken into account when analyzing the IF noise measurements of Section 7.6.
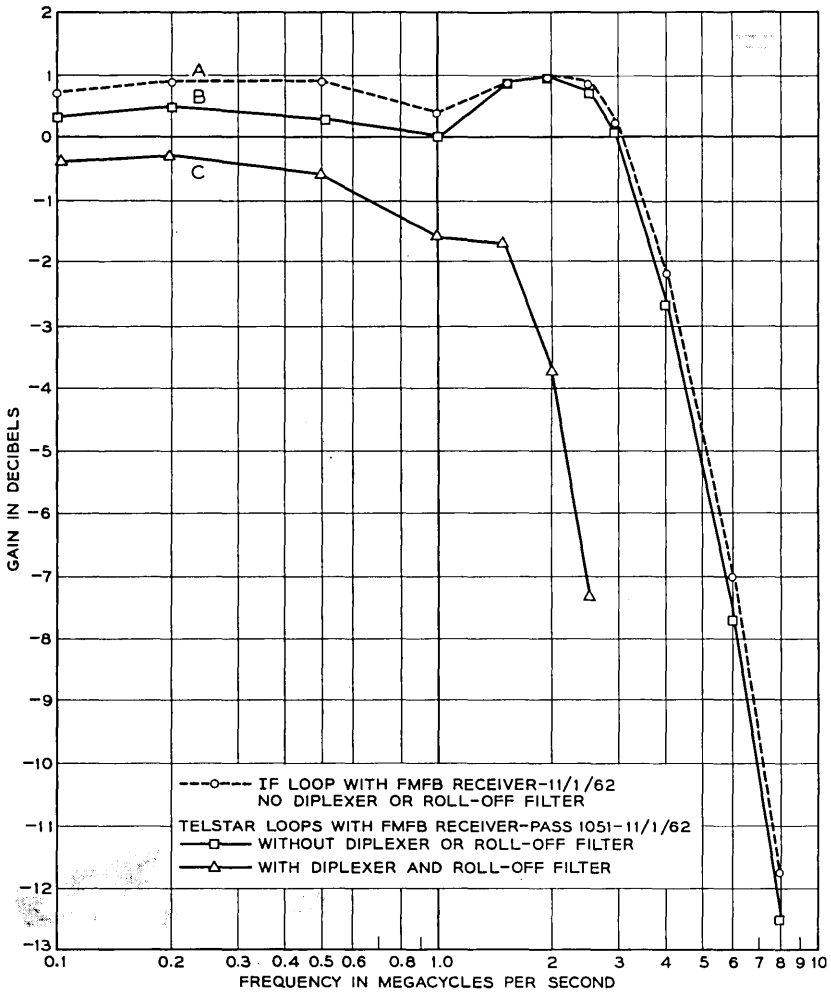
Fig. 17 — Baseband frequency response (FMFB receiver).

6.3 *Baseband Stability*

Stability measurements of the baseband gain-vs-frequency charac-
teristic were made on several passes under conditions of varying slant
range (or received carrier powers) and spin angle. The test was made by
applying a 450-kc tone to the input of each of the five type "L" super-
groups Nos. 2, 4, 6, 8, and 10.[4] The 450-kc tone was then translated to
the frequencies 415, 915, 1411, 1907 and 2651 kc, respectively, and trans-

BEFORE   AFTER
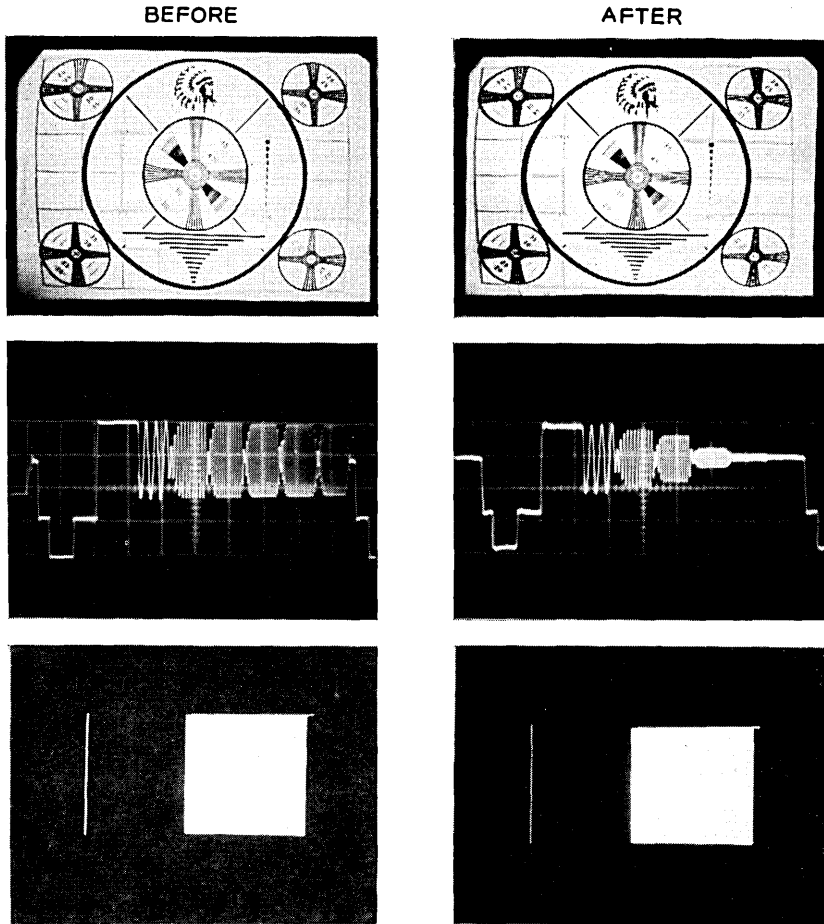
Fig. 18 — Effect of transmission on various test signals.

mitted over the satellite communications repeater. The five received
signals were shifted back to 450 kc by means of the receiving supergroup
equipment, detected and recorded on a strip chart. An expanded db
scale capable of discerning changes of 0.05 db was used. In all cases the
stability was better than ±0.1 db, most of which is attributable to drift
in the measuring equipment.

VII. NOISE

Various measurements of baseband and IF noise are described in this
section. In view of the many varying parameters affecting the system's

79.6 MC   70.5 MC   79.0 MC   69.5 MC   77.8 MC   68.6 MC

1 DB   1 DB   1 DB

UNIVERSAL TIME 2154   UNIVERSAL TIME 2217   UNIVERSAL TIME 2233
AZIMUTH = 222.28°   AZIMUTH = 172.51°   AZIMUTH = 78.61°
EARTH MAGNETIC FIELD   EARTH MAGNETIC FIELD   EARTH MAGNETIC FIELD
AT MASER ≈ −0.125 GAUSS   AT MASER ≈ 0 GAUSS   AT MASER ≈ +0.15 GAUSS
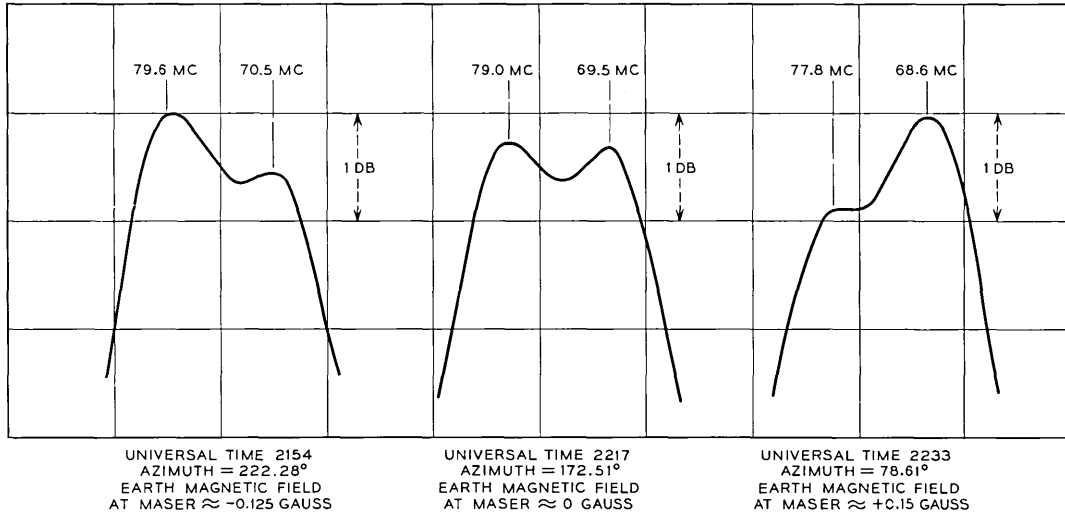
Fig. 19 — IF-RF transmission characteristics; pass 188, July 30, 1962.
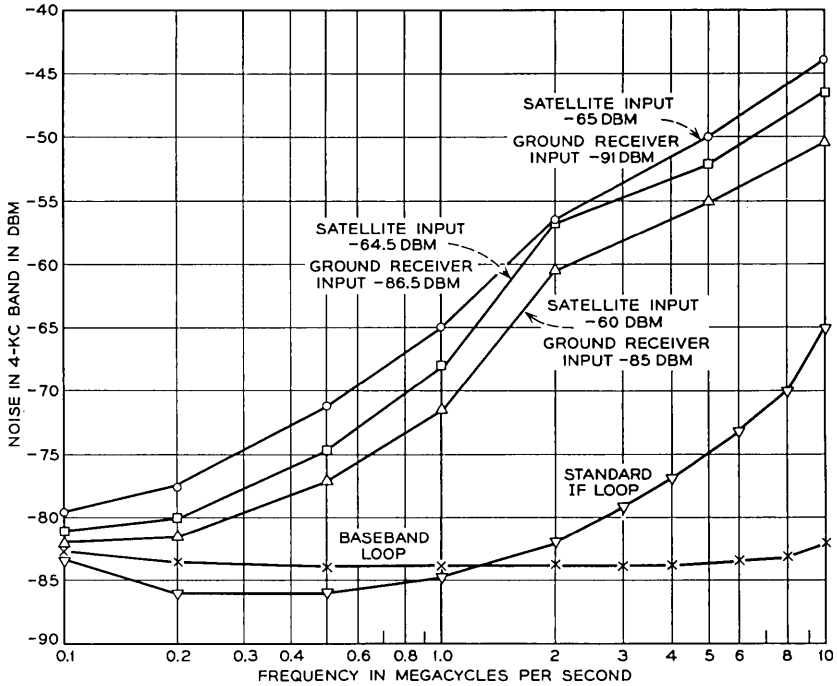
Fig. 20 — Baseband noise spectra: standard FM receiver; no diplexer or clamper; measured at test area; pass 62, July 17, 1962.

baseband noise, i.e., satellite elevation above the horizon, slant range, spin angle, power transmitted to the satellite, and ground receiver used, most noise measurements have been repeated often in order to obtain sufficient data for statistical analysis.

7.1 Baseband Noise Spectrum

Typical measurements of the baseband noise spectrum made from the test area* during pass 62 are shown in Fig. 20. These noise measurements, made in a 4-kc band, have been corrected for the transmission characteristic of Fig. 16. The figure clearly exhibits the effect of changing slant range on received carrier power and on the system's noise performance. In addition, noise measurements for the standard IF loop and the baseband loop are also shown. The latter show that significant noise is contributed by the video circuits and FM terminals below 200 kc.

* Fig. 1 shows the system block diagram.

Baseband noise spectrum measurements were repeated often during the first four months after the launch of the Telstar satellite. The results are consistently similar to those of Fig. 20.

To relate baseband noise measurements made at various points in the system to RF signal-to-noise performance, the following constants of the Telstar system must be defined:

(a) A tone (or a one-cycle band of noise) X dbm at the test area is $X - 5$ dbm at the deviator input (or at the FM receiver output).

(b) Zero dbm of a sine wave at the deviator input corresponds to an rms frequency deviation of 7.07 mc.

If the RF noise spectrum is white, the expected baseband noise spectrum is triangular. In practice, the baseband noise is decreased at the high-frequency end due to the IF-RF transmission characteristic (see Fig. 19) and increased at low frequencies due to noise in the terminal and baseband equipment, as well as FM noise from the satellite carrier supplies.

To obtain data under carefully controlled conditions of range and satellite attitude, eleven complete noise spectrum measurements were made at one-minute intervals at the test area during pass 297. The total system noise at each frequency was plotted against time, and smooth curves drawn. The smoothed values obtained at 20:32 UT for a satellite slant range of 4000 miles are shown in Fig. 21, curve A.

To isolate the satellite or up-path contribution to the total noise for comparison with pre-launch measurements, the down-path baseband noise is computed. Assuming a receiving system noise temperature of 35°K and a 4-kmc received carrier of −88.6 dbm, the down-path noise at 10 mc in a 4-kc band is −50.4 dbm at the test area and decreases at 20 db/decade. The calculated down-path noise is shown by the dotted line on Fig. 21. At low frequencies, the noise contribution of the baseband trunks and FM terminals is added in to get the total down-path noise. Subtraction (on a power basis) of the down-path noise from the total system noise gives the up-path noise, shown as curve B of Fig. 21.

Fig. 21, curve C, shows the up-path noise measured in the laboratory prior to launch. The two curves, B and C, agree within the measurement error. It is therefore concluded that the satellite's noise performance has not been changed by the launch or by space environment. This is further substantiated by the IF noise measurements of Section 7.6. Fig. 21 shows that the contribution of the up-path to the total system noise is somewhat greater than the down-path for this pass. The data consistently show that two paths contribute about equally to total noise, with a tendency for the up-path to be the larger contributor.
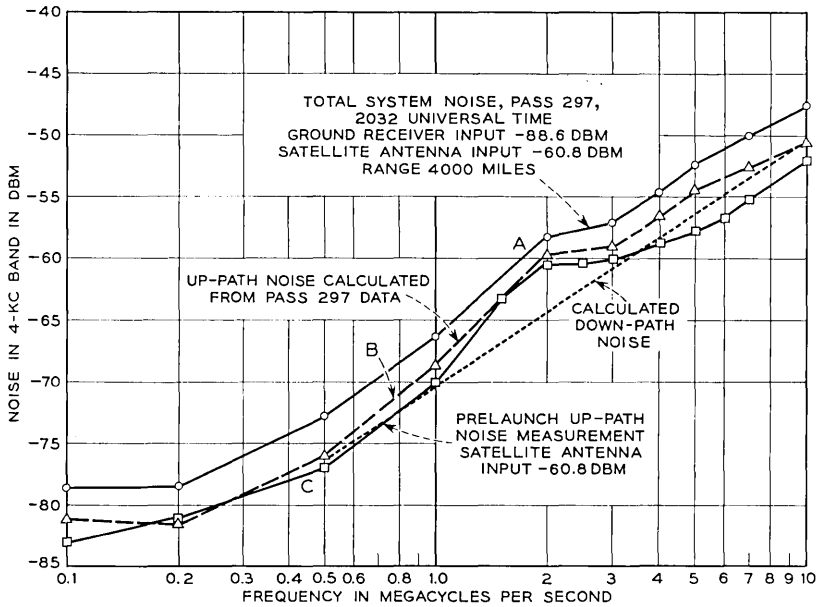
Fig. 21 — Comparison of pre-launch and post-launch baseband noise spectra: post-launch data from pass 297, Aug. 11, 1962.

7.2 *Noise at 6 mc*

Since typical monochrome television signals have negligible energy at 6 mc, the system noise at this frequency serves as a monitor of the system performance during video transmissions and noise tests and is therefore recorded continuously at the test area. Such a recording, made during pass 988, is shown at the top of Fig. 22. This figure clearly exhibits the dependence of the baseband noise on the range and received carrier powers tabulated thereon. Further, it shows that after appropriate adjustments are made for transmission losses (see Figs. 16 and 17), the two FM receivers detect the same noise at 6 mc, everything else being equal.* The 6-mc noise is measured at the same point as the baseband noise spectra of Section 7.1, but in a 6.3-kc band.

Of the several parameters affecting the noise at 6 mc, the slant range and spin angle are both reflected in the 4170-mc carrier power received at the ground receiver. Therefore, Fig. 23, which is the scatter diagram

---

* At the time of switching between FM receivers, the sensitivity of the measuring equipment was decreased 10 db. This accounts for the apparent decrease in 6-mc noise on Fig. 22.
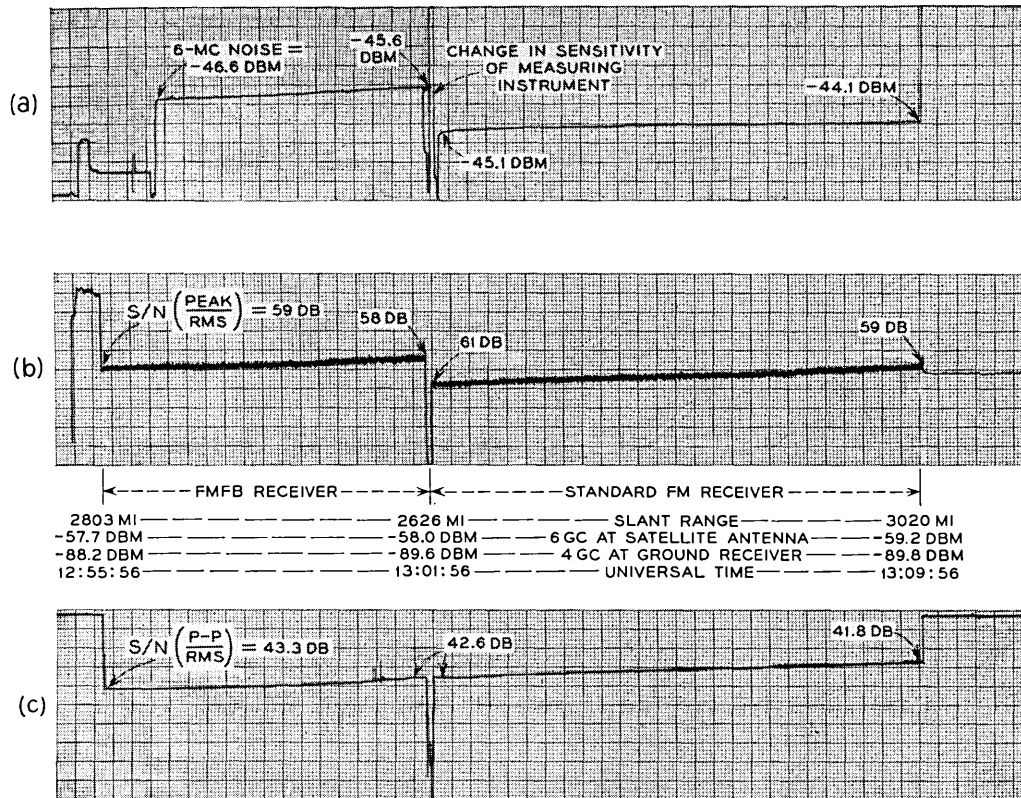
Fig. 22 — Baseband noise recordings; pass 988, Oct. 26, 1962. (a) Noise at 6 mc in 6.3-kc band; (b) weighted audio noise; (c) weighted video noise.
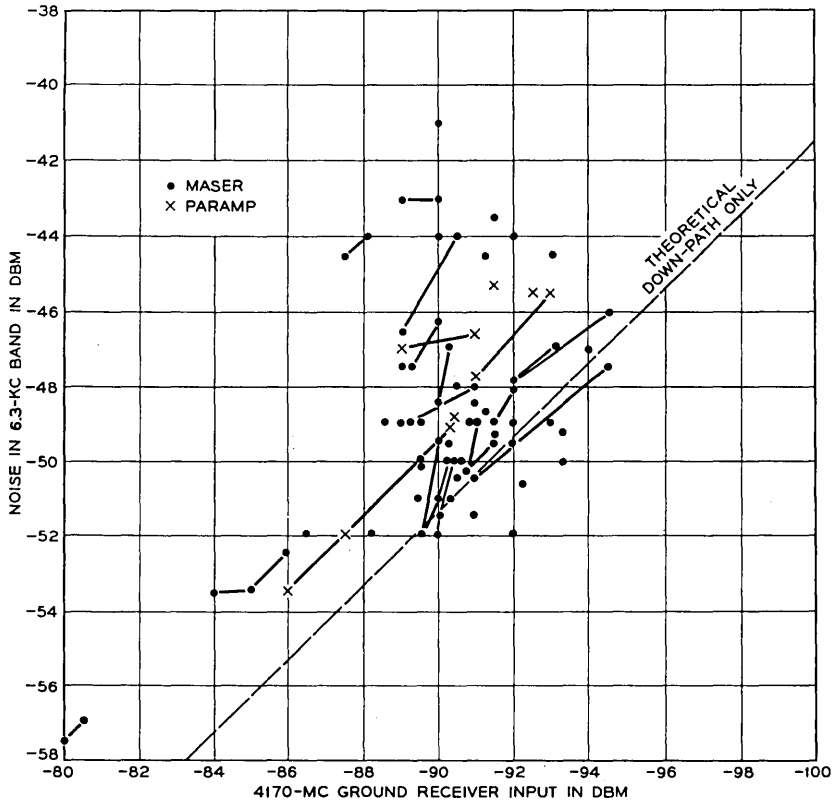
Fig. 23 — 6-mc noise vs received carrier power.

of 6-mc noise vs received carrier power,* shows the effect on the noise of
the remaining parameters and of the measurement errors. The principal
known parameter is the carrier power transmitted to the satellite. This
affects the up-path contribution to the total noise. Since the maximum
available power of 2 kw was not always transmitted to the satellite, only
noise measurements corresponding to received carrier powers within the
satellite's 20-db AGC range were used for this figure. The satellite's ele-
vation angle, which determines the ground receiver's effective noise tem-
perature, is of secondary importance in Fig. 23 since all values used cor-
respond to elevations of 15° or more. The effect of using the parametric
amplifier instead of the maser at the ground receiver is also shown ex-
plicitly on the figure.

---

* The straight lines on the figure represent continuous measurements during a
pass.

There are two principal sources of measurement error in the data of Fig. 23: human errors and the different system configurations. The human errors are particularly acute, because of the relatively short time available for both measurements and calibrations, and because of inability to reproduce exactly any given set of testing conditions. The use of different system configurations for various tests has resulted in variations of the baseband transmission characteristics which were not always observed and recorded, thus leading to errors.

The large variance of the data on Fig. 23 thus reflects the measurement uncertainties and the increases in noise due to decreases in transmitted power to the satellite. The theoretical line shown on the figure gives the down-path noise alone, based on a 35°K system noise temperature and on the assumption of a triangular noise spectrum. The fact that the mean value of the figure is above the theoretical down-path line substantiates the assertion of the previous section, namely, that the up-path contributes about as much noise to the total as does the down-path.

The contribution of the baseband and IF loops to the 6-mc noise is negligible in every measurement: about −70 dbm for the IF loops and −80 dbm for the baseband loop.

7.3 *Television Noise*

7.3.1 *Video Noise*

The noise in the video channel is weighted using the latest Bell System video noise weighting network ahead of the measuring instrument. The detected video noise is recorded continuously during a pass simultaneously with the 6-mc noise and often with the audio channel noise. A typical recording of these noises is shown on Fig. 22, with the video noise at the bottom.

As expected, the video signal-to-noise ratio (SNR) is the same for both FM receivers, since their transmission characteristics are both essentially flat in the band of interest for video noise, i.e., below 2 mc. This is also evidenced by the scatter diagram of video noise vs received carrier power, Fig. 24, which shows the scattering to be the same for both receivers. The comments on the variance of the 6-mc noise data apply here equally well.

To account for the clampers used in the video circuit between the FM receiver and the test area in the computation of SNR, 1.0 db has been added to noise measured without clampers. Thus, the signal-to-noise ratios shown represent the practical situation for television receptions.
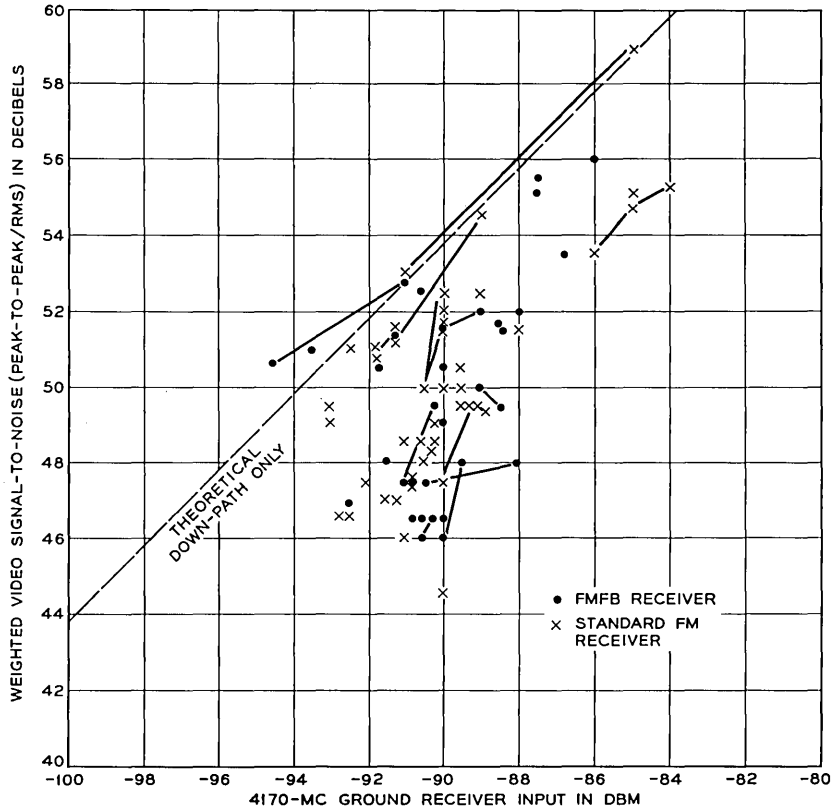
Fig. 24 — Video noise vs received carrier power.

The calculation of the theoretical value of the SNR for the down-path of Fig. 24 again assumes a triangular noise spectrum, plus the effect of the clamper and of the noise weighting. In this case, however, a triangular noise spectrum is too optimistic an assumption, as can be seen from the baseband noise spectra, Figs. 20 and 21. Because the up- and down-path noise contributions are about equal at 1 mc and because of the excess noise in the 1- to 3-mc band, it is not surprising that the average total video noise is about 5 db higher than the theoretical down-path noise.

As can be predicted from the baseband noise spectra measurements of Section 7.1, the IF loop video noise is at least 12 db lower than the satellite loop noise and the baseband loop noise is 2 to 3 db lower than the IF loop noise. The IF loop SNR is about 72 db.

TABLE IV — AUDIO SIGNAL/NOISE RATIO

	Audio SNR
Baseband loop	80 db
IF loop with FMFB receiver	75 db
IF loop with standard FM receiver	77 db
Satellite loop	55-65 db

7.3.2 *Audio Noise*

The Bell System 8-kc program noise-weighting network is used for the measurement of noise in the sound channel of the television signal. A continuous recording of the audio noise using the two FM receivers is also shown on Fig. 22, curve B.

This figure shows that under identical conditions the audio noise measured with the FMFB receiver is about 3 db higher than with the standard FM receiver. For the purpose of computing SNR, the signal is taken to be the peak power of a 1000-cps sine wave, resulting in a peak frequency deviation of the aural subcarrier of ±50 kc.*

The audio SNR measurements range from about 55 db to 65 db for 4-kmc received carrier powers of -95 dbm to -85 dbm. These measurements are not extensive enough to warrant presenting them in the form of a scatter diagram. The audio signal-to-noise ratios for the baseband. IF and RF loops are shown in Table IV.

7.4 *Telephone Noise*

The noise in five telephone channels located across a 3-mc band has been measured using the Telstar repeater. In addition to the circuits of Fig. 1, supergroups 2, 4, 6, 8 and 10 of the type L multiplex system were used for these measurements. The measuring equipment connected at the output of each supergroup consisted of a selective voltmeter† and a six-channel pen recorder. The noise was thus monitored continuously for several complete passes in order to observe the variation in noise with range, spin angle and satellite elevation.

The pen recordings for these measurements are very similar to those made for 6-mc and video noise shown on Fig. 22 and therefore are not reproduced here. However, typical values of noise in dbrn at 0 db TL (transmission level), measured during pass 1088, are shown in Table V.

---

* The so-called "program level" signal sometimes used for the calculation of SNR is 10 db lower than the signal assumed for the above computations.

† The voltmeters have a noise bandwidth of 6.3 kc and were each tuned to 450 kc. The values of Table V are corrected to a 3-kc bandwidth and for "C" message weighting.

TABLE V — TELEPHONE NOISE — PASS 1088

	11:52:00 UT	12:03:00 UT	12:07:30 UT	12:11:00 UT
Satellite antenna input (dbm)	−58.5	−60	−61	−62
Ground receiver input (dbm)	−88.5*	−92	−93	−94.3
Spin angle (degrees)	63	50	49	50
Range (miles)	2800	3115	3550	3960
Elevation (degrees)	20	27	22	18
Supergroup 2 (450 kc) ⎫ dbrn	27	30	31.5	31.5
Supergroup 4 (915 kc) ⎪ at	34.5	36	37.5	38
Supergroup 6 (1411 kc) ⎬ 0 db	40.5	42	42.5	43
Supergroup 8 (1907 kc) ⎪ TL	42	45.5	47	47.5
Supergroup 10 (2651 kc) ⎭	44	46	47.5	48

* This value, although inconsistent with other entries in the table, has been carefully rechecked against the original pen recording.

This table also shows the location of the measured channel in the baseband frequency spectrum.

7.5 *Impulse Noise*

Impulse noise measurements were made on the Telstar system during passes 208, 217, and 226 (August 1–3, 1962). These measurements were made primarily on voice circuits using an impulse counter and an experimental peak noise distribution measuring set. A standard noise measuring set was used to monitor the rms value of the noise.

The distribution of the noise peaks was recorded by the peak noise distribution set on voice circuits at levels of 6 to 10 db above rms value. These data indicate that only random thermal noise was present. The results of counting the noise peaks with the impulse counter also support the conclusion that very little impulse noise is present in the Telstar system.

7.6 *IF Noise Spectrum*

The IF noise spectrum is measured directly in the IF band using a selective analyzer covering the range of 55 to 95 mc. The analyzer used has nominal bandwidths of either 100 or 10 kc, a sensitivity of −100 dbm, and an accuracy and stability in the order of 0.2 db. The analyzer is connected at an intermediate point of the IF amplifier of Fig. 1. This IF amplifier consists of two separate amplifiers in tandem, the first being fixed-gain and the second having AGC. The analyzer is connected at the output of the first amplifier, where the nominal power is −22.5 dbm for a −80-dbm, 4-kmc input carrier to the maser.

Fig. 25 shows the results obtained during pass 1664, January 8, 1963. After the pass, the Andover antenna was pointed at the zenith and the
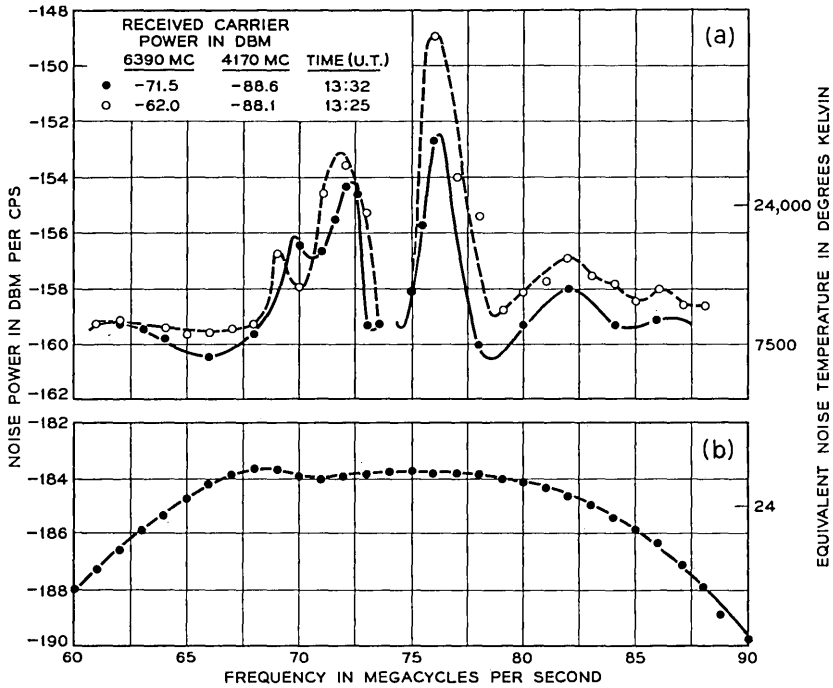
Fig. 25 — IF noise spectra: (a) Telstar satellite noise referred to satellite down-converter input; pass 1664, Jan. 8, 1963; (b) Andover zenith noise referred to maser input.

IF noise was measured. This measurement is referred to the output of the horn-reflector antenna (maser input) by correcting for the gain from this point to the point of measurement.* The bottom curve of Fig. 25 shows this result. The shape of this curve is consistent with the maser's transmission characteristic (see Section 6.2) with a bandwidth of 25 mc at 3-db points. The apparent ground station noise temperature is 30°K, which agrees closely with other observations.

To enhance the accuracy for the noise measurements with the satellite, a technique similar to that described in Section 7.1 was used. Four complete spectrum measurements were first made at about 2-minute intervals with maximum 6-kmc power transmitted to the satellite. The transmitted power was subsequently reduced, in order to increase the satellite's contribution to the total noise, and a detailed spectrum meas-

---

* This gain was measured only once, at the center frequency, and is therefore taken as fixed and uniform. In addition, the measured gain is increased by 1 db to account for the difference in maser gain when the input is broadband noise as opposed to carrier plus noise.

urement was made. The total noise was plotted as a function of time and smoothed values obtained corresponding to 13:25 UT (for full power transmitted) and 13:32 UT (reduced power). These smoothed values for the total IF noise were corrected on a power basis, for the ground station noise already discussed, to obtain the satellite's noise. Since the 6-kmc input to the satellite is known from telemetry and the 4-kmc input to the ground receiver is known from direct measurement with the selective analyzer,* it is possible to refer the satellite noise to the satellite down-converter input by making the appropriate corrections. The results are shown at the top of Fig. 25.

Several features of these curves are of interest. The humps at 72 and 76 mc, 6 to 10 db above the general noise level, clearly correspond to the hump at about 2 mc in the baseband noise, Figs. 20 and 21, and to the peak at 1.7 mc in the baseband frequency response, Fig. 16. The presence of the two humps suggests that the noise is leaving the satellite as modulation of the carrier.

The general noise level, excluding the humps, is −159 dbm/cps ±2 db, corresponding to a noise figure of 15 db ±2 db. The inclusion of the noise humps results in an integrated noise figure of 16.5 db ±2 db (integrated over a 20-mc band), referred to the satellite's down-converter input. A separate measurement made prior to launch[6] using a noise lamp resulted in a satellite noise figure of 13.5 db ±1 db, for the region where the noise spectrum is flat.

It was stated in Section 7.1 that the baseband noise attributable to the satellite has not been affected by launch or space environment. The same conclusion is reached from a comparison of Fig. 25, for pass 1664, with Fig. 26, the calculated† pre-launch IF noise spectrum. The exact symmetry of Fig. 26 is due to the fact that these curves were calculated from measurements of baseband noise such as shown on Fig. 21, curve C. As expected, the peaks of the calculated noise of Fig. 26 lie between the levels of the measured, unequal peaks of Fig. 25.

VIII. NONLINEARITY AND CROSS-MODULATION

8.1 Envelope Delay Distortion

The envelope delay distortion (EDD) discussed here is that found in in the IF and RF circuitry of the system. It is to be distinguished from

---

* For this test, the 6-kmc carrier transmitted to the satellite is derived from a crystal-controlled oscillator. The stability of this source is sufficient to enable accurate measurement of the received 4-kmc carrier within the 100-kc band of the selective analyzer used.

† The measurement of noise at IF was not made prior to the launch of the Telstar satellite.
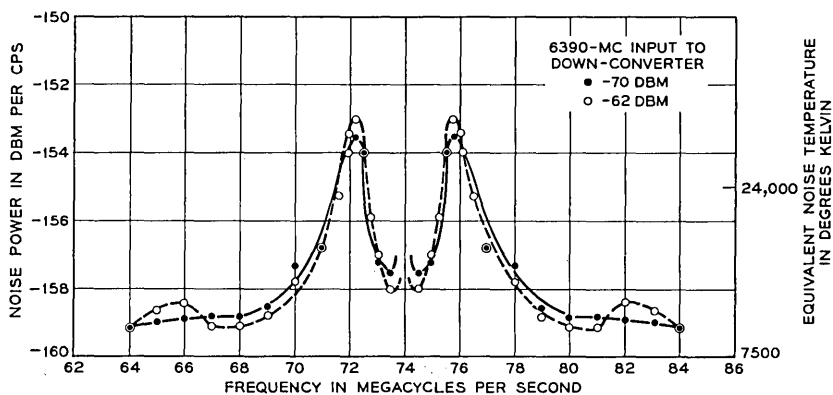
Fig. 26 — Pre-launch IF noise spectra of Telstar satellite referred to satellite down-converter input; calculated from baseband noise measurements.

the over-all baseband delay distortion of the system. This latter, which causes baseband waveform distortion, is of importance in the total baseband when transmitting TV and in individual segments of baseband when data-type signals are transmitted. Measurements of baseband distortion are not presented here for the Telstar satellite because available test equipment does not have adequate resolution in the presence of signal-to-noise ratios typical of those encountered in this experiment. It is inferred that it is satisfactory from examination of television test signal transmissions.

EDD, which causes cross-modulation in FM systems, is measured by the two-frequency sweep method, using the standard test set used on TD-2 and TH radio systems. The test set is located adjacent to the FM terminals, to which it is connected directly.

Briefly, this set operates as follows. A 100-cps sine wave is applied to the BO klystron of the FM deviator[5] so that the output IF sweeps from 62 to 86 mc. Simultaneously, a 278-kc sine wave from a crystal oscillator is applied to the video (baseband) input of the deviator to give a peak deviation of about 200 kc. At the FM receiver video output, the 100-cps and 278-kc signals are recovered and separated. The 100-cps tone is used for horizontal scope deflection. The 278-kc tone is phase-modulated by the transmission delay distortion of the system (at 278 kc, $1° = 10$ ns). Its phase is compared with that of a 278-kc crystal oscillator located in the delay receiver. The latter oscillator is phase locked to the long-term average phase of the received 278-mc tone by suitable circuitry. The phase variations are used for vertical scope deflection, with a customary EDD sensitivity of 5 ns per small division (0.2 inch). As may be seen

from the photos presented, the signal-to-noise ratio of this set is really not satisfactory for the Telstar system, but is not so poor as to obscure essential results.

Each of the elements shown in the block diagram of Fig. 1 contributes to the total EDD of the system. The EDD is mostly parabolic and is inherent in the bandpass characteristic of the system. Delay equalization provides the inverse characteristic and improves the cross-modulation performance of the system for telephone operation and the differential phase for TV operation. It is desirable to equalize each element individually, but this is frequently impractical.

On pass 925 (October 19, 1962) the over-all system was equalized. The equalization was in four parts, as shown in Table VI.

In the feedback FM receiver, the IF swing is reduced by the feedback to less than 1 mc, and therefore, its EDD is negligible.

Fig. 27 shows the measured EDD of the IF loop, which includes the equipment and equalizers of the first three items of Table VI. Fig. 28 shows the EDD measured through the boresight repeater and Fig. 29 shows the EDD measured through the satellite on pass 925.

8.2 *Differential Gain and Phase*

The differential gain and phase measurements are similar to the EDD test, but are specifically designed to measure the ability of a video system to transmit color TV. The details are therefore different. The low frequency is 15.75 kc and is adjusted to sweep the IF ± 7 mc (67 mc to 81 mc). The high frequency is 3.58 mc and is applied at a power level 14 db below that of the 15.75 kc. The test set is located in the test area where it is connected to the video lines. For this test, the low-pass filter and the diplexers of Fig. 2 are removed from the video lines, and

TABLE VI — EDD EQUALIZATION

Equalization for	Location	Amount of Eqn* (ns)
FM deviator	Output of deviator	†
Intermediate IF amplifier	Input of IF amp.	$-0.25(\Delta F) - 0.07(\Delta F)^2$
Standard FM receiver	Input of FM receiver	$+0.44(\Delta F) - 0.10(\Delta F)^2$
RF circuits, including modulator-amplifier, power amplifier, satellite repeater, and RF amplifier	Output of RF amp.	$+0.95(\Delta F) - 0.13(\Delta F)^2$

  * This is expressed as a power series, in which ΔF is the difference in mc from 74 mc.
  † This is a gain equalizer for the delay equalizer of the standard FM receiver and has negligible EDD.
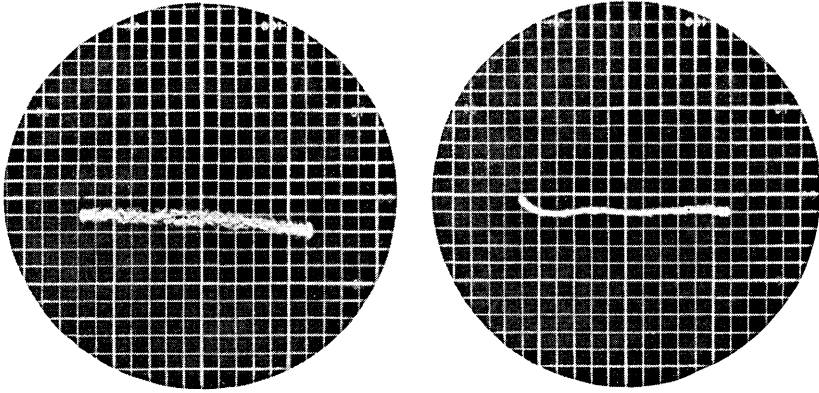
Fig. 27 — Envelope delay distortion of IF loop, Oct. 19, 1962. Left: FMFB receiver. Right: standard FM receiver. Horizontal scale: 1 division = 2 mc (sweep = 62–86 mc). Vertical scale: 1 division = 5 ns.
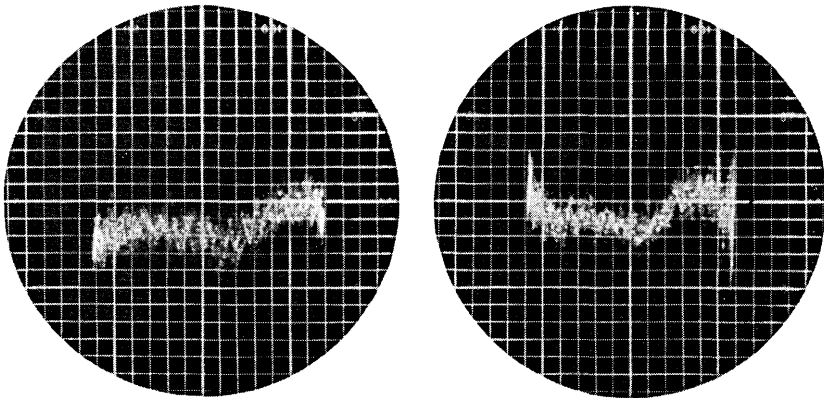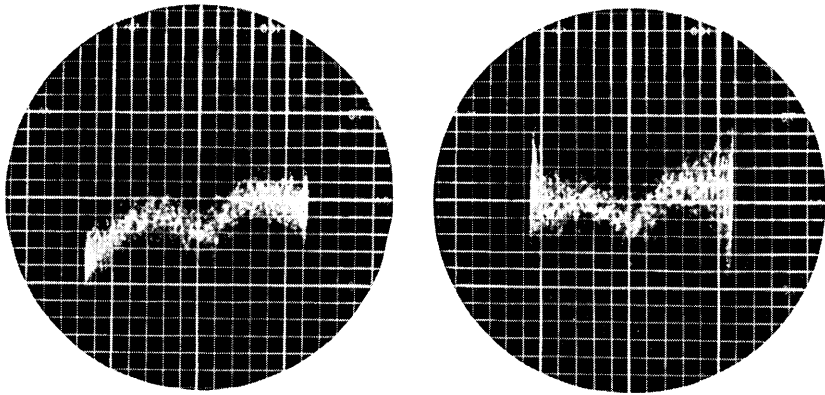

Fig. 28 — Envelope delay distortion of equalized loop through boresight repeater, Oct. 19, 1962. Left: FMFB receiver. Right: standard FM receiver. Scales same as Fig. 27.

only the standard FM receiver is used. At the receiving end, the recovered 15.75-kc tone drives the scope horizontally. Either the gain or phase variations of the 3.58-mc tone can be shown as the vertical deflection. Typically the sensitivity is 0.2 db and 1° per small scope division. The SNR of this test set when used with the satellite system is poor.

On pass 1113 (November 9, 1962) photos were made of the equalized system. Fig. 30 shows the results. The baseband loop has no discernible distortion on this test, and therefore no photo is presented here.

Fig. 29 — Envelope delay distortion of equalized loop through Telstar satellite; pass 925, Oct. 19, 1962. Left: FMFB receiver. Right: standard FM receiver. Scales same as Fig. 27.

8.3 Noise Loading

Noise loading simulates the operation of the system with 600 channels of multiplex telephony. The test set used for the noise loading measurements generates white noise in the band of 60 to 2660 kc and has slots cleared of noise at 70, 1248, and 2438 kc. With flat loading, the calculated normal TL at the test point is −18 db TL. The total noise power corresponding to the 600 telephone channels is −7 dbm. The system has an over-all net loss of 0 db, and therefore the receiving TL is the same as the transmitting TL. The noise loading equipment measures the total received noise power (sum of thermal noise and cross-modulation noise) in the noise slots. This is converted, for plotting purposes, into dbrn at the zero db TL point.

There is 5 db loss from the test area to the FM deviator input; hence, at nominal TL, the noise power at the FM deviator is −12 dbm. The deviator sensitivity is set so that 0 dbm of a sine wave gives 20-mc peak-to-peak, or 7.07-mc rms, deviation. Therefore, the rms deviation for nominal TL is 1.77 mc. By varying the applied noise power (the drive on the system) the rms deviation can be changed; this corresponds to changing the assigned TL.

Fig. 31 shows the results obtained on pass 1015.* When circuit noise is controlling, the SNR improves db for db as the drive (rms deviation) is increased. This accounts for the 45° down-sloping line at the left.

---

* At this time, one of the components of the equalizer for the RF circuit was defective and was removed, so that +0.5 ns/mc of EDD slope equalization was missing from the satellite loop. The measured EDD for this condition (taken on pass 1042, November 1, 1962) is shown in Fig. 32.
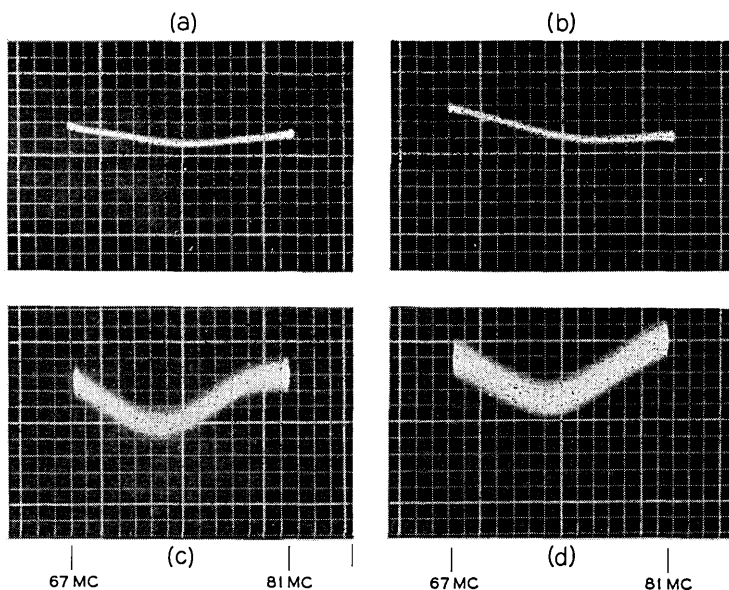
(a) (b)

(c) (d)
67 MC 81 MC 67 MC 81 MC

Fig. 30 — Differential gain and phase of equalized loops; standard FM receiver. Sweep: 67–81 mc. (a) Differential gain of IF loop. Vertical scale: 1 division = 0.2 db. (b) Differential phase of IF loop. Vertical scale: 1 division = 1°. (c) Differential gain of Telstar satellite loop; pass 1113, Nov. 9, 1962. Vertical scale: 1 division = 0.4 db. (d) Differential phase of Telstar satellite loop; pass 1113, Nov. 9, 1962. Vertical scale: 1 division = 2°.

However, as the drive is raised, the cross-modulation products increase 2 db per db for second order, 3 db per db for third order, and eventually become controlling. The very sharp upward break at the right shows that very high order modulation products are involved, indicative of severe overload or clipping.

Overloading (or overdrive) occurs when the peaks of the noise substantially exceed the design peak deviation. The peak deviation due to noise is 6 db higher than rms 5 per cent of the time, 9 db higher 0.4 per cent of the time, and 12 db higher 0.01 per cent of the time. For example, with a drive corresponding to an assigned −12 db TL at the test point, or 6 db above normal, the rms deviation is 3.54 mc and the peak deviation exceeds 10 mc 0.4 per cent of the time. At −9 db TL drive, the peak deviation exceeds 10 mc 5 per cent of the time and 20 mc 0.01 per cent of the time. The system bandwidths cannot accomodate such overdrives.

Fig. 33 shows noise loading curves for the IF loop. This shows the modulation break to be generated, to a considerable extent, in the
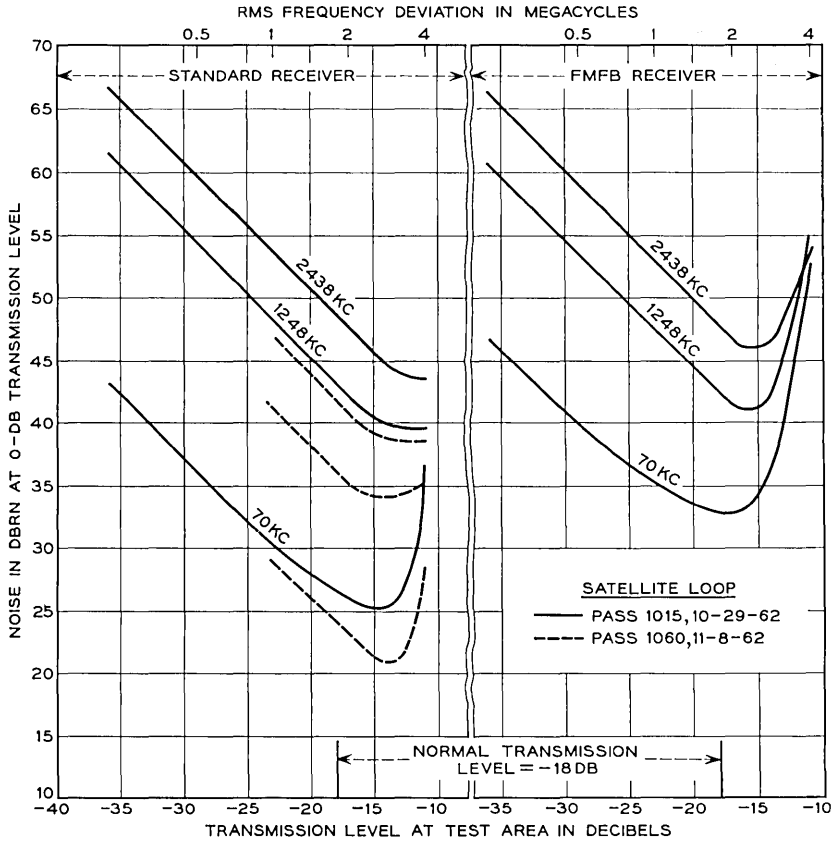
Fig. 31 — Telstar satellite loop noise loading measurement; passes 1015 and 1060.

terminal equipment. The FMFB receiver overloads sooner than the standard FM receiver since its noise performance at normal TL is nearly 10 db poorer than the standard receiver.

Since the video transmission system (Fig. 1) is also included in these tests, Fig. 34 shows noise loading performance of the baseband loop. This graph indicates that the baseband has third-order cross-modulation.

It appears from the noise loading data that for the EDD equalized system carrying 600 telephone channels and using the standard FM receiver, the contribution of cross-modulation to total system noise is small at the normal operating TL. Operation would probably be satisfactory at 3 db higher TL, giving 3 db less noise. The modulation break
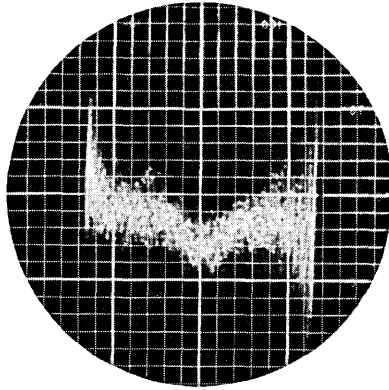
Fig. 32 — Envelope delay distortion of Telstar satellite loop with 0.5 ns/mc EDD equalization missing; pass 1042, Nov. 1, 1962; standard FM receiver. Scales: same as Fig. 27. Compare with Fig. 29, right.
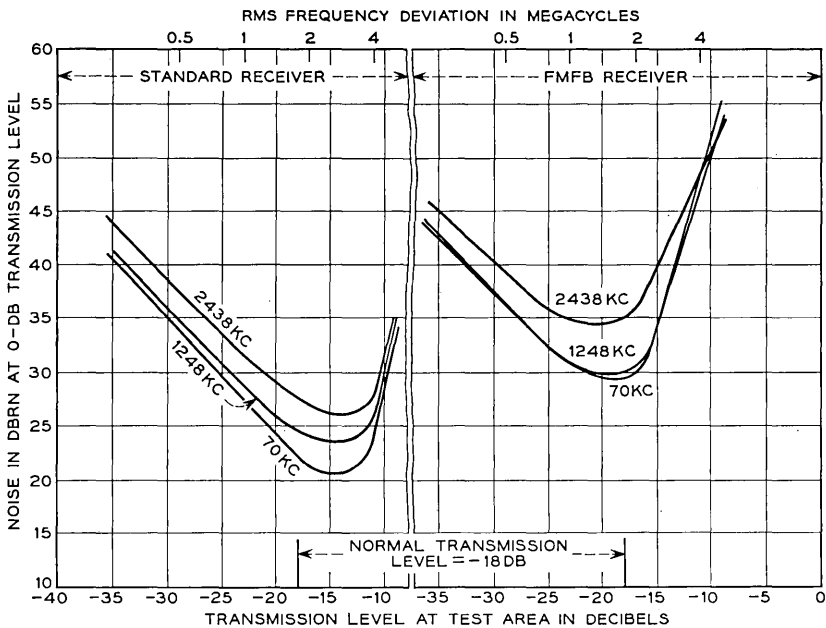
Fig. 33 — IF loop noise loading measurements, Nov. 1, 1962 (no pre-emphasis).

appears to be controlled by the video and IF equipment. However, the tests and calculations are based on telephone loading and take advantage of talker volume distribution and idle time. If a substantial part of base-band is carrying data service, the allowable TL will be reduced.
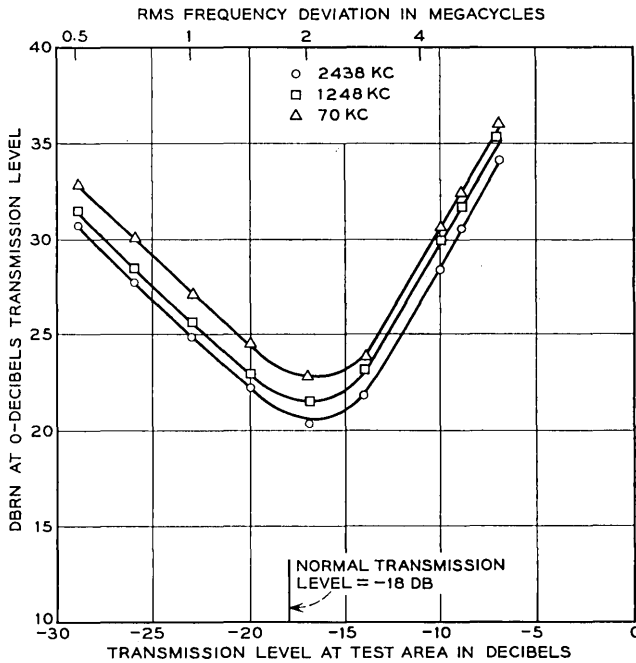
Fig. 34 — Baseband loop noise loading measurements, Sept. 27, 1962.

An acceptable value for channel noise at zero TL is 45 dbrn. Fig. 31 shows this to be exceeded by 3 db at 2438 kc. However, high-frequency noise is determined by the radio path. The dotted lines on Fig. 31 illustrate a noise loading test made during pass 1060 (November 3, 1962) when the range was about 1500 miles instead of the approximately 4000 miles for pass 1015. The channel noise performance therefore is a statistical process, and the data at hand are not sufficient to plot a noise probability distribution curve.

It is clear from Fig. 31 that the noise performance could be equalized across the band by the use of pre-emphasis. Tests have been made using the standard TD-2 pre-emphasis, shown in Fig. 35. The pre-emphasis and de-emphasis networks are patched in ahead of the FM deviator and after the FM receiver (see Fig. 1). Their total loss is a flat 14 db. This was compensated for by removing a 3-db pad in the transmitting line and 11 db of loss in the receiving line. Over the range of 60-2660 kc, the pre-emphasis network reduces the total noise power by 6.5 db with a resulting net power loss of 3.5 db in the transmitting path. Therefore, the normal TL at the test area is -14.5 db TL.
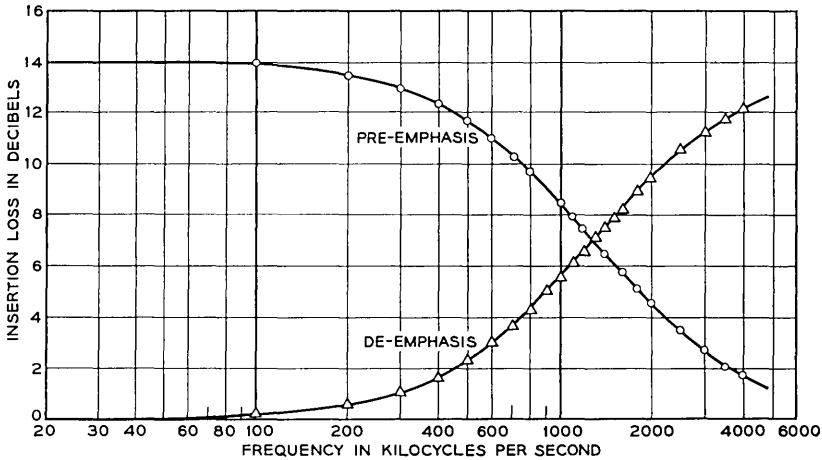
Fig. 35 — Insertion loss for telephony pre- and de-emphasis networks.

Fig. 36 shows noise loading measurements with pre-emphasis. These results show that TD-2 pre-emphasis is not the optimum for this system.

8.4 *Intermodulation: Video to Audio*

The audio noise measurements discussed in Section VII and shown in Fig. 22 are for the condition of no video signal being transmitted. When video material is transmitted, the audio noise increases. Presumably, the additional noise is due to cross-modulation (video-to-audio) due to nonlinearity of the over-all system. Tests of diplexers back-to-back show that direct interference due to power in the video signal at 4.5 mc is not significant, except possibly for the multiburst test signal.

Audio noise was measured repeatedly with no video present and also with a monoscope (Indian Head) signal. The 2-mc roll-off filter was omitted. No EDD equalization or video pre-emphasis was used in the system for this test. Examination of the data shows no clear correlation between audio noise and 6- or 4-kmc received carrier. Accordingly, the data for each pass have been averaged with the results shown in Table VII.

These data show the monoscope signal to give a weighted audio SNR of about 56 db. Tests made on early passes with other types of video test signals (multiburst, stairstep, window) showed the monoscope to have about as much effect as any. No audio to video cross-modulation interference has ever been observed, even under exaggerated laboratory tests.
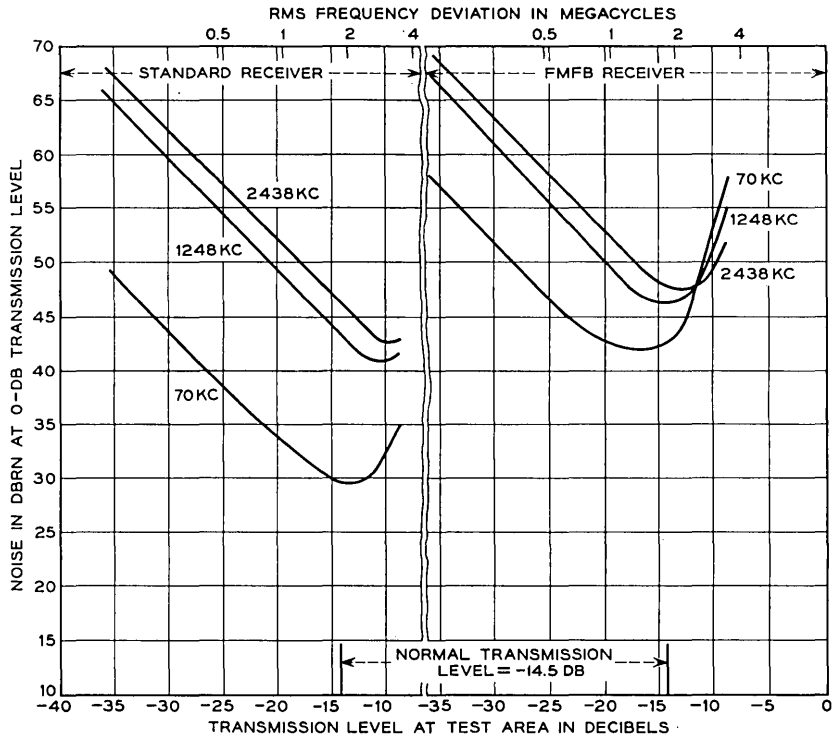
Fig. 36 — Telstar satellite loop noise loading measurements; pass 1016, Oct. 29, 1962 (with pre-emphasis).

IX. TELEVISION

Television transmission over the Telstar system has been highly successful for both monochrome and color signals. Most of the signal impairment which has been observed was expected and is in agreement with calculated performance. One type of impairment which was not anticipated is also reported here.

Probably the most noticeable signal impairment is some loss in picture definition. This is almost entirely attributable to the low-pass characteristics of the ground station equipment. The principal contributors are the 2-mc low-pass filter, the transmission characteristics of the 4.5-mc diplexers, and the roll-off in the FMFB receiver. This impairment was intentionally accepted in order to make possible the transmission of the audio signal as well as the video signal. As indicated by the baseband transmission characteristics presented in Section 6.1, the

TABLE VII — VIDEO-TO-AUDIO INTERMODULATION

Pass	FM Recvr.	Avg. Recd. Carr. (dbm)		Weighted Audio SNR*	
		6 kmc	4 kmc	No Video	Monoscope
316	Std	−61.5	−90	63	56
326	FB	−61	−89	61.5	55
341	FB	−61.5	−88	61.5	56.5
350	FB	−61	−92.5	60.5	56
350	Std	−62.5	−93	62	58
570	Std	−63	−91	60.5	57 (Monoscope)
					55 (Multiburst)

* SNR is defined in Section 7.3.2.

removal of the filter and diplexers and the use of the standard FM receiver eliminate this impairment.

A second impairment, also anticipated, was somewhat noticeable noise at maximum range. Under this condition the predicted (and measured) weighted signal-to-noise performance of the system is somewhat less than the normal Bell System objectives for commercial service. Typical values for the weighted signal-to-noise ratio have already been discussed in Section 7.3.

A third impairment, not anticipated, occurred during several of the demonstration transmissions from Andover to Europe. In these demonstrations, the transmitted signal originated in other parts of the country and was transmitted to Andover via the microwave radio system between Boston and Andover. Coincident with switches at the originating studio from one camera pickup to another, there were very annoying bursts of noise occurring in both the video and audio channels received over the satellite system. These noise bursts were not present in the signal applied to the ground transmitter. The difficulty was apparently caused by the transients which accompanied the switch from one signal to the other. In the signal as received for transmission at Andover, these appeared as relatively long (100 milliseconds or greater) negative pulses which were large compared to the normal peak-to-peak value of the video signal. Since the system itself uses a high-index deviation (14 mc peak-to-peak) in a 25-mc system bandwidth, these pulses were apparently large enough to cause the FM deviator to shift momentarily out of the 25-mc band. This resulted in momentary loss of signal at the various ground receivers, and the automatic gain control circuit increased the receiver gains long enough to cause substantial noise bursts in both the video and audio outputs.
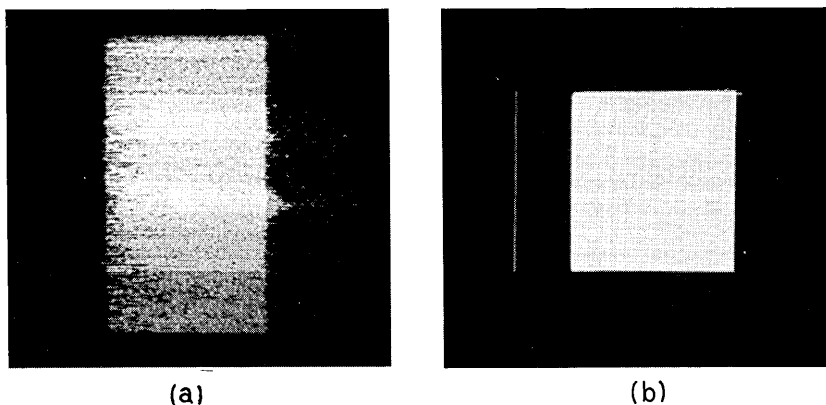
<div align="center">(a)   (b)</div>

Fig. 37 — First video signals from Telstar satellite; pass 6, July 10, 1962. (a) Noisy pulse and window; (b) clear pulse and window.

9.1 Early Transmissions

This section includes samples of some of the early picture material transmitted over the Telstar satellite. In all cases the television signal was a standard 525-line signal. The photographs were all taken at Andover using a standard picture monitor and oscilloscope and a Polaroid camera. A substantial amount of picture degradation has occurred in the reproduction processes, but the results are believed to be of sufficient historical interest to warrant their inclusion here.

Pass 6—July 10, 1962

During this pass the satellite repeater was turned on for the first time following the successful launch earlier in the day. Some of the significant events of this pass are recorded in Table VIII; the table explains the signals shown in Figs. 37 and 38.

Pass 15—July 11, 1962

On the following day the first television pictures were received from Europe. Fig. 39(a) shows the first signal received from France during pass 15 and Figure 39(b) shows a subsequent picture received during the same pass. The French material had been prerecorded on video tape.

Pass 16—July 11, 1962

A little less than three hours later the first transmissions from England took place. The first signal and a subsequent picture received from the

(a)
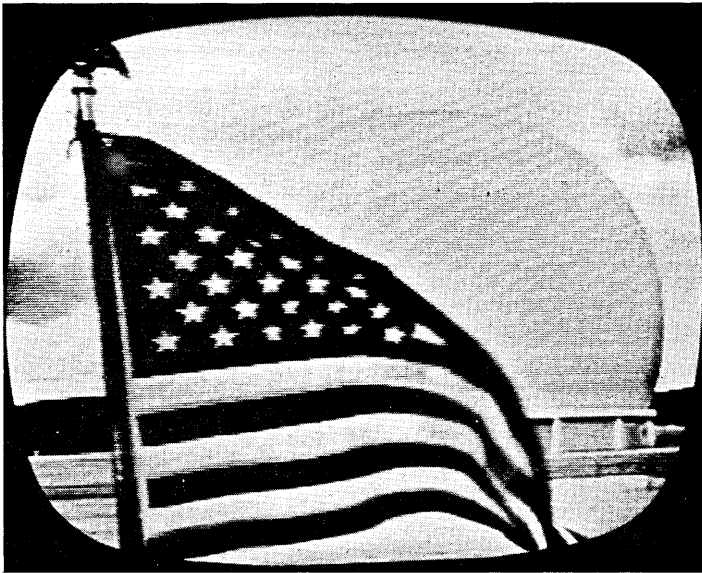
(b)

Fig. 38 — First public demonstration of television via Telstar satellite; pass 6, July 10, 1962. (a) American flag in front of radome; (b) Mr. Frederick R. Kappel.

TABLE VIII — SIGNIFICANT EVENTS — JULY 10, 1962

Time (UT)	Event
23:18	Andover command tracker acquires Telstar satellite.
23:20	Andover telemetry in synchronism. First command sent to turn on traveling-wave tube.
23:21	Second command sent to turn on traveling-wave tube.
23:23:36	Third and final command completed turn on of traveling-wave tube.
23:23:56	Precision tracker in autotrack.
23:24:34	Autotrack system for horn antenna in lock.
23:25:00	First video signal from Telstar satellite, a noisy pulse and window, received at Andover. Transmitter not yet at full power. [Fig. 37 (a)].
23:25:30	A clear pulse and window being received [Fig. 37(b)].
23:30	Start telephone conversation from Mr. Frederick R. Kappel, AT&T Board Chairman, to the Vice President of the United States, Mr. Lyndon Johnson.
23:33	Taped television transmission sent to Telstar satellite. The first received picture is shown in Fig. 38(a). The picture shown in Fig. 38(b) was taken about 2 minutes later.
23:47:30	Television pictures were received in France.

Goonhilly Downs station are shown respectively in Figs. 40(a) and 40(b). The picture material is from a live pickup at the Goonhilly station.

9.2 Color Television

Color television signals have been transmitted via the Telstar satellite on several occasions. The first such transmission took place during pass 60 on July 16, 1962, when several color slides were transmitted from the Goonhilly Downs station to the Andover station. A similar transmission took place during pass 88 on July 19. Photographs taken at the Andover station of the Goonhilly signals are shown in Fig. 41 (color plates, opposite p. 1614). In addition, several color slides were originated at the Murray Hill location of Bell Telephone Laboratories and were transmitted from Andover to Goonhilly Downs on this pass. Additional test transmissions in both directions took place during pass 178 on July 29, 1962. For all of these tests the 4.5-mc aural diplexers and low-pass filter were removed from the circuit and the standard FM receiver was used.

9.3 Two-Way Television

The first two-way transatlantic television tests were conducted during pass 142 on July 25, 1962, between the Andover station and the Pleumeur-Bodou ground station. Separate FM carriers were used for the two directions. The signal from Andover to Pleumeur-Bodou was trans-
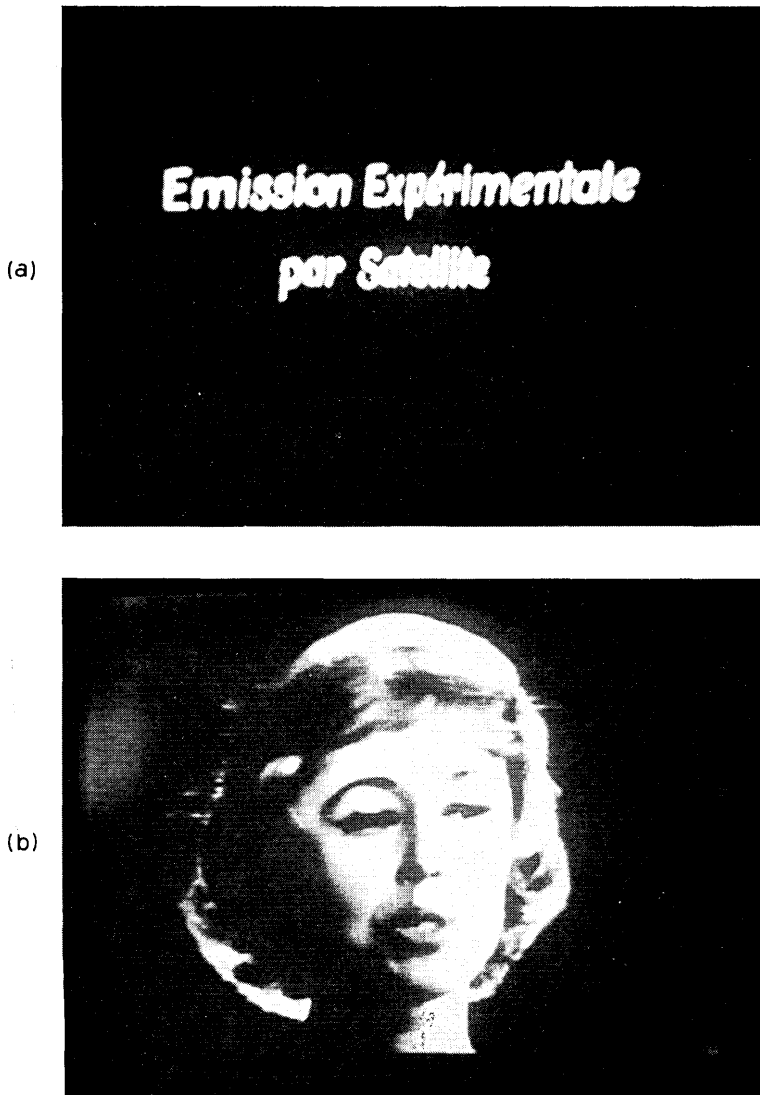
Fig. 39 — First television signals received from France; pass 15, July 11, 1962. (a) First signal received; (b) video tape transmission.

mitted at 6394.58 mc, or 5 mc above the nominal center frequency. The signal in the other direction was transmitted 5 mc below the nominal center frequency, or at 6384.58 mc. Fig. 42 shows a test pattern received from France during this test.
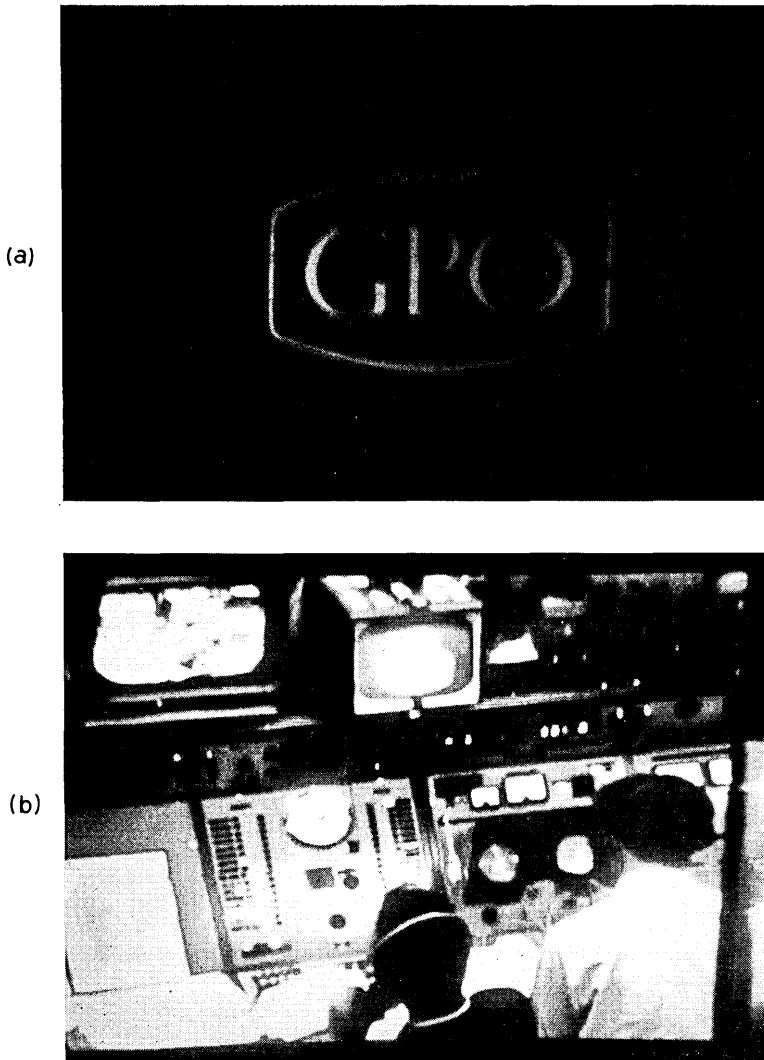
(a)

(b)

Fig. 40 — First television signals received from England; pass 15, July 11, 1962. (a) First signal received; (b) live video from Goonhilly Downs.

In addition to the simultaneous transmission in two directions, some two-way loop tests were made. Fig. 43 shows a photograph of video tape material after transmission to Pleumeur-Bodou, where the signal was looped and returned to Andover after traveling twice through the satellite repeater.

For these tests, IF bandpass filters 6 mc wide were used in both stations. The frequency deviation was adjusted to be approximately 2 mc peak-to-peak. Audio signals were transmitted in both directions by means of the 4.5-mc diplexers, but with definite degradation in audio quality.

A stabilizing amplifier was used to insert new sync pulses in the received signal. This resulted in definite improvement in the synchronization of the monitors.

In an attempt to optimize signal-to-noise ratios at the ground receivers, the ground transmitter power was programmed at both stations to provide -63 dbm at the satellite converter (assuming an isotropic antenna at the satellite).

The principal degradation to picture quality was noise, which was probably about 20 db poorer than in normal one-way transmissions. About 16 db was due to the reduction in frequency deviations from 14 mc to 2 mc peak-to-peak. The additional degradation was due to the reduced transmitter power per carrier at the satellite output. The ratio of peak-to-peak signal to rms noise was probably between 25 and 30 db. Crosstalk between channels was not noticeable.

X. TWO-WAY TELEPHONY

10.1 *Early Transmissions*

The Andover and Goonhilly Downs stations were arranged for two-way telephone tests for pass 24 on July 12, 1962. Transmission and noise were checked on each of the two-way channels. One of the channels was used as an order wire by technicians in the two stations to coordinate the test procedure. These tests indicated that a successful demonstration of two-way telephony could be expected on the following day.

During pass 33 on July 13, 1962, the first demonstration of two-way telephony took place between Kingston, New York, and Paris, France. The first call was placed by Mr. E. J. McNeely, President of the A.T.&T. Co., to M. Jacques Marette, Minister of Communications, and other French government officials. This was followed by other calls.

10.2 *Channel Noise*

Noise measurements in at least a portion of the telephone channels have been made on nearly all of the many two-way message transmissions. Typically, the channel noise has been in the range between 40 and 48 dbrn at 0 db TL, depending on the satellite range and the relative

power in the two signals at the satellite input. Although range information is available for all of the passes, the determination of the relative input power of the two signals is not possible during a normal transmission test. This is because the AGC circuit in the satellite responds only to the total signal. On pass 706 more complete data were obtained in an Andover and Pleumeur-Bodou test. By alternately turning off the two ground transmitters, their individual contributions to the input power at the satellite was measured and adjusted. In this way, it was possible to determine the noise in telephone channels of both carriers being transmitted by the satellite under known conditions. On pass 1014 a similar test was made, at which time the satellite range was substantially less. The results are shown in Table IX and are in good agreement with expected performance. Just as one would expect, when the power of one of the carriers is reduced at the input to the satellite, the noise increases for the channels on that carrier. At the same time, the other carrier gets an increased portion of the total power at the satellite output and the noise decreases in the telephone channels on the stronger carrier.

10.3 *Crosstalk*

The simultaneous amplification of the FM signals in the single satellite repeater gives rise to some crosstalk from one carrier to the other. No problems have been encountered in actual two-way telephone transmissions. However, the mechanism is such that with reduced circuit noise, intelligible cross-talk would occur from a particular telephone channel on one carrier to the corresponding channel on the other carrier. With sufficient noise, the crosstalk falls below the noise level and is not objectionable.

To evaluate quantitatively the crosstalk loss, specific tests were made such that the crosstalk could be measured above the background noise. The results of one such test made during pass 697 are included in Table X. The 6395-mc carrier transmitted at Andover was modulated with either a 100- or 200-kc sine wave. Peak frequency deviations of 1.0, 0.5 and 0.25 mc were used. A 6385-mc unmodulated carrier was transmitted by the Goonhilly station. At Andover the 100- or 200-kc modulation of the carrier received from Goonhilly was measured and compared with the modulation applied to the Andover carrier. The difference was recorded as the crosstalk loss.

Fig. 41 (Opposite page) — Color test signals from Goonhilly Downs to Andover; pass 88, July 19, 1962. ———————————→

British Post Office

BBC

EXPERIMENTAL

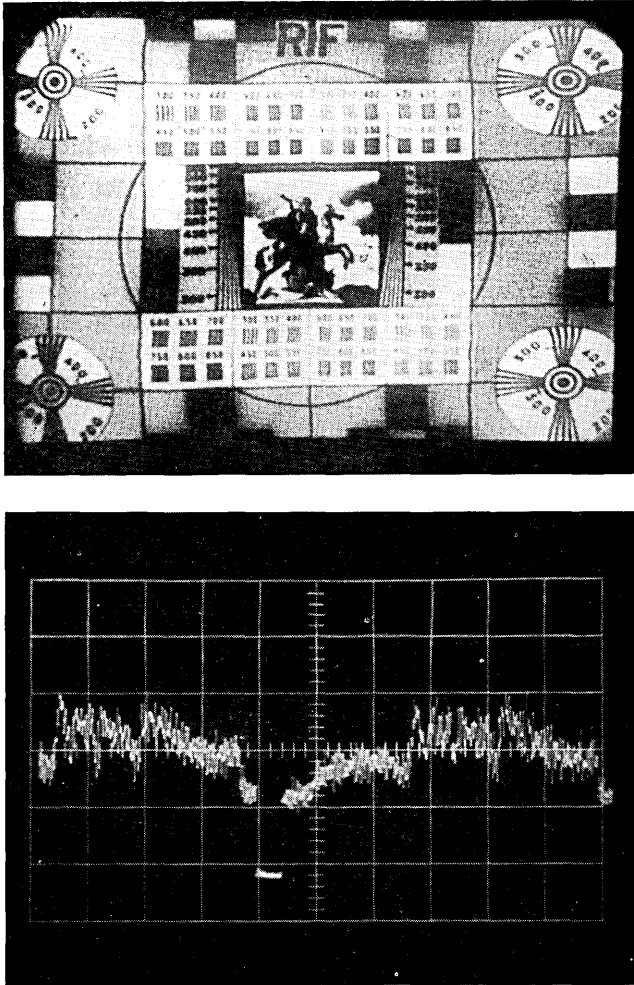COLOUR

TRANSMISSION

by Telstar Satellite
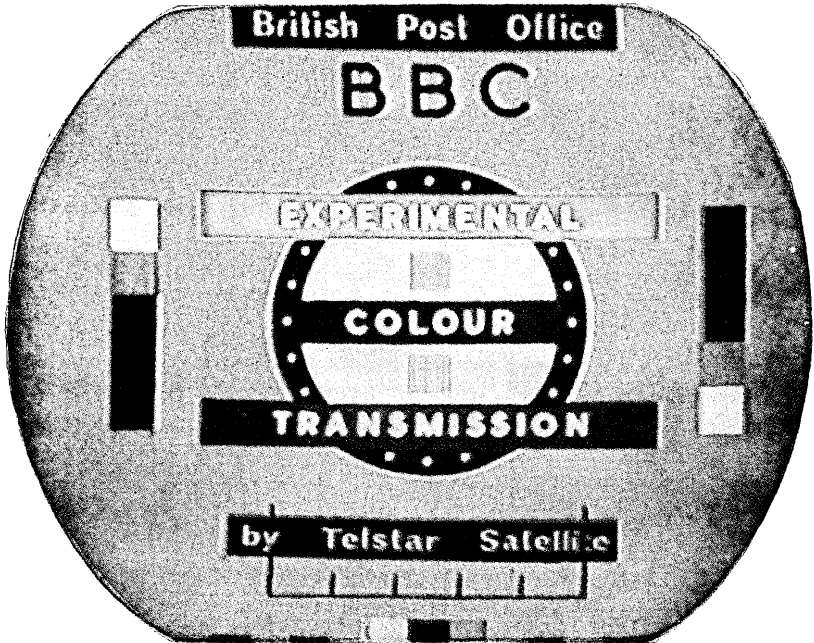
Fig. 42 — Signal received from France during two-way television transmission; pass 142, July 25, 1962. Top: test pattern. Bottom: oscilloscope presentation of individual lines.

XI. DATA TRANSMISSION

The suitability of the Telstar system for handling various types of data signals has been verified by means of tests ranging from the transmission of ordinary 60-wpm teletypewriter signals to 875,000 bit per second serial data, as well as various types of facsimile signals. Bell System data terminals were used for most of these tests. In order to
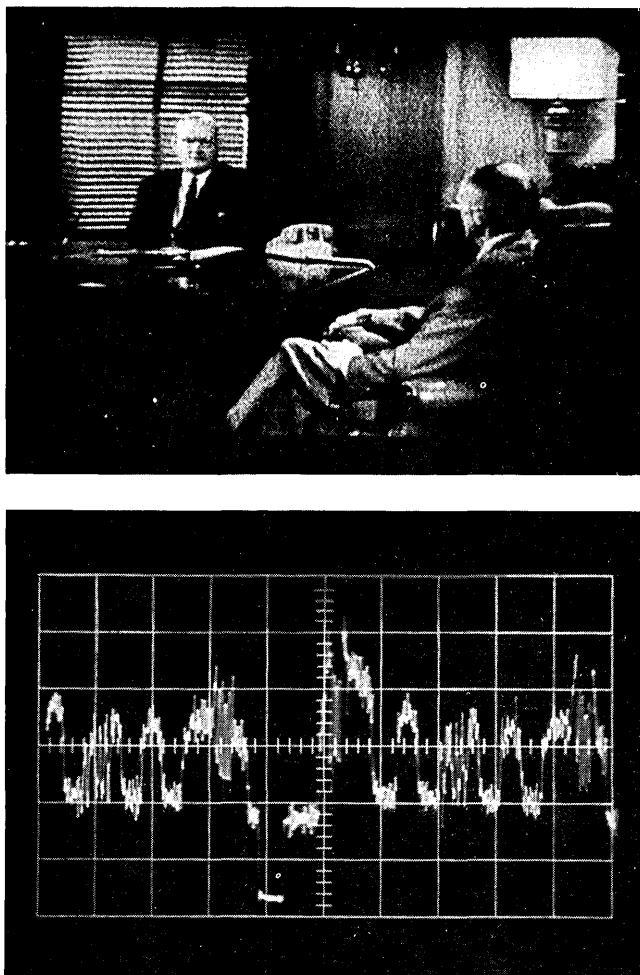
Fig. 43 — Television signal transmitted to France and returned to Andover; pass 142, July 25, 1962. Top: monitor presentation. Bottom: oscilloscope presentation of individual lines.

predict the performance of other signals and data terminals, basic transmission parameters in the voice-frequency band were also measured.

The transmission path for these tests included approximately 800 miles of land telephone circuits* in addition to that shown in Fig. 1,

---

* Most of the U. S.-based terminal equipment was located at 32 Avenue of the Americas, New York City. The tests described herein were principally conducted by personnel of the Long Lines Dept., A.T.&T. Co., from August 6 to October 18, 1962.

TABLE IX — TWO-WAY TELEPHONE NOISE

Pass No.	Time (UT)	Andover to Satellite Range (SM)	Signal Power at Satellite (dbm)		Telephone Noise (dbrn at 0 db TL)*				Received Carrier Power at Andover (dbm)	
			Andover Carrier	Pleumeur-Bodou Carrier	Andover Carrier		Pleumeur-Bodou Carrier		And. Car.	P-B Car.
					Channel 1	Channel 11	Channel 1	Channel 11		
706	15:54:30	3390	−65	−65	—	—	43.5	43.5†	—	−95
	15:56:30	3490	−65	−65	40.0	42.0†	—	—	−95	—
	15:59:30	3760	−68	−65	47.0	45.2†	—	—	<−95	—
	16:01:30	3850	−68	−65	—	—	43.0	43.0†	—	−94
	16:04:30	4030	−71	−65	—	—	42.0	42.0†	—	<−95
	16:08:30	4420	−71	−65	51.0	52.0†	—	—	<−95	—
	16:09:30	4470	−71	−65	43.0	44.0†	—	—	<−95	—
	16:10:30	4580	−65	−65	—	—	44.0	46.0†	—	<−95
1014	09:17:30	1800	−61	−61	—	—	36.5	36.0	—	−90.0
	09:18:30	1930	−61	−61	35.0	34.0	—	—	−85.8	—
	09:19:30	2070	−64	−61	37.5	36.0	—	—	−89.6	—
	09:21:00	2300	−64	−61	—	—	37.0	36.0	—	−88.4
	09:22:00	2460	−67	−61	—	—	36.0	35.0	—	−88.5
	09:24:00	2790	−67	−61	41.0	39.0	—	—	−96.0	—
	09:26:00	3120	−58	−61	35.0	34.5	—	—	−91.0	—
	09:27:00	3280	−58	−61	—	—	41.0	39.0	—	−101.0

* All measurements are with "C" message weighting except those denoted †, which are with 3-kc flat weighting.

TABLE X — TELEPHONE CHANNEL CROSSTALK LOSS

(Pass 697 — September 24, 1962)

Andover Carrier Power at Satellite (dbm)	Goonhilly Carrier Power at Satellite (dbm)	Frequency Deviation at Andover (mc)	Crosstalk* on Goonhilly Carrier	
			100 kc	200 kc
−70	−70	1.0	51.6	52.8
−70	−70	0.5	52.6	51.6
−70	−70	0.25	49.0†	50.5†
−64	−70	1.0	48.9	51.2
−64	−70	0.5	48.8	47.0
−64	−70	0.25	46.2†	47.2†
−73	−70	1.0	58.0	
−73	−70	0.5	55.4	
−73	−70	0.25	51.0†	

* Defined as the ratio of modulating signal on the modulated carrier to the received signal plus noise on the unmodulated carrier.
† The crosstalk was below the background noise level.

thereby simulating a typical service offering. Analysis of all the results of these extensive tests has not been completed to date. However, the analyses made indicate that the system performance is as predicted — in fact, very similar to a 4000-mile microwave radio relay system except

TABLE XI — SUMMARY OF DATA TESTS

Type of Test	Equipment	Signal or Modulation	Transmission Rate	Results
Low-speed digital	(a) 43A1 VF carrier terminals (b) 101B DATA-PHONE Data Set	Standard teletypewriter FSK	(a) 60 wpm, 5 level (b) 100 wpm, 8 level	Highly satisfactory. See Fig. 44 for per cent distortion on pass 914.
Medium-speed digital	63-bit word generator with either: (a) 202B DATA-PHONE Data Set (b) 201A DATA-PHONE Data Set	(a) FSK (b) Four-phase	(a) 1200 bauds (b) 2000 bauds	(a) See Fig. 45 for eye patterns, pass 542. (b) See Fig. 46 for eye patterns, pass 578. Eye patterns* indicate sufficient margin against errors. Error rates averaged better than generally accepted standards.
High-speed digital	(a) Bell System high-speed data terminal with IBM 729 magnetic tape units, a 1945 data transmission terminal and a 1401 computer (b) 301A-X1 data set† using as terminal equipment: (1) 63-bit word generator (2) IBM 729 mag. tape units, 7287 data trans. term., and a 1401 computer (c) Experimental high-speed data system‡	(a) Seven parallel double-sideband AM channels, each using a bandwidth of 480 kc and keyed at 62,500 bauds. (b) Four-phase (c) Four-phase	(a) 62,500 characters per second (b) 42,000 bauds (c) 875,000 bauds	(a) Some timing problems experienced due to changing absolute delay. Error-free transmission achieved for several minutes on pass 353. (b1) 69.5 million bits received error-free on pass 270. (b2) 2.8 million characters received error-free on pass 270. See Fig. 47 for eye patterns. (c) On pass 833, 970 million bits transmitted in 18.5 minutes with only one bit in error. Slight signal deterioration observed, probably due to change in slant range.¶ See Fig. 48.

* Eye patterns are formed by overlaying successive demodulated mark and space pulses before reshaping or retiming.
† The signals for these tests originated from Murray Hill, N. J. and were received at Holmdel, N. J.
‡ This test was conducted from Pleumeur-Bodou to New York City.
¶ The slant range to Andover varied from 2996 to 4809 miles during the test.

for the expected frequency shift due to Doppler effect and for the change in absolute time delay due to changing slant range. The test results were satisfactory to excellent. Doppler shift caused some distortion in low-speed data signals; however, transmission results were satisfactory. Changes in absolute time delay caused some degradation in high-speed data and facsimile transmission which can be compensated for in equipment design.

11.1 *Digital Data*

Table XI outlines the digital data tests made and summarizes the results obtained. Some further results are presented in Figs. 44 to 48. The results indicate that digital data can be successfully transmitted over the Telstar system.

11.2 *Facsimile*

Facsimile copy using both voice-band and broadband circuits were transmitted over the satellite repeater via landline facilities between New York and Andover.

Voice-band facsimile* was transmitted on pass 461 at keying frequency rates of 555 cps (60 rpm) and 1110 cps (120 rpm) over ordinary equalized L-type multiplex voice-band channels (nominal 4 kc). Envelope delay distortion was equalized to within 460 microseconds, while amplitude distortion was held to ±1 db over the band 1000 to 3000 cycles for the system. Fig. 49 shows a typical voice-band reception of an IRE test chart copied at 60 rpm. With the exception of a slight increase in noise evident in mid-gray tones, receptions copied at 60 and 120 rpm are subjectively equivalent to those copied over the facilities looped at Andover.

High-speed, two-tone facsimile,† utilizing a keying frequency rate of 675 kilocycles, was transmitted on pass 352 over the Telstar repeater via unclamped video facilities between New York and Andover. Figs. 50 and 51 are copies of portions of two consecutive transmissions conducted during a single satellite pass. Fig. 50 illustrates the result of employing an out-of-band transmitted synchronizing signal to drive the receiving drum motor. Some jitter is noticeable due to unfiltered low-frequency transients located in the landline facilities. Fig. 51 shows the results obtained when local (separate, stable) synchronization is employed. Here, frame skew due to the change of slant range (absolute

---

* Muirhead D-628-F, D-700-AM, DSB-AM, 1300-cps carrier.
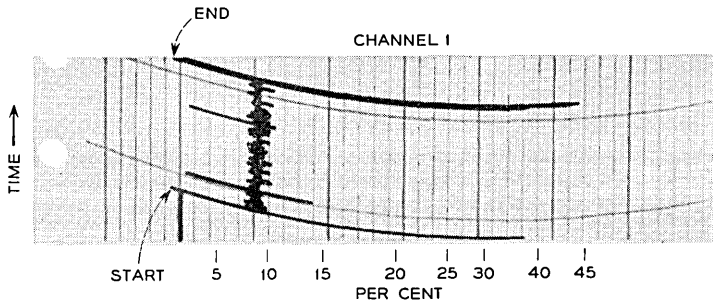† Westrex modified CTRT-5, DSB-AM, 2-mc carrier.

Fig. 44 — Per cent distortion vs time, using 43A1 VF terminals at 60 wpm from London to New York; pass 914, Oct. 18, 1962.
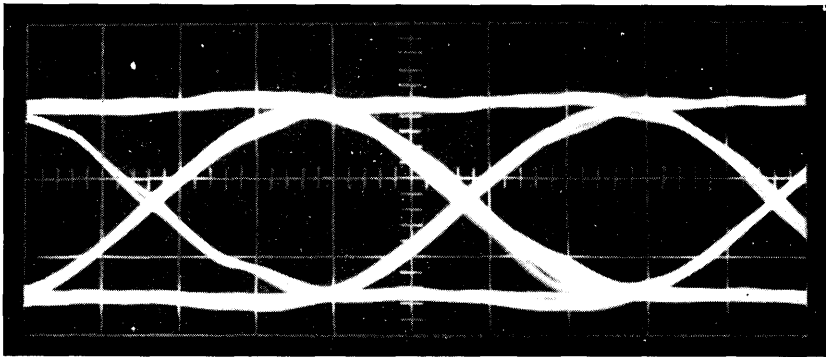

Fig. 45 — Eye pattern; 202B DATA-PHONE Data Set. Satellite loop, pass 542, Sept. 7, 1962.

delay change), is pronounced. This is to be expected at the 3000-rpm scanning rate of 675 linear inches per second.

It is concluded that transmission of facsimile signals via the Telstar satellite repeater, at both voice and video bandwidth rates, is entirely feasible. For wideband, high-speed systems, it will be necessary to utilize a transmitted synchronizing signal to eliminate frame skew in the recorded copy. Voice bandwidth systems require no change in operation.

XII. MISCELLANEOUS

This section includes a few tests not otherwise classified and one test in which the first measurements have been made only very recently and on which testing is still in progress.
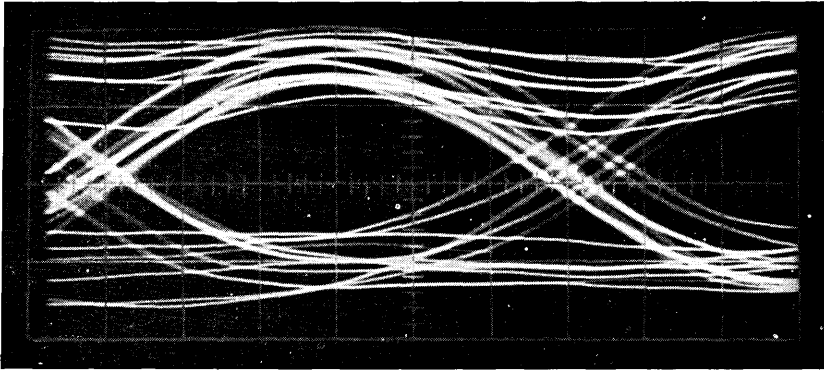
Fig. 46 — Eye pattern; 201A DATA-PHONE Data Set. Satellite loop, pass 578, Sept. 11, 1962.
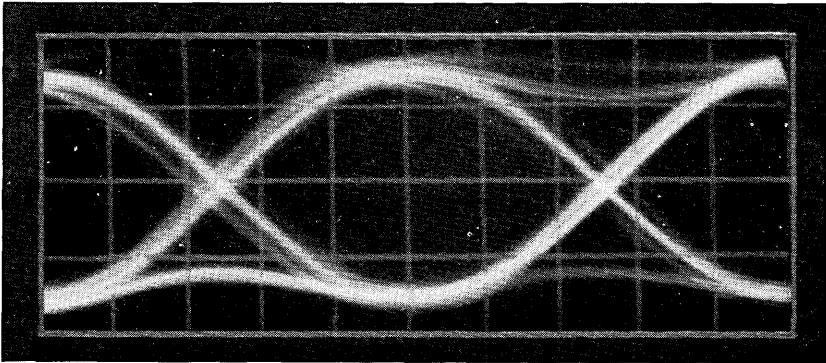
Fig. 47 — Eye pattern; 301A-XI Wideband Data Set. Satellite loop, pass 270, Aug. 8, 1962.

12.1 *Doppler Shift*

Fig. 52 shows measured and calculated Doppler shifts of the communications carrier in Andover and Goonhilly. Andover transmitted a crystal-controlled carrier at 74.13 mc, received it and measured the frequency in a counter connected to the 74-mc output of the IF amplifier. Goonhilly likewise measured the frequency at the output of the 70-mc IF amplifier. The measured frequency values were set to be zero at the same point where the calculated ones cross zero. This was necessary because zero-doppler is not known with this method. The measured and calculated curves agree to within 1 kc, and this occurs over a period of about 45 minutes.
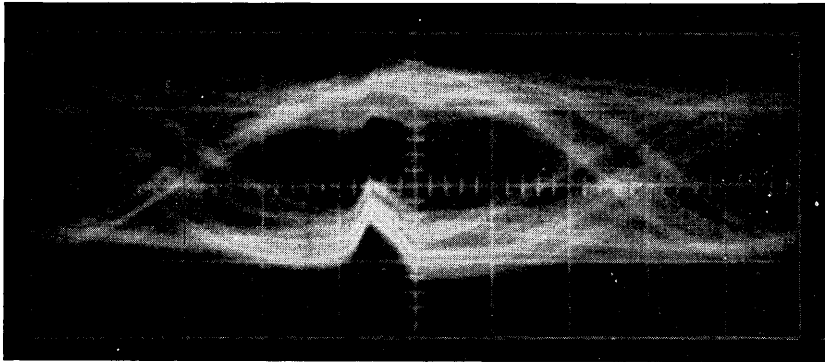
Fig. 48 — Eye pattern; experimental four-phase, high-speed data system. Pleumeur-Bodou to NewYork, pass 833, Oct. 9, 1962.

12.2 *Absolute Delay*

During most of pass 463, the signal delay in an Andover loop was measured. Fig. 53 shows the measured as well as calculated delays based on range information. A maximum error of about 20 microseconds or 2 miles was found.

12.3 *Time Synchronization*

On pass 424, the precision clocks at Andover and Goonhilly were compared by transmitting time pulses simultaneously in both directions. The accuracy of the method was believed to be about 20 microseconds, and a difference in clock time of 2 milliseconds was found. A more detailed description of the experiment is given in Ref. 7.

12.4 *Interference*

Measurements of propagation from potentially interfering TD-2 transmitters were made during October and November, 1962. Special crystal-controlled 4170-mc transmitters were located at the two nearest existing TD-2 stations and were equipped with antennas aimed directly at Andover. Study of the profile between Andover and West Paris, Me., 23.5 miles away, indicated that the controlling mode of propagation would be diffraction over a single obstacle about three miles from Andover. Study of the profile to Cornish, Me., 55 miles away, indicated that the controlling mode of propagation would be tropospheric forward scatter. These expectations were verified by the characteristics of the signal received at Andover. The signal from West Paris was very steady,
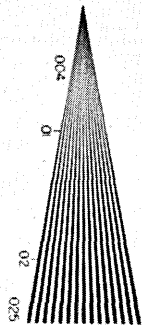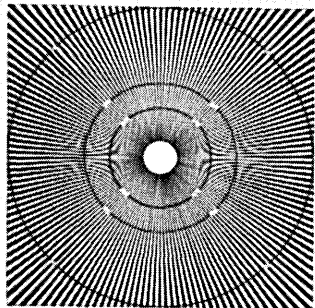
Fig. 49 — Voice-band facsimile transmission; satellite loop, pass 461, Aug. 29, 1962.

Fig. 50 — High-speed, two-tone facsimile; satellite loop, pass 352, Aug. 17, 1962. (Keying rate is 675 kc. Jitter is due to unfiltered transients in the landline facilities.)

with negligible long-term and short-term variations. The signal from Cornish, on the other hand, showed the very rapid fading characteristic of tropospheric forward scatter. The median signal from Cornish was within about 5 db of what had been predicted, taking into account the "gain loss" of the transmitting and receiving antennas. The signal from West Paris, however, was about 30 db less than had been computed on the basis of knife-edge diffraction. The actual diffracting obstruction was a mountain covered with pine trees.

About 100 hours of measurements of the signal from Cornish were made with the Andover antenna elevated a few degrees above optical horizon. Several short periods of enhancement were noted, usually during the early evening hours, in which the received signal rose as much as 30 db for a few seconds. Several one-hour recordings were made on antenna lobe peaks near elevations of 2, 4, 6, 8 and 10 degrees. No anomalous effects were observed.

During reception from West Paris, elevation sweeps from horizon to zenith were made during moderately heavy rainfall and during dry weather. The rain appeared to augment the received signal when the Andover antenna was elevated more than about 40 degrees, but the augmentation was only about 3–4 db. Several slow-speed azimuth scans

Fig. 51 — High-speed, two-tone facsimile; satellite loop, pass 352. (Frame skew is due to changing absolute time delay for the synchronizing signal.)

were made at several low elevations to define the "hot spot" at the true bearing of the interfering transmitter. At very low elevations the signal was increased in some directions, apparently by reflections from hills surrounding the Andover station.

Analysis of these data is continuing.

XIII. CONCLUSIONS

With economic, administrative, and hardware design considerations set aside and attention confined to technical transmission aspects, the Telstar satellite communication system is closely related to the FM microwave radio relay systems operating in the same frequency bands, i.e., the TD-2 and TH systems. The design parameters are somewhat different and subject perhaps to different state-of-the-art limitations, but the performance is just as predictable.

The communications tests show that the transmission performance of the Telstar satellite system is as good as or better than an equivalent length of the related land lines, when the satellite is visible to the terminal stations. Certain problems of great design importance in the land
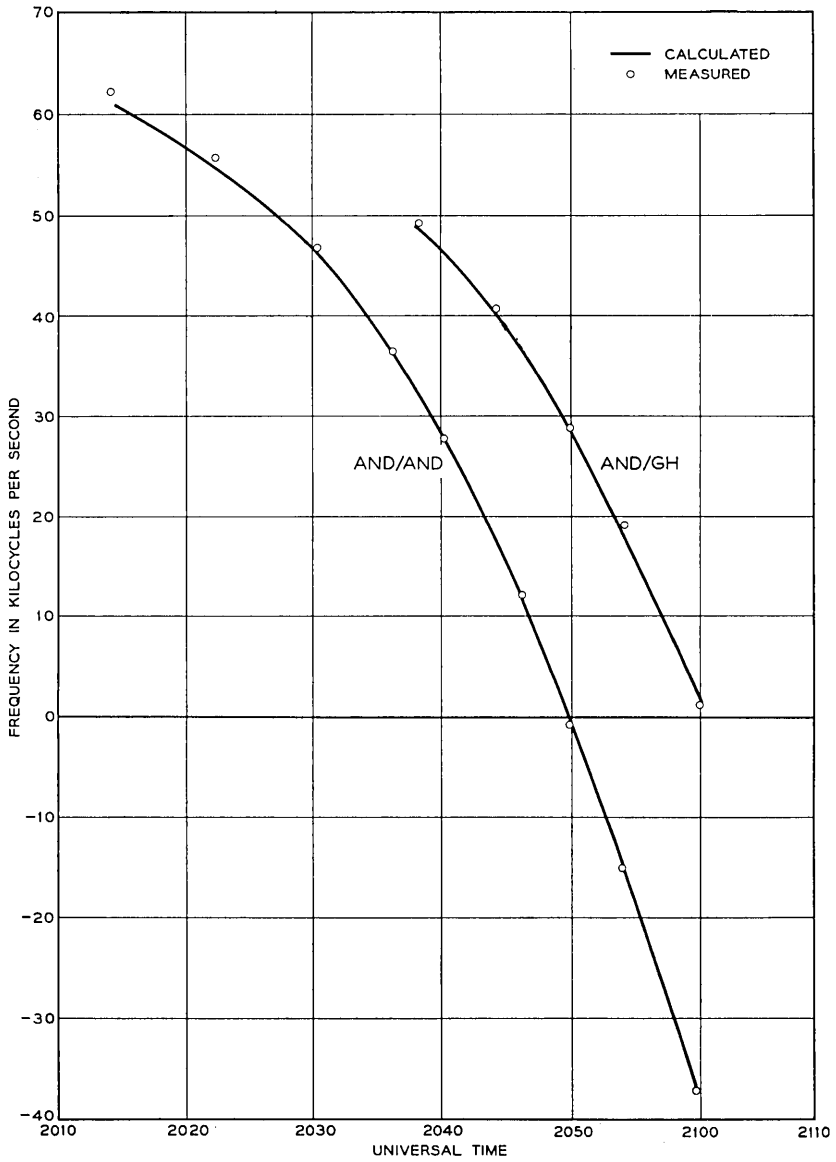
Fig. 52 — Doppler shift of communications carrier; pass 443, Aug. 27, 1962.
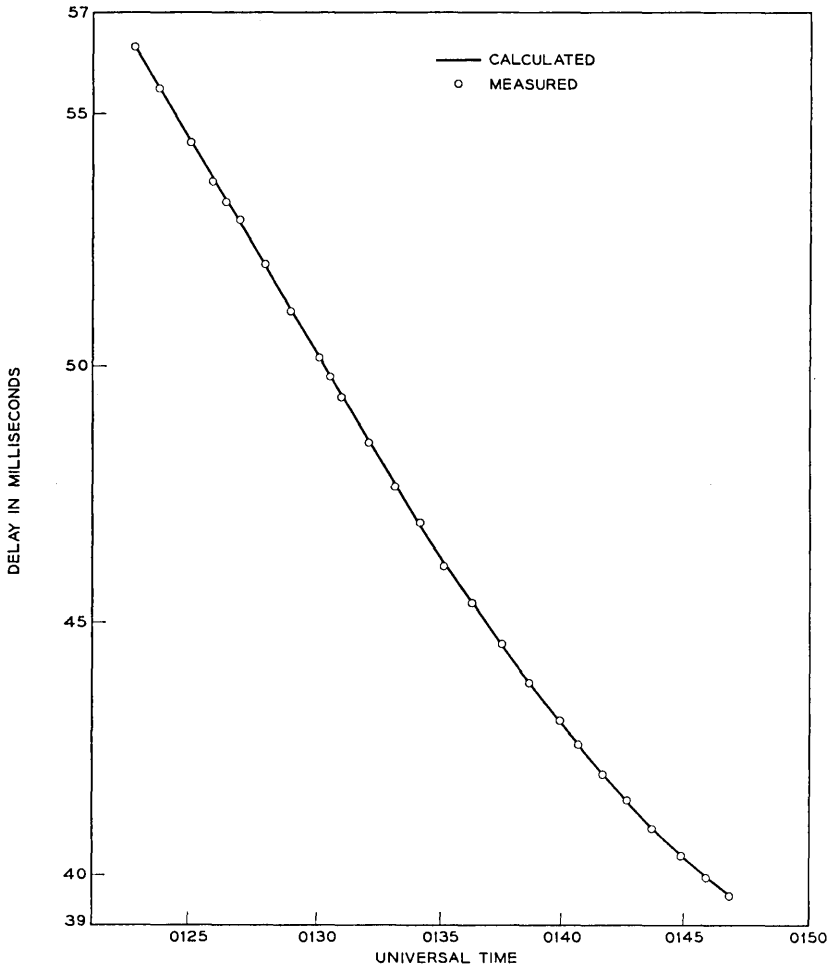
Fig. 53 — Absolute time delay of 5-μs pulse over satellite loop; pass 463, Aug. 30, 1962.

systems mentioned above are not present in the satellite system. These are (a) fading, (b) the need for highly accurate transmission equalization, and (c) the need for extraordinarily good frequency accuracy. The latter two arise from the large number of tandem relay sections in the landline systems.

On the other hand, some problems peculiar to a low-orbit satellite system are a direct result of its orbital nature, and are due to the vary-

ing range and spin angle. Although these variable parameters do not affect the transmission gain or delay distortion shapes, so far as is known, the variations in path loss do affect the noise performance. Although satellite spin (about its axis) is clearly seen on some of the recordings, there is no evidence to date of any effects on signal transmission. In addition, there are the Doppler and variable absolute delay effects to consider, particularly when transmission is transferred from a setting to a rising satellite; no tests were made on these effects.

XIV. ACKNOWLEDGMENTS

REFERENCES

1. Jakes, W. C., Jr., Participation of the Holmdel Station in the *Telstar* Project, B.S.T.J., this issue, p. 1421.
2. Recommendation No. 277, CCIR, 9th Plenary Assembly, Los Angeles, 1959.
3. Bangert, J. T., Engelbrecht, R. S., Harkless, E. T., Sperry, R. V., and Walsh E. J., The Spacecraft Antennas, B.S.T.J., this issue, p. 869.
4. Crane, R. E., Dixon, J. T., Huber, G. H., Frequency Division Techniques for a Coaxial Cable Network, Trans. AIEE, 66, 1947, pp. 1451–1459.
5. Giger, A. J., Pardee, S., Jr., and Wickliffe, P. R., Jr., The Ground Transmitter and Receiver, B.S.T.J., this issue, p. 1063.
6. Davis, C. G., Hutchison, P. T., Witt, F. J., and Maunsell, H. I., The Spacecraft Communications Repeater, B.S.T.J., this issue, p. 831.
7. International Time Comparison by Telstar, Electronic Engineering, 34, No. 146, October, 1962, p. 681.

The Command System Malfunction of the *Telstar* Satellite

By J. S. MAYO, H. MANN, F. J. WITT, D. S. PECK,
H. K. GUMMEL and W. L. BROWN

Loss of the command function of the Telstar satellite first occurred on November 24, 1962. There had been earlier indications of degraded performance. Facts are presented which led to the conclusion that the malfunction of the command system was due to surface damage to certain transistors in the redundant command decoders by the enhanced radiation in the inner Van Allen belt.

Correction steps have included laboratory experiments to gain a better understanding of the cause of failure, the use of continuous normal commands, commands transmitted from Johannesburg, South Africa, and specially modified commands to circumvent failure of the more vulnerable transistors. The operations which aided in the gradual rejuvenation of both command decoders are described. Also covered are the subsequent reappearance of the command system malfunction on February 21, 1963, and its correlation with the variation of the average radiation intensity seen by the satellite.

I. INTRODUCTION

After more than four months of successful performance, difficulties were experienced with the Telstar satellite command system. Early in the week of November 18, 1962, the command system became sluggish — the satellite responded only after a long string of continuous commands had been sent. Normally, a command is carried out as soon as it is received. On November 24, after five days of increasingly sluggish performance, the command system failed to respond.

There had been signs of deterioration earlier, which, however, did not affect command system performance. On August 7, about one month after launch, there was an indication that one of the redundant command decoders may have been operating intermittently. By August 21, failure of one decoder appeared to be complete. However, intermittent

operation of that decoder was again possible for a three-day period
during October.

A program was initiated to determine the cause of failure and the
action to be taken to recover the command function. Several steps were
taken as a result of this study and, on December 20, through the use
of modified command pulses, certain commands were executed by the
satellite. With the command function recovered (in a limited sense),
operations were performed on the satellite, and evidence suggests that
these operations aided in gradual rejuvenation of both command de-
coders. On January 3, 1963, with both decoders responding to *normal*
commands, the communications-experiment equipment in the satellite
was turned on and tests indicated normal performance.

This paper describes the stages of failure and recovery of the com-
mand system. An explanation is suggested for both failure and recovery
in light of the available evidence.

Complete failure of the command system again occurred on February
22, 1963. The pattern of malfunction in many ways resembled that of
late 1962. Detailed treatment is given of only those events which oc-
curred during November, December, and January.

II. COMMAND DECODER

The failure of the command system of the satellite was traced to the
command decoders through the examination of telemetry data. Hence,
a brief discussion of the command decoders, which are described in de-
tail elsewhere in this issue,[1] is in order here.

There are two virtually identical command decoders in the command
system. Each is driven by one of the two command receivers and each
drives a command switch unit, as shown in Fig. 1. Each command
relay is normally driven by both command switch units in parallel;
the design is such that a pulse from either or both command switch
units is sufficient to operate a relay. Thus, redundancy exists between
the input to the command receivers and the output of the command
switch units.

Several checks are available on the health of the redundant command
circuits: The AGC and output voltages of the command receivers are
telemetered. Also, two commands are used to disable the decoders.
T-1 command disables decoder 2 for 15 seconds and permits testing of
decoder 1; T-2 command disables decoder 1 for the same length of time
and permits testing of decoder 2. These and the 13 other commands are
described in Table I of Ref. 1. Information is telemetered, telling whether

or not T-1 or T-2 commands have been executed, as well as indicating the state of the relays in the command switch.

III. MALFUNCTION OF THE COMMAND SYSTEM

3.1 *Failure to Respond to T-2 Command*

The first indication of trouble in the command system of the satellite came on pass 260 on August 7 when there was no response to the T-2 command. On the next visible pass that same day, T-2 command was carried out in a normal manner. Table I shows the erratic response to the T-2 command between August 7 and October 21, when the T-2 command function had apparently failed completely. Note that there is a gap of approximately two months during which no acknowledgement of T-2 command was received.

Failure to respond to the T-2 command is not conclusive evidence that decoder 2 has failed. The same symptom could result from failure of command receiver 2, T-2 relay, or T-2 relay-state telemetry channel
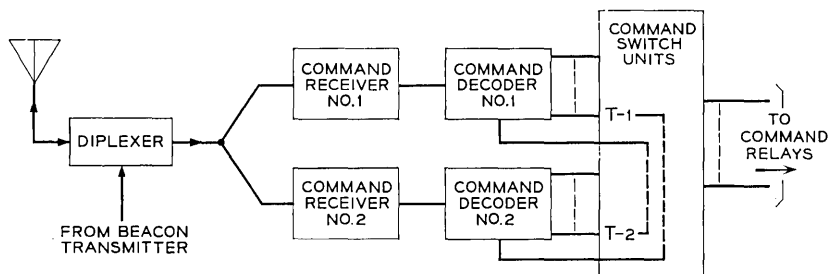
Fig. 1 — Block diagram of command system.

TABLE I — FAILURE OF DECODER 2

Date	Pass	Observation
Aug. 7, 1962	260	No response to T-2 command
	261	Normal operation
Aug. 8	268,9	No response to T-2 command
	270	Intermittent T-2 command response
	271	Normal operation
Aug. 9–20		Intermittent T-2 command response
Aug. 21		Decoder 2 apparently completely failed
Oct. 17–20		Intermittent T-2 command response
Oct. 21		Decoder 2 apparently completely failed

or of the circuits in the command decoders and switch unit associated with T-2 command.

3.2 *Gradual Failure of Command System*

Except for the difficulty described in the previous section, the command function was satisfactory until November 18; the response to commands from the ground appeared to be instantaneous. On November 18, however, it took 8 minutes before the satellite responded to a command. Delay between command and response became gradually greater and, on November 23, complete failure of the command system occurred.

The chronology of events of the week of November 18 is given in Table II. During this week, one important consistency was apparent: After the first command was executed on a pass, other commands were carried out immediately in a normal way, even if the first command took several minutes to go through. One can see from Table II that three different commands were used to bring about recovery (for at least one pass). The duration of continuous pulsing to bring about recovery gen-

TABLE II — THE WEEK OF NOVEMBER 18

Date	Pass	Duration of Commands Before Recovery	Command at Recovery	Successful Commands After Recovery	Final Command of Pass
Nov. 18	1203	8 min	T-1	DD, D, T-1	T-1
	04	0	—	A, AA, B, C, CC	AA
	05	0	—	A, AA, B, C, CC	AA
	06	0	—	T-1	T-1
19	1212	0	—	A, AA, B, C, CC	AA
	13	0	—	A, AA, B, C, CC	AA
	14	0	—	A, AA, B, C, CC	AA
	15	No commands sent	—	—	—
20	1221	No recovery	—	—	T-1
	22	2 min	A	A, AA, B, T-1	T-1
	23	20 sec	T-1	F, FF, T-1	T-1
	24	0	—	F, FF, T-1	T-1
21	1230	No recovery	—	—	T-1
	31	3 min	C	C, CC, F, FF, T-1	C
	32	15 sec	T-1	C, CC, F, FF, T-1	T-1
	33	0	—	C, CC, F, FF, T-1	T-1
22	1239	No recovery	—	—	T-1
	40	No recovery	—	—	C
	41	11 min	T-1	C, CC, F, FF, T-1	F
	42	3 min	T-1	C, CC, F, FF, T-1	T-2
23	1247	No recovery	—	—	—

erally decreased for succeeding passes on a given day. Increased degrada-
tion was apparent from day to day. Also, during a period when commands
were not executed, several different commands were sent with no
response; the failure appeared to be in the part of the decoder which is
common to all command channels.

When it was apparent that the command system was deteriorating,
care was taken to hold the satellite in the condition which would be
most useful in the event of failure of the command function. The com-
munications experiment could not be left on because, under that condi-
tion, energy would have been drained from the storage cells faster than
it would have been replenished by the solar plant. The resultant dropping
battery voltage would have automatically tripped the low-voltage
trigger circuit which disconnects the storage cells from the power supply
circuit* and turns off all circuits except the switching regulator in the
power supply, the command receivers, the command decoders, and the
two-year timer. Power restoration to all other circuits can only be
accomplished through use of the command system. Incidentally, the
action of the low-voltage trigger circuit is the same as that accomplished
by sending the SS command; knowledge of the function of this command
is essential to the understanding of Section V. The low-voltage trigger
circuit and the SS command control the same S relay.

Hence, during the week of November 18, care was taken to assure
that the satellite was left with the VHF beacon, radiation experiment
and telemetry circuits powered; the command system is permanently
connected to the switching regulator and always receives power except
when the S relay is open and the satellite is in darkness. Thus, even
without an operative command system, valuable information was re-
layed from the Telstar satellite; radiation field mapping data, battery
charging rate (from which solar cell quality could be ascertained), solar
aspect data, temperatures throughout the satellite, pressures and the
performance of the command receivers were among the useful pieces of
information received.

The failure of the command system which began on November 18
suggests that the T-2 command difficulty was indeed a failure of a
circuit common to all commands in decoder 2. The later pinpointing of
the exact failure in decoder 2 further supports this idea. Hence, most
of the time since launch, command signals were probably being inter-
preted only by decoder 1.

---

* There is an exception; the storage cells can be charged by the solar plant
through a diode.

IV. FAILURE MECHANISM

4.1 *Possible Causes of Failure*

The earth satellite environment creates a number of effects which should be suspected as possible causes of failure. The pertinent effects are enumerated and discussed in this section.

4.1.1 *Temperature Variation*

Because of the thermal design of the satellite, the assemblies within the electronics canister are subjected to relatively small temperature excursions. In particular, the temperature of the decoders has been between 22 and 37 degrees C since launch. During a given pass, the temperature of the decoders will vary by only one degree and may go up or down depending on the state of circuits in the satellite, solar aspect and the time of occurrence of an eclipse. The range of temperature is small and is well within the design limits of the decoders. There appears to be no correlation between temperature and the recovery of the command function during a pass.

One can hypothesize the following: The decoder circuit has failed because a component has deteriorated badly but can be made "good enough" if warmed slightly. Further, assume that one can heat the faulty component by means of the application of command signals to the decoder. In practice, the amount by which the temperature of a device can be changed by this method is only a few degrees. If one assumes, however, that the component in question is cool enough at the beginning of a pass so that the circuit has failed, then behavior of the sort listed in Table II might be explained. Final collapse of the command function could be attributed to further deterioration of the component. However, the data show that the deterioration is slow and that it does not correlate with decoder ambient temperature. Hence, one might suppose that the recovery is caused by a temperature variation which has been brought about by application of command signals, but that the damage itself results from some other effect. It is shown below that there is a much more probable cause of recovery.

4.1.2 *Eclipse*

Whether the satellite is in sunlight or the shadow of the earth greatly affects the temperature on the outer surfaces of the satellite. However,

the electronics canister is hardly affected by a single eclipse.* Study of the data has indicated that there is no correlation between the occurrence of an eclipse and the failure of the command system.

4.1.3 *Magnetic Field Variations*

The command switch unit drives nine magnetic latching relays. Satisfactory operation is achieved in the leakage field of the traveling-wave tube, which is as large as 10 gauss at some of the relays. The external magnetic flux density never exceeds 0.44 gauss. No evidence supports magnetic effects as the cause of decoder failure, especially since it would take a very strong magnetic bias to render *all* relays inoperative.

4.1.4 *Noise*

Galactic noise was considered as a possible cause of failure, but was ruled out because there were no indications of a noisy signal entering the decoder. Commanding under extremely noisy conditions usually results in the execution of incorrect commands, but there were no errors during the week of November 18. No unusual noise conditions were detected at the ground station during the period the command system was inoperative. Telemetry signals indicated that normal signals were entering the two decoders and that the command receiver AGC voltage was consistent with the range and aspect of the satellite.

4.1.5 *Aging*

Another possible cause of failure would be aging failure of a component. Even though very reliable components were used, the large numbers in this experimental model do raise the question of the statistical probability of such a failure. On the basis of estimated random failure rates under operating conditions of one in 10^9 component hours for passive components (largely resistors and capacitors), and 10 in 10^9 for semiconductor components, there results a 9 per cent probability of one component failure in the entire system or a 1 per cent probability of failure in each decoder in a four-month life. This is not consistent with the occurrence of two failures, one at even a shorter time, each occurring in the same portion of the system. Furthermore, the failure of the command system was gradual rather than catastrophic. Gradual failure would be expected if one component were undergoing a gradual

---

* Unless, of course, S relay is in the SS state. For this case, eclipse will turn off all circuits, including the command system.

change in characteristics and thus causing a circuit to become marginal. Since the components used were carefully screened under power aging conditions to eliminate those with drifting characteristics, only a catastrophic equipment failure is reasonable by residual random failure mechanisms. The absence of catastrophic failure points to the presence of a wear-out mechanism distinct from power aging.

4.1.6 Radiation Damage

Bulk damage to semiconductor materials by energetic particles, i.e., protons and electrons, is a well known phenomenon which leads primarily to degradation of minority carrier lifetime. This degradation is the failure mechanism for solar cells and must be considered for wide-base, low-frequency transistors. The effect is negligible for the diodes and narrow-base transistors used in the decoder. Therefore, this mechanism can be ruled out as an explanation for the failure.

4.1.7 Ionization Damage

Exposure of certain types of transistors to ionizing radiation can cause failure at radiation doses appreciably lower than those necessary to cause bulk damage.[2] Parameters which are dependent on the semiconductor surfaces, such as the collector reverse current or the transistor gain, will degrade gradually under radiation (with considerable variation in degradation rates among different transistors), and will typically recover temporarily to some degree when removed from exposure or when exposed with a reduced (or zero) collector-to-emitter voltage. Issuance of a command to the satellite turns some "off" (V_{CE} high, I_C low) transistors "on" (V_{CE} low, I_C high), and hence could cause recovery of those transistors. Recovery is not instantaneous with either voltage reduction or removal from exposure. Therefore, ionization damage could explain why (i) during the failure of decoder 1 during the week of November 18, delayed response to commands was observed, but once commands were obeyed, the command function was operative during at least that pass, and (ii) the temporary recovery of decoder 2 in October occurred during an experiment which involved continuous transmission of commands.

Since many transistors in the command decoder are of a type sensitive to ionizing radiation such as that encountered in the Telstar satellite orbit, it is reasonable to consider this phenomenon as a plausible cause of failure. In fact, since the other possible causes of failure do not satisfactorily account for the deterioration observed, ionization damage is

thought to be the most probable cause. The next section describes the evidence which supports this contention.

4.2 Radiation Effects

4.2.1 Ionization Damage to Transistors

The effect of ionizing radiation on transistors has been described in considerable detail.[2] It appears to result from the interaction of semi-conductor surface contaminants with gaseous ions produced in the transistor enclosure by radiation, and with electrical bias applied to the transistor. A few of the features of this effect, pertinent to the immediate consideration, are:

(a) Transistors encapsulated in a gaseous atmosphere are generally most susceptible to surface radiation damage.

(b) Parameters sensitive to surface states are affected; these parameters include I_{CBO}, h_{FE} and noise figure at low frequencies.

(c) Transistors removed from radiation will typically recover usable characteristics.

(d) A degraded transistor will tend to recover when the collector voltage is removed, or even reduced, while either in radiation or out of radiation. This recovery may be quite appreciable even within the first few seconds.

(e) Collector junction degradation rate is dependent upon the magnitude of reverse collector voltage, so that a marginal transistor may be more or less degraded, depending upon its voltage condition.

These effects were recognized while the Telstar circuits were being assembled. Where possible, units of the sensitive types were irradiated and the most resistant ones selected for use. Screening experiments indicated that pre-irradiation up to one tenth of the expected orbital dose could reasonably predict the behavior in orbit. However, test results had also indicated that the reliability of screening predictions decreases with increasing ratio between the actual and screened radiation levels. Because the average dose rate encountered in the Telstar orbit was found to be approximately two orders of magnitude greater than expected at the time of launch (see Section 4.2.2), and because only a part of the transistors in the command decoder were screened, ionization damage remains the prime suspect as the cause of circuit malfunction.

4.2.2 Radiation Intensity Seen by Telstar Command Circuits in Orbit

The radiation effects on the devices in the Telstar satellite are produced by the Van Allen belt, which is composed of energetic electrons and

protons trapped in the earth's magnetic field. The surface effects depend
only on the ionization caused by these particles inside a transistor's
encapsulation. Protons and electrons which actually penetrate the tran-
sistor's container contribute directly. In addition, there may be a con-
tribution from the bremsstrahlung, X-rays, created in stopping energetic
electrons. It is convenient to express the integrated radiation dose in
rads, a unit of energy deposited by the ionizing particle flux per unit
mass of material.* In principle, the dose is calculable for any location
in the satellite from a knowledge of the energy distribution of the particle
flux at the surface of the satellite and the shielding provided by the
satellite skin and frame, the wall of the canister housing the electronic
circuits, other components, etc. Only approximate calculations are fea-
sible in view of the complex geometry of the shielding in the satellite and
the incomplete information concerning the electron energy distribution.

The highest intensity in the inner Van Allen belt is around the mag-
netic equator of the earth and extends between about 1200 and 2500
statute miles above the earth's surface at the equator. The Telstar satel-
lite's orbit is in the region about 20 per cent of the time. Because the
earth's magnetic field which controls the motion of the trapped particles
is misaligned with respect to the earth's geographic axis, the particle
flux incident on the satellite varies from orbit to orbit. The daily aver-
age also varies as the apogee of the orbit precesses between its extremes
at 45° north and south latitudes with a period of 181 days. In addition,
of course, there are time variations of the radiation belt.

The estimated upper limit of the radiation dose contributed by ener-
getic protons in the region of highest intensity is illustrated in Fig. 2
as a function of aluminum absorber thickness. The radiation dose rate
is shown under the assumption of uniform shielding and exposure to a
uniform omnidirectional proton flux. For the decoders which are very
close to the surface of the electronics canister, the minimum shield thick-
ness is only about 0.1 inch of aluminum, but the solid angle for accept-
ance of particles through this thickness is between $\frac{1}{4}$ and $\frac{1}{2}$ of the total
4π solid angle. The curve applied to this case gives an orbital average
of between 5 and 10 rads per hour. The proton exposure of the satellite
has been quite close to the pre-flight estimate.

Trapped electrons can also contribute directly to ionization. For an
electron to reach the average component in the canister, it must have
an energy of more than 5 Mev, and for a circuit shielded by 0.1 inch
of aluminum, such as the decoder, the electron energy must exceed

---

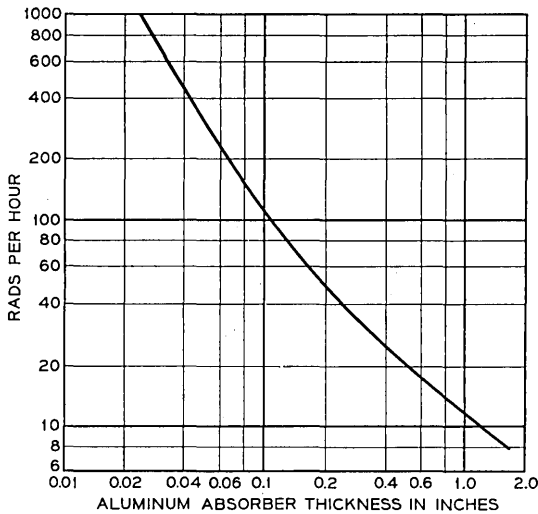* One rad equals 100 ergs of absorbed energy per gram of material.

Fig. 2 — The radiation due to high-energy protons in the peak of the inner Van Allen belt.

about 1.5 Mev. It was believed before launch that there were very few electrons with energies this high in the inner Van Allen Belt, and thus it was concluded that direct electrons were of no importance. Consequently, with the expected orbital average flux less than 10 rads/hour, which implied a total dose of 1.8×10^5 rads over the two-year expected useful life of the satellite, the screening dose for sensitive transistors was held to 1.4×10^4 rads.

From measurements by the Telstar and Explorer XV satellites, it has been concluded that a very substantial fraction of the electrons in the inner Van Allen Belt have energies above 1.5 Mev. In parts of the inner belt region, the energy distribution can be reasonably represented by an expression of the form $\exp -E/E_0$ where $E_0 = 1.2$ Mev. A large part of these high-energy electrons are believed to have been introduced by the high-altitude nuclear explosion of July 9, 1962.

The omnidirectional electron flux averaged over the first four months of the Telstar satellite's orbit is about 10^8 electrons/cm² sec. The radiation dose rate for electrons with this flux and the above spectrum is shown as a function of shield thickness in Fig. 3. The curve represents the radiation in the Telstar canister for shielding thicknesses small compared to that in the middle of the canister.* For transistors in the

* The curve includes the influence of the solar cells and the canister itself in reducing the effective solid angle for incident electrons. It also contains the effect of nonnormal incidence on the effective shielding.
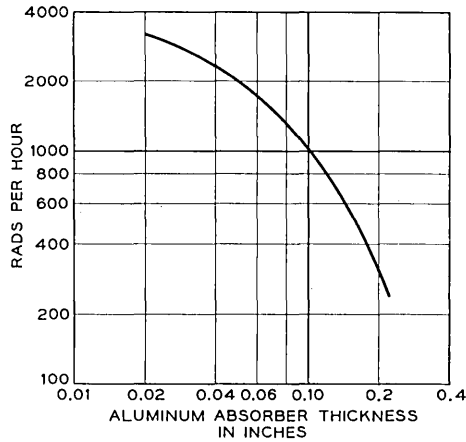
Fig. 3 — The average radiation due to high-energy electrons in the Telstar orbit.

decoder the dose rate due to electrons is approximately 10^3 rads/hour. The estimated dose rate due to protons is only 5 to 10 rads/hour. Hence the components in the Telstar command decoder have been exposed to approximately 100 times the anticipated radiation intensity, and the major contribution is not from protons but from high-energy electrons. It is believed that the peak radiation intensity could be as high as 10^4 rads/hour. The bremsstrahlung is insignificant in comparison with the direct electron effects.

4.2.3 *Transistor Ionization Damage Experiments**

Two kinds of experiments were conducted to evaluate the hypothesis that radiation was the cause of command decoder malfunction and to pinpoint the problem areas in the circuit with the ultimate hope that some corrective action could be taken. Transistors of the same code as those used in the decoders were cycled in a radiation field (gamma rays from a cobalt 60 source) with a period about the same as the Telstar satellite orbital period. Also, complete command decoder circuits were subjected to gamma irradiation. These experiments confirmed what was already known about surface ionization damage, summarized in Section

---

* The experiments described in this section are a direct extension and application of experience gained in work on surface effects of radiation in semiconductor devices, a part of which was performed under contract with Electron Technological Laboratories, Aeronautical Systems Division of the United States Air Force Systems Command.

4.2.1, but the data obtained were more directly applicable to the Telstar command problem.

Since there is a very large variation in radiation damage for different transistors of the same code and because the experiments did not duplicate the environment of the transistors in orbit,* the conclusions are qualitative or, at most, quasi-quantitative. The following statements can be made regarding the radiation-sensitive transistor type used in the command decoder, which is a nitrogen-filled diffused silicon npn unit.

(i) Those units which were heavily degraded in the high-intensity field partially recovered in the low-intensity field. The time constant for I_{CBO} and h_{FE} degradation ranged from 1 to 20 minutes; recovery has logarithmic time dependence. Typical cycles are shown in Fig. 4 for a transistor which had been pre-irradiated to degrade I_{CBO} from a few nanoamperes to several microamperes.

(ii) Short-term reciprocity does not hold; i.e., during cycling tests it was apparent that a given total dose applied at a fast rate caused more degradation than the same dose applied at a slower rate. Note from Fig. 5 that 3.6 hours at 4.5 kilorads per hour induce less effect than 1 hour at 16 kilorads per hour, although the total dose is the same for both cases.

(iii) Removal of power from the device during cycling resulted in temporary improvement, and the improvement was generally greater if power was removed during the high-intensity interval. The degree of memory of this improvement varied widely from one transistor to another.

Although irradiation tests on an actual command decoder are less useful from a statistical point of view than the experiments conducted with individual devices, they offer the possibility of focusing attention on vulnerable areas in the circuit and can possibly bring to light certain subtleties which might be overlooked in a perusal of circuit diagrams. Two command decoders (referred to here as decoder A and decoder B) were irradiated, both at high intensities (0.68 and 0.34 megarad per hour) to cause early failure; then decoder A was disassembled to study the failed component, and decoder B was placed in a low-intensity field (500 rads per hour) to study various recovery techniques. A summary of the results of these tests follows:

(i) Decoder A failed at a total dose of 2.3 megarads. (If reciprocity were to hold between time and dose rates, then this total dose would

---

* In most of the experiments the units were cycled between a level of 10 kilorads per hour for one hour and 30 rads per hour for one and one-half hours. This high average dose rate (5 kilorads per hour) was used to accelerate deterioration.
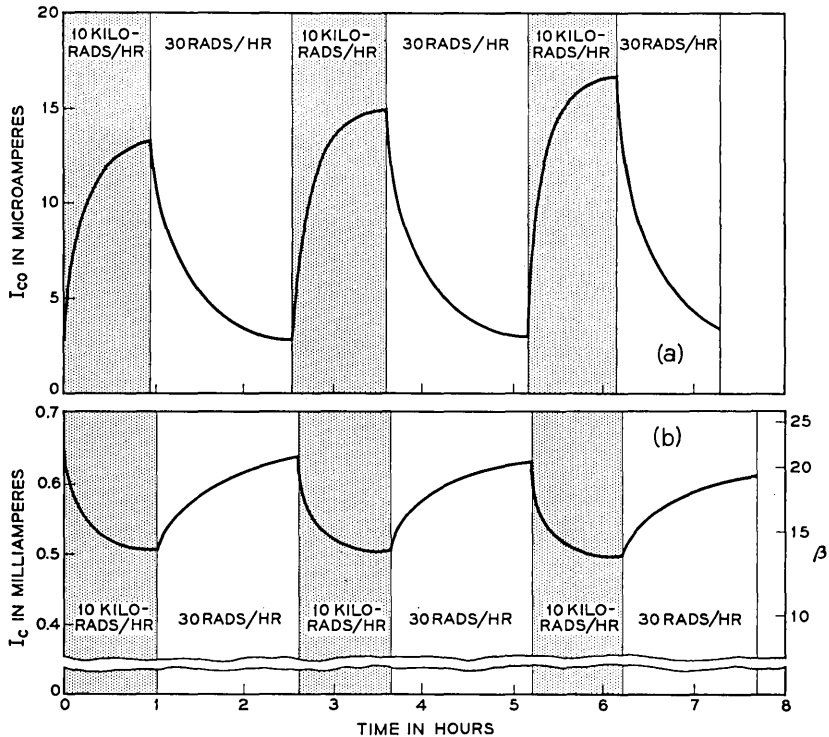
Fig. 4 — Leakage current and gain of a transistor cycled between high and low radiation field intensities.

correspond to 26.5 years at 10 rads per hour or 3.2 months at 1 kilorad per hour.) Up to this dose level, continuous commands had been sent to the decoder and some degradation (but not failure) had been observed. Failure occurred immediately after the continuous commands ceased, which indicates that the commanding had retarded failure.

When the circuit was removed from radiation, it recovered and operated satisfactorily.

The failure was traced to low h_{FE} in the "zero" digit gate transistor, which, because of its load configuration, had a turn-on time which was too slow to advance the digit counter.[1] Measurements on the device confirmed the diagnosis.

(ii) For tests on decoder B, commands were sent only intermittently until failure had occurred. The failure occurred at a total dose of 0.62 megarad (7 years at 10 rads per hour; 25 days at 1 kilorad per hour). The decoder did not respond to the first of a continuous train of com-
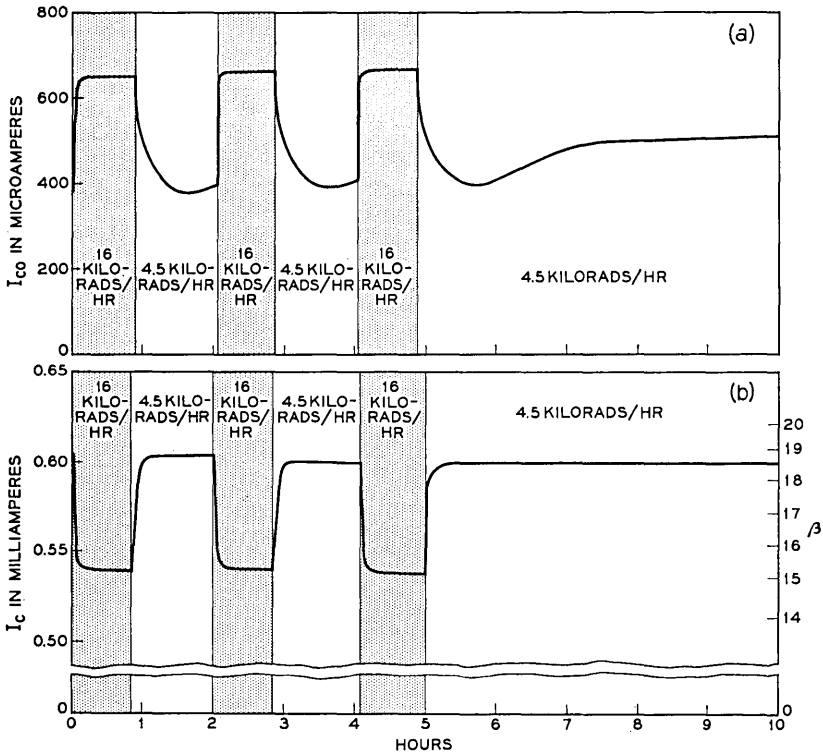
Fig. 5 — Leakage current and gain of a transistor cycled between two high radiation field intensities.

mands, but did react properly to all succeeding commands. (Each command lasts about 0.1 second.)

Deterioration was gradual: Continuous commands caused recovery in 2 seconds at a total dose of 2.4 megarads and in 14 seconds at a total dose of 4.0 megarads.

Even after the command decoder had received a total dosage of 10 megarads, recovery occurred when it was removed from the radiation field.

The failure occurred in the shaping network which controls the pulse generator.[1] The pulse generator, a gated astable circuit, is held off most of the time by the shaping network, but due to increased I_{CBO} of either the first or the second stage of that circuit,* the astable circuit became free-running, independent of the decoder input signal.

---

* See Appendix Sections A.2 and A.3.

(*iii*) After a total dose of 10 megarads at the high dose rate, decoder
B was placed in the low-intensity field (500 rads per hour). Failure again
occurred, but the malfunction was not in the shaping network. The
trouble, which occurred at an additional exposure of about 0.3 megarad,
was traced to the one digit gate, which has several output functions.
One of these, which is the resetting of the timer circuit, was not being
performed by the digit gate.[1]

Eventually the shaping network did fail in the low-intensity radiation
field. However, since the total exposure to cause this failure was much
greater for the low-intensity field than for the high one, it is suggested
that either an out-of-radiation recovery mechanism exists or that de-
terioration is rate-sensitive for some transistors.

Continuous commands, power removal or extraction of the circuit
from the radiation field could bring about recovery of the circuit.

4.2.4 *Ionization Damage as the Cause of Failure*

Two significant facts which pertain to the failure are apparent from
the previous three sections: (*i*) High radiation dose rates were en-
countered by the satellite prior to the failure of the command system,
and (*ii*) the gradual failure with temporary recovery after a successful
command is consistent with the kind of failure observed in the labora-
tory when transistors were irradiated.

In addition to their usefulness in pinning down the cause of failure,
the data described above also helped lead to the recovery of the com-
mand function. The action which was taken to this end is described in
the next section.

V. RECOVERY OF THE COMMAND SYSTEM

5.1 *Corrective Measures*

Since previous tests had provided evidence that either reduced radia-
tion field or voltage removal from certain transistor stages might lead to
recovery of the command function, certain corrective steps were taken.

5.1.1 *Turning "Off" Transistors "On"*

The command decoder is basically a digital logic circuit and, as such,
contains mostly transistor and diode stages which are normally in
either a "conducting" or "nonconducting" state. When a command
pulse train is being interpreted by the decoder, its stages alternate one
or several times between these states, and the majority of them end up

in a particular state at the end of each command pulse train. There are, however, several circuits whose resting state is a function of the last received command signal. Out of the 34 transistors of the radiation-sensitive type in each decoder, 24 can be controlled to be "off" (high V_{CE}, low I_C) or "on" (low V_{CE}, high I_C). Any of the 24 transistors could have been triggered into the more desirable "on" state (from the standpoint of radiation damage), and, of course, if it had been known that a particular one of these devices was the cause of malfunction, such action would have been taken. Even though response to commands would not be expected initially, the healing effect of reduced V_{CE} might have led ultimately to recovery. Unfortunately, no device could be "tagged" as the most probably faulty one,* and further, acquisition of the more desirable state by one device usually resulted in forcing an adjacent device into the "off" state. Several experiments, which were designed to control the states of the various stages, were carried on over a period of three weeks, but to no avail.

5.1.2 Continuous Commands

Although the command function was inoperative, it was felt that some benefit could be gained from sending continuous commands from the ground terminals whenever the satellite was in view.† The probability was high that such action would reduce the average V_{CE} applied to the damaged transistors. Command signals were designed to benefit particular transistors; e.g., a train of signals consisting of "ones" only was sent to exercise optimally the one digit gate. A number of such commands were tried, all with no success, in attempts to "heal" the satellite after the command failure.

5.1.3 Commands from Johannesburg

The normal operating procedure called for issuance of commands from Cape Canaveral, Florida, or Andover, Maine. However, at the time of the failure of the command system, the apogee of the orbit, at which the radiation field is at a minimum value, was in the southern hemisphere and was not visible to either normal command station. The NASA command and telemetry station at Johannesburg, South Africa, was selected as a third Telstar satellite command terminal. In addition

---

* Examination of the data taken during the week of November 18 was carried out to see if any correlation between the last command sent and depth of recovery existed. No conclusive correlation was apparent.

† That recovery can be brought about with continuous commands had been demonstrated in the laboratory. See Section 4.2.3.

to the advantage of apogee visibility, it also had sight of the satellite as it passed through the region where radiation was thought to be a minimum because of the anomalies in the earth's magnetic field.

The tests were begun on December 6. On at least one pass each day, conditions were thought to be favorable from the standpoint of passage through the radiation belt. As many commands as possible were sent during each visible pass on the assumption that the cumulative effect of a large number of commands would increase the probability of response in the reduced radiation field. All results were negative, although telemetry indicated a normal signal at the output of the command receiver. These tests were terminated on December 17.

5.1.4 *Modified Commands*

By far the most fruitful approach to the recovery of the command function was the use of command signals which were designed to circumvent some assumed failed circuit. Such a procedure, if successful, would lead to full use of the satellite for communications experiments and would also locate the exact area of the decoder circuit in which the failure had occurred.

The first procedure was a process of elimination to focus attention on those stages for which the probability of failure was highest. The considerations which greatly reduced the number of suspects are listed below:

1. Only those circuits which had a function common to all command channels were considered, since failure existed for all commands. Also, during the week of November 18, when the circuit recovered, all commands which were issued were carried out.

2. Only stages containing the device-type known to be radiation sensitive were examined in detail.

3. Stages which were normally in the "on" state except during a command pulse train were excluded.

4. First priority in the investigation was given to those devices with especially high V_{CE} and in circuit positions known to have stringent leakage current and gain requirements.

The results of this study suggested that six transistors were most vulnerable. For only one of these, the reset digit gate transistor,[1] was it not possible to design a satisfactory modified command. However, this device could be set into the "on" state by means of the transmission of a start pulse (normally at the beginning of each command) as the last pulse of a pass. This procedure was carried out as soon as its importance

was realized. The other five transistors were the first two stages of the pulse shaping network, the normally "off" transistor of the astable pulse generator, and the zero and one digit gate transistors.[1]

The modified commands were designed either to permit satisfactory circuit operation without the use of the stage under study or to enable circuit operation to occur even after the normal operating margin had been reduced to zero. Refer to the Appendix for a description of each of the modified command procedures.

Prior to use of the modified commands on the orbiting satellite, a laboratory test was carried out on a decoder which had a condition simulating the probable failure. In this way, the reliability of the procedure was evaluated.

An interesting aspect of use of modified commands involved the experiments on irradiated decoders which were described in Section 4.2.3. The failures observed in those experiments were all in regions which were thought to be most vulnerable to radiation damage and which were arrived at through the process of elimination described earlier. Furthermore, in each instance, it was demonstrated that modified commands could restore the command function. This fact is indeed a fortunate coincidence, for one could point to other stages, which are thought to be less vulnerable to radiation damage, where increased leakage or reduced gain would lead to a failure about which nothing could be done.

5.2 *Return to Normal Operation*

On December 19, two different test signals were transmitted to the satellite. They were designed to override high leakage in the first and second stages of the shaping network. Neither test was successful. A third test, which was established to circumvent failure of the zero digit gate, was successfully tried on December 20. The C command was carried out on pass 1492, and during the next pass CC command was properly executed.*

Following the success of the test on December 20, on December 21 it was decided that commands C, CC, T-1 and T-2 would be tried. The C, CC and T-2 commands were successful; T-1 command was not successful but, because of the nature of that command, one could not definitely say that decoder 1 was not functioning (see the Appendix).

---

* The C command, which normally turns on the traveling-wave tube anode voltage, is not executed unless A and B commands are sent first and, since a telemetry channel indicates the state of the C relay, C and CC commands provide a convenient means for checking the command system.

The significance of execution of the T-2 command was substantial for it meant that the zero digit gate failure was in decoder 2. This decoder was the first to exhibit command system difficulties (one month after launch).

With the failure pinpointed in one decoder, the plan was to increase the size of the list of commands which would be obeyed. For operating convenience, magnetic tape recordings were made of the modified command signals. As outlined in the Appendix, application of the modified command which circumvents the zero digit gate failure is somewhat difficult because of the bandwidth limitations of the satellite command receiver system. Through a gradual increase in confidence in operation of the command system, it was expected that all features of the satellite repeater would be recovered. On December 27, on pass 1555, after a successful C command, CC command was interpreted as an SS command and the S relay opened; this removed the connection between the nickel-cadmium battery and the solar plant and left the command system powered by only the solar plant. This occurrence, which has since been duplicated in the laboratory, was unexpected since it meant that the CC command had been converted into its complement. Within one minute the S relay opened, closed and opened again, and it was left in this state as the satellite disappeared over the horizon.

While out of view of Cape Canaveral and Andover, the satellite went into eclipse for a period of 25 minutes. Thus power was removed from the ailing decoders for that length of time On the next pass the satellite first became visible to Cape Canaveral, which had not yet been equipped to send the modified command signals. With the hope that power removal might have caused enough recovery of the damaged transistors, a continuous normal S command was transmitted from Cape Canaveral for 12 minutes; however, the satellite did not respond. When the satellite came in view of Andover, a modified S command was sent and properly executed. Telemetry, which is automatically turned off through the interpretation of an SS command, was turned on again with a modified D command.

On December 28 and 29, continuous normal command signals were transmitted to the satellite and, during pass 1574, a repetitive *normal* C command was executed after 37 minutes. The time to execute repetitive normal C, CC and T-2 commands gradually decreased, and, during pass 1602 on January 1, 1963, the first nonrepetitive command (C) was executed. Up until that date, there had been no response to T-1; all successful commands had been decoded by decoder 2. On that day, however, T-1 command was also properly interpreted, and it was clear that both decoders were responding to normal commands, although some sluggishness was still apparent.

On the last visible pass of January 1, the SS command was executed erroneously by the satellite during a sequence of normal T-2 commands. The S relay was not closed and the decoders were left powered by only the solar plant; the satellite went through five 20-minute eclipses during which power was removed from the command equipment. On the next visible pass (1609) the following day, normal operation was observed for decoder 1; response to T-2 command was less sluggish. The S relay was deliberately left open on the last pass of January 2 (1613), and on January 3 complete recovery of both decoders had taken place.

The traveling-wave tube was turned on, for the first time since November, on January 3, and normal operation of all systems was reported. Since that time, commands have been successfully carried out through the use of both normal and modified commands. The latter commands do not use the zero digit gates of either decoder. On only four different occasions have the modified commands been misinterpreted by the satellite.

Since January 2, the SS command has been sent intentionally whenever it was operationally convenient to do so to retard radiation damage and hopefully to increase the circuit operating margins. The length of an eclipse varies with time, however, and dropped to zero from January 6 to February 4.[3] Hence, power was applied continuously to both decoders during that period. Nevertheless, normal commands gave satisfactory performance throughout that interval.

5.3 Cause of Recovery

There is no conclusive evidence that there is any one cause of recovery of the normal command function. Laboratory experiments have shown that reduction of V_{CE} and/or reduction of the radiation field intensity can bring about recovery, although the degree of improvement varies greatly among devices. The facts related in the previous section show that there is a definite correlation between recovery and V_{CE} reduction through the use of continuous commands and the occurrence of eclipse with the S relay open. However, simultaneous with the efforts to regain the command function, there was a reduction in the radiation flux seen by the Telstar satellite due to decay of the particle density in space and the oscillatory change in the orbital average as the line of apsides of the orbit precessed. On January 1, 1963, the average flux had dropped to less than 20 per cent of the value it had on November 15, and to less than 10 per cent of that measured during the month of July.* The re-

---

* The temporary recovery of the T-2 command on October 17 occurred at the time of a minimum in the radiation intensity with apogee of the satellite's orbit at the equator.

covery was probably due to a complex combination of the effects described above.

5.4 *Reappearance of Command System Malfunction*

Throughout the month of January, the command system responded normally. On February 5, however, the malfunction of the zero gate in decoder 2 again appeared, and it was necessary to command through that decoder with the use of the modified command signals described in Section A.4. Decoder 1 continued to function normally until February 14, and, to assure reliable operation, taped modified commands were used almost exclusively for commanding the satellite through decoder 2. On February 21, however, the command system apparently misinterpreted a modified T-2 command and the S relay was opened. Thus the storage batteries were disconnected from the solar plant and power was supplied to only the command system. The satellite has failed to respond to further command attempts.

The cyclic behavior of the average radiation intensity to which the Telstar satellite is exposed has a period of approximately three months. It is significant that the February malfunction, like that of November, occurred near the peak of the cycle.

The phenomenon of the conversion of a modified command to the SS command has been demonstrated in the laboratory. It occurs when I_{CBO} of the reset digit gate transistor attains a critical value. Circumstances indicate, therefore, that the problem in decoder 2 might be failure of both the one and reset digit gates.

VI. CONCLUSION

The facts have been presented which led to the conclusion that the malfunction of the command system was due to surface damage to certain transistors by enhanced radiation in the inner Van Allen belt. Correction steps have included laboratory experiments to gain a better understanding of the cause of failure, the use of continuous normal commands, commands transmitted from Johannesburg, South Africa, and specially modified commands to circumvent failure of the more vulnerable transistors.

VII. ACKNOWLEDGMENTS

Other members of the technical staff of Bell Telephone Laboratories were instrumental in planning and conducting the experiments and tests which led to the diagnosis and cure of the command system mal-

function. Contributions were made by R. H. Shennum, R. C. Chapman, H. H. Henning, D. B. Cuttriss, W. Rosenzweig, J. D. Gabbe, E. R. Schmid, and W. Gianopulos.

APPENDIX

Modified Command Signals

A.1 *General*

The five most vulnerable transistor stages, selected in the manner described in Section 5.1.4, require the use of different modified command signal structures to accomplish proper decoding in failed units. The relative location of each of these stages can be determined from the block diagram of the command decoder shown in Fig. 6. A detailed description of the operation of the decoder circuit is given in Ref. 1.

A.2 *First Stage of the Pulse Shaping Network*

This circuit is an emitter follower with a high V_{CE} ; high I_{CBO} (>25 microamperes) will force the base voltage of this stage above a threshold level and will consequently cause the pulse generator to free-run. The input of the emitter follower is coupled to the output of the command
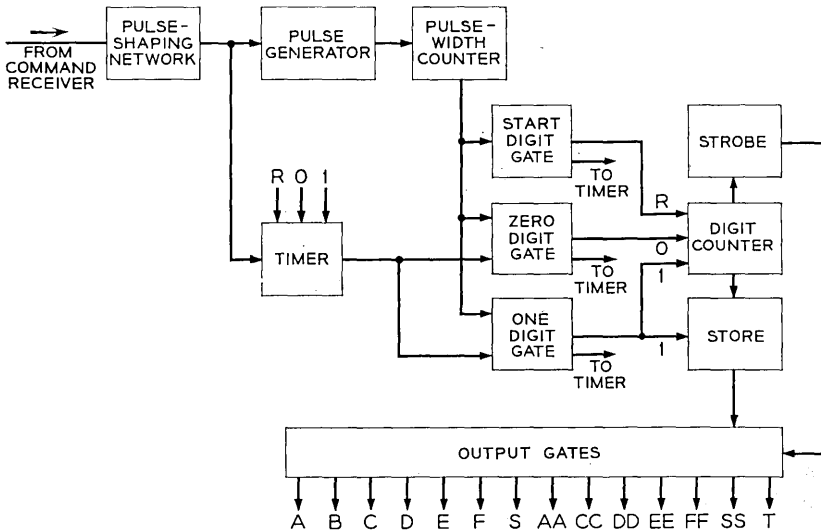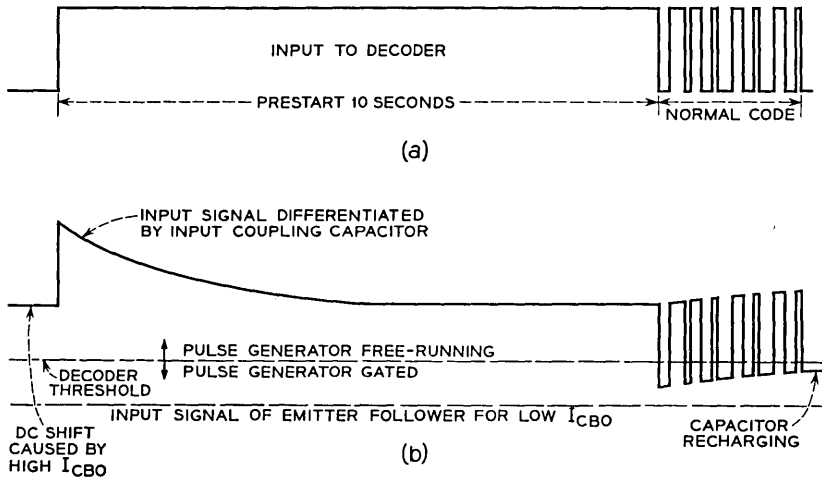

Fig. 6 — Command decoder block diagram.

Fig. 7 — Modified command for high I_{CBO} in pulse shaping network first stage.

receiver through a capacitor. By preceding a normal command signal by a long pulse, as shown in Fig. 7(a), the input capacitor is charged to the full pulse amplitude level. When the pulse is removed, the charged capacitor will serve to pull the base of the emitter follower below the threshold level so that a command may be transmitted during the interval that the capacitor is being discharged by the leakage current (see Fig. 7b).

A.3 Second Stage of the Pulse Shaping Network

If the leakage current of this stage is above 150 microamperes, the pulse generator will free-run. Leakage currents in excess of 300 micro-amperes will cause the digit gates to be held off; consequently, the modified command signal described here will be effective only for a leakage current below 300 microamperes. Normally, the pulse generator, a gated astable circuit, is allowed to free-run only when an input pulse is present, as shown in Fig. 8(a). The modified command consists of a near-standard command set up on a shorter time interval basis, so that the input pulses are occasionally "in phase" with the free-running astable circuit, as shown in Fig. 8(b). With the shortened code it is possible to cause spurious decoder response when proper phasing does not exist. Errors can be avoided if the command pulse sequence is very carefully established.
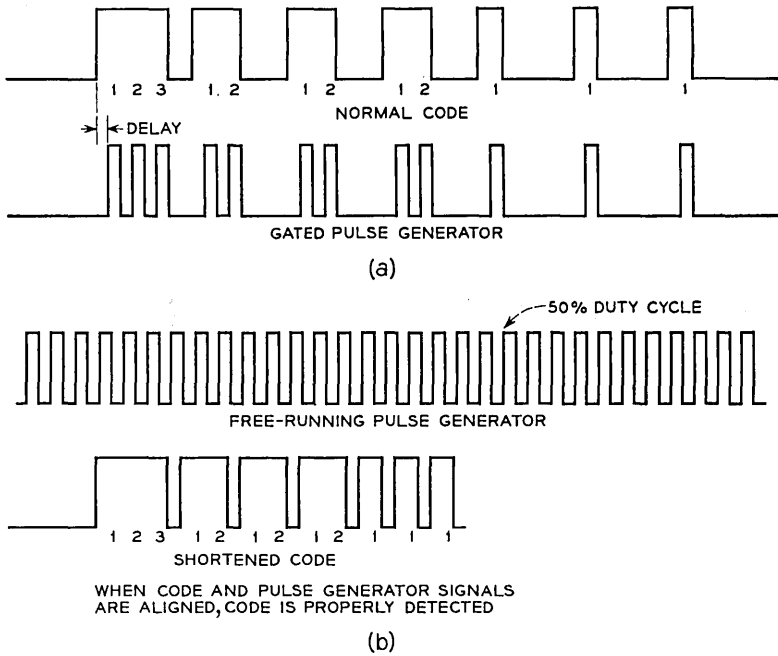
NORMAL CODE

DELAY

GATED PULSE GENERATOR

(a)

50% DUTY CYCLE

FREE-RUNNING PULSE GENERATOR

SHORTENED CODE

WHEN CODE AND PULSE GENERATOR SIGNALS
ARE ALIGNED, CODE IS PROPERLY DETECTED

(b)

Fig. 8 — Modified command for high I_{CBO} in pulse shaping network second stage.

A.4 Zero Digit Gate

If the gain of the zero digit gate transistor becomes sufficiently low in value, that stage will not be capable of driving the digit counter. As one sees from Fig. 6, the zero digit gate drives the digit counter and the timer; the one digit gate drives the digit counter, and, after a small amount of delay, drives the store. The scheme for circumventing the failed zero digit gate is to send in place of a "zero" a modified "one" code in such a way that the one digit gate is turned on and almost immediately turned off again. By use of the notched and shortened pulse in Fig. 9(c), it is possible to advance the digit counter but not to build up sufficient voltage to set a "one" into the store. Thus this notched "one" causes the same response in the digit counter and store as a "zero." Unfortunately, the notched "one" does not fully enable the timer circuit, and it is difficult to handle codes containing three sequential "zeros," unless these "zeros" are at the end of the code.*

---

* Since the T-1 command contains three "zeros" in sequence, there is uncertainty regarding the reason why a modified T-1 command caused no response on December 21. See Section 5.2.
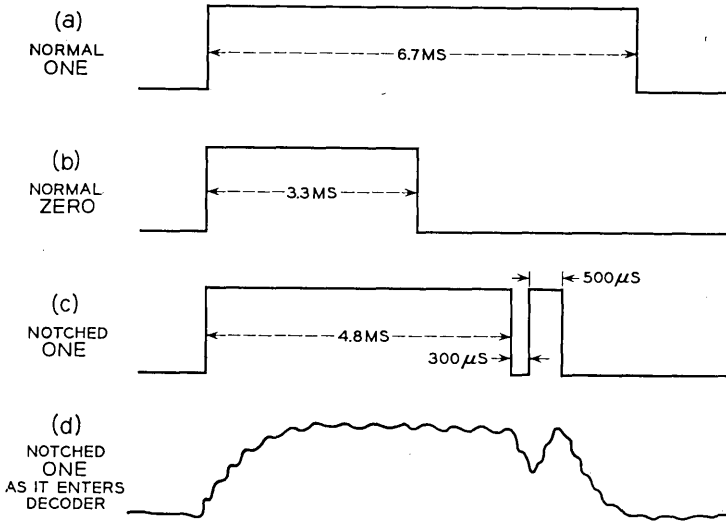
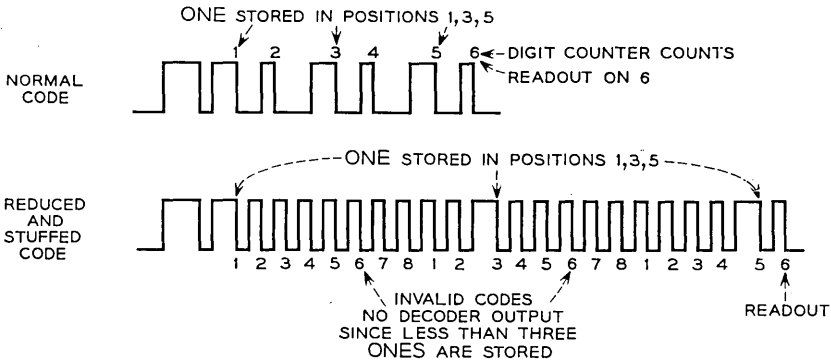Fig. 9 — Modified "one" to circumvent failed zero digit gate.

Fig. 10 — Modified command for low gain in one digit gate.

Proper detection of this modified command is difficult (but completely workable) since a code must be transmitted which produces a very marginal "one" out of the one digit gate. The margin involved is of the order of 30 microseconds in a system where the residual ripple from the subcarrier occurs with a period of 100 microseconds. Also, the notch is greatly distorted by the bandwidth limiting which occurs ahead of the decoder (see Fig. 9d). However, through the use of width modulation of the notch, the one digit gate output jitters through the region of un-

certainty. As the notch width decreases, the "one" digit notch provides outputs ranging from a "one" to a "zero." One therefore establishes a reliable mode of operation by randomly modulating the notch widths in a manner such that the desired response of the one digit gate to a notched "one" occurs with finite and acceptable probability. The number of commands that must be transmitted to execute a given order is increased. However, since the normal command time is about one-tenth second, an exchange of command time for operating margin is acceptable.

A.5 *One Digit Gate*

There are two ways in which loss of gain in the one digit gate transistor will most probably first show up. Either the gate will fail to advance the digit counter (but still set the store and reset the timer), or it will fail to fully reset the timer (but still set the store and advance the digit counter). Failure to advance the digit counter is easily overcome by preceding each legitimate "one" by a zero. (The zero advances the counter.) Thus 111000 is transmitted as 010101000.

A failure which prevents full resetting of the timer can be combated by sending a code with shortened pulse widths and pulse intervals. If that method is not satisfactory, extra zeros may be inserted in the code (to reset the timer) so that a "one" is stored in the proper slot each cycle of counter operation. See Fig. 10 for an example of this procedure.

A.6 *Normally "Off" Transistor in Pulse Generator*

The effect of excessive leakage or low gain in this stage is to increase the natural frequency of the astable multivibrator, which is the basic pulse generator circuit. To circumvent this problem it is only necessary to set up standard commands on a contracted time scale. This procedure will work up to the point that degradation is so severe that astable operation is no longer possible.

REFERENCES

1. Chapman, R. C., Jr., Critchlow, G. F., and Mann, F., Command and Telemetry Systems, B.S.T.J., this issue, p. 1027.
2. Peck, D. S., Blair, R. R., Brown, W. L., and Smits, F. M., Surface Effects of Radiation on Transistors, B.S.T.J., **42**, January, 1963, pp. 95–129.
3. Hutchison, P. T., and Swift, R. A., Results of *Telstar* Satellite Space Experiments, B.S.T.J., this issue, p. 1475; see Fig. 6.